

Investigation on Band Gap Characteristics in a Two-dimensional Photonic Crystal with Honeycomb Structure

Shanglin Hou, Rui Lv, Yanjun Liu, Jingli Lei, and Suoping Li
School of Science, Lanzhou University of Technology, Lanzhou 730050, China

Abstract— The plane wave expansion method is used to calculate the band gap width of two-dimensional photonic crystal based on honeycomb structure for the transversal electric polarized mode, transversal magnetic polarized mode and absolute photonic band gap by taking into account the effects of the relative dielectric constant and filling ratio on the band gap. The results show that a largest complete photonic band gap is obtained, with the normalized band gap width $\Delta G_{\max}/\omega_0 = 25\%$ for the circular dielectric rods structure. We conclude that forming band gap in the circular dielectric rods structure is easier than in the air hole structure.

1. INTRODUCTION

Photonic crystal is a periodic arrangement of dielectric materials in one, two or three dimensions, which exhibits a “forbidden” frequency region where electromagnetic waves cannot propagate along any direction [1, 2]. In a two-dimensional (2D) photonic crystal, the electromagnetic waves can be decoupled into two different polarized modes. These polarized modes are known as transversal magnetic (TM) polarized mode and transversal electric (TE) polarized mode. An absolute photonic band gap (complete TEM band gaps) exists for a 2D photonic crystal only when photonic band gaps in both polarization modes are present and they overlap each other. Photonic crystals have many potential applications [3–6] and most of them rely on their band structures.

Photonic band gaps for TE and TM modes occur at different frequency regions and only in select structures both of them exist at the same frequency region giving rise to complete photonic band gap. In order to obtain a large absolute photonic band gap, a sufficient overlap between both TE and TM band gaps is important. Many attempts have already been made to design various kinds of photonic crystal structures [7–10], which are not easy for fabrication and the geometric shape is complex, although these structures can offer larger complete photonic band. Yuan et al. have studied the band gap characteristics of two-dimensional photonic crystal with triangular lattice structure and square lattice structure [11], however it hasn't been reported the TE band gaps and TM band gaps are responsible for the formation of complete TEM band gaps.

In this letter, we investigate the band gap characteristics of a two-dimensional photonic crystal consisting of honeycomb lattices for the TE mode, TM mode and complete TEM gaps by using the plane-wave expansion method. We concentrate on the effect of the relative dielectric constant and filling ratio. The results indicate that the TE band gaps and TM band gaps are responsible for the formation of complete TEM gaps; When $r/a = 0.32$, $\varepsilon_b = 26$, for the circular dielectric rods structure, the largest complete photonic band gap appears, with the normalized gap width $\Delta G_{\max}/\omega_0 = 25\%$. The study can prove useful in the design of various complete photonic band gap-based devices, where it will be important to find or engineer structures with correct band structure characteristics and hence in the design of compact all integrated photonic circuits.

2. THEORETICAL ANALYSIS

This section presents a brief description of plane-wave expansion method to obtain the band diagram of two-dimensional photonic crystal. First, the electromagnetic fields are expanded into plane waves of wave vector \vec{k} with respect to the 2D reciprocal lattice vectors \vec{G} and the Maxwell's equations are turned into the eigenvalue equations. Then the eigenvalue equations are solved to get the intrinsic frequency of the propagation photons and the dispersion relation of electromagnetic wave propagation in photonic crystals. Finally the band structures are obtained [12].

Solving Maxwell's equations for the magnetic field H leads to the following vector wave equation,

$$\nabla \times \frac{1}{\varepsilon(r)} \nabla \times \vec{H}(r) = \frac{\omega^2}{c^2} \vec{H}(r) \quad (1)$$

where $\varepsilon(r)$ is the dielectric function, ω is the angular frequency and c is the speed of light in vacuum. Because of the two-dimensional lattice periodicity, the dielectric constant ε can be described by

$$\varepsilon(r) = \sum_{\vec{G}} \varepsilon_G e^{i\vec{G}\cdot\vec{r}} \quad (2)$$

The magnetic field H is then expanded into plane waves of wave vector \vec{k} with respect to the 2D reciprocal lattice vectors \vec{G} .

$$\vec{H}(r) = \sum_{\vec{G},\lambda} h_{G,\lambda} \hat{e}_\lambda e^{i(\vec{k}+\vec{G})\cdot\vec{r}} \quad (3)$$

where $\lambda = 1, 2$, \vec{k} are the wave vector of the plane wave, \vec{G} is the reciprocal lattice vector, \hat{e}_λ represents the two unit axis perpendicular to the propagation direction $\vec{k} + \vec{G}$. ($\hat{e}_1, \hat{e}_2, \text{veck} + \vec{G}$) are perpendicular to each other. $h_{G,\lambda}$ is the coefficient of the H component along the axes \hat{e}_λ . Finally, the eigenvalue equation of the magnetic field H is obtained as,

$$\sum_G \varepsilon^{-1}(\vec{G} - \vec{G}') \left| \vec{k} + \vec{G} \right| \left| \vec{k} + \vec{G}' \right| \cdot \begin{bmatrix} \vec{e}_2 \cdot \vec{e}'_2 & -\vec{e}_2 \cdot \vec{e}'_1 \\ -\vec{e}_1 \cdot \vec{e}'_2 & \vec{e}_1 \cdot \vec{e}'_1 \end{bmatrix} \begin{bmatrix} h'_1 \\ h'_2 \end{bmatrix} = \frac{\omega^2}{c^2} \begin{bmatrix} h'_1 \\ h'_2 \end{bmatrix} \quad (4)$$

$$\varepsilon^{-1}(G) = \begin{cases} \frac{1}{\varepsilon_b} + \left(\frac{1}{\varepsilon_a} - \frac{1}{\varepsilon_b} \right) f, & G = 0, \\ f \left(\frac{1}{\varepsilon_a} - \frac{1}{\varepsilon_b} \right) \frac{2J_1(GR)}{GR}, & G \neq 0 \end{cases} \quad (5)$$

where f is the filling ratio, $J_1(x)$ is the Bessel function. Substituting Eq. (5) into Eq. (4), the eigenfrequency is obtained for TM polarization. By using the same theory, the eigenfrequency of the electric field E is obtained.

3. SIMULATIONS AND DISCUSSIONS

In this letter, the band gap characteristics of a two-dimensional photonic crystal consisting of honeycomb lattices with circular dielectric rods and air holes are investigated for the TE mode, TM mode and complete TEM gaps. The effects of relative dielectric constant and filling ratio on the band gap are analyzed. Fig. 1 shows the structure of two-dimensional photonic crystal. ε_a is the relative dielectric constant of background material. ε_b is the relative dielectric constant of circular rods. For the air hole structure, $\varepsilon_a > 1$, $\varepsilon_b = 1$. For the circular dielectric rods structure, $\varepsilon_a = 1$, $\varepsilon_b > 1$. r is the air hole radius, a is the lattice constant. The photonic band structure is presented in Fig. 2 ($\varepsilon_a = 1$, $\varepsilon_b = 26$, $r/a = 0.32$). The shaded regions represent photonic band gaps. We can see that there are several gaps but we only consider the largest band-gap. For this particular choice of the parameters there is a largest complete photonic band gap, with the normalized band gap width $\Delta G_{\max}/\omega_0 = 25\%$. ΔG_{\max} is the largest band gap width. ω_0 is the central frequency of band gap.

3.1. Band Gap Characteristics in the Air Hole Structure

In this model, the largest band gap width ΔG_{\max} is discussed for the TE mode, TM mode and complete TEM gaps. The relative dielectric constant of background material ε_a varies from 3 to 36, setting the relative dielectric constant of circular rods $\varepsilon_b = 1$ for three different filling ratios, namely, $r/a = 0.47, 0.48$ and 0.49 .

Figure 3 shows the dependency of the largest band gap width on the relative dielectric constant and filling ratios with regard to the TE mode. It shows that the peak values of ΔG_{\max} appear in low-dielectric regions and they move to high dielectric regions with the increasing filling ratios. For the fixed dielectric constant, the peak values increase as the filling ratios increase. When $r/a = 0.49$, $\varepsilon_a = 8$, the peak value is the largest, with the largest band gap width $\Delta G_{\max} = 0.523$.

Figure 4 displays the peak values of ΔG_{\max} increase rapidly with the relative dielectric constant varying from 3 to 9 for the fixed filling ratios and then decrease slowly with regard to the TM mode. These values move to low dielectric regions as the filling ratios increase. When $r/a = 0.49$, $\varepsilon_a = 8$, the peak value is the largest, with the largest band gap width $\Delta G_{\max} = 0.442$.

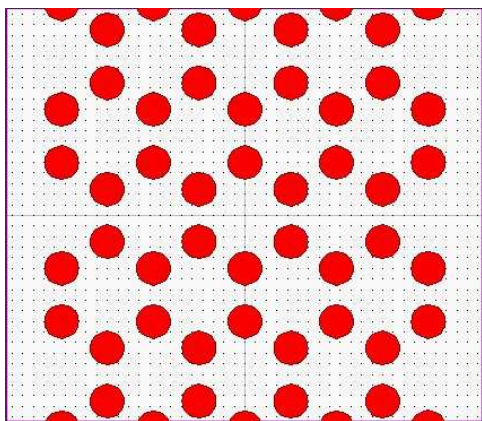


Figure 1: The structure of two-dimensional photonic crystal.

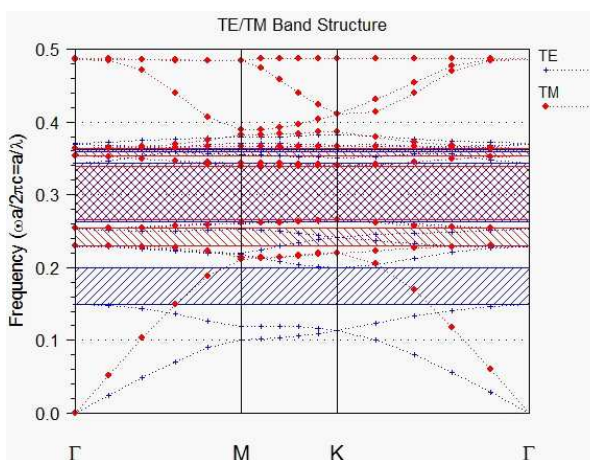


Figure 2: The photonic band structure.

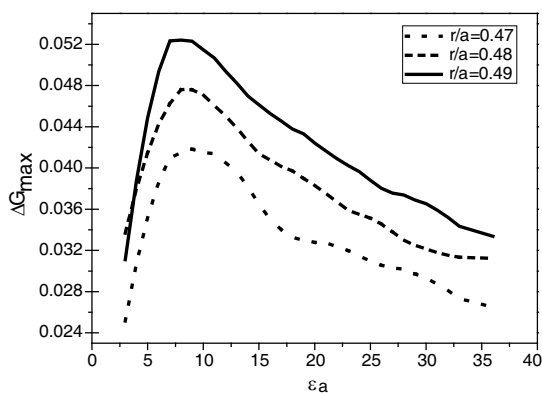


Figure 3: ΔG_{\max} versus ε_a and r/a for TE mode.

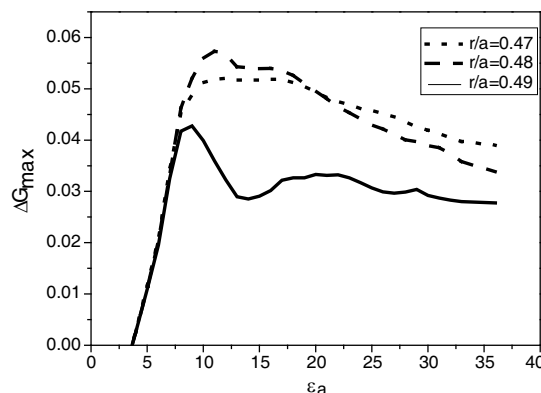


Figure 4: ΔG_{\max} versus ε_a and r/a for TM mode.

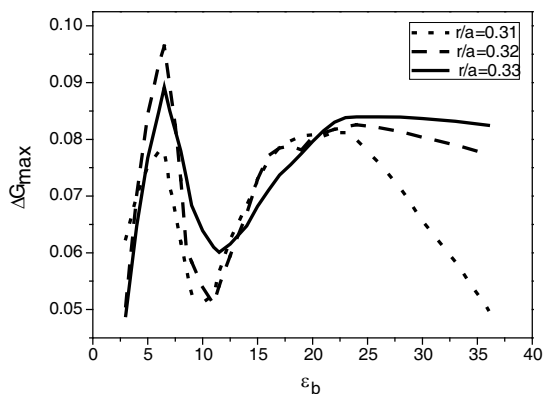
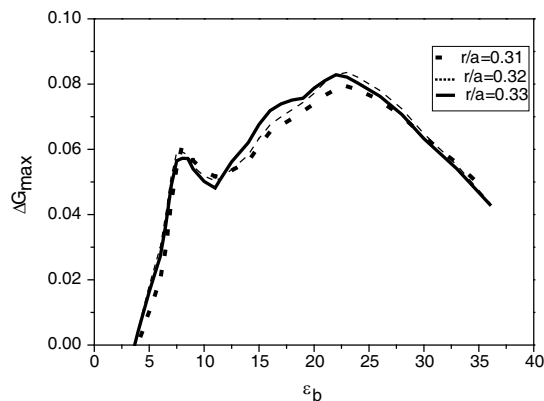
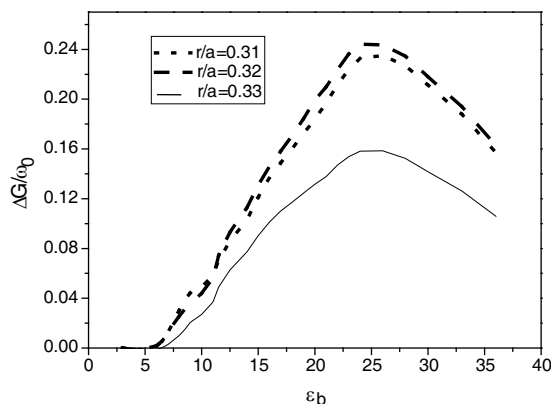
3.2. Band Gap Characteristics in the Circular Dielectric Rods Structure

Following this model, we also consider the dependency of the largest band gap width ΔG_{\max} on the relative dielectric constant and filling ratios for the TE mode, TM mode and complete TEM gaps. Setting the relative dielectric constant of background material $\varepsilon_a = 1$, the relative dielectric constant of circular rods ε_b varies from 3 to 36 for three different filling ratios, namely, $r/a = 0.31$, 0.32 and 0.33.

Figure 5 displays the largest band gap width versus the relative dielectric constant and filling ratios with regard to the TE mode. There are two larger peak values of ΔG_{\max} . The first peak values which are the largest value appear in low-dielectric regions and the second peak values arise in high-dielectric regions. The largest peak values move to high dielectric regions with the increasing filling ratios.

Figure 6 illustrates how the largest band gap width varies with the relative dielectric constant and filling ratios for the TM mode. There are also two larger peak values of ΔG_{\max} . The second peak values which are the largest value appear in high-dielectric regions and the first peak values arise in low-dielectric regions. The largest peak values move to low dielectric regions with the increasing filling ratios.

The results indicate that the TE band gaps and the TM band gaps are responsible for the formation of complete TEM band gaps. Therefore, as shown in Fig. 7, the larger complete photonic band gaps appear in high-dielectric regions. When $r/a = 0.32$, $\varepsilon_b = 26$, for the circular dielectric rods structure, the largest complete photonic band gap appears, with the normalized band gap width $\Delta G_{\max}/\omega_0 = 25\%$. It is remarkable that forming band gap in the circular dielectric rods structure is easier than in the air hole structure.

Figure 5: ΔG_{\max} versus ε_b and r/a for TE mode.Figure 6: ΔG_{\max} versus ε_b and r/a for TM mode.Figure 7: $\Delta G_{\max}/\omega_0$ versus ε_b and r/a for TEM gap.

4. CONCLUSIONS

In conclusion, by using the plane-wave expansion method, we have studied the band gap characteristics of a two-dimensional photonic crystal consisting of honeycomb lattices varying the relative dielectric constant and filling ratio for the TE mode, TM mode and complete TEM gaps. We have considered the two possible situations: (i) the air hole structure and (ii) the circular dielectric rods structure. The results indicate: the TE band gaps and TM band gaps are responsible for the formation of complete TEM band gaps; When $r/a = 0.32$, $\varepsilon_b = 26$, for the circular dielectric rods structure, the largest complete photonic band gap appears, with the normalized band gap width $\Delta G_{\max}/\omega_0 = 25\%$; It is remarkable that forming band gap in the circular dielectric rods structure is easier than in the air hole structure; For a given filling ratio, with the increase of relative dielectric constant, the maximum band gap width does not always increase, but it is peaked; Similarly, for a given relative dielectric constant, with the increase of filling ratio, it is also peaked for the maximum band gap width. These findings should be useful in the design of 2D photonic crystals when a large absolute PBG is desired.

ACKNOWLEDGMENT

This work is financially supported by the National Natural Science Foundation of China (Grant No. 61167005), the Natural Science Foundation of Gansu province of China (Grant No. 1112RJZA018).

REFERENCES

1. Yablonovitch, E., "Inhibited spontaneous emission in solid-state physics and electronics," *Phys. Rev. Lett.*, Vol. 58, No. 20, 2059–2062, 1987.
2. Joannopoulos, J. D., P. R. Villeneuve, and S. Fan, "Photonic-bandgap microcavities in optical waveguides," *Nature*, Vol. 390, No. 13, 143–145, 1997.
3. Boutami, S., B. B. Bakir, H. Hattori, and X. Letartre, "Broadband and compact 2-D photonic

- crystal reflectors with controllable polarization dependence,” *IEEE Photonics Technol. Lett.*, Vol. 18, No. 7, 835–837, 2006.
4. AhsanHabib, M. and Z. U. S. Mohammad, “Band gap calculation of a 2-D photonic crystal and its application towards a thin film solar cell,” *Photonics. PL*, Vol. 3, No. 4, 162–164, 2011.
 5. Chen, C., S. Shi, D. W. Prather, and A. Sharkawy, “Beam steering with photonic crystal horn radiators,” *Opt. Eng.*, Vol. 43, No. 1, 174–180, 2004.
 6. Chien, F. S. S., Y. J. Hsu, W. F. Hsieh, and S. C. Cheng, “Dual wavelength demultiplexing by coupling and decoupling of photonic crystal waveguides,” *Opt. Express*, Vol. 12, No. 6, 1119–1125, 2004.
 7. Goh, J., I. Fushma, D. Englund, and J. Vukovic, “Genetic optimization of photonic band gap structures,” *Opt. Express*, Vol. 15, 8218–8230, 2007.
 8. Shen, L. F., Z. Ye, and S. L. He, “Design of two-dimensional photonic crystals with large absolute band gaps using a genetic algorithm,” *Phys. Lett. B*, Vol. 68, No. 3, 035109, 2003.
 9. Shen, L. F., Z. Ye, S. L. He, and S. S. Xiao, “Large absolute band gaps in two-dimensional photonic crystals formed by large dielectric pixels,” *Phys. Lett. B*, Vol. 66, No. 16, 165315, 2002.
 10. Wen, F., S. David, and X. Checoury, “Two-dimensional photonic crystals with large complete photonic band gaps in both TE and TM polarizations,” *Opt. Express*, Vol. 16, No. 16, 12278–12289, 2008.
 11. Yuan, G. F. and L. H. Han, “Two-dimensional photonic crystal band gap characteristics,” *Acta Phys. Sin.*, Vol. 60, No. 10, 104214, 2011.
 12. Guo, S. P. and S. Albin, “Simple plane wave implementation for photonic crystal calculations,” *Opt. Express*, Vol. 11, No. 2, 167–175, 2003.

Study on Characteristics of the Photonic Crystal Fibers with Three Zero-dispersion Points

Shanglin Hou, Yu Du, Rui Lv, Yanjun Liu, Jingli Lei, and Suoping Li

School of Science, Lanzhou University of Technology, Lanzhou, Gansu 730050, China

Abstract— The properties of the PCFs, which have three zero-dispersion wavelengths, are investigated by adjusting the air-hole diameters of the structure parameters in the cladding and the influence of the structure parameters on dispersion and nonlinearity are studied. The results show that in these PCFs broad anomalous dispersion region around the wavelength of 1550 nm, the lower dispersion in the normal dispersion region and larger effective mode area of the PCFs and lower nonlinearity coefficient, where the effective mode area A_{eff} are sufficiently larger than that of the multicore fibers.

1. INTRODUCTION

Photonic crystal fibers (PCFs) have attracted considerable attention as optical fiber transmission media and fiber-optic devices owing to the flexible tailor of their chromatic dispersion over a wide wavelength range, the controllability of their effective mode area and nonlinearities as well as their low confinement loss. So many novel optical properties are due to the position and size of the air-holes around the core of the PCFs [1]. PCFs have been considered for fiber-optic devices but also as a candidate optical transmission medium for future large capacity photonic networks. And now wavelength division multiplexing (WDM) systems are widely used to improve the capacity of networks. Though the realization of higher bit-rate WDM transmission will be required in the future, the dispersion and the nonlinearity of the optical fiber degrade the transmission characteristics. So far people use dispersion compensation techniques to compensate for the dispersion and enlarge the effective area of optical fiber for reducing nonlinearity [2].

The photonic crystal fibers with three zero-dispersion points present a very rich phase-matching topology enabling enhanced control over the spectral locations of the four-wave-mixing and resonant-radiation bands emitted by solitons and short pulses, because of the presence of a third zero-dispersion point [3]. The spectral evolution and the time-frequency characteristics of the soliton in PCFs owning three zero-dispersion wavelengths have been reported and the result shows that in high frequency normal dispersion region the blue-shifted dispersive wave was emitted by the dispersion wave soliton [4].

In this paper, we investigated the properties of the PCFs, which have three zero-dispersion wavelengths, by adjusting the air-hole diameters of the structure parameters in the cladding and studied the influence of dispersion and nonlinearity on the structure parameters. The results show that in these PCFs broad anomalous dispersion region around the wavelength of 1550 nm, the lower dispersion in the normal dispersion region and larger effective mode area of the PCFs, where the effective mode area A_{eff} are sufficiently larger than that of the multicore fibers (effective area about $120 \mu\text{m}^2$ at 1550 nm [5]). These PCFs are expected to be used in optical networks with wavelength of 1260 nm–1625 nm (O-L bands), such as access networks and long haul networks [2].

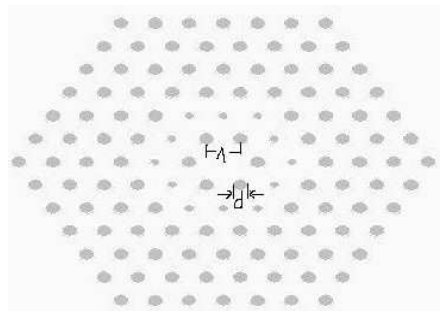


Figure 1: A cross-section of the PCF with three zero-dispersion points.

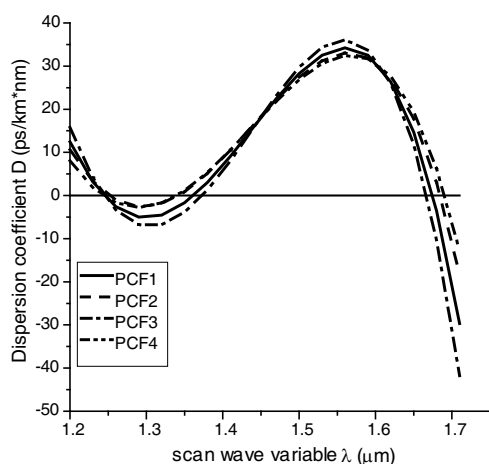


Figure 2: Varying the air-hole diameters of the three air-hole rings, the curves of the dispersion and zero-dispersion points dependent of the wavelength.

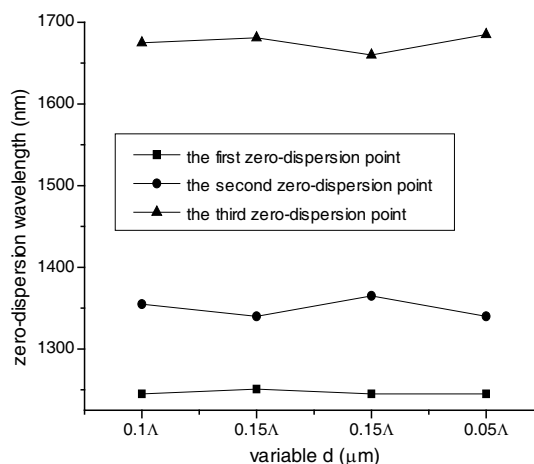


Figure 3: The curves of three zero-dispersion points dependent of the PCF1, PCF2, PCF3, PCF4, respectively.

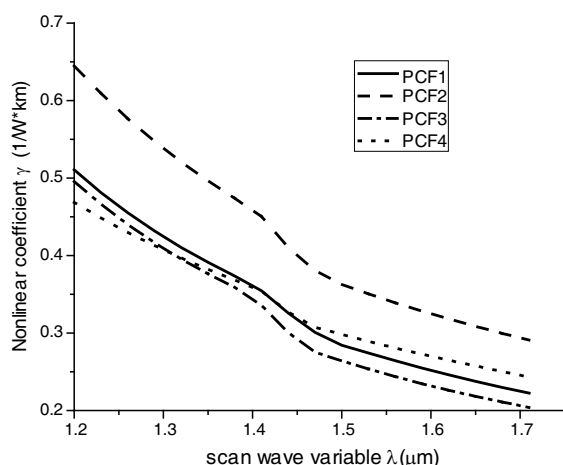


Figure 4: The curves of the nonlinearity dependence of the wavelength changing with the PCF1, PCF2, PCF3, PCF4 respectively.

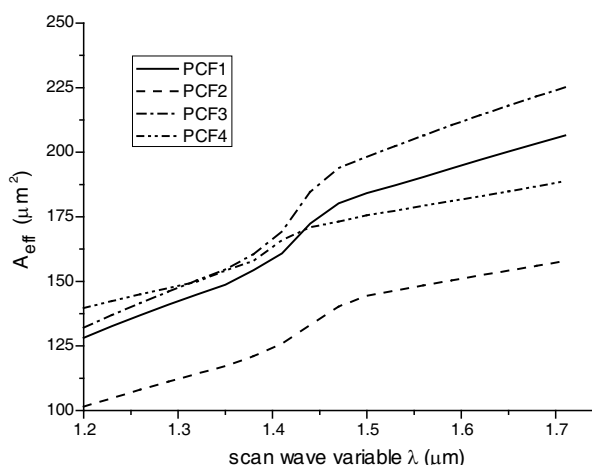


Figure 5: The effective mode area A_{eff} dependence of the wavelength changing with the PCF1, PCF2, PCF3, PCF4 respectively.

2. DESIGN OF THE PCFS, SIMULATION AND DISCUSSION

The properties of the chromatic dispersion and the nonlinearity as well as the effective mode area are investigated by varying the air-hole diameters of the three air-hole rings around the core of the PCF. We set the rings of air hole $N = 6$ to obtain a well-confined fundamental mode. The hole to hole space is $\Lambda = 5 \mu\text{m}$ and d is the air-hole diameter. Setting $d_1 = d_2 = 0.1\Lambda$, $d_3 = d_4 = d_5 = d_6 = 0.2\Lambda$ which called PCF1 in the PCFs we designed. The PCF2 is $d_2 = 0.15\Lambda$, PCF3 is $d_3 = 0.15\Lambda$, and PCF4 is $d_1 = 0.05\Lambda$. Fig. 1 shows a cross-section of the PCF with three zero-dispersion points, which consists of a central high-index defect in a regular hexagonal array of air-holes.

Figure 2 shows the curves of the dispersion and zero-dispersion points dependence of the wavelengths when change the air-hole diameters of the three air-hole rings around the core of the PCF, and keep the rest air-hole rings as constant. When the air-hole diameters of the first air-hole ring around the core of the PCF decrease, the dispersions both of the anomalous dispersion regions and the normal dispersion regions decrease in short wavelength of 1600 nm, and the waveband between the second zero-dispersion point and the third one become large as well as that the second zero-dispersion point shifts towards the short wavelength while the third one towards the long wavelength. Increasing the air-hole diameters of the second air-hole layer, the tendencies of the dispersion curves and the three zero-dispersion points are respectively similar with that of decreasing the air-hole diameters of the first air-hole layer, except the wavelengths which are shorter than

Table 1: The wavelengths of three zero-dispersion points dependence of the PCF1, PCF2, PCF3, PCF4, respectively.

	PCF1	PCF2	PCF3	PCF4
First zero-dispersion point (nm)	$\lambda_1 = 1245$	$\lambda_1 = 1251$	$\lambda_1 = 1245$	$\lambda_1 = 1245$
Second zero-dispersion point (nm)	$\lambda_2 = 1355$	$\lambda_2 = 1340$	$\lambda_2 = 1365$	$\lambda_2 = 1340$
Third zero-dispersion point (nm)	$\lambda_3 = 1675$	$\lambda_3 = 1681$	$\lambda_3 = 1660$	$\lambda_3 = 1685$

1250 nm and longer than 1600 nm. In this case, owing to the moving of the three zero-dispersion points can get largely anomalous dispersion areas. Decreasing the air-hole diameters of the third layer, the values of the dispersion coefficient D both increase in the anomalous dispersion region and the normal dispersion region from 1245 nm to 1622 nm. However the second zero-dispersion point shifts towards the longer wavelength and the third one towards the shorter wavelength. So the waveband between the first zero-dispersion wavelength and the second zero-dispersion one, become large, on the other hand the waveband between the second zero-dispersion wavelength and the third zero-dispersion one become narrow. Then the normal dispersion regions are enlarged. Fig. 3 presents the curves of three zero-dispersion points while varying the air-hole diameters of the three air-hole rings around the core of the PCF. From both the Fig. 2 and Fig. 3, we can see that the increase of the wavelength range between the first zero-dispersion point and the second, namely the normal dispersion region, enlarge the maximum of the dispersion and subsequently make the dispersion not flat during this range, but the increase of the wavelength range between the second zero-dispersion point and the third, namely the anomalous dispersion region, make the maximum of the dispersion reduce and the dispersion flat among its area. Table 1 presents the wavelengths of the three zero-dispersion points dependence of the PCF1, PCF2, PCF3, PCF4, respectively. The simulation results show that there are a much flatter dispersion PCF owning three zero-dispersion points if decrease the air-hole diameters of the first layer or increase the ones of the second layer, and the widely anomalous dispersion regions are obtained.

Figure 4 presents the curves of the nonlinearity dependence of the wavelength changing with the PCF1, PCF2, PCF3, PCF4 respectively. The nonlinear effects decrease quickly when the wavelength increases. The lowest nonlinearity coefficient r of PCF3 is $0.221 \text{ W}^{-1}\text{km}^{-1}$ (the wavelength 1550 nm). The reason is that the nonlinearity is inversely proportional to the wavelength. The nonlinear effects also decrease if the air-hole diameters of the three air-hole layers around the core of the PCF decrease. Decreasing the air-hole diameters of the third layer, the PCF3's curve of the nonlinearity is wholly below the one of the criterion PCF1. However, when the air-hole diameters of the first ring decrease, the values of the dispersion coefficient D are smaller than that of the criterion between the waveband from 1200 nm to 1410 nm, but bigger between the wavelength range from 1410 nm to 1710 nm. The phenomenon can be accounted for that the core diameter of the PCF gets rise following the decreasing of the air-hole diameters of the first layer. When the air-hole diameters of the second layer of PCF2 increase, the values of the dispersion coefficient D are much larger than that of PCF1 in the whole waveband, on the other hand, decreasing the air-hole diameters of the second layer can achieve very low nonlinear effects. The simulation results confirm that the impacts of the varying the air-hole diameters of the first and second layers are more significant than that of the third one.

Figure 5 shows that the effective mode area A_{eff} dependence of the wavelength changing with the PCF1, PCF2, PCF3, PCF4 respectively. As a result, the tendencies of the curves of the effective mode area are respectively on the contrary of the ones of the nonlinearity while varying the air-hole diameters of the three air-hole layers around the core of the PCF. Here through reducing the air-hole diameters of the third air-hole layer, obtain a very large A_{eff} about $206 \mu\text{m}^2$ at the wavelength of 1550 nm and expect to obtain a larger A_{eff} by decreasing the air-hole diameters of the second air-hole layer.

3. CONCLUSIONS

In this paper, the PCFs with three zero-dispersion points are designed and the properties of the PCFs while varying the air-hole diameters of the PCFs are investigated. From the above results, we can conclude that the effects of the air-hole diameters of the three air-hole rings around the core of the PCF are considerable to the properties of the PCFs, there is a more smaller and flatter dispersion PCF by decreasing the air-hole diameters of the first air-hole layer or increasing the

ones of the second, and decreasing the air-hole diameters of the second and third air-hole layers, particularly the second one, we will get the very largely effective mode area. The large effective mode area decrease the nonlinearity and increase the input power of the communication channels. For the reason that it is capable of suppressing dispersion, nonlinear impairments and improving the input power of every channel of the WDM system simultaneously.

ACKNOWLEDGMENT

This work was supported by the National Natural Science Foundation of China (No. 61167005), the Natural Science Foundation of Gansu province of China (No. 1010RJZA036), the Natural Science Foundation of Gansu province of China (No. 1112RJZA018), the Natural Science Foundation of Guangdong province of China (No. 10451170003004948), the Doctoral Fund of Lanzhou University of Technology, and the Dongguan Science and Technology Program (No. 2008108101002).

REFERENCES

1. Florous, N., K. Saitoh, and M. Koshiba, "The role of artificial defects for engineering large effective mode area, flat chromatic dispersion, and low leakage losses in photonic crystal fibers: Towards high speed reconfigurable transmission platforms," *Opt. Express*, Vol. 14, No. 2, 901–913, 2006.
2. Matsui, T., K. Nakajima, and C. Fukai, "Applicability of photonic crystal fiber with uniform air-hole structure to high-speed and wide-band transmission over conventional telecommunication bands," *J. Lightwave Technol.*, Vol. 27, No. 23, 5410–5416, 2009.
3. Stark, S. P., F. Biancalana, A. Podlipensky, and P. S. J. Russell, "Nonlinear wavelength conversion in photonic crystal fibers with three zero-dispersion points," *Phys. Rev. A*, Vol. 83, No. 2, 1–5, 2011.
4. Hao, Z., C. Zhao, J. Wen, S. Wen, and D. Fan, "Dispersive-wave soliton generation in photonic crystal fiber with three zero-dispersion wavelengths," *Acta Optica Sinica*, Vol. 31, No. 10, 1–5, 2011.
5. Matsuo, S., K. Takenaga, Y. Arakawa, Y. Sasaki, S. Taniagwa, K. Saitoh, and M. Koshiba, "Large-effective-area ten-core fiber with cladding diameter of about 200 μm ," *Opt. Lett.*, Vol. 36, No. 23, 4626–4628, 2011.
6. Abdelaziz, I., H. Ademgil, F. Abdelmalek, S. Haxha, T. Gorman, and H. Bouchriha, "Design of a large effective mode area photonic crystal fiber with modified rings," *Opt. Commun.*, Vol. 283, 5218–5223, 2010.
7. Hou, S., J. Han, Z. Qiang, and Q. Kong, "The dispersive and nonlinear properties of photonic crystal fibers with modified honeycomb lattice structure," *Chin. J. Lumin.*, Vol. 32, No. 2, 179–183, 2011.

Investigation on Slow Light of Uniform Fiber Bragg Gratings

Jingli Lei, Shanglin Hou, Rui Lv, Yan-Jun Liu, and Suo-Ping Li
School of Science, Lanzhou University of Technology, Lanzhou 730050, China

Abstract— The impact of the grating of length, “dc” index change spatially averaged over a grating period and fringe visibility of the index change on group delay of uniform fiber Bragg grating are investigated in detail by means of numeric simulation and slow light delay characteristics this kind grating is presented emphatically. The calculated results indicate that the influence of “dc” index change spatially averaged over a grating period on group delay is most obviously, the maximum value of group delay is 140.087 ns, especially slow light delay is rapidly decaying. This provides theoretical basis for designing novel delay devices.

1. INTRODUCTION

The tremendous interest in slow light research has been spurred partly by its potential to communication components and sensors devices in optics. Such as, slow light has been applied to strengthen the nonlinear interaction between the light and medium [1, 2], and to shorten the required fiber path length in an interferometric device [3, 4]. Other proposed applications of slow light include fiber delay lines and buffers. In 2007, J. T. Mok, etc. [5] reported the dispersionless slow light with 5-pulse-width delay in fiber Bragg grating. The excitation of gap solitons in a 30 cm fiber Bragg grating using 0.68 ns pulses, which emerge with a tunable delay of up to 3.2 ns, corresponding to almost five pulse widths, and without broadening. In 2008, Myungjun Lee, Ravi Pant and Mark A. Neifeld [6], reported the improved slow-light delay performance of a broadband SBS system using fiber Bragg gratings: they present a technique for improving the pulse-delay performance of a SBS based broadband slow-light system by combining with fiber Bragg grating and optimize the physical device parameters of three systems. Pump power consumption is reduced by 15% as compared to the broadband SBS system at the same bit rate. In 2009, Qian Kai, Zhan Li, etc. [7] reported the tunable delay slow-light in an active fiber Bragg grating: to achieve tunable optical delay by using the Er/Yb codoped fiber Bragg grating, a controllable delay of 0.9 ns can be obtained through changing the 980 nm pump power. It provides a very simple approach to control the light group delay. However, it does not take into consideration the maximum delay.

In this paper, the uniform fiber Bragg grating to the main research objective, the effect of the grating of length, “dc” index change spatially averaged over a grating period and fringe visibility of the index change on group delay are focus on discussed by means of numeric simulation and slow light delay characteristics is studied emphatically. The research results indicate that the impact of “dc” index change spatially averaged over a grating period on group delay is most obviously, the maximum value of the group delay of 140.087 ns can be obtained and slow light delay this kind grating is rapidly decaying.

2. THEORY

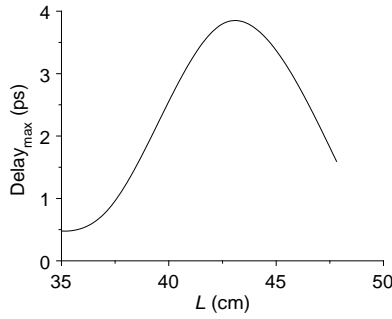
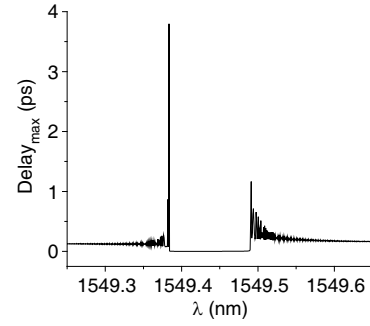
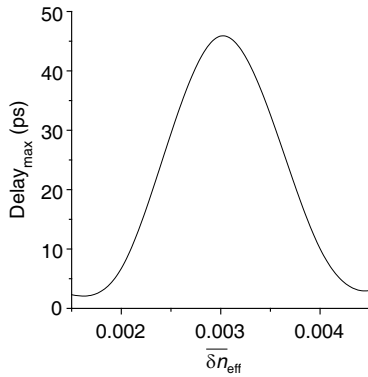
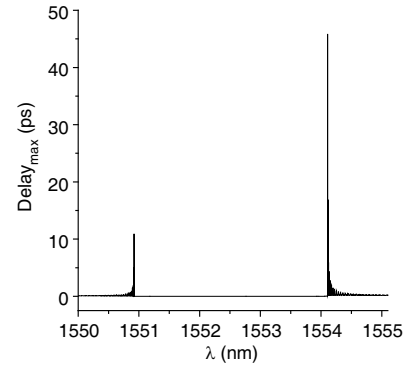
Fiber phase gratings are produced by exposing an optical fiber to a spatially varying pattern of ultraviolet intensity. For sake of simplicity, we studied an unchirped uniform refractive index of grating only can be described as follows [8]

$$n(z) = \overline{\delta n_{eff}} \left[1 + \nu \cos \left(\frac{2\pi}{\Lambda} z \right) \right] \quad (1)$$

where $\overline{\delta n_{eff}}$ is “dc” index change spatially averaged over a grating period, ν is the fringe visibility of the index change, Λ is the grating period, L is the grating length, N is the total number of the grating periods and $\Lambda = L/N$.

According to coupled mode theory, synchronous approximation and the boundary condition of the fiber Bragg grating [9, 11]. The amplitude reflection coefficient can be written as

$$\rho = \frac{-\kappa \sinh \left(\sqrt{\kappa^2 - \hat{\sigma}^2} L \right)}{\hat{\sigma} \sinh \left(\sqrt{\kappa^2 - \hat{\sigma}^2} L \right) + i \sqrt{\kappa^2 - \hat{\sigma}^2} \cosh \left(\sqrt{\kappa^2 - \hat{\sigma}^2} L \right)} \quad (2)$$

Figure 1: Influence of L on delay_{\max} .Figure 2: delay_{\max} as a function of wavelength with $L = 42.5008$ cm.Figure 3: delay_{\max} versus $\overline{\delta n_{eff}}$.Figure 4: delay_{\max} as a function of wavelength with $\overline{\delta n_{eff}} = 0.003$.

where $\kappa = \pi v \overline{\delta n_{eff}} / \lambda$ is the “ac” coupling coefficient, $\sigma = 2\pi \overline{\delta n_{eff}} / \lambda$ is the “dc” coupling coefficient, $\hat{\sigma}$ is a general “dc” self-coupling coefficient and $\hat{\sigma} = \sigma + \delta$, the detuning δ is defined as $\delta = 2\pi n_{eff}(1/\lambda - 1/\lambda_B)$, the Bragg wavelength λ_B is expressed as $\lambda_B \equiv 2n_{eff}\Lambda$.

The group delay of the reflected light by the fiber Bragg grating can be determined from the phase of the amplitude reflection coefficient ρ in (2). If we denote $\theta = \text{phase}(\rho)$.

Then at a local frequency ω_0 we may expand θ in a Taylor series about ω_0 . Since the first derivative $d\theta/d\omega$ is directly proportional to the frequency ω , this quantity can be identified as a time delay. Thus, the group delay time τ for light reflected off of a grating is [12, 13]

$$\tau = \frac{d\theta}{d\omega} = -\frac{\lambda^2}{2\pi c} \frac{d\theta}{d\lambda} \quad (3)$$

3. CALCULATED RESULTS AND ANALYSIS

3.1. Influence of Grating Length on Group Delay

Setting $n_0 = 1.46$, $\Delta = 0.002$, $N = 20000$, $L = 1.06252$ cm, $a = 5$ μm , $\overline{\delta n_{eff}} = 0.0001$ and $v = 1$ in Equation (3), a delay-wavelength curve of a mode can be obtained, in order to studied the slow light delay of the uniform fiber Bragg grating, though not shown here. Let us first discuss the effects of grating length on the group delay this kind grating. When the grating length L is changed, the others were determined, the group delay as functions of the wavelength λ can be obtained, then, the value of maximum group delays are obtained. The influence of L on delay_{\max} is shown in Figure 1. It can be seen that when $L < 42.5008$ cm, the delay_{\max} increases with L increasing, when L tends to 42.5008 cm have a maximum delay_{\max} , the value increased to 3.797 ps, but when $L > 42.5008$ cm, delay_{\max} decreases with L increasing.

Figure 2 shows that delay_{\max} as a function of wavelength with $L = 42.5008$ cm in uniform fiber Bragg grating. It is found that the group delay was changed rectangle wave and the maximum value of group delay is preceded in fast ray. Moreover, the bandwidth increased to 0.1 nm because of the bandwidth is decided to length in weak grating.

3.2. Effect of “dc” Index Change Spatially Averaged over a Grating Period on Group Delay

When the “dc” index change spatially averaged over a grating period $\overline{\delta n_{eff}}$ is changed, the others are determined, the group delay of the uniform fiber Bragg grating can be obtain. Figure 3 shows that the curve of delay max versus $\overline{\delta n_{eff}}$, it can be seen that when $\overline{\delta n_{eff}} < 0.003$, the delay max increases with $\overline{\delta n_{eff}}$ increasing, when $\overline{\delta n_{eff}}$ tends to 0.003 has a maximum delay max, the value is 45.869 ps, but when $\overline{\delta n_{eff}} > 0.003$, the delay_{max} decreases with $\overline{\delta n_{eff}}$ increasing. This means that group delay has a strong influenced of the $\overline{\delta n_{eff}}$.

As show in Figure 4, the delay_{max} as a function of wavelength with $\overline{\delta n_{eff}} = 0.003$ in uniform fiber Bragg grating. It indicates that the delay_{max} is also changed rectangle wave and clearly right-shifted, the delay max increased to 45.869 ps. Can not pass through the entire grating only under strong grating condition, bandwidth and the length have nothing to do with the change direct proportion that $\overline{\delta n_{eff}}$ leads, therefore, the bandwidth increased to 3 nm.

3.3. Influence of Fringe Visibility of the Index Change on Group Delay

Figure 5 shows that the curve of delay_{max} as a function of fringe visibility of the index change ν . When ν is deepened, the others are determined, the value of maximum group delay can be obtained. This means that when $\nu < 25$, the delay max increases with the deepening of the ν in uniform fiber of Bragg grating, when ν tends to 25 has a maximum delay max, which increased to 14.046 ps, but when $\nu > 25$, delay max decreases with the deepening of the ν . It indicates that fringe visibility of the index change has a remarkable impact on delay_{max} of the uniform fiber Bragg grating.

Delay_{max} versus wavelength with $\nu = 25$ in uniform fiber Bragg grating is shown in Figure 6. It can be seen that the delay_{max} is also obviously right-shifted and changed rectangle wave. At the same time, to the strong grating, bandwidth with ν direct proportion. So, the bandwidth has also increased with 3 nm. The maximum value of group delay increased to 14.046 ps.

It follows from the above discussion that the L , $\overline{\delta n_{eff}}$ and ν can lead to the group delay variation in uniform fiber Bragg grating while the other parameters as constants. The impact of $\overline{\delta n_{eff}}$ on group delay is most obviously. In addition, the delays max right-shifted, changed rectangle wave and the bandwidth changes broaden. These characteristics provide an important basis for further designing fiber Bragg grating for sensing.

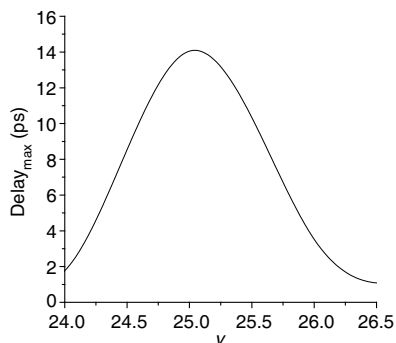


Figure 5: Delay max as a function of ν .

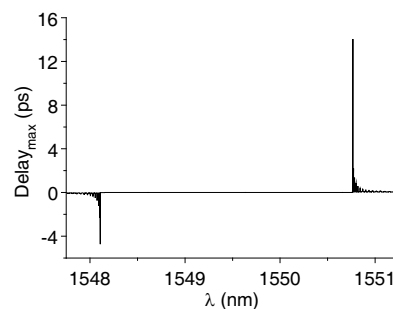


Figure 6: Delay max versus wavelength with $\nu = 25$.

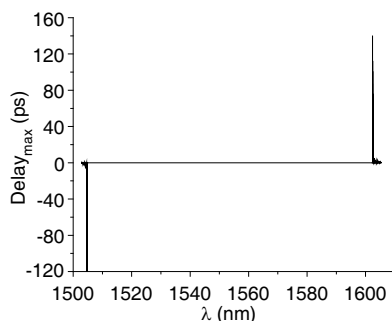


Figure 7: Delay_{max} as a function of wavelength with $L = 42.5008$ cm, $\overline{\delta n_{eff}} = 0.004$ and $\nu = 23$.

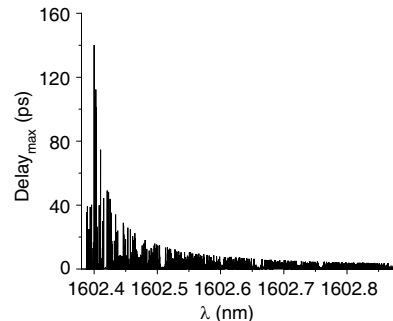


Figure 8: Slow light delay of uniform fiber Bragg grating with $L = 42.5008$ cm, $\overline{\delta n_{eff}} = 0.004$ and $\nu = 23$.

3.4. Slow Light Delay of Uniform Fiber Bragg Grating

As shown in Figure 7, the delay_{max} as a function of wavelength λ for uniform fiber Bragg grating with $L = 42.5008$ cm, $\overline{\delta n_{eff}} = 0.004$ and $\nu = 23$. It can be seen that the delay_{max} is apparently right-shifted, changed rectangle wave and the bandwidth has tends to 100 nm, especially the maximum value of group delay increased to 140.087 ns.

In order to further study the influence of the L , $\overline{\delta n_{eff}}$ and ν on slow light delay of uniform fiber Bragg grating. Figure 8 shows that the slow light delay with $L = 42.5008$ cm, $\overline{\delta n_{eff}} = 0.004$ and $\nu = 23$. It can be seen that the slow light delay is rapidly decaying, which rapidly reduced to 0 ns from 140.087 ns and shocks of the deviation is 0.4 nm, because coupled model theory is hit by inclusion have the speedy oscillating items. For the future design of new properties of slow light delay devices provide a theoretical reference.

4. CONCLUSIONS

The influence of the grating of length, “dc” index change spatially averaged over a grating period and fringe visibility of the index change on group delay of a mode uniform fiber Bragg grating are studied by means of numeric simulation and slow light delay characteristics this kind grating is presented emphatically. The calculated results show that the impact of “dc” index change spatially averaged over a grating period on group delay is most obviously. Moreover, the delay max of 140.087 ns with $L = 42.5008$ cm, $\overline{\delta n_{eff}} = 0.004$ and $\nu = 23$ can be obtained, curve is right-shifted, changed rectangle wave and the bandwidth changes broaden, especially slow light delay is rapidly decaying. These studies provides theoretical basis for designing novel delay devices.

ACKNOWLEDGMENT

This work is financially supported by the National Natural Science Foundation of China (Grant No. 61167005), the Natural Science Foundation of Gansu province of China (Grant No. 1112RJZA0-18).

REFERENCES

1. Jacobsen, R. S., K. N. Andersen, P. L. Borel, J. Fage-Pedersen, L. H. Frandsen, O. Hansen, M. Kristensen, A. V. Lavrinenko, G. Moulin, H. Ou, C. Peucheret, B. Zsigri, and A. Bjarklev, “Strained silicon as a new electro-optical material,” *Nature*, Vol. 441, No. 7090, 199–202, 2006.
2. Janner, D., G. Galzerano, G. D. Valle, P. Laporta, S. Longhi, and M. Belmonte, “Slow light in periodic superstructure Bragg gratings,” *Phys. Rev. E*, Vol. 72, No. 5, 056605, 2005.
3. Gu, L., W. Jiang, X. Chen, L. Wang, and R. T. Chen, “High speed silicon photonic crystal waveguide modulator for low voltage operation,” *Appl. Phys. Lett.*, Vol. 90, No. 7, 071105, 2007.
4. Mok, J. T., C. M. de Sterke, I. C. M. Little, and B. J. Eggleton, “Dispersion slow light using gap solitons,” *Nat. Phys.*, Vol. 2, No. 11, 775–780, 2006.
5. Mok, J. T., M. Ibsen, C. M. de Sterke, and B. J. Eggleton, “Dispersionless slow light with 5-pulse-width delay in fiber Bragg grating,” *Electron. Lett.*, Vol. 43, No. 25, 1418–1419, 2007.
6. Lee, M., R. Pant, and M. A. Neifeld, “Improved slow-light delay performance of a broadband SBS system using fiber Bragg gratings,” *Appl. Opt.*, Vol. 47, No. 34, 6404–6415, 2008.
7. Qian, K., L. Zhan, H. Li, X. Hu, J. Peng, L. Zhang, and Y. Xia, “Tunable delay slow-light in an active fiber Bragg grating,” *Opt. Exp.*, Vol. 17, No. 24, 22217–22222, 2009.
8. Erdogan, T., “Fiber grating spectra,” *IEEE J. Lightwave. Technol.*, Vol. 15, No. 8, 1277–1294, 1997.
9. Kogelnik, H. and C. V. Shank, “Coupled-wave theory of distributed feedback lasers,” *J. Appl. Phys.*, Vol. 43, No. 5, 2327–2335, 1972.
10. Kogelnik, H., “Theory of optical waveguides,” *Guided-wave Optoelectronics*, T. Tamir, Ed., Springer-Verlag, New York, 1990.
11. Ball, G. A., W. H. Glenn, and W. W. Morey, “Programmable fiber optical delay line,” *IEEE Photon. Technol. Lett.*, Vol. 6, No. 6, 741–743, 1994.
12. Gauthier, D. J., “Slow light brings faster communications,” *Phys. World*, Vol. 18, No. 12, 30–32, 2005.
13. Boyd, R. W., D. J. Gauthier, and A. L. Gaeta, “Applications of slow light telecommunications,” *Opt. Photon. News*, Vol. 17, No. 4, 18–23, 2006.

Optical Fiber Nonlinear Coefficient Measurements Using FWM

A. Supe, J. Porins, and G. Ivanovs

Institute of Telecommunications, Riga Technical University, Azenes st. 12, Riga LV-1010, Latvia

Abstract— In this article is given research results about nonlinear phenomena four-wave mixing (FWM) potential use in the optical fiber (OF) nonlinear coefficient γ and polarization mode dispersion (PMD) evaluation. First of all we give theoretical review about FWM causes in the OF. Afterwards the γ parameter measurement technique based on FWM is proposed. Fiber used in the experimental measurements is highly non-linear fiber (HNLF) with γ parameter is unknown and therefore is suitable for this research work.

1. INTRODUCTION

Continuously increasing amount of data in telecommunication networks requires higher and higher data rates. Nonlinear fiber optics plays an important role in the design of high capacity lightwave systems. Mostly due to the huge advantage over other technologies by achievable data rates and promising future development. One of the research areas is related with optical fiber non-linear characteristics. From one side non-linearity is not desirable because it causes distortions to the transmitted optical signals. It is very essential in the case of wavelength division multiplexed transmission systems for long transmission distances with several amplification regions. But nonlinear optical effects (NOE) also can be utilized in optical signal processing. In this case it is desirable to use the medium with increased non-linearity to achieve better NOE manifestation. For this reason very suitable are HNLFs [1].

Several approaches are used to determine optical fiber's γ parameter. Both interferometer based measurements or realization of some specific NOE in the OF [2, 3]. From wide range of NOEs that can be observed in OF, very promising is FWM. It is simple to induce and provide not only γ parameter characterization possibility, but also optical fiber PMD characteristics [5].

This paper consists of four parts. In Section 2 FWM process is described in details. The background of FWM is described in relation to OF and optical radiation parameters. FWM dependency on the two optical component — pump and signal — polarization state reciprocal matching is explained. Section 3 is devoted to describe the measurement scheme that was used to estimate γ and PMD parameters for the HNLF fiber. In Section 4 the main results and conclusions are given.

2. FOUR-WAVE MIXING IN OPTICAL FIBER

Four-wave mixing (FWM) is referred to as a parametric process. These processes only involve modulation of an OF refractive index or so called nonlinear refractive index [2, 3]. It is caused by ultrafast third-order nonlinear susceptibility $\chi^{(3)}$ of the SiO₂ [2]. FWM is a very harmful for a multichannel fiber optics transmission systems such as wavelength division multiplexing (WDM). It is because FWM can significantly reduce WDM performance by increasing crosstalk between all the system channels. This is due to optical signal generation at new frequencies that are defined by intermediate frequencies between any two initial optical signal frequencies.

In general FWM involve nonlinear interaction among four and more optical waves. But for simplicity let's consider case with two waves with different frequencies usually called pump and signal that generate third optical wave called as idler. According with the publication by S. Jung et al. [6] the idler component can be expressed as

$$P_3(L) = (\gamma P_1(0) L_{eff})^2 P_2(0) \exp(-\alpha L) \eta \quad (1)$$

where L is the fiber length, L_{eff} — effective length, α — fiber losses, $P_1(0)$ — pump power, $P_2(0)$ — signal power and η is the efficiency of the FWM that can be expressed as

$$\eta = \frac{\alpha^2}{\alpha^2 + \Delta\beta^2} \left(1 + \frac{4 \exp(-\alpha L) \sin^2(\Delta\beta L/2)}{(1 - \exp(-\alpha L))^2} \right) \quad (2)$$

where $\Delta\beta$ is the phase-matching condition.

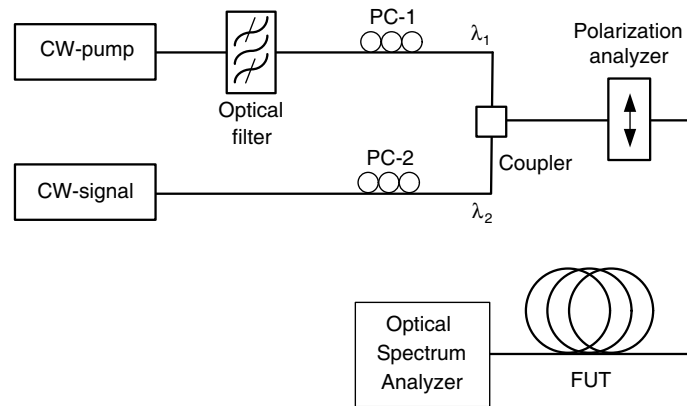


Figure 1: Experimental OF nonlinear coefficient measurement scheme based on FWM.

The efficiency of the FWM process is also dependent of the relative polarization of pump and signal fields. The best efficiency is obtained when pump and signal are co-polarized, whereas the orthogonal scheme leads to the worst efficiency [2]. When pump and signal are orthogonal the optical power of the idler component is approximately 8/9 times smaller than in the co-polarized state [2]. This polarization state influence to the FWM origins from the $\chi^{(3)}$ dependence of polarization state.

3. MEASUREMENTS USING FWM

To determine HNLF fiber nonlinear parameter the FWM based measurements were performed. The actual experimental measurement layout is shown in the Figure 1.

In this scheme two laser sources are used to generate pump and signal optical components with wavelength λ_1 and λ_2 . Both lasers are DFB and are working in the continuous radiation mode. Since the pump laser is working with higher optical output power there is an optical filter to reduce the laser radiation sideband noisiness at the output signal. To achieve co-polarized state between pump and signal there are two polarization controllers (PC-1 and PC-2). Afterwards both optical waves are coupled together and goes through the polarization analyzer. That allows us to control that both components has the same state of polarization. After polarization analyzer the fiber under test is connected. In our experiment it is 860 meters long HNLF. To see the FWM induced idler component at the wavelength:

$$\lambda_{\text{idler}} = 2\lambda_{\text{pump}} - \lambda_{\text{signal}} \quad (3)$$

From the HNLF output spectrums we can define what is the idler component's power level. Since the FWM process is dependent of OF γ it can be used to determine this parameter for the specific fiber. The relation between parameter γ and the FWM generated idler wave can be seen in the Equation (1). To estimate HNLF γ parameter the pump and signal wavelength separation was set to 1 nm. Larger wavelength separations could be used, but then we have to take into account polarization induced FWM efficiency reduction. From HNLF fiber output spectrum measurements it was estimated that γ parameter for this specific OF is $10.7 \text{ W}^{-1} \text{ km}^{-1}$. It is approximately 4 times higher than standard single mode fiber γ . It means this fiber is much more effective for NOE generation and it does not require so high optical power to achieve the same nonlinear manifestation as standard OFs.

To find out OF PMD characteristics the FWM measurements were performed for different pump and signal wavelength separations. Pump wavelength is kept constant while the signal wavelength is gradually increased. In the Figure 2, all the measured spectrums are represented in the same graph (legend shows the difference between the pump and signal wavelengths). It allows to better observe the evolution of the idler component. From measured output spectrums it can be seen that at certain threshold the idler components start to decrease. Nearer image to the FWM generated idler components is given in the Figure 3. Calculated results were achieved using Equation (1). Up to 3 nm separation between pump and signal wavelengths the idler remains almost constant, but afterwards start to decrease. It can be explained by the theory of the principal states of polarization. Exist a small frequency region over which the PMD vector is reasonably constant [7]

$$\Delta\omega \approx \frac{\pi}{4\langle\text{DGD}\rangle} \quad (4)$$

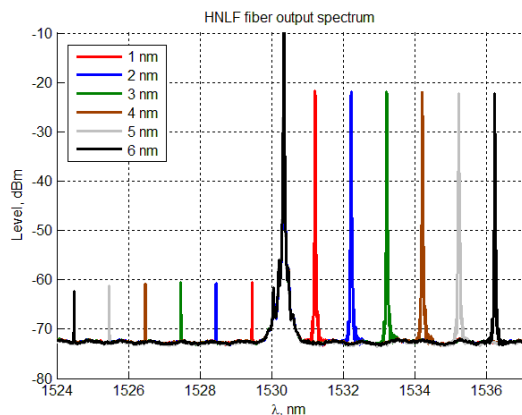


Figure 2: Measured HNLf output spectrums. Six different signal wavelength are shown in the graph.

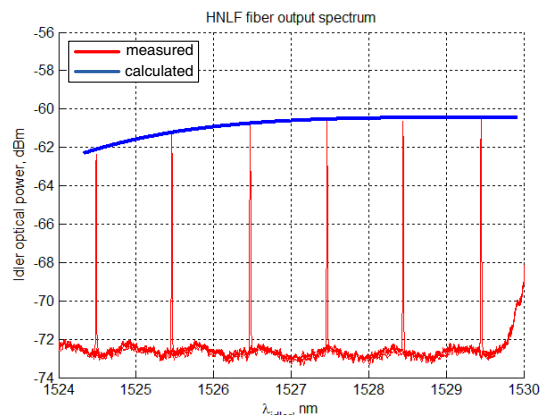


Figure 3: Calculated and measured idler components for six different signal wavelengths.

where $\langle \text{DGD} \rangle$ is the mean differential group delay or fiber PMD. From here it is possible to express the PMD depending on the frequency region over which the two signals propagating in the OF remain co-polarized. In this case the indication of co-polarized state existence in the OF is the FWM generated idler signals. From Figure 3, it can be seen, that region over which the PMD vector is almost constant is ~ 3 nm. Using Equation (4) the estimated HNLf fiber PMD value is 2.19 ps.

4. CONCLUSIONS

FWM use in fiber parameter measurements is very topical and promising. This NOE is easy to initiate and therefore does not require very complicated techniques. In this research we have shown the relation between FWM nonlinear effect and OF γ and PMD parameters. Afterwards it is used to determine both parameters for the HNLf fiber. Nonlinear parameter γ is $10.7 \text{ W}^{-1} \text{ km}^{-1}$ and PMD is estimated to be 2.19 ps.

ACKNOWLEDGMENT

The travel costs and participation fee to conference was supported by the European Regional Development Fund project “Development of international cooperation projects and capacity in science and technology Riga Technical University”, Nr. 2DP/2.1.1.2.0/10/APIA/VIAA/003.

REFERENCES

1. Ferreira, M. F. S., *Nonlinear Effects in Optical Fibers*, Wiley & Sons, New Jersey, 2011.
2. Agrawal, G. P., *Nonlinear Fiber Optics*, 3rd Edition, Academic Press, San Diego, 2001.
3. Supe, A. and J. Porins, “Methods for estimation of optical fiber non-linearity using self-phase modulation effect,” *Latvian Journal of Physics and Technical Sciences*, No. 6, 29–40, 2011.
4. Namihira, Y., et al., “Comparison of six techniques for nonlinear coefficient measurements of various single mode optical fibers,” *12th Symposium on Optical Fiber Measurements*, 15–19, Boulder, 2002.
5. Lin, Q. and G. P. Agrawal, “Effects of polarization-mode dispersion on fiber-based parametric amplification and wavelength conversion,” *Opt. Letters*, Vol. 29, No. 10, 1114–1116, 2004.
6. Jung, S. J., J. Y. Lee, and D. Y. Kim, “Novel phase-matching condition for a four wave mixing experiment in an optical fiber,” *Opt. Express*, Vol. 14, 35–43, 2005.
7. Jopson, R. M., L. E. Nelson, and H. Kogelnik, “Measurement of second-order polarization-mode dispersion vectors in optical fibers,” *IEEE Photon. Tech. Lett.*, Vol. 11, No. 9, 1153–1155, 1999.

Design of Quantum Secure Communication System Based on FPGA

Jun Li¹, Jie Chen², Heping Zeng², and Hui Li¹

¹Shenzhen Graduate School, Peking University, China

²State Key Laboratory of Precision Spectroscopy, ECNU, China

Abstract— Nowadays, quantum secure communication has been recognized as one of the most secure communication techniques, and plug-play scheme is one of the most practical case in QKD (quantum key distribution) experiment. This paper mainly introduces how to use FPGA (field programming gate array) to control the optical components in order to implement quantum key distribution system. The system works based on phase coding mode with optical pulse frequency being 10 MHz, communication distance being 50 km, code generating rate being 2 kbps and error rate being 10^{-6} . Also we have developed an application software which can take text chat and secure file transmit for the QKD hardware system using Qt IDE on Linux OS.

1. INTRODUCTION

As we all know, now is the age of information technology, where information security plays an important role in all works of life. In the trend of higher performance computer, the information secure technology depending on traditional mathematical algorithm has become lame and awkward. Especially with the rise of quantum information technology, study of quantum computer has been promoted in many ways. If quantum computer were developed, the cryptographic system would be broken easily. But quantum mechanics is a double-edged sword. In the meantime of bringing us the quantum computer which can easily break the classical cryptographic system, it also brings the new absolutely secure encryption techniques. Relying on uncertainty principle and non-cloning theorem in quantum mechanics, we use single photons as the key carrier to ensure that the quantum secure communication system is an absolutely secure communication system which cannot be wiretapped.

In recent years, quantum secure communication research has developed very rapidly. Many research groups have made lots of contributions to quantum communication system. China has already made the study of quantum secure communication as a national science and technology's long-term strategic development project. Quantum secure communication has been commonly recognized as one of the most secure communication methods in the future [1,2]. Due to the wide application of information security in National security department, military department and financial system, quantum secure communication is considered more and more important.

There are two key parts in practical quantum communication system, optical component and electronic component. In electronic part, we choose FPGA chip as the main device because FPGA is configurable [3,4] that we can upgrade our system easily. Furthermore, FPGA has rich IO interfaces that can support interconnection between optical devices and electronic devices. Also FPGA's high frequency can easily upgrade our system to be high speed level.

2. BB84 PROTOCOL & PLUG-PLAY SCHEME

2.1. Introduction of BB84 Protocol

In 1984, Bennett and Brassard put forward the first QKD (quantum key distribution) protocol — BB84 protocol [5] which is the most popular protocol in laboratory, and it has been theoretically proved as the absolutely safe and reliable protocol. Now we describe the advanced BB84 protocol based on phase coding [6–14]. Protocol details as follows:

(1) Alice makes four kinds of single photon phase state randomly among which two of them are orthogonal mutually. It means that Alice makes a random phase state among phase 0, π , $\pi/2$, $3 * \pi/2$ in one clock cycle and then send it to Bob after recording these random sequence.

(2) Bob also chooses ground state randomly (0 or 1) to measure single photon state. Because Bob doesn't know that which ground state the photon was made, so there are only 50 percent photon state be measured correctly.

(3) Bob announces the measured ground sequence to Alice, but doesn't announce the measured result. Then Alice tells Bob which measured ground state is correct according to the sequence recorded by Alice.

(4) Alice and Bob preserve the bit under the same ground state, and delete the others. Now both have the same bit sequence.

(5) Alice and Bob announce some part of the keys to make sure that there are no wiretappers. And the rest is the final cipher code.

2.2. Plug-play Scheme with Phase Coding and QKD System Architecture

Quantum key distribution architecture is described in Figure 1. It shows the connection between QKD processor (FPGA) and optical devices. Our system uses the plug-play scheme which was put forward by University of Geneva and IBM lab independently [15–20]. The plug-play optical path is shown in the wire-frame. In the scheme, the optical source and photon detector are both at Bob's place. The process is as follows: Bob sends single photon pulse, then the pulse is divided into 'fast' and 'slow' paths after passing through M-Z interferometer, then the two path photons are modulated into two mutual orthogonal states after passing through PBS (Polarization Beam Splitter). These two kinds of photons then arrive at Alice's side after passing through long distant optic fiber and then modulator #2 just modulates the 'slow' photons. Then all of the photons exchange the phase state after passing through Faraday rotator mirror, and all return back to Bob through long optic fiber. At this time, fast photons will go long-arm path but slow photons will go short-arm path. Then modulator #1 will modulate the fast photons. After that, the photons will arrive at the coupler at the same time, then interference will happen. The influence of interference will be different according to the difference between phase state of Alice and Bob. Assuming that the wave function of single photon state that Bob sends is $|\psi\rangle = a|0\rangle + b|1\rangle$, then the probability of single photon being detected will be $p = [1 + \cos(\varphi_a - \varphi_b)]/2$, where φ_a and φ_b are Alice's and Bob's modulator phases respectively. So we can know from the equation that the probability of photon being detected is 1 when phase difference is 0, $1/2$ when phase difference is π , 0 when phase difference is $\pi/2$ or $3 * \pi/2$.

While FPGA is in charge of generating synchronous clock, driving random number chip, collecting data from single photon detector, controlling system running abode by BB84 protocol, storing and correcting cipher code. Among them, the random number chip aims to generate random sequence for random measuring ground state and optic phase state. Single photon detector uses SPDIII [21] which works at 10 MHz frequency and is developed by ECNU state key laboratory of precision spectroscopy.

3. QKD SYSTEM DESIGN AND FPGA MODULAR DESIGN

Here we only consider the Bob's QKD processor, because it is basically identical with Alice's. There are just a few differences in some algorithms.

3.1. QKD Processor Architecture

The overall design includes many small modules, and the architecture shows as in Figure 2. Among these modules, module "synchronous clock" is in charge of generating synchronous clock and driving random number chip. Module "Protocol Controller Unit" takes charge of the scheduling to make sure that the system runs abode by the BB84 protocol. Memory module is mainly used to store the

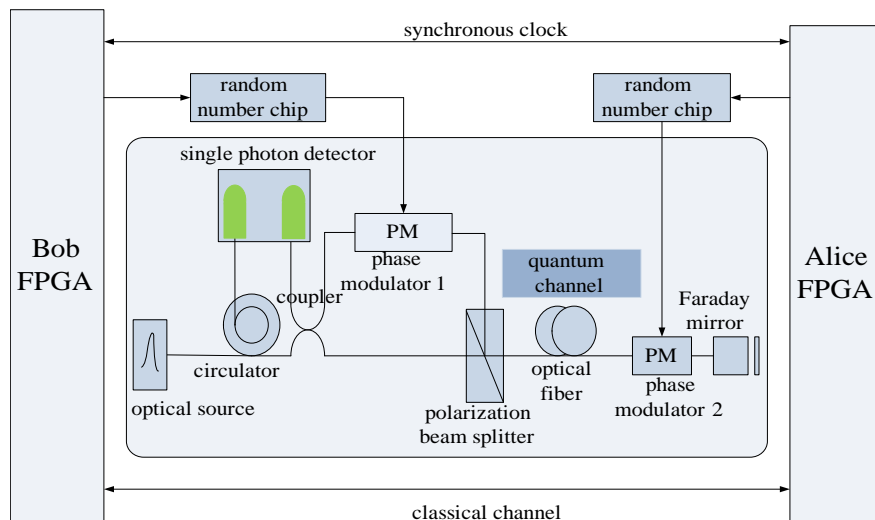


Figure 1: Quantum key distribution architecture based on phase coding plug-play scheme.

bit information that produced in the process of data collecting and operating, as well as store the final cipher code sequence. ALU is the main unit for data operation, including ground state sequence comparison and ground state sifting. It's the main data path in the architecture. The function of UART controller is to debug cipher code and upload what is used for encrypting messages for PC user. These modules are interconnected by address bus, controller bus and data bus.

3.2. Protocol Controller Unit

This module mainly takes in charge of system's work schedule. By using state machine, we can make sure that the system runs abode by BB84 protocol. FSM shows as in Figure 3. While the memory mainly stores logic sequences generated in the process of BB84 protocol. In memory system, we divide it into three sub memory modules: ram 0, ram 1 and ram 2, where ram 0 takes in charge of storing random sequence generated by random number chip, ram 1 stores bit information which are detected by single photon detector and coded as simple coding rule (coding rule shows as in Table 1 where symbol 'xx' means the detected information cannot be sure), ram 2 stores the cipher code after code sifting.

Here we consider the process flow in detail. In the state machine, state 'Initial' is used to initialize the registers, such as the memory's address registers, read registers and write registers. State 'write_ram 0.ram 1' is used to execute write operation to ram 0 and ram 1. Our system is a two-way system that Bob generates random numbers after synchronous clock returns back from Alice. This method has a big advantage that it can automatically compensate polarization jitter, making the system more stable. At the same time, Bob will receive the photon interference results, encode it as simple coding rule and store it into ram 1. Bob detects the interference results at random ground states, so the only 50% results are right (regardless of other factor). And if take the single photon detector's detect efficiency and dark count into consideration, there are only 0.1% photons will be detected correctly. Thus, in state 'read_ram 0.ram 1', Bob must sift the wrong

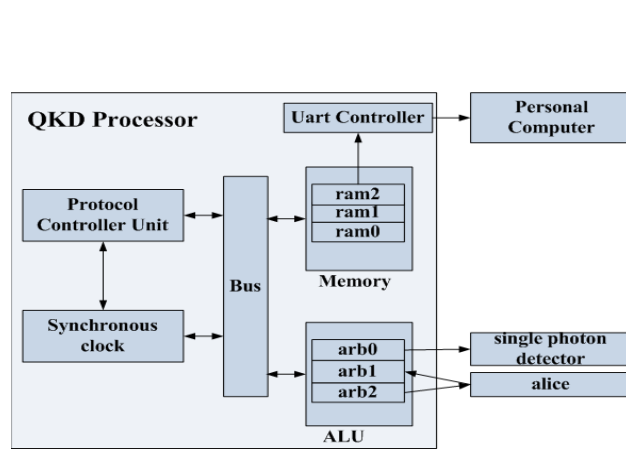


Figure 2: QKD processor architecture.

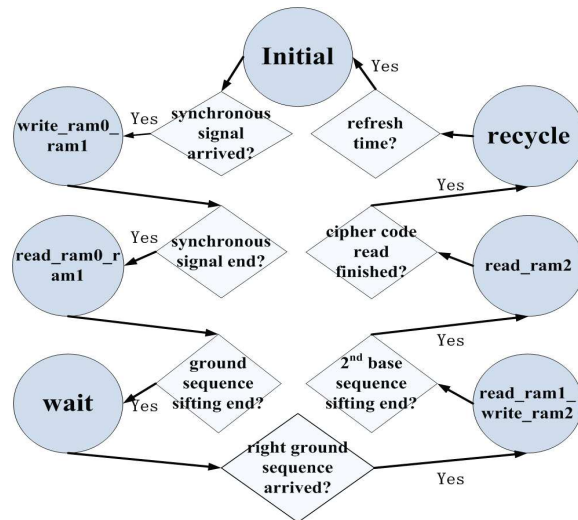


Figure 3: QKD controller Unit State machine.

Table 1: Ram 1 coding rule.

Acode	Aphase	Bcode	Bphase	APD	Code
[00]	0	0	0	[01]	[00]
[01]	180	0	0	[10]	[01]
[10]	45	0	0	[xx]	[11]
[11]	270	0	0	[xx]	[11]
[00]	0	1	45	[xx]	[11]
[01]	180	1	45	[xx]	[11]
[10]	90	1	90	[01]	[00]
[11]	270	1	90	[10]	[01]

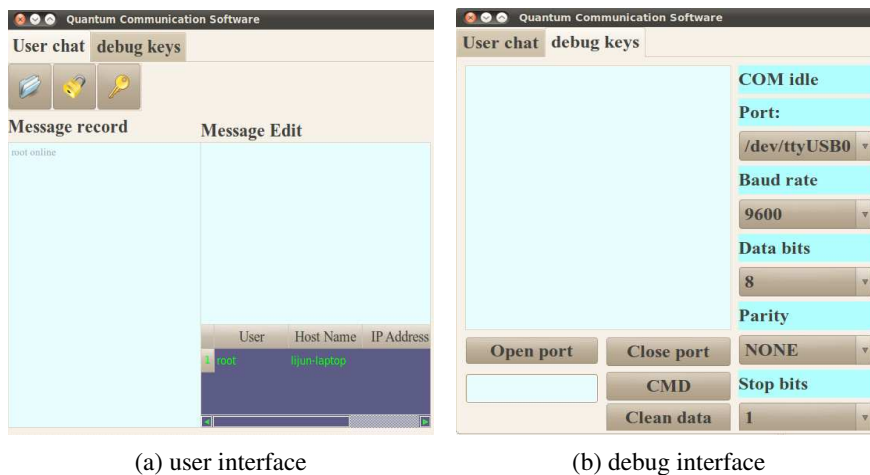


Figure 4: QKD application software.

bit sequences out by telling Alice his detect ground state. Then Alice is able to distinguish the right ground sequences by comparing Bob's sequences and her own sequences (stored in Alice's ram 0), and then tells Bob the right ground states. Bob gets the right sequences and selects the corresponding results store in ram 1. Therefore Bob can get the right cipher code and store them in ram 2. Then in state 'read_ram 2', Bob reads the cipher code to PC terminal or other application terminal such as voice process module. In state 'recycle', we can make system update the quantum keys periodically.

4. QKD APPLICATION SYSTEM

The hardware system introduced above is used to generate and distribute secure cipher code. But in the real system, we must construct a platform for the secure communication system. We promote a QKD application software using Qt [22] IDE under Linux OS. Using the software, we can have a secure text chat or secure file transmission. The GUI shows as Figure 4. User interface shows as Figure 4(a), and debugging interface which is used for the hardware system debugging shows as Figure 4(b).

In debug interface, we can read secure keys from RS232 port by typing read command, and then secure keys will display in the key display area. And we distinguish the consistency between Alice's and Bob's keys so that we can debug the hardware system. In practical application, for example, Alice sends ciphertext Bob by performing bitwise XOR on plaintext and cipher keys. And Bob receives this ciphertext and decode it just by performing bitwise XOR on this received ciphertext and cipher keys. By this simple mathematical operation we can take absolutely secure communication and improve the speed of users' encoding and decoding, but for wiretappers, they can not obtain the message forever.

5. CONCLUSION

In this paper, we have promoted the QKD application system based on the phase coding mode. The system we developed takes FPGA as main control unit for QKD protocol so that it can run normally abode by BB84 protocol. And we developed an application software using Qt IDE under Linux OS for practical quantum communication. The QKD application system we promoted can make the secure quantum keys distributed in 50 km, the code generating rate being about 2 kbps and error rate being 10^{-6} after error correcting. And our system can work stably more than 1 week. For more extern work, we can use FPGA to implement it due to its configurable feature.

ACKNOWLEDGMENT

The work is supported by National Basic Research Program of China (973 Program) (No. 2012CB-315904), National Natural Science Foundation of China (No. NSFC61179028), Natural Science Foundation of Guang Dong (No. GDNSF S201101000923), Basic Research of Shen Zhen (No. Shen-zhen JC201104210120A) and Basic Research of Shen Zhen (No. Shenzhen JC201005260234A).

REFERENCES

1. Gisin, N., G. Ribordy, W. Tittel, and H. Zbinden, *Quantum Cryptography, Reviews of Modern Physics*, Vol. 74, No. 1, 145–195, 2002.
2. Dusek, M., N. Lütkenhaus, and M. Hendrych, “Quantum cryptography,” *Progress in Optics*, Vol. 49, E. Wolf, Ed., Elsevier, 2006.
3. Sun, H., L. Hu, and L. Yu, *Xilinx FPGA Application and System Design*, Publishing House of Electronics Industry, Beijing, May 2008.
4. He, B., *Xilinx FPGA Design Technology Details*, Tsinghua University Press, Beijing, Mar. 2010.
5. Bennett, C. H. and G. Brassard, “Quantum cryptography: Public key distribution and coin tossing,” *Proceedings of the IEEE International Conference on Computers, Systems and Signal Processing*, 175, Bangalore, India; IEEE, New York, 1984.
6. Bennett, C. H., “Quantum cryptography using any two non-orthogonal states,” *Phys. Rev. Lett.*, Vol. 68, 3121–3124, 1992.
7. Townsend, P. D., J. D. Rarity, and P. R. Tapster, “Single photon interference in a 10 km long optical fiber interferometer,” *Electron. Lett.*, Vol. 29, 634–639, 1993.
8. Townsend, P. D., J. D. Rarity, and P. R. Tapster, “Enhanced single photon fringe visibility in a 10 km-long prototype quantum cryptography channel,” *Electron. Lett.*, Vol. 29, 1291–1293, 1993.
9. Marand, C. and P. D. Townsend, “Quantum key distribution over distances as long as 30 km,” *Opt. Lett.*, Vol. 20, 1695–1697, 1995.
10. Hughes, R., G. Morgan, and C. Peterson, “Quantum key distribution over a 48-km optical fiber network,” *J. Mod. Opt.*, Vol. 47, 533–547, 2000.
11. Muller, A., T. Herzog, B. Huttner, W. Tittel, H. Zbinden, and N. Gisin, “Plug and Play’ systems for quantum cryptography,” *Appl. Phys. Lett.*, Vol. 70, 793–795, 1997.
12. Zhou, C. Y. and H. P. Zeng, “Time-division single-photon Sagnac interferometer for quantum key distribution,” *Appl. Phys. Lett.*, Vol. 82, 832, 2002.
13. Zbinden, H., J. D. Gautier, N. Gisin, B. Huttner, A. Muller, and W. Tittel, “Interferometry with Faraday mirrors for quantum cryptography,” *Electron. Lett.*, Vol. 33, 586–588, 1997.
14. Mo, X. F., B. Zhu, et al., “Faraday-Michelson system for quantum cryptography,” *Opt. Lett.*, Vol. 30, 2632, 2005.
15. Muller, A., T. Herzog, et al., “‘Plug and play’ systems for quantum cryptography,” *Appl. Phys. Lett.*, Vol. 70, 793, 1996.
16. Bourennace, M., F. Gibsona, et al., “Experiments on long wavelength (1550 nm) ‘plug and play’ quantum cryptography systems,” *Opt. Express*, Vol. 4, 383, 1999.
17. Ribordy, G., J. D. Gautier, et al., “Fast and user-friendly quantum key distribution,” *J. Mod. Opt.*, Vol. 47, 517, 2000.
18. Bethune, D. S. and W. P. Risk, “An auto compensating fiber-optic quantum cryptography system based on polarization splitting of light,” *IEEE J. of Quantum. Electron.*, Vol. 36, 340, 2000.
19. Zhou, C. and G. Wu, “Quantum secure communication over 50 km optic fiber,” *Science*, Vol. 33, 538, China, 2003.
20. Wu, G., C. Y. Zhou, et al., “A stable long-distance quantum key distribution system,” *Acta Phys. Sin.*, Vol. 54, 3662, 2005.
21. Wu, G., C. Zhou, and X. Chen, “Long distant and stable quantum key distribution system,” Vol. 54, No. 8, 3626, 2005.
22. Blanchette, J. and M. Summerfield, *C++ GUI Programming with Qt 4*, Prentice Hall, Feb. 4, 2008.

Numerical Study of Effective Plasma Frequency for a Plasma Photonic Crystal in the Presence of Magnetic Field

Heng-Tung Hsu¹, Jin Jei Wu², Chi-Chung Liu³, and Chien-Jang Wu⁴

¹Department of Communications Engineering, Yuan Ze University, Chungli 320, Taiwan, R.O.C.

²Department of Electrical Engineering, Chung Hua University, Hsinchu 300, Taiwan, R.O.C.

³Department of Electro-Optical Engineering
National Formosa University, Yunlin 632, Taiwan, R.O.C.

⁴Institute of Electro-Optical Science and Technology
National Taiwan Normal University, Taipei 116, Taiwan, R.O.C.

Abstract— In this paper, based on the transmittance spectrum calculated by making use of the transfer matrix method, we numerically study the effective plasma frequency for a ternary plasma photonic crystal (PPC) in the presence of static magnetic field. The results illustrate that the effective plasma frequency for the PPC will be red-shifted as a function of the static magnetic field. In the case of oblique incidence, we find that the effective plasma frequency is found to be insensitive to the angle of incidence in the TM wave.

1. INTRODUCTION

It is known that the wave property of a metal can be characterized by the so-called plasma frequency, $\omega_p = 2\pi f_p$. In the absence of damping frequency, an electromagnetic wave with frequency higher than ω_p can propagate inside the metal whereas it is prohibitive to propagate at $\omega < \omega_p$ because wave is evanescent. However, wave can propagate in a metal-dielectric photonic crystal (MDPC) even at $\omega < \omega_p$. In the MDPC, the lowest frequency, at which wave can begin to propagate, is defined as an effective plasma frequency $\omega_{p,eff} = 2\pi f_{p,eff}$ for the MDPC system. It has been shown that $\omega_{p,eff}$ is, in general, smaller than ω_p [1–3]. The concept of effective plasma frequency is that, the wave property at lower frequency for a PC can be effectively replaced by a semi-infinite medium with a effective permittivity related to the effective plasma frequency [2].

In the early stage, photonic crystals made of all dielectrics or of metal-dielectric are of main interest to the community. In recent years, a special type of photonic crystal called the plasma photonic crystal (PPC) was first proposed by Hojo and Mase [4]. A superior feature for a PPC is to possibly tunable photonic band gaps (PBGs) at microwave frequency. A similarity between metal and plasma is that both have the same mathematical form of permittivity, i.e., the Drude-like expression [5, 6].

$$\varepsilon(\omega) = 1 - \frac{\omega_p^2}{\omega^2 + j\gamma\omega}, \quad (1)$$

where γ is the damping frequency, and the plasma frequency is $\omega_p = (\tilde{N}e^2/m\varepsilon_0)^{1/2}$, where \tilde{N} is the electron concentration, ε_0 is the permittivity of free space, m is the electron mass, and e is the electronic charge. In Eq. (1), and in what follows in this paper, the temporal part for all fields is assumed to be $\exp(-j\omega t)$. The typical value of ω_p for various bulk metals is 100 THz whereas it is at microwave frequency for the plasma. The best understanding for the characteristic frequency of ω_p is in the lossless case where $\gamma = 0$. In a plasma system, ω_p can be changed by controlling \tilde{N} in the plasma, leading to a tunable property in wave propagation when it is introduced in the PPC system. That is, the photonic band structure (PBS) is tunable in a plasma-based photonic crystal. Since the effective plasma frequency of a PC is a characteristic frequency that plays a fundamental role in the wave propagation, we are thus motivated to study the effective plasma frequency in a PPC.

In this paper, we consider a ternary finite PPC of $(ABC)^N$, as depicted in Fig. 1 where the first period is shown. The PPC structure is embedded in the air with N being the number of periods. In what follows, A is quartz, B is plasma, and C is MgF_2 will be considered. In addition, we are specifically interested in a magnetized PPC, i.e., the PPC is exerted by an externally applied static magnetic field. The incident wave with TM -polarization is obliquely incident on the left plane boundary of $z = 0$. The effective plasma frequency will be extracted from the transmittance spectrum calculated by making use of the transfer matrix method (TMM) [7]. We investigate effective plasma frequency as a function of the static magnetic field as well as the angle of incidence.

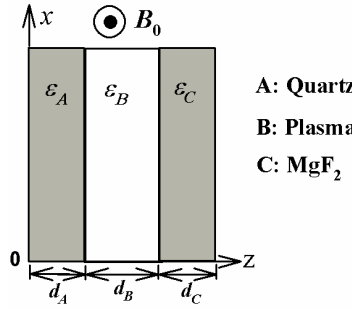


Figure 1: The first period of the ternary dielectric-plasma-dielectric photonic crystal. The structure is $Air/(ABC)^N/Air$, where A is quartz, B is plasma, and C is MgF_2 .

2. BASIC EQUATIONS

The finite ternary PPC has a structure $Air/(ABC)^N/Air$, as illustrated in Fig. 1, where the first period is shown and layer B is the plasma, A (quartz) and C (MgF_2) are two dielectric materials. The incident wave with TM polarization is obliquely incident on the left plane boundary of $x = 0$. The angle of incident is denoted by θ . The PPC is magnetized by an externally applied static magnetic field, $\mathbf{B}_0 = \mathbf{y}B_0$. It is worth mentioning that in a magnetized PPC the angular dependence is shown to be seen in the TM polarization since TE polarization has the same properties as the unmagnetized PPC [8, 9].

The effective plasma frequency will be extracted from the transmittance spectrum calculated from the TMM [7]. The transfer matrix for the magnetized plasma layer B under TM -polarization can be written by [10]

$$M_B = \begin{pmatrix} \cos(k_{Bx}d_B) + \varepsilon_{21} \tan \theta_B \sin(k_{Bx}d_B) & -\frac{j}{\eta_B} \left[1 + (\varepsilon_{21} \tan \theta_B)^2 \right] \sin(k_{Bx}d_B) \\ -j\eta_B \sin(k_{Bx}d_B) & \cos(k_{Bx}d_B) - \varepsilon_{21} \tan \theta_B \sin(k_{Bx}d_B) \end{pmatrix}, \quad (2)$$

where

$$k_{Bx} = k_B \cos \theta_B, \quad k_B = (\omega/c) \sqrt{\varepsilon_{TM}}, \quad \eta_B = \sqrt{\varepsilon_{TM}} \sqrt{\varepsilon_0/\mu_0} (1/\cos \theta_B), \quad (3)$$

and

$$\varepsilon_{21} = \frac{-\omega_p^2 \omega_c}{\omega \left[(\omega + j\gamma)^2 - \omega_c^2 \right] - \omega_p^2 (\omega + j\gamma)}, \quad (4)$$

Here, the effective permittivity of a magnetized plasma is given by

$$\varepsilon_{TM} = \frac{[\omega(\omega + j\gamma) - \omega_p^2]^2 - \omega^2 \omega_c^2}{\omega^2 \left[(\omega + j\gamma)^2 - \omega_c^2 \right] - \omega \omega_p^2 (\omega + j\gamma)}, \quad (5)$$

where $\omega_c = eB_0/m$ is the cyclotron frequency. As for the dielectric layers A and C , the transfer matrix is expressed as

$$M_q = \begin{pmatrix} \cos(k_{qx}d_q) & -\frac{j}{\eta_q} \sin(k_{qx}d_q) \\ -j\eta_q \sin(k_{qx}d_q) & \cos(k_{qx}d_q) \end{pmatrix}, \quad q = A, C \quad (6)$$

where

$$k_{qx} = k_q \cos \theta_q, \quad k_q = (\omega/c) \sqrt{\varepsilon_q}, \quad \text{and} \quad \eta_q = \sqrt{\varepsilon_q} \left(\sqrt{\varepsilon_0/\mu_0} \right) (1/\cos \theta_B). \quad (7)$$

The total transfer matrix for the finite ternary PPC is thus given by

$$\mathbf{M} = \begin{pmatrix} m_{11} & m_{12} \\ m_{21} & m_{22} \end{pmatrix} = (\mathbf{M}_A \mathbf{M}_B \mathbf{M}_C)^N. \quad (8)$$

The reflectance coefficient r and transmission coefficient t are expressed as

$$r = \frac{m_{11}\eta_0 + m_{12}\eta_0\eta_s - m_{21} - m_{22}\eta_s}{m_{11}\eta_0 + m_{12}\eta_0\eta_s + m_{21} + m_{22}\eta_s}, \quad t = \frac{2\eta_0}{m_{11}\eta_0 + m_{12}\eta_0\eta_s + m_{21} + m_{22}\eta_s} \quad (9)$$

where $\eta_0 = \sqrt{\varepsilon_0/\mu_0} (1/\cos \theta)$ and $\eta_s = \sqrt{\varepsilon_s} (\sqrt{\varepsilon_0/\mu_0}) (1/\cos \theta_s)$. In our design, the substrate is simply taken as air, i.e., $\eta_s = \eta_0$. All the ray angles are related to the angle of incidence by the Snell's law of refraction,

$$n_0 \sin \theta = n_A \sin \theta_A = n_B \sin \theta_B = n_C \sin \theta_C = n_s \sin \theta_s. \quad (10)$$

The reflectance and transmittance are given by

$$R = |r|^2 \quad \text{and} \quad T = \frac{n_s \cos \theta_s}{n_0 \cos \theta_0} |t|^2. \quad (11)$$

3. NUMERICAL RESULTS AND DISCUSSION

First, let us consider the simple case of normal incidence ($\theta = 0$). Fig. 2 shows the calculated transmittance spectra at different static magnetic fields, $B_0 = 0, 2$, and 4 T, respectively. Here, the electron concentration is $\tilde{N} = 10^{13} \text{ cm}^{-3}$, $\gamma = 0$, and the thicknesses are $d_A = 0.5 \mu\text{m}$, $d_B = 5 \mu\text{m}$, and $d_C = 0.5 \mu\text{m}$. The cutoff frequency marked by the red arrow is defined as the effective plasma frequency, $f_{p,eff}$, for the plasma photonic crystal. It can be seen that $f_{p,eff}$ is shifted to the lower frequency when the static magnetic field B_0 increases. The values of $f_{p,eff}$ are $4.146, 1.84$, and 0.844 GHz for $B_0 = 0, 2$, and 4 , respectively. In fact, $f_{p,eff}$ will approach zero at $B > 10$ T. This indicates that the magnetized PPC at higher magnetic field will behaves like a dielectric-dielectric photonic crystal (DDPC) because $f_{p,eff}$ is zero in a DDPC. In addition, it can be seen from the figure that the bandwidth of the first transmission band is enlarged as a function of B_0 . Moreover, the second PBG at $B_0 = 0$ becomes narrower for $B_0 > 0$.

Figure 3 shows the transmittance spectra at $B_0 = 0$ for three different angles of incidence, $\theta = 10^\circ, 45^\circ$, and 75° , respectively. It is seen that the effective plasma frequency is insensitive to the angle of incidence. The values of $f_{p,eff}$ are $4.157, 4.187$, and 4.22 GHz, for $\theta = 10^\circ, 45^\circ$, and 75° , respectively. However, the first transmission band and second gap are enhanced as a function of angle of incidence in this case. The weak dependence in the angle of incidence is also seen when the static magnetic field is applied.

In Fig. 4, we plot the transmittance at $B = 4$ T for three different thicknesses of the plasma layer, $d_B = 2, 0.5$, and $0.1 \mu\text{m}$, respectively. Here, the conditions are $d_A = d_C = 0.5 \mu\text{m}$, $N = 50$, and the electron concentration is 10^{13} cm^{-3} . The corresponding effective plasma frequencies are 1.525 ,

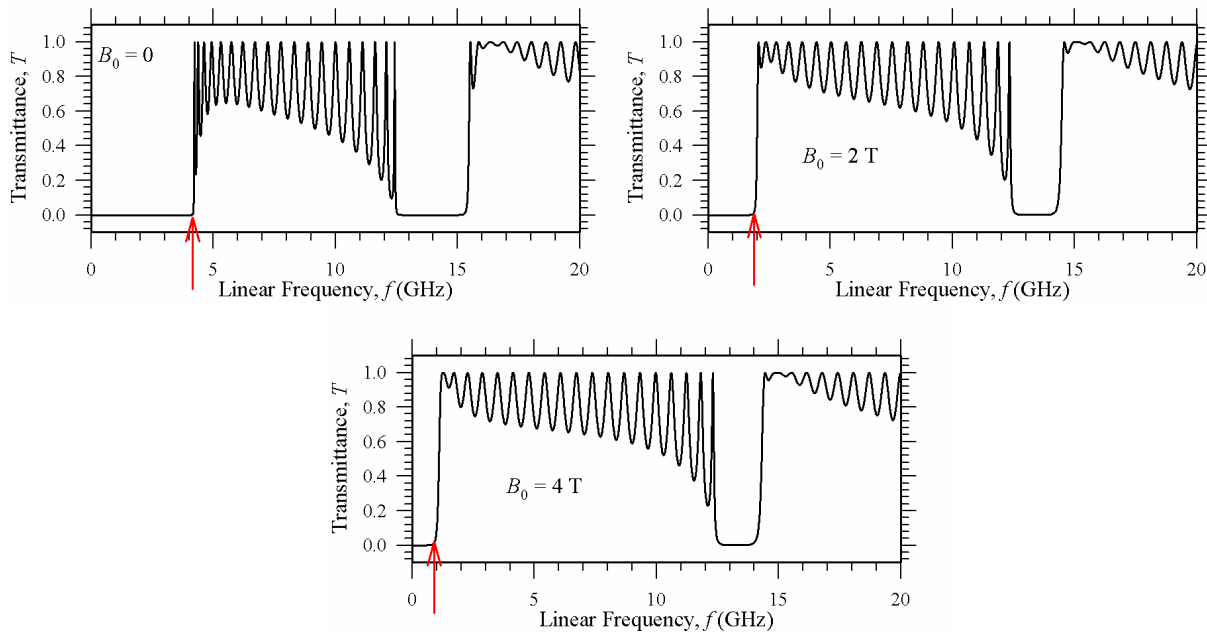


Figure 2: The calculated normal-incidence transmittance at various static magnetic fields, $B_0 = 0, 2$, and 4 T, respectively. The number of periods is $N = 20$, the thicknesses are $d_A = 0.5 \mu\text{m}$, $d_B = 5 \mu\text{m}$, and $d_C = 0.5 \mu\text{m}$. The electron concentration is 10^{13} cm^{-3} .

2.447, and 3.3 GHz. It is of interest to see that the effective plasma is shifted to the higher frequency as the thickness of plasma layer decreases. This trend is opposite to that of the unmagnetized PPC, in which the effective plasma frequency is shifted to the lower frequency as the thickness of plasma layer decreases [3]. This opposite trend can be ascribed to the presence of magnetic field that leads to the more dielectric-like material for the plasma, as mentioned previously.

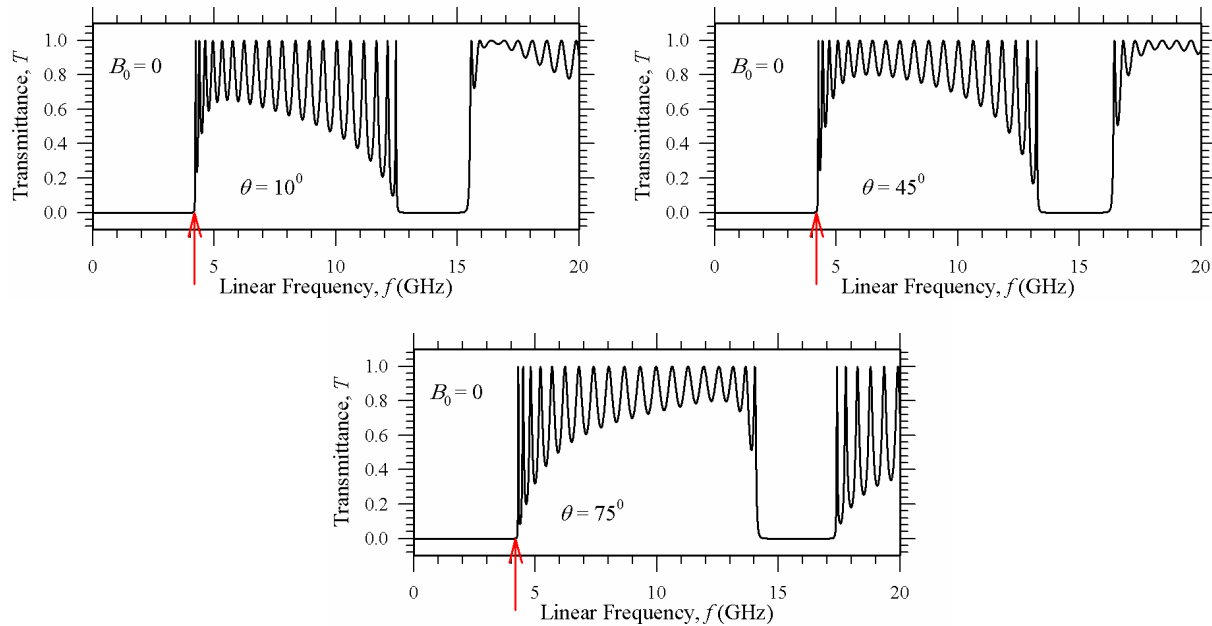


Figure 3: The calculated TM-wave transmittance at $B_0 = 0$ for various angles of incidence, $\theta = 10^\circ$, 45° , and 75° , respectively. The number of periods is $N = 20$, the thicknesses are $d_A = 0.5 \mu\text{m}$, $d_B = 5 \mu\text{m}$, and $d_C = 0.5 \mu\text{m}$. The electron concentration is 10^{13}cm^{-3} .

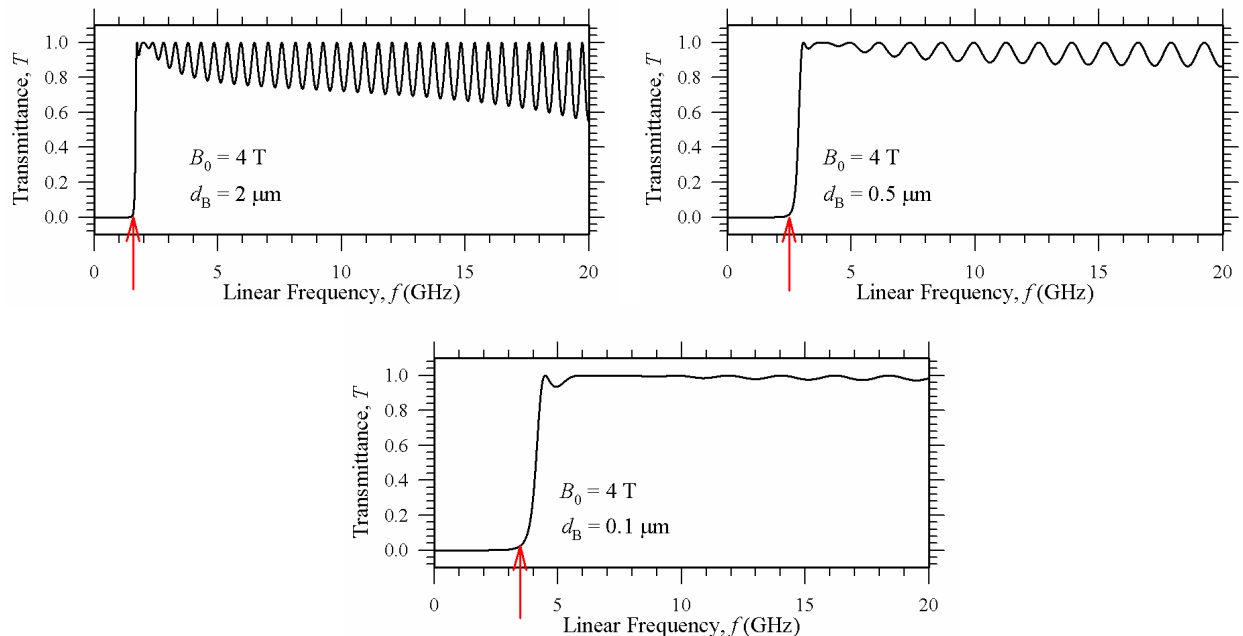


Figure 4: The calculated normal-incidence transmittance at $B_0 = 4 \text{ T}$ for various thicknesses of plasma layer, $d_B = 2$, 0.5 , and $0.1 \mu\text{m}$, respectively. The number of periods is $N = 50$, the thicknesses are $d_A = 0.5 \mu\text{m}$, and $d_C = 0.5 \mu\text{m}$. The electron concentration is 10^{13}cm^{-3} .

4. CONCLUSION

The effective plasma frequency for a magnetized plasma photonic crystal has been analyzed based on the calculated transmittance spectrum. The conclusion can be drawn as follows: First, the effective plasma frequency is moved to the lower frequency when the static magnetic field increases. Second, the effective plasma frequency is a weak function of the angle of incidence. Finally, we find that the effective plasma frequency is shifted to the higher frequency as the thickness of plasma layer decreases. The study thus gives some fundamental information about the effective plasma frequency for a magnetized plasma photonic crystal.

ACKNOWLEDGMENT

The author is indebted to the financial support from the National Science Council of the Republic of China (Taiwan) under grant No. NSC-100-2112-M-003-005-MY3.

REFERENCES

1. Xu, X., Y. Xi, D. Han, X. Liu, J. Zi, and Z. Zhu, *Appl. Phys. Lett.*, Vol. 86, 09112, 2005.
2. Manzanares-Martinez, J., “Analytic expression for the effective plasma frequency in one-dimensional metallic-dielectric photonic crystal,” *Progress In Electromagnetics Research M*, Vol. 13, 189–202, 2010.
3. Wu, C.-J., T.-J. Yang, C.-C. Li, and P.-Y. Wu, “Investigation of effective plasma frequencies in one-dimensional plasma photonic crystals,” *Progress In Electromagnetics Research*, Vol. 126, 521–538, 2012.
4. Hojo, H. and A. Mase, *J. Plasma Fusion Res.*, Vol. 8, 477, 2005.
5. Zhang, H. F., et al., *J. Appl. Phys.*, Vol. 110, 026104, 2011.
6. Zhang, H. F., et al., *Phys. Plasmas*, Vol. 19, 022103, 2012.
7. Yeh, P., *Optical Waves in Layered Media*, John Wiley & Sons, New York, 1998.
8. Guo, B., *Phys. Plasmas*, Vol. 16, 043508, 2009.
9. Guo, B., *Plasma Sci. Technol.*, Vol. 11, 18, 2009.
10. Qi, L., Z. Yang, F. Lan, X. Gao, and Z. Shi, *Phys. Plasmas*, Vol. 17, 042501, 2010.

The Studies of Enhanced Optical Single Sideband Modulation Using by Laser's Cavity Mode and Nonlinear Optical Fiber Effect

H. Y. Shao¹, W. S. Tsai¹, G. C. Lin¹, and H. H. Lu²

¹Department of Electrical Engineering, Ming Chi University of Technology, Taipei 24301, Taiwan

²Department of Electro-Optical Engineering, National Taipei University of Technology
Taipei 10608, Taiwan

Abstract— We propose a transmission system based on injection-locked Fabry-Perot (FP) Lasers and stimulated Brillouin scattering (SBS) to achieve modulation in fiber. These two kinds of technologies fall on frequency band approximately nearby 10.87 GHz~11 GHz to enhance optical single sideband (OSSB) signal. The first step based on injection-locked FP Lasers to achieve modulation. The right sideband is amplified and the unlocked mode signal is attenuated by the cavity mode to produce OSSB modulation. The second step is to drive the radio-frequency (RF) signal into the modulation and then use the SBS effect to enhance performance of OSSB modulation. This results in an OSSB modulation signal after 25-km of single-mode fiber (SMF) is transmitted. We then can observe the sideband power ratio (SBPR) > 17 dB and phase noise < -80.07 dBc/Hz.

1. INTRODUCTION

In the optical modulation, utilizing optical double sideband (ODSB) ways to do modulation; it is very serious on the fiber dispersion to optical double sideband, resulting in a significant attenuation of the microwave power. ODSB modulation comprises an optical carrier signal and two modulation sidebands, these two sidebands in the optical fiber transmission will generate different phase shifts with different fiber length. The microwave frequency and fiber dispersion factors in when the two sidebands phase shift too much difference. This cause the microwave signals to disappear. Therefore, the microwave power attenuation caused by fiber dispersion is the radio-over-fiber (ROF) system needs to be addressed by key technology. Power loss due to fiber dispersion, optical single-sideband (OSSB) modulation techniques and optical frequency reduction technology can effectively reduce the impact of the fiber dispersion. OSSB modulation bandwidth is half the double-sideband modulation. The dispersion limit to relay distance can be doubled, increase the transmission quality of fiber optic communications systems to meet the needs of the users, ultimately reaching the ideal of service.

The fiber dispersion caused by the microwave power of the attenuation is needed to improve the key issues in the fiber optic microwave transmission system. The OSSB not only can effectively suppress the dispersion, but the efficiency of transmission more advance than tradition of double sideband modulation and the further transmission distance.

In recent years many optical single sideband signal modulation techniques have been proposed to solve the problem caused by the dispersion of the RF attenuation, but must be using the papers presented that are a special component architecture, resulting in the increase of system complexity and system costs. Instead, another optical single-sideband modulation method can be used to narrow the bandwidth optical filter. Single-sideband modulation along side a narrow bandwidth optical can filter its ODSB signal. But the signal band wavelength range must be set for the filter to work. However, the shorter range of the signal band can be adjusted.

2. EXPERIMENTAL SETUP

Figure 1 uses FP laser based on injection locking and SBS techniques to generate optical single sideband.

As the signal transmitter uses the tunable laser as the master laser, the FP laser as slave laser, the FP laser belongs to the multimode light source. We propose an optical injection-locked (OIL) structure. The laser wavelength is about 1530 nm passing the Mach-Zender modulator (MZM) to generate a double sideband signal, and use the semiconductor optical amplifier (SOA), increasing optical power into the optical circulator.

Through the injection locking technique and SBS, the two kinds of technologies are fall on frequency bands approximately nearby 10.87 GHz and 11 GHz. Therefore, the microwave signal

generates frequencies between 10.87 GHz and 11GHz. The corresponding frequency bands gain cavity modes, and effectively achieve strengthening the right sideband. The master laser transmits through the circulator port 1 to port 2 via injection-locked technology by the gain cavity mode. The light signals the double sideband modulation signal and is converted into a single-sideband signal, via circulator port 2 to port 3, and transmits the 25-km single-mode fiber. Through the 10:90 coupler, 10% of the light source is through SOA amplifier power, through the circulator port 1 to port 2 into the 25-km single-mode fiber to do transmission, this produces the SBS scattering 10.87 GHz~11 GHz the drift, another access 90% light source into MZM modulated double sideband signal, and 10% of the light sources do combine enhanced right sidebands, enhancing performance and gain OSSB modulation signal.

After EDFA adjusts the optical attenuator, and does optical detecting, EDFA is a compensation optical power, when optical power decreases in transmission. The receiver has limited optical power; therefore optical attenuation is performed to adjust the optical power to the appropriate power, and then observing the OSSB signal by the spectrum analyzer, sideband power ratio to calculate the optical signal in the system. The sideband power ratio is defined as the non suppressed sideband with suppression behind with optical power dB values does divide.

Optical signal through the PD photoelectric conversion, to observe in the spectrum, the signal output by the spectrum analyzer, we evaluate the phase noise by spectrum calculated frequency

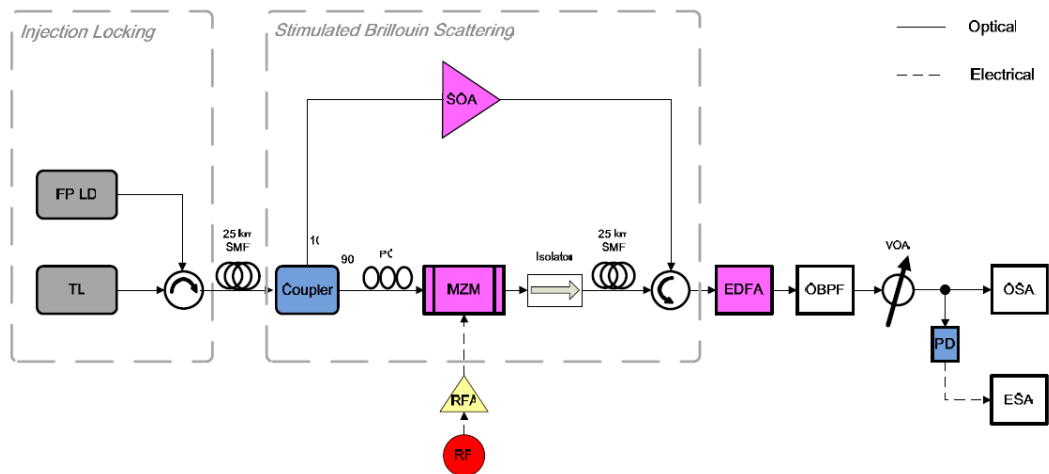


Figure 1: Based on injection locking and stimulated Brillouin scattering techniques to generate optical single sideband of structure chart.

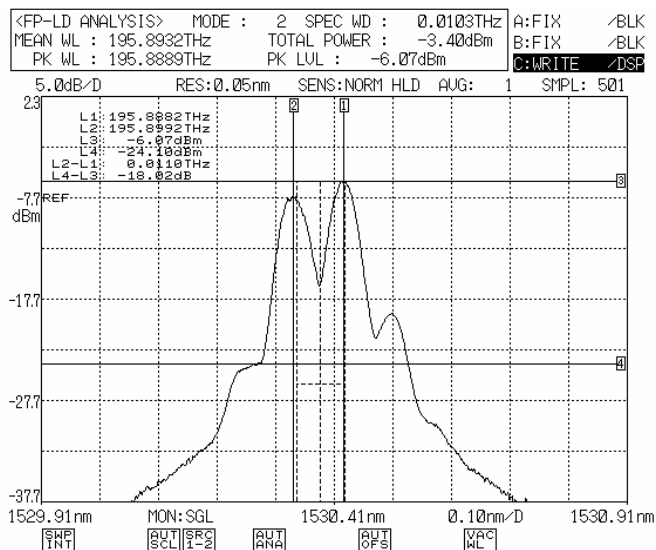


Figure 2: Through the PD before the OSSB signal optical spectrum (25-km).

signals, analysis of the degree of stability of its frequency signal, the calculation of the offset frequency power master signal power ratio action, and then RBW generated by thermal noise into consideration, were taken to 100 Hz, 500 Hz, 1 kHz, 5 kHz, 10 kHz, 50 kHz, 100 kHz, 500 kHz and 1 MHz the phase noise calculation.

3. EXPERIMENT RESULTS

Figure 2 shows the measured spectrum by the transmission of 25-km single-mode fiber, this source is observed in the spectrum analyzer by the photo detector (PD). Due to injection-locked reduction, most optical power is in the fiber transmission; therefore one would need the erbium-doped fiber amplifier (EDFA) to amplify the optical power, utilizing the optical band-pass filter for filtering out noise. Finally, one should adjust the appropriate optical power by the optical attenuator into the spectrum analyzer.

Figure 3 shows the measured the electrical signals by the spectrum analyzer, operated at optical single-sideband modulation signal 11 GHz after 25-km single-mode fiber are measured -39.60 dBm.

Figure 4 shows a demonstration through the hypothetical experiment Stimulated Brillouin gain at 10.87 GHz and near the injection-locked gain cavity mode 11 GHz, considering a different modulation frequency of optical single sideband signal, and calculating its OSSB signal sideband power ratio, with and without the stimulated Brillouin gain, after 25-km of single-mode fiber to measure. In this architecture with stimulated Brillouin gain, the Sideband power ratio of the optical signal measured after 25-km transmission can achieve approximately 18.02 dB.

Figure 5 shown is an optical single sideband signal generated based on optical injection-locked technology transmission of 25-km SMF measured phase noise chart, modulation frequency at 11 GHz and high-power slave signal, drifted frequency 100 Hz, 500 Hz, 1 kHz, 5 kHz, 10 kHz, 50 kHz, 100 kHz, 500 kHz, 1 MHz to do phase noise, the measurement of the phase noise is -80.07 dBc/Hz.

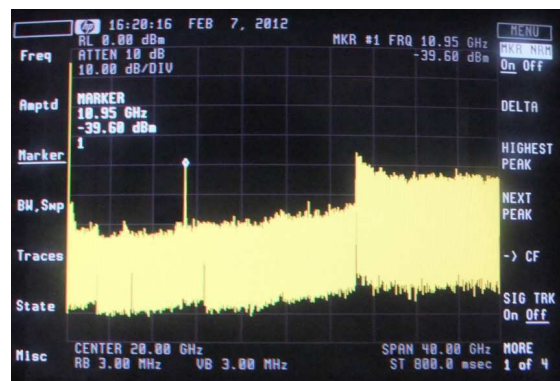


Figure 3: Detected after the optical detector 11 GHz spectrum (25-km).

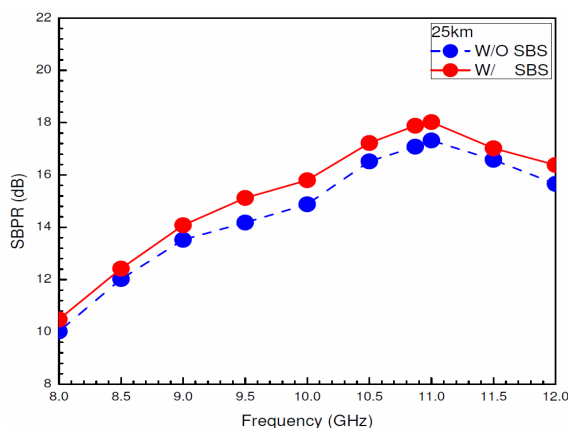


Figure 4: With the change of the modulation frequency of the sideband power proportion of measured.

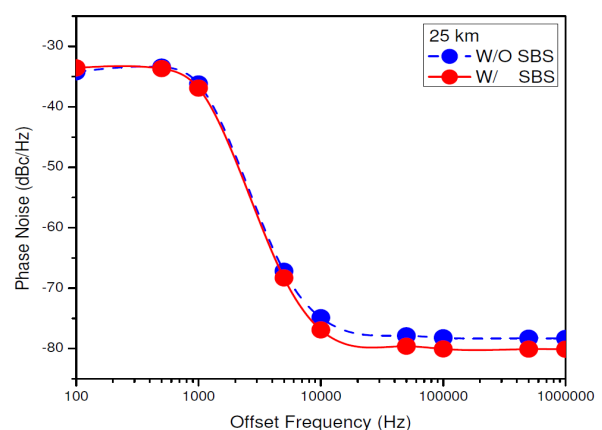


Figure 5: 11 GHz band OSSB phase noise of figure (25-km).

4. CONCLUSION

We successfully demonstrated an optical single sideband based on injection-locked Fabry-Perot (FP) laser and stimulated Brillouin scattering (SBS) to achieve modulation, combining two different modulation techniques, the gain range between 10.87 GHz and 11 GHz, this gain is enhanced right sideband and generates an OSSB modulation signal.

Radio-on-fiber (ROF) systems do utilize single-sideband modulation techniques. The transmission is efficient and more advanced than traditional double sideband modulation, not only effectively suppressing the dispersion, but also achieving long-distance optical fiber transmission, to optimize the transmission quality of communications systems and reaching the ideal of service and broadband for users.

Finally, the OSSB modulation signal after a 25-km of single-mode fiber transmission test, we can observe the sideband power ratio (SBPR) > 17 dB and phase noise < -80.07 dBc/Hz.

REFERENCES

1. Chi, H. and J. Yao, "Frequency quadrupling and upconversion in a radio over fiber link," *Journal of Lightwave Technol.*, Vol. 26, 2706–2711, 2008.
2. Zhou, M. T., A. B. Sharma, Z. H. Shao, and M. Fujise, "Optical single-sideband modulation at 60 GHz using electro-absorption modulators," *International Topical Meeting on Microwave Photonics, 2005, MWP 2005*, 121–124, 2005.
3. Park, J., W. V. Sorin, and K. Y. Lau, "Elimination of the fiber chromatic dispersion penalty on 1550 nm millimeter-wave optical transmission," *Electron. Lett.*, Vol. 33, 512–513, 1997.
4. Fonseca, D., P. Monteiro, and A. V. T. Cartaxo, "Adaptive optical single sideband filter based on a phase modulator," *Electron. Lett.*, Vol. 41, 760–761, 2005.
5. Fonseca, D. D., A. V. T. Cartaxo, and P. P. Monteiro, "Opto-electrical filter for 40 Gb/s optical single sideband signal generation," *Conference on Opt. Fiber Communication*, 2006.

A Study of Enhanced Optical Single Sideband Modulation Based on Scattering Effects and Semiconductor Laser Injection Locked Technology

Y. L. Chen¹, W. S. Tsai¹, G. Z. Lin¹, and H. H. Lu²

¹Department of Electrical Engineering, Ming Chi University of Technology, Taiwan

²Department of Electro-Optical Engineering, National Taipei University of Technology, Taiwan

Abstract— We propose a transmission system based on stimulated Brillouin scattering (SBS) and Distributed-Feedback (DFB) Lasers to achieve OSSB modulation in fiber. These two kinds of technologies fall on frequency band approximately nearby 10.8 GHz, to enhance OSSB signal. The first step drive radio-frequency (RF) signal into the modulation and then used SBS effect to enhance right sideband. The second step based on injection-locked DFB Lasers to achieve OSSB modulation. After 25-km of single-mode fiber (SMF) transmission test, we can observe the sideband power ratio (SBPR) > 15.81 dB and power penalty is 5.2 dB.

1. INTRODUCTION

In Radio-on-fiber (ROF) transmission system, the microwave signal is converted into the optical signal and distributed to the remote base station by fiber link, which provide broad bandwidth and low attenuation characteristics. The conventional fiber optical communication system usually adopts light intensity modulation with optical double sideband (ODSB) modulation format. After transmission for a long distance, dispersion effect will make the microwave signal produced serious fading [1].

Optical single sideband (OSSB) signal, which can remove a half of the optical spectrum, solving dispersion induce microwave signal degradation [2–4]. By eliminating one of the sidebands, OSSB modulation not only immunizes to fiber dispersion, but also increases the spectral efficiency. The study proposes the improved and enhanced OSSB modulation method, which can suppress the dispersion caused between carrier and sideband, then can be transmitted over a longer distance.

We propose a transmission system based on stimulated Brillouin scattering (SBS) and Distributed-Feedback (DFB) Lasers to achieve OSSB modulation in fiber. These two kinds of technologies fall on frequency band approximately nearby 10.8 GHz, to enhance OSSB signal. The first step drive radio-frequency (RF) signal into the modulation and then used SBS effect to enhance right sideband. The second step based on injection-locked DFB Lasers to achieve OSSB modulation. The results show that good performance is achieved in this ROF system.

2. EXPERIMENTAL SETUP

The experimental setup for based on stimulated Brillouin scattering (SBS) and Distributed-Feedback (DFB) Lasers to achieve OSSB modulation in fiber is shown in Fig. 1. The tunable laser is used for master laser and the DFB laser is used for slave laser. The wavelength of DFB laser is 1546.49 nm. The main parts of transmitter consists of a tunable laser, a DFB laser, a microwave signal generator, a digital signal generator, a RF power amplifier, a RF power splitter, a optical isolator, a optical interleaver, high-frequency signal mixer, a optical circulator, a semiconductor optical amplifier (SOA), and a Mach-Zehnder modulator (MZM).

Based on injection-locked Distributed-Feedback (DFB) Lasers and stimulated Brillouin scattering (SBS) to achieve modulation, the two kinds of technologies fall on frequency band approximately nearby 10.8 GHz. Therefore, the microwave signal generates frequencies about 10.8 GHz. The light signals through the 10 : 90 coupler, 10% of the light source is through SOA amplifier power, through the circulator port 1 to port 2 into the 25-km single-mode fiber (SMF) to do transmission, this produces the SBS scattering 10.8 GHz the drift, another access 90% light source into MZM modulated double sideband signal, and 10% of the light sources do combine enhanced right sidebands, enhancing performance and gain OSSB modulation signal. After EDFA adjusts the optical attenuator, and does optical detecting, EDFA is a compensation optical power, when optical power decreases in transmission. The receiver has limited optical power, therefore optical attenuation is performed to adjust the optical power to the appropriate power, and then observing the OSSB signal by the spectrum analyzer, sideband power ratio to calculate the optical signal in the system.

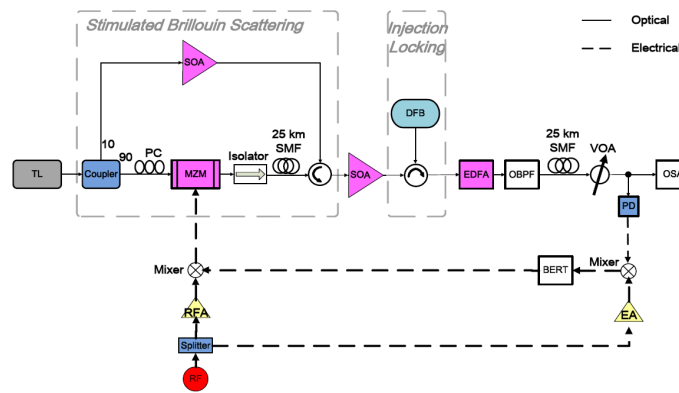


Figure 1: The experimental architecture diagram.

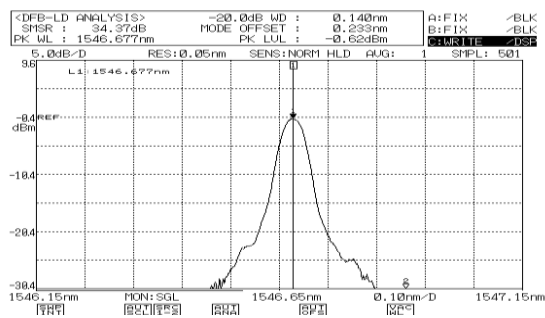


Figure 2: Optical spectra at the output of the tunable laser.

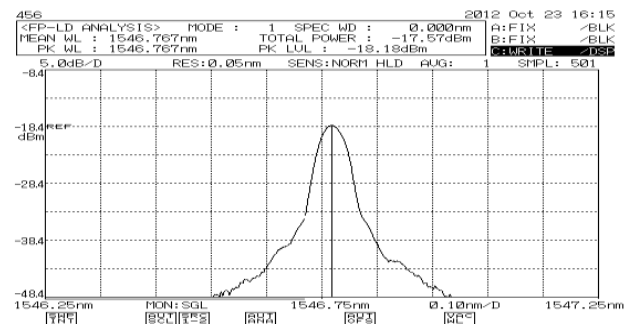


Figure 3: Optical spectra at the output of the DFB laser.

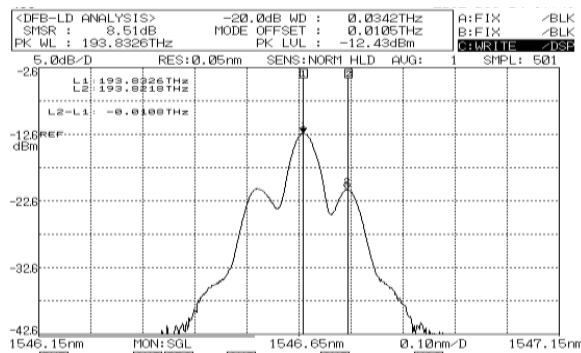


Figure 4: Optical spectra at the output of the MZM.

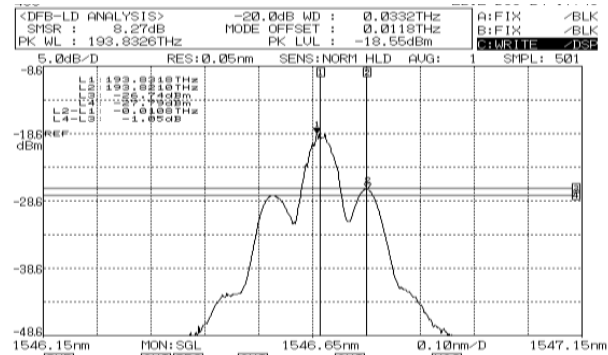


Figure 5: Optical spectra of the SBS scattering effects.

3. RESULTS AND DISCUSSION

Figures 2 and 3 show the optical spectra of the tunable (master) laser and DFB (slave) laser, respectively. The current of DFB was 15.02 mA, and the optical power was -18.18 dBm.

Figure 4 shows the optical spectra at the output of the MZM. Since MZM has the sensitive characteristic regarding the input light source's polarization state. A polarization controller (PC) needs to be added on in front of the MZM input section. This function is to adjust the state of polarization (SOP) of the input light. In Fig. 5, the 10% of the light source went through a semiconductor optical amplifier (SOA), the use of the optical circulator port 2 transmitted over 25-km SMF with combined by MZM output signal. Fig. 6 shows the optical spectra of the OSSB modulation based on SBS effect and injection-locked technology. Optical spectra of the OSSB signal filtered by optical interleaver are shown in Fig. 7. The eye diagrams at both back-to-back and 25-km SMF transmission are shown in Fig. 8(a) and Fig. 8(b), respectively.

Figure 9 shows the measured bit error rate (BER) curves of 622-Mbps/10.8-GHz signal. The

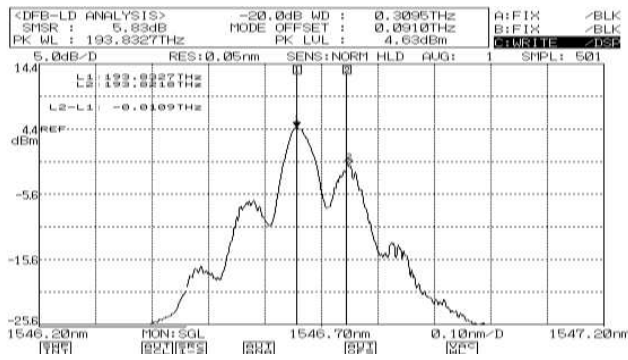


Figure 6: Optical spectra of the SBS effects and injection-locked technology.

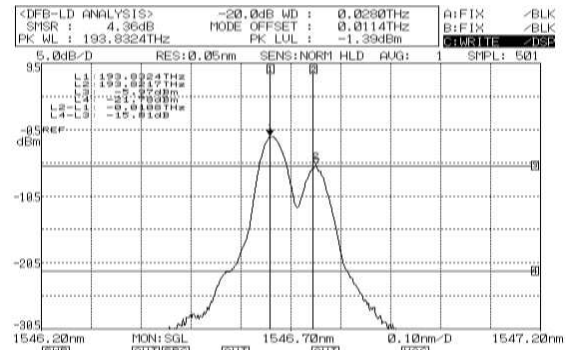


Figure 7: Optical spectra of the OSSB signal by optical interleaver.

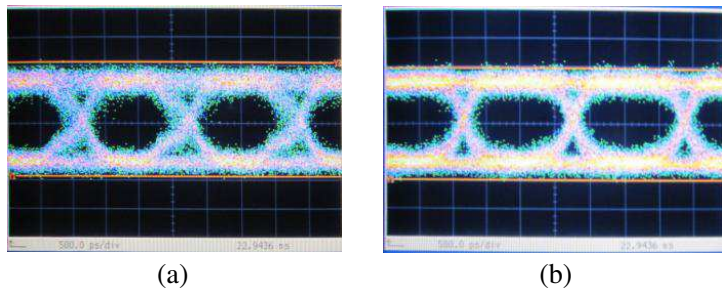


Figure 8: The eye diagrams (a) back-to-back (b) after 25-km SMF transmission.

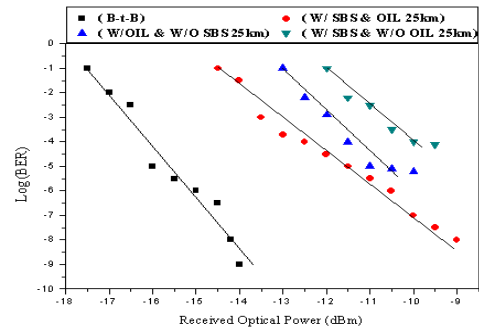


Figure 9: BER curves of the OSSB signal.

received optical power levels at the BER of 10^{-8} are -14.2 (back-to-back) and -9 (25-km SMF transmission) dBm. Power penalty of about 5.2 dB for the downlink is observed at a BER of after 25-km SMF transmission.

4. CONCLUSIONS

We experimentally demonstrated a transmission system based on stimulated Brillouin scattering (SBS) and Distributed-Feedback (DFB) Lasers to achieve OSSB modulation in fiber. Using the proposed scheme, a 622-Mbps data stream is mixed with a 10.8-GHz RF carrier to generate the 622 Mbps/10.8 GHz RF signal for both directions are successfully transmitted over a 25-km single-mode fiber link, we can observe the sideband power ratio (SBPR) > 15.81 dB and power penalty is 5.2 dB.

REFERENCES

1. Chi, H. and J. Yao, "Frequency Quadrupling and upconversion in a radio over fiber link," *Journal of Lightwave Tech.*, Vol. 26, 2706–2711, 2008.
2. Lee, U.-S., H.-D. Jung, and S.-K. Han, "Optical single sideband signal generation using phase modulation of semiconductor optical amplifier," *IEEE Photon. Tech. Lett.*, Vol. 16, 1373–1375, 2004.
3. Blais, S. R. and J. Yao, "Optical single sideband modulation using an ultranarrow ual-transmission-band fiber Bragg grating," *IEEE Photon. Tech. Lett.*, Vol. 18, 2230–2232, 2006.
4. Sung, H. K., E. K. Lau, and M. C. Wu, "Optical single sideband modulation using strong optical injection-locked semiconductor lasers," *IEEE Photon. Tech. Lett.*, Vol. 19, 1005–1007, 2007.

Development of Optical Wave Microphone Measuring Sound Waves with No Diaphragm

Yoshito Sonoda, Takashi Samatsu, and Toshiyuki Nakamiya

Graduate School of Industrial Engineering, Tokai University, Toroku 9-1-1, Kumamoto 862-8652, Japan

Abstract— The optical wave microphone with no diaphragm (or the optophone), which can detect sound waves wave-optically by using a laser beam without disturbing a sound field and an air flow, is presented as a novel sound measurement technique. In the optical receiving system, the diffraction light generated by sound waves is passed through an optical Fourier-transform system and is focused on an observing plane. The spatial position of diffraction light pattern in the plane is rotated around the laser beam axis when changing the sound incidence angle to the axis, which property can be used as a separation method of sounds with different incidence angles and a hand control method of directivity. In the present experiment, an optical fiber bundle with 16ch fibers is used to detect the diffraction light patterns generated by sounds with different incidence angle. The experimental results show that it is possible to separate two sounds with incidence angle difference of 90 degree and to control the receiving directivity by synthesizing some of fiber output signals.

1. INTRODUCTION

As a standard technique to measure sound waves, various types of microphone have been developed and used over one hundred years. However, they have many restrictions on practical applications because they use a diaphragm or any vibrating object to detect sound waves.

On the other hand, the optophone based on the wave optical principle [1] can transform a sound signal to an electrical signal by detecting an ultraweak diffraction light, which is generated by sounds crossing the laser beam. By experiments carried out so far, it was shown that sounds from about 100 Hz to 100 kHz could be simultaneously detected by a visible laser beam of 5 to 20 mW [2]. In this method, it is possible to change the sound receiving property such as directivity, signal amplification and frequency response by transforming the construction of a laser beam antenna (or a sound antenna). Furthermore, as the position of diffraction light pattern appeared in the observing plane is varied by the incidence angle of sound, it is expected that the separation of sounds with different incidence angles and the hand control of directivity become possible by using a divided photo detector or an optical fiber bundle connected to photo detectors.

In this paper, the principle and theory of the method is shortly introduced and the experimental results about the receiving property of optophone using an optical fiber bundle with 16ch fibers in the light detection plane are presented and discussed.

2. PRINCIPLE AND THEORY

The method is based on the theory of the Fraunhofer diffraction method, which has been developed as a new means to detect the electromagnetic radiation scattered by long-wavelength plasma waves within the penetrating laser beam in the plasma nuclear fusion research [3, 4]. By using the theory, the method has been applied to sound measurement from audio to ultrasonic waves and developed [5, 6].

An image figure of the optophone of one-dimensional straight laser beam type is shown in Figure 1. The abstract of the model for theoretical analysis is shown in Figure 2. When an incidence probing laser beam crosses a sound wave, diffraction light waves are generated and propagate with and in the penetrating beam through the Fourier optical system and reach the detection plane, which is set in the back focal plane of a receiving lens. The diffracted light is heterodyne-detected there by using the penetrating laser light as a local oscillating power. The spatial intensity of diffraction light signal for the theoretical model shown in Figure 2 is given by the following equation [3, 4].

$$I_{ac}^{(1)} = I_0 \Delta \phi_0 \exp(-u^2) [\exp\{-(u - \theta)^2\} - \exp\{-(u + \theta)^2\}] \cos \omega_a t \quad (1)$$

where $I_0 = (2P_0/\pi w_f^2) \exp[-2(y_f/w_f)^2]$ [W/m²], $\Delta \phi = k_i(\mu_0 - 1)\Delta z \Delta p/\gamma p$, μ_0 : refractive index of air, γ : specific heat ratio, Δz : width of sound, p : atmospheric pressure, Δp : sound pressure,

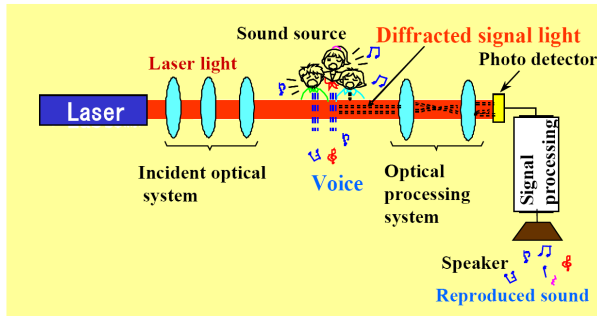


Figure 1: Image of the optical wave microphone.

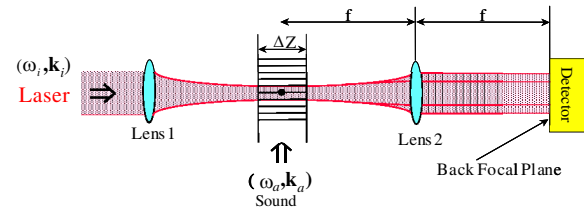


Figure 2: Optical setup for theoretical analysis.

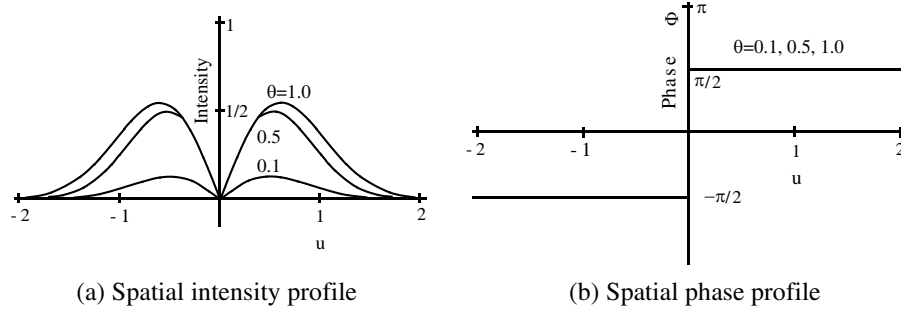


Figure 3: Theoretical profiles of diffracted light distribution.

k_l : wave number of laser light, ω_a : angular frequency of sound wave, P_0 : laser power, $u = x_f/w_f$: the normalized x -coordinate in the back focal plane, $\theta = k_a w_0/2$: the normalized wave number, k_a : wave number of sound wave, w_0 : radius of laser beam waist in sound incident region, w_f , x_f , y_f : radius of the beam cross section, x -coordinate and y -coordinate in the observing plane, respectively.

Based on the above equations, numerical calculations of the diffraction pattern are carried out, in which a visible laser was assumed as a probing laser beam. Examples of spatial distributions of the intensity and the phase of the diffraction light pattern are shown in Figures 3(a) and (b), respectively.

The spatial profile of diffracted light pattern (I) oscillating at the sound frequency has two peaks, which spatial positions do not change with frequency in the audio-wave or the low frequency ultrasonic band. On the other hand, the temporal phase difference (Φ) between the right and left diffraction patterns oscillating at ω_a is π , as shown in Figure 3(b). From Equation (1), it is found that the optical signal intensity is theoretically in proportion to the frequency of sound wave. In application to sound measurement, the frequency response of the optophone system is made flat over the whole frequency band by an electric signal processing circuit.

If many sounds enter a laser beam from different directions, the diffraction patterns appear at different positions in the observing plane as shown in Figure 4(a). This property can be used to separate sound signals to each incident direction and/or control the sound receiving directivity by using a divided multiple photo-detector, as shown in Figure 4(b), or an optical fiber bundle connected to photo detectors, as shown in Figure 6 in the next chapter.

3. EXPERIMENTAL APPARATUS AND METHOD

The experimental apparatus is shown in Figure 5 where a visible diode laser (wavelength 635 nm, output power 25 mW) was used. The radius of laser beam is 1.5 mm. The optical Fourier transform and setting of light diffraction pattern size are controlled by three lenses in front of the observing plane. The radius of laser beam at detection plane is about 1.6 mm. Two low-frequency ultrasonic oscillators of 25 kHz (diameter 16 mm) and 40 kHz (diameter 16 mm) are used as sound sources. Sounds are perpendicularly injected to the laser beam. As shown in Figure 5, the ultrasonic oscillators of 40 kHz is attached to metal ring (diameter 100 mm) and rotated from 0° to 360° around the optical axis. The incidence angle 0° is set just above the laser beam. The 40 kHz sound source is rotated to clock hand rotation direction. The sound source of 25 kHz is fixed at angle of 180° (just below the laser beam) and 60 mm apart from the metal ring position. As the laser

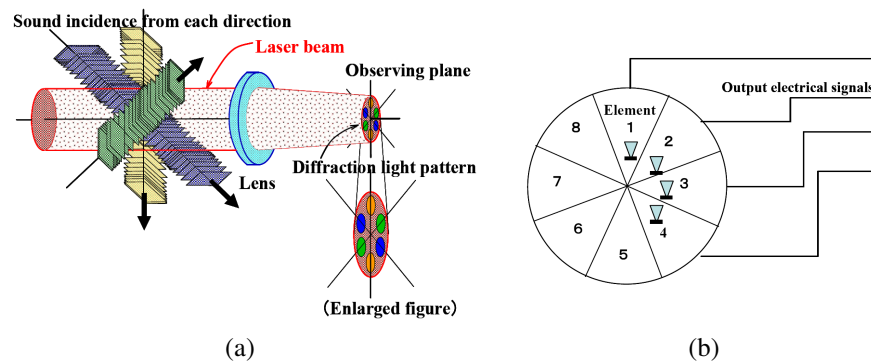


Figure 4: Relation between sound incidence direction and diffraction light pattern. (a) Physical image. (b) Control of directivity by multiple photo detectors.

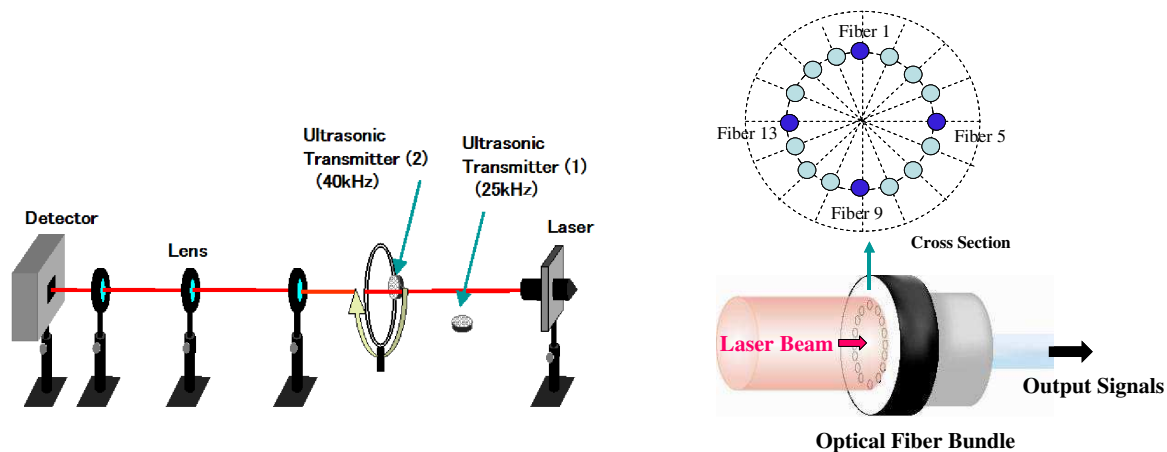


Figure 5: Experimental apparatus.

Figure 6: Optical fiber bundle.

beam is parallel beam in the sound injection area, the sensitivity is same at two injection positions of 25 kHz and 40 kHz sounds. A 1/4 inch electrostatic microphone is used as a monitor of sound pressure level. The sound pressure level at the laser beam position is set 90 dB for both 25 kHz and 40 kHz. The output of photo-detector is input to a preamplifier and a band path filter and finally measured by a FFT analyzer or a digital oscilloscope with a computer.

The abstract of optical fiber bundle used in the light detection part of optophone is shown in Figure 6, where 16 fibers of 0.2 mm diameter are set on the circle of 3 mm diameter. The fiber is connected to avalanche photodiode module with a FC connector.

4. EXPERIMENTAL RESULTS

Experiment using an optical fiber bundle shown in Figure 6 in optical signal detection part was carried out. The sound source of 25 kHz was used and fixed at incidence angle of 180°. The result is shown in Figure 7 in which the signal intensities from each fiber are plotted at each fiber position (or angle) on a circle. The signal has the maximum value at fiber No. 1 (0°) and the minimum at fiber No. 5 (90°). It is found that if a single fiber is used, the bidirectional property is obtained, which is similar to the experimental result using a single photodiode.

In the next experiment, the sound source of 25 kHz was fixed at incidence angle of 180° and the 40 kHz source was fixed at 90°. The experimental result is shown in Figure 8. The signal of 40 kHz has the maximum value at fiber 5 (90°) and fiber 13 (270°) and is nearly zero at fiber 1 (0°) and fiber 9 (180°). The shape of plotted line is similar to a bidirectional curve. Inversely, the signal of 25 kHz has the maximum value at fiber 1 (0°) and fiber 9 (180°) and is nearly zero at fiber 5 (90°) and fiber 13 (270°).

By the experimental result described above, it is shown that when the incidence angle difference between two sound waves is about 90°, nearly perfect separation of these can be achieved. If the incidence angle difference becomes smaller than 90°, the performance becomes a little less good.

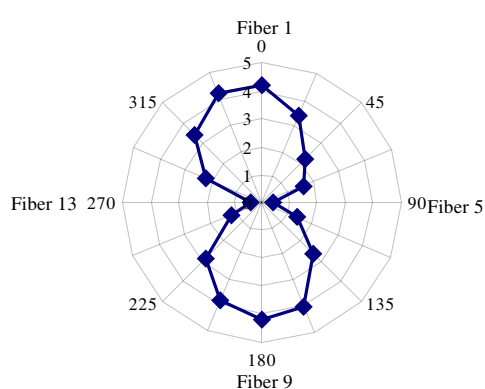


Figure 7: Output signal intensity of each optical fiber.

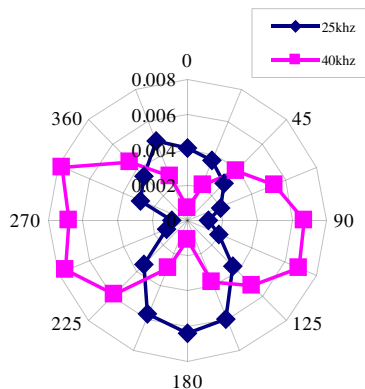


Figure 8: Output signal intensity of each optical fiber for two sounds with different frequency and different incidence angle.

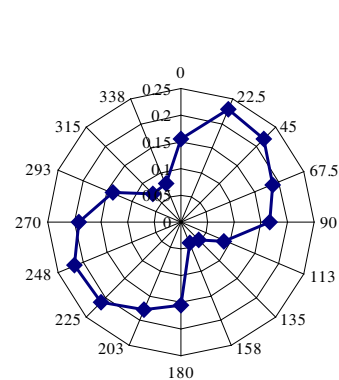


Figure 9: Synthesized directivity by two optical fibers.

From a view of directivity control, the bidirectional property of $\pm 40^\circ$ is obtained in case of using a single fiber. The 16ch fibers positioned on a circle compose a set of sound sensor, each of which has bidirectional directivity and maximum sensitivity at the radius direction (or on the line connecting the center of fiber bundle and the fiber position).

Next experiment synthesizing output signals from some fibers was carried out. The optical fibers of No. 1 and No. 5 were used and output electrical signals from these were electrically added by using audio transformers. The sound source of 40 kHz was rotated around the laser axis. The output signal intensity for each incidence angle is plotted on Figure 9. It is found that the maximum point of the synthesized directivity is around 45° and the directivity wider than Figure 7 is obtained.

From these results, if many fibers output signals from No. 1 to No. 8 are used, we can realize a variable directivity or a hand control sound receiver by synthesizing some of output signals from the 16ch fibers.

5. CONCLUSION

The final purpose of this study is to establish the separation measurement method of sounds with different incidence angle and the hand control method of sound receiving directivity. The main result obtained in the present study is as follows: 1) Experiments using an optical fiber bundle with 16ch fibers set on a circle of 3 mm diameter as optical detectors to measure the diffraction light generated by sounds with different incidence angle were carried out 2) Two sounds injected with incidence angle difference of 90° can be separated by using two fibers set at 0° and 90° , respectively. 3) It is possible to control the receiving directivity by synthesizing the output electrical signals from some fibers.

ACKNOWLEDGMENT

The authors acknowledge the supports of the Grant-in-Aid for Scientific Research (C; No. 22560429) from Japan Society for the Promotion of Science.

REFERENCES

1. Goodman, J. W., *Introduction to Fourier Optics*, 3rd Edition, Roberts & Company Publishers, 2005.
2. Sonoda, Y., "Direct detection of acoustic waves by laser light diffraction and proposals of the optophone," *Proc. 16th Int. Cong. on Acoust. and 135th Meet. of Acoust. Soc. America*, Vol. 1, 427–428, 1996.
3. Evans, D. E., M. von Hellermann, and E. Holzauer, "Fourier optics approach to far forward scattering and related refractive index phenomena in laboratory plasmas," *Plasma Phys.*, Vol. 24, 819–834, 1982.
4. Sonoda, Y., Y. Suetsugu, K. Muraoka, and M. Akazaki, "Applications of the Fraunhofer-diffraction method for plasma-wave measurements," *Plasma Phys.*, Vol. 25, 1113–1132, 1983.

5. Sakoda, T. and Y. Sonoda, “Visualization of sound field with uniform phase distribution using laser beam microphone coupled with computerized tomography method,” *Acoustical Science and Technology*, Vol. 29, No. 4, 295–299, 2008.
6. Sonoda, Y. and Y. Nakazono, “Development of optophone with no diaphragm and application to sound measurement in jet flow,” *Advances in Acoustics and Vibration*, Vol. 2012, Article ID 909437, 17 pages, 2012.

Visualization of Electric Discharge Sound Fields in Atmospheric Pressure Plasma Using Fraunhofer Diffraction

Toshiyuki Nakamiya¹, Fumiaki Mitsugi², Yoichiro Iwasaki¹, Tomoaki Ikegami²,
Ryoichi Tsuda¹, and Yoshito Sonoda¹

¹Graduate School of Industrial Engineering, Tokai University
9-1-1, Toroku Higashi-ku, Kumamoto 862-8652, Japan

²Graduate School of Science and Technology, Kumamoto University
2-39-1, Kurokami Chuo-ku, Kumamoto 860-0082, Japan

Abstract— The Most of electric discharges emit acoustic (20 ~ 20,000 Hz) and ultrasonic (over 20 kHz) waves. Continuous and pulsed voltages initiate the electric breakdown which generates pressure deviation from equilibrium pressure. The sound waves are generated by the pressure change causing local compression and rarefaction. We have examined the sound signals which are emitted from the discharge area. Because the sound signals contain about the information of discharge and atmospheric condition around the discharge.

However, it's not easy to detect the sound signal in plasma reactor by the conventional condenser microphone technique. Therefore, we have developed a new diagnostic method, in which sound wave is measured by an optical sensor based on a Fraunhofer diffraction effect between the sound wave and laser beam. The light diffraction technique, which we call the “Optical Wave Microphone (OWM)” technique, is an effective sensing method to detect the sound. This technique is very useful to detect the sound wave without disturbing the sound field. Moreover, OWM can be applied for the visualization of sound field by computerized tomography (CT) because the ultrasmall modulation by the sound field is integrated along the laser beam path.

1. INTRODUCTION

Atmospheric pressure plasmas are used in various fields such as the formation of nanocarbon-based materials [1], coating and modification of materials [2], ozone synthesis, pollution control including the removal of the environmental pollutant [3] and biomedical applications [4]. For the successful applications, plasma parameters need to be obtained for better understanding of the interactions between plasma and process material. Spectroscopic or electric diagnostics have the limitation in the investigations of discharge behavior such as distribution of electric field and plasma particles over discharge gap. Therefore, we have focused on the discharge sound from energetic aspect. The sound signals contain about the information of discharge and atmospheric condition around the discharge [5].

In the previous study [6, 7], we introduced a novel sound detection technique of Optical Wave Microphone (OWM) and applied to detect the sound of atmospheric pressure discharges such as gliding arc discharge and DBD. Moreover, we developed the computerized tomography technique to show the two-dimensional sound field visualization for coplanar DBD in air. The OWM is based on a Fraunhofer diffraction effect between sound wave and laser beam. This new method can realize high accuracy measurement of slight density change of atmosphere without disturbing electric and sound field [8]. In addition, it can be applied for the visualization of sound field using computerized tomography (CT) method because it integrates sound field along the laser beam path [9].

2. PRINCIPLES OF OWM-CT METHOD

Fundamental optical setup of OWM including the definition of the coordinates is shown in Fig. 1. When the incident probing laser beam crosses perpendicular to refractive index change such as sound wave, the diffracted waves are generated. They propagate with the penetrating beam through the Fourier optical system and reach the back focal plane, which is set at the Fraunhofer diffraction region. The sound wave is assumed to be a plane wave. It can be considered that the diffracted optical waves are homodyne-detected by using the penetrating optical wave as a local oscillating power. The intensity of diffracted waves of higher orders is much smaller than that of the first order wave and can be neglected. We are calling this setup the OWM system. The time-dependent component of the spatial intensity (I_{ac}) along z_f -axis is given by the following equation [10].

$$I_{ac} = I_0 \Delta \phi_0 \left[\exp \left\{ - \left(u^2 + (u - n)^2 \right) \right\} - \exp \left\{ - \left(u^2 + (u + n)^2 \right) \right\} \right] \sin \omega p t \quad (1)$$

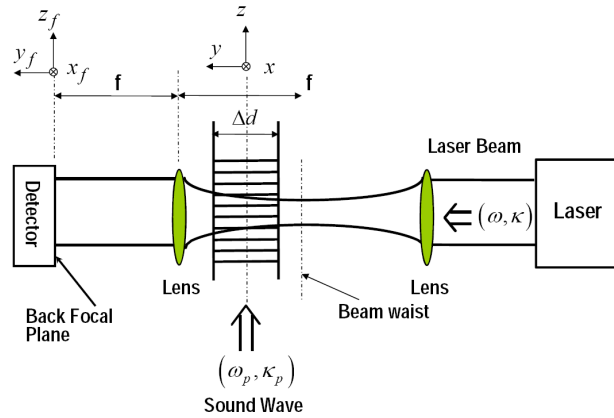


Figure 1: Fundamental optical setup of OWM.

where $I_0 = (2P_0/\pi W_f^2) \exp[-2(y_f/W_f)^2]$,

$$\Delta\phi_0 = \frac{\kappa_i (\mu_0 - 1) \Delta d \Delta p}{\gamma p},$$

u : normalized z -coordinate in the back focal plane (z_f/ω_f), n : normalized wave number ($k_p\omega_0/2$), ω_f : beam waist in the focal plane, k_p : wave number of refractive index change ($2\pi/\lambda_p$), ω_0 : spot size of laser, ω_p : the angular frequency of refractive index change, P_0 : laser power, k_i : wave number of laser beam ($2\pi/\lambda_i$), λ_i : wave length of laser, μ_0 : reflective index of atmosphere, Δd : width of sound wave, Δp : sound pressure, γ : specific heat ratio, p : atmospheric pressure.

If the sound pressure distribution $\tilde{p}(\rho)$ is integrated along the ρ -axis for the interaction length (L) between the sound wave and laser beam, Eq. (1) is rewritten as

$$I_{ac} = I_0 \Delta\phi_0 \left[\exp \left\{ - \left(u^2 + (u - n)^2 \right) \right\} - \exp \left\{ - \left(u^2 + (u + n)^2 \right) \right\} \right] \sin \omega_p t \int_L \tilde{p}(\rho) d\rho. \quad (2)$$

CT method can reconstruct a cross-sectional image of sound field using projected data from 0 to 180 degrees.

Figure 2 shows the relation between x - y and x' - y' coordinates. The two-dimensional sound field $S(x, y)$ along the propagation direction of the sound signal is the analytical area. If the output voltage signal of the OWM is proportional to I_{ac} or $\Delta p \Delta d$ is normalized by the maximum signal amplitude, the detected signal, i.e., the projected data $D(\rho, \theta)$ along the interaction length (L) between the laser beam and the sound field, can be written as

$$D(\rho, \theta) = \int_L S(x, y) dx dy, \quad (3)$$

θ : rotated angle from x - y coordinates to x' - y' coordinates.

The reconstruction image can be obtained by inversely projecting the data to the x - y coordinates, in which the filtered back-projection method and Lamp filter function are used as the reconstruction algorithm [19].

3. EXPERIMENTAL APPARATUS AND RESULTS

Figure 3 shows the experimental apparatus to detect the sound signal from coplanar DBD using OWM-CT. The electrodes module was set up between the diode laser and Lens 1, which was mounted on a $x - \theta$ stage. The center position of the electrodes module was set to be $x = 0$ mm with $z = 0$ mm (electrodes module surface). The proving laser beam (685 nm, 28 mW, $\phi 2$ mm) of OWM passed through above the electrodes module. The distance of the laser beam and the electrodes module was set 2 cm. The sound signals generated by the electrodes module crossed the laser beam between the diode laser and Lens 1. The diffracted laser beam was performed the optical Fourier transform by the Lens 1 and detected by the photodiode detector. The diameter of the laser to reach to the photodiode detector was adjusted by the beam expander (Lens 2 and Lens 3). The acoustic signals detected by OWM were stored in the digital oscilloscope (Tektronix

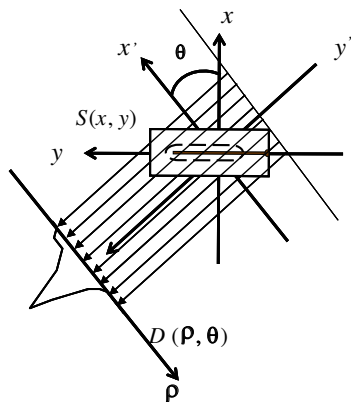


Figure 2: Top view of electrodes module and relation between the coordinates of (x, y) and (x', y') .

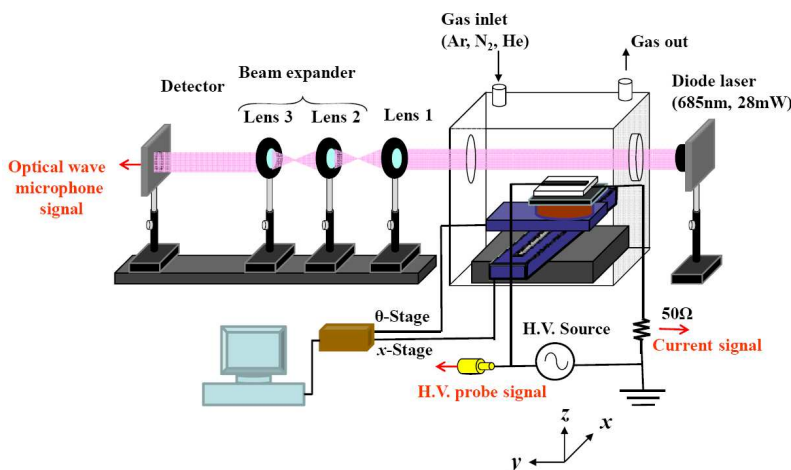


Figure 3: Experimental setup to detect the sound of coplanar DBD using OWM-CT.

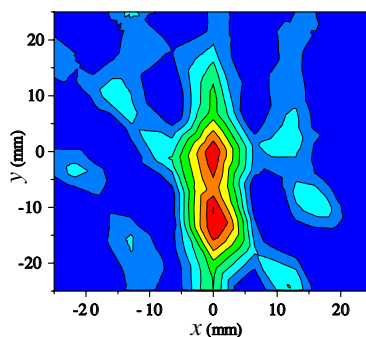


Figure 4: Reconstructed distribution of the discharge sound in the x - y plane (Top view) in Ar atmosphere. The area of the strong sound pressure is shown by bright color. HV electrodes is located in $x = 0$ mm, $y = -25$ to 4.5 mm.

TDS3034) and analyzed. To obtain projection data for CT analysis, the sound field was rotated in the θ direction and moved toward the x direction. The rotation step angle was set to 20 degrees from 0 to 180 degrees, and the driving range in the x direction was from $x = -25$ to 25 mm with the step length of 5 mm.

The reconstruction image could be obtained by inversely projecting the data to the x - y coordinates. Figure 4 shows a reconstructed distribution of the discharge sound field on the x - y plane in Ar atmosphere. The applied voltage was 5 kV_{p-p} with the frequency of 45 kHz. The strongest sound field was observed at just above the top electrode along the y direction and the strong sound area was separated in two peaces.

4. CONCLUSION

The OWM was very convenient to detect the acoustic and the ultrasonic wave generated by coplanar DBD. We applied the CT method to the OWM and could clarify the strong sound pressure area which was located around the electrodes of coplanar DBD in Ar atmosphere.

ACKNOWLEDGMENT

This work was supported by the Japan Grant-in-Aid for Scientific Research (23560510), the Japan Science and Technology Agency (15-138), and the Research and Study Project of Tokai University Educational System General Research Organization.

REFERENCES

1. Kyung, S., Y. Lee, C. Kim, J. Lee, and G. Yeom, "Deposition of carbon nanotubes by capillary-type atmospheric pressure PECVD," *Thin Solid Films*, Vol. 268, 506–507, 2006.

2. Dubreuil, M. F. S., E. M. Bongaers, and P. F. A. Lens, “Incorporation of amino moieties through atmospheric pressure plasma: Relationship between precursor structure and coating properties,” *Surface & Coatings Technology*, Vol. 206, 1439, 2011.
3. Doubla, A., S. Laminsi, S. Nzali, E. Njoyim, J. Kamsu-Kom, and J.-L. Brisset, “Organic pollutants abatement and biodecontamination of brewery effluents by a non-thermal quenched plasma at atmospheric pressure,” *Chemosphere*, Vol. 69, 332, 2007.
4. Seo, Y. S., H. W. Lee, H. C. Kwon, J. Choi, S. M. Lee, K. C. Woo, K. T. Kim, and J. K. Lee, “A study on characterization of atmospheric pressure plasma jets according to the driving frequency for biomedical applications,” *Thin Solid Films*, Vol. 519, 7071, 2011.
5. Nakamiya, T., K. Ebihara, T. Ikegami, Y. Sonoda, and R. Tsuda, “Acoustic signal analysis in the creeping discharge,” *Journal of Physics: Conf.*, Vol. 100, 062016, 2008.
6. Nakamiya, T., F. Mitsugi, S. Suyama, T. Ikegami, Y. Sonoda, Y. Iwasaki, and R. Tsuda, “Investigation of electric discharge sound in atmospheric pressure plasma,” *Journal of AOT's*, Vol. 13, 43–49, 2010.
7. Nakamiya, T., Y. Iwasaki, F. Mitsugi, R. Kozai, T. Ikegami, Y. Sonoda, and R. Tsuda, “Investigation of electric discharge sound in atmospheric pressure plasma using optical wave microphone,” *J. Adv. Oxid. Technol.*, Vol. 14, 43, 2011.
8. Sonoda, Y. and M. Akazaki, “Measurement of low-frequency ultrasonic waves by fraunhofer diffraction,” *Jpn. J. Appl. Phys.*, Vol. 33, 3110–3114, 1994.
9. Sakoda, T. and Y. Sonoda, “Visualization of sound field with uniform phase distribution using laser beam microphone coupled with computerized tomography method,” *Acoust. Sci. & Tech.*, Vol. 29, No. 4, 295, 2008.
10. Nakamiya, T., Y. Sonoda, T. Ikegami, F. Mitsugi, K. Ebihara, and R. Tsuda, “Measurement of electric discharge sound by Fraunhofer diffraction and analysis,” *Przegląd Elektrotechniczny (Electrical Review)*, Vol. 2009, No. 5, 143–146, 2009.
11. Gonzalez, R. C. and R. E. Woods, *Digital Image Processing*, Pearson Education, NJ, 2008.

An Overview of Metamaterials in Biomedical Applications

S. Raghavan and V. Rajeshkumar

Department of Electronics and Communication Engineering
National Institute of Technology, Tiruchirappalli 620015, India

Abstract— Communication technologies and biomedical sensors can provide services for the patient's vital signs to be monitored outside the clinical environment. The need for implantable telecommunication devices for medical applications has been growing rapidly over the past ten years. Microwave antennas and sensors are key components of telemetry systems related to medical applications. Metamaterials are artificial materials which have the electromagnetic properties that may not be found in nature. The unusual properties of a metamaterial have led to the development of metamaterial antennas, sensors and metamaterial lenses for miniature wireless systems which are more efficient than their conventional counterparts. Metamaterials exhibit a very sensitive response to the strain, dielectric media, chemical and biological sensing applications. A wide area of biomedical applications using metamaterials has been discussed in this review. The design concept of metamaterial antennas in ISM band is presented. Later, the fundamental theory and recent progress of metamaterial in sensors, lenses and absorbers are reviewed for various healthcare applications towards its practical implementation.

1. INTRODUCTION

In Recent years, need for the deployment of wireless telemetry systems in medicine has significantly increased due to necessity for early diagnosis of diseases and continuous monitoring of physiological parameters. Microwave antennas and sensors are key components of these telemetry systems since they provide the communication between the patient and base station. Metamaterials can have their electromagnetic properties altered to something beyond what can be found in nature. Hence metamaterials have been attracted great interest among microwave engineers and physicists, due to showing exotic electromagnetic properties at microwave frequencies. A split-ring resonator (SRR) is one of the metamaterial particles that offer negative permeability [1], while complementary split-ring resonator (CSRR), the duality of SRR, interacts with the electric field and introduces negative permittivity [1], which are most commonly used in biomedical sensors. It is well known that SRRs are resonant structures, and consequently, it is possible to employ these resonances as well as radiating modes. SRRs are very compact and it is easy to design them with dual band characteristic. The review of metamaterials towards various healthcare applications is described in the subsequent sections.

2. METAMATERIAL ANTENNAS FOR ISM BAND

The Industrial, Scientific and Medical (ISM) radio bands are portions of the radio spectrum reserved internationally for the use of radio frequency (RF) energy for industrial, scientific and medical purposes other than communications. By using metamaterial like EBG (Electromagnetic Band Gap) structures in slotted microstrip antenna the increased efficiency and better return loss characteristics can be achieved [2]. A patch antenna with slotted ground plane has been developed in which EBG structure is used as a metamaterial above the ground plane. The designed antenna has suitable characteristics at two frequency bands (2067–2245 MHz) covering UMTS band and (2390–2795 MHz) covering ISM band [2].

A wireless endoscope is a capsule-shaped system used for gastrointestinal monitoring and/or treatment. A 2.4-GHz ISM-band folded patch antenna is designed, fabricated, and characterized by Xiaoyu Cheng et al. for a wireless capsule endoscope application. A CSRR loaded patch has been fabricated on a flexible substrate and folded in a cylindrical shape, forming a self-packaged folded patch antenna with a quasi-omnidirectional radiation pattern [3]. The designed CSRR loaded patch, featuring compact size, EMI shielding and quasi-omnidirectional radiation pattern for a wireless endoscope [3]. The CSRR contributes a 74% size reduction compared to its traditional patch counterpart without CSRR loading [3]. The large enclosed space would be available for placing digital controllers, EMI sensitive sensors, cameras, batteries, or drug delivery systems [3].

A high gain pencil beam array antenna for the applications within the 24 GHz ISM band has been designed by A. Rennings et al. [4]. The high-gain pencil-beam array antenna based on composite right/left-handed (CRLH) metamaterial transmission-lines, referred as CRLH meta-lines.

A metamaterial-inspired handset antenna designed to reduce the specific absorption rate (SAR) for mobile communication. The SAR reduction was achieved by miniaturizing the physical size of the antenna for the resonance frequency of 2.4 GHz, by devising a metamaterial-inspired radiator much smaller than the conventional planar inverted F antenna (PIFA) [5]. Further, the dual band microstrip patch antenna has been designed for implantable medical devices, which covers the ISM (2.4–2.48 GHz) band. The antenna has a multilayer configuration where the feeding line and the radiating elements are located at different levels. The radiating elements of the antenna are a split ring resonator (SRR) coupled to a spiral and both elements are short-circuited to the ground plane to achieve size reduction [6].

3. METAMATERIALS IN CANCER DETECTION

Cancer is the uncontrolled growth of abnormal cells in the body, called as malignant cells. By developing microwave devices and combining it with structures inspired by metamaterials, it can lead to a very cost-effective device that can localize with high precision an abnormality within the human body. The basic principle behind the cancer detection is, a small change in the water content of biological tissues produces changes in the permittivity (ϵ) and conductivity (σ) values of the tissues [7]. The malignant cells have significantly higher water content than normal tissues. Hence the permittivity and the conductivity of the tumor are higher than those ones of a normal tissue at microwave frequencies. The proposed biosensor consists of an array of complementary metallic metamaterial resonators. The reason for choosing SRRs are their strong response to an electromagnetic field [7].

An electromagnetic source generates an electromagnetic wave impinging on the metamaterial array and a detector is placed to reveal the signal after the array. The biosensor without any material under test has a specific resonant frequency [7]. The variation of the permittivity caused by the presence of the material under test, acts on the capacitance of the resonators, leading to a high-sensitive variation of the sensor resonant frequency. Thus the shift in resonant frequency and the shape of the response is extremely useful to detect the tumor. Further, the frequency multiplexed two dimensional sensor array based on SRR for organic tissue analysis has been proposed by Margarita Puente et al.. A frequency multiplexed 2-dimensional sensor array was developed using microstrip-line excited SRRs which are designed to have different resonant frequencies is shown in Fig. 1(a) [8]. Therefore the resonant frequency of individual SRR will indicate the dielectric properties of the MUT around the ring and also its location within the array [8].

4. METAMATERIALS IN MEDICAL IMAGING

A super lens or perfect lens is a lens which uses metamaterials to go beyond the diffraction limit. The diffraction limit is an inherent limitation in conventional optical devices or lenses. In 2000, a type of lens was proposed, consisting of a metamaterial that compensates for wave decay and reconstructs images in the near field [9]. And most importantly the both propagating and evanescent waves contribute to the resolution of the image. In 2004, the first superlens with a negative refractive index provided resolution three times better than the diffraction limits and was demonstrated at microwave frequencies. In 2005, the first near field superlens which exceeded the diffraction limit was demonstrated by N. Fang et al. [10].

The higher focusing resolution will be provided by flat left-handed metamaterial (LHM) lens if compared to convex dielectric lens and elliptical reflector focusing system. High-resolution near-field microwave target detection and imaging with flat LHM lens can be implemented which is shown in Fig. 1(b) [11]. Due to higher focusing resolution the LHM lens has the potential to acquire higher imaging resolution and easy in-depth scanning, which will simplify the detection system design [11].

5. METAMATERIALS IN MICROWAVE HYPERTHERMIA

Microwaves are used to destroy or ablate diseased soft-tissue by heating the tissue to a temperature that causes cell death is called hyperthermia. The generator produces microwave energy which is transmitted through the antennas and into the patient. Elevating the temperature of tumor cells causes cell membrane damage, which leads to the destruction of the cancer cells. Hyperthermia treatment of cancer requires directing a carefully controlled dose of heat to the cancerous tumor and surrounding body tissue. The most prominent property of metamaterial lens is the ability of negative-refractive index (NRI) to focus the electromagnetic field of a source [11]. Hence it can generate appropriate focusing spot in biological tissue as required in microwave hyperthermia treatment shown in Fig. 1(c) [12]. Flat metamaterial slab has been used as a lens to focus microwave

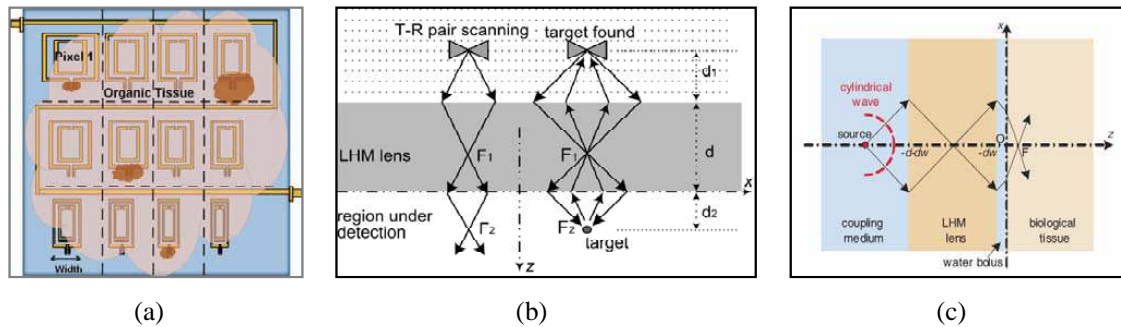


Figure 1: (a) Two dimensional organic tissue analysis. (b) Imaging. (c) Hyperthermia treatment.

energy emitted from the microwave source. In this, a planar array of split-ring resonators placed between two parallel metallic plates and it is fed by a small loop antenna to excite the split-rings [13].

Further the convenient adjustment of position of focusing or heating spot in tissue region gives the great potential to successful microwave hyperthermia [14]. By moving the source, the heating spot in tissue can be adjusted, without any complex deployment and control system as required in the conventional array applicator [12]. Recently, conformal microwave array applicators proposed with proper source spacing, low loss left-handed metamaterial lens can be useful for hyperthermia treatment of large area tumors. In this, microwave hyperthermia can be performed by joint heating of multiple microwave sources [14].

6. METAMATERIALS IN WIRELESS STRAIN SENSING

RF-microelectromechanical systems (MEMS) strain sensors that take advantage of the recent advances in metamaterials. A wireless strain sensor to monitor the healing processes of fractured long bones has been developed by R. Melik et al.. Approximately 10% of the fractures do not heal properly because of the inability to monitor fracture healing. The SRR-based sensor displays a characteristic resonance frequency under no load, by measuring the magnitude of operating frequency shift under applied load; the progression of fracture healing can be monitored [15]. Initially, the single SRR based wireless metamaterial strain sensor was developed and then the nested SRR based strain sensor developed to enhance the sensitivity. The nested metamaterial-based strain sensors incorporate multiple SRRs in a compact nested architecture on a single chip to significantly achieve enhanced sensitivity in telemetric sensing [16]. By comparing the parameters such as unloaded operating frequency, sensitivity and nonlinearity errors of the nested SRR based strain sensor outperforms the classical SRR sensor [16].

7. METAMATERIAL ABSORBERS FOR SAR REDUCTION

Specific absorption rate is a measure of how much radiation is absorbed by human body, given in Watts per kilogram (W/kg). The basic principle behind the metamaterial absorbers is, when one of the effective medium parameter is negative and the other is positive, the medium will display a stop band. The stop band of metamaterials can be designed at operating bands of cellular phone. The SRRs has been designed to operate at 900 and 1800 MHz bands [17]. The structure parameters of SRRs were chosen in order to be the effective medium parameter is negative around 900 and 1800 MHz bands. The use of metamaterial absorber is compared with other SAR reduction techniques such as ferrite sheet attachment and the use of perfect electric conductor which shows the use of metamaterials can reduce the peak for 22.2% [17]. The ferrite sheet attachment can reduce the peak SAR effectively but the degradation on radiated power from antenna is also significant. Compared to the use of ferrite sheet, the metamaterials can be designed at the desired operating frequency. The metamaterials can be designed on circuit board so it may be easily integrated to the cellular phone [17].

8. CONCLUSION

There is growing need for engineers and physicists to concentrate and develop equipments specifically suitable for healthcare. Metamaterials is one of the active field of research in the past decade which has potential application in healthcare. This paper summarizes the extensive use of metamaterials in biomedical applications. In particular, an overview of the existing metamaterial antennas designed to operate at ISM band and the use of metamaterials in cancer detection, imaging, mi-

crowave hyperthermia, strain sensing, and reduction of SAR are presented. Apart from these, metamaterials are also applied in glucose monitoring for diabetes management. Also, the use of resorbable metamaterials will overcome the issues associated with retrieval of implantable devices after their operational lifetime. The metamaterials in biomedical applications opens a wide area of research in the near future.

REFERENCES

1. Pendry, J. B., A. J. Holden, D. J. Robbins, and W. J. Stewart, "Magnetism from conductors and enhanced nonlinear phenomena," *IEEE Trans. on Microwave Theory and Tech.*, Vol. 47, No. 11, Nov. 1999.
2. Kumar, H., R. K. Kanth, P. Liljeberg, and H. Tenhunen, "Metamaterial based slotted patch antenna," *IEEE 10th International Conference on Telecommunication in Modern Satellite Cable and Broadcasting Services (TELSIKS)*, 43–46, 2011.
3. Cheng, X., E. David, C. Kim, and Y.-K. Yoon, "A compact omnidirectional self-packaged patch antenna with complementary split-ring resonator loading for wireless endoscope applications," *IEEE Antennas and Wireless Propagation Letters*, Vol. 10, 1532–1535, 2011.
4. Rennings, A., B. Zhou, A. Al-Bassam, Z. Chen, S. Otto, K. Solbach, and D. Erni, "Metabeam: A high-gain pencil-beam array antenna based on corporately fed CRLH meta-lines for the 24 GHz ISM band," *IEEE Microwave Conference (GeMIC)*, 1–4, German, 2011.
5. Kahng, S., K. Kahng, D. Eom, B. Lee, S. Mok, S. Yoo, J.-G. Kim, J.-H. Cho, and K. Kim, "A metamaterial-inspired handset antenna with the SAR reduction," *IEEE Int. Symp. on Components, Circuits, Devices & Systems*, 307–310, 2012.
6. Sanchez-Fernandez, C. J., O. Quevedo-Teruel, J. Requena-Carrion, L. Inclan-Sanchez, and E. Rajo-Iglesias, "Dual-band microstrip patch antenna based on short-circuited ring and spiral resonators for implantable medical devices," *IET Microwaves, Antennas & Propagation*, 1048–1055, 2010.
7. La Spada, L., F. Bilotti, and L. Vegni, "Metamaterial biosensor for cancer detection," *IEEE Sensors*, 627–630, 2011.
8. Puentes, M., M. Maasch, M. Schubler, and R. Jakoby, "Frequency multiplexed 2-dimensional sensor array based on split-ring resonators for organic tissue analysis," *IEEE Trans. on Microwave Theory and Tech.*, Vol. 60, No. 6, 1720–1727, Jun. 2012.
9. Pendry, J. B., "Negative refraction makes a perfect lens," *Phys. Rev. Lett.*, Vol. 85, 3966–3969, Oct. 2000.
10. Fang, N., H. Lee, C. Sun, and X. Zhang, "Sub-diffraction-limited optical imaging with a silver superlens," *Science Magazine*, 2005.
11. Wang, G., J. Fang, and X. Dong, "Resolution of near-field microwave target detection and imaging by using flat LHM lens," *IEEE Trans. Antennas Propag.*, Vol. 55, No. 12, 3534–3541, 2007.
12. Gong, Y. and G. Wang, "Superficial tumor hyperthermia with flat left-handed metamaterial lens," *Progress In Electromagnetics Research*, Vol. 98, 389–405, 2009.
13. Velazquez-Ahumada, M. C., M. J. Freire, and R. Marques, "Metamaterial applicator for microwave hyperthermia," *IEEE General Assembly and Scientific Symposium*, 1–4, 2011.
14. Tao, Y. and G. Wang, "Hyperthermia of large superficial tumor with a flat LHM lens," *IEEE Microwave Symposium Digest (MTT)*, 2012.
15. Melik, R., E. Unal, C. Puttlitz, and H. V. Demir, "Wireless metamaterial RF-MEMS strain sensors," *Appl. Phys. Lett.*, Vol. 95, 2009.
16. Melik, R., E. Unal, N. K. Perkgoz, B. Santoni, D. Kamstock, C. Puttlitz, and H. V. Demir, "Nested metamaterials for wireless strain sensing," *IEEE Journal of Selected Topics in Quantum Electronics*, Vol. 16, No. 2, 450–458, 2010.
17. Hwang, J.-N. and F.-C. Chen, "Reduction of the peak SAR in the human head with metamaterials," *IEEE Trans. Antennas Propag.*, Vol. 54, No. 12, 3763–3770, 2006.

Interfacial Properties of Modified Natural Polysaccharide Carbohydrate Surfactants

Mou-Chuan Hwang¹, Li-Huei Lin², and Wei-Min Hwang¹

¹Department of Materials and Textiles, Oriental Institute of Technology
Pan-Chiao City, Taipei County 22061, Taiwan, R.O.C.

²Department of Cosmetic Science, Vanung University
Chung-Li City, Taoyuan County 32061, Taiwan, R.O.C.

Abstract— New natural polysaccharide carbohydrate derivatives of sodium alginate surfactants were prepared by condensation of sodium bisulfite onto the polysaccharide linkages at different hydrophobic chain of Fatty acids. We were synthesis and solution properties of hydrophobically modified alginate-ester derivatives in which dodecyl or octadecyl chains were grafted onto the polysaccharide backbone via ester functions. In semi-dilute aqueous solution, intermolecular hydrophobic associations result in the formation of physical networks, the physico-chemical properties of which can be controlled through polymer concentration, hydrophobic chain content and non-chaotropic salts such as sodium chloride. Alginate is a biomaterial widely used in the food industry as thickener and in biotechnological applications including cell encapsulation, protein delivery or tissue engineering. Alginate is a negatively charged polysaccharide obtained from marine algae and various bacteria, with solution properties ranging from viscous to gel-like structures in the presence of divalent cations. In this study, the structure of final products was confirmed by FT-IR and ¹H-NMR. The interfacial properties were evaluated by surface tension, foaming properties and conductivity. The result showed that the novel material is capable of encapsulating both hydrophilic and hydrophobic molecules. Crucially, the all-important gelling and non-toxic properties of native alginate have been retained.

1. INTRODUCTION

During the past few years, many natural waters have been polluted by chemicals from various sources. Some of them are surfactants which originate mainly from household detergents, personal care products, washing agents, and processing supplies used in industry. A great deal of work has been done in trying to take into account biodegradability in the use of surfactants [1]. Many natural and processed food products consist either partly or wholly in emulsions whose formation and stability are achieved by the use of emulsifiers. Emulsifiers are commonly used in food emulsion systems to increase their short- and long-term kinetic stability. There is a trend within the food industry to replace synthetic emulsifiers with more natural ones. The most commonly used polysaccharides in food emulsions are gum arabic, modified starch, modified cellulose, galactomannans, and pectin [2–4]. However, these molecules are not particularly surface active and/or have to be used in relatively large quantities to make stable emulsions. Alginate has a number of free hydroxyl and carboxyl groups distributed along the backbone, therefore it is an ideal candidate for chemical functionalization. By forming alginate derivatives through functionalizing available hydroxyl and carboxyl groups, the properties such as solubility, hydrophobicity and physicochemical and biological characteristics may be modified. Alginates are widely used as a gelling agent for thickening foods and cosmetics. Our strategy is based on hydrophobic modification of alginate, which is regarded as an emulsifier used in emulsions [5].

2. EXPERIMENTAL

Figure 1 illustrates the three steps followed to prepare the alginate surfactants. In step 1, Sodium Alginate and Epichlorohydrin (1:1 mol) were mixed evenly at 50°C ~ 60°C for 2 hours (SA-E). In step 2, Myristic Acid and Sodium Bisulfite were mixed evenly at 90°C ~ 100°C for 2 hours (MA-S). Then, In step 3, the SA-E and MA-S were reaction at 100°C ~ 105°C for 2 hours. This raw product was then dissolved in EtOH. The undissolved impurities were filtered off and then the solvents (EtOH and water) were evaporated from the filtrate under reduced pressure in a rotary evaporator. The final product was dried in a vacuum desiccator. The products were purified by using ethanol to remove the impurities; the structure of the final products was confirmed by infrared (IR), proton nuclear magnetic resonance (NMR) spectral analysis. The analyses of the final products are shown in Figure 2 and Figure 3.

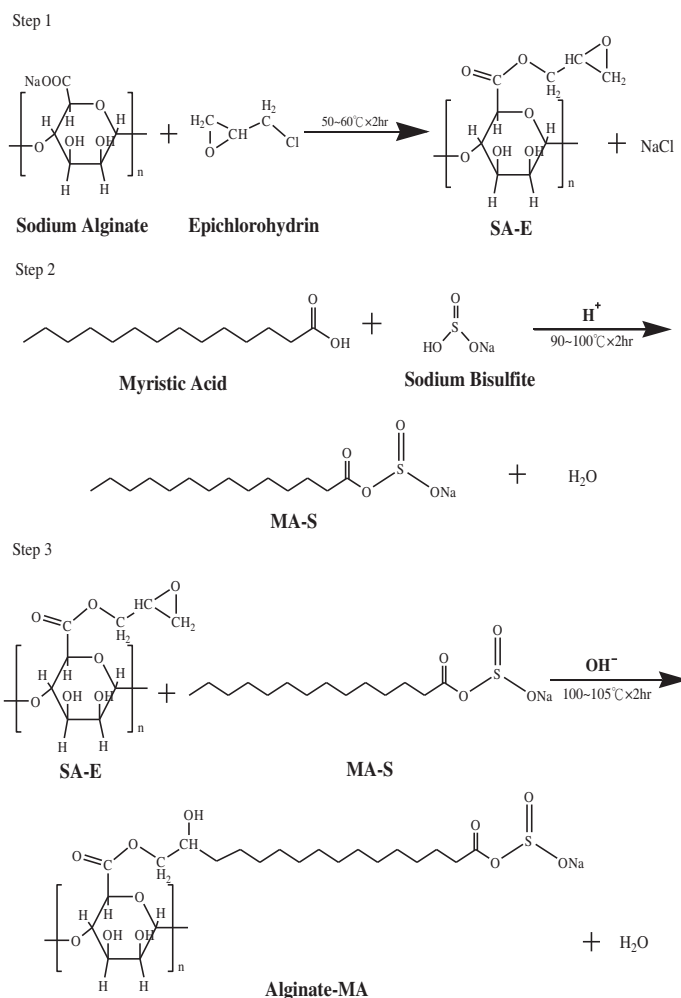


Figure 1: Synthesis of novel alginate-derived surfactants.

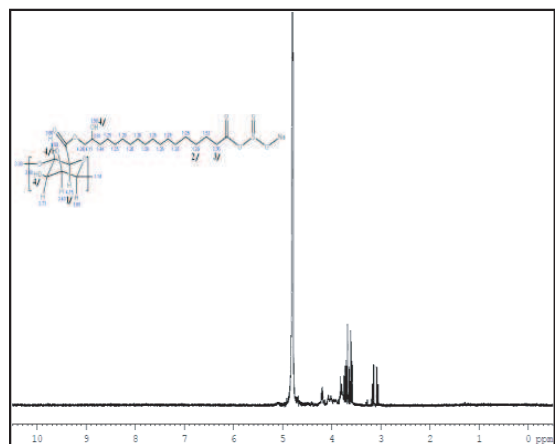


Figure 2: NMR spectra of novel alginate-derived surfactants.

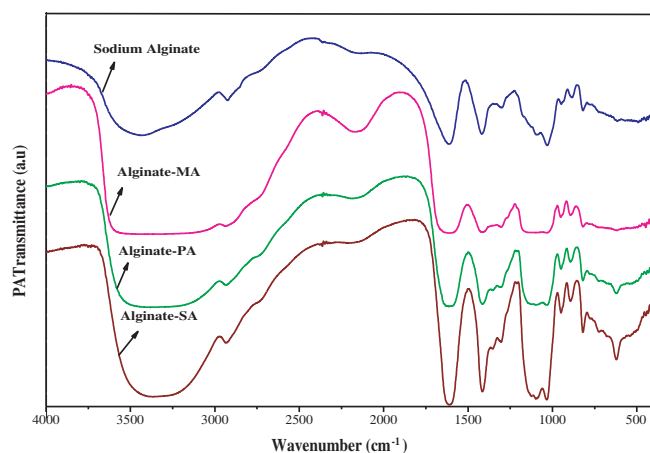


Figure 3: IR spectra of novel alginate-derived surfactants.

Surface tensions were determined at 25°C using a Japan Kaimenkagaku CBVP-A3 surface tensiometer, which was calibrated with ultra-pure water prior to use. The platinum plate was cleaned by flaming, while the glassware was rinsed with tap water and ultra-pure water. Conductivities were measured using a WTW FL538 conductivity meter (cell constant: 0.475 cm⁻¹; Germany). The experimental temperature was maintained at 25°C (water bath) for each series of measurements;

distilled water (50 mL) was added to the bath and the conductivity was then measured after each addition. Foaming properties were determined using the Ross-Miles method. Foam production was measured by the height of the foam produced initially; the foam stability was measured by the height after 3 min.

3. RESULTS AND DISCUSSION

The structures of the addition products were confirmed through IR and NMR spectroscopic analyses. Figure 2 and Figure 3 present the results. The IR spectra display bands at $3,250\text{--}3,500\text{ cm}^{-1}$ (O-H), $3000 \sim 2800\text{ cm}^{-1}$ ($-\text{CH}_2$), $1610 \sim 1560\text{ cm}^{-1}$ (COO^-), $1260 \sim 1210\text{ cm}^{-1}$ and $810 \sim 770\text{ cm}^{-1}$ (ROSO_3^-), $1200 \sim 1000\text{ cm}^{-1}$ (C-OH). The ^1H NMR spectra of these products provided further support for the assigned structures, with signals at $\delta = 4.75$ ($-\text{CH}$, 1/), $\delta = 1.30$ ($-\text{CH}_2-$, 2/), $\delta = 2.30$ ($-\text{CH}_2\text{-CH}_2\text{-C-}$, 3/), $\delta = 3.50 \sim 4.50$ ($\text{R-CH}_2\text{-OH}$, 4/) ppm. Figure 4 reveals the increase in surface tension that occurred for solutions containing the alginate-derived surfactants. Increasing the length of the alkyl chain led to decreased surface activity. More specifically, the increased hydrophobic chain length improved the ability of the alginate-derived surfactants to increase surface tension. The surface tension of the solution decreased upon increasing the concentration of the alginate-derived surfactant, reaching a clear breakpoint that we consider to be the critical micelle concentration (CMC). Figure 5 presents a plot of the conductivity with respect to the surfactant concentration at 298 K. The conductivities increased linearly upon increasing the surfactants' concentrations; in addition, longer hydrophobic chains provided larger conductivities. When micelles are formed, the binding of counter ions to the micellar surfaces reduces the mobility of the micelles relative to that of their monomeric forms. Thus, we would expect some type of discontinuity to appear in the plot of the conductivity versus concentration (i.e., at the concentration where the micelles begin to form).

Recent advances in the design of dyeing machines, such as their having a more rapid circulation of the liquor, have resulted in foam formation commonly occurring in dye baths. This inconvenience has increased the importance of developing low-foaming dyeing auxiliaries. Table 1 lists the low-foaming properties of our surfactants. Each compound exhibited not only low foam production (measured by the height of foam initially produced) but also low-foaming stability (measured by the height after 3 min).

Table 1: Foaming properties of novel alginate-derived surfactants.

	Foam height (cm)	Foam stability (cm)	Defoaming rate (%)
SDS	30.5	26	14.7
Alginate	2	0.75	62.5
Alginate-MA	1.25	0.25	80
Alginate-PA	0.25	0	100
Alginate-SA	0.25	0	100

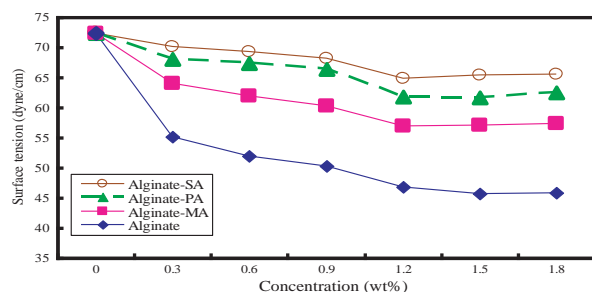


Figure 4: Surface tension plotted with respect to the concentration of novel alginate-derived surfactants.

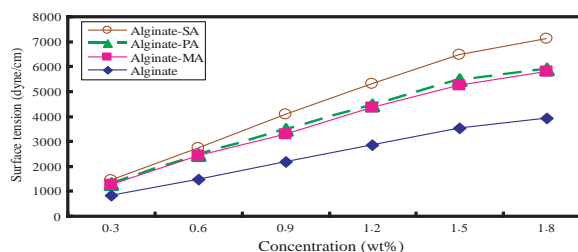


Figure 5: Conductivity plotted with respect to the concentration of alginate-derived surfactants.

4. CONCLUSIONS

We have prepared a novel series of surface-active alginate-derived surfactants through the reaction of alginate with fatty acids. These novel compounds exhibited good surface activities, including good surface tension, wetting ability, and foaming properties. The surface activities of these compounds in aqueous solution increased upon increasing the alkyl chain length in the hydrophobic fragment of the surfactants. Furthermore, we found that the surface activity of the alginate-SA surfactant was poorer than those of the alginate-PA and alginate-MA surfactants, presumably because of the stronger attractive interactions between the hydrocarbon chains of alginate-SA.

REFERENCES

1. Chen, K. M., L. H. Lin, M. Y. Dong, C. F. Wang, and M. C. Hwang, "Preparation and surface activity of phosphated Alkyl oligoglucosides," *Journal of Surfactants and Detergents*, Vol. 13, 417–422, 2010.
2. Ji, S. Y., J. Biao, H. Wen, and M. X. Yong, "Hydrophobically modified alginate for emulsion of oil in water," *Carbohydrate Polymers*, Vol. 87, 1503–1506, 2012.
3. Lin, L. H., K. M. Chen, H. J. Liu, H. C. Chu, T. C. Kuo, M. C. Hwang, and C. F. Wang, "Preparation and surface activities of modified gelatin-glucose conjugates," *Colloids and Surfaces A: Physicochem. and Eng. Asp.*, Vol. 408, 97–103, 2012.
4. Lin, L. H., C. C. Wang, K. M. Chen, and P. C. Lin, "Synthesis and physicochemical properties of casein-derived surfactants," *Colloids and Surfaces A: Physicochem. and Eng. Asp.*, Vol. 346, 47–51, 2009.
5. Su, S. K., L. H. Lin, and Y. C. Lai, "Synthesis and emulsification properties of novel modified polyoxyethylenated stearylamine surfactants," *Colloids and Surfaces A: Physicochem. and Eng. Asp.*, Vol. 414, 26–32, 2012.

Indoor Broadband Spectrum Survey Measurements for the Improvement of Wireless Systems

R. Urban, T. Kriz, and M. Cap

Department of Theoretical and Experimental Electrical Engineering
Brno University of Technology, Kolejní 2906/4, Brno 612 00, Czech Republic

Abstract— This paper presents a unique measurement campaign focused on indoor spectrum survey. This type of results should be used by many ways. Firstly, the spectrum regulators have to know which frequencies are used at the measured locations. Secondly, the spectrum survey data could be used to simulate cognitive systems, which have become a significant part of wireless communication during the past decade. The presented measurement is specific as we used one wideband omnidirectional antenna and a portable receiver which measures the wideband results (9 kHz–7.5 GHz) with sufficient sensitivity (not worse than -113 dBm) in the whole band. The receiver was controlled by a specially designed program that communicates via TCP/IP and therefore provides sufficient connection for downloading an extensive amount of data to the controlling PC. The results are processed to detect the primary users (users of the frequency spectrum) and calculate utilization of the frequency spectrum. Based on the results, the potential for the improvement of wireless traffic is observable. The optimization of the radiated electromagnetic waves has a positive effect on biological tissues.

1. INTRODUCTION

Modern wireless communication is focused on improving data transmission speed and prioritizing specific services (VOIP). The current situation in the overfilled frequency spectrum leads to the use of higher frequency bands [1] and the increase of radiation power. Most of the propagation parameters such as penetration or diffraction are more suitable for lower frequency bands. An increase in the radiation power goes hand in hand with a decrease in the SINR (signal-to-noise ratio including interferences) of the other services. The effects on biological tissues are also discussed in the context of enormous usage of microwave power [2]. According to the spectrum survey measurements, the problem of overfilled frequency spectrum could be solved using a cognitive system, which is mainly represented by dynamic spectrum sharing.

Cognitive radio is an intelligent autonomous system capable of adapting to the current area and time [3, 4]. We could change transmitter parameters such as the operation frequency and radiation power. A prerequisite for correct functioning of the cognitive system is the awareness feature, which is represented by sensing of the environment. These data are managed by a cognitive engine that controls available resources. In a cognitive system, we define primary users (wireless devices using the spectrum according to the assigned licence) and secondary or cognitive users (new entrants to the shared frequency spectrum whose traffic is coordinated by the cognitive engine). It is obvious that the spectrum sensing is a crucial feature for correct operation of the cognitive radio. Real-time wideband spectrum sensing is still one of the main challenges for system developers. Therefore cognitive radio is now working in limited bands [5] and simulations are provided in a large scale. For the simulations it is necessary to obtain the data related to the frequency spectrum utilization [6, 7].

These offline spectrum scans (spectrum surveys) are prepared mainly for outdoor scenarios and measured in a limited bandwidth given by the antennas. We prepared an indoor measurement campaign to be realized by means of a wideband receiver with sufficient sensitivity and a wideband double disc antenna. This setup provided us with sufficient measurement speed and dynamics. Fast scans are very important for monitoring the time development of white spaces. White space is an unused part of the frequency spectrum at the current location and time. Wireless traffic is routed to these free bands by the cognitive engine, which is essential for dynamic spectrum sharing [8].

This paper is organized as follows: Firstly, short measurement description including the scenario description is provided. Secondly, evaluation of the measurement is presented. Finally, the conclusion part summarizes the obtained results.

2. MEASUREMENT DESCRIPTION

Generally, the measurement setup (Figure 1) was designed for measurements up to 7.5 GHz; in reality, however, we concentrated on indoor wireless systems that are mainly located in frequency

bands up to 3 GHz. The presented measurement system offers several advantages: It is portable, fast and sensitive. The omnidirectional wideband antenna has suitable parameters in the frequency band from 100 kHz to 12 GHz. The wideband, battery powered receiver R&S PR100 [9] is designed for the frequency range of 300 kHz–7.5 GHz with the worst sensitivity of -113 dBm (RBW 12.5 kHz, the worst value in the measured band). We controlled the receiver by native commands from the controlling laptop through the TCP/IP protocol. The communication was established via a shielded, noise minimizing Ethernet cable.

We measured at urban indoor locations (Figure 2) such as a lecture hall, a public library or as hopping mall. We also considered the effect of people present in the area. In all the measurements the antenna was placed on a tripod at the reference height of 1.5 meter above the floor. While most wireless communication is located up to 3 GHz, we measured in the band from 100 MHz to 3 GHz. We also measured several significant bands in greater detail (e.g., the WI-FI band). The resolution of the receiver was set to the values of 1250 Hz or 12500 Hz respectively.

A very important parameter is also the scanning repetition rate. We are able to scan at the speed of 6.4s per 1 GHz with the resolution rate of 1250 Hz and at 0.88s per 1 GHz with there solution rate of 12500 Hz respectively. Such fast frequency scans are crucial in terms of considering other factors for the cognitive system evolution (such as time evolution).

2.1. Calibration and Data Post-processing

The calibration process was realized in several consecutive steps. Firstly, it was necessary to prepare the calibration measurement. We placed the entire measurement setup into the anechoic chamber (Figure 1) and ran the measurement. The calibration baseline was estimated as the average (Figure 3) of more than 200 consecutive samples within the whole bandwidth (100 MHz up to 3 GHz). The anechoic chamber guaranteed the isolation of -110 dB from the outside environment, which provided a sufficient value for our measurements.

During the post-processing we subtracted the calibration data from the measured data. While losing the information about the absolute amplitude value for each measured frequency point, we removed the noise caused by the receiver and the antenna; the noise was varying around 0 dB afterwards. It is possible to recalculated absolute value back, because we used one calibration curve for each measurement type. To determine the utilization of the frequency spectrum it is

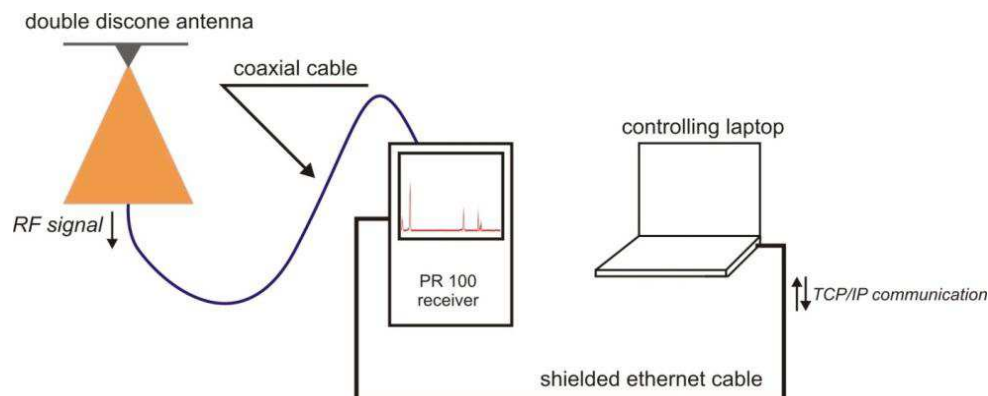


Figure 1: Typical measurement setup.

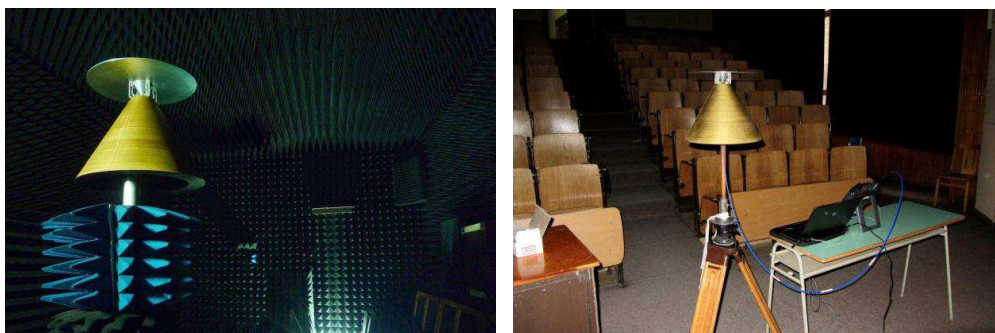


Figure 2: Measurement setup in an anechoic chamber and in an empty lecture hall.

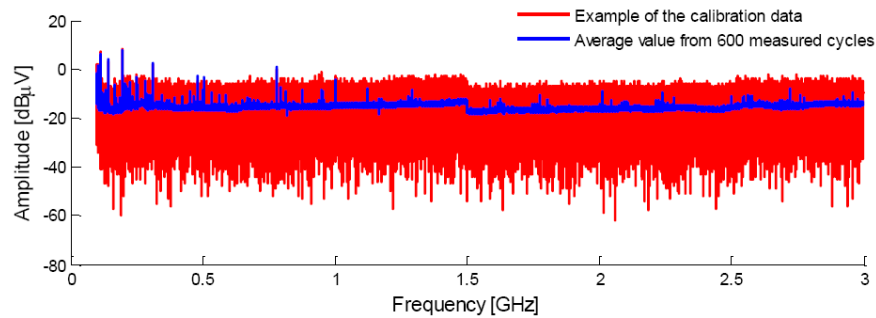


Figure 3: Calibration data example (the resolution was 12500 MHz).

not necessary to have information about the amplitude. Finally, the primary users are marked as signals above the specific threshold level. We also diagnosed time evolution of the white spaces.

3. MEASUREMENT RESULTS

Firstly, RAW data from the measurement are cleaned from the missing data. It is possible that some UDP packets are lost during the transfer from the receiver to the controlling PC. During the post-processing, we replaced the missing data with the data from the previous measured cycle. This enabled us to use all the measured data. The typical error rate in the measured data before correction is less than 0.1% (typically 0.01%). We compared each measured frequency step with the threshold level, which had been set to the value of 10 dB. All frequency points above this level were selected as occupied by a primary user. The parameter describing the utilization of the frequency spectrum is called *Duty Cycle* and is defined by (1):

$$Duty\ Cycle = \frac{N_{detected}}{N_{total}}, \quad (1)$$

where $N_{detected}$ is the number of detected peaks above the threshold and N_{total} is the number of total measured points. *Duty Cycle* is normally presented as a percentage value.

As mentioned above, we also took into account the effect of people within the area. Figure 5 presents the utilization of the frequency spectrum during a public holiday and compares the detected conditions with the fully occupied lecture hall. Utilization decrease occurred mainly in the WI-FI bands (2.4 GHz) and (somewhat less) the GSM bands. Nobody was using the public WI-FI network (checked with the network admins) and the traffic in the WI-FI band was produced only by the pilot signals.

It is obvious that the frequency spectrum is used quite inefficiently in the presented example. Utilization of the frequency spectrum corresponds to 5.2% for the occupied lecture hall and 3.5% for the empty lecture hall respectively. Therefore, some parts should be used more efficiently. In the current licensing system licensed frequency bands cannot be used by other services. The permission to use the frequency band is granted for large geographical areas. Naturally, certain regions of the frequency band are unused at some locations.

In contrast to the whole measured bandwidth, some of the bands are used quite well. The best example is provided by the GSM band measured in a shopping mall (TESCO) and presented in Figure 5. It is remarkable that some channels exhibit nearly 100% use during the whole measured time. Total utilization of the selected band was 23.5%.

Finally, we examined the WI-FI band (from 2400 MHz up to 2495 MHz). This band operates under ISM (Industrial, science and medical) licensing and is rarely limited. There is thirteen of 20 MHz wide channels in this band and only 3 channels (#1, #6, #11) [10] are not overlapped by the others. Due to channel overlapping, most providers are using the “full” channels and there are a lot of interferences caused by wrong wireless network planning. As presented in Figure 6, several services were using close channels during the measurement in the public library.

Figure 6 shows that if one of the services shifts to the other channel there will be significant improvement (up to 30 dB) in the SINR. In the cognitive system, the cognitive engine should estimate the frequency band collision and change the parameters of one of the above-mentioned services. In this case, the whole system needs to communicate with the other cognitive nodes to coordinate the cognitive system decisions. This should also cause significant reduction in radiation power, which will decrease power consumption of the whole system.

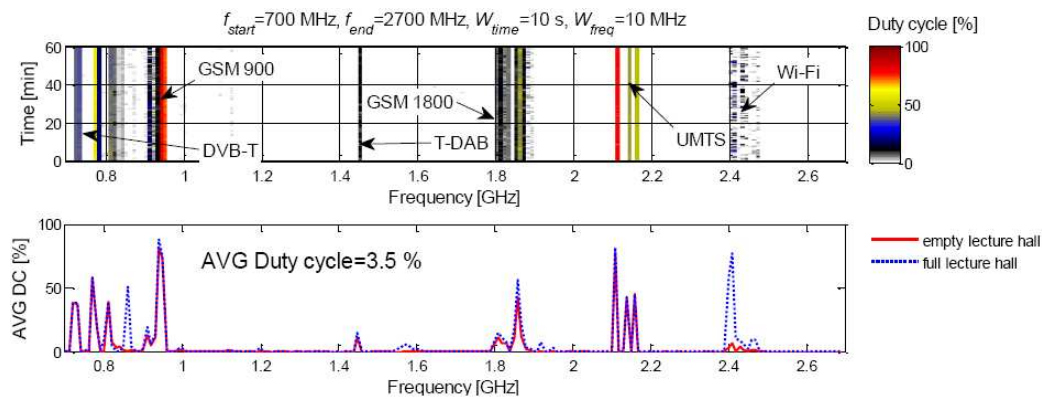


Figure 4: Measurement in an empty lecture hall (0.7 GHz–2.7 GHz).

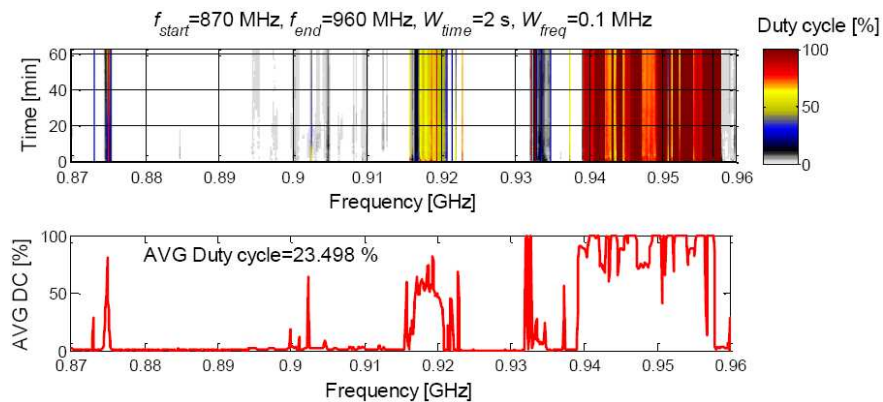


Figure 5: Utilization of the GSM band in the shopping mall.

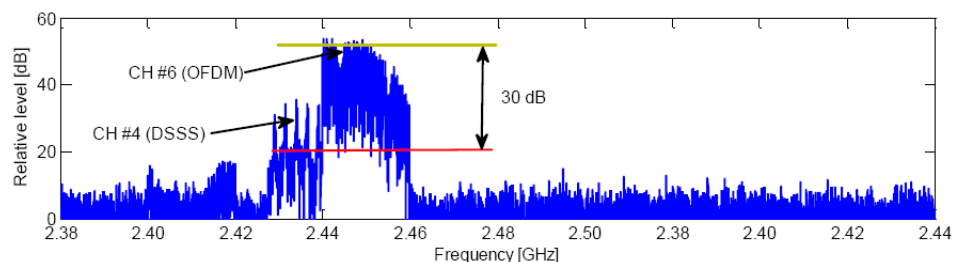


Figure 6: Collision in the WI-FI band: the public library measurement.

4. CONCLUSION

A unique measurement campaign for indoor environment was presented, including the results. Our measurements were focused on frequency bands starting in the GSM region (700 MHz) and ending with the WI-FI band (2.5 GHz). Generally, the frequency spectrum utilization values calculated for a large frequency bandwidth are commonly on a very low level. We calculated the spectrum utilization values between 3.5% and 5.2% according to the number of people in the area. We also examined significant services such as the GSM and WI-FI. For example the GSM bands were utilized up to 24.5% in the TESCO shopping mall. In the WI-FI band we found interference between the channels. An improvement of the SINR (30 dB) was presented due to better channel organization. We are convinced that cognitive radio has its niche on the market with wireless technologies and assume that the system could solve many topical problems within wireless networks.

ACKNOWLEDGMENT

This work was supported by the project CZ.1.07/2.3.00/30.0005, Brno University of Technology.

REFERENCES

1. Daniels, R. C. and R. W. Heath, “60 GHz wireless communications: Emerging requirements and design recommendations,” *IEEE Vehicular Technology Magazine*, Vol. 2, 41–50, 2007.
2. Adair, E. R., K. S. Mylacraine, and B. L. Cobb, “Partial-body exposure of human volunteers to 2450 MHz pulsed or CW fields provokes similar thermoregulatory responses*,” *Bioelectromagnetics*, Vol. 22, 246–259, 2001.
3. Mitola, J., *Cognitive Radio Architecture: The Engineering Foundations of Radio XML*, Wiley-Interscience, Hoboken, N.J., 2006.
4. Mitola, J., “Cognitive radio architecture evolution,” *Proceedings of the IEEE*, Vol. 97, 626–641, 2009.
5. *Cognitive Radio Experimentation Platform*, Available 2011, <http://asgard.lab.es.aau.dk/joomla/index.php/home>.
6. *Shared Spectrum Company (SSC)*, Available 2011, <http://www.sharedspectrum.com/company-overview/>.
7. Valenta, V., R. Marsalek, G. Baudoin, M. Villegas, M. Suarez, and F. Robert, “Survey on spectrum utilization in Europe: Measurements, analyses and observations,” *Proceedings of the Fifth International Conference on Cognitive Radio Oriented Wireless Networks & Communications (CROWNCOM)*, 1–5, 2010.
8. Akyildiz, I. F., L. Won-Yeol, M. C. Vuran, and S. Mohanty, “A survey on spectrum management in cognitive radio networks,” *IEEE Communications Magazine*, Vol. 46, 40–48, 2008.
9. *R&S PR100 Portable Receiver*, Available 2011, http://www2.rohde-schwarz.com/en/products/radiomonitoring/receivers/PR100-|-Key_Facts-|-4-|-3473.html.
10. IEEE, “Part 11: Wireless LAN Medium Access Control (MAC) and Physical Layer (PHY) specifications,” *Amendment 4: Further Higher Data Rate Extension in the 2.4 GHz Band*, Ed: The Institute of Electrical and Electronics Engineers, Inc., 2003.

Measurement of Inhomogeneity in the B_0 and B_1 Fields Performed via the Spin-Echo and Gradient-Echo MR Imaging Techniques

R. Kubasek, E. Gescheidtova, and K. Bartusek

Department of Theoretical and Experimental Electrical Engineering
Brno University of Technology, Kolejní 4, Brno 612 00, Czech Republic

Abstract— The authors describe a method for the basic and RF field inhomogeneity estimation in NMR based on the measurement of T_2 and T_2^* . The method combines the gradient and spin echo acquisition techniques to differentiate the T_2 and T_2^* relaxation times. Exponential approximation of the relaxation process has to be performed. Experimental results for the plastic and copper specimens are shown.

1. INTRODUCTION

The physical phenomenon in which the magnetic field of the nuclei of some atoms contained in the examined substance reacts with a rotating magnetic field is referred to as NMR (Nuclear Magnetic Resonance). NMR spectroscopy and tomography require the basic magnetic field B_0 to be generated with a high homogeneity [1]. Homogeneity of the basic magnetic field can be distorted by the measured object, and this object does not necessarily have to be magnetic: image distortion may occur already as a result of different susceptibility.

High homogeneity of the RF field in the working space of an MR tomograph depends on the structure and setting of the applied probe. Mapping of the RF magnetic field is commonly based on MR image measurement of the homogeneous test specimen; in the measurement, the flip angle is optimally determined to ensure the maximum contrast of the measured RF magnetic field map [2, 3]. The local B_1 field strength in each slice can be obtained using repeated acquisitions with different RF-impulse amplitudes ('transmit gain', 'flip angle') [4]. The inhomogeneity can be corrected by the use of a map of the spatial distribution of the B_1 field acquired either through computer simulation or through the measurement of the field. The actual measurement of the B_1 distribution provides two major advantages: it makes the registration of the map against the MR images easier, and the measured B_1 field compensates for imperfections in the coil design. The paper describes the first instance of relaxation measurement using the SE and GE methods applied for the B_0 inhomogeneity estimation. The method of B_1 estimation from the relaxation times via the magnetization transfer ratio is described in the following chapter of this article.

2. INHOMOGENEITY ESTIMATION FROM RELAXATION TIMES

The GE and SE methods are well known within NMR measurement techniques [4]. We can measure the relaxation process after excitation by changing the echo time, Fig. 2(a). The number of realized measurements depends on the requirements and the time available. The measurement proper can be performed by a hard excitation pulse on the whole specimen, on a selectively chosen layer or area of the specimen, or on a pixel/voxel in an imaging sequence.

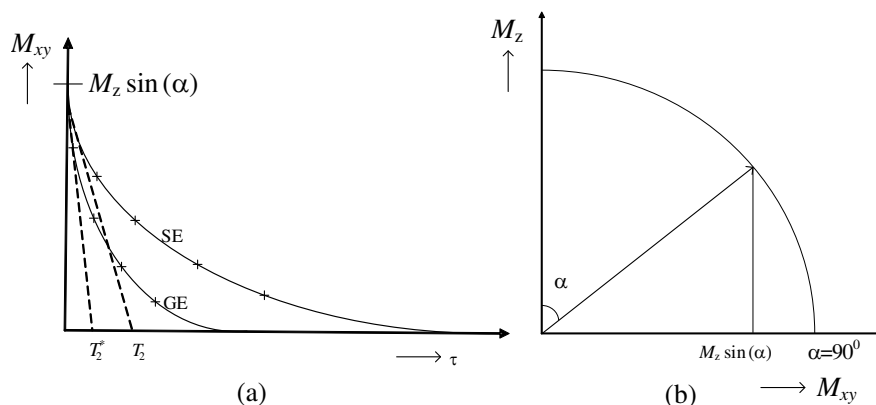


Figure 1: (a) Relaxation process after excitation. (b) Flip angle representation.

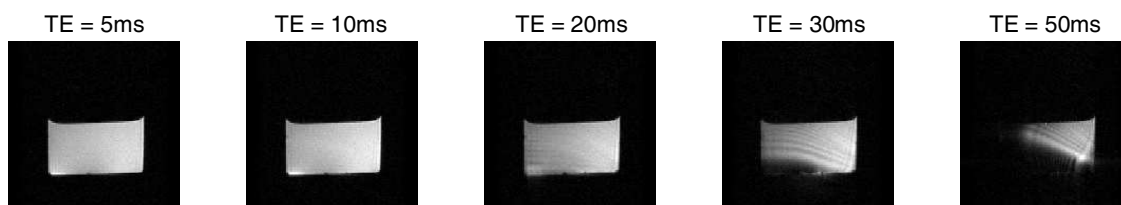
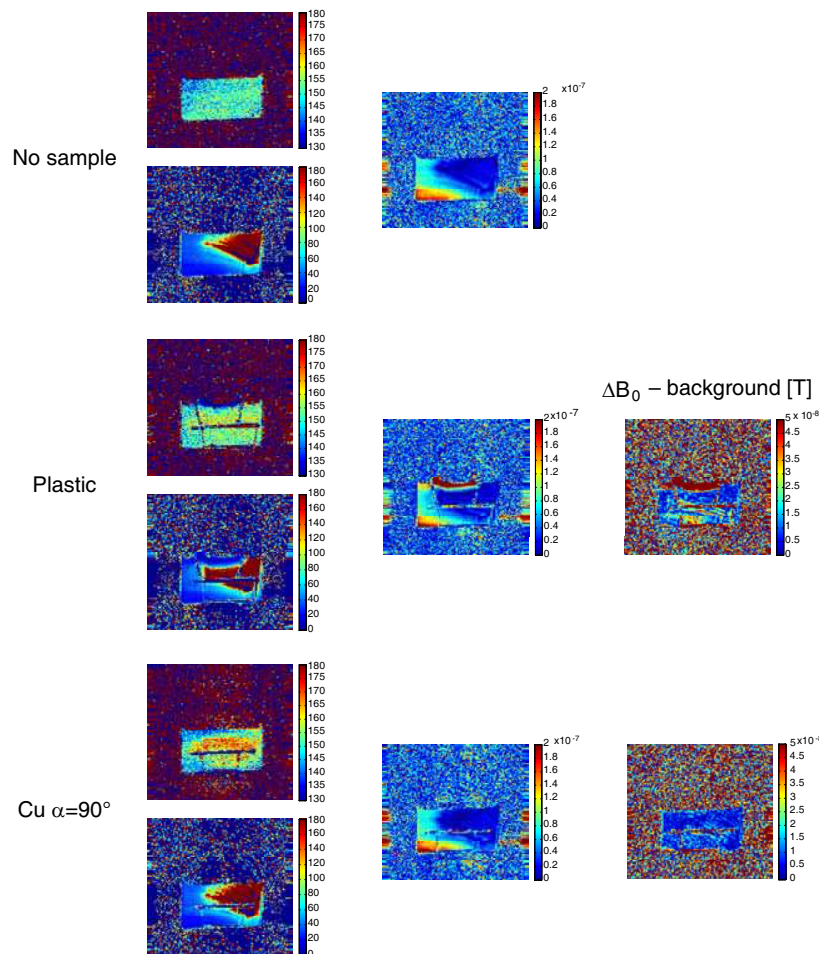


Figure 2: Magnitude images for the GE sequence.

Figure 3: Maps of the B_0 inhomogeneity estimation, and the final results.

The measured data must be approximated by an exponential function. Both constants of the exponential course, namely the magnetization after excitation M_{xy} and the time constant T_2 or T_2^* , are needed. At least three measured magnitudes of the FID (Free Induction Decay) signal at different TE echo times are necessary for the approximation. The TE echo times should be chosen with care. The first echo time should be set to the lowest possible value with respect to technical parameters of the tomograph. The last echo time can be chosen either on the basis of the known inhomogeneity or experimentally. Other echo times can be distributed linearly between these two points. If a whole image is measured, we need to perform approximation in every pixel/voxel of the image. For high-resolution images, it is important to consider the computational complexity of the approximation algorithm. For example, the genetic algorithm is not a suitable option.

The basic field inhomogeneity B_0 exerts influence on the relaxation process; thus, any deformation of B_0 causes the dephasing of magnetization. Dephasing leads to a faster drop of the FID signal and shortens the relaxation time T_2^* . Fig. 2 shows five magnitude images obtained by the GE technique. Magnitude drop in the bottom left corner is marginal; it is caused by the B_0 inhomogeneity not successfully corrected by the shim coils. This is a limiting factor for any successful

approximation of relaxation.

The SE method compensates inhomogeneity B_0 ; therefore, we measure true relaxation T_2 . It is, however, necessary to select a suitable specimen to exclude the influence of diffusion and movements. The basic field inhomogeneity B_0 is given by

$$\frac{1}{T_2^*} = \frac{1}{T_2} + \frac{1}{T_2'} = \frac{1}{T_2} + \gamma \Delta B_0,$$

$$\Delta B_0 = \frac{\frac{1}{T_2^*} - \frac{1}{T_2}}{\gamma}, \tag{1}$$

where γ is the gyromagnetic ratio of H_2 . The value ΔB_0 is the overall and, in a way, average value of the B_0 inhomogeneity in any pixel/voxel.

Figure 3 shows the B_0 inhomogeneity maps measured using a 4.7 T tomograph. A cube filled by long-relaxing water was used. The specimen, namely a plastic or copper plate placed on a glass vessel, was inserted in the cube. The B_0 inhomogeneity with no sample is presented as

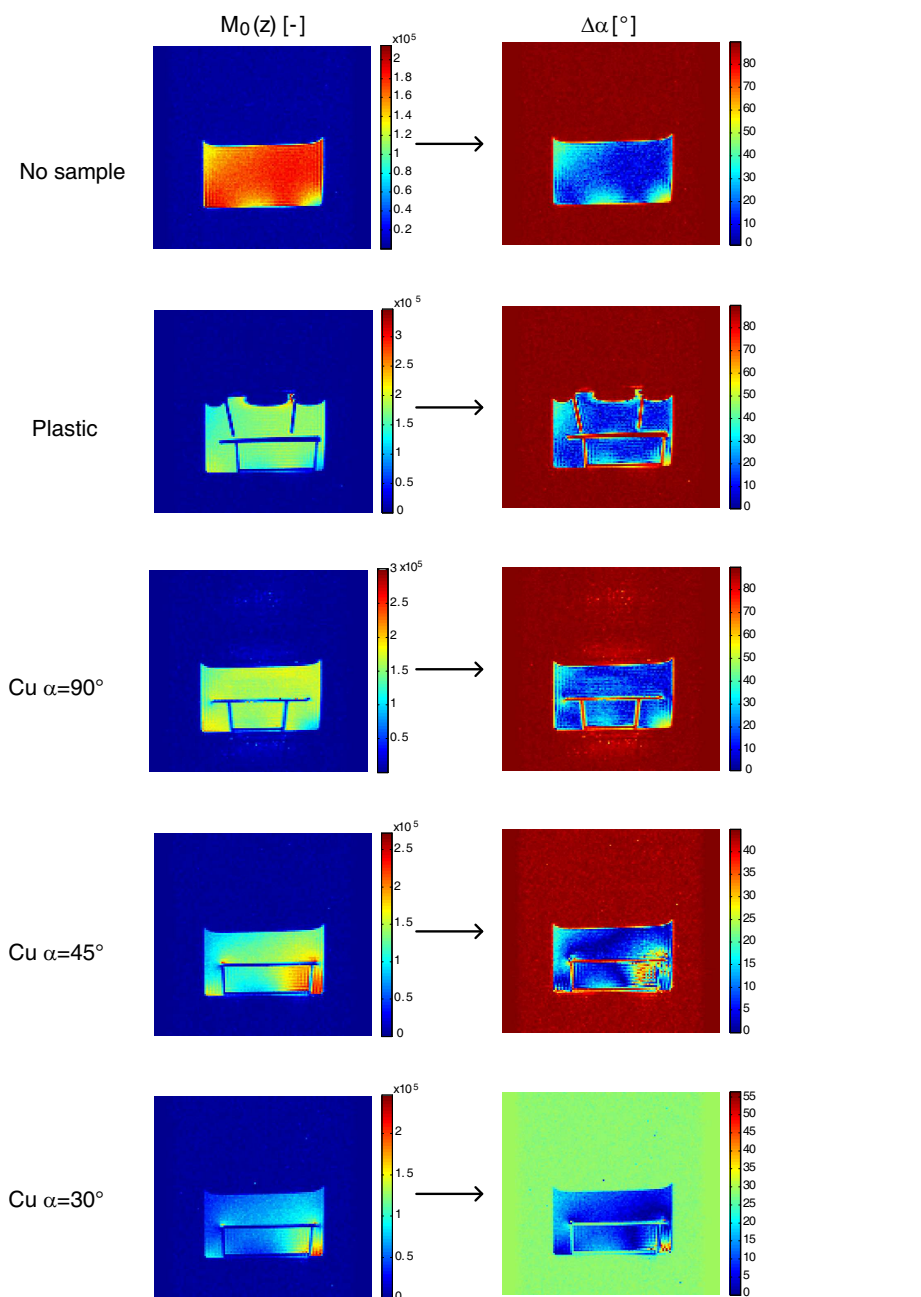


Figure 4: Flip angle errors.

background and can be subtracted from the measurement. The plastic sample is non-conducting and exhibits a significant (not exactly determined) value of susceptibility. Conversely, the copper sample is a good conductor with a low susceptibility value; this sample exerts minimal influence on the B_0 inhomogeneity. Traces of distortion are visible only in the immediate vicinity of the copper plate; the distortion is probably caused by a flip angle error and possible inaccuracy in the T_2 approximation. In the plastic sample, B_0 changes significantly in the whole space of the water-filled cube. The maximal value of B_0 inhomogeneity is $4 \cdot 10^{-7}$ T.

Immediately after excitation, the NMR signal magnitude is proportional to the basic field strength represented by M_{xy} and flip angle α . The magnetization is expressed by:

$$M_{xy} = M_z \cdot \sin(\alpha). \quad (2)$$

The flip angle is a linear function of the B_1 field strength and length of the excitation pulse t_e :

$$\alpha = \gamma B_1 t_e. \quad (3)$$

The B_1 inhomogeneity map can be represented by the map of flip angle α . The task is to find M_{xy} in time $t = 0$. The M_{xy} ratio is theoretically the same for both the GE and SE methods. We can use the average M_{xy} of the GE and SE weighted by the exponential approximation accuracy.

Figure 4 shows the flip angle error $\Delta\alpha$ for the same copper and plastic specimens used previously for the B_0 inhomogeneity measurement. A comparison of background in the different samples will show that the plastic sample exhibits minimal influence of excitation in the whole space. Conversely, the copper sample has a substantial effect on the RF field; there are regions where the nuclei are overstimulated or inadequately excited. This significant region can be clearly seen in a small flip angle. The major disadvantage of the proposed method is that we cannot recognize if the flip angle is over or below 90° . For example, the magnitude of the signal after excitation is the same for flip angles of 80° and 100° .

3. CONCLUSION

Estimation of the B_0 and B_1 inhomogeneity from relaxation times T_2 and T_2^* and initial magnetization after excitation M_{xy} is a useful method. The benefit consists in the fact that there does not have to exist any mutual influence between the inhomogeneities. The described approach is limited by two aspects, namely loss of the FID signal magnitude below the noise level in the case of a high inhomogeneity and the fact that we know only the absolute flip angle error. The quality of the B_0 inhomogeneity strongly depends on successful approximation of T_2 .

ACKNOWLEDGMENT

This work was supported within the Czech Science Foundation project No. 102/09/0314 and a project funded by the Education for Competitiveness Operative Programme CZ.1.07.2.3.00.20.0175 (Electro-researcher).

REFERENCES

1. Vlaardingerbroek, M., *Magnetic Resonance Imaging*, Springer-Verlag, 2000.
2. Cunningham, H. C., J. M. Pauly, and K. S. Nayak, "Saturated double-angle method for rapid B_1 mapping," *Magnetic Resonance in Medicine*, Vol. 55, 1326–1333, 2006.
3. Zuehlsdorff, D. W. S. and A. C. Larson, "Rapid 3D radiofrequency field mapping using catalyzed double-angle method," *NMR Biomedicine*, Vol. 22, 882–890, 2009.
4. Bartusek, K., E. Gescheidtova, and R. Kubasek, "Mapping of radiofrequency magnetic field in MR tomography," *International Conference on Fundamentals of Electrotechnics and Circuit Theory*, 135–138, Gliwice, 2006.
5. Haacke, E. M., R. W. Brown, M. R. Thompson, and R. Vankatesan, *Magnetic Resonance Imaging Physical Principles and Sequence Design*, Wiley & Sons, 1999.

Processing of Magnetic Resonance Images of Adipose Tissues

Michaela Pokludová, Eva Gescheidtová, and Jan Mikulka

Department of Theoretical and Experimental Electrical Engineering
Brno University of Technology, Kolejní 4, Brno 612 00, Czech Republic

Abstract— Sufficiently meaningful picture of tissue structure can be obtained by the correct processing of the image data. This can be done by using image analysis, which takes place in several steps: acquisition of data, image adjustment, segmentation, and image description. At first, digital images are obtained, in our case these are the images of soft tissue obtained with using magnetic resonance tomograph (MR). This device is mainly used to display human tissue in medicine. MR is one of the non-destructive methods, does not cause harmful radiation, whose main advantage is the high contrast in the imaging of soft tissues. The contrast of the resulting images can be changed by setting of the pulse sequence (Spin Echo and Inversion Recovery) timing parameters used to measure the monitored tissue. The data acquired by tomograph is necessary reconstruct by using Fourier Transform reconstruction from K-space in to the MAT file as complex data. The next step of image analysis is image improvement, usually by suppression of noise, histogram equalization and segmentation. Noise should be suppressed to improve results of image processing. Linear transform of histogram was adjusted using a median filter. This is an expansion of the range of brightness in order to cover the entire width of the available brightness. The last step of image processing is multiparametric segmentation. It is a process that divides the image to objects of different characteristic. The main methods include the use of edge detector to highlight certain edges. The last step of the analysis is a description of the image; it is a statistical description of segmented objects in an image with subsequent classification. The aim of this paper is to demonstrate the internal morphology of chicken thigh by using MR. All MR images were evaluated using programs Marevisi and Matlab.

1. INTRODUCTION

To study the internal morphology of chicken thighs it is necessary to process the data by using the image analysis, which is applied not only in the research of living matter, but also inanimate. However, the most significant application is in the biological sciences, where with the help of image analysis such information as the number of cells in the sample or the intensity of colour reaction are assessed. The greatest emphasis is placed on medical image processing, which is used to diagnose a disease or to monitoring the development of the disease.

The image analysis proceeds in several basic steps: data acquisition, image improvement, image segmentation, and description. The process of image analysis is shown in Figure 1. Individual techniques of the process are described in the text below [1].

Primarily it is necessary to obtain the digital images via imaging techniques. To obtain medical images X-Ray (hard tissue) and MRI or CT tomography (mostly for displaying soft tissue) are applied. For monitoring of very small structures microscopic method is used. In this paper, there are images of biological tissues obtained thorough magnetic resonance imaging (MRI). MRI is one of the non-destructive methods, which does not cause harmful radiation. The main advantage of MR imaging of soft tissues is high contrast. The contrast depends on the characteristics of the monitored tissue, especially on the proton density and relaxation properties. In addition, the contrast is dependent on the setting of three parameters (flip angle, the T_R and the T_E times) of pulse sequence. To obtain an image with the largest information value the best image contrast is necessary to achieve [2].

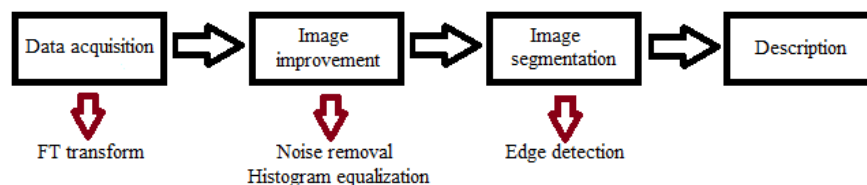


Figure 1: Diagram of image analysis.

2. EXPERIMENTAL MEASUREMENTS

The sample material selected for the experimental measurements was the biological tissue of thighs, which was scanned by the magnetic resonance tomograph 4.7 T/200 MHz. The output of the MR tomograph is an image of the monitored tissue, which is displayed in the frequency domain (k -space) (see Figure 2(a)). This image is converted into the time domain using the Fourier transform. The result is the image of the real distribution of tissues in a given spatial region (see Figure 2(b)) [2].

The next step in image analysis is image improvement, typically the suppression (removal) of noise, histogram equalization, and segmentation, Figure 3. Individual techniques in the chain are described in the text below [3].

Unwanted interference (noise) was filtered using wavelet transform. The principle of wavelet transform (WT) lies in a mutual comparison of the analog signal $x(t)$ with the chosen model shape known as the wavelet ψ . Figure 4 shows two images: (a) before filtering (with the noise which can be seen around the tissue) and (b) after filtering (in which the noise is removed around the tissue) [3].

Histogram equalization is a method of regulating the image contrast. This is an expansion of the range of brightness in order to cover the entire width of the available grey-scale spectrum. The method is useful for images that are underexposed or overexposed. In Figure 5, you can see a representation of the grey levels (0–255) [3].

The last step of image improvement is multiparametric segmentation, which is a process that divides the image to objects of different types. Segmentation methods can be divided into two groups: methods based on pixel (techniques based on edges and thresholding) and methods based on areas (search technique based on homogeneous areas in the image). The main segmentation method in our paper is the edge enhancement using the edge detector. In Figure 6, you can see the

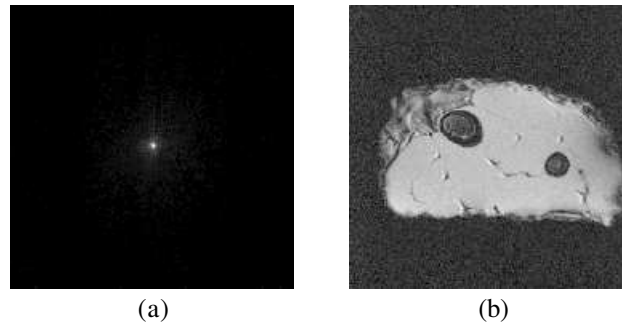


Figure 2: MR images of the monitored tissue. (a) The frequency domain. (b) The time domain.

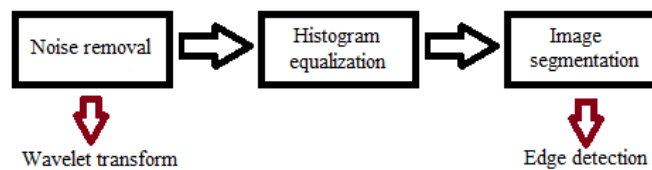


Figure 3: Diagram of image improvement.

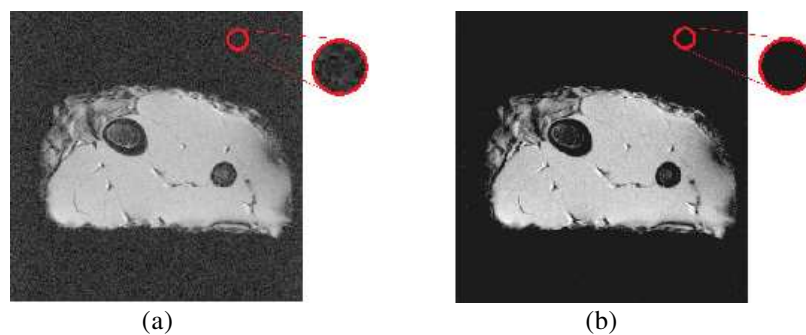


Figure 4: (a) The image before filtering. (b) The resulting image after noise removal filtering.

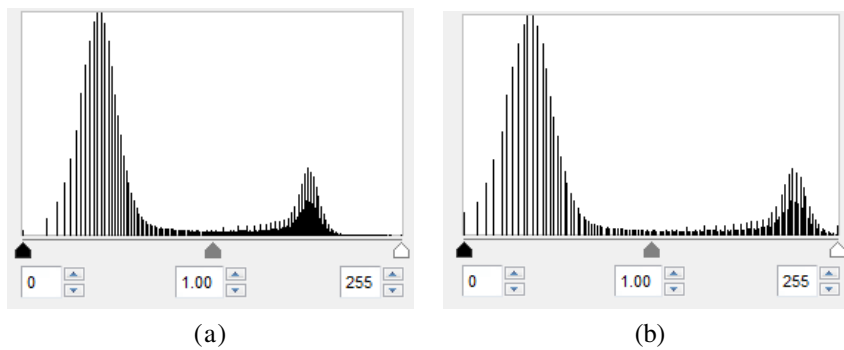


Figure 5: Histogram equalization (a) before and (b) after the application method.

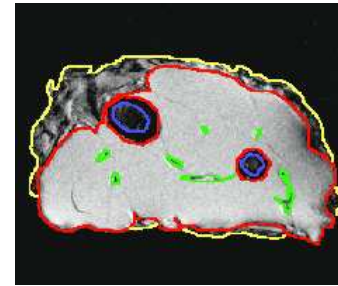


Figure 6: Resulting image after the edge enhancement.

Table 1: Diagram of image analysis.

Tissue	Colour identification	Total surface	Number of pixel	Maximum intensity of image	Standard deviation
Muscle	Red	6721,97	54026	115796	37758,5
Adipose tissue	Yellow	1198,67	2994	28165	17269,3
Bone tissue	Blue	372,517	9634	59291	34598,4
Muscle tendrils	Green	79,6457	458	127390	28166,9

edge enhancement of the chicken tissue: red colour indicates the muscle, yellow the adipose tissue, blue the bone tissue, and green the muscle tendrils [4].

The last step of image analysis consists in the description of tissues. This is the classification of segmented objects in an image. In Table 1, the obtained parameters of tissues are listed. The chicken thigh contains mostly muscles and adipose tissues. Further, the image indicates (in the biggest tissue) muscle tendrils with the highest intensity of the image signal, which corresponds to a larger amount of water contained in this tissue [5].

3. CONCLUSIONS

The aim of this paper was to display the internal morphology of chicken thighs using magnetic resonance tomograph. The images taken by MR tomograph having parameters of 4.7 T/200 MHz were reconstructed and pre-processed by means of Marevisi software. In these images, analysis was performed by Matlab software application. In the resulting images soft tissue and consequently their parameters can be distinguished. It is obvious from the image that muscle tendrils contain the largest amount of water. The adipose tissue set out around the muscle forms a significant part of the total weight.

ACKNOWLEDGMENT

This work was supported within the framework of projects Nos. 102/11/0318 and 102/12/1104 of the Czech Science Foundation and the project of the BUT Grant Agency FEKT-S-11-5/1012.

REFERENCES

1. Jan, J., *Medical Image Processing, Reconstruction and Restoration: Concepts and Methods*, CRC Press, USA, 2006, ISBN 0-8247-5849-8.
2. Haacke, E. M., R. W. Brown, M. R. Thompson, and R. Venkatesan, *Magnetic Resonance Imaging: Physical Principles and Sequence Design*, John Wiley & Sons, 1999, ISBN 0-471-35128-8.
3. Mikulka, J., E. Gescheidtová, and K. Bartušek, "Wavelet filtering and level set segmentation of NMR images for monitoring the development of growing cultures," *PIERS Proceedings*, 1124–1127, Beijing, China, Mar. 23–27, 2009.
4. Grau, V., et al., "Improved watershed transform for medical image segmentation using prior information," *IEEE Transactions on Medical Imaging*, Vol. 23, No. 4, 2004.
5. Liang, P. and P. Lauterbur, *Principles of Magnetic Resonance Imaging*, IEEE Press, New York, 1999.

The Effect of Extremely Low Frequency (ELF) Pulsed Electromagnetic Field (PEMF) on Bacteria *Staphylococcus Aureus*

Istiaque Ahmed¹, Taghrid Istivan², and Elena Pirogova¹

¹School of Electrical and Computer Engineering
Royal Melbourne Institute of Technology (RMIT) University
Melbourne, Victoria 3001, Australia

²Department of Biotechnology and Environmental Biology, School of Applied Science
Royal Melbourne Institute of Technology (RMIT) University
Bundoora, Victoria 3083, Australia

Abstract— Current interest in the application of pulsed electromagnetic fields (PEMF) as alternative therapy for different medical conditions has proven to be successful. There are studies that demonstrate the effectiveness of low frequency PEMF in facilitating wound healing. There are many factors that can affect wound healing and cause improper or impaired tissue repair. Of particular interest are the infected wounds where bacteria or other microorganisms have colonized that cause either a delay in wound healing or deterioration of the wound. In most cases, wounds are typically contaminated by bacteria. In this study, we investigate the application of the applied PEMF on the selected bacterial cultures. In our previous study [1], we presented and discussed the design and development of an extremely low frequency (ELF) PEMF system that produces time varying magnetic field in the range of 0.5 mT to 2.5 mT for a frequency range of 2–500 Hz. Here, we report simulation results of the induced magnetic field distribution and the region of uniformity produced by the system of two pairs of air core Helmholtz coils. We also present the experimental evaluation of varying parametric changes in the applied ELF PEMF on the bacteria *Staphylococcus aureus*. The selection of this gram-positive bacterium for this study is attributed to the versatile role of these bacteria in infecting wounded tissues. These bacteria are also within easy reach and can be bred at a temperature of 37°C. Here, the *Staphylococcus aureus* bacteria in broth were exposed to the ELF PEMF of magnetic flux density, $B = 0.5\text{--}2.5\text{ mT}$, frequency (f) range of 2–500 Hz and time of exposure, $t = 90\text{ min}$. This is done in order to compare studied bacterial cultures viability (number of colony-forming units (CFU)). The number of colony-forming units aids in quantifying the experimental result. Fresh bacterial culture is used throughout the experiment. Findings from our investigation have direct implication in determining the optimal characteristics of the applied ELF PEMF for possible treatment of infected tissue and thus, wound healing promotion.

1. INTRODUCTION

The effect of extremely low frequency (ELF) electromagnetic field on biological media has been studied by many researchers using a variety of *in vitro* exposure systems [2]. Almost all of these laboratory-based experiments utilized electric coils to generate electromagnetic exposures. A Classic Helmholtz coil design ascertains that the first and second spatial derivatives of the applied fields are zero at the central point of the applied system [3]. Much larger volume of uniform field space inside the coil setup results from the assembly of more coils [4]. Computational modelling and simulation of the ELF uniform magnetic field exposure system, prior to the actual practical design and development process, is extremely important in terms of design flexibility and efficiency.

ELF magnetic field therapy is considered as useful and beneficial treatment for different diseases, especially those involving skin and bones [5]. Studies have shown that application of pulsed electromagnetic field (PEMF) to damaged cells can accelerate the re-establishment of normal potentials, promote cell proliferation, increase the rate of healing, reduce swelling and bruising [6]. A good model system for studying effects of magnetic fields is bacterial cultures [7]. A few investigations have been conducted using prokaryotes, mostly examining bacterial growth [8]. However, the effects of the entire range of ELF PEMF on bacteria have yet to be reported. In our previous work [1, 9], we presented and discussed the design and development of an ELF PEMF system that produces time varying magnetic field in the range of 0.5 mT to 2.5 mT for a frequency range of 2–500 Hz. Here, we report the simulation results of the induced magnetic field distribution and the region of uniformity produced by the system of two pairs of air core Helmholtz coils. To test

the efficacy of the developed ELF PEMF and evaluate the simulation results experimentally, the exposure system was used to irradiate gram-positive bacteria *Staphylococcus aureus* ATCC 25923, which were selected for their versatility in infecting wounded tissues, and be bred at 37°C.

2. MATERIALS AND METHODS

2.1. Experimental Setup

The experimental setup (Figure 1(a)) is used to generate the uniform time varying magnetic fields in the frequency range of 2–500 Hz and magnetic induction (magnetic flux density) of 0.5–2.5 mT. The uniformity of magnetic field is extremely important for the irradiated sample. Therefore, the uniform magnetic field was first simulated using the software Maple 14. The simulated uniform magnetic field of 1 mT, produced by the system of two pair of Helmholtz coils, is shown in Figure 1(b). This simulation result was then practically verified by the direct measurement of the generated field using “Wandel and Golterman” EFA-200 EMF Analyzer fitted with an external B-probe.

The temperature inside the coils was maintained at 22–24°C by airflow, and measured by the thermometer to ensure that any heat generated from the coil has not affected the experimental conditions. The sample was placed on the non-conductive stand in the centre of the coil as shown in Figure 1(a). The region of uniformity, where the total magnetic field is uniform within 1% in the xy - and xz -axis, was also simulated using Maple 14 (Figure 2).

2.2. Experimental Procedure

Colony-forming unit (CFU) is an estimate of viable bacterial number. CFU was used to quantify the effects of applied ELF on fresh bacterial cultures used throughout the experiments. A preliminary experimentation using the ELF of the selected frequencies was conducted to estimate a required duration of the exposures. It was observed that irradiating a sample with the magnetic field of

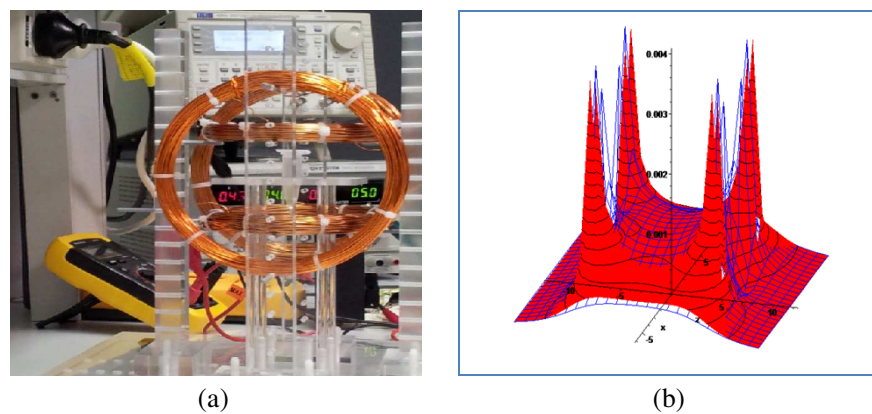


Figure 1: (a) ELF PEMF system setup for irradiating *Staphylococcus aureus* in broth and (b) total magnetic field intensity of 1 mT as projected in the xz -axis.

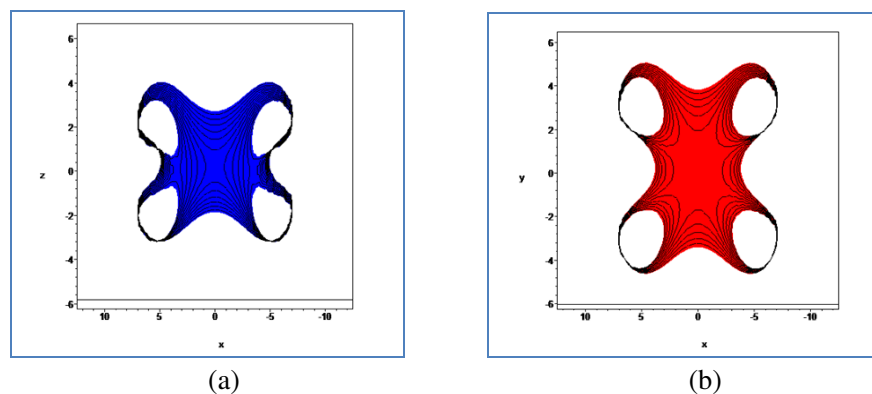


Figure 2: Region in which total magnetic field is uniform within 1% (a) in the xz -axis and (b) in the xy -axis.

0.5–2.5 mT over a period of 90 minutes can significantly increase the value of CFU count, when compared with the control sample. Therefore, the irradiation exposure for all frequencies and corresponding magnetic field intensities were fixed to 90 minutes.

The bacteria *Staphylococcus aureus* was cultivated in an agar Petri dish and left to incubate for 24 hours at 37°C. The culture was then checked for any form of contamination and the inoculum from the bacterial culture was picked and transferred to broth. Diluted bacterial culture in 100 μ l of broth having unknown concentration was measured using Optical Density Photometer. The optical density reading was always adjusted to 0.1 *a priori* to commencing irradiation of the sample. This step was necessary for maintaining a consistency/standardization for all conducted experiments. Bacterial cultures were then placed inside of a 2.5 ml centrifuge tube and exposed for 90 minute to ELF PEMF. To determine the CFU/mL count, a serial dilution using the bacterial culture was performed. Next, the each dilution prepared was transferred to agar plates through the method of spread plating. Finally, after incubation at 37°C for 24 hours, the colonies on the plates were counted.

For statistical analysis, each experiment was repeated three times for each unique combination of frequency and magnetic field. Control cultures (non-exposed) were kept in the same conditions as the exposed ones except the sole exposition to the magnetic fields.

3. RESULTS AND DISCUSSION

We have compared the changes in the CFU number after the ELF PEMF exposures of 90 minutes. Comparison was done as a function of magnetic field strength in mT and extremely low frequency in Hz. All data were compared with the controlled sample. We can conclude from this study that ELF PEMF have a profound effect on the bacteria *Staphylococcus aureus*. The maximum decrease of CFU was observed at 300 Hz for both the magnetic field intensities of 0.5 mT (Figure 3) and 1.5 mT (Figure 4). The minimum decrease of CFU was observed at 10 Hz for both the magnetic field intensity of 0.5 mT and 1.5 mT. The CFU count shows that at 300 Hz the number of bacteria counts n equals 27 upon irradiation with 0.5 mT and 24 upon irradiation with 1.5 mT. These bacteria counts are significantly lower in comparison with their respective sample control counts of 77 and 79.

Figure 5 clearly shows that, apart from two frequencies 50 Hz and 100 Hz, the effect of the ELF PEMF of 1.5 mT appears to be more significant on the studied the bacterial culture of *Staphylococcus aureus* as opposed to the exposures of 0.5 mT. After irradiation with 0.5 mT and 1.5 mT, the relative (%) decrease of CFU was above 35% and 25% respectively for all counts at the frequencies from 100 Hz to 500 Hz. Results obtained thus far reveal that the effect of ELF PEMF is more profound on *Staphylococcus aureus* at frequencies in the upper end of the ELF spectrum as opposed to the lower end of the spectrum. In addition, the increase in magnetic field strength generally seems to stop bacterial growth more in comparison to a smaller value of magnetic field strength. For all the selected cases shown, the error bars are at 95% confidence level.

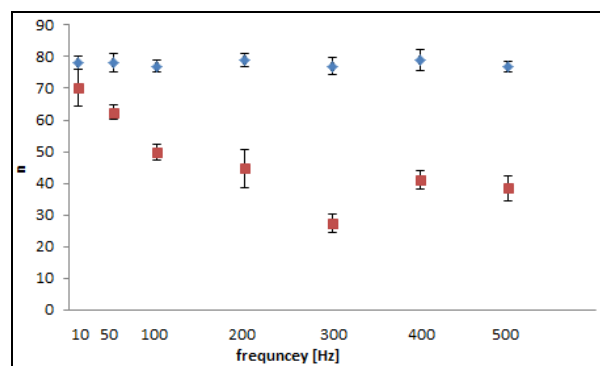


Figure 3: Dependence of the CFU number of *S. aureus* after ELF PEMF exposure (n — number of bacteria in 100 μ l of suspension), \diamond — control sample at 0.5 mT, \square — exposed sample.

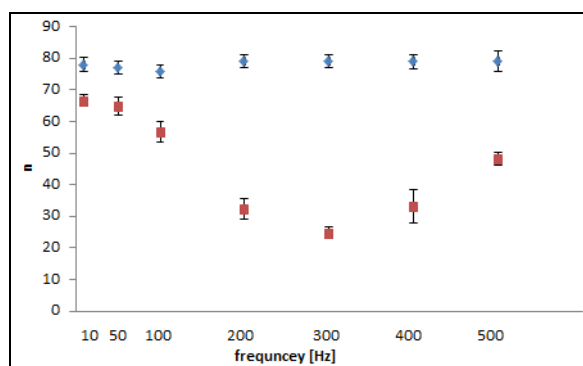


Figure 4: Dependence of the CFU number of *S. aureus* after ELF PEMF exposure (n — number of bacteria in 100 μ l of suspension), \diamond — control sample at 1.5 mT, \square — exposed sample.

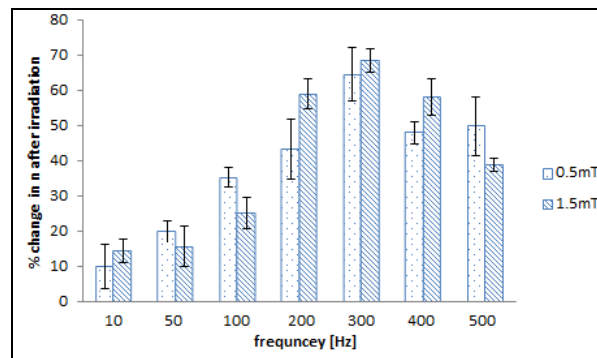


Figure 5: Relative change (%) in the number of bacteria count after ELF PEMF exposure for selected frequency.

4. CONCLUSIONS

We investigated the effect of the applied ELF PEMF on the bacteria *Staphylococcus aureus* in broth. The results demonstrated that magnetic field causes the decrease of CFU in all exposed samples. The findings of this study clearly showed that the generated exposures of the magnetic field densities of 0.5 mT and 1.5 mT in the range of 2–500 Hz decrease the CFU count when compared to the non-irradiated samples. These outcomes have direct implication for determining the optimal characteristics of the applied ELF PEMF for possible treatment of the infected tissue and thus, wound healing promotion.

REFERENCES

1. Ahmed, I., V. Vojisavljevic, and E. Pirogova, "Design and development of extremely low frequency (ELF) pulsed electromagnetic field (PEMF) system for wound healing promotion," *IFMBE Proceedings World Congress on Medical Physics and Biomedical Engineering*, Vol. 3, 27–30, 2012.
2. Bassen, H., T. Litovitz, M. Penafiel, and R. Meister, "ELF in vitro exposure systems for inducing uniform electric and magnetic fields in cell culture media," *Bioelectromagnetics*, Vol. 13, 183–198, 1992.
3. Herceg, D., A. Juhas, and M. Milutinov, "A design of four square coil system for biomagnetic experiment," *Facta University Series: Electronics and Energetics*, Vol. 22, No. 3, 285–292, 2009.
4. Kirschvink, J. L., "Uniform magnetic fields and double-wrapped coil systems: Improved techniques for the design of bioelectromagnetics experiments," *Bioelectromagnetics*, Vol. 13, 401–411, 1992.
5. Kraus, W., "Magnetfeldtherapie?," *Der Praktische Tierarzt*, Vol. 70, 46–69, 1989.
6. Gougarzi, I., S. Hajizadeh, M. E. Salmani, and K. Abrari, "Pulsed electromagnetic fields accelerate wound healing in the skin of diabetic rats," *Bioelectromagnetics*, Vol. 31, No. 4, 318–323, 2010.
7. Fojt, L., L. Strasak, V. Vetterl, and J. Smarda, "Comparison of the low-frequency magnetic field effects on bacteria, *Escherichia coli*, *Leclercia adecarboxylata* and *Staphylococcus aureus*," *Bioelectrochemistry*, Vol. 63, 337–341, 2004.
8. Alipov, Y. D., I. Y. Belyaev, and O. A. Aizenberg, "Systematic reaction of *Escherichia coli* cells to weak electromagnetic fields of extremely low frequency," *Bioelectrochem. Bioenergy*, Vol. 34, 5–12, 1994.
9. Istiaque, A., V. Vojisavljevic, and E. Pirogova, "The effect of extremely low frequency (ELF) pulsed electromagnetic field (PEMF) on collagenase enzyme kinetics," *MD — Medical Data*, Vol. 4, No. 4, 357–362, 2012.

The Effects of Visible Light Radiation (400–500 nm) on Enzymatic Activity of Collagenase

J. Hu, V. Vojisavljevic, and E. Pirogova
School of Electrical and Computer Engineering
RMIT University, Melbourne 3001, Australia

Abstract— Debridement is the process of removing necrotic burden or contaminated tissue from a wound bed until surrounding healthy tissue is exposed. Enzymatic debridement helps to remove non-viable tissue which can otherwise delay wound healing and lead to infection [1]. Collagenase enzyme is known to be able to promote cellular responses to injury and wound healing *in vivo*. Collagenase shows more selectivity on denatured collagen in devitalized tissue. This selectivity is beneficial as it keeps the vital tissue and growth factors crucial to wound healing intact. There are studies which have shown that applied electromagnetic radiation (EMR) in the visible light range can modulate protein and cellular activity. Here we validate experimentally the hypothesis of the Resonant Recognition Model (RRM) that selectivity of protein activities is based on specific resonant electromagnetic interactions [2]. The computational analysis of 28 collagenase sequences was performed and the activation frequency/wavelength range was determined to be 450–460 nm. To evaluate this range, the Collagenase enzyme solutions were irradiated by monochromatic light of 400 to 500 nm. The kinetics of the chemical reaction was measured by continuous monitoring of the changes in absorbance of collagen at 570 nm. The results revealed that collagenase activity can be modulated at the particular wavelengths of 450 nm, 456 nm, and 460 nm, which is within the activation wavelength range defined computationally. This finding indicates that enzyme function can be modified by an applied electromagnetic radiation of defined frequency, which may contribute to the development of a new clinical therapy for wound healing promotion.

1. INTRODUCTION

Debridement is an essential treatment process used in wound bed preparation. Since devitalized tissue can obstruct healing of a wound, debridement offers a comprehensive approach to removing barriers to healing and creating a wound environment for healing promotion and thus, reducing risk of local infection [1]. There are a number of methods currently used for debridement of wounds. These include surgical, chemical, enzymatic, mechanical and biological techniques [5, 6]. Although enzymatic debridement is a time consuming process, it is still a primary technique for wound debridement in certain cases, especially when alternative methods such as surgical or conservative sharp wound debridement are not feasible due to bleeding disorders or other complication [5]. Of particular interest to this study are the enzymatic debridement method and the possibility of accelerating/promoting this process aiming at its enhanced clinical practice in wound management.

There is evidence that applied EMR in the visible light range can modulate protein and cellular activity [7, 8]. Reported studies show that endochondral bone formation can be regulated by exogenously applied biophysical stimuli that include EMR. Some studies revealed that exposures to pulsed electromagnetic fields (PEMF) enhance chondrogenic differentiation and the synthesis of cartilage extracellular matrix proteins. Studies focused on investigating the effects of visible light on cell proliferation and their metabolisms were reported [9]. Biological processes can be modulated by induction of light of particular frequencies of applied EMR [3, 4]. Our previous studies show that activity of L-Lactate Dehydrogenase can be affected by external light of particular wavelengths, computed using the Resonant Recognition Model [3, 4]. The RRM theory states that an external EMR at a particular frequency would produce resonant effects on protein biological activity [2, 3]. The resonant absorption and resonant interactions have been proposed as an explanation for the marked sensitivity of living systems to EMR [10]. Each biological process involves a number of interactions between proteins and their targets, which are based on energy transfer between the interacting molecules. Protein interactions are highly selective, and this selectivity is defined within a protein's structure. The RRM is designed for analysis of protein (DNA) interactions and their interaction with EMR [2–4]. In our previous work [2], a relationship between the RRM spectra of some protein groups and their interaction with visible light has been established. The RRM concept states that external EMR at a particular activation frequency would produce resonant effects on protein biological activity [3, 4]. This hypothesis is validated experimentally here by irradiating

collagenase enzyme (that plays a crucial role in enzymatic debridement) by visible light in the frequency range of 400–500 nm.

2. MATERIALS AND METHODS

The RRM is a physico-mathematical approach based on digital signal processing [2]. The application of the RRM involves two stages of calculation. The first is the transformation of the amino acid sequence into a numerical sequence. Each amino acid is represented by its Electron-Ion Interaction Potential (EIIP) value which describes the average energy states of all valence electrons in a given amino acid [2]. A unique number can thus represent each amino acid or nucleotide, irrespective of its position in a sequence. Then the numerical series obtained are analyzed by digital signal analysis methods, Fourier and Wavelet transforms, in order to extract information pertinent to the biological function. A multiple cross-spectral function is defined and calculated to obtain the common frequency components from the spectra of a group of proteins. Peak frequencies in such a multiple cross-spectral function denote common frequency components for all sequences analyzed.

It was shown in our previous studies that all protein sequences with a common biological function have a common frequency component in the free energy distribution of electrons along the protein backbone. This characteristic frequency was shown to be related to protein biological function [2–4]. It was also shown that proteins and their targets share a characteristic frequency. Thus, it can be postulated that RRM frequencies characterize not only a general function but also a recognition/interaction between the particular proteins and their target at a distance. Thus, protein interactions can be viewed as a resonant energy transfer between the interacting molecules. This energy can be transferred through oscillations of a physical field, possibly electromagnetic in nature [2]. Since there is evidence that proteins have certain conducting or semi-conducting properties, a charge moving through the protein backbone and passing different energy stages caused by different amino acid side groups can produce sufficient conditions for a specific electromagnetic radiation or absorption [2]. A strong linear correlation exists between the predicted and experimentally determined frequencies corresponding to the absorption of electromagnetic radiation of such proteins [2]. It is inferred that approximate wavelengths in real frequency space can be calculated from the RRM characteristic frequencies for each biologically related group of sequences. These calculations can be used to predict the wavelength of the light irradiation, which might affect the biological activity of exposed proteins. The frequency range predicted for protein interactions is from 10^{13} Hz to 10^{15} Hz. This estimated range includes IR, visible and UV light. These computational predictions were confirmed by comparison of: (i) absorption characteristics of light absorbing proteins and their characteristic RRM frequencies [2]; (ii) frequency selective light effects on cell growth and characteristic RRM frequencies of growth factors [2]; and (iii) activation of enzymes by laser radiation [2].

These results indicate that the specificity of protein interaction is based on a resonant electromagnetic energy transfer at the frequency specific for each interaction. A linear correlation between the absorption spectra of proteins and their RRM spectra with a regression coefficient of $K = 201$ was established. Using RRM postulates, a computationally identified characteristic frequency for a protein functional group can be used to calculate the wavelength of applied irradiation, λ , defined as $\lambda = 201/f_{\text{RRM}}$, which could activate this protein sequence and modify its bioactivity [2, 3]. Here, we utilize this relationship to calculate the frequencies/wavelengths that modulate the bioactivity of the selected enzyme and investigate/evaluate their activation experimentally.

3. EXPERIMENTAL STUDY

3.1. Chemicals

TES free acid, Calcium Chloride with Dihydrate, Collagen Type 1, Collagenase were all obtained from Sigma.

3.2. Equipment

As a source of visible light radiation we used Monochromators SPEX 270M: (Princeton Instruments, Trenton, NJ, USA) 1200 g/mm grating, focal length 270 mm, resolution 0.1 nm at 500 nm, dispersion 3.1 nm/mm, range 400–890 nm, RS232 connection with HP 34001A, controlled by LabView 6.1 (National Instruments). For measurement of absorbance of the analyzed enzyme solutions we used Ocean Optics USB2000 spectrometer coupled with USBISS-UV/VIS, (Ocean Optics, FL, USA) range 190–870 nm, USB-2 connection with Pentium IV (Windows XP). Software automatically monitors and saves the absorption coefficient at 570 nm wavelength every 10 sec.

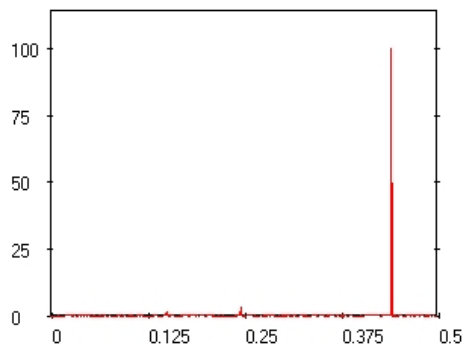


Figure 1: Multiple cross spectral function of 28 vertebrate collagenase sequences. The x axis represents the relative RRM frequency. The y axis represents the normalized intensity.

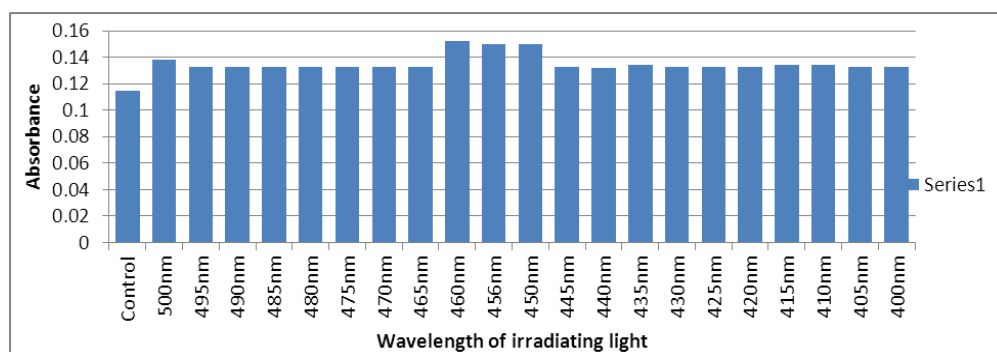


Figure 2: The effect of irradiating light on absorbance of Collagen.

3.3. Enzymatic Assay

Experimental solutions were prepared according to the standard enzymatic assay of collagenase from Sigma-Aldrich. The experiments were divided into two groups: (i) Group 1 (sham-exposure), collagenase sample not exposed to applied irradiation. This sample was used as a control for evaluating effects of irradiation on exposed *vs.* non-exposed samples; and (ii) Group 2, collagenase samples irradiated with light of different wavelengths (400–500 nm, with 5 nm steps) for 600 sec. All experiments were performed at 37°C.

3.4. Experimental Protocol

1. The cuvette, filled with the collagenase solution, was irradiated with light of a particular wavelength (400–500 nm) for 600 sec or incubated for 600 sec for the control enzyme sample;
2. The irradiated or incubated non-exposed samples were added to the already prepared enzymatic substrate solution of Collagen Type I (pH 7.4);
3. The optical density of digested collagen solution is measured at 570 nm (Sigma assay) for each selected irradiating wavelengths (400 nm–500 nm, with a step of 5 nm) and the control sample. With the aim at eliminating the effect of all possible artifacts (PH, temperature, and concentrations), the measurements were repeated three (3) times for each irradiating wavelength to evaluate changes in collagenase absorbance (changes in activity of collagenase solutions) before and after the light exposures.

4. RESULTS

In this study, the RRM was used to compute the RRM characteristic frequency of 28 vertebrate collagenase proteins, that corresponds to their common biological activity. Collagenase primary protein sequences were collected from the NCBI protein database. A multiple cross-spectral analysis was performed resulting in one prominent RRM characteristic frequency identified at $f = 0.4385$ (Fig. 1). This frequency is related to the biological activity of the analyzed Collagenase proteins, as was found in our previous studies.

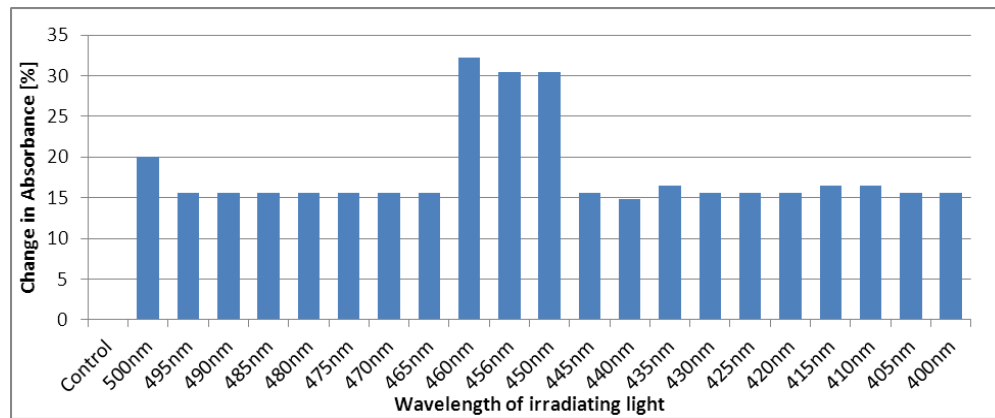


Figure 3: Relative change in Collagen absorbance upon light irradiation, %.

This RRM frequency $f = 0.4385$ is used to calculate the wavelength of external irradiation, λ , which can activate Collagenase protein and modify its bioactivity, $\lambda = 201/f_{\text{RRM}}$. Thus, the wavelength of the EMR required for Collagenase enzyme activation will be at or near 456 nm. To validate this predicted activation wavelength, the experiments were conducted according to the experimental protocol outlined above with the results presented in Fig. 3 and Fig. 4. The results revealed that light (400–500 nm) affects the absorbance of digested collagen (the influence of irradiated collagenase solution) at different degrees.

Figure 2 shows that the selected light exposures increase Collagenase absorbance and thus, affect its enzyme activity. A significant effect (compared to the control sample) is seen at the wavelengths of 450, 456, and 460 nm (Fig. 3) with the increase of 30–32% in Collagen absorbance achieved at these particular wavelengths. The maximum change in absorbance of digested collagen is in the range predicted computationally by the RRM. A change of 20% in absorbance can be seen at 500 nm, and even smaller changes of 15–16% are seen at all other wavelengths (Fig. 3). These findings support the hypothesis that protein activity of Collagenase can be modulated by external light of the particular wavelengths predicted by the RRM approach.

5. CONCLUSIONS

The results presented reinforce the previously developed linear relationship between the calculated RRM frequencies and wavelengths of light radiation. With this correlation in mind, it is now possible to calculate wavelengths of light irradiation which will affect different biological processes. These findings suggest that EMR can be used as a non-invasive treatment to promote enzymatic debridement and thus assist wound healing. The possibility to computationally calculate the RRM frequencies, followed by the use of IR and visible light to produce the desired biological mutations and alterations in proteins will benefit the development of new biomaterials, and advanced technologies.

ACKNOWLEDGMENT

We acknowledge support by Robert and Josephine Shanks Scholarship and Australian Postgraduate Award.

REFERENCES

1. Falanga, V., “Wound bed preparation and the role of enzymes: A case for multiple actions of therapeutic agents,” *Wounds — A Compendium of Clinical Research and Practice*, Vol. 14, No. 2, 47–57, 2002.
2. Cosic, I., *The Resonant Recognition Model of Macromolecular Bioactivity: Theory and Applications*, Birkhauser Verlag, Basel, 1997.
3. Vojisavljevic, V., E. Pirogova, and I. Cosic, “Review of studies on modulating enzyme activity by low intensity electromagnetic radiation,” *Proc. 32nd Annual Intl. Conf. IEEE EMBS*, 835–838, 2010.
4. Vojisavljevic, V., E. Pirogova, and I. Cosic, “The effect of electromagnetic radiation (550–850 nm) on l-Lactate dehydrogenase kinetics,” *Intl. J. Radiation Biology*, Vol. 83, No. 4, 221–230, 2007.

5. Shi, L. and D. Carson, “Collagenase santyl ointment: A selective agent for wound debridement,” *Journal of Wound Ostomy Continence Nurs.*, Vol. 36, No. 6, 12–16, 2009.
6. Ramundo, J. and M. Gray, “Enzymatic wound debridement,” *Journal of Wound Ostomy Continence Nurs.*, Vol. 35, No. 3, 273–280, 2008.
7. Blank, M. and L. Soo, “Optimal frequencies for magnetic acceleration of cytochrome oxidase and NaK-ATPase reactions,” *Bioelectrochemistry and Bioenergetics*, Vol. 53, No. 2, 171–174, 2001.
8. Kujawa, J., L. Zavodnik, and I. Zavodnik, “Low-intensity near-infrared laser radiation-induced changes of acetylcholinesterase activity of human erythrocytes,” *Journal of Clinical Laser Medicine Surgery*, Vol. 21, No. 6, 351–355, 2003.
9. Karu, T. I., L. V. Pyatibrat, and G. S. Kalendo, “Photobiological modulation of cell attachment via cytochrome c oxidase,” *Photochem and Photobiol. Science*, Vol. 3, No. 2, 211–216, 2004.
10. Frohlich, H., “Coherent excitation in active biological systems,” F. Gutmann & H. Keyzer, Eds., *Modern Bioelectrochemistry*, 241–261, Plenum, NY, 1986.

The Comparison of the Contrasts of Magnetic Resonance Images of Plants

M. Pokludová and E. Gescheidtová

Department of Theoretical and Experimental Electrical Engineering
Brno University of Technology, Kolejní 4, Brno 612 00, Czech Republic

Abstract— To obtain an image with the largest information value, the best image contrast during the measurement of the object in the magnetic resonance tomograph is necessary to achieve. This contrast depends on the physical properties of the object, in particular a proton density and relaxation properties of the material. Furthermore, the contrast depends on parameter characteristic for each MR method: Spin Echo, Gradient Echo and Inversion Recovery. The echo time and repetition time are included between the two most important parameters of pulse sequence. We can create four different variants of contrast by combining these two mentioned times: the contrast spin density, the T_1 weighted contrast, the T_2 weighted contrast, and the last one is inappropriate setting for the contrast. Each resulting contrast is suitable for displaying different plant stem tissues. An increase in the contrast can also be achieved by adding contrast (paramagnetic) substances for differentiation of isomagnetics tissues. The aim of this paper is to display the internal morphology of plants by various methods with subsequent comparison of contrast and identification of an appropriate method for the study of transport of substances in the stem of the plant. Euphorbia cactus was chosen for the study of the image contrasts. This plant was inserted into working space of the tomograph. Images of the plant stem were acquired by a magnetic resonance tomograph with the magnetic field induction of 4.7 T (200 MHz). The evaluation of the results obtained via the applied methods as related the last measurement. The data processing was performed by using Marevisi and Matlab programs. Monitored parameters of individual plant samples were inserted into a table and inserted into graphs. By evaluating and comparing the relaxation times, it can be determined that, in the same selected points, the relaxation time T_2 exhibits shorter values than the relaxation time T_1 . This holds true despite the fact that method for weighted by relaxation time T_2 is a faster method. Moreover, the final image acquired via this method is of inferior quality. The resulting image after weighted relaxation time T_1 nevertheless exhibits a lower value of image intensity.

1. INTRODUCTION

The contrast depends on the following characteristics of the monitored tissue: the density of protons, relaxation properties of the tissue, and the setting of three parameters of the pulse sequence. The first parameter of the pulse sequences is the energy used of the RF pulse; this parameter is known as the flip angle. Correlation applies here the more energy is emitted in the monitored tissue the longer time interval is needed for the full relaxation. The second parameter is the repetitive time T_R , which describes the time interval between two successive RF pulses applied to the same slice. With shorter time T_R needed for less relaxation time T_1 . The third parameter is the echo time T_E , which indicates the time between the excitation pulse and detection of the resonance signal. In the Table 1 below the possibilities of times with the resulting contrasts are listed [1].

2. EXPERIMENTAL MEASUREMENTS

Euphorbia cactus was chosen for the study of contrast in the MR images (plant stem). The plant was placed into the magnetic resonance tomograph with magnetic field induction of 4.7 T/75 mm. The parameters used by the MRI methods are given in Table 2.

2.1. The Proton Density Contrast

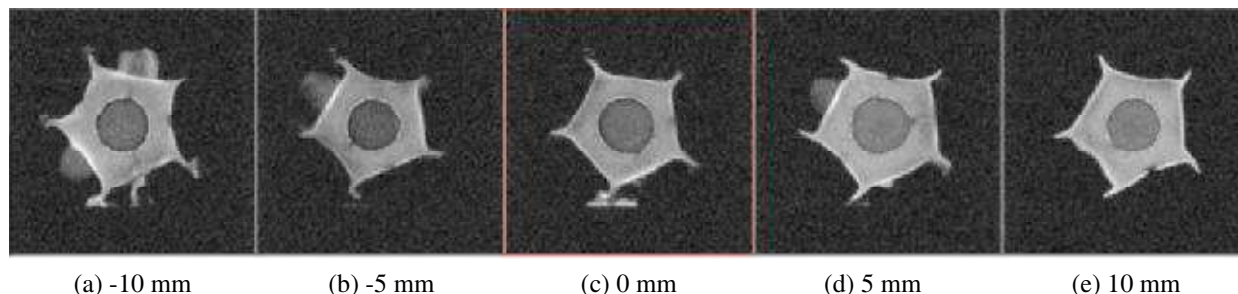
To determine the intensity of the image weighted by proton density, the data were loaded in the Marevisi program where they were transferred from the K-space into the spatial domain using the

Table 1: The resulting contrasts to the basis of times changes.

Contrast	Short time T_E	Long time T_E
Short time T_R	T_1 weighted	Inappropriate image
Long time T_R	Proton density contrast	T_2 weighted

Table 2: The parameters of chosen pulse sequences.

Spine Echo method	Gradient Echo method	Inversion Recovery method
$T_R = 3\text{ s}$	$T_R = 3\text{ s}$	$T_R = 3\text{ s}$
$T_E = 14, 20, 50, 100, 200\text{ ms}$	$T_E = 5, 6\text{ ms}$	$T_E = 14, 50, 200, 500, 1000, 2500\text{ ms}$

Figure 1: The series of slices obtained by the SE method at various distances from the z axis.

Selected point	SE method [$\times 10^3$]	GE method [$\times 10^3$]
1	129.3	44.6
2	65.1	Noise
3	15.2	14.1
4	90.2	105.7
5	34.2	Noise

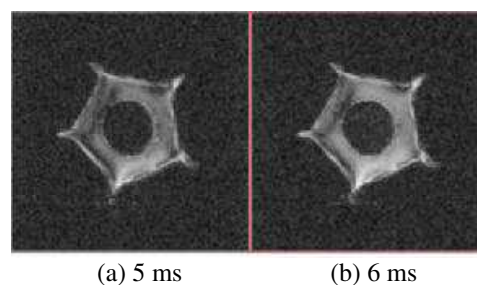


Table 3: The mean value of intensity from selected areas of SD images.

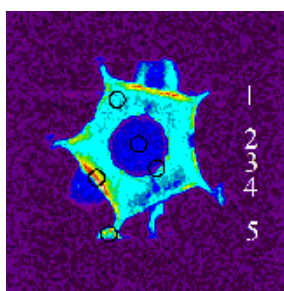
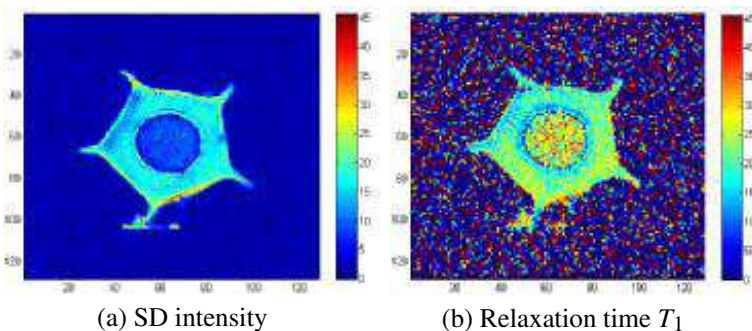
Figure 2: The series of slices acquired by GE method at different times T_E .

Figure 3: The image of stem slice with numbered areas.

Figure 4: The images of intensity weighted by relaxation time T_1 .

Fourier transform [2]. In Figure 1, the reconstructed images of the cactus stem are introduced. These images were obtained by application the spin echo (SE) method with the time $T_E = 14\text{ ms}$ and at different distances from the centre of the reference sample in z axis. In Figure 1, the leaves around the stem can be seen. Some large leaves were removed before the stem was inserted in the tomograph, and therefore, spilled sap can be seen in Figure 1(c). The slices obtained by the gradient echo (GE) method at time $T_E: 5$ and 6 ms are shown in Figure 2. We can see there much worse contrast in comparison with the previous images (Figure 1). In the centre of the images obtained via GE method (Figure 2), an artefact of susceptibility caused by inhomogeneity of the external magnetic field can be observed [3].

The slices (SE and IR method) with the highest contrast were selected to calculate the mean value of intensity of the weighted spin density images. There are two images, the first obtained by the SE method in the time $T_E = 14\text{ ms}$, and the second by the GE method in the time $T_E = 6\text{ ms}$.

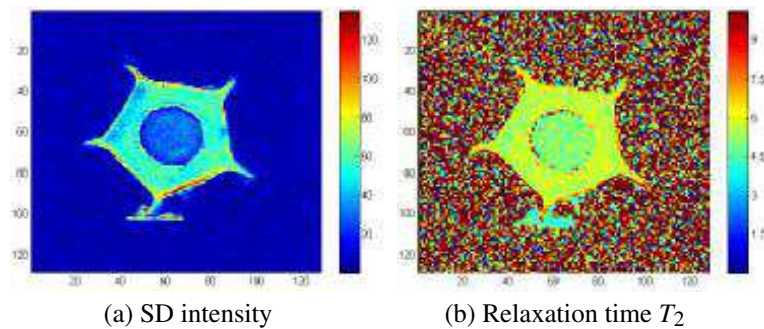
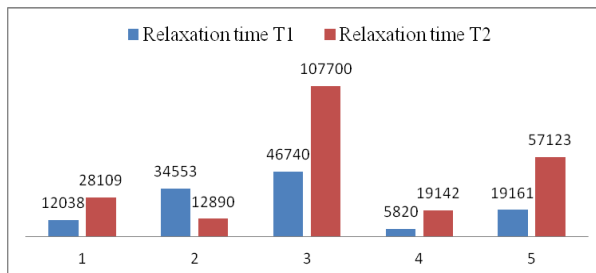
Figure 5: The images of intensity weighted by relaxation time T_2 .

Figure 6: Comparison of the values of relaxation times in selected areas of the image.

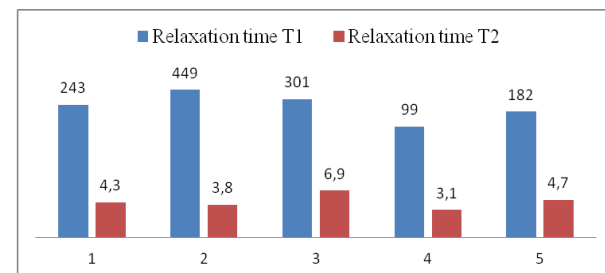


Figure 7: Comparison of image intensity values in selected areas of the image.

Table 4: The intensity values weighted by relaxation time T_1 .

Selected point	SD intensity [$\times 10^3$]	Relaxation time T_1 [$\times 10^{-3}$]
1	19.2	182
2	12.0	243
3	5.8	99
4	46.7	301
5	34.5	449

Table 5: The intensity values weighted by relaxation time T_2 .

Selected point	SD intensity [$\times 10^3$]	Relaxation time T_2 [$\times 10^{-3}$]
1	57.1	4.7
2	28.1	4.3
3	19.2	3.1
4	107.7	6.9
5	128.9	3.8

The mean values of intensity (Table 3) were from selected areas of slices (Figure 3) computed in the Marevisi program. In Table 3, the values of image intensity determined as a noise are can be seen (lines 2 and 5 of GE methods). This noise is caused by artefact of susceptibility [3]. The colours in Figure 3 correspond to the intensities, which is proportional to the number of proton nuclei in a given location of cactus stem. The higher values of image intensity correspond to a larger amount of water, while the shorter values correspond to a firmer structure of plant tissue culture.

2.2. The Contrast Weighted by Relaxation Time T_1

To obtain the image weighted by relaxation time all images (obtained via IR method) were loaded into the Marevisi program (for different times T_E). These images had to be adjusted by using two phase corrections: the first order correction to create a homogeneous environment (the resulting image has a solid colour), and the second order correction for finding the maximum signal (resulting image exhibits the clearest contrast of all structures). Then a series of images was weighted to provide the resulting weighted image displayed in Figure 4. Each selected area (according to Figure 3) corresponds to one line in Table 4 with listed measured relaxation times and signal intensities. From the images weighted by relaxation time T_1 follows that a longer relaxation time corresponds to a higher intensity of the point. The relaxation time is longer at the nutritive fibre (in Table 4, marked line 5). Therefore, the particles return more slowly to the equilibrium position [4].

2.3. The Contrast Weighted by Relaxation Time T_2

Weighting by relaxation time T_2 is carried out in the same way as in the case of time T_1 . The images obtained by SE method were loaded in the program Marevisi. Since it was a multi sequence method, images in the axis $z = 0$ had to be saved under different names (for all times T_E) and reloaded for further processing. The resulting image after weighting by relaxation time T_2 is shown in Figure 5. Each selected area (according to Figure 3) corresponds to one measured relaxation time and signal intensity (Table 5). From Table 5, it can be seen that the firmly bounded structure (centre sample) has a shorter relaxation time than the other sections containing larger admixtures of water [4].

3. CONCLUSIONS

Gradual application of the MRI method with subsequent weighting can detect the internal structure of plants to acquire basic knowledge about the morphology of plants. This knowledge is necessary for the non-destructive detection of any anomalies in plants. By comparing the values of relaxation times from the graph in, we can see that in the same selected points the values of relaxation time T_2 exhibits shorter than the values of relaxation time T_1 . By comparison of the image intensity values from the graph in Figure 7, we can see that weighting by relaxation time T_1 has lower values.

ACKNOWLEDGMENT

This work was supported within the framework of projects Nos. 102/11/0318 and 102/12/1104 of the Czech Science Foundation of the Czech Republic and the project of the BUT Grant Agency FEKT-S-11-5/1012.

REFERENCES

1. Liang, Z. P. and P. Lauterbur, *Principles of Magnetic Resonance Imaging*, IEEE Press, New York, 1999.
2. Morris, G. A. and R. Freeman, "Selective excitation in Fourier transform nuclear magnetic resonance," *Journal of Magnetic Resonance*, Vol. 213, No. 2, 2011.
3. Steibauer, M. and K. Bartusek, "Magnetic susceptibility measurement using magnetic resonance tomograph," *Acta Technica ČSAV*, Vol. 53, No. 1, 2008, ISSN 0001-7043.
4. Bartušek, K., E. Gescheidtová, R. Kízek, and Z. Dokoupil, "Zpracování dat při studiu růstu raných smrkových embryí zobrazovacími MR technikami," *Elektrorevue*, Vol. 43, 2008 (in Czech), ISSN 1213-1539.

Electromagnetic Structures and Inertias of Particles including the Higgs Boson

Michael J. Underhill

Underhill Research Ltd, Lingfield, UK

Abstract— The underlying thesis is that all particles and fields are electromagnetic and all particles have defined shapes and density profiles in the three spatial dimensions and in the two dimensions of time and frequency. Electromagnetic string structures suitable for photons [1] and the main sub-atomic particles [2] have previously been presented. The strings are high density currents and line charges, collectively named ‘substance’ ψ , in loops and toroids and these make up the central core of a particle. By ‘electromagnetic coupling’ a particle core induces a ‘potential region’, which is a ‘dark matter atmosphere’ surrounding the core. The atmosphere is a finite region, and thus a finite energy region, where the ‘potential’ Φ_1 from the core ‘substance’ ψ dominates but induces an atmosphere of low density secondary substance ψ_2 with potential Φ_2 . In this way ‘electromagnetic coupling’ with finite energy constraints establishes the shapes and profiles of the sub-atomic particles. These particle models have electromagnetic frequency spectra with discrete lines. The total energy E of the spectral lines and any coupling between them is the gravitational mass m of a particle according to $E = mc^2$.

With an additional assumption the EM model explains the high inertial mass of any particle having a dense core. The additional assumption is that EM coupling between the core and the atmosphere has a small definite time delay. Thus inertia of particles comes from ‘time delayed EM coupling’. It follows that diffuse energy with low density, such as for dark matter, fields, photons and neutrinos, should have low inertial mass relative to gravitational mass.

Young’s double slit diffraction of electrons is explained by the substance cores of the electrons passing through either slit, but with the EM wave potential atmosphere passing through both slits to create a ‘potential diffraction pattern’ that steers the electron cores probabilistically into the observed diffraction patterns. The effective frequency for the diffraction of electrons is the electron (string) frequency Doppler shifted by the electron stream velocity.

The lifetime of the Higgs Boson is predicted to be short $\sim 1.6 \times 10^{-22}$ sec. The Higgs particle is found to have a dominant line spectrum with a line width corresponding to a $Q \sim 380$. The peak of the spectrum is $\sim 6 \times 10^{21}$ Hz, which is at least an order of magnitude greater than for Gamma rays. The Higgs particle is thus a rather unstable quantum and its EM strings may not be easily represented or measured.

A layered and twisting EM string arrow model is considered as a possible structure for neutrinos.

1. INTRODUCTION

The underlying thesis for this paper is that all particles and fields are electromagnetic and have defined shapes and density profiles in the three spatial dimensions and in the two dimensions of time and frequency. Most particles are assumed to have an EM string structure and frequency spectrum of a few discrete ‘lines’. But the Higgs boson or particle can be envisaged to be spherically symmetric without a well defined string structure, and to have a broad line spectrum.

Electromagnetic string structures suitable for photons [1] and the main sub-atomic particles [2] have previously been presented. A photon is an ‘electromagnetic string arrow’ with a single line frequency spectrum as in Figures 1(a) and 1(b). It is envisaged to be ‘dark matter’ with low inertia. A photon is a boson and has zero or unit spin. The unit spin can be taken to correspond to left-hand or right-hand circular polarisation.

Protons, electrons and neutrons can be described by two or more interlaced toroidal string loops arguably having two or more dominant line frequency components in the particle’s spectrum [2]. Electron core string structures are shown in Figures 1(c) to 1(g). The interlacing can be regarded as a representation of circular polarisation and characterises ‘intrinsic spin’. These three particles have half unit spin and so are classified as ‘fermions’. All these particle models have an electromagnetic frequency spectrum with discrete lines. The total energy of the spectral lines is the mass m of a particle according to $E = mc^2$.

However the lifetime of the Higgs Boson is possibly too short for it to have a well defined electromagnetic string structure and a narrow line spectrum. This paper extends the ‘Physical

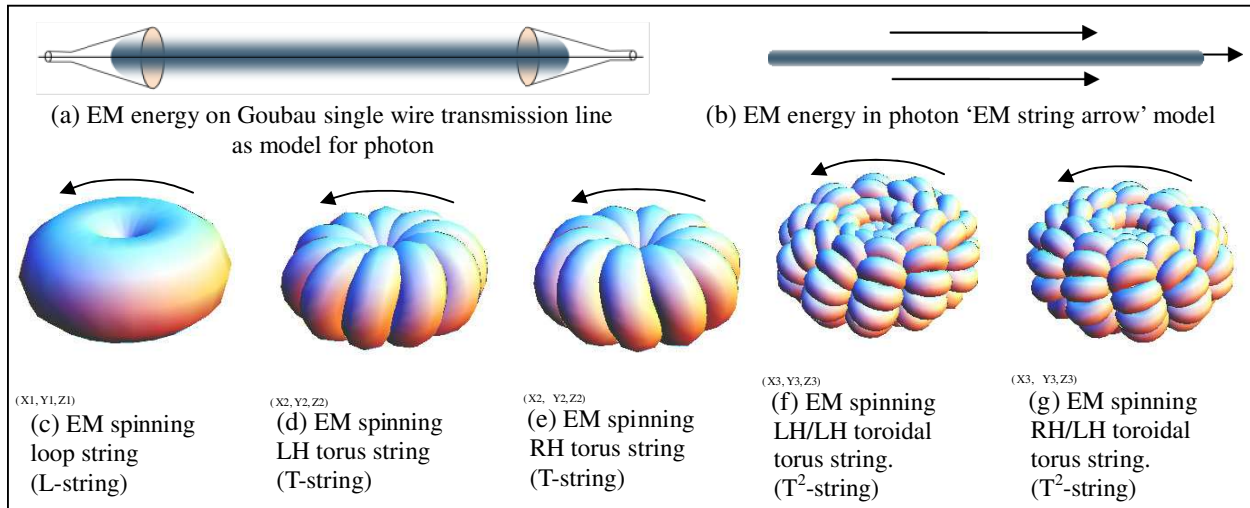


Figure 1: EM String models for photons and sub-atomic particles: (a) EM energy on Goubau single wire transmission line. (b) EM energy in photon ‘EM string arrow’ model, with similar energy distribution to (a). (c) EM spinning loop string; an L-string. (d) EM spinning LH torus string; a T-string. (e) EM spinning LH torus string; a T-string and a mirror image of (d). (f) EM spinning LH/LH toroidal torus string; a T²-string. (g) EM spinning RH/LH toroidal torus string; a mirror image of (f).

Model of Electromagnetism’ [2] to include a spherical particle structure proposed for the Higgs Boson. Whether this is a string structure or not will have to await experimental confirmation that $E = hf$ holds for the core of the Higgs particle. The truth of $E = mc^2$ is not being challenged.

The Physical EM model is also extended to include mechanisms for particle inertia, particle beam diffraction, charged particles and a possible EM neutrino structure.

Figures 1(d) and 1(e) are possible EM string models for electrons with opposite (intrinsic) spins. The spin multiplicity is 2. It is a matter of opinion and possible debate whether the multiplicity should be considered as two extra ‘dimensions’.

Figures 1(f) and 1(g) are possible models for quarks. They allow three dimensions or independent variables of spin that in combination could define the six flavours of up, down, strange, charm, bottom and top [3].

2. INERTIA

All particles are defined as a compact high density ‘substance’ core surrounded by a low density potential (evanescent wave) ‘atmosphere’. Substance ψ is essentially all forms of electromagnetic currents and charges in a volume RSS summed according to their energies. (RSS means ‘Root-Sum-of-the-Squares’). The core substance creates a surrounding (spherical) potential distribution Φ that decays as $1/r$ outside the core, where r is the radial distance from the core centre. For any of the particles having a ‘coherent’ line spectrum, the potential has the same spectrum.

At any point potential Φ and substance ψ are partially coupled by the asymptotic local coupling factor κ_0 . For EM strings and current filaments $\kappa_0 = 1/2\pi$ [4, 5], and for compact quasi-point sources $\kappa_0 = 1/4\pi$. The latter value can be derived from the formula that defines the directivity D of an antenna of capture aperture area A as $D = 4\pi A/\lambda^2$.

For convenience we can define both Φ and ψ in units of the square root of energy. Then we find that just outside the surface of the core $\Phi_2 = \kappa_0\psi_1$ and $\Phi_1 \propto 1/r$. In turn the potential Φ_2 induces or creates substance with density ψ_2 . This means that the atmosphere has energy density $U = \Phi_2\psi_2$.

A more accurate representation of the combined core and atmosphere potential distribution for the dominant line in the particle spectrum is given by Equation (1) of reference [2] as

$$\Phi_n = \left(1 - e^{-\kappa_1/(\sqrt{f} \times r)}\right) \quad (1)$$

This function of r is meromorphic and so advantageously has no central singularity. Away from the centre a $1/r$ law holds. In the case of the Higgs particle the \sqrt{f} term can be combined into

κ_1 and this can be estimated when the size of the Higgs particle has been measured, or calculated from some other assumed physical process.

With respect to Special Relativity we note that for constant particle and observer frame velocities the offset as is seen to be zero in the particle velocity observer frame and to be a finite value as observed from any other observer velocity frame. The observed offset is proportional to the difference between the particle and observer frame velocities.

The atmosphere is primarily a potential distribution created by the core substance. It is taken to be ‘dark matter’ which has gravitational mass in accordance with $E = mc^2$. But because it is diffuse with no dense point-like cores dark matter has a much lower inertial mass for the same amount of energy or gravitational mass.

3. FINITE ENERGY REGIONS AND PARTICLE DENSITY PROFILES

The atmosphere of a particle has energy density $U = \Phi_2\psi_2 \propto 1/r_2$. It follows that the energy added per unit radial distance is constant. The energy of the atmosphere has to be a finite value. We therefore assume that the atmosphere has a finite energy that is less than the core energy by a coupling factor κ_2 and therefore terminates at a finite radial distance $r_2 = r_1/\kappa_2$ where r_1 is the radius of the core. This fundamental process has to hold at all frequencies down to static fields as from a static charge. The energy of the field atmosphere can never become infinite. For the ‘coherent’ coupling that occurs for a particle with a line spectrum, the termination distance can be expected to be κ_2 times the Goubau distance [1, 2].

Figure 2 shows the particle energy density spherical ‘regions’ for two cases having different (EM) coupling factors. Calibration of the coupling and sizes of these two types of particles is under further investigation. More measurement data is needed. Existing theoretical assumptions may have to be modified.

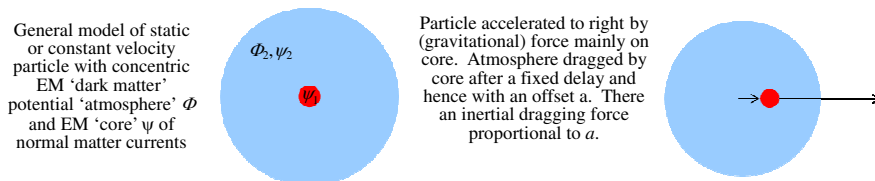


Figure 2: General model of a particle with an explanation for the inertia of normal matter.

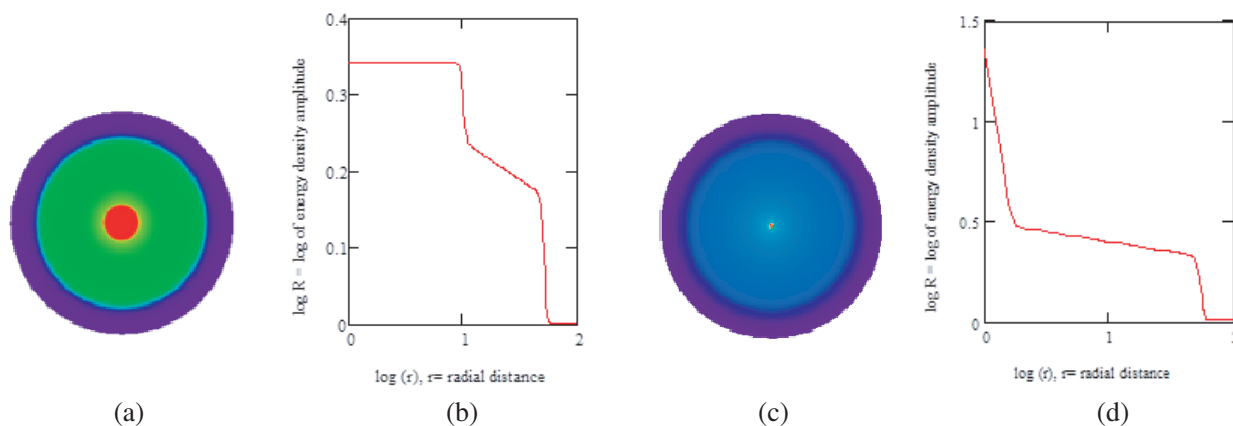


Figure 3: Particle spherical energy density ‘regions’ consisting of central dense ‘substance’ dominated ‘core’ (red) surrounded by $1/r$ potential density dominated ‘atmosphere’, which is size limited by a defined energy constraint, and abruptly descends to the free-space energy density level (violet): (a) Profile of highly self-coupled particles with dominant line spectra with cores as in Figures 1(c) to 1(f). (b) Plot of log of energy density amplitude against log of radial distance for (a). (c) Profile of lightly self-coupled Higgs particle with broadband energy spectrum. (d) Plot of log of energy density amplitude against log of radial distance for (c).

4. EM MODEL OF HIGGS BOSON

The proposed structure for the Higgs particle is a sphere with a core mass/energy density that is constant out to a radial distance at which it decays moderately rapidly towards zero density. This is as shown in Figures 3(c) and 3(d). The density law is assumed to be caused by (electromagnetic) self coupling. Surrounding the dense core is a region, an ‘atmosphere’ dominated by the (gravitational?) potential, giving an inverse square law of field/potential energy density. At a further distance the energy density decays more rapidly than the inverse square law to avoid the total field energy becoming greater than the core energy. The short predicted Higgs particle lifetime may be comparable to the delay between core and atmosphere in Figure 1 and its inertia may be uncertain.

The lifetime of the Higgs Boson is known to be short $\tau \sim 1.6 \times 10^{-22}$ sec [6] and so the Higgs Boson is expected to have a wideband spectrum with no discrete lines. It is believed to have an energy of about 125 GeV and thus a mass of about 125 GeV/c² (a proton is 0.938 GeV/c²). We can apply $E = hf$ as a guess for the dominant line frequency. Then the Higgs particle core is predicted to have a dominant line frequency $f = 125 \times 10^9 \times 0.242 \times 10^{15} = 3 \times 10^{25}$ Hz. The minimum line width is $\sim 2 \times 2\pi/\tau = 7.85 \times 10^{22}$ Hz and this corresponds to a Q of ~ 380 . Thus the Higgs particle does exist for just sufficient time to be assigned a particle line frequency. The particle size is difficult to measure with such a short lifetime. More data is needed. The Higgs boson is thought to be a spin-zero particle. If it does have a string structure then the strings are unlikely to be in the form of simple loops and toroids shown in Figures 1(c) to 1(g). The internal structure of the Higgs Boson has not yet been discovered nor unequivocally established by theory. Thus at this moment in time a simple electromagnetic structure for the Higgs Boson as in Figures 3(c) and 3(d) can be considered to have as much credence as any other offering from theoretical physics.

5. PARTICLE BEAM DIFFRACTION

The initial assumption is that particles are electromagnetic and in general have line spectra with one dominant line. The steady (dc) potential of a charged particle is assumed to be modulated by the particle line frequency f_p . For a particle travelling at velocity towards a pair of slits there is a Doppler shifted potential component of the particle potential atmosphere at a Doppler shift frequency f_d . This potential wave excites the two slits in phase for motion that normal to the plane of the slits. A potential wave distribution in the form of an interference pattern of the Doppler difference frequency is then formed to the right of the slits. The massive particle core passes through one of the slits. It is steered by the potential distribution towards one of the maxima positions on the screen. Which maximum is chosen depends on the precise phases of the Doppler frequency f_d and the line frequency f_p potential components at the moment the core passes through the slits.

Thus Young’s double slit diffraction of electrons is explained by the substance cores of the electrons passing through either slit, but with the EM wave potential atmosphere passing through both slits to create a ‘potential diffraction pattern’ that steers the electron cores probabilistically into the observed diffraction patterns. The effective frequency for the diffraction of electrons is the electron (string) frequency Doppler shifted by the electron stream velocity.

6. EM NEUTRINO STRUCTURE

The neutrino has very low energy, low gravitational mass and even lower inertia, and it conveys a half unit of spin [7]. Neutrinos are assumed to travel at about the speed of light. Recent claims of faster than light travel are now thought to be suspect (See ‘OPERA collaboration’ in [8]). As quoted from Wikipedia [7]: “Neutrino oscillation is a quantum mechanical phenomenon predicted by Bruno Pontecorvo whereby a neutrino created with one of the three lepton flavours (electron, muon or tau) can later be measured to have a different flavour. The probability of measuring a particular flavour for a neutrino varies periodically as it propagates. A given detector type only detects one of the three flavours. The oscillation wavelength of nuclear reactor anti-neutrinos has been measured as about 34 km in the KamLAND facility [9] which corresponds to a beat frequency of 8.8 kHz. Neutrino energies are expected to be measured by the KATRIN experiment [10] in 2015 to be between 0.2 and 2 eV corresponding to dominant line frequencies between 48.4 THz (infrared) and 484 THz (orange), where THz = 10¹² Hz.

Two possible basic neutrino structures, which incorporate a mechanism for the observation of ‘neutrino oscillation, are shown in Figures 5(a) and 5(b). Essentially they are variants of the EM string arrow photon shown in Figure 1(b). The elliptical arrows show phase velocity to be slightly greater than the neutrino speed on the outside of the cores of the arrows and slightly less on the

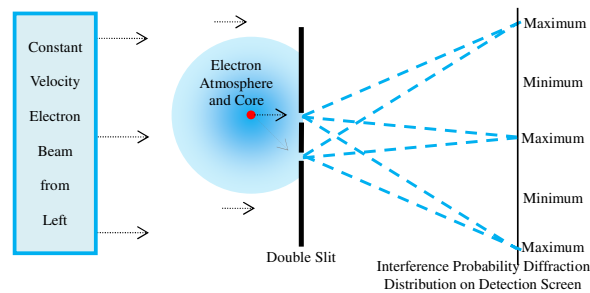


Figure 4: Electromagnetic model of electron and its diffraction pattern depending on velocity and Doppler frequency shift of electron dominant spectral line frequency.

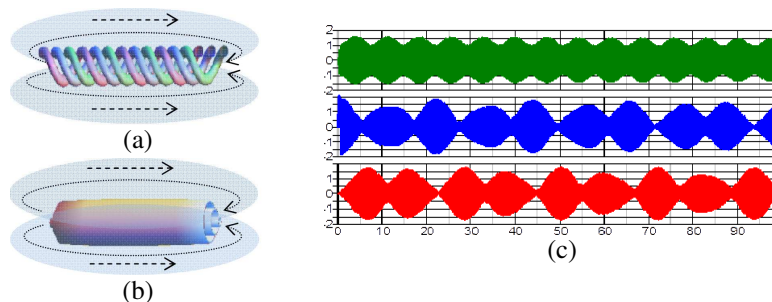


Figure 5: Two possible electromagnetic models of neutrinos incorporating a neutrino oscillation mechanism. (a) Interlaced EM strings. (b) Concentric tubular layers. (c) Coupled tuned circuit modelling of neutrino oscillation.

inside. The exchange of energy between the three strings or layers defining the six flavours is expected to be akin to the exchange of energy between three lightly coupled tuned circuits shown in Figure 5(c). The relative phases provide additional degrees of freedom.

7. CONCLUSION

The main conclusion is that all particles, including the Higgs Boson, and their fields, potentials and physical properties can be expressed in terms of an electromagnetic structure and profile in the three spatial dimensions and the two dimensions of time and frequency. The key enabling factor is ‘electromagnetic coupling’. Its importance as the basis for an Electromagnetic Theory of Everything [2] has once again been demonstrated. The ‘electroweak’ force appears to be related to EM coupling [11]? The neutrino can be considered to be a ‘dark matter’ quantum like the photon and it oscillates between three different EM forms. Two possible EM structures for neutrinos have been put forward as an initial basis. In the ‘Standard Theory’ the Higgs field is said to give mass to all particles. Thus the Higgs field and EM coupling have some features in common.

REFERENCES

- Underhill, M. J., “The phase noise spectrum and structure of photons?,” *Proc. 16th EFTF-2010*, 8 pages, Noordwijk, Netherlands, Apr. 13–16, 2010.
- Underhill, M. J., “A physical model of electro-magnetism for a theory of everything,” *PIERS Online*, Vol. 7, No. 2, 196–200, 2011.
- Wikipedia, <http://en.wikipedia.org/wiki/Quark>.
- Underhill, M. J., “Maxwell’s transfer functions,” *PIERS Proceedings*, 1766–1770, Kuala Lumpur, Malaysia, Mar. 27–30, 2012.
- Underhill, M. J., “Wideband small loop-monopole HF transmitting antenna with implications for Maxwell’s equations and the Chu Criterion,” *PIERS Proceedings*, Taipei, March 25–28, 2013.
- Wikipedia, http://en.wikipedia.org/wiki/Higgs_boson.
- Wikipedia, <http://en.wikipedia.org/wiki/Neutrino>.
- Wikipedia, http://en.wikipedia.org/wiki/Neutrino_oscillation.
- Cheng, G., <http://www.astro.caltech.edu/~golwala/ph135c/20ChengNeutrinoOscillations.pdf>.
- Wikipedia, <http://en.wikipedia.org/wiki/KATRIN>.
- Wikipedia, http://en.wikipedia.org/wiki/Electroweak_interaction.

A Low Phase Noise CMOS VCO for the Millimeter Wave Application

Mingzhu Zhou¹, Jincal Wen¹, Jie Wang¹, and Zhili Liu²

¹The Institute of Electronic and Information Engineering
Hangzhou Dianzi University, China

²Hangzhou C-Sky Microsystems Co. Ltd., China

Abstract— In this paper, a low phase noise VCO for millimeter application is presented. The phase noise introduced by the NMOS channel current and the tank loss resistance are modeled to give approximate evaluation of the circuit character, and an optimization of the phase noise has been done according to this model. An inductor is inserted between the drain of one transistor and the gate of the other transistor, and then the transistor g_m generation efficiency is improved. To acquire an optimization inductor value, HFSS is used to model the device. The circuit has been simulated in a 90 nm CMOS technology. The result indicates that the frequency of the VCO is from 42 to 74 GHz, and the phase noise is -100.738 dBc/Hz @ 1 MHz in 58 GHz. The VCO core consumes 1.225 mA with 0.7 V power supply and the FOM is -195.124 dBc/Hz in 58 GHz. The chip layout occupies $500 \times 800 \mu\text{m}^2$ areas.

1. INTRODUCTION

As the IEEE Standard 802.15.3c allows transmitting in a wide bandwidth within 57.0 GHz to 66.0 GHz containing 4 channels [1], 60 GHz becomes an important candidate for multi-gigabit Wireless Personal Area Network (WPAN) communication. In recent researches, CMOS technology is becoming a good choice for millimeter wave components designs to integrate with baseband circuits.

This paper presents a millimeter oscillator which is realized in 90 nm CMOS technology for IEEE 802.15.3c wireless communication applications. As the phase noise performance of the VCO is difficult to be modeled, many researches about this topic have been done. The LTV (linear Time Invariant) model which addressed by Hajimiri is widely used in the phase noise analysis. To apply this model in a millimeter oscillator and analyze the phase noise introduced by different devices is a difficult question. In this paper, a phase noise model is used to enhance the VCO performance, the transistor level design and the simulation results are also described.

2. CIRCUIT ANALYSIS AND IMPLEMENTATION

The circuit schematic of the VCO is shown in Fig. 1 [2–4]. M1 and M2 are the cross coupled pair; L1 ~ 3, Cvar1 and Cvar2 are consisting of the LC-Tank; M3, M4, L5 and L6 are the buffer circuit. The NMOS cross coupled pair M1 and M2 contributes the negative g_m for the LC tank. According to the phase noise model in [5], the inductor L1 and L2 is set to 60 pH to lower the phase noise induced by the tank loss resistance.

The inductor is modeled in HFSS which is shown in Fig. 2. The inductor value versus the frequency is shown in Fig. 3: The inductor is 56 pH at 60 GHz and the quality is 341. The inductor L3 and L4 are inserted between the drain of one transistor and the gate of the other transistor, and then the transistor g_m generation efficiency is improved.

With an S -parameter simulation at 60 GHz, GA versus the gate voltage V_{bias} is generated. As shown in Fig. 4, GA is a bathtub curve. Based on this curve, the voltage region around 0.6 V is a good biasing region. So the supply voltage of the VCO core is 0.7 V, and the supply voltage of the VCO buffer is 1.2 V.

3. SIMULATION RESULT AND LAYOUT

The post-layout simulation based on the caliber R+C+CC parasitic extraction is performed using Cadence RF spectre tool. The layout of the proposed LC VCO is presented in Fig. 5, and the total chip size is $500 \times 800 \mu\text{m}^2$ including output buffers and I/O pads. With a 0.7 V supply voltage, the oscillator consumes a dc current of 1.232 mA, and with a 1.2 V supply voltage the buffer consumes a dc current of 0.769 μA . The simulated centre frequency of the VCO is 54 GHz with a tuning range of 54.3% from 42.5 to 74.2 GHz. The tuning curve of the oscillator is given in Fig. 6, with the tuning voltage ranging from 0 to 1.2 V. The phase noise curve at 58 GHz is shown in Fig. 7.

The oscillator demonstrates -100.738 dBc/Hz at 1 MHz offset from the oscillation frequency. Fig. 8 shows the phase noise results at 1 MHz offset across the tuning range.

The overall performance of the proposed VCO is listed in Table 1 and compared with other reported works. To make a comparison of the performance of the oscillators, figure of merits FOM [6]. It is defined as

$$FOM = L\{\Delta f\} - 20 \log \left(\frac{f_0}{\Delta f} \right) + 10 \log \left(\frac{P_{DC}}{1 \text{ mW}} \right) \quad (1)$$

where $L\{\Delta f\}$ is the phase noise at an offset frequency Δf from the carrier frequency f_0 , P_{DC} is

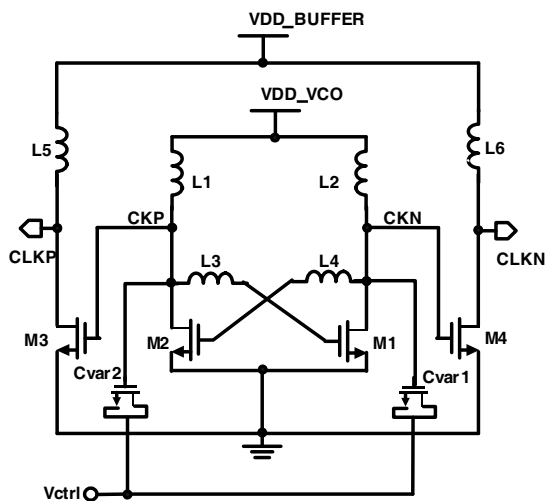


Figure 1: The VCO architecture.

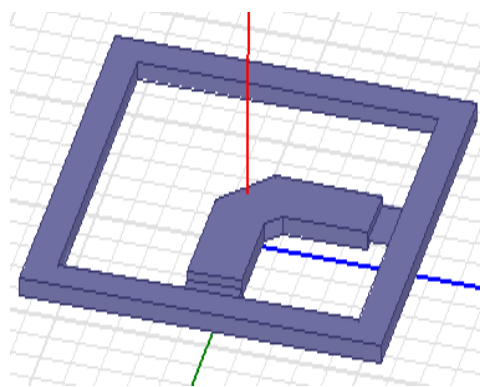


Figure 2: The inductor model in HFSS.

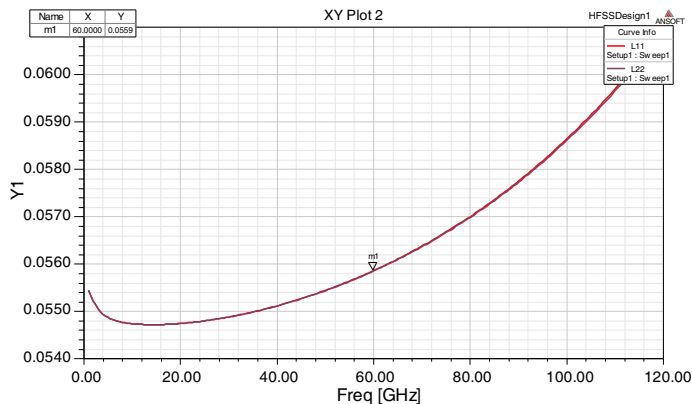


Figure 3: The inductor value versus frequency.

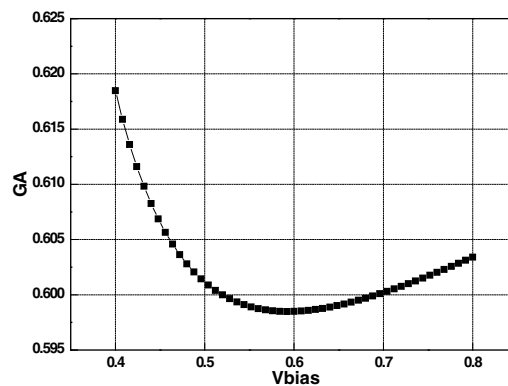


Figure 4: GA versus Vbias at 60 GHz.

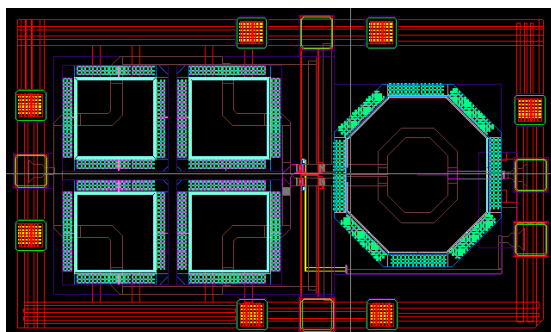


Figure 5: Layout of the VCO.

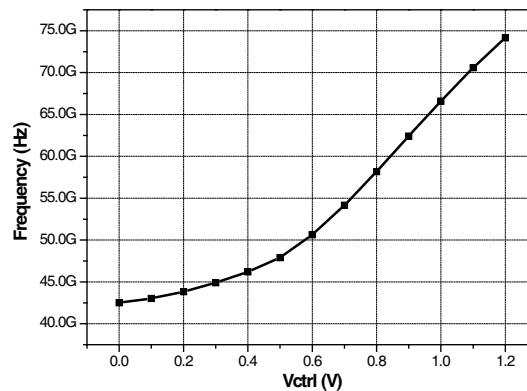


Figure 6: Tuning curve.

Table 1: A comparison with previous designs.

Ref	[7]	[8]	[9]	[10]	[11]	[12]	This work (simulated)
Year	2004	2006	2007	2008	2008	2010	2012
Tech	90 nm SOI	0.13 μm	65 nm SOI	0.13 μm	0.13 μm	90 nm	90 nm
f (GHz)	56.5	56.5	70.2	69.8	62.1	42.6–45.6	42.5–74.2
FTR (%)	14.7	10.27	9.55	4.5	10	6.8	54.3
PDC (mW)	21	9.8	5.4	4.32	3.9	4.8	1.785
P_{noise} (dBc/Hz @ 1 MHz)	-92	-108@10 M	-98.8	-95	-118 ~ -128	-93.7	-100.738
FOM	-173.8	-173.1	-175.8	-188.9	-185	-180.5	-195.12
FOM_{T}	-177.3	-173.4	-175.4	-182	-185	-177.15	-209

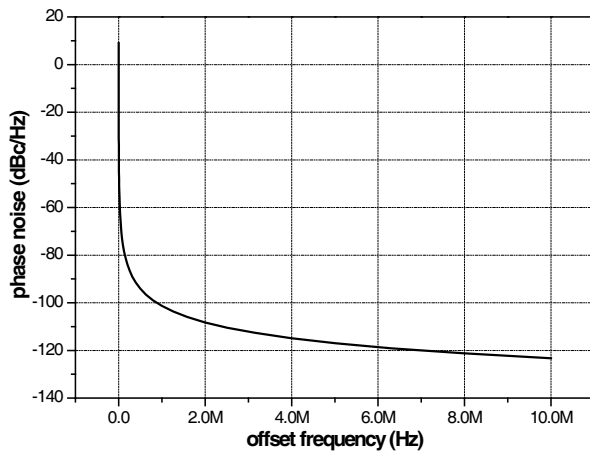


Figure 7: The phase noise.

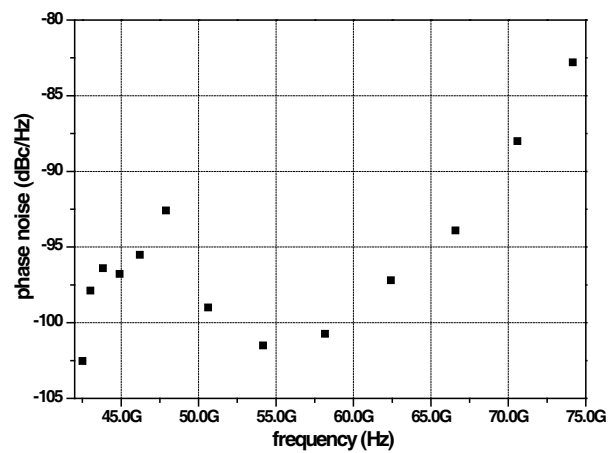


Figure 8: The phase noise @ 1 MHz.

the VCO power consumption in milliwatts. Based on the measurement results, the fabricated VCO exhibits a FOM of -195.124 at 58 GHz carrier frequency. To evaluate the wideband performance of the VCO, figure of merit including the frequency tuning range (FOM_{T}) are employed [6]. It is defined as

$$\text{FOM}_{\text{T}} = L\{\Delta f\} - 20 \log \left(\frac{f_0}{\Delta f} \cdot \frac{\text{FTR}}{10\%} \right) + 10 \log \left(\frac{P_{\text{DC}}}{1 \text{ mW}} \right) \quad (2)$$

where FTR stands for frequency tuning range in percentage. The FOM_{T} of this wideband VCO is -209 dBc/Hz.

4. CONCLUSIONS

A low power and low phase noise mm-wave oscillator using phase noise optimum techniques is demonstrated. Using a 90 nm CMOS, the oscillator achieves a tuning range from 42.5 GHz to 74.2 GHz. The oscillator core consumes 1.785 mW through 0.7 V supply voltage. The phase noise is -100.738 dBc/Hz @ 1 MHz in 58 GHz and the FOM is -195.124 dBc/Hz in 58 GHz.

ACKNOWLEDGMENT

Project supported by the Zhejiang Provincial Natural Science Foundation of China (No. Y1110991), the National Natural Science Foundation of China (No. 61102027), and the Major State Basic Research Development Program of China (973 Program) under Grant 2010CB327403.

REFERENCES

1. IEEE 802.15.3c-2009, IEEE 802.15 WPAN Task Group 3c (TG3c) Millimeter Wave Alternative PHY, Dec. 18, 2012.

2. Li, L. M. and P. Reynaert, “A 60-GHz CMOS VCO using capacitance-splitting and gate-drain impedance-balancing techniques,” *IEEE Transactions on Microwave Theory and Techniques*, Vol. 59, No. 2, 406–413, 2011.
3. Li, L. M., P. Reynaert, and M. Steyaert, “A low power mm-wave oscillator using power matching techniques,” *IEEE Radio Frequency Integrated Circuits Symposium*, 469–472, Boston, America, Jun. 2009.
4. Chai, S. W., J. Yang, and B.-H. Ku, “Millimeter wave CMOS VCO with a high impedance LC tank,” *IEEE Radio Frequency Integrated Circuits Symposium*, 545–548, Anaheim, America, May 2010.
5. Zhou, M. Z., “A low phase noise wideband VCO in 65 nm RF CMOS for low power applications,” *ICMMT*, May 2012.
6. Chien, J.-C., “Design of wide-tuning-range millimeter-wave CMOS VCO with a standing-wave architecture,” *IEEE Journal of Solid-State Circuits*, Vol. 46, No. 9, 1950–1951, 2007.
7. Ellinger, F., T. Morf, and G. Buren, “60 GHz VCO with wideband tuning range fabricated in VLSI SOI CMOS technology,” *IEEE MTT-S Int. Microw. Symp. Dig.*, 1329–1332, Jun. 2004.
8. Cao, C. H. and O, K. K., “Millimeter-wave voltage controlled oscillator in 0.13 μm CMOS technology,” *IEEE Journal of Solid-State Circuits*, Vol. 41, No. 6, 1297–1304, Jun. 2006.
9. Kim, D. D., H. Wohlmuth, and W. Simburger, “A 70 GHz manufacturable complementary LC-VCO with 6.14 GHz tuning range in 65 nm SOI CMOS,” *Int. Solid-State Circuits Conf. Tech. Dig.*, 540–541, Feb. 2007.
10. Chen, H.-K., H.-J. Chen, D.-C. Chang, Y.-Z. Juang, and S.-S. Lu, “A 0.6 V, 4.32 mW, 68 GHz low phase noise VCO with intrinsic-tuned technique in 0.13 μm CMOS,” *IEEE Microw. Wireless Compon. Lett.*, Vol. 18, No. 7, 467–469, Jul. 2008.
11. Borremans, J., M. Dehan, K. Scheir, M. Kuijk, and P. Wambacq, “VCO design for 60 GHz using differential shielded inductors in 0.13 μm CMOS,” *IEEE Radio Freq. Integr. Circuits Symp.*, 135–138, 2008.
12. Huang, Z.-Y. and C.-C. Hung, “1 V 4.8 mW 42.6–45.6 GHz CMOS voltage controlled oscillator for IEEE 802.15.3c wireless communication system,” *Proceedings of Asia-Pacific Microwave Conference*, 485–487, 2010.

The Influence of an Electromagnetic Wave on the Acoustoelectric Current in a Rectangular Quantum Wire with an Infinite Potential

Nguyen Van Nghia¹, Nguyen Quang Bau², Nguyen Van Hieu^{2,3}, and Nguyen Vu Nhan²

¹Department of Physics, Water Resources University, Hanoi, Vietnam

²Department of Physics, College of Natural Sciences, Hanoi National University, Hanoi, Vietnam

³Department of Physics, Danang University of Education, Danang University, Danang, Vietnam

Abstract— The analytic expression for the acoustoelectric (AE) current in the presence of an electromagnetic wave (EMW) induced by the electron-external acoustic wave (external phonons) interactions and electron-internal acoustic wave (internal phonons) scattering in a rectangular quantum wire (RQW) with an infinite potential is calculated by using the quantum kinetic equation for electrons. The dependence of the AE current on the temperature, the external acoustic wave frequency, the frequency of the EMW and the parameters of the RQW is analyzed. The theoretical results are numerically evaluated, plotted and discussed for the specific rectangular quantum wire with an infinite potential GaAs. These results are also compared with those for normal bulk semiconductors and RQW in the case of the absence of the EMW to show difference.

1. INTRODUCTION

It is well known that the propagation of the acoustic wave in conductors is accompanied by the transfer of the energy and momentum to conduction electrons which may give rise to a current usually called the acoustoelectric (AE) current. The study of this problem is crucial, because of the complementary role it may play in the understanding of the properties of the low-dimensional systems (superlattices, quantum wells, quantum wires, quantum dots . . .) which, we believe, should find an important place in the acoustoelectronic devices. The AE effect has been studied in detail in bulk semiconductors by using both the Boltzmann classical kinetic equation and quantum kinetic equation [1–3].

Recently, the acoustoelectric effect in low-dimensional structures has been extensively studied experimentally and theoretically. There have been growing interests in observing this effect in mesoscopic structures [4–8]. The interaction between surface acoustic wave and mobile charges in semiconductor layered structures and quantum wells are an important method to study the dynamic properties of low-dimensional systems. Especially, in recent time the acoustoelectric current was studied in both a one dimensional channel [9] and in a finite-length ballistic quantum channel [10–12]. The acoustoelectric effect was measured by an experiment in a submicron-separated quantum wire [13] and in a carbon nanotube [14].

It is well known that the quantum kinetic equation method have shown the advantage. So, in a recent work we have used this method to calculate the quantum acoustomagnetolectric field in a parabolic quantum well [15], in a CQW with an infinite potential [16], in a RQW with an infinite potential [17]. However, the calculation of the AE current and influence of the electromagnetic wave on AE current in the RQW with an infinite potential by using the quantum kinetic equation method is still open for study. Therefore, the purpose of this work is to examine this effect in the RQW with an infinite potential. In this paper, we use the quantum kinetic equation method to study the influence of the EMW on the AE current induced by the electron-external acoustic wave interactions and the electron-internal acoustic wave (internal phonons) scattering in a RQW with an infinite potential. We have obtained influence of the EMW on the AE current in the RQW with an infinite potential. The dependence of the expression for the AE current on acoustic wave numbers q , the frequency Ω of the EMW, the temperature of the system T , the width and the length of the RQW has been shown. Numerical calculations are carried out a specific the RQW with an infinite potential GaAs to clarify our results.

2. THE QUANTUM KINETIC EQUATION FOR ELECTRONS IN THE PRESENCE OF AN ULTRASOUND

It is well known that the eigenfunction of an unperturbed electron in a RQW with an infinite potential is expressed as

$$\psi_{n,N,\vec{p}}(\vec{r}) = \frac{2}{\sqrt{abL}} \sin\left(\frac{n\pi^2}{a}x\right) \sin\left(\frac{N\pi^2}{b}y\right) \exp\left(i\frac{p_z}{\hbar}z\right), \quad (1)$$

where a and b are, respectively, the cross-sectional dimensions along x - and y -directions, n , N are the subband indexes, L is the length of the quantum wire, and $\vec{p} = (0, 0, p_z)$ is the electron momentum vector along z -direction.

The electron energy spectrum takes the form

$$\varepsilon_{\vec{p}_z}^{n,N} = \frac{\vec{p}_z^2}{2m} + \frac{\pi^2\hbar^2}{2m} \left(\frac{n^2}{a^2} + \frac{N^2}{b^2} \right), \quad (2)$$

where m is the electron effective mass.

Let us suppose that the external acoustic wave of frequency ω_q is propagating along the RQW with an infinite potential axis (Oz). We consider the most realistic case from the point of view of a low-temperature experiment, when $\omega_q/\eta = v_s|q|/\eta \ll 1$ and $ql \gg 1$, where v_s is the velocity of the acoustic wave, q is the external acoustic wave number and l is the electron mean free path. If the conditions $\omega_q/\eta = v_s|q|/\eta \ll 1$ and $ql \gg 1$ are satisfied, a macroscopic approach to the description of the acoustoelectric effect is inapplicable and the problem should be treated by using quantum mechanical methods. We also consider the external acoustic wave as a packet of coherent phonons. Therefore, we have the Hamiltonian describing the interaction of the electron- internal and external phonons system in the RQW in the secondary quantization representation can be written as

$$\begin{aligned} H = & \frac{1}{2m} \sum_{n,N,\vec{p}_z} \left[\hbar^2\pi^2 \left(\frac{n^2}{a^2} + \frac{N^2}{b^2} \right) + \left(\vec{p}_z - \frac{e}{m}\vec{A}(t) \right)^2 \right] a_{n,N,\vec{p}_z}^+ a_{n,N,\vec{p}_z} + \sum_{\vec{k}} \hbar\omega_{\vec{k}} b_{\vec{k}}^+ b_{\vec{k}} \\ & + \sum_{n,N,n',N',\vec{k}} C_{\vec{k}} I_{n,N,n',N'} a_{n',N',\vec{p}_z+\vec{k}}^+ a_{n',N',\vec{p}_z} (b_{\vec{k}} + b_{-\vec{k}}^+) \\ & + \sum_{n,N,n',N',\vec{q}} C_{\vec{q}} U_{n,N,n',N'} a_{n',N',\vec{p}_z+\vec{q}}^+ a_{n',N',\vec{p}_z} b_{\vec{q}} \exp(-i\omega_q t), \end{aligned} \quad (3)$$

where $C_{\vec{k}} = i\Lambda\sqrt{\frac{k}{2\rho v_s S L}}$ is the electron-internal phonon interaction factor, ρ is the mass density of the medium, Λ is the deformation potential constant, $C_{\vec{q}} = i\Lambda v_l^2 \sqrt{\frac{\hbar\omega_q^3}{2\rho F S}}$ is the electron-external phonon interaction factor, with $F = q[\frac{1+\sigma_t^2}{2\sigma_t} + (\frac{\sigma_t}{\sigma_l} - 2)\frac{1+\sigma_t^2}{2\sigma_t}]$, $\sigma_l = \sqrt{1 - (v_s/v_l)^2}$, $\sigma_t = \sqrt{1 - (v_s/v_t)^2}$, v_l (v_t) is the velocity of the longitudinal (transverse) bulk acoustic wave, $S = ab$ is the surface area, a_{n,N,\vec{p}_z}^+ (a_{n,N,\vec{p}_z}) is the creation (annihilation) operator of the electron, $b_{\vec{k}}^+$ ($b_{\vec{k}}$) is the creation (annihilation) operator of the internal phonon and $b_{\vec{q}}$ is the annihilation operator of the external phonon. $|n, \vec{k}\rangle$ and $|n', \vec{k} + \vec{q}\rangle$ are the electron state before and after scattering, $\vec{A}(t) = \frac{e}{\Omega} \vec{E}_0 \sin(\Omega t)$ is the vector potential of an external EMW (where E_0 and Ω are the amplitude and the frequency of the EMW, respectively), $U_{n,N,n',N'} = \frac{1}{abL} \int_V \psi_{n,N,\vec{p}}^*(\vec{r}) U \psi_{n,N,\vec{p}}(\vec{r}) dV$ is the matrix element of the operator $U = \exp(iqy - k_l z)$ (where $k_l = \sqrt{q^2 - (\omega_q/v_l)^2}$ is the spatial attenuation factor of the potential part the displacement field), and the electronic form factor, $I_{n,N,n',N'}$ is written as

$$\begin{aligned} I_{n,N,n',N'} = & \frac{32\pi^4 (q_x a n n')^2 [1 - (-1)^{n+n'} \cos(q_x a)]}{[(q_x a)^4 - 2\pi^2 (q_x a)^2 (n^2 + n'^2) + \pi^4 (n^2 - n'^2)^2]^2} \\ & \times \frac{32\pi^4 (q_y b N N')^2 [1 - (-1)^{N+N'} \cos(q_y b)]}{[(q_y b)^4 - 2\pi^2 (q_y b)^2 (N^2 + N'^2) + \pi^4 (N^2 - N'^2)^2]^2}, \end{aligned} \quad (4)$$

here q_x and q_y are the components of the wave vector in the x - and y -directions.

In order to establish the quantum kinetic equation for electrons in the presence of an ultrasound, we use equation of motion of statistical average value for electrons

$$i\hbar \frac{\partial \langle f_{n,N,\vec{p}_z}(t) \rangle_t}{\partial t} = \langle f_{n,N,\vec{p}_z}(t), H \rangle_t \quad (5)$$

where $\langle X \rangle_t$ is means the usual thermodynamic average of operator X and $f_{n,N,\vec{p}_z}(t) = \langle a_{n,N,\vec{p}_z}^+ a_{n,N,\vec{p}_z} \rangle_t$ is the particle number operator or the electron distribution function.

Substituting the Hamiltonian in Eq. (3) into Eq. (5) and realizing operator algebraic calculations, we obtain a quantum kinetic equation for the electron.

$$\begin{aligned} \frac{\partial f_{n,N,\vec{p}_z}(t)}{\partial t} = & -\frac{1}{\hbar^2} \sum_{K,v=-\infty}^{+\infty} J_K \left(\frac{e\vec{E}_0 \vec{k}_z}{m\Omega^2} \right) J_v \left(\frac{e\vec{E}_0 \vec{k}_z}{m\Omega^2} \right) \exp[i(v-K)\Omega t] \sum_{n',N',\vec{k}} |C_k|^2 |U_{n,N,n',N'}|^2 N_k \\ & \times \int_{-\infty}^t dt' \{ [f_{n,N,\vec{p}_z} - f_{n',N',\vec{p}_z+\vec{k}_z}] \exp \left[\frac{i}{\hbar} \left(\varepsilon_{\vec{p}_z+\vec{k}_z}^{n',N'} - \varepsilon_{\vec{p}_z}^{n,N} + \hbar\omega_q - \hbar\omega_k - K\hbar\Omega + i\delta \right) (t-t') \right] \right. \\ & - [f_{n',N',\vec{p}_z-\vec{k}_z} - f_{n,N,\vec{p}_z}] \exp \left[\frac{i}{\hbar} \left(\varepsilon_{\vec{p}_z}^{n,N} - \varepsilon_{\vec{p}_z-\vec{k}_z}^{n',N'} + \hbar\omega_q - \hbar\omega_k - K\hbar\Omega + i\delta \right) (t-t') \right] \left. \right\} \\ & - \frac{1}{\hbar^2} \sum_{K,v=-\infty}^{+\infty} J_K \left(\frac{e\vec{E}_0 \vec{q}_z}{m\Omega^2} \right) J_v \left(\frac{e\vec{E}_0 \vec{q}_z}{m\Omega^2} \right) \exp[i(v-K)\Omega t] \sum_{n',N',\vec{q}} |C_q|^2 |I_{n,N,n',N'}|^2 N_q \\ & \times \int_{-\infty}^t dt' \{ [f_{n,N,\vec{p}_z} - f_{n',N',\vec{p}_z+\vec{q}_z}] \exp \left[\frac{i}{\hbar} \left(\varepsilon_{\vec{p}_z+\vec{q}_z}^{n',N'} - \varepsilon_{\vec{p}_z}^{n,N} - \hbar\omega_q - K\hbar\Omega + i\delta \right) (t-t') \right] \right. \\ & + [f_{n,N,\vec{p}_z} - f_{n',N',\vec{p}_z+\vec{q}_z}] \exp \left[\frac{i}{\hbar} \left(\varepsilon_{\vec{p}_z+\vec{q}_z}^{n',N'} - \varepsilon_{\vec{p}_z}^{n,N} + \hbar\omega_q - K\hbar\Omega + i\delta \right) (t-t') \right] \left. \right\} \\ & - [f_{n',N',\vec{p}_z-\vec{q}_z} - f_{n,N,\vec{p}_z}] \exp \left[\frac{i}{\hbar} \left(\varepsilon_{\vec{p}_z}^{n,N} - \varepsilon_{\vec{p}_z-\vec{q}_z}^{n',N'} - \hbar\omega_q - K\hbar\Omega + i\delta \right) (t-t') \right] \left. \right\} \\ & - [f_{n',N',\vec{p}_z-\vec{q}_z} - f_{n,N,\vec{p}_z}] \exp \left[\frac{i}{\hbar} \left(\varepsilon_{\vec{p}_z}^{n,N} - \varepsilon_{\vec{p}_z-\vec{q}_z}^{n',N'} + \hbar\omega_q - K\hbar\Omega + i\delta \right) (t-t') \right] \left. \right\}, \quad (6) \end{aligned}$$

with N_q is the particle number external phonon, N_k is the particle number internal phonon, $J_s(x)$ is the s th order Bessel function of the first kind of argument x and δ is the Kronecker delta symbol.

3. ANALYTIC EXPRESSION FOR THE ACOUSTOELECTRIC CURRENT IN A RECTANGULAR QUANTUM WIRE WITH AN INFINITE POTENTIAL

The density of the acoustoelectric current is generally expressed as

$$j = \frac{e}{\pi\hbar} \sum_{n,N} \int \vec{v}_{\vec{p}_z} f_{n,N,\vec{p}_z}(t) d\vec{p}_z, \quad (7)$$

here $\vec{v}_{\vec{p}_z}$ is the average drift velocity of the moving charges.

Solving the Eq. (6), we linear the equation by replacing f_{n,N,\vec{p}_z} by $f_F + f(t)$. With f_F is the equilibrium Fermi contribution function and $f(t)$ function takes the form

$$\begin{aligned} f_{n,N,\vec{p}_z}(t) = & \frac{2\pi\tau}{\hbar} \sum_{s=1}^{\infty} \frac{\sin(s\hbar\Omega t)}{s\hbar\Omega} \sum_{K=-\infty}^{\infty} \frac{Km\Omega^2}{e\vec{E}_0 \vec{q}_z} J_K^2 \left(\frac{e\vec{E}_0 \vec{q}_z}{m\Omega^2} \right) \sum_{n',N',\vec{q}} |C_q|^2 |I_{n,N,n',N'}|^2 N_q \\ & \times \left\{ [f_{n',N',\vec{p}_z+\vec{q}_z} - f_{n,N,\vec{p}_z}] \delta \left(\varepsilon_{\vec{p}_z+\vec{q}_z}^{n',N'} - \varepsilon_{\vec{p}_z}^{n,N} - K\hbar\Omega - \hbar\omega_q \right) \right. \\ & + [f_{n',N',\vec{p}_z+\vec{q}_z} - f_{n,N,\vec{p}_z}] \delta \left(\varepsilon_{\vec{p}_z+\vec{q}_z}^{n',N'} - \varepsilon_{\vec{p}_z}^{n,N} - K\hbar\Omega + \hbar\omega_q \right) \left. \right\} \\ & + \frac{2\pi\tau}{\hbar} \sum_{s=1}^{\infty} \frac{\sin(s\hbar\Omega t)}{s\hbar\Omega} \sum_{K=-\infty}^{\infty} \frac{Km\Omega^2}{e\vec{E}_0 \vec{k}_z} J_K^2 \left(\frac{e\vec{E}_0 \vec{k}_z}{m\Omega^2} \right) \sum_{n',N',\vec{k}} |C_k|^2 |U_{n,N,n',N'}|^2 N_k \\ & \times \left[f_{n',N',\vec{p}_z+\vec{k}_z} - f_{n,N,\vec{p}_z} \right] \delta \left(\varepsilon_{\vec{p}_z+\vec{k}_z}^{n',N'} - \varepsilon_{\vec{p}_z}^{n,N} - K\hbar\Omega + \hbar\omega_q - \hbar\omega_k \right), \quad (8) \end{aligned}$$

where τ is relaxation time of momentum.

Substituting Eq. (8) into Eq. (7), we obtain for the acoustoelectric current

$$j = \frac{e^2 \Lambda^2 m E_0 \tau e^{\beta \varepsilon_F}}{\rho v_s S \hbar^3 \beta^2 \Omega^3} \sum_s \frac{1}{[(s \hbar \Omega \tau)^2 + 1]} \times \sum_{n, N, n', N'} \exp\left(-\frac{\beta \pi^2 \hbar^2}{2m} \left(\frac{n^2}{a^2} + \frac{N^2}{b^2}\right)\right) \left[\frac{D_1 + D_2}{\pi \omega_q L \beta} |I_{n, N, n', N'}|^2 + \frac{2 \phi v_l^4 \omega_q^3 D_3}{\omega_k F} |U_{n, N, n', N'}|^2 \right], \quad (9)$$

with

$$D_1 = \xi_1^3 \exp(\xi_1) [K_3(\xi_1) - 3K_2(\xi_1) + 3K_1(\xi_1) - K_0(\xi_1)]; \quad \xi_1 = \frac{\hbar \beta}{2} \left(\Omega + \omega_q - \frac{\Delta_{n', N', n, N}}{\hbar} \right), \quad (10)$$

$$D_2 = \xi_2^3 \exp(\xi_2) [K_3(\xi_2) - 3K_2(\xi_2) + 3K_1(\xi_2) - K_0(\xi_2)]; \quad \xi_2 = \frac{\hbar \beta}{2} \left(\Omega - \omega_q - \frac{\Delta_{n', N', n, N}}{\hbar} \right), \quad (11)$$

$$D_3 = \chi^3 \exp(\chi) [K_3(\chi) - 3K_2(\chi) + 3K_1(\chi) - K_0(\chi)]; \quad \chi = \xi_1 - \frac{\hbar \beta \omega_k}{2}, \quad (12)$$

$$\Delta_{n', N', n, N} = \frac{\pi^2 \hbar^2}{2ma^2} (n'^2 - n^2) + \frac{\pi^2 \hbar^2}{2mb^2} (N'^2 - N^2); \quad \beta = \frac{1}{k_B T}, \quad (13)$$

where k_B is Boltzmann constant, T is the temperature of the system, ε_F is the Fermi energy and $K_n(x)$ is the modified Bessel function of the second kind.

The Eq. (9) is the analytical expression for the AE current in a RQW with an infinite potential when the momentum relaxation time is a constant. In the case of the vanishing electron-internal phonon interaction, this result is the same as that obtained by using the Boltzmann classical kinetic equation in the RQW with an infinite potential.

4. NUMERICAL RESULTS AND DISCUSSIONS

To clarify the results that have been obtained, in this section, we considered the influence of an electromagnetic wave on the acoustoelectric current in a RQW with an infinite potential. This quantity is considered as a function the length of the RQW with an infinite potential GaAs, the frequency Ω of the EMW, the temperature of system T . The parameters used in the numerical calculations are as follow: $E_0 = 5 \times 10^5 \text{ Vm}^{-1}$; $\tau = 10^{-12} \text{ s}$; $\Lambda = 13.5 \text{ eV}$; $a = b = 40 \text{ \AA}$; $\phi = 10^4 \text{ Wm}^{-2}$; $\rho = 5320 \text{ kgm}^{-3}$; $v_s = 5370 \text{ ms}^{-1}$; $\omega_{\bar{q}_z} = 10^9 \text{ s}^{-1}$; $v_l = 2 \times 10^3 \text{ ms}^{-1}$, $v_t = 18 \times 10^2 \text{ ms}^{-1}$; $m = 0.067 m_e$, m_e being the mass of free electron.

In the Figure 1, we show the dependence of the acoustoelectric current on the length of the RQW at different values of temperature $T = 100 \text{ K}$, $T = 130 \text{ K}$ and $T = 200 \text{ K}$. The value of the

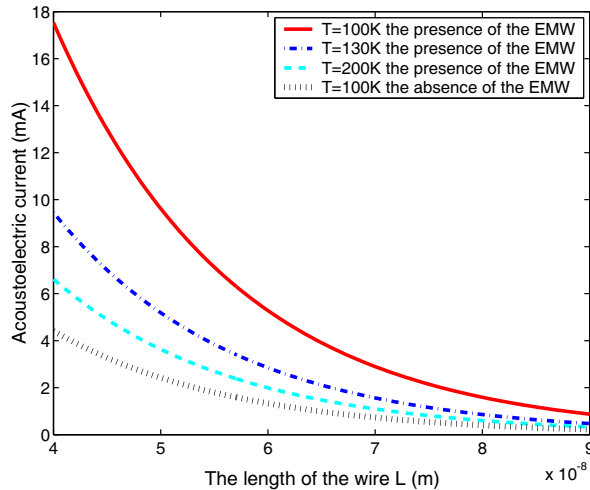


Figure 1: The dependence of the AE current on the length of the RQW at different values of temperature and $\Omega = 5 \times 10^{14} \text{ s}^{-1}$.

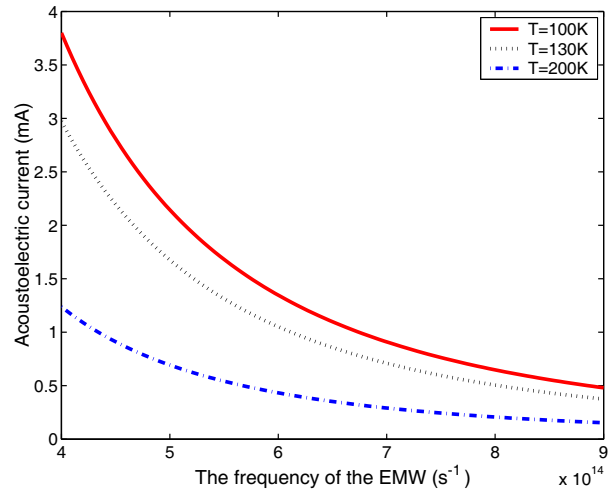


Figure 2: The dependence of the AE current on the frequency Ω of electromagnetic wave at different values of temperature.

AE current strongly decreases with the length of the RQW when the length increases. This value is also smaller as the temperature of the quantum wire increases when other quantities are unchanged. The result showed the different behavior from results in the bulk semiconductor [1–3] and the RQW with an infinite potential in the case of the absence of the EMW. Like the RQW in the case of the absence of the EMW, the results are non-linear but its value is greater than. Unlike the bulk semiconductor [1–3], in the RQW with an infinite potential the AE current is non-linear. The cause of the difference between our result and other results is the effect of the one-dimensional systems characteristic and in the one-dimensional systems the energy spectrum of electron is quantized.

In the Figure 2, we show the dependence of the acoustoelectric current on the frequency Ω of electromagnetic wave with the temperature $T = 100$ K, $T = 130$ K and $T = 200$ K. The value of the AE current decreases as the frequency Ω of EMW increases.

5. CONCLUSION

In this paper, we have analytically investigated the possibility of the influence of the electromagnetic wave on the acoustoelectric current in the RQW with an infinite potential. We have obtained analytical expressions for the influence of the EMW on the AE current in the RQW with an infinite potential. The strong dependences of AE current on the acoustic wave number q , the frequency Ω of the EMW, the temperature T of the system, the width and the length of the RQW. The result showed that the cause of the AE current is the existence of partial current generated by the different energy groups of electrons, and the dependence of the electron energy due to momentum relaxation time.

The numerical result obtained for RQW with an infinite potential GaAs shows that in the dependence of the AE current on the frequency Ω of electromagnetic wave is strong and non-linear. In the dependence of the AE current on the length of the RQW is significantly reduced the length of the quantum wire. This dependence has differences in comparison with that in normal bulk semiconductors [1–3] and the results are similar to those for RQW with an infinite potential in the case of the absence of the EMW. This differs from bulk semiconductors, because in bulk semiconductors [1–3], the AE current vanishes for a constant relaxation time and a geometrical dependence of the AE current due to the confinement of electrons in RQW.

ACKNOWLEDGMENT

This work is completed with financial support from the National Foundation for Science and Technology Development of Vietnam (NAFOSTED) (No. 103.01-2011.18) and the Vietnam National University, Ha Noi (No. QG.TD.12.01).

REFERENCES

1. Parmenter, R. H., "The acousto-electric effect," *Phys. Rev.*, Vol. 89, 990, 1953.
2. Epshtein, E. M. and Y. V. Gulyaev, "Acoustomagnetolectric effect in conductors with monopolar conductivity," *Fiz. Tverd. Tela.*, Vol. 9, No. 2, 376–381, 1967; *Sov. Phys. Solids State*, Vol. 9, No. 2, 288–293, 1967.
3. Galperin, M. Y. and V. D. Kagan, "On the acoustoelectric effect in a strong magnetic field," *Fiz. Tverd. Tela; Sov. Phys. Solid. State.*, Vol. 10, 2038–2045, 1968.
4. Rotter, M., A. V. Kalameitsev, A. O. Grovorov, W. Ruile, and A. Wixforth, "Charge conveyance and nonlinear acoustoelectric phenomena for intense surface acoustic waves on a semiconductor quantum well," *Phys. Rev. Lett.*, Vol. 82, No. 10, 2171, 1999.
5. Afonin, V. V. and Y. M. Galperin, "Acoustoelectric effect and phonon-drag electron thermoelectric-power under weak localization conditions," *Semiconductors.*, Vol. 27, No. 1, 61–65, 1993.
6. Shilton, J. M., D. R. Mace, and V. I. Talyanskii, "Experimental study of the acoustoelectric effects in GaAs-AlGaAs heterostructures," *J. Phys: Condens. Matter.*, Vol. 7, 7675, 1995.
7. Shilton, J. M., V. I. Talyanskii, M. Pepper, D. A. Ritchie, J. E. F. Frost, C. J. B. Ford, C. G. Smith, and G. A. C. Jones, "High-frequency single-electron transport in a quasi-one-dimensional GaAs channel induced by surface acoustic waves," *J. Phys: Condens. Matter.*, Vol. 8, 531, 1996.
8. Maa, F. A. and Y. Galperin, "Acoustoelectric effects in quantum constrictions," *Phys. Rev. B.*, Vol. 56, 4028–4036, 1997.

9. Shilton, J. M., D. R. Mace, V. I. Talyanskii, Y. Galperin, M. Y. Simmons, M. Pepper, and D. A. Ritchie, “On the acoustoelectric current in a one-dimensional channel,” *J. Phys: Condens. Matter.*, Vol. 8, No. 24, 337–341, 1996.
10. Wohlman, O. E., Y. Levinson, and Y. M. Galperin, “Acoustoelectric effect in a finite-length ballistic quantum channel,” *Phys. Rev. B.*, Vol. 62, 7283–7288, 2000.
11. Zimbovskaya, N. A. and G. Gumbs, “The effect of a magnetic field on the acoustoelectric current in a narrow channel,” *J. Phys.*, Vol. 13, No. 20, 409–416, 2001.
12. Galperin, Y. M., O. E. Wohlman, and Y. Levinson, “Quantized acoustoelectric current in a finite-length ballistic quantum channel: The noise spectrum,” *Phys. Rev. B*, Vol. 63, No. 15, 153309–153313, 2001.
13. Cunningham, J., M. Pepper, and V. I. Talyanskii, “Acoustoelectric current in submicron-separated quantum wires,” *Appl. Phys. Lett.*, Vol. 86, 152105, 2005.
14. Reulet, B., A. Y. Kasumov, M. Kociak, R. Deblock, I. I. Khodos, Y. B. Gorbatov, V. T. Volkov, C. Journet, and H. Bouchiat, “Acoustoelectric effects in carbon nanotubes,” *Phys. Rev. Lett.*, Vol. 85, 2829–2832, 2000.
15. Bau, N. Q., N. V. Hieu, and N. V. Nhan, “The quantum acoustomagnetoelectric field in a quantum well with a parabolic potential,” *Superlattices and Microstructures.*, Vol. 52, No. 5, 921930, 2012.
16. Bau, N. Q., N. V. Nhan, and N. V. Nghia, “The dependence of the acoustomagnetoelectric current on the parameters of a cylindrical quantum wire with an infinite potential in the presence of an external magnetic field,” *PIERS Proceedings*, 1452–1456, Suzhou, China, Sep. 12–16, 2011.
17. Nghia, N. V., N. Q. Bau, N. V. Nhan, and D. Q. Vuong, “Calculation of the acoustomagnetoelectric field in a rectangular quantum wire with an infinite potential,” *PIERS Proceedings*, 772–777, Kuala Lumpur, Malaysia, Mar. 27–30, 2012.

Influence of a Strong Electromagnetic Wave (Laser Radiation) on the Hall Coefficient in Doped Semiconductor Superlattices with an In-plane Magnetic Field

N. Q. Bau¹, N. V. Nghia¹, N. V. Hieu¹, and B. D. Hoi^{1,2}

¹Department of Physics, College of Natural Science, Vietnam National University, Hanoi, Vietnam

²Department of Physics, National University of Civil Engineering, Hanoi, Vietnam

Abstract— The Hall effect is studied theoretically in a doped semiconductor superlattice (DSSL) with a periodical superlattice potential in the z -direction, subjected to a crossed dc electric field $\vec{E}_1 = (0, 0, E_1)$ and magnetic field $\vec{B} = (0, B, 0)$ (\vec{B} is oriented in the plane of free motion of electrons) in the presence of a strong electromagnetic wave (EMW) characterized by electric field $\vec{E} = (E_0 \sin(\Omega t), 0, 0)$ (where E_0 and Ω are the amplitude and the frequency of EMW, respectively). By using the quantum kinetic equation method for electrons interacting with optical phonons at high temperatures, we obtain analytical expressions for the components σ_{zz} and σ_{xz} of the Hall conductivity as well as the Hall coefficient with a dependence on B , E_1 , E_0 , Ω , temperature T of the system and the characteristic parameters of DSSL. These expressions are fairly different in comparison to those obtained for bulk semiconductors. The influence of the EMW is interpreted by using the dependencies of the Hall conductivity and the Hall coefficient on the amplitude E_0 and the frequency Ω of the EMW. The numerical results for the GaAs:Si/GaAs:Be DSSL show that the Hall coefficient reaches saturation when the magnetic field or the EMW frequency increases. The Hall coefficient varies strongly at small values and reaches saturation at large values of the doped concentration.

1. INTRODUCTION

The Hall effect in two-dimensional electron systems has been studied in many aspects (see Ref. [1] for a recent review). However, most of the previous works only considered the case when the electromagnetic wave (EMW) was absent and when the temperature so that electron-electron and electron-impurity interactions were dominant (conditions for the integral and fractional quantum Hall effect). This effect in bulk semiconductors in the presence of EMW has been studied in much details by using quantum kinetic equation method [2–6]. In Refs. [2, 3] the odd magnetoresistance was calculated when the nonlinear semiconductors are subjected to a magnetic field and an EMW with low frequency, the nonlinearity is resulted from the nonparabolicity of distribution functions of carriers. In Refs. [4, 5], the magnetoresistance was derived in the presence of a strong EMW for two cases: the magnetic field vector and the electric field vector of the EMW are perpendicular [4], and are parallel [5]. The existence of the odd magnetoresistance was explained by the influence of the strong EMW on the probability of collision, i.e., the collision integral depends on the amplitude and frequency of the EMW. This problem was also studied in the presence of both low and high frequency EMWs [6]. Moreover, the dependencies of magnetoresistance as well as magnetoconductivity on the relative angle of applied fields have been considered carefully [2–6]. Throughout these problems, the quantum kinetic equation method have been seen as a powerful tool. So, in a recent work [7], we have used this method to calculate the quantum acoustomagnetolectric field in a parabolic quantum well subjected to a crossed electric field and magnetic field in the presence of a sound wave. The acoustomagnetolectric field is similar to the Hall field in the bulk semiconductor where the sound flux plays the role of the electric current.

To our knowledge, the Hall effect in low-dimensional semiconductor systems in the presence of an EMW remains a problem to study. Therefore, in this work, by using the quantum kinetic equation method we study the Hall effect in a doped semiconductor superlattice (DSSL) subjected to a crossed dc electric field $\vec{E}_1 = (0, 0, E_1)$ and magnetic field $\vec{B} = (0, B, 0)$ in the presence of an EMW characterized by electric field $\vec{E} = (E_0 \sin \Omega t, 0, 0)$. We only consider the case of high temperatures when the electron-optical phonon interaction is assumed to be dominant and electron gas is nondegenerate. We derive analytical expressions for the Hall conductivity tensor and the Hall coefficient (HC) taking account of arbitrary transitions between the energy levels. The analytical result is numerically evaluated and graphed for the GaAs:Si/GaAs:Be DSSL to show clearly the dependence of the HC on above parameters. The present paper is organized as follows. In the next

section, we briefly present the electronic structure and the Hamiltonian of electron-phonon system in a DSSL. The expressions for the conductivity and the HC are given in Section 3. Numerical results and discussion are given in Section 4. Finally, remarks and conclusions are shown briefly in Section 5.

2. HAMILTONIAN OF ELECTRON-PHONON SYSTEM IN A DSSL IN THE PRESENCE OF A STRONG EMW

We consider a simple model of a DSSL (*n-i-p-i* superlattice), in which electron gas is confined by an additional potential along the *z*-direction and free in the (*x-y*) plane. It is well-known that the motion of an electron is confined in each layer of the system and that its energy spectrum is quantized into discrete levels in the *z*-direction [8]. If the DSSL is subjected to a crossed dc electric field $\vec{E}_1 = (0, 0, E_1)$ and magnetic field $\vec{B} = (0, B, 0)$ and a strong EMW (laser field) is applied in the *z* direction with the electric field vector $\vec{E} = (E_0 \sin \Omega t, 0, 0)$ (where E_0 and Ω are the amplitude and the frequency of the EMW, respectively), then the Hamiltonian of the electron-optical phonon system in the second quantization representation can be written as

$$H = H_0 + U, \quad (1)$$

$$H_0 = \sum_{N, \vec{k}_x} \varepsilon_N \left(\vec{k}_x - \frac{e}{\hbar c} \vec{A}(t) \right) a_{N, \vec{k}_x}^+ a_{N, \vec{k}_x} + \sum_{\vec{q}} \hbar \omega_{\vec{q}} b_{\vec{q}}^+ b_{\vec{q}}, \quad (2)$$

$$U = \sum_{N, N'} \sum_{\vec{q}, \vec{k}_x} D_{N, N'}(\vec{q}) a_{N', \vec{k}_x + \vec{q}_x}^+ a_{N, \vec{k}_x} (b_{\vec{q}} + b_{-\vec{q}}^+), \quad (3)$$

where $|N, \vec{k}_x\rangle$ and $|N', \vec{k}_x + \vec{q}_x\rangle$ are electron states before and after scattering; $\vec{k}_x = (k_x, 0, 0)$; $\hbar \omega_{\vec{q}}$ is the energy of an optical phonon with the wave vector $\vec{q} = (q_x, q_y, q_z)$; a_{N, \vec{k}_x}^+ and a_{N, \vec{k}_x} ($b_{\vec{q}}^+$ and $b_{\vec{q}}$) are the creation and annihilation operators of electron (phonon), respectively; $\vec{A}(t)$ is the vector potential of the EMW; and $D_{N, N'}(\vec{q})$ is the matrix element of interaction which depends on the initial and final states of electron and the interacting mechanism. In our model, the DSSL potential can be considered as a multiquantum-well structure with the parabolic potential in each well, and if we neglect the overlap between the wavefunctions of adjacent wells, the single-particle wave function and corresponding eigenenergy of an electron in a single potential well can be obtained from the model of a parabolic quantum well in Ref. [9] as

$$\Psi(\vec{r}) = \frac{1}{2\pi} e^{i\vec{k}_\perp \vec{r}} \phi_N(z - z_0), \quad (4)$$

$$\varepsilon_N(\vec{k}_x) = \hbar \tilde{\omega} \left(N + \frac{1}{2} \right) + \frac{1}{2m} \left[\hbar^2 k_x^2 - \left(\frac{\hbar k_x \omega_c + e E_1}{\tilde{\omega}} \right)^2 \right], \quad N = 0, 1, 2, \dots, \quad (5)$$

where m and e are the effective mass and the charge of a conduction electron, respectively, $\vec{k}_\perp = (k_x, k_y)$ is its wave vector in the (*x-y*) plane; $z_0 = (\hbar k_x \omega_c + e E_1) / m \tilde{\omega}^2$; $\tilde{\omega}^2 = \omega_p^2 + \omega_c^2$, $\omega_c = eB/m$ is the cyclotron frequency and ω_p is the plasma frequency characterizing for the DSSL confinement in the *z*-direction, given by $\omega_p = (4\pi e^2 n_D / \varepsilon_0 m)^{1/2}$, where ε_0 is the electronic constant (vacuum permittivity) and n_D is the doped concentration; and

$$\phi_N(z - z_0) = H_N(z - z_0) \exp \left[-(z - z_0)^2 / 2 \right], \quad (6)$$

with $H_N(z)$ being the Hermite polynomial of N th order. The matrix element of interaction, $D_{N, N'}(\vec{q})$, is given by

$$|D_{N, N'}(\vec{q})|^2 = |C_{\vec{q}}|^2 |I_{N, N'}(\pm q_z)|^2, \quad (7)$$

where $C_{\vec{q}}$ is the electron-phonon interaction constant which depends on the interacting mechanism, for electron-optical phonon interaction, $|C_{\vec{q}}|^2 = 2\pi e^2 \hbar \omega_{\vec{q}} (\chi_\infty^{-1} - \chi_0^{-1}) / (\varepsilon_0 V_0 q)$ [10–12], where V_0 is the normalization volume of specimen, χ_0 and χ_∞ are the static and the high-frequency dielectric constants, respectively; $I_{N, N'}(\pm q_z)$ is the form factor of electron, given by

$$I_{N, N'}(\pm q_z) = \sum_{\wp=1}^{s_0} \int_0^d e^{\pm i q_z d} \phi_N(z - z_0 - \wp d) \phi_{N'}(z - z_0 - \wp d) dz. \quad (8)$$

Here, d is the period and s_0 is the number of periods of the DSSL. In the following, we will use Hamiltonian (1) to derive the Hall conductivity tensor as well as the HC.

3. EXPRESSIONS FOR THE HALL CONDUCTIVITY AND THE HALL COEFFICIENT

By using Hamiltonian (1) and the procedures as in the previous works [2–7], we obtain the equation for the partial current density $\vec{j}_{N,N'}(\varepsilon)$ (the current caused by electrons that have energy of ε) in the single (constant) relaxation time approximation as

$$\frac{\vec{j}_{N,N'}(\varepsilon)}{\tau} + \omega_c \left[\vec{h} \wedge \vec{j}_{N,N'}(\varepsilon) \right] = \vec{Q}_N(\varepsilon) + \vec{S}_{N,N'}(\varepsilon), \quad (9)$$

where

$$\vec{Q}_N(\varepsilon) = -\frac{e}{m} \sum_{N, \vec{k}_x} \vec{k}_x \left(\vec{F} \frac{\partial f_{N, \vec{k}_x}}{\hbar \partial \vec{k}_x} \right) \delta(\varepsilon - \varepsilon_N(\vec{k}_x)), \quad \vec{F} = e\vec{E}_1, \quad (10)$$

and

$$\begin{aligned} \vec{S}_{N,N'}(\varepsilon) = & \frac{2\pi e}{m\hbar} \sum_{N', \vec{q}} \sum_{N, \vec{k}_x} |D_{N,N'}(\vec{q})|^2 N_{\vec{q}} \vec{k}_x \left\{ \left[\bar{f}_{N', \vec{k}_x + \vec{q}_x} - \bar{f}_{N, \vec{k}_x} \right] \left[\left(1 - \frac{\lambda^2}{2\Omega^2} \right) \right. \right. \\ & \times \delta(\varepsilon_{N'}(\vec{k}_x + \vec{q}_x) - \varepsilon_N(\vec{k}_x) - \hbar\omega_{\vec{q}}) + \frac{\lambda^2}{4\Omega^2} \delta(\varepsilon_{N'}(\vec{k}_x + \vec{q}_x) - \varepsilon_N(\vec{k}_x) - \hbar\omega_{\vec{q}} + \hbar\Omega) \\ & \left. \left. + \frac{\lambda^2}{4\Omega^2} \delta(\varepsilon_{N'}(\vec{k}_x + \vec{q}_x) - \varepsilon_N(\vec{k}_x) - \hbar\omega_{\vec{q}} - \hbar\Omega) \right] + \left[\bar{f}_{N', \vec{k}_x - \vec{q}_x} - \bar{f}_{N, \vec{k}_x} \right] \left[\left(1 - \frac{\lambda^2}{2\Omega^2} \right) \right. \right. \\ & \times \delta(\varepsilon_{N'}(\vec{k}_x - \vec{q}_x) - \varepsilon_N(\vec{k}_x) + \hbar\omega_{\vec{q}}) + \frac{\lambda^2}{4\Omega^2} \delta(\varepsilon_{N'}(\vec{k}_x - \vec{q}_x) - \varepsilon_N(\vec{k}_x) + \hbar\omega_{\vec{q}} + \hbar\Omega) \\ & \left. \left. + \frac{\lambda^2}{4\Omega^2} \delta(\varepsilon_{N'}(\vec{k}_x - \vec{q}_x) - \varepsilon_N(\vec{k}_x) + \hbar\omega_{\vec{q}} - \hbar\Omega) \right] \right\} \delta(\varepsilon - \varepsilon_N(\vec{k}_x)). \quad (11) \end{aligned}$$

In these expressions, $\vec{h} = \vec{B}/B$ is the unit vector along the magnetic field, the notation ‘ \wedge ’ represents the cross product (or vector product), τ is the electron momentum relaxation time which is assumed to be constant in this calculation, $\bar{f}_{N, \vec{k}_x}(N_{\vec{q}})$ is the time-independent component of the distribution function of electrons (phonons), and $\lambda = (eE_0q_x/m\Omega)(1 - \omega_c^2/\tilde{\omega}^2)$. Solving (9) we have

$$\begin{aligned} \vec{j}_{N,N'}(\varepsilon) = & \frac{\tau}{1 + \omega_c^2\tau^2} \left\{ \left(\vec{Q}_N(\varepsilon) + \vec{S}_{N,N'}(\varepsilon) \right) - \omega_c\tau \left([\vec{h} \wedge \vec{Q}_N(\varepsilon)] + [\vec{h} \wedge \vec{S}_{N,N'}(\varepsilon)] \right) \right. \\ & \left. + \omega_c^2\tau^2 \left(\vec{Q}_N(\varepsilon)\vec{h} + \vec{S}_{N,N'}(\varepsilon)\vec{h} \right) \vec{h} \right\}. \quad (12) \end{aligned}$$

The total current density is given by

$$\vec{J} = \int_0^\infty \vec{j}_{N,N'}(\varepsilon) d\varepsilon \quad \text{or} \quad J_i = \sigma_{im} E_{1m}. \quad (13)$$

Inserting (12) into (13) we obtain the expressions for the current density J_i as well as the Hall conductivity σ_{im} after carrying out the analytical calculation. To do this, we assume that the electron-optical phonon interaction is dominant at high temperatures, so the electrons system is nondegenerate and obeys the Boltzmann distribution function in this case. Also, we assume that phonons are dispersionless, i.e., $\hbar\omega_{\vec{q}} \approx \hbar\omega_0$, $N_{\vec{q}} \equiv N_0 \approx k_B T / (\hbar\omega_0)$, where ω_0 is the frequency of the longitudinal optical phonons, assumed to be constant, k_B being Boltzmann constant. After some mathematical manipulation, we obtain the expression for the conductivity tensor:

$$\sigma_{im} = \frac{\tau}{1 + \omega_c^2\tau^2} \left[\delta_{ij} - \omega_c\tau \epsilon_{ijk} h_k + \omega_c^2\tau^2 h_i h_j \right] \left\{ a \delta_{jm} + \frac{be}{m} \frac{\tau}{1 + \omega_c^2\tau^2} \delta_{jl} \times \left[\delta_{lm} - \omega_c\tau \epsilon_{lmp} h_p + \omega_c^2\tau^2 h_l h_m \right] \right\}, \quad (14)$$

where δ_{ij} is the Kronecker delta; ϵ_{ijk} being the antisymmetrical Levi-Civita tensor; the Latin symbols i, j, k, l, m, p stand for the components x, y, z of the Cartesian coordinates;

$$a = \frac{e^2 L_x}{2\pi m \hbar} \sqrt{\frac{\pi}{\alpha \beta}} \sum_N \exp \left\{ \beta \left[\epsilon_F - \left(N + \frac{1}{2} \right) \hbar \tilde{\omega} + \frac{e^2 E_1^2}{2m\tilde{\omega}^2} + \frac{\gamma^2}{4\alpha} \right] \right\} \quad (15)$$

with ϵ_F is the Fermi level; L_x is the normalization length in the x -direction;

$$b = \frac{2\pi e N_0}{m \hbar} \sum_{N, N'} \{b_1 + b_2 + b_3 + b_4 + b_5 + b_6 + b_7 + b_8\}, \quad (16)$$

$$\begin{aligned} b_1 &= \frac{-\beta A L_x}{64\pi^3 \alpha^2} I(N, N') \exp \left\{ \beta \left[\epsilon_F - \left(N + \frac{1}{2} \right) \hbar \tilde{\omega} + \frac{e^2 E_1^2}{2m\tilde{\omega}^2} - \frac{C_1}{2} + \frac{\gamma^2}{4\alpha} \right] \right\} \\ &\quad \times \left\{ \alpha \left(\frac{C_1^2}{\alpha^2} \right)^{\frac{1}{4}} K_{\frac{1}{2}} \left(\frac{\beta |C_1|}{2} \right) - \gamma K_0 \left(\frac{\beta |C_1|}{2} \right) + C_1 \left(\frac{C_1^2}{\alpha^2} \right)^{-\frac{1}{4}} K_{-\frac{1}{2}} \left(\frac{\beta |C_1|}{2} \right) \right\}, \\ b_2 &= \frac{-\beta \theta A L_x}{64\pi^3 \alpha^2} I(N, N') \exp \left\{ \beta \left[\epsilon_F - \left(N + \frac{1}{2} \right) \hbar \tilde{\omega} + \frac{e^2 E_1^2}{2m\tilde{\omega}^2} - \frac{C_1}{2} + \frac{\gamma^2}{4\alpha} \right] \right\} \\ &\quad \times \left\{ \alpha \left(\frac{C_1^2}{\alpha^2} \right)^{\frac{3}{4}} K_{\frac{3}{2}} \left(\frac{\beta |C_1|}{2} \right) - \gamma \left(\frac{C_1^2}{\alpha^2} \right)^{\frac{1}{2}} K_1 \left(\frac{\beta |C_1|}{2} \right) + C_1 \left(\frac{C_1^2}{\alpha^2} \right)^{\frac{1}{4}} K_{\frac{1}{2}} \left(\frac{\beta |C_1|}{2} \right) \right\}, \\ b_3 &= \frac{-\beta \theta A L_x}{128\pi^3 \alpha^2} I(N, N') \exp \left\{ \beta \left[\epsilon_F - \left(N + \frac{1}{2} \right) \hbar \tilde{\omega} + \frac{e^2 E_1^2}{2m\tilde{\omega}^2} - \frac{C_2}{2} + \frac{\gamma^2}{4\alpha} \right] \right\} \\ &\quad \times \left\{ \alpha \left(\frac{C_2^2}{\alpha^2} \right)^{\frac{3}{4}} K_{\frac{3}{2}} \left(\frac{\beta |C_2|}{2} \right) - \gamma \left(\frac{C_2^2}{\alpha^2} \right)^{\frac{1}{2}} K_1 \left(\frac{\beta |C_2|}{2} \right) + C_2 \left(\frac{C_2^2}{\alpha^2} \right)^{\frac{1}{4}} K_{\frac{1}{2}} \left(\frac{\beta |C_2|}{2} \right) \right\}, \\ b_4 &= \frac{-\beta \theta A L_x}{128\pi^3 \alpha^2} I(N, N') \exp \left\{ \beta \left[\epsilon_F - \left(N + \frac{1}{2} \right) \hbar \tilde{\omega} + \frac{e^2 E_1^2}{2m\tilde{\omega}^2} - \frac{C_3}{2} + \frac{\gamma^2}{4\alpha} \right] \right\} \\ &\quad \times \left\{ \alpha \left(\frac{C_3^2}{\alpha^2} \right)^{\frac{3}{4}} K_{\frac{3}{2}} \left(\frac{\beta |C_3|}{2} \right) - \gamma \left(\frac{C_3^2}{\alpha^2} \right)^{\frac{1}{2}} K_1 \left(\frac{\beta |C_3|}{2} \right) + C_3 \left(\frac{C_3^2}{\alpha^2} \right)^{\frac{1}{4}} K_{\frac{1}{2}} \left(\frac{\beta |C_3|}{2} \right) \right\}, \quad (17) \end{aligned}$$

$$\begin{aligned} b_5 &= b_1(C_1 \rightarrow D_1), \quad b_6 = b_2(C_1 \rightarrow D_1), \quad b_7 = b_3(C_2 \rightarrow D_2), \quad b_8 = b_4(C_3 \rightarrow D_3), \\ \beta &= 1/(k_B T), \quad \alpha = (\hbar^2/2m) (1 - \omega_c^2/\tilde{\omega}^2), \quad \gamma = e E_1 \hbar \omega_c / m \tilde{\omega}^2, \quad (18) \end{aligned}$$

$$\theta = \frac{e^2 E_0^2}{m^2 \Omega^4} (1 - \omega_c^2/\tilde{\omega}^2), \quad A = \frac{2\pi e^2 \hbar \omega_0}{\epsilon_0} (\chi_\infty^{-1} - \chi_0^{-1}), \quad (19)$$

$$\begin{aligned} C_1 &= (N' - N) \hbar \tilde{\omega} - \hbar \omega_0, \quad C_2 = C_1 + \hbar \Omega, \quad C_3 = C_1 - \hbar \Omega, \\ D_1 &= (N' - N) \hbar \tilde{\omega} + \hbar \omega_0, \quad D_2 = D_1 + \hbar \Omega, \quad D_3 = D_1 - \hbar \Omega; \quad (20) \end{aligned}$$

and

$$I(N, N') = \int_{-\infty}^{\infty} |I_{N, N'}(q_z)|^2 dq_z. \quad (21)$$

The HC is given by the formula [13]

$$R_H = \frac{\rho_{xz}}{B} = -\frac{1}{B} \frac{\sigma_{xz}}{\sigma_{xz}^2 + \sigma_{zz}^2}, \quad (22)$$

where σ_{xz} and σ_{zz} are given by Eq. (14).

Equations (14) and (22) show the complicated dependencies of the Hall conductivity tensor and the HC on the external fields, including the EMW. It is obtained for arbitrary values of the indices N and N' . However, it contains the term $I(N, N')$ which is difficult to find out the exact analytical result due to the presence of the Hermite polynomials. We will numerically evaluate this term by the computational method. In the next section, we will give a deeper insight into these results by carrying out a numerical evaluation and a graphic consideration by the computational method.

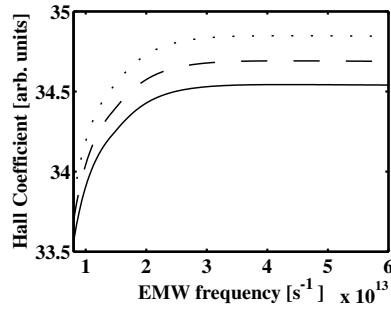


Figure 1: Hall coefficients (arb. units) as functions of the EMW frequency Ω at $B = 4.00$ T (solid line), $B = 4.05$ T (dashed line), and $B = 4.10$ T (dotted line). Here, $\omega_p = 4 \times 10^{13} \text{ s}^{-1}$, $E_1 = 5 \times 10^5 \text{ V}\cdot\text{m}^{-1}$, $E_0 = 10^5 \text{ V}\cdot\text{m}^{-1}$, and $T = 270$ K.

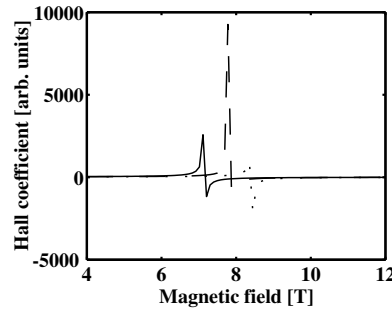


Figure 2: Hall coefficients (arb. units) as functions of the magnetic field at temperatures of 260 K (solid line), 270 K (dashed line), and 280 K (dotted line). Here, $\omega_p = 4 \times 10^{13} \text{ s}^{-1}$, $E_1 = 5 \times 10^5 \text{ V}\cdot\text{m}^{-1}$, $E_0 = 10^5 \text{ V}\cdot\text{m}^{-1}$, and $\Omega = 5 \times 10^{13} \text{ s}^{-1}$.

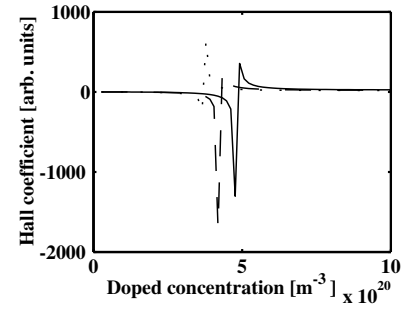


Figure 3: Hall coefficients (arb. units) as functions of the doped concentration at temperatures of 260 K (solid line), 270 K (dashed line), and 280 K (dotted line). Here, $B = 4$ T, $E_1 = 5 \times 10^5 \text{ V}\cdot\text{m}^{-1}$, $E_0 = 10^5 \text{ V}\cdot\text{m}^{-1}$, and $\Omega = 5 \times 10^{13} \text{ s}^{-1}$.

4. NUMERICAL RESULTS AND DISCUSSION

In this section we present detailed numerical calculations of the Hall conductivity and the HC in a DSSL subjected to the uniform crossed magnetic and electric fields in the presence of a strong EMW. For the numerical evaluation, we consider the *n-i-p-i* superlattice of GaAs:Si/GaAs:Be with the parameters [8, 11, 12]: $\varepsilon_F = 50$ meV, $\chi_\infty = 10.9$, $\chi_0 = 12.9$, $\hbar\omega_0 = 36.25$ meV (optical phonon frequency), and $m = 0.067 \times m_0$ (m_0 is the mass of a free electron). For the sake of simplicity, we also choose $N = 0$, $N' = 1$, $\tau = 10^{-12}$ s, and $L_x = 10^{-9}$ m.

The HC is plotted as function of the EMW frequency at different values of the magnetic field in Figure 1. The HC can be seen to increase strongly with increasing EMW frequency for the region of small values ($\Omega < 2.5 \times 10^{13} \text{ s}^{-1}$) and reaches saturation as the EMW frequency continues to increase. Moreover, the HC is very sensitive to the magnetic field at the chosen values of the other parameters; concretely, the value of the HC raises remarkably when the magnetic field increases slightly.

In Figure 2 and Figure 3, we show the dependence of the HC on the magnetic field and on the doped concentration, respectively, at different values of the temperature T ; the necessary parameters involved in the computation are the same as those in Figure 1. We can describe the behavior of the HC in Figure 2 as follows: Each curve has one maximum and one minimum. As the magnetic field increases, the HC is positive, reaches the maximum value and then decreases suddenly to a minimum with a negative value. When the magnetic field is increased further, the HC increases continuously (with negative values) and reaches saturation at high magnetic fields. This behavior is similar to the case of low temperatures in two-dimensional electron systems have been observed before for both the in-plane and perpendicular magnetic fields (see Ref. [14] and references therein). Particularly, the values of HC at the maxima are much larger and at the minima, they are much smaller than other values. Moreover, the dependence of the HC on the temperature is complicated. As the temperature increases the maxima and the minima shift to the right. Also, the values of the HC at maxima (minima) at different temperatures are very different. Thus, we can conclude that the HC is very sensitive to the temperature. The dependence of the HC on the doped concentration in Figure 3 can be analyzed similarly. However, the main difference here is that as the doped concentration increases the HC is negative, reaches minimum and then reaches maximum.

5. CONCLUSION

In this work, we have studied the influence of laser radiation on the Hall effect in a DSSL subjected to crossed dc electric and magnetic fields. The electron-optical phonon interaction is taken into account at high temperatures, and the electron gas is nondegenerate. We obtain the expressions for the Hall conductivity as well and the HC. The influence of the EMW is interpreted by using the dependencies of the Hall conductivity and the HC on the amplitude E_0 and the frequency Ω of the EMW and by using the dependencies on the magnetic B and the dc electric field E_1 as

in the ordinary Hall effect. The analytical results are numerically evaluated and plotted for the GaAs:Si/GaAs:Be DSSL to show clearly the dependence of the Hall conductivity on the external fields and the parameters of the system. From the numerical results, we can summarize the main points as follows: The HC increases strongly with increasing EMW frequency for the small values of the EMW frequency and reaches saturation as the EMW frequency continues to increase. As the magnetic field increases, the HC is positive, reaches its maximum value and then decreases suddenly to a minimum with a negative value; also, the values of the HC at a maxima are much larger and at the minima are much smaller than other values. Furthermore, as the magnetic field increases the HC reaches saturation, this behavior is similar to the results obtained at low temperatures in some two-dimensional electron systems.

ACKNOWLEDGMENT

This work was completed with the financial support from the National Foundation for Science and Technology Development of Vietnam (NAFOSTED) (Grant No. 103.01-2011.18).

REFERENCES

1. Goerbig, M. O., “Quantum hall effects,” arXiv:0909.1998v2, [cond-mat.mes-hall], 2009.
2. Epshtein, E. M., “Odd magnetophotoresistance effect in semiconductors,” *Sov. Phys. Semicond.; Fiz. Tekh. Poluprovodn.*, Vol. 10, 1414–1415, 1976 (in Russian).
3. Epshtein, E. M., “Odd magnetoresistance of nonlinear conductors in time-dependent electric fields,” *Sov. J. Theor. Phys. Lett.*, Vol. 2, No. 5, 234–237, 1976 (in Russian).
4. Malevich, V. L. and E. M. Epshtein, “Photostimulated odd magnetoresistance in semiconductors,” *Sov. Phys. Solid State; Fiz. Tverd. Tela*, Vol. 18, 1286–1289, 1976 (in Russian).
5. Pankratov, A. A. and E. M. Epshtein, “Kinetic theory of longitudinal Hall effect in high-frequency electric field,” *Sov. Phys. Semicond.; Fiz. Tekh. Poluprovodn.*, Vol. 16, No. 9, 1689–1691, 1982 (in Russian).
6. Shmelev, G. M., G. I. Tsurkan, and N. H. Shon, “The magnetoresistance and the cyclotron resonance in semiconductors in the presence of strong electromagnetic wave,” *Sov. Phys. Semicond.; Fiz. Tekh. Poluprovodn.*, Vol. 15, No. 1, 156–161, 1981 (in Russian).
7. Bau, N. Q, N. V. Hieu, and N. V. Nhan, “The quantum acoustomagnetolectric field in a quantum well with a parabolic potential,” *Superlattices and Microstructures*, Vol. 52, No. 5, 921–930, 2012.
8. Ploog, K. and G. H. Dohler, “Compositional and doping superlattices in III-V semiconductors,” *Adv. Phys.*, Vol. 32, No. 3, 285–359, 1983.
9. Chen, X., “Local-field study of optical intersubband saturation in a parabolic quantum well under crossed magnetic and electric fields,” *J. Phys.: Condens. Matter*, Vol. 9, 8249–8256, 1997.
10. Vasilopoulos, P., M. Charbonneau, and C. M. Van Vliet, “Linear and nonlinear electrical conduction in quasi-two-dimensional quantum wells,” *Phys. Rev. B*, Vol. 35, No. 3, 1334–1344, 1987.
11. Lee, S. C., “Optically detected magnetophonon resonances in quantum wells,” *J. Korean Phys. Soc.*, Vol. 51, No. 6, 1979–1986, 2007.
12. Bau, N. Q and D. M. Hung, “Calculation of the nonlinear absorption coefficient of a strong electromagnetic wave by confined electrons in doping superlattices,” *Progress In Electromagnetics Research B*, Vol. 25, 39–52, 2010.
13. Charbonneau, M., K. M. van Vliet, and P. Vasilopoulos, “Linear response theory revisited III: One-body response formulas and generalized Boltzmann equations,” *J. Math. Phys.*, Vol. 23, 318–336, 1982.
14. Hwang, E. H. and S. Das Sarma, “Hall coefficient and magnetoresistance of two-dimensional spin-polarized electron systems,” *Phys. Rev. B*, Vol. 73, No. 12, 121309(R), 2006.

Effects of Tuning Condition, Head Size and Position on the SAR of a MRI Dual-row Transmit Array at 400 MHz

M. Kozlov and R. Turner

Max Planck Institute for Human Cognitive and Brain Sciences, Leipzig, Germany

Abstract— We numerically investigated the effects of tuning condition, head size and position on the specific absorption ratio (SAR) of a dual row 16-channel transmit array used for magnetic resonance imaging (MRI) at 400 MHz. The array was loaded by typical human head models with three scaling factors, at eight locations specified by four axial and two transverse positions. The circuit-level array performance was fine-tuned for each head location using two independent optimization strategies. Then the SAR was evaluated for different array excitation modes and all variants of the array tuning condition. The tuning condition may have a significant impact on the spatial-average 10-gram SAR of a dual row array. It is therefore essential for reliable SAR assessment of such an array to precisely match the tuning conditions in the numerical and actual domains.

1. INTRODUCTION

Manufacturers of magnetic resonance imaging (MRI) scanners and most national standards organizations (e.g., FDA) recommend the use of numerical simulation for the evaluation of specific absorption ratio (SAR) of MRI radio frequency (RF) arrays, because actual SAR measurement is not easily feasible for human subjects in-vivo. The SAR can be readily calculated for several excitation modes, and/or complex parallel transmit pulses, if array elements have unambiguous (well-defined) coupling and matching parameters [1]. Usually the actual and simulated element matching and adjacent element coupling are compared in decibels. The influence of coupling phase on SAR has generally been neglected, despite the well-known existence of under-coupled and over-coupled cases. However, for reliable SAR assessment the numerical model must be equivalent to the constructed MRI array.

The transmit performance of UHF MRI coils benefits from a dual-row array configuration [2]. However, it is more difficult to match an actual dual-row array and its numerical model, due to the significantly increased complexity of dual-row array fabrication. A global optimum for a constructed dual-row array may not be reached by circuit-level optimization. In previous work, we developed a simulation work-flow that closely corresponds to the fabrication steps of such an array, but the results reported were obtained for circuit-level optimization that reached a global minimum [2]. Our numerical simulation goals in this study were: a) to investigate the effect of different tuning conditions on SAR of an already-constructed 400 MHz dual-row array [3]; and b) to explore the sensitivity of SAR to both head size and position within an array. Low sensitivity to these variables would simplify safety supervision.

2. METHOD

Our investigation was performed using RF circuit and 3-D EM co-simulation. This allows the effects of tuning conditions on the SAR to be studied on the basis of only one multi-port 3-D EM simulation for a given head in each of its several positions. The fundamentals of the co-simulation work-flow have been described in our previous report [2]. The RF circuit simulator was Agilent ADS 2011.10, and Ansoft HFSS 14 was chosen as the 3-D EM tool. The realistic 3-D EM model of the array included all radiative element construction details, simulated with precise dimensions and material electrical properties. However, neither RF cable traps nor coax cable interconnection wiring were included in the model.

The transmit array was mounted on fiber glass tube with an inner diameter of 28 cm and thickness of 2.5 mm. 16 identical loop type radiative elements, made of 2 mm diameter silver wire and with height 85 mm and length 100 mm, were arranged in two rows of eight elements each. The lower row elements were rotated by 22.5° with respect to the upper row. In each element, one variable and 13 fixed capacitors were placed in positions shown as gaps in the copper wire (Fig. 1). The axially and circumferentially adjacent elements were separated by a space of 12 mm and decoupled by inductive decoupling networks. The network consisted of the inductors, placed in series with the distributed capacitor, with inductance $\mathbf{L}_{\text{inductor}}$ and coupling factor $\mathbf{K}_{\text{inductor}}$.

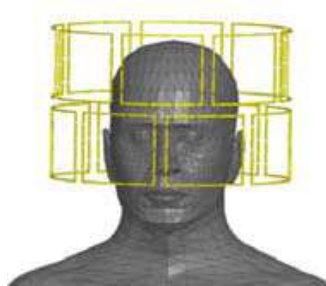


Figure 1: Array geometry setup. Only radiative elements and human model are shown.

To actively detune the radiative elements, a PIN diode connected in series with an inductor was attached in parallel to one of the distributed capacitors in each element. The Q factor of all capacitors was equal to 200. The array decoupling PIN diode resistance was 0.2 Ohm. All inductors and coil conductors were modelled with the same wire gauge as in the actual implementation. The head gradient shield and the magnet bore were included in the 3-D EM model.

The loads utilized were the multi-tissue Ansoft human body models, cut in the middle of the torso, with different scaling factors: human body model #1 with scaling factors $X = 0.9$, $Y = 0.9$, $Z = 0.9$ (simulating an average head), human body model #2 with scaling factors $X = 0.85$, $Y = 0.85$, $Z = 0.9$ (simulating a small head), and human body model #3 with scaling factors $X = 0.95$, $Y = 0.975$, $Z = 0.9$ (simulating a large head). We analyzed geometries where the head was placed symmetrically in the transverse plane, and where the head was positioned 22 mm lower, to allow space for the mirror of a visual stimulus system. In both geometries each human body model was located at four axial positions so that the distance between crown of the head and array top was 16, 21, 26, and 31 mm. We use the following abbreviations for head displacement from end of coil: “16 mm”, “21 mm”, “26 mm”, and “31 mm”. In the first geometry the human body model #1 was also shifted to both sides by 5 and 10 mm.

Six components (feed-point, variable capacitor, and 4 sub-circuit of distributed capacitors and decoupling inductor connected in series) in each resonance element were substituted as 3-D EM lumped ports. Other distributed capacitors retained in 3-D EM domain to reduce the time required for post-processing as well as to maintain the amount of simulation data less than 60 GB for each 3-D EM simulation.

In the RF circuit domain, substituted components were connected to the corresponding ports of the S -parameter simulation block representing the array 3-D EM model. To obtain values of the variable array components — The decoupling inductors, tune and match capacitors, which ensured that the array’s field generation was optimal at 400 MHz — We used two circuit-level array optimization strategies: 1) optimization based on S parameters, that mimics the commonly used tuning during coil fabrication, where the reflection coefficients (\mathbf{S}_{xx}) for each individual array element and the coupling coefficients (\mathbf{S}_{xy}) for each decoupled pair of array elements were minimized at the array operating frequency (\mathbf{F}_{MRI}); 2) mode optimization, minimizing an error or cost function (\mathbf{EF}), which consisted of individually weighted sums derived from the S parameter matrix and power reflected by array rows, for a given set of excitation modes [2]. All optimizations were performed in two steps: 30,000 random tries, followed by the “Quasi-Newton” optimization method until no further improvement was possible.

Because such an array would desirably be used without adjustment of array components for each subject, dedicated circuit-level optimizations were performed for the human body model #1, which represented an average head, at eight locations specified by four axial and two transverse positions. Sixteen tuning conditions, that is sixteen values for the variable components obtained, were grouped in two sets (one per each geometry), which each consisted of eight different tuning conditions.

The tuning conditions from the given geometry set were sequentially used for RF circuit and 3-D EM co-simulations of all human body models. This approximately mimicked situations when a human subject was placed in the array, either tuned for different subject positions or for another subject, or for both. After each co-simulation, the \mathbf{E} and \mathbf{H} fields (on an equidistant 1 mm mesh) for 16 independently excited radiative elements were exported from HFSS to temporary ASCII files, and then converted into files in Matlab format. The field export time, originally about 30 minutes for each radiative element, was reduced by a factor of two by exporting only the field data

for the part of the human model that was included in the numerical domain. An in-house Matlab procedure guided the co-simulation, data export and conversion of ASCII files into files in Matlab format.

The near field distribution was calculated as a weighted sum of all radiative element \mathbf{E} - and \mathbf{H} - fields for each tuning condition applied. The weighting factors were defined by the applied excitation mode. We investigated circular polarization (CP) and some other modes. The total number of modes applied was 12. A power of 0.5 watt was applied to each radiative element, in CP mode. The total transmit power ($\mathbf{P}_{\text{transmit}}$) was maintained at 8 W in the other excitation modes.

The spatial-average 10-gram specific absorption rate ($\mathbf{SAR}_{10\text{g}}$) was calculated using an in-house MATLAB procedure, developed consistently with the draft of IEEE/IEC 62704-1 standard and validated by means of an IEEE TC 34 interlab comparison study [4]. For each 3-D EM simulation, the total number of calculated $\mathbf{SAR}_{10\text{g}}$ values was 96 (the number of tuning conditions ‘8’ multiplied by the number of excitation modes ‘12’). We also calculated the safety excitation efficiency — $\mathbf{B}_{1+\mathbf{v}}/\sqrt{\mathbf{SAR}_{10\text{g}}}$, where $\mathbf{B}_{1+\mathbf{v}}$ is the transverse magnetic field magnetic field component (\mathbf{B}_{1+}) with clockwise circular polarization averaged over averaged over the brain, because it defines MRI scanner performance from the MRI perspective, not the peak $\mathbf{SAR}_{10\text{g}}$, which we have included for comparison with other results.

3. RESULTS AND DISCUSSION

The array loaded by human body model #1 at all positions appeared to be properly tuned: The magnitude of all values of \mathbf{S}_{xx} and \mathbf{S}_{xy} was lower than -20 dB and -18 dB, respectively, when any of the eight tuning conditions were applied. When variable component values were used from simulations of other head locations, the \mathbf{S}_{xx} magnitude slightly increased (remaining below -20 dB) and the \mathbf{S}_{xy} slightly decreased. Variation of the \mathbf{S}_{xx} and \mathbf{S}_{xy} for human body model #2 and #3 simulations was more pronounced, but the array properties in all configurations still appeared to be reasonably tuned (only a couple of \mathbf{S}_{xx} were about -16 dB, other $\mathbf{S}_{xx} < -20$ dB and all $\mathbf{S}_{xy} < -18$ dB).

For the human body model placed symmetrically in the transverse plane, and using the first circuit-level optimization strategy value of $\mathbf{K}_{\text{inductor}}$, \mathbf{S}_{xy} phases were significantly different between head displacement “26 mm” and other locations, as shown on Figs. 2 and 3.

To obtain a sensitivity analysis, the circuit level optimization strategy #1 was applied 100 times, for geometry case #1 and displacement “26 mm”. We obtained solutions where the values

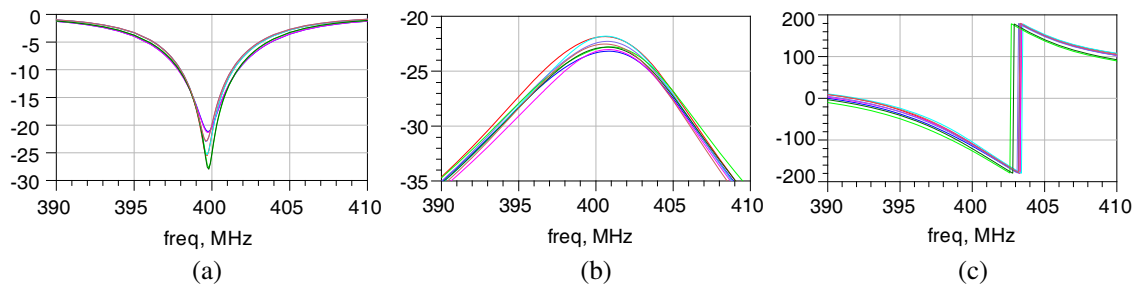


Figure 2: Circuit level data for displacement “26 mm”. (a) S_{xx} in dB, (b) diagonal adjacent coupling in dB, (c) diagonal adjacent coupling phase in degree.

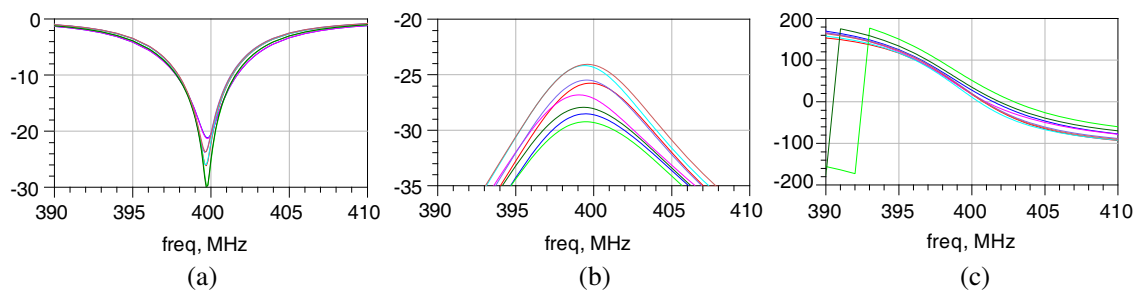


Figure 3: Circuit level data for displacement “16 mm”. (a) S_{xx} in dB, (b) diagonal adjacent coupling in dB, (c) diagonal adjacent coupling phase in degree.

of $\mathbf{K}_{\text{inductor}}$ were grouped around two values with small dispersion: the first value was close to the value of the original optimization for human body model with displacements “16 mm”, “21 mm”, and “31 mm”; and the second value was close to the value of the original optimization for displacement “26 mm”. The probability to obtain the first value was 83%.

When the variable component values previously obtained for the displacement “16 mm” were used for co-simulation of the human body model with displacements “26 mm”, for CP excitation the mean \mathbf{B}_1+ across the brain was $0.82 \mu\text{T}$, and $\text{SAR}_{10\text{g}}$ was 2.01 W/kg , both very close to the values (mean \mathbf{B}_1+ across brain = $0.82 \mu\text{T}$, $\text{SAR}_{10\text{g}} = 2.02 \text{ W/kg}$) obtained for co-simulation of the human body model with displacements “26 mm” with variable component values obtained for displacement “26 mm” (Figs. 4 and 5). But for the “+90” excitation mode, the mean \mathbf{B}_1+ across brain was $0.77 \mu\text{T}$ and the $\text{SAR}_{10\text{g}}$ was 1.99 W/kg for the first case, differing significantly from the second case, for which the mean \mathbf{B}_1+ across brain was $0.83 \mu\text{T}$, and the $\text{SAR}_{10\text{g}}$ was 1.61 W/kg . The reasons for this behaviour were: i) significant variation of current through radiative elements; ii) different pattern of the constructive E -field interference; and iii) finally, significantly changed spatial location of the peak $\text{SAR}_{10\text{g}}$.

For geometry case #2, circuit level optimization strategies #1 and #2 both resulted in values of \mathbf{S}_{xx} and \mathbf{S}_{xy} of similar magnitude, but the \mathbf{S}_{xy} phases were different and the values of $\mathbf{K}_{\text{inductor}}$ were grouped around two values (one for each strategy) with small dispersion. The behaviour of the magnitudes of \mathbf{S}_{xx} and \mathbf{S}_{xy} for different head positions and head sizes was similar to geometry

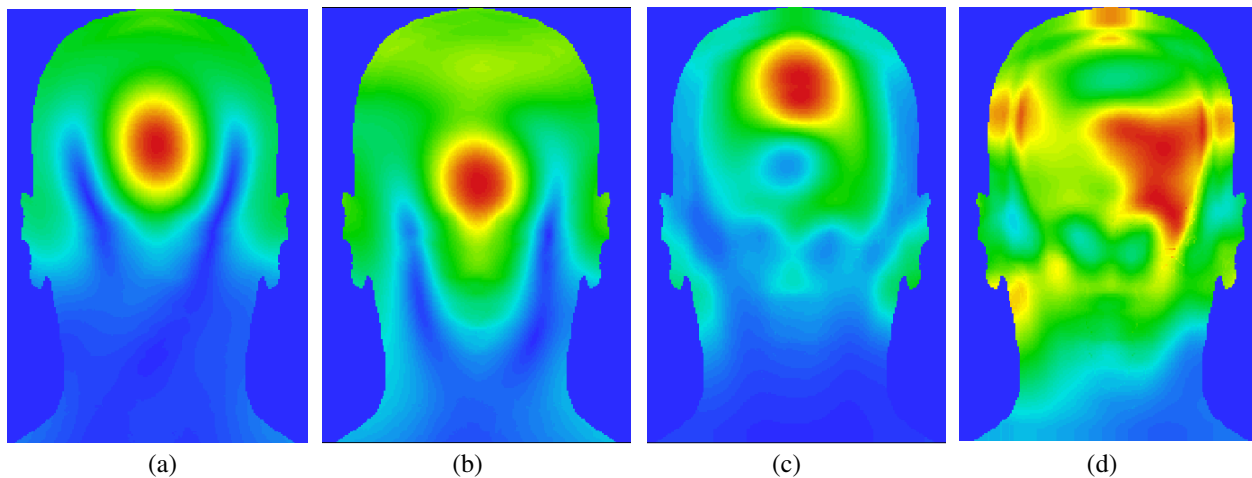


Figure 4: Variable component values for displacement “16 mm”. (a) and (b) \mathbf{B}_1+ slices rescaled to individual maximum, (c) and (d) $\text{SAR}_{10\text{g}}$ slices rescaled to individual maximum; (a) and (c) CP mode, (b) and (d) “+90” mode.

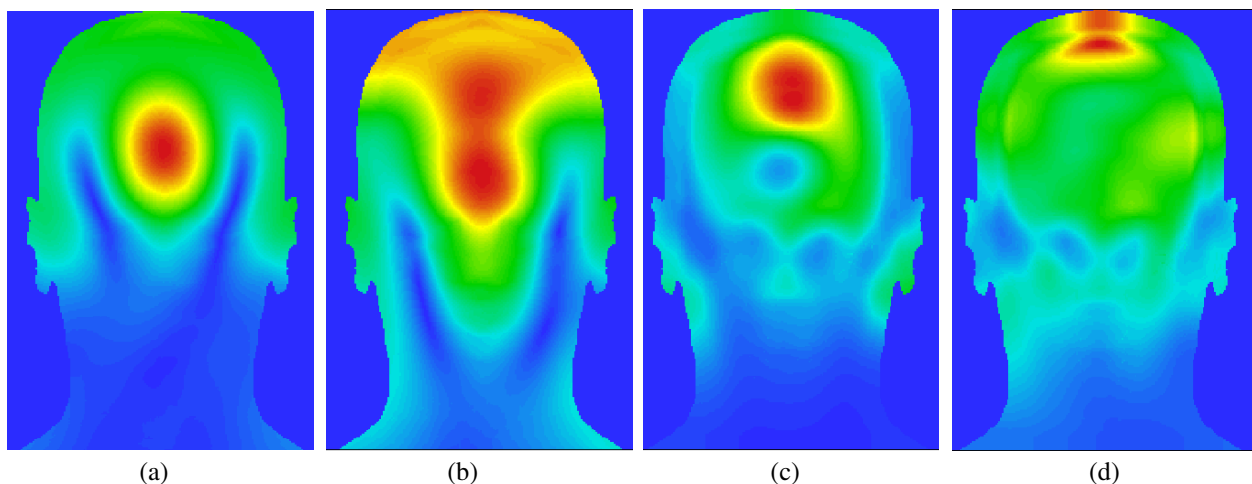


Figure 5: Variable component values for displacement “26 mm”. (a) and (b) \mathbf{B}_1+ slices rescaled to individual maximum, (c) and (d) $\text{SAR}_{10\text{g}}$ slices rescaled to individual maximum; (a) and (c) CP mode, (b) and (d) “+90” mode.

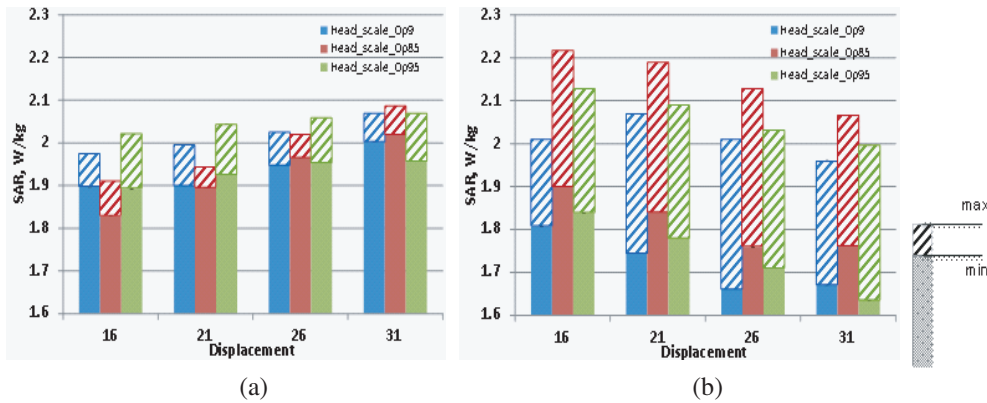


Figure 6: SAR_{10g} for geometry case #2. (a) CP mode, (b) “+90” mode.

case #1. For geometry case #2 for CP excitation mode, SAR_{10g} variations were less than $\pm 5\%$ for both optimization strategies (Fig. 6), but about 30% (peak to peak) for the “+90” excitation mode.

If results for the head displacement “26 mm” of geometry case #1 were excluded from the database, SAR_{10g} variations for both geometry cases would be very similar. But including these results gave variations of SAR_{10g} that were increased by up to 30% for some excitation modes.

4. CONCLUSIONS

The tuning condition may provide a significant impact on the SAR_{10g} of a dual row RF array. The similarity of the experimental and numerical B_1+ , or even the SAR_{10g} for the CP mode, cannot guarantee similarity of these quantities for other excitation modes. A precise match of dual row array conditions in numerical and actual domains is essential for reliable SAR assessment. When the array diameter is relatively large, and variations of head position result in insignificant variations of array circuit level measures, SAR_{10g} differences are expected to be relatively small (less than 20%) and can be easily covered by the typical array safety margin. However it is impossible to provide a general conclusion that a variation of an array property provides negligible influence on SAR_{10g} for any dual row array. A dual-row array of interest should be comprehensively and reliably investigated (including a sensitivity analysis) in order to define scanner SAR assessment parameters. If the precise match of conditions or a sensitivity analysis cannot be obtained, the coil safety margin should be increased considerably.

REFERENCES

1. Guerin, B., M. Gebhardt, E. Adalsteinsson, and L. Wald, “PTx pulse design with explicit hard constraints on local and global SAR and maximum and average forward power,” *Proceedings of the 20th Annual Meeting*, 2215, Melbourne, Australia, May 2012.
2. Kozlov, M. and R. Turner, “Engineering of 7 T transmit multi-row arrays,” *Proceedings of 34th Annual International Conference of the IEEE EMBS*, 1089–1092, San Diego, California, USA, Aug. 28–Sep. 1, 2012.
3. Shajan, G., M. Kozlov, J. Hoffmann, R. Turner, K. Scheffler, and R. Pohmann, “A 16-channel dual-row transmit array in combination with a 31-element receive array for human brain imaging at 9.4 T,” *Magnetic Resonance in Medicine*, 2013, DOI 10.1002/mrm.24726.
4. Monebhurrun, V., Y. Braux, H. Devos, M. Kozlov, W. Simon, and T. Wittig, “An interlaboratory comparison of SAR calculations using a CAD phone: A new step towards standardized procedures,” *Proceedings of the BEMS2012*, 315–317, Australia, Jun. 2012.

Three Dimensional Radar Imaging by Using Spherical Near Field Range

Dau-Chyrh Chang¹, Chih-Hung Lee^{2,3}, and Tsung-Yuan Yang³

¹Oriental Institute of Technology, Taiwan

²Yuan Ze University, Taiwan

³Electronics Testing Center, Taiwan

Abstract— In this paper, a high performance three dimensional radar image with size 1.5 meter by 1.5 meter and far field RCS versus aspect angle is performed by using the spherical near field range. By using the near field to far field transformation, the high fidelity radar image and radar cross section (RCS) can be generated. The radar system is impulse time domain system. The pulse width and pulse repetition frequency of radar are 30 ps and 1 MHz respectively. Figure 2 shows the simulation image result of 12 scatter points target model, distributed on 1.5 meter by 1.5 meter plane, by using the near field spherical range. Figure 2 shows the structure of near field scanner. The target is mounted on the horizontal positioner. By the rotation of the target, the near field ISAR image can be generated at special aspect angle. The impulse time domain radar system is moved along the arch. By using the radar movement along the arch and the target rotation on the positioner the three dimensional near field ISAR radar image can be generated. By using the field transformation from near field to far field, the high performance radar image and RCS can be generated.

1. INTRODUCTION

Usually, the high quality inverse synthetic aperture radar (ISAR) radar image is generated inside anechoic microwave chamber with far field test range or compact far field test range. The radar cross section (RCS) of target is measured to meet the quadratic phase error 11.25° . The RCS depends on size, surface roughness and material of target, while the target size bigger and bigger, the test range will be longer. Using the field transformation in the spherical near field test range can provide larger size of quite zone for target size of RCS measurement. So, to get high resolution must raise frequency and size of antenna. The radar image can be generated by ISAR techniques without the anechoic chamber.

The RCS value is the reflection signal from the target, the equation is shown Equation (1).

$$\sigma = 4\pi R^2 \left| \vec{E}_s \right|^2 / \left| \vec{E}_{in} \right|^2 \quad (1)$$

σ : RCS value, \vec{E}_s : The electric field density of reflection wave, \vec{E}_{in} : The electric field density of incident wave, R : The range from target to radar.

To get the scatter points on down range is the capability of down range resolution. That depends on bandwidth as shown in Equation (2). To get the scatter points on cross range is the capability of cross range resolution. That depends on rotate angle and given by Equation (3). The rotate angle is relation to frequency and size of antenna.

$$\Delta X = \lambda/4 \sin(\Delta\theta/2) \quad (2)$$

θ : The rotate angle.

$$\Delta R = C/2B \quad (3)$$

C : the speed of light, B : bandwidth.

2. THEORETICAL ANALYSIS

The purpose in this paper is that by using spherical near field measurement and gets the high quality ISAR radar image. To raise resolution of cross range and down range in the impulse time domain radar system is very easy. The pulse width and pulse repetition frequency of radar are 30 ps and 1 MHz respectively that the multi-path and the noise signal can be reduced in this system. The input scatter of the target shows as Table 1. The simulation image result of 12 scatter points target model are distributed on 1.5 meter by 1.5 meter plane. The simulation results of points

Table 1: Input scatter of the target.

Target	X	Y	RCS
No.1	-70	70	1000
No.2	0	70	1000
No.3	70	70	1000
No.4	-70	0	1000
No.5	0	0	1000
No.6	70	0	1000
No.7	-70	-70	1000
No.8	0	-70	1000
No.9	70	-70	1000

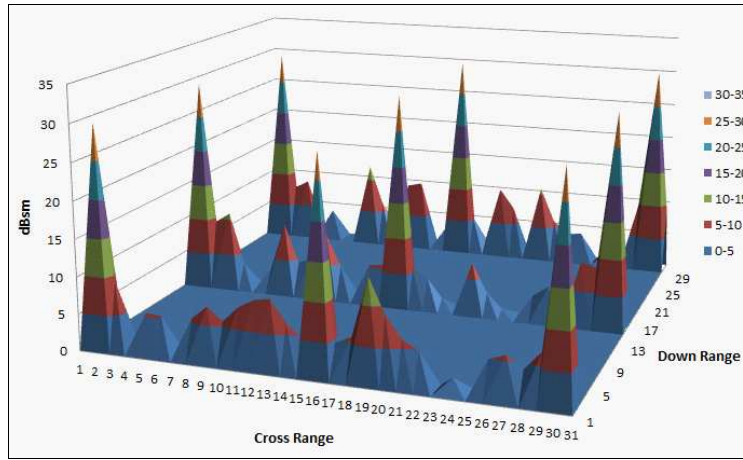


Figure 1: Simulation results of points scatter target.

scatter target with and without modification are show as the Figure 1, Figure 2. Following the ISAR techniques, then collect the reflected signal from different rotate angles of target and use these data to combine the microwave image with mathematics. The receive reflection signals for different aspect angles to synthesize radar image by the mathematical formula. These equations are shown as Equations (4) ~ (7):

Let $V(\theta, x, y)$ is the receive reflection signal for scatter point at (x, y) .

$$V(\theta, x, y) = A \cdot e^{j2kr(\theta, x, y)} \quad (4)$$

A : The amplitude of receive signal, $j2kr(\theta, x, y)$: The phase of receive signal, $r(\theta, x, y)$ is the range from radar to the target.

The range between target and radar can be expressed by Equation (5)

$$r(\theta, x, y) = \left\{ 1 + 2 \frac{y \cos \theta - x \sin \theta}{R_0} + \frac{x^2 + y^2}{R_0^2} \right\}^{1/2} \quad (5)$$

Then Equation (6) can be rewritten as

$$V(\theta, x, y) = A \cdot \exp \left[j4\pi(R_0/\lambda) \left\{ [1 + 2(y \cos \theta - x \sin \theta)/R_0 + (x^2 + y^2)/R_0^2]^{1/2} \right\} \right] \quad (6)$$

The result of image $g(x, y)$ is Equation (7).

$$g(x, y) = \sum V(\theta, x, y) \cdot \exp \left[-j4\pi(R_0/\lambda) \left\{ [1 + 2(y \cos \theta - x \sin \theta)/R_0 + (x^2 + y^2)/R_0^2]^{1/2} \right\} \right] \quad (7)$$

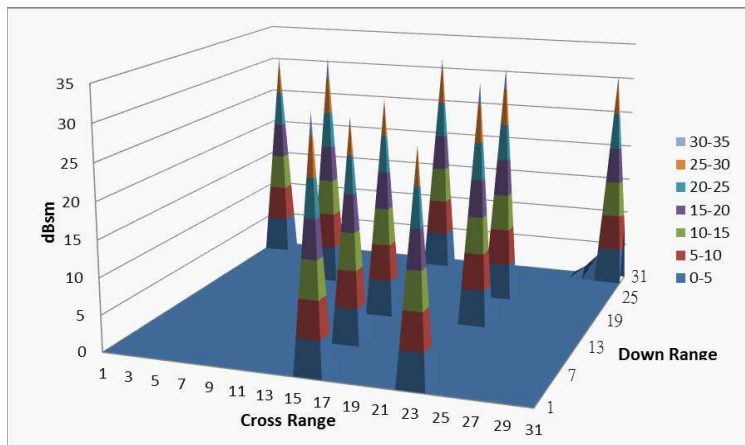


Figure 2: Simulation results of points scatter target with modification.

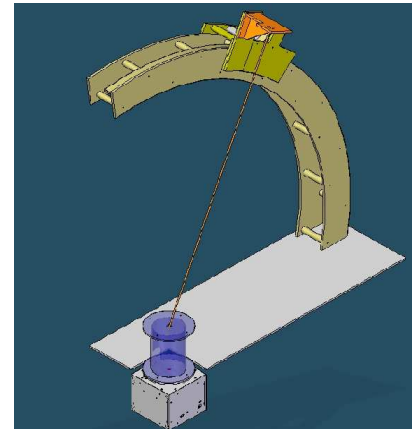


Figure 3: Spherical near field scanner.

3. SIMULATION AND EXPERIMENT

Figure 3 shows the structure of near field scanner. In order to increase the size of measurement target, the radius of spherical near field scanner might be large. Size of target 1.5 meter is located 70 cm above ground plane. The target is mounted on the horizontal positioner. By the rotation of the target, the near field ISAR image can be generated at special aspect angle. The maximum random angular positioned error 0.5 degrees may be acceptable for image quality. The impulse time domain radar system is moved along the arch and increases the scan area for large radar image. By using the radar movement along the arch and the target rotation on the positioner the three dimensional near field ISAR radar image can be generated.

4. CONCLUSIONS

Three dimensional radar imaging generated by using spherical near field range is developed. The performance of this system includes at least the following items: 1. Without the anechoic microwave chamber for radar image. 2. High quality radar image generated by the ISAR technique. 3. Three dimensional near field scanner for application. The simulation and test result of radar image is from the data collected by the impulse time domain radar system. The high performance radar image and RCS can be generated.

REFERENCES

1. Chang, D. C., "Course note on special topic of EM theory: PO, GO, GTD," 2001.
2. Mensa, D. L., "High resolution radar image," 1981.
3. Tasi, M.-Z., "Far field target image by near field RCS measurement," 2002.
4. Haykin, S., *Communication System*, Wiley, 1994.

Study of DNA Fingerprint of Pine Wood Nematode Based on Terahertz Spectroscopic Technology at 0–10 THz

Ling Jiang¹, Chun Li¹, Lin Huang², Zhenwei Zhang³, Cunlin Zhang³, and Yunfei Liu¹

¹College of Information Science and Technology, Nanjing Forestry University, Nanjing 210037, China

²Forest Resources and Environment Institute, Nanjing Forestry University, Nanjing 210037, China

³Terahertz Laboratory, Department of Physics, Capital Normal University, Beijing, China

Abstract— In this paper, we investigate the fingerprint characteristics of harmful *Bursaphelenchus xylophilus* (*Bx*) nematode and harmless *Bursaphelenchus mucronatus* (*Bm*) nematode by applying terahertz spectroscopic techniques. We measure and analyze the transmission features of the deoxyribose nucleic acid (DNA) of the *Bx* and the *Bm* samples, and their corresponding polymerase chain reaction (PCR) amplification segments of the DNA molecules by using terahertz domain spectroscopy (THz-TDS) and Fourier transform infrared spectroscopy (FTIR). According to the low frequency measurement below 2.5 THz by THz-TDS, the calculated relative refractive index of the *Bm*-PCR segment is found to be much smaller compared with other three samples. The higher frequency characteristics of the four samples measured by the FTIR spectroscopy shows similar absorption peaks, except that the *Bm*-DNA provides a smooth differential feature of absorption at 5.46 THz. These measurement results indicate the *Bm* samples including DNA and PCR segment have different spectroscopic behaviors from the *Bx* samples. It demonstrates that the terahertz spectroscopic technique is a useful method to distinguish the *Bx* and the *Bm*'s DNA and PCR segments by locating the absorption frequency.

1. INTRODUCTION

The pine wood nematode, *Bursaphelenchus xylophilus* (*Bx*), is a harmful insect living in pine wood. It is the main reason of pine wilt disease called pine cancer. *Bursaphelenchus mucronatus* (*Bm*) is a harmless insect living in the healthy pine wood, however which is quite similar to the *Bx* in shape. Currently the conventional method to diagnose the *Bx* and *Bm* nematodes is real-time fluorescence *polymerase chain reaction* (PCR) technique, which focus on the investigation of the PCR segment of deoxyribose nucleic acid (DNA) molecule of the *Bx* and the *Bm* samples by introducing the fluorescence marker [1, 2]. This method has several defects, for instance, time-consuming, high cost, relative high error rate due to the fluorescence marker. It's mainly employed for quarantine purposes. To early diagnose the pine wilt disease, it's necessary to find a fast and exact method. Terahertz spectroscopic technology has been successfully used to biology and medicine to study the animal and plant protein, nucleic acid, and amino acid and so on [3–6]. However, the spectral property of DNA has not been investigated thoroughly due to its huge mass. In this paper, we employ the THz spectroscopic method to study the absorption characteristics of the DNA and its PCR amplification segment of the *Bx* and *Bm* nematodes, i.e., *Bx*-DNA, *Bx*-PCR, *Bm*-DNA, and *Bm*-PCR samples by using terahertz time domain spectroscopy (THz-TDS) and Fourier transform infrared spectroscopy (FTIR). This is a continued study based on our previous work [7, 8]. In this paper, we obtain the different characteristic peaks of the *Bm* and the *Bx* samples. The experimental results will be analyzed by phonon modes in DNA macromolecules and dielectric resonances in terahertz spectra.

2. MEASUREMENT SETUP AND METHODS

2.1. Measurement Setup

The characterization of the *Bx*-DNA, *Bx*-PCR, *Bm*-DNA, and *Bm*-PCR samples are performed by the THz-TDS and the FTIR spectroscopy respectively. By measuring the change of the intensity of probe beam, we can obtain the THz wave signal which carries the information of the sample in the frequency range of 0–2.5 THz. In order to understand the spectral property of DNA molecule at high frequencies, we measure its absorbance by using Fourier transform infrared spectroscopy (FTIR), which is a technique used to obtain an infrared spectrum of absorption, emission, photoconductivity or Raman scattering of a solid, liquid or gas. The conventional FTIR system consists of optical source, Michelson Interferometer, and detector. In our measurement, the transmission spectral data were obtained. The measurement setup of the THz-TDS is shown in Fig. 1. The information of DNA and PCR samples can be recorded by THz detector.

2.2. Sample Preparation

The *Bx*-DNA, *Bm*-DNA, *Bx*-PCR, and *Bm*-PCR samples were measured by the THz-TDS and FTIR spectroscopy respectively. The *Bx*-DNA and the *Bm*-DNA were distilled from the *Bx* and the *Bm* nematodes by biological methods. The polymerase chain reaction (PCR) is a technique in molecular biology to amplify a single or few copies of a piece of DNA across several orders of magnitude, generating thousands to millions of copies of a particular DNA sequence. The *Bx*-PCR and the *Bm*-PCR samples are the special segments extracted from the *Bx*- and *Bm*-DNA molecules. The pure *Bx*-DNA, *Bm*-DNA, *Bx*-PCR, and *Bm*-PCR samples have the weight about 20 μg , which were mixed with the polyethylene (PET) powder and compressed into a thin pill under high pressure. The final pill has a 0.5-mm thickness, 13-mm diameter, 30-mg weight, after drying by vacuum drying oven until the water content is below 5%. The pure PET powder is also made into a pill with same thickness and weight as the other four samples for comparison. Given the PET is transparent to THz signal, the measured results will reflect the absorption characteristics of the *Bx* and the *Bm* nematodes.

2.3. Data Analysis Method

In the THz-TDS measurement, The refractive index $n_s(\omega)$, absorption coefficient $\alpha_s(\omega)$, and extinction coefficient $k_s(\omega)$ of the four samples are obtained by means of the physical model developed by the research groups [9, 10]

In our experiment, the expressions of the refractive index $n_s(\omega)$, the absorption coefficient $\alpha_s(\omega)$, and the extinction coefficient $k_s(\omega)$ can be achieved as follows:

$$n_s(\omega) = \phi(\omega) \cdot \frac{c}{\omega d} + 1 \quad (1)$$

$$\alpha_s(\omega) = \frac{2}{d} \ln \left(\frac{4n_s(\omega)}{\rho(\omega) \cdot (n_s(\omega) + 1)^2} \right) \quad (2)$$

$$k_s(\omega) = \frac{\alpha_s \cdot c}{2\omega} = \frac{c}{\omega d} \cdot \ln \left(\frac{4n_s(\omega)}{\rho(\omega) \cdot (n_s(\omega) + 1)^2} \right) \quad (3)$$

where $\rho(\omega)$ and $\phi(\omega)$ are the ratio of the amplitude and the phase difference between the sample and the reference which are obtained from the THz-TDS experiment.

3. MEASUREMENT RESULTS

3.1. THz Transmission Measured by THz-TDS

We have employed the conventional THz-TDS spectroscopy to measure the transmission characteristics of the *Bx*-DNA, *Bm*-DNA, *Bx*-PCR, and *Bm*-PCR samples. The time domain spectra of the *Bx*-PCR and *Bm*-PCR were measured to be similar to that of DNA samples, all of which have time delay compared with the case of the pure PE powder. The frequency domain characteristic of the four samples shows same absorption amplitude.

According to the Eqs. (1) and (2), the refractive index and absorption coefficient were calculated for the *Bx*-DNA, *Bx*-PCR, *Bm*-DNA, *Bm*-PCR samples, as shown in Fig. 2. It should be noted that the calculated refractive index are relative ones based on that of the pure PET sample. The calculated refractive index of the *Bm*-PCR sample is quite different from the other three samples with the discrepancy of larger than 0.1.

The measurement by THz-TDS indicate the *Bm* and the *Bx* DNA samples have similar variation trend of absorption features, however no fingerprint is found at 0–2.5 THz. Generally the elastic nature of DNA polymer results in structural vibrations that are acoustic modes below approximately 0.01 THz. DNA phonon modes in the microwave and millimeter-wave regime, with frequency smaller than 0.1 THz, are for the most part optically inactive and absorption spectrum from this region cannot be expected to yield a great deal of information about the internal structure of the polymer [11]. Our measurement results demonstrate the lower edge of millimeter-wave DNA phonon modes does not reflect the structural information. As a supplement of the whole terahertz region, we make the measurement at higher frequencies above 3 THz by FTIR spectroscopy.

3.2. Transmission Measured by FTIR

We measure the response above 1 THz by using broadband FTIR spectroscopy. In the frequency range of 1–10 THz, the measured FTS responses exhibit several similar peaks for the four samples. Fig. 3 displays the absorbance of the four samples in terms of FTIR spectroscopy. In order to find

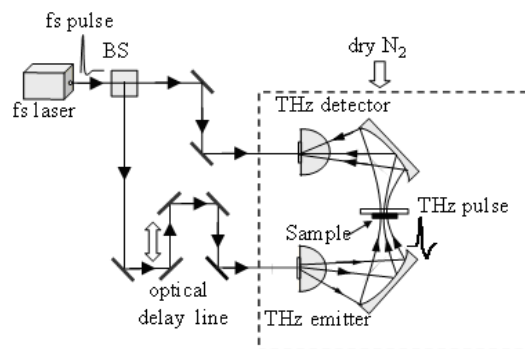


Figure 1: Schematic of THz-TDS measurement system, which mainly consists of THz coupling path, THz emitter, and THz detector.

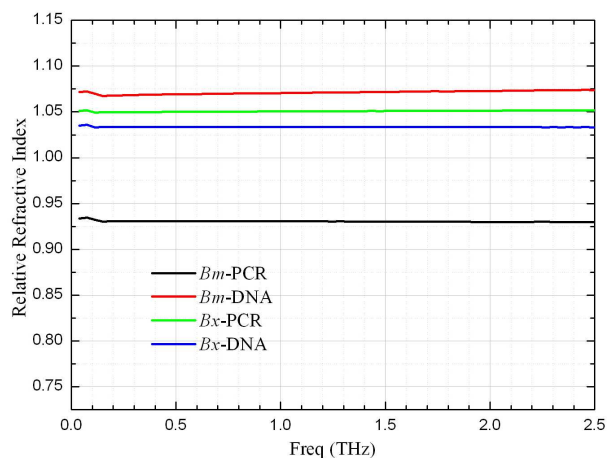


Figure 2: Relative refractive index as a function of frequency for the *Bx*-DNA, *Bx*-PCR, *Bm*-DNA, *Bm*-PCR samples, based on the refractive index of the pure PET sample.

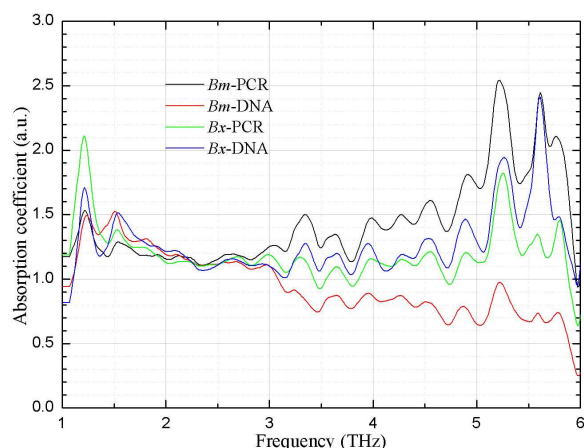


Figure 3: Absorption as a function of frequency for the *Bx*-DNA, *Bx*-PCR, *Bm*-DNA, *Bm*-PCR samples by using FTIR.

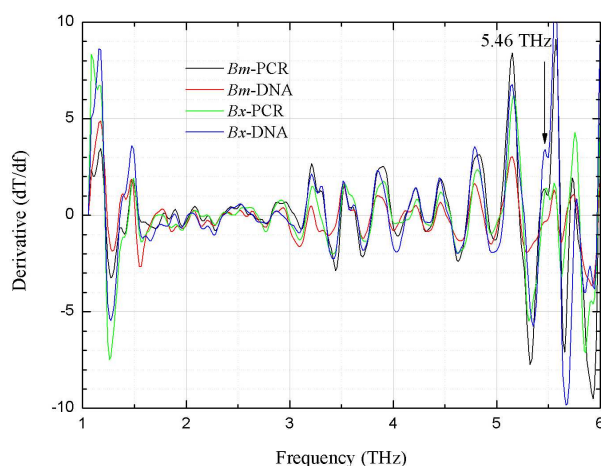


Figure 4: Differential plot of the absorbance characteristic for the *Bm*-PCR, *Bm*-DNA, *Bx*-PCR, *Bx*-DNA.

the signature feature to discriminate the *Bm* and the *Bx*, the differential plots of the transmission characteristic versus frequency (i.e., dT/df calculated from smoothing over nine data points) from the DNA and PCR segments of the *Bm* and *Bx* are compared, as shown in Fig. 4. Here, approximately similar results for the four different samples are observed. Furthermore, the differential plots reveal a discrepancy at 5.46 THz between *Bm*-DNA and the other three samples. The *Bm*-DNA shows a smooth curve while the other three samples exhibit a weak shoulder feature, which probably results from soft phonon modes that are obscured by the absorption feature at Fig. 3.

4. CONCLUSIONS

We have measured the time domain and frequency domain responses of the *Bx*-DNA, *Bx*-PCR, *Bm*-DNA, and *Bm*-PCR by using the terahertz time domain spectroscopy (THz-TDS) and the Fourier transform infrared spectroscopy (FTIR). The calculated relative refractive index of the *Bm*-PCR is smaller than that of another three samples according to the measurement of THz-TDS. Further measurement of the absorption characteristics and differential curves at higher terahertz frequencies above 1 THz by the FTIR demonstrates a different feature exist of the *Bm*-DNA at 5.46 THz, which indicate different phonon modes existing in the *Bm*-DNA. Therefore, we can clearly distinguish the *Bm* and the *Bx* nematodes by observing the differential peak at 5.46 THz derived from the absorption characteristic. This investigation will provide a new method based on terahertz spectroscopy technology to detect pine wood nematode.

ACKNOWLEDGMENT

This work was supported by the National Natural Science Foundation of China under Contracts 31170668 and 31200541, by the Natural Science Foundation of Jiangsu Province under Contract BK2012417, by the Scientific Research Foundation of the Education Ministry for Returned Chinese Scholars of China, and by the foundation of high level and returned personnel of Nanjing Forestry University.

REFERENCES

1. Cao, A. X., et al., “Detection of the pinewood nematode, *Bursaphelenchus xylophilus*, using a real-time polymerase chain reaction assay,” *Phytopathology*, Vol. 95, No. 5, 566–571, 2005.
2. Wang, Y., et al., “Comparative analyses on three kinds of molecular detection technique of *Bursaphelenchus xylophilus*,” *Journal of Nanjing Forestry University*, Vol. 31, No. 4, 2007.
3. Markelz, A. G., A. Roitberg, and E. J. Heilweil, “Pulsed terahertz spectroscopy of DNA, bovine serum albumin and collagen between 0.1 and 2.0 THz,” *Chemical Physics Letters*, Vol. 320, 42–48, 2000.
4. Fischer, B. M., M. Walther, and P. Uhd Jepsen, “Far-infrared vibrational modes of DNA components studied by terahertz time-domain spectroscopy,” *Physics in Medicine and Biology*, Vol. 47, 3807–3814, 2002.
5. Siegel, P. H., “Terahertz technology in biology and medicine,” *IEEE Trans. on Microwave Technology and Techniques*, Vol. 52, No. 10, 2004.
6. Kutteruf, M. R., C. M. Brown, L. K. Iwaki, M. B. Campbell, T. M. Korter, and E. J. Heilweil, “Terahertz spectroscopy of short-chain polypeptides,” *Chemical Physics Letters*, Vol. 375, 337–343, 2003.
7. Liu, Y. F., J. J. Tan, L. Jiang, S. C. Shi, B. B. Jin, and J. L. Ma, “Diagnostic technique of pine wood nematode disease based on THz spectrum,” *Proceedings of the SPIE*, Vol. 7277, 72770V-1–8, 2009.
8. Liu, Y. F., et al., “Application of terahertz spectroscopic technology in identification of pine wood nematode disease,” *Proc. of Asia-Pacific Microwave Conference*, WE3C-1, 2010.
9. Timothy, D. D., G. B. Richard, and M. M. Daniel, “Material parameter estimation with terahertz time-domain spectroscopy,” *Journal of the Optical Society of America A*, Vol. 18, No. 7, 1562–1571, 2001.
10. Duvillaret, L., F. Garet, and J. L. Coutaz, “Highly precise determination of optical constants and sample thickness in terahertz time-domain spectroscopy,” *Applied Optics*, Vol. 38, No. 2, 409–415, 1999.
11. Woolard, D. L., et al., “Submillimeter-wave phonon modes in DNA macromolecules,” *Physics Review E*, Vol. 65, 0519, 2002.

Terahertz Functional Tissue Imaging

S. M. Kim and P. Kung

Department of Electrical and Computer Engineering
The University of Alabama, Tuscaloosa, USA

Abstract— In recent years, biomedical imaging techniques using electromagnetic radiation in the terahertz (THz) spectral band, between 0.2 THz and 10 THz, has drawn considerable interest and made progress due to the ability of THz radiation to interact with biological tissue at the molecular structure level, in addition to being non-ionizing. For example, THz waves have been used to identify tissue changes in tooth enamel, cartilage, and malignant cancer cells. Terahertz Time-Domain Spectroscopy (THz-TDS) is one of the most versatile methods for spectroscopic image acquisition because of its ability to simultaneously determine the amplitude and phase of the traveling wave over a broad spectral range.

In this work, we investigate the use of THz-TDS imaging techniques to uniquely identify changes in tissue samples for both forensic and treatment applications. Using THz-TDS imaging in both transmission and reflection modes, we examine tissue samples that have been damaged by an acid. The structural deterioration to the tissue leads to a distinct fingerprint on the tissue that creates a contrast visible in the THz. In this study, we correlate the observed spectroscopic change in the THz time domain spectra and the frequency spectra.

1. INTRODUCTION

In recent years, electromagnetic waves in the Terahertz (THz) spectral region have received increasing attention for a growing number of spectroscopy and sensing applications, including in biomedical research, because of their non-ionizing characteristics, the presence of many molecule vibrational modes at THz frequencies, and their ability to penetrate a wide variety of materials [1–7]. However, THz based technologies are still in the early stages of development. We have already reported the use THz electromagnetic waves for imaging studies of undamaged bone tissue, skin tissues, and inorganic objects, including the development of THz image reconstruction algorithms [8, 9].

In this work, we examine the THz spectroscopic response and imaging of bone and cartilage tissue samples that have been damaged using hydrofluoric (HF) acid (Tissue I), as well as skin tissue damaged by both nitric (HNO_3) and hydrochloric (HCl) acids (Tissue II). One of the primary effects of direct exposure to HF is acute hypocalcaemia, i.e., removal of calcium from the tissue, which is expected to lead to significant changes in the THz response of the tissue due to structural changes and traces of acid.

2. EXPERIMENTAL PROCEDURE

The Tissue I samples consisted of thin (1 ± 0.1 mm) flat slices taken from the long bone of chickens and included both bone and cartilage parts. A small amount of HF acid was dropped in various small regions on the samples, at concentrations from 48 to 12% in water, and left to burn for 1 minute prior to rinsing off with deionized water. The samples were then dried with nitrogen prior to fixing using a 10% formalin neutral buffer for 2 hours. The Tissue II samples consisted of chicken skin tissue. Small drops of 100% HNO_3 and 100% HCl acid were applied to the tissue on adjacent spots and allowed to react until visible discoloration occurred. The tissue was then rinsed with de-ionized water, dried at room temperature using compressed nitrogen.

THz imaging of samples was conducted at room temperature using a THz Time-Domain Spectrometer (TDS) pumped by a mode-locked, ultrafast laser emitting at 790 nm with pulse width of 120 fs and a repetition rate of ~ 80 MHz. The sliced samples were mounted vertically with their surface plane perpendicular to the incident THz electromagnetic wave propagation direction. They were mounted between two thin, transparent plastic sheets which allow for $> 95\%$ transmission of the propagating THz radiation. The in-plane position was precisely controlled using a 3-axis motion controlled mount. All measurements were performed with the spectrometer under a nitrogen purge to minimize humidity for the duration of the measurement. For Tissue I the THz signal consisted of the transmitted wave, while for Tissue II the reflected wave was detected. Detection was achieved by means of electro-optic sampling using ZnTe crystal. The collected data consisted of the time domain amplitude for each pixel, i.e., each position of the sample. From this time domain signal,

frequency data is generated through the use of Fast-Fourier Transform (FFT) that gives frequency resolution of 25 GHz, which is sufficiently small for the observation of features and trends in the power spectrum. Since such full spectroscopic data is thus obtained for each pixel/point, an image can be reconstructed by showing the contrast associated to a specific attribute — either the time or the frequency domain — as a function of position [8].

3. RESULTS AND DISCUSSION

3.1. Tissue I: THz Imaging of Bone and Cartilage in Transmission Mode

Figure 2 shows the studied Tissue I before and after HF burn. The bottom right dark color area is where the compact bone is located and the part above is the cartilage. The region which was exposed to the HF has marked discoloration both on the bone and cartilage regions.

Figure 3 shows the THz imaging results obtained using different image reconstruction techniques based on the time domain amplitude signal. The image dimension was $\sim 20 \text{ mm} \times 20 \text{ mm}$, with a 0.5 mm pixel pitch. Figures 3(a) and 3(c) are obtained by using the peak amplitude in the time domain signal between fresh tissue and HF acid burned tissue, respectively; while Figures 3(b) and 3(d) are obtained by considering the amount of time delay that the transmitted wave peak experienced for both samples with respect to the free-path propagation peak position in time. We observed that the intensity of transmission through the sample is dramatically increased in both the cartilage and bone regions where the HF acid burn occurred, which is consistent with a loss of material due to the acid. Furthermore, the bone and cartilage exhibited a different response to HF. Before acid reaction (Figure 3(a)), the transmitted THz wave peak intensity was uniform for both cartilage and bone areas. After HF acid (Figure 3(c)), the transmitted intensity in the bone was still relatively uniform and higher, but the cartilage area showed a more fractured pattern with more contrasted transmission. In the time delay contrast, we can see that the cartilage exhibited a transmission peak that was delayed by 0.5 ps after HF burn, while the bone area did not show such large change.

Figure 4 shows the images reconstructed using the THz power spectra obtained after FFT of the time domain scan data for each pixel. These images are obtained at different frequencies, and the specific frequencies shown have been chosen after analysis of the power spectra for selected pixels.

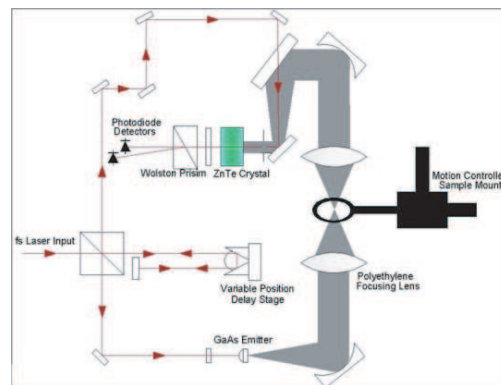


Figure 1: Schematic diagram of the THz-TDS used for tissue imaging study, shown here in transmission mode.

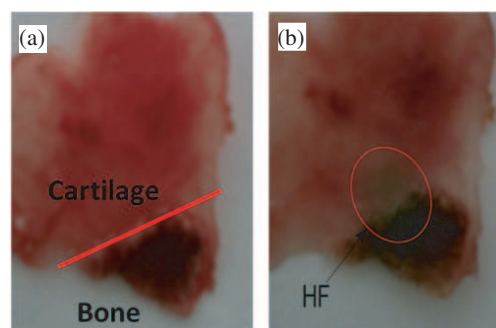


Figure 2: (a) Tissue I before and (b) after HF exposure burn.

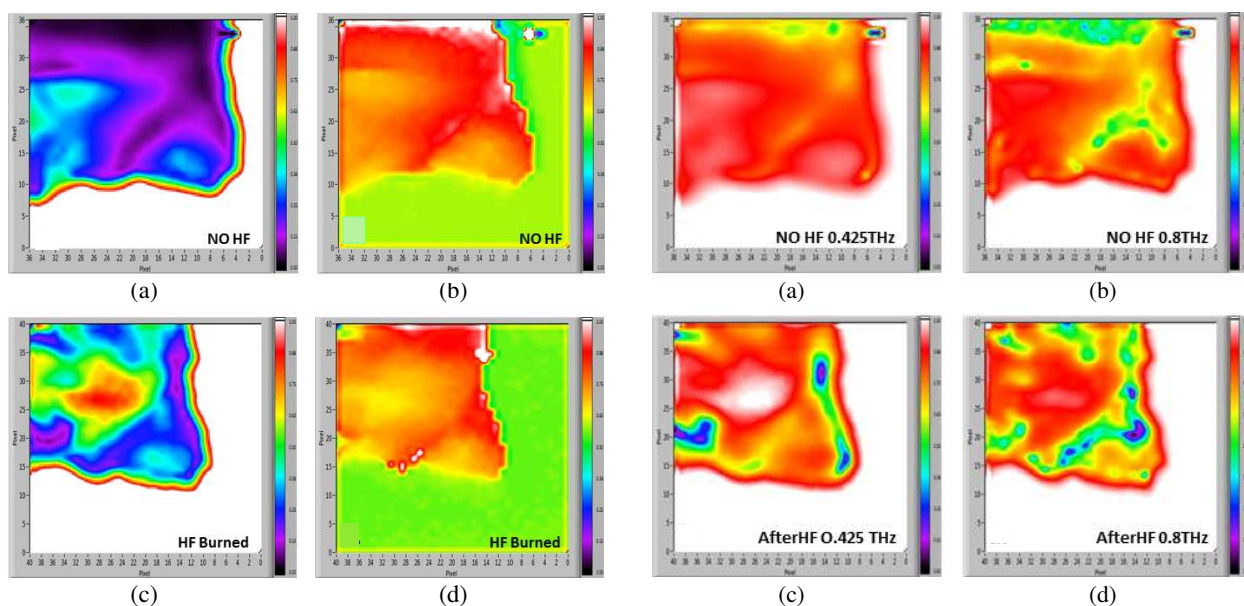


Figure 3: THz reconstructed images from signal in the time domain: (a) before and (c) after burn using peak signal; (b) before and (d) after burn using the delay of the signal peak in the time domain.

Figure 4: THz reconstructed images from power in the frequency domain at various frequencies: (a) before and (c) after burn at 0.425 THz; (b) before and (d) after burn at 0.8 THz.

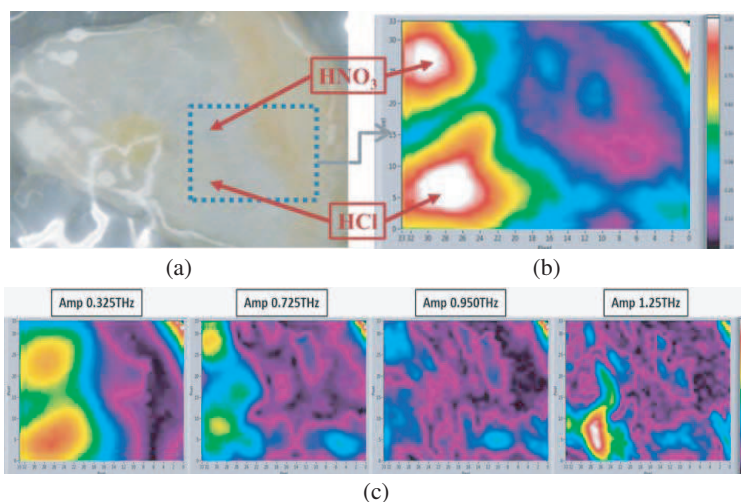


Figure 5: (a) Photo image of skin sample. (b) Time domain images reconstructed using peak intensity. (c) Images reconstructed at select frequencies in the power spectra: 0.325 THz, 0.725 THz, 0.950 THz, and 1.25 THz.

Below 0.5 THz, the HF damaged areas in both bone and cartilage exhibited higher transmitted THz power than the undamaged tissue, which can be easily shown in Figures 4(a) and 4(b) at 0.425 THz. A much larger contrast between fresh and HF burned tissue could be seen in the cartilage area than in the bone area. This behavior is similar to what was seen in Figure 3(c). Above 0.5 THz (Figures 4(c) and 4(d)), the burned areas do not become both more transmissive in the THz, but the burned bone area becomes less transparent than the cartilage (either burned or not). This enables us to distinguish between bone and cartilage at the higher THz frequency. Such contrast could not be easily obtained from the time domain data alone.

3.2. Tissue II: THz Imaging of Chicken Skin in Reflection Mode

Figure 5 shows the studied skin (Tissue II) with the two acid burned spots marked. The dashed frame region corresponds to the area that was imaged in reflection mode in the THz-TDS. Image acquisition was performed over a 20 mm \times 20 mm window with a 0.6 mm pixel pitch.

The image in Figure 5 (Top right) shows the image reconstructed by considering the peak

THz signal amplitude in the time domain. The areas affected by acids exhibited the highest reflected THz wave intensity compared to the normal skin area (right half of the imaged area). Image reconstructions were also accomplished using the THz power spectra obtained after FFT of the time domain scan for each pixel, and are shown in the lower row of Figure 5 for selected frequencies: 0.325, 0.725 THz, 0.950 and 1.25 THz. The area affected by the HNO₃ acid exposure on the tissue revealed an increased reflectance only at the lower frequencies (0.325 and 0.725 THz). At 0.950 THz, the acids do not appear to affect the interaction behavior of the THz radiation with the skin tissue. However, in the case of the hydrochloric acid, an increased reflection was observed again in a spectral window centered on 1.25 THz. From this difference in frequency dependent response, the nature of the two burns can be qualitatively differentiated.

4. CONCLUSIONS

We have investigated the use of THz-TDS imaging techniques to identify changes in tissue samples. Chicken bone and cartilage tissue samples have first been damaged locally using HF acid and imaged in the THz in transmission mode. The structural deterioration to the tissue leads to a distinct fingerprint on the tissue that creates a contrast visible in the THz. Image reconstructions from both the time and frequency domain data have been compared and clearly showed that the THz transparency increased in areas exposed to the acid, although the effect appears to be broad-spectrum, without clearly identifiable frequency specific results. Chicken skin tissue samples have been studied under reflection mode after local exposure to HNO₃ and HCl acids. Image reconstructions using both time and frequency domain data have also been compared. An analysis of frequency domain images showed that the nature of tissue degradation (i.e., which acid was used) could be differentiated; indicating that forensic medical applications may be possible with THz based techniques. With these results, a better understanding of the nature and precision of THz based biomedical imaging and imaging reconstruction can be developed.

ACKNOWLEDGMENT

We would like to acknowledge the National Science Foundation (EECS-0824452, CAREER, and IIT-1127831) for support of this work.

REFERENCES

1. Siegel, P., "Terahertz technology," *IEEE Trans. Microw. Theory Tech.*, Vol. 50, No. 3, 910–918, 2002.
2. Woolard, D. L., E. R. Brown, A. C. Samuels, J. O. Jensen, T. Globus, B. Gelmont, and M. Wol-ski, "Terahertz-frequency remote-sensing of biological warfare agents," *2003 IEEE MTT-S International Microwave Symposium Digest*, Vol. 2, No. 763, 2003.
3. Mellinger, J. S., N. Laman, and D. Grischkowsky, "The underlying terahertz vibrational spec-trum of explosive solids," *Appl. Phys. Lett.*, Vol. 93, No. 011102, 2008.
4. Dexheimer, S., *Terahertz Spectroscopy: Principles and Applications*, CRC Press, Boca Raton, FL, 2008.
5. Duvillaret, L., F. Garet, and J.-L. Coutaz, "A reliable method for extraction of material parameters in terahertz time-domain spectroscopy," *IEEE J. Sel. Top. in Quant. Electr.*, Vol. 2, No. 3, 739–746, 1996.
6. Dorney, T. D., G. Richard, G. Baraniuk, and D. M. Mittleman, "Material parameter estimation with terahertz time-domain spectroscopy," *J. Opt. Soc. Am. A*, Vol. 18, 1562–1571, 2001.
7. Laman, N., S. Harsha, D. Grischkowsky, and J. Mellinger, "High resolution waveguide thz spectroscopy of biological molecules," *Biophys. Journal*, Vol. 94, 1010–1020, 2008.
8. Baughman, W. E., D. S. Wilbert, S. Balci, M. Bolus, M. Baker, P. Kung, S. M. Kim, M. S. He-imbeck, and H. O. Everitt, "Comparative reconstructions of THz spectroscopic imaging for non-destructive testing and biomedical imaging," *Proc. of SPIE*, Vol. 8363, 2012.
9. Kim, S. M., W. Baughman, D. S. Wilbert, L. Butler, M. Bolus, S. Balci, and P. Kung, "High sensitivity and high selectivity terahertz biomedical imaging," *Chinese Opt. Lett.*, Vol. 9, No. 10, 2011.

Characterization of High Intense Pulse Amplified by Yb-doped Fiber Chirped Pulse Amplification System for THz Wave Generation

J. Hamazaki, N. Sekine, S. Saito, and I. Hosako

National Institute of Information and Communications Technology, Japan

Abstract— To obtain high power THz pulse, we construct fiber chirped pulse amplification system using double-clad Yb-doped fiber. We obtain output pulse power of 700 mW and pulse width of 230 fs. Using this amplified pulse, THz wave generation is achieved.

1. INTRODUCTION

Optical frequency comb is the technique to measure absolute optical frequency very precisely [1]. It is one of the fundamental techniques for the development of various advanced technologies. In terahertz region, optical frequency comb (THz comb) is in an early phase of development [2]. Since mode intensity of THz comb is not high enough, it is not utilized for measuring absolute THz wave frequencies. To measure absolute THz wave frequency, high mode intensity and mode spacing over 10 MHz are necessary. Therefore, high-power broad-band THz pulse generation with high repetition rate is required.

To generate THz pulse suitable for THz comb technique, optical rectification effect using ultra-short high-power pump pulse and nonlinear crystal (e.g., GaP, ZnSe, DAST) is a promising technique [3]. In this technique, broader-band THz pulse is obtained by using shorter pump pulse. Moreover, higher-power THz pulse is obtained by using higher-power pump pulse. Therefore, shorter and higher-power pump pulse is required. Recently, ultra-broadband THz pulse generation (spectral range of 0.1 ~ 100 THz) using ultra-short pulse (< 10 fs) [4] and high power THz generation (> 6.5 μ W) using high-power pulse (> 1 W) [5] were reported.

In these days, double-clad Yb-doped fiber (DC-YDF) has attracted much attention for realizing high-power highly-efficient amplifier. It is known that Yb-doped fiber (YDF) has large gain and broad gain spectrum (1.0–1.1 μ m). Furthermore, DC-YDF has extremely larger gain than usual YDF. Therefore, output power over 1 W is easily expected by using DC-YDF. Thus, fiber chirped pulse amplification (FCPA) technique using DC-YDF is suitable for high-power ultra-short pulse generation [5].

In this paper, we present our FCPA system using DC-YDF and characterize amplified output pulse. We obtain average output power of 700 mW with a pulse width of 230 fs at high repetition rate of 100 MHz. Moreover, we generate THz pulse by using our amplified pulse. We investigate effects of pump pulse dispersion on THz generation. Finally, we discuss improvements of our system for high-power broadband THz pulse generation toward THz comb.

2. HIGH INTENSE PULSE AMPLIFICATION

2.1. Experimental Setup of DC-YDF CPA System

Figure 1 shows experimental setup of our pulse amplifier system, which consists of pulse stretcher, double-clad Yb-doped fiber amplifier (DC-YDFA) and dispersion compensator. We used mode-locked pulse as a seed pulse (pulse width of 120 fs, repetition rate of ~ 100 MHz). The pulse stretcher was 90-m-long single mode fiber (HI-1060, Corning *inc.*). The pulse width of the seed was stretched from 120 fs to 130 ps. In the amplifier, the stretched seed pulse was amplified by 3.5-m-long DC-YDF (PLMA-YDF-10/125-VIII, Nufern *inc.*) pumped by a high power laser diode (LD). In the dispersion compensator, the amplified pulse was compressed by using grating pair (G_1 and G_2 , 1200 lines/mm) in the free space.

2.2. Characteristics of Amplified Pulse

As shown in Fig. 2, black squares denote output power as a function of launched pump LD power, measured just after DC-YDFA. The corresponding extraction efficiency and the maximum output power were 20% and 1.2 W, respectively. Red circles in Fig. 2 denote output power after pulse compressor. Maximum output power of 700 mW was obtained. Owing to four-times of diffraction losses, loss of pulse compressor was estimated to be ~ 40%.

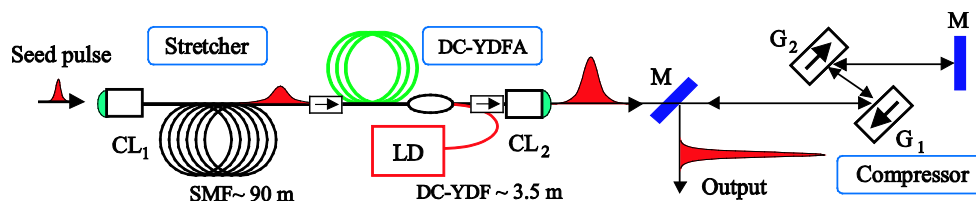


Figure 1: Experimental setup of our FCPA system using DC-YDF. CL: Collimating lens, SMF: Single mode fiber, LD: Laser diode, G: Grating, M: Mirror.

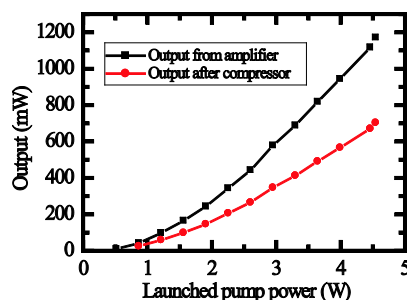


Figure 2: Output power from amplifier (black square) and output power after compressor (red circle), as a function of launched pump power.

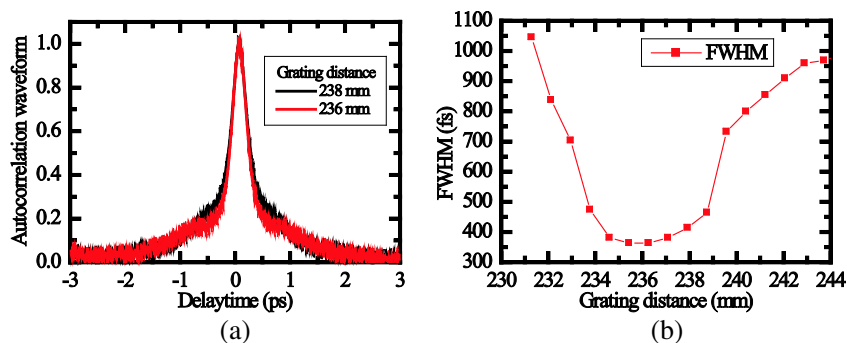


Figure 3: (a) Autocorrelation waveforms of amplified pulses from our FCPA. (b) FWHMs of autocorrelation waveforms as a function of grating distance.

In Fig. 3(a), red and black lines denote autocorrelation waveforms at grating distances of 236 mm and 238 mm, respectively. Full width at half maximums (FWHMs) at 236 mm and 238 mm were 360 fs and 415 fs, respectively. Fig. 3(b) shows FWHMs of autocorrelation waveforms as a function of grating distance. A minimum of FWHMs was 360 fs at 236 mm. So that, dechirped pulse width was estimated to be ~ 230 fs.

3. THz GENERATION AND DETECTION USING OUR AMPLIFIED PULSE

3.1. Experimental Setup for THz Generation and Detection

Figure 4 shows experimental setup for THz generation and detection. The pump pulses were produced by our FCPA system. The pump pulses were focused on a DAST crystal with a convex lens ($f = 100$ mm). THz pulses emitted from the DAST were collected and collimated by a Tsurupica lens of 35 mm focal length and 50 mm diameter (Pax *inc.*). Tsurupica is a lens generally used for THz waves. The power of the THz pulses was measured by a cooled Ge bolometer. Note that, Black polyethylene (BP) was used to prevent the strong pump pulse.

3.2. Result

Figure 5(a) shows a power of THz pulse as a function of input pump pulse power. A square-law dependence of the THz power on pump power was observed. We also investigated effects of pump pulse dispersion on THz generation power. Fig. 5(b) shows THz power as a function of grating distance. A maximum THz power was obtained at grating distance of 238 mm, although narrowest pump pulse width was observed at the distance of 236 mm. Moreover, generated THz power at

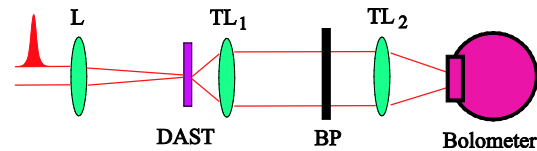


Figure 4: Experimental setup of THz generation and detection. L: Lens, TL: Tsurupica lens, BP: Black polyethylene.

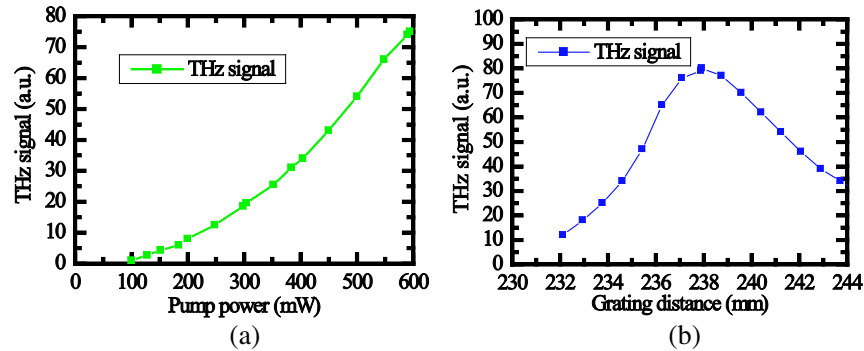


Figure 5: (a) THz power as a function of pump power. (b) THz power as a function of the grating distance.

239.5 mm was ~ 3.5 times higher than that at 233 mm. In spite of the fact, the FWHMs at 233 mm and at 239.5 mm were roughly the same width of ~ 700 fs (see Fig. 3(b)).

4. DISCUSSION

4.1. DC-YDF CPA System

It is clarified that our FCPA system deteriorates pulse qualities, as explained below. The pulse width of amplified pulse was estimated to be ~ 230 fs, in spite of the fact that pulse width of seed pulse was ~ 110 fs. Moreover, FWHM of autocorrelation waveform shows asymmetric dependence on grating distance, centering on the distance at 236 mm (see Fig. 3(b)). We claim the origin of these deteriorations is higher order dispersion effect. Since the pulse was stretched by 90-m-long SMF in the stretcher, third order dispersion (TOD) was roughly evaluated to be 7×10^6 fs³. Note that, compressor using grating pair can compensate only group velocity dispersion (GVD), it can not compensate TOD. To reduce effects of TOD on amplified pulse, shorter SMF in the pulse stretcher and/or higher order dispersion compensator is required.

4.2. THz Generation Using Our DC-YDF CPA System

As shown in Fig. 5(b), maximum THz power was obtained not in the case of shortest pulse width, as explained in the Section 3.2. We suggest the origin of this result is higher order dispersion of the pump pulse. As a result of the higher order dispersion, phase matching condition for THz generation was not well matched in DAST crystal. Therefore, by compensating TOD as well as GVD, THz generation efficiency must become improved.

Above all, in our experiments, THz power as a function of pump pulse power shows a square dependence and saturation effect was not observed. Therefore, further power scaling of THz generation is expected by increasing pump pulse power.

5. CONCLUSIONS

We presented our FCPA system and characterized our amplified output pulse. Average output power of 700 mW with a pulse width of 230 fs at 100 MHz was obtained. Using the amplified pulse, we achieved THz pulse generation from DAST crystal. Since saturation effect was not observed in THz generation, further power increasing of THz generation is expected by power scaling of pump pulse. By comparing the results in Figs. 3(b) and 5(b), we claimed TOD of amplified pulse deteriorates not only pulse width but also THz generation efficiency. Thus, we suggest TOD compensation as well as GVD is necessary to generate THz pulse more efficiently.

REFERENCES

1. Jones, D. J., S. A. Diddams, J. K. Ranka, A. Stentz, R. S. Windeler, J. L. Hall, and S. T. Cundiff, “Carrier-envelope phase control of femtosecond mode-locked lasers and direct optical frequency synthesis,” *Science*, Vol. 288, 635–639, 2000.
2. Yasui, T., Y. Kabetani, E. Saneyoshi, S. Yokoyama, and T. Araki, “Terahertz frequency comb by multifrequency-heterodyning photoconductive detection for high-accuracy, high-resolution terahertz spectroscopy,” *Appl. Phys. Lett.*, Vol. 88, 241104-1–3, 2006.
3. Dexheimer, S. L. (Ed.), *Terahertz Spectroscopy: Principles and Applications (Optical Science and Engineering)*, CRC Press, New York, 2008.
4. Ashida, M., “Ultra-broadband terahertz wave detection using photoconductive antenna,” *Jpn. J. Appl. Phys.*, Vol. 47, 8221–8225, 2008.
5. Chang, G., C. J. Divin, C. Liu, S. L. Williamson, A. Galvanauskas, and T. B. Norris, “Power scalable compact THz system based on an ultrafast Yb-doped fiber amplifier,” *Opt. Express*, Vol. 15, 16308–16315, 2007.
6. Strickland, D. and G. Mourou, “Compression of amplified chirped optical pulses,” *Opt. Commun.*, Vol. 56, 219–221, 1985.

Reflection and Transmission of Electromagnetic Waves from the Boundaries of Anisotropic Magneto Dielectric Plate in the Waveguide

E. A. Gevorkyan and V. I. Steshkin

Moscow State University of Economics, Statistics and Informatics
7, Nezhinskaya Str., Moscow 119501, Russia

Abstract— The propagation of transverse-electric (TE) and transverse-magnetic (TM) electromagnetic waves in the waveguide of arbitrary cross section with anisotropic magneto dielectric plate is considered. With help of received generalized Fresnel's formulas the power reflection and transmission coefficient for the plate are obtained. The dependence of these coefficients on thickness of the plate at various values of the parameters describing the parametric interaction of TE and TM waves with anisotropic and magneto dielectric plate in the waveguide is found.

The investigation of the propagation of TE and TM electromagnetic waves in the waveguide with anisotropic magneto dielectric plate of finite thickness represents the great interest, because these mediums have wide practical implementation in various regions of microwave electronics, thin-film and integrated optics, etc. [1, 2].

Let in the waveguide of arbitrary cross section whose axis coincides with oz axis of some Cartesian coordinate frame is placed the anisotropic magneto dielectric plate ($-d \leq z \leq d$). Consider the reflection and transmission of signal TE and TM waves with unit amplitude and frequency ω_0 from the boundary of the plate in the waveguide (Figure 1). Let the permittivity and permeability of the plate have a form.

Let the permittivity and permeability of the plate have a form

$$\widehat{\varepsilon} = \begin{pmatrix} \varepsilon_1 & 0 & 0 \\ 0 & \varepsilon_1 & 0 \\ 0 & 0 & \varepsilon_2 \end{pmatrix}, \quad \widehat{\mu} = \begin{pmatrix} \mu_1 & 0 & 0 \\ 0 & \mu_1 & 0 \\ 0 & 0 & \mu_2 \end{pmatrix} \quad (1)$$

where ε_1 , ε_2 , μ_1 , μ_2 are the constant quantities and the TE and TM waves incident on the plate from the side $z \leq -d$. TE and TM fields in the waveguide, as in our early articles (see, [3–6]), we can describe with help of longitudinal Fourier components of the magnetic and electric vectors

$$H_z = \sum_{n=0}^{\infty} H_{nz}(z) \widehat{\Psi}(x, y), \quad E_z = \sum_{n=0}^{\infty} E_{nz}(z) \psi_n(x, y), \quad (2)$$

where $\widehat{\psi}_n(x, y)$, $\psi_n(x, y)$ are the eigenfunctions of the second and first boundary-value problems for the cross section of the waveguide and satisfy the Helmholtz equations [4]. Solving the wave equations for the Fourier components of the TE and TM fields in the waveguide, received from the Maxwell equations, with help of the method, developed in the articles [3, 4], we shall receive for H_{nz} and E_{nz} in different regions of the waveguide the following expressions:

I and III regions, $z \leq -d$ and $z \geq d$

$$H_{nz1} = \widehat{b}_n^R \exp(i\widehat{\gamma}_n z) + \exp(-i\widehat{\gamma}_n z), \quad H_{nz3} = \widehat{b}_n^T \exp(-i\widehat{\gamma}_n z), \quad (3)$$

$$E_{nz1} = b_n^R \exp(i\gamma_n z) + \exp(-i\gamma_n z), \quad E_{nz3} = b_n^T \exp(-i\gamma_n z) \quad (4)$$

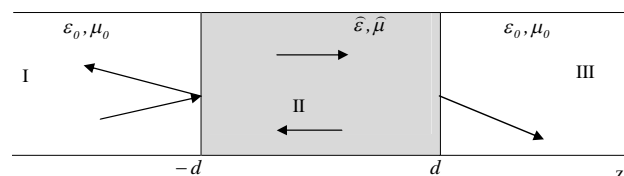


Figure 1: The geometry of the cross section of the waveguide.

where

$$\widehat{\gamma}_n^2 = \varepsilon_0^2 \mu_0^2 \omega_0^2 - \widehat{\lambda}_n^2, \quad \gamma_n^2 = \varepsilon_0^2 \mu_0^2 \omega_0^2 - \lambda_n^2. \quad (5)$$

II region, $-d \leq z \leq d$

$$H_{nz2} = \widehat{a}_n \exp(i\widehat{\Gamma}_n z) + \bar{\widehat{a}}_n \exp(-i\widehat{\Gamma}_n z), \quad E_{nz2} = a_n \exp(i\Gamma_n z) + \bar{a}_n \exp(-i\Gamma_n z), \quad (6)$$

where

$$\widehat{\Gamma}_n^2 = \frac{\mu_1}{\mu_2} \left(\varepsilon_0 \mu_0 \varepsilon_1 \mu_2 \omega_0^2 - \widehat{\lambda}_n^2 \right), \quad \Gamma_n^2 = \frac{\varepsilon_1}{\varepsilon_2} \left(\varepsilon_0 \mu_0 \varepsilon_2 \mu_1 \omega_0^2 - \lambda_n^2 \right), \quad (7)$$

$\varepsilon_0 = (4\pi \cdot 9 \cdot 10^3)^{-1}$ (F/m), $\mu_0 = 4\pi \cdot 10^{-7}$ (Gn/m), $\widehat{\lambda}_n$ and λ_n are the eigenvalues of the second and first boundary-value problems for the cross section of the waveguide. The unknown coefficients \widehat{b}_n^R , \widehat{b}_n^T , \widehat{a}_n , $\bar{\widehat{a}}_n$, b_n^R , b_n^T , a_n , \bar{a}_n in (3), (4), (6) can be found from the following boundary conditions at $z = \pm d$:

$$z = -d: \quad \begin{aligned} \mu_0 H_n^{(1)}(z) &= \mu_2 H_n^{(2)}(z), & \frac{\partial H_n^{(1)}(z)}{\partial z} &= \frac{\mu_2}{\mu_1} \frac{\partial H_n^{(2)}(z)}{\partial z}, \\ \varepsilon_0 E_n^{(1)}(z) &= \varepsilon_2 E_n^{(2)}(z), & \frac{\partial E_n^{(1)}(z)}{\partial z} &= \frac{\varepsilon_2}{\varepsilon_1} \frac{\partial E_n^{(2)}(z)}{\partial z}, \end{aligned} \quad (8)$$

$$z = +d: \quad \begin{aligned} \mu_2 H_n^{(2)}(z) &= \mu_0 H_n^{(3)}(z), & \frac{\mu_2}{\mu_1} \frac{\partial H_n^{(2)}(z)}{\partial z} &= \frac{\partial H_n^{(3)}(z)}{\partial z}, \\ \varepsilon_2 E_n^{(2)}(z) &= \varepsilon_0 E_n^{(3)}(z), & \frac{\varepsilon_2}{\varepsilon_1} \frac{\partial E_n^{(2)}(z)}{\partial z} &= \frac{\partial E_n^{(3)}(z)}{\partial z}. \end{aligned} \quad (9)$$

The obtained expressions for the coefficients allow to find the power reflection and transmission coefficients for the anisotropic magneto dielectric plate in the waveguide in the form

$$\widehat{T}_n = \frac{16\mu_0^2 \frac{\mu_4}{\mu_1^2} \widehat{\gamma}_n^2 \widehat{\Gamma}_n^2}{\left(\widehat{\Delta}_{n1}\right)^2 + \left(\widehat{\Delta}_{n2}\right)^2}, \quad (10)$$

$$T_n = \frac{16\varepsilon_0^2 \frac{\varepsilon_4}{\varepsilon_1^2} \gamma_n^2 \Gamma_n^2}{\left(\Delta_{n1}\right)^2 + \left(\Delta_{n2}\right)^2}, \quad (11)$$

where

$$\widehat{\Delta}_{n1} = \left(\widehat{\beta}_n^+\right)^2 \cos[2(\widehat{\Gamma}_n - \widehat{\gamma}_n)d] - \left(\widehat{\beta}_n^-\right)^2 \cos[2(\widehat{\Gamma}_n + \widehat{\gamma}_n)d], \quad \widehat{\beta}_n^\pm = \mu_2 \widehat{\gamma}_n \pm \frac{\mu_0 \mu_2}{\mu_1} \widehat{\Gamma}_n, \quad (12)$$

$$\widehat{\Delta}_{n2} = \left(\widehat{\beta}_n^+\right)^2 \sin[2(\widehat{\Gamma}_n - \widehat{\gamma}_n)d] + \left(\widehat{\beta}_n^-\right)^2 \sin[2(\widehat{\Gamma}_n + \widehat{\gamma}_n)d], \quad (13)$$

$$\Delta_{n1} = \left(\beta_n^+\right)^2 \cos[2(\Gamma_n - \gamma_n)d] - \left(\beta_n^-\right)^2 \cos[2(\Gamma_n + \gamma_n)d], \quad \beta_n^\pm = \varepsilon_2 \gamma_n \pm \frac{\varepsilon_0 \varepsilon_2}{\varepsilon_1} \Gamma_n, \quad (14)$$

$$\Delta_{n2} = \left(\beta_n^+\right)^2 \sin[2(\Gamma_n - \gamma_n)d] + \left(\beta_n^-\right)^2 \sin[2(\Gamma_n + \gamma_n)d]. \quad (15)$$

The dependences of power reflection and transmission coefficients from thickness of the anisotropic magneto dielectric plate in the waveguide at various values of the parameters, describing the interaction between the signal wave and the plate, resulted in the Figures 2–7.

The resulted graphs show (see, Figures 2–7) that the power reflection coefficients \widehat{R}_n and R_n have oscillating character and the envelopes of maxima of \widehat{R}_n and R_n are decreasing functions of d . It should be noted, that the points of maxima and minima of \widehat{R}_n are displaced aside smaller d when ε_1 increases at the fixed values of parameters μ_1 , μ_2 , ε_2 , $\widehat{\lambda}_n$ and ω_0 . The power transmission coefficients aspire to zero when $d \rightarrow \infty$.

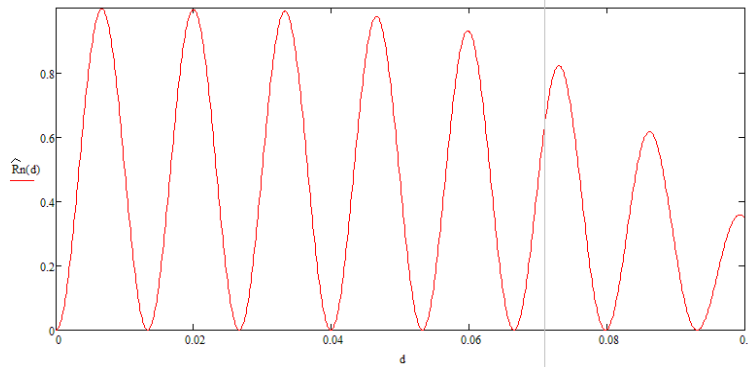


Figure 2: Dependence of \widehat{R}_n on width of the plate when $\varepsilon_1 = 1.5$; $\mu_1 = 1000$; $\mu_2 = 14$; $d \in [0.0005; 0.1]$; $\lambda_n = 20$; $\omega_0 = 1.2 \cdot 10^6$.

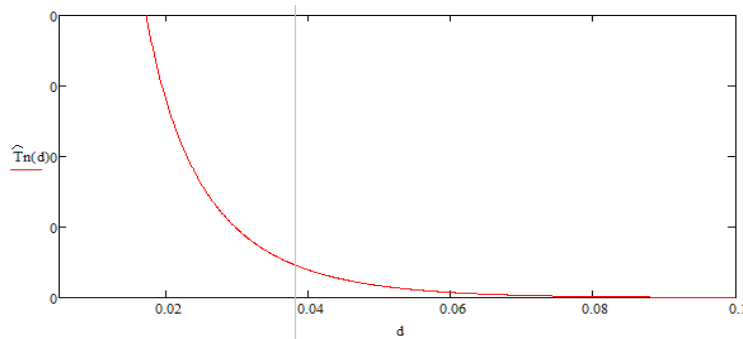


Figure 3: Dependence of \widehat{T}_n on width of the plate when $\varepsilon_1 = 1.5$; $\mu_1 = 1000$; $\mu_2 = 14$; $d \in [0.0005; 0.1]$; $\lambda_n = 20$; $\omega_0 = 1.2 \cdot 10^6$.

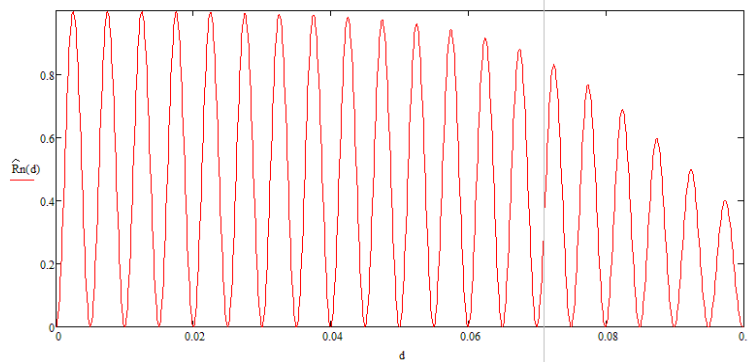


Figure 4: Dependence of \widehat{T}_n on width of the plate when $\varepsilon_1 = 4.5$; $\mu_1 = 1000$; $\mu_2 = 14$; $d \in [0.0005; 0.1]$; $\lambda_n = 20$; $\omega_0 = 1.2 \cdot 10^6$.

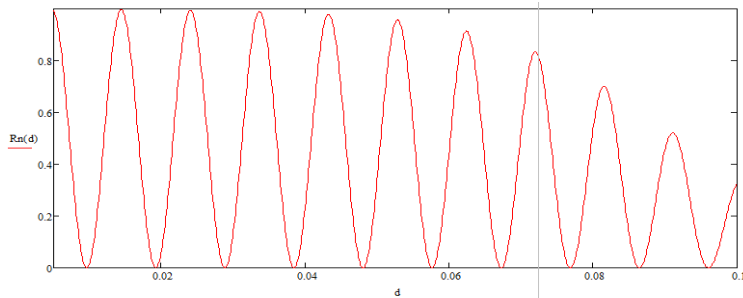


Figure 5: Dependence of R_n on thickness of the plate when $\varepsilon_1 = 1.5$; $\varepsilon_2 = 1.3$; $\mu_1 = 1000$; $\mu_2 = 1500$; $\lambda_n = 20$; $\omega_0 = 1.2 \cdot 10^6$; $0.005 \leq d \leq 0.1$.

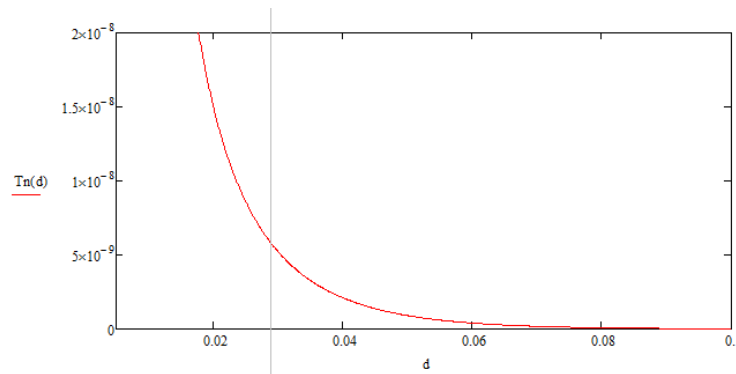


Figure 6: Dependence of T_n on thickness of the plate when $\varepsilon_1 = 1.5$; $\varepsilon_2 = 1.3$; $\mu_1 = 1000$; $\varepsilon_1 = 1.5$; $\varepsilon_2 = 1.3$; $\mu_1 = 1000$; $\mu_2 = 1500$; $\lambda_n = 20$; $\omega_0 = 1.2 \cdot 10^6$; $0.005 \leq d \leq 0.1$.

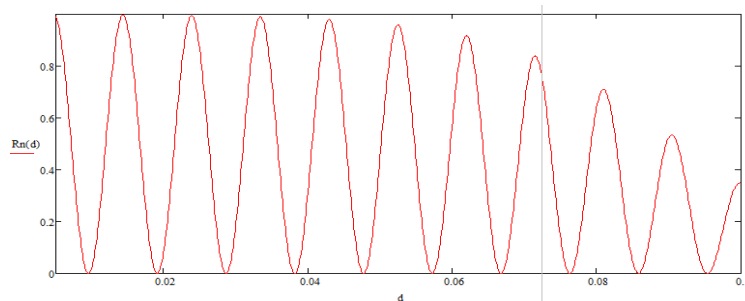


Figure 7: Dependence of R_n on thickness of the plate when $\varepsilon_1 = 1.5$; $\varepsilon_2 = 8.4$; $\mu_1 = 1000$; $\mu_2 = 6500$; $\lambda_n = 20$; $\omega_0 = 1.2 \cdot 10^6$; $0.005 \leq d \leq 0.1$.

REFERENCES

1. Yariv, A. and P. Yeh, *Optical Waves in Crystals*, Moscow, Mir, 1987.
2. Delitsin, A. L. and I. K. Troshina, "Complex waves in a waveguide with anisotropic filling," *Radiotekhnika Elektronika*, Vol. 50, No. 7, 815–820, 2005.
3. Gevorkyan, E. A., "On the electrodynamic of space — Time periodic mediums in the waveguides of arbitrary cross section," *Uspekhi Sovremennoy Radioelektroniki*, No. 1, 3–29, 2006.
4. Gevorkyan, E. A., "Interaction of electromagnetic waves with anisotropic magnetodielectric filling of the waveguide," *Elektromagnitnie Volni I Elektronnie Sistemi*, Vol. 14, No. 10, 65–72, 2009.
5. Gevorkyan, E. A., "On the electrodynamic of space-time periodic mediums in a waveguide of arbitrary cross section," *Wave Propagation*, Chapter 13, 267–284, INTECH Open Access Publisher, Croatia, 2011, www.intechopen.com, orders@intechweb.org.
6. Gevorkyan, E. A., "The theory of propagation of electromagnetic waves in a waveguide with magnetoactive anisotropic modulated filling," *Radiotekhnika I Elektronika*, Vol. 53, No. 5, 565–659, 2008.

Wiener-Hopf Method for Problems of Diffraction of Asymmetric Waves by a Circular Cylinder

Seil Sautbekov, Gulnar Alkina, and Merrey Sautbekova
Eurasian National University, 5, Munaitpassov Str., Astana, Kazakhstan

Abstract— Diffraction of an unsymmetrical electromagnetic wave by a long pipe coaxially oriented inside an infinite waveguide is considered. The corresponding boundary value problem is reduced to a system of singular integral equations concerning the Fourier component of the surface current density. The exact solution of the above system of equations is constructed by the Wiener-Hopf-Fok method in a class of analytical functions and it is defined in the form of sum of partial waves.

1. INTRODUCTION

Unsymmetrical E_{nm} (electrical or TM) and H_{nm} (magnetic or TE) waves ($m = 1, 2, 3, \dots$) differ from symmetrical waves ($m = 0$) that the diffraction field of unsymmetrical waves is characterized by two scalar functions which correspond to a longitudinal component of electric and magnetic Hertz's vectors according to the following equations [1]:

$$\Pi_z^e = \sin(m\varphi + \varphi_0)\Pi(r, z), \quad \Pi_z^m = \cos(m\varphi + \varphi_0)\tilde{\Pi}(r, z).$$

The presence of the two Hertz potentials complicates the derivation of the boundary value problem by Wiener-Hopf-Fok method [2, 3]. However the exact solution of this problem can be obtained by some generalization of the corresponding axially symmetrical problem.

Electromagnetic fields are expressed in terms of the functions Π and $\tilde{\Pi}$ as follows:

$$\begin{aligned} E_r &= \sin(m\varphi + \varphi_0) \left(\frac{\partial^2}{\partial r \partial z} \Pi - i \frac{mk}{r} W \tilde{\Pi} \right), \\ E_\varphi &= \cos(m\varphi + \varphi_0) \left(\frac{m}{r} \frac{\partial}{\partial z} \Pi - ikW \frac{\partial}{\partial r} \tilde{\Pi} \right), \\ E_z &= \sin(m\varphi + \varphi_0) \left(\frac{\partial^2}{\partial z^2} + k^2 \right) \Pi, \\ H_r &= \cos(m\varphi + \varphi_0) \left(\frac{\partial^2}{\partial r \partial z} \tilde{\Pi} - i \frac{mk}{r} W^{-1} \Pi \right), \\ H_\varphi &= -\sin(m\varphi + \varphi_0) \left(\frac{m}{r} \frac{\partial}{\partial z} \tilde{\Pi} - ikW^{-1} \frac{\partial}{\partial r} \Pi \right), \\ H_z &= \cos(m\varphi + \varphi_0) \left(\frac{\partial^2}{\partial z^2} + k^2 \right) \tilde{\Pi}, \quad W = \sqrt{\frac{\mu}{\varepsilon}}, \quad k = \frac{\omega}{c}. \end{aligned}$$

The constant angle φ_0 is determined by polarization of the wave impinging on the end of the circular waveguide.

Note that electromagnetic field of E_{mn} waves is defined by electric Hertz function Π from the abovementioned formulas, and electromagnetic field of waves H_{mn} by magnetic Hertz function $\tilde{\Pi}$.

Thus it is necessary to consider jointly unsymmetrical waves E_{m1}, E_{m2}, \dots and H_{m1}, H_{m2}, \dots for the given value m ($m = 1, 2, 3, \dots$), as they are transformed each other at reflection from the end of the waveguide.

2. STATEMENT OF THE PROBLEM

Let two waves are incident from the right to the left at the end of the long pipe with infinitely thin wall of radius a_1 located coaxially in the basic waveguide of radius a : one is unsymmetrical TM-wave with amplitude A and wave number h and the other is unsymmetrical TE-wave with amplitude B and wave number \tilde{h} (Figure 1).

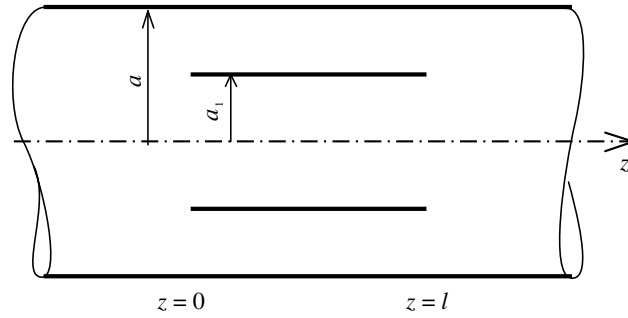


Figure 1.

The problem solution should satisfy the following boundary conditions:

$$E_z = E_\varphi = 0 \text{ at } r = a, \quad -\infty < z < \infty; \quad r = a_1, \quad 0 \leq z \leq l, \quad (1)$$

$$J_\varphi = H_z(a_1 - 0, \varphi, z) - H_z(a_1 + 0, \varphi, z) = 0 \text{ at } z < 0, \quad z > l, \quad (2)$$

$$J_z = H_\varphi(a_1 + 0, \varphi, z) - H_\varphi(a_1 - 0, \varphi, z) = 0 \text{ at } z \leq 0, \quad z \geq l, \quad (3)$$

where J_φ , J_z are azimuthally and longitudinal components of the surface current density.

The electrical and magnetic Hertz functions Π and $\tilde{\Pi}$ should be the solutions of the equation:

$$\frac{1}{r} \frac{\partial}{\partial r} \left(r \frac{\partial}{\partial r} \Pi \right) + \frac{\partial^2}{\partial z^2} \Pi + \left(k^2 - \frac{m^2}{r^2} \right) \Pi = 0. \quad (4)$$

3. SOLUTION OF THE PROBLEM

We are looking for Hertz functions according to Equation (4) in the following form [1]:

$$\Pi = -i \frac{\pi a_1}{2k} W \int_C \exp(iwz) L(r, w) F(w) dw, \quad (5)$$

$$\tilde{\Pi} = \frac{\pi a_1}{2} \int_C \exp(iwz) L(r, w) \frac{F(w)}{v} dw, \quad (6)$$

where $v = \sqrt{k^2 - w^2}$,

$$L(r, w) = \frac{1}{J_m(va)} \begin{cases} J_m(vr)(a_1, a), & r \leq a_1 \\ J_m(va_1)(r, a), & r \geq a_1 \end{cases},$$

$$L(r, w) = \frac{1}{J'_m(va)} \begin{cases} J_m(vr)(a'_1, a'), & r \leq a_1 \\ J'_m(va_1)(r, a'), & r \geq a_1 \end{cases},$$

$$(r, a) = J_m(vr)N_m(va) - J_m(va)N_m(vr),$$

$$(r, a') = J_m(vr)N'_m(va) - J'_m(va)N_m(vr),$$

$$(r', a') = J'_m(vr)N'_m(va) - J'_m(va)N'_m(vr),$$

$J_m(x)$ is the Bessel function, $N_m(x)$ is the Neumann function, C is the integration contour in the complex plane w lying along the real axis and consisting of an infinitely narrow loop enveloping a point h and \tilde{h} from below, F and F are the decision functions.

The boundary value problem is reduced with the help of the boundary conditions (1)–(3) to the system of the following functional integral equations:

$$\int_C \exp(iwz) \left(i \frac{mw}{k^2 a_1} LF(w) + LF(w) \right) dw = 0 \text{ at } 0 \leq z \leq l, \quad (7)$$

$$\int_C \exp(iwz) v^2 LF(w) dw = 0 \text{ at } 0 \leq z \leq l, \quad (8)$$

$$\int_C \exp(iwz)F(w)dw = 0 \text{ at } z < 0, z > l \quad (9)$$

$$\int_C \exp(iwz) \left(F(w) + i \frac{mw}{a_1 v^2} F(w) \right) dw = 0 \text{ at } z \leq 0, z \geq l, \quad (10)$$

where the following notation is introduced: $L \equiv L(a_1, w)$, $\tilde{L} \equiv L(a'_1, w)$.

Taking into account that the edges of the pipe are secondary sources of waves, the Fourier-component of the current density is constructed by Wiener-Hopf-Fok method as a sum from two analytical sources in the form of natural space harmonics forward and backward:

$$F(w) = \frac{1}{(k-w)L_-} \left(C_1^+(w) + \frac{C_1}{w+k} \right) + \frac{\exp(-iwl)}{(k+w)L_+} \left(C_2^-(w) + \frac{C_2}{w-k} + \frac{D_2}{w+h} \right), \quad (11)$$

$$F(w) = \frac{1}{L_-} \left(\frac{B_1}{w+k} + \frac{A_1}{w-k} + E_1^+(w) \right) + \frac{\exp(-iwl)}{L_+} \left(\frac{B_2}{w+k} + \frac{A_2}{w-k} + E_2^-(w) + \frac{F_2}{w+\tilde{h}} \right), \quad (12)$$

where $C_1, C_2, D_2, A_1, A_2, B_1, B_2, F_2$ are constants, $C_1^+(w), E_1^+(w)$ are analytical functions on the upper complex w plane, $C_2^-(w), E_2^-(w)$ are analytical functions on the lower complex plane.

As the integral along an infinitely narrow loop of the contour C corresponds to amplitude of the incident wave, it is easy to calculate the values of the following constants:

$$D_2 = A \frac{k}{\pi^2 a_1} \frac{L_-(a_1, h)}{(k+h)} \exp(-ihl) \frac{J_m(va)}{(a_1, a)} \Big|_{v=\sqrt{k^2-h^2}}, \quad (13)$$

$$F_2 = -i \frac{B}{\pi^2 a_1} L_-(a_1, \tilde{h}) \exp(-i\tilde{h}l) \frac{J'_m(va)}{(a'_1, a')} \Big|_{v=\sqrt{k^2-\tilde{h}^2}}. \quad (14)$$

Similarly we have

$$B_1 = -B_2 \frac{L_+(a_1, k)}{L_-(a_1, k)} \exp(ikl),$$

$$A_2 = -A_1 \frac{L_+(a_1, k)}{L_-(a_1, k)} \exp(ikl).$$

By substituting expressions (11), (12) into the system of the integral Equations (7)–(10) and closing the integration contour C in the upper half-plane or in the lower half-plane along the infinite semicircle according to Jordan's lemma, it is easy to obtain the system of the linear algebraic and functional equations, as following:

$$\begin{aligned} & \frac{C_1}{2kL_+(a_1, k)} + \frac{1}{L_-(a_1, k)} \left(C_2^-(-k) - \frac{C_2}{2k} + \frac{D_2}{h-k} \right) \exp(ikl) \\ &= \frac{im}{2a_1} \left[\frac{1}{L_+(a_1, k)} \left(E_1^+(-k) - \frac{A_1}{2k} \right) + \frac{1}{L_-(a_1, k)} \left(E_2^-(-k) - \frac{A_2}{2k} + \frac{F_2}{\tilde{h}-k} \right) \exp(ikl) \right], \quad (15) \end{aligned}$$

$$\begin{aligned} & \frac{1}{L_-(a_1, k)} \left(\frac{C_1}{2k} + C_1^+(k) \right) + \frac{C_2}{2kL_+(a_1, k)} \exp(-ikl) \\ &= \frac{im}{2a_1} \left[\frac{1}{L_-(a_1, k)} \left(E_1^+(k) + \frac{B_1}{2k} \right) + \frac{1}{L_+(a_1, k)} \left(E_2^-(k) + \frac{B_2}{2k} + \frac{F_2}{\tilde{h}+k} \right) \exp(-ikl) \right]. \quad (16) \end{aligned}$$

$$\begin{aligned} & \left(\frac{im}{a_1 k} \frac{L_-(a_1, k)}{2k} C_2 + L_-(a_1, k) A_2 \right) \exp(-ikl) + L_+(a_1, k) A_1 \\ &= \frac{im}{a_1 k} L_+(a_1, k) \left(\frac{C_1}{2k} + C_1^+(k) \right), \quad (17) \end{aligned}$$

$$\begin{aligned} & \frac{im}{a_1 k} \left(L_-(a_1, k) \frac{C_1}{2k} + L_+(a_1, k) \left(\frac{C_2}{2k} - C_2^-(-k) + \frac{D_2}{k-h} \right) \exp(ikl) \right) \\ &= L_-(a_1, k) B_1 + L_+(a_1, k) B_2 \exp(ikl). \end{aligned} \quad (18)$$

$$C_1^+(w) = - \sum_{n=1}^{\infty} \frac{\exp(iw_n l)}{w + w_n} \frac{L_+(a_1, w_n)}{L_-^*(a_1, w_n)} \frac{(k + w_n)}{(k - w_n)} \left(C_2^-(-w_n) - \frac{C_2}{k + w_n} + \frac{D_2}{h - w_n} \right), \quad (19)$$

$$C_2^-(w) = - \sum_{n=1}^{\infty} \frac{\exp(iw_n l)}{w - w_n} \frac{L_+(a_1, w_n)}{L_-^*(a_1, w_n)} \frac{(k + w_n)}{(k - w_n)} \left(C_1^+(w_n) + \frac{C_1}{k + w_n} \right), \quad (20)$$

where w_n are the zeros of L_- ($n = 1, 2, \dots$),

$$L_-^*(a_1, w_n) = \lim_{w \rightarrow w_n} (w - w_n)^{-1} L_-(a_1, w).$$

It is necessary to note, reasonably, the convergence of the infinite series, on account of exponential convergence, and in consideration of all traveling spatial harmonics and of some damped harmonics with imaginary wave numbers. Thus, the boundary value problem was reduced to the solution of a finite system of linear algebraic equations.

REFERENCES

1. Weinstein, L. A., *The Theory of Diffraction and the Factorization Method*, The Golem Press, Boulder, Colorado, 1969.
2. Daniele, V. G. and G. Lombardi, "Wiener-Hopf solution for impenetrable wedges at skew incidence," *IEEE Trans. Antennas and Propagation*, Vol. 54, No. 9, 2472–2485, 2006.
3. Noble, B., *Methods Based on the Wiener-Hopf Technique*, 2nd Edition, Chelsea, New York, 1988.

Design and Implementation of Low Phase Noise Oscillator Based on Film Bulk Acoustic Resonator

Wei-Wei Cheng¹, Shu-Rong Dong¹, and Sheng-Yun Luo²

¹Institute of Microelectronics and Optoelectronics
Zhejiang University, Hangzhou, Zhejiang 310027, China
²Physical Electronics Lab, Department of Materials Science
Fudan University, Shanghai 200433, China

Abstract— A novel low phase noise oscillator with film bulk acoustic resonator (FBAR) technology is presented. The longitudinal mode FBAR and shear mode FBAR are fabricated. The High Q FBAR also obtained from cutting AVAGO's FBAR produce. The Clapp oscillator based on FBAR at 1881 MHz is designed with PMBVD model and fabricated on printed circuit board. The testing results show that the output power of this FBAR oscillator is -3.5 dBm, while the phase noise is -130 dBc/Hz at 1 MHz.

1. INTRODUCTION

Film Bulk Acoustic Resonator (FBAR), a thin film piezoelectric resonator based on bulk acoustic, is a good candidate of integrated mass sensor chip owing to its high operating frequency, very high Q factor (above 1000), integrated process and small size [1, 2]. Considering the high Q factor of FBAR, using FBAR as a part of resonant network in oscillator is helpful to reduce noise. In this paper a novel low phase noise oscillator with FBAR technology is proposed.

2. FBAR OSCILLATOR DESIGN AND FABRICATION

Considered about higher Q factor, we also get the FBAR by cutting AVAGO's produce HPMD7904. Figure 1 shows the transmitting part of HPMD7904 duplexer which composed with six FBAR parts to perform the transmitting filtering. The middle FBAR at right side is used in this paper after being decapped, cut and re-bonded. Its Q factor is over 1200. Compared with the fabricated longitudinal mode FBAR and shear mode FBAR, the FBAR cut from HPMD7904 has a highest Q factor. The following oscillator is designed with this type of FBAR.

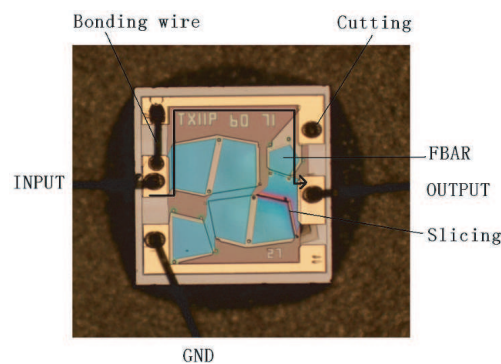


Figure 1: FBAR cut from HPMD7904.

3. DESIGN AND IMPLEMENTATION OF OSCILLATOR

Figure 2 shows the Clapp oscillator circuit based on FBAR, which is modified from Colpitts oscillator [3, 4].

The FBAR oscillator circuit is implemented with discrete components on the radio frequency printed circuit board, shown in Figure 3.

We design FBAR at 1880 MHz based on PMBVD model. PMBVD [5] is a new FBAR model, which adds pad parasitic parameter and bonding effect into MBVD (Modified Butterworth Van Dyke) model [6].

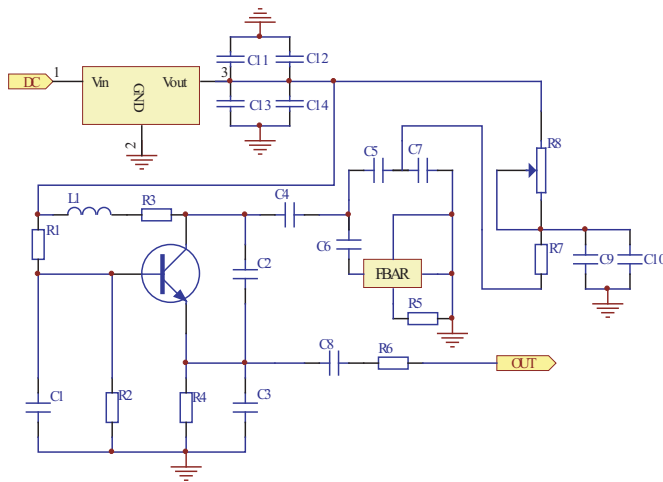


Figure 2: Schematic of FBAR oscillator.

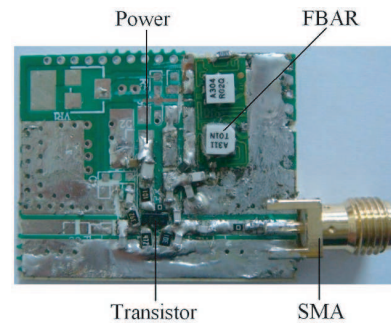


Figure 3: PCB Circuit of FBAR oscillator.

4. TEST RESULTS AND ANALYSIS

The FBAR oscillator is measured by the spectrum analyzer is 8563EC of Agilent and results are shown in Figure 4 and Figure 5. The output power of FBAR oscillator is -3.50 dBm in Figure 4, while the phase noise of FBAR oscillator is 132 dBc/Hz at 1 MHz in Figure 5 with the center frequency 1881 MHz, RBW 100 KHz and VBW 100 KHz. This phase noise is much lower than traditional Clapp oscillator. Testing results show that the oscillating frequency shifts from the designed resonant frequency by about 1 MHz. The frequency shift results from the slicing, cutting and bonding. The depth of slicing and the shape of single FBAR part affect the resonant frequency. And the remaining of the wire in cutting increases the insertion loss. In fact, the GND pad used as transmission may mismatch the impedance. At last, the new bonding wire brings some parasitic effect. Besides, all the above factors may affect the stabilization of FBAR oscillator [7].

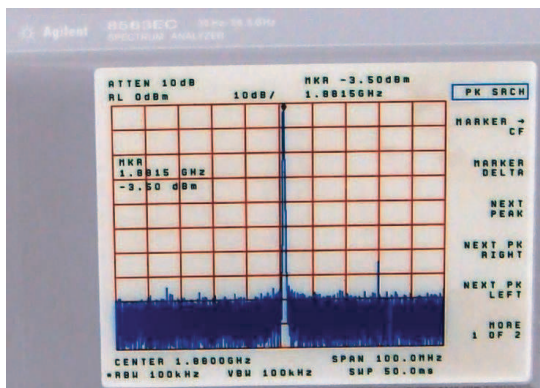


Figure 4: Test results of FBAR oscillator: output power.

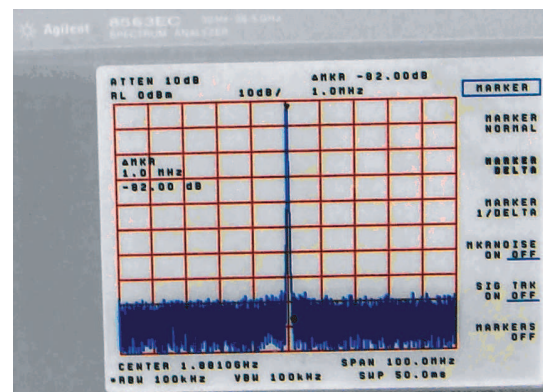


Figure 5: Test results of FBAR oscillator: phase noise.

5. CONCLUSION

This paper introduces a novel low phase noise oscillator with film bulk acoustic resonator (FBAR) technology, the longitudinal mode FBAR and shear mode FBAR are fabricated. It proposes a Clapp oscillator based on FBAR at 1881 MHz with PMBVD model and fabricated on printed circuit board, and the testing results show that the output power of this FBAR oscillator is -3.5 dBm, while the phase noise is -130 dBc/Hz at 1 MHz.

ACKNOWLEDGMENT

This work is supported by a grant from the National Natural Science Foundation Key Program of China (No. 60936002).

REFERENCES

1. Zhang, H. and E. S. Kim, “Micromachined acoustic resonant mass sensor,” *Journal of Microelectromechanical Systems*, Vol. 14, No. 4, 699–706, 2005.
2. Wingqvist, G., V. Yantchev, and I. Katardjiev, “Mass sensitivity of multilayer thin film resonant BAW sensors,” *Sensors and Actuators A: Physical*, Vol. 148, No. 1, 88–95, 2008.
3. Jiang, T., S. Qiao, Z.-G. Shi, L. Peng, J. Huangfu, W.-Z. Cui, W. Ma, and L.-X. Ran, “Simulation and experimental evaluation of the radar signal performance of chaotic signals generated from a microwave Colpitts oscillator,” *Progress In Electromagnetics Research*, Vol. 90, 15–30, 2009.
4. Shi, Z.-G., S. Qiao, K. S. Chen, W.-Z. Cui, W. Ma, T. Jiang, and L.-X. Ran, “Ambiguity functions of direct chaotic radar employing microwave chaotic Colpitts oscillator,” *Progress In Electromagnetics Research*, Vol. 77, 1–14, 2007.
5. Zhao, S. H., S. R. Dong, H. J. Zhang, W. W. Cheng, and X. X. Han, “Modeling of RF filter component based on film bulk acoustic resonator,” *IEEE Transactions on Consumer Electronics*, Vol. 55, No. 2, 351–355, May 2009.
6. Larson, J. D., P. D. Bradley, S. Wartenberg, and R. C. Ruby, “Modified butterworth-van dyke circuit for FBAR resonators and automated measurement system,” *IEEE Ultrasonics Symposium*, 863–868, San Juan, Pr, 2000.
7. Vahdati, H. and A. Abdipour, “Nonlinear stability analysis of an oscillator with distributed element resonator,” *Progress In Electromagnetics Research*, Vol. 80, 241–252, 2008.

DOA Estimation via Phase Measurement

Andrew Im, Matthew Gialich, Zekeriya Aliyazicioglu, and H. K. Hwang
 Electrical and Computer Engineering, California State Polytechnic University-Pomona
 3801 W. Temple Ave, Pomona, CA 91768, USA

Abstract— This paper investigates direction of arrival (DOA) estimation using array antenna with large inter-element spacing. The estimation technique is based on measuring the phases of the array elements. Since the inter-element spacing is larger than signal wavelength, the measured phase of each element has ambiguity. The possible phase combination of array elements is a large number. The proper phase combination is derived from the least square method. Once the proper phase combination is defined, the signal's DOA can be computed. Simulation results are presented in this paper.

1. INTRODUCTION

Estimating a signal's DOA with resolution exceeding conventional limitation has been investigated by many authors [1–5]. Simulation studies of eigen-analysis based techniques such as MUSIC, Root MUSIC, PRIME, ESPRIT for array antenna with inter-element spacing less than or equal to half of signal's wavelength have been carried out at California State Polytechnic University-Pomona [6–8]. Studies show that these advanced signal processing techniques provide satisfactory results. If the inter-element spacing is greater than half of a signal's wavelength, the MUSIC spectrum has spurious peaks. One method to identify signal's DOA is to partition the array into two independent subsets. The common MUSIC spectrum peak is the signal's DOA [9]. This paper presents the method of estimating the signal's DOA by measuring the relative phase of array elements.

Assume the array elements are placed on the x - y plane. The signal impinging the array antenna from elevation angle θ and azimuth angle ϕ . The array geometry is shown in Figure 1(a). The array antenna used in this simulation study is a 5 element non-uniformly spaced array as shown in Figure 1(b). λ is the signal wavelength.

The received waveform at k th element $u_k(n) = s_k(n) + w_k(n)$ where $s_k(n)$ is the signal component and $w_k(n)$ is the white noise component. Signal $s_k(n) = s(n) \exp(j\beta_k)$, where $\beta_k = \frac{2\pi}{\lambda} \sin \theta (x_k \cos \phi + y_k \sin \phi)$ is the relative phase of k th element and $s(n)$ is the signal of the reference element.

Setting the signal phase of reference element to be zero at every snapshot, the equivalent received waveform of k th element at sample n $u_k(n) = A \exp(j\beta_k) + w(n)$, where A is the signal amplitude.

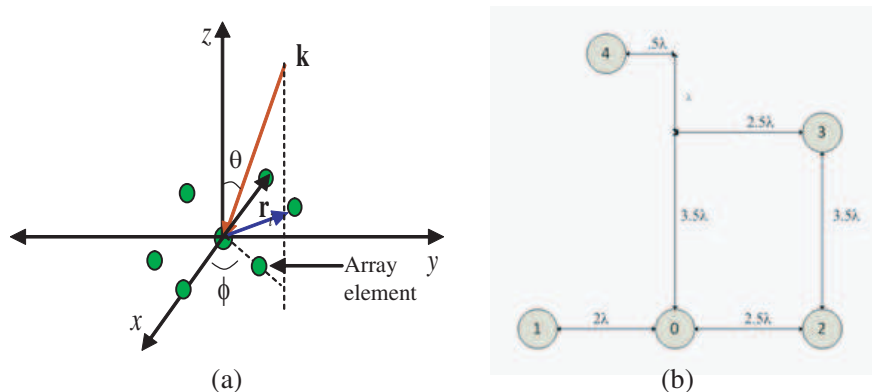


Figure 1: (a) Array antenna geometry. (b) Elements two dimensional array.

The received power of k th element after integrating over N snapshot is

$$\begin{aligned}
 P_k &= E \left[\left| \sum_{n=0}^{N-1} u_k(n) \right|^2 \right] = E \left[\sum_{n=0}^{N-1} s_k(n) \sum_{n'=0}^{N-1} s_k^*(n') \right] + E \left[\sum_{n=0}^{N-1} w_k(n) \sum_{n'=0}^{N-1} w_k^*(n') \right] \\
 &+ E \left[\sum_{n=0}^{N-1} s_k(n) \sum_{n'=0}^{N-1} w_k^*(n') \right] + E \left[\sum_{n=0}^{N-1} w_k(n) \sum_{n'=0}^{N-1} s_k^*(n') \right] \quad (1)
 \end{aligned}$$

The first term can be simplified to

$$E \left[\sum_{n=0}^{N-1} s_k(n) \sum_{n'=0}^{N-1} s_k^*(n') \right] = E \left[\sum_{n=0}^{N-1} A e^{j\beta_k} \sum_{n'=0}^{N-1} A e^{-j\beta_k} \right] = N^2 A^2 = N^2 \sigma_s^2$$

Since the noise is assumed to have a mean of zero, the 3rd and 4th terms are zero. The second term can be simplified to

$$E \left[\sum_{n=0}^{N-1} w_k(n) \sum_{n'=0}^{N-1} w_k^*(n') \right] = \sum_{n=0}^{N-1} \sum_{n'=0}^{N-1} E [w_k(n) w_k^*(n')] = \sum_{n=0}^{N-1} \sum_{n'=0}^{N-1} \sigma_w^2 \delta_{nn'} = N \sigma_w^2$$

The received power of the k th element is:

$$P_k = N^2 \sigma_s^2 + N \sigma_w^2 \quad (2)$$

The SNR can be given as

$$SNR = \frac{N^2 \sigma_s^2}{N \sigma_w^2} = \frac{N \sigma_s^2}{\sigma_w^2} \quad (3)$$

Thus integrating the received waveform over N samples improves the SNR by a factor of N .

The estimated phase of the k th element is

$$\hat{\beta}_k = \tan^{-1} \left[\text{Im} \left(\sum_{n=0}^{N-1} u_k(n) \right) / \text{Re} \left(\sum_{n=0}^{N-1} u_k(n) \right) \right] \quad (4)$$

The estimated phase of Equation (4) is the apparent phase. The true phase could be the value given by Equation (4) plus/minus the integer multiple of 2π .

The signal's DOA (θ, ϕ) can be obtained by solving the simultaneous nonlinear equations

$$\hat{\beta}_k = \frac{2\pi}{\lambda} \sin \theta (x_k \cos \phi + y_k \sin \phi) \quad \text{for } k = 1, 2, \dots, K \quad (5)$$

where K is the number of element of the array.

Equation (5) shows that the signal's DOA (θ, ϕ) related to the measured phase $\hat{\beta}_k$ in a nonlinear manner. To simplify the computation complexity, define $u = \sin \theta \cos \phi$, $v = \sin \theta \sin \phi$, Equation (5) transformed into linear form.

$$x_k u + y_k v = \frac{\lambda}{2\pi} \hat{\beta}_k \quad \text{for } k = 1, 2, \dots, K \quad (6)$$

The unknowns of Equation (6) are u and v . This set of linear equations can be expressed in a compact matrix form as:

$$\mathbf{A} \mathbf{w} = \mathbf{b} \quad (7)$$

where

$$\mathbf{A} = \begin{bmatrix} x_1 & y_1 \\ x_2 & y_2 \\ \vdots & \vdots \\ x_K & y_K \end{bmatrix}, \quad \mathbf{w} = \begin{bmatrix} u \\ v \end{bmatrix}, \quad \mathbf{b} = \frac{\lambda}{2\pi} \begin{bmatrix} \hat{\beta}_1 \\ \hat{\beta}_2 \\ \vdots \\ \hat{\beta}_K \end{bmatrix} \quad (8)$$

The number of equations K is greater than the number of unknowns, thus this is an over-determined system of linear equations. The optimal solution in the least square error sense is [10]:

$$\hat{\mathbf{w}} = \begin{bmatrix} u \\ v \end{bmatrix} = (A^T A)^{-1} \mathbf{A}^T \mathbf{b} \quad (9)$$

Suppose the number of possible phases of the k th element is p_k , for $k = 1, \dots, K$. Equation (9) has to solve for all $p_1 \times p_2 \times \dots \times p_K$ possible combinations of vector \mathbf{b} . A particular vector \mathbf{b} that yields the minimum error energy is the desired solution. The error energy is defined as

$$E_o = \min_{\hat{\mathbf{w}}} E = \sum_{k=1}^K \left(x_k u + y_k v - \frac{\lambda}{2\pi} \hat{\beta}_k \right)^2 \quad (10)$$

Once the optimal solution u_o, v_o are found, the DOA angles are:

$$\hat{\phi} = \tan^{-1} \left(\frac{v_o}{u_o} \right) \quad (11)$$

$$\hat{\theta} = \sin^{-1} \left(\frac{u_o}{\cos \hat{\phi}} \right) \quad (12)$$

Using the 5 element array antenna shown in Figure 1(b), the received waveform of k th element $u_k(n)$ is $u_k(n) = s_k(n) + w_k(n)$ where $s_k(n) = A \exp(j2\pi f n) \exp(j\beta_k)$ is the signal component and $w_k(n)$ is the white noise. The element 1 is used as the reference element. The reference phase β_k is the difference of the measured phase at element k and element 1. The angle error α_e is defined as the angle between the estimated DOA (θ_e, ϕ_e) and the true signal DOA (θ_s, ϕ_s) .

$$\alpha_e = \cos^{-1}(\mathbf{v}_e \cdot \mathbf{v}_s) \quad (13)$$

where $\mathbf{v}_e = \sin \theta_e \cos \phi_e \mathbf{i} + \sin \theta_e \sin \phi_e \mathbf{j} + \cos \theta_e \mathbf{k}$ and $\mathbf{v}_s = \sin \theta_s \cos \phi_s \mathbf{i} + \sin \theta_s \sin \phi_s \mathbf{j} + \cos \theta_s \mathbf{k}$, are the unit direction vectors of the true signal and estimated signal and $\mathbf{i}, \mathbf{j}, \mathbf{k}$ are the unit vectors along x, y, z directions.

2. COMPUTER SIMULATION

Suppose a signal impinging the array from $(\theta = 50^\circ, \phi = 50^\circ)$, the phase calculation is based on averaging over 100 snapshots, the scatter plots for SNR of 0 dB and 10 dB are plotted in Figure 2. The red dot is the true signal's DOA where the blue circles are the estimated signal's DOA. The scatter plots are obtained from 300 independent simulations.

When the phase estimation is based on averaging over 100 samples, the angle error for SNR ranging between 0 dB and 10 dB are plotted in Figure 3. Blue circles are the angle error of individual test and the red stars are the averaged angle error. The average angle error is around 0.29° when SNR is 0 dB and monotonically decreases as the SNR is improved.

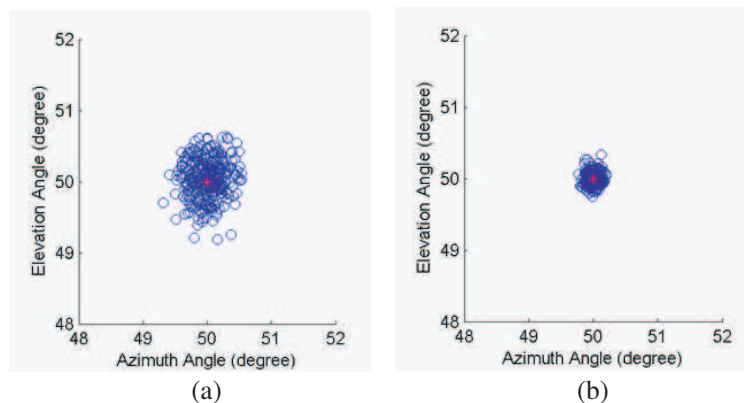


Figure 2: Scatter plot for (a) $SNR = 0$ dB. (b) $SNR = 10$ dB.

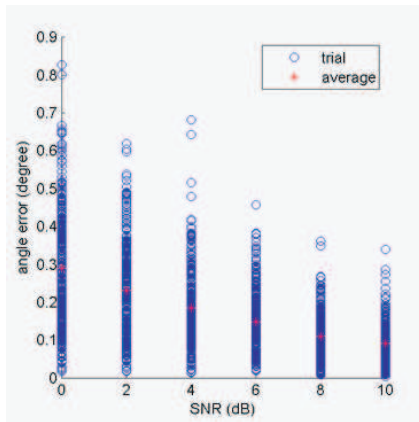


Figure 3: Angle error as function of SNR.

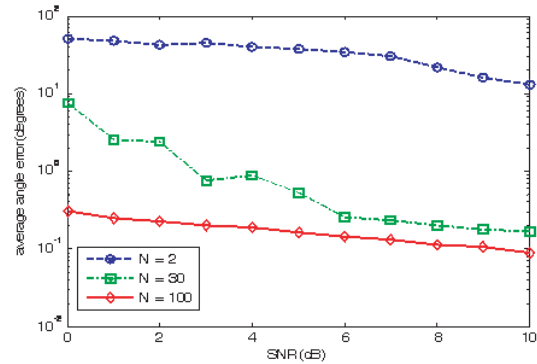


Figure 4: Average angle error as function of SNR.

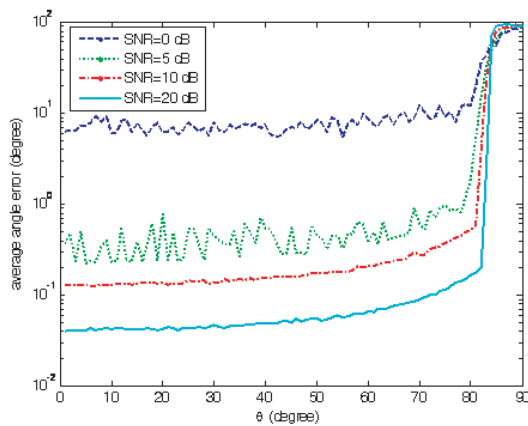


Figure 5: Angle error as function of SNR and elevation angle.

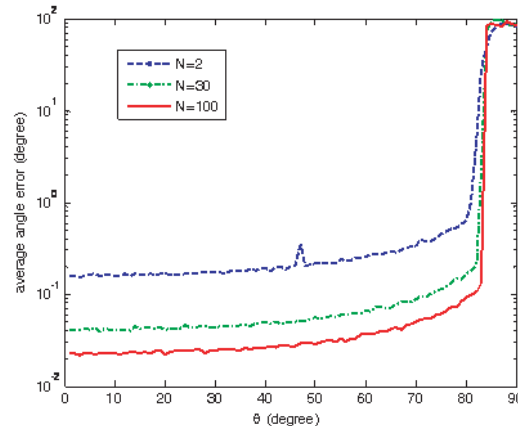


Figure 6: Angle error as function of number of snapshot and elevation angle.

The average angle error as function of SNR and number of sample (N) to compute the received phases is plotted in Figure 4. The dotted, dash and solid curves are the averaged angle error when the phase computation is based on averaging over 2, 30 and 100 samples. This Figure shows that increasing the number of averaging samples improves the accuracy of phase estimation. Consequently, the average angle error is reduced to a smaller value.

The simulation study shows the average angle error depends on the elevation angle θ . For example, fixing the signal's azimuth angle ϕ at 90° and phase estimation is based on averaged over 30 snapshots, the average angle error as a function of SNR and elevation angle θ is shown in Figure 5. Figure 5 shows that as the elevation angle approaches to 90° , average angle error suddenly jumps to a very large value. This processing algorithm is not very effective at detecting signals from a large elevation angle.

With SNR fixed at 10 dB, Figure 6 shows the average angle error as a function of elevation angle and number of snapshots. As indicated in Equation (3), increasing the number of snapshot by a factor of N has the equivalent effect of improving the SNR by the same factor of N . The average angle error for 100 snapshots is orders of magnitude lower than $N = 2$. Again, as the elevation angle approaching 90° the average angle error suddenly increases by an order of magnitude.

3. CONCLUSIONS

When the inter-element spacing is greater than half of the signal wavelength, MUSIC spectrum has multiple peaks. Rather than using the MUSIC method, this paper presents DOA estimation based on measuring the relative phases of the array elements. Conclusions of this simulation study are:

- (1) Better DOA estimation can be achieved by averaging the phase estimation over larger number of samples.

- (2) Improved DOA estimation can be obtained in a better SNR environment.
- (3) Estimated angle error increases by order of magnitude as the signal's elevation approaching 90° .
- (4) Results of this simulation study are based on array antenna shown in Figure 2. Different array antenna may have different result. Optimal array antenna is subject to further study.

REFERENCES

1. Burg, J. P., "Maximum entropy spectral analysis," Ph.D. Dissertation, Stanford University, May 1975.
2. Schmidt, R., "Multiple emitter location and signal parameter estimation," *IEEE Transactions on Antennas and Propagation*, Vol. 34, No. 3, 276–280, Mar. 1986.
3. Hatke, G. and K. Forsythe, "A class of polynomial rooting algorithms for joint azimuth/elevation estimation using multidimensional arrays," *28th Asilomar Conference on Signals, Systems and Computers*, 694–699, 1994.
4. Chandran, S., *Advances in Direction-of-Arrival Estimation*, Artech House Publisher, 2006.
5. Roy, R. and T. Kailath, "ESPRIT-estimation of signal parameters via rotational invariance techniques," *IEEE Transactions on Acoustics, Speech and Signal Processing*, 1989.
6. Aliyazicioglu, Z., H. K. Hwang, M. Grice, and A. Yakovlev, "Sensitivity analysis for direction of arrival estimation using a root-MUSIC algorithm," *Engineering Letters*, Vol. 16, No. 3, 353, 2008.
7. Aliyazicioglu, Z. and H. K. Hwang, "Performance analysis for DOA estimation using the PRIME algorithm," *10th International Conference on Signal and Image Processing*, 2008.
8. Bermudez, J., R. C. Chin, P. Davoodian, A. T. Y. Lok, Z. Aliyazicioglu, and H. K. Hwang, "Simulation study on DOA estimation using ESPRIT algorithm," *Proceedings of World Conference on Engineering & Computer Science*, 2009.
9. Gialich, M., A. Im, T. Lee, Z. Aliyazicioglu, and H. K. Hwang, "DOA estimation using array antenna with large inter-element spacing," *11th International Conference on Signal Processing*, 2012.
10. Haykin, S., *Adaptive Filter Theory*, 4th Edition, Prentice Hall, 2001.

Universal Properties of Electromagnetic Pulses

John Lekner

MacDiarmid Institute and School of Chemistry and Physics
Victoria University, Wellington, New Zealand

Abstract— We survey the existing known universal properties of electromagnetic pulses, and discuss their consequences. The established universal properties are (i) the time invariance of the total electromagnetic energy U , momentum P_z and angular momentum J_z of the pulse, and (ii) the inequality $cP_z < U$. (Pulse propagation is along the z -direction.) In both (i) and (ii), the theorems follow directly from Maxwell's equations.

The conservation of energy, momentum and angular momentum is no surprise, but the inequality $cP_z < U$ implies that all localized electromagnetic pulses have a zero-momentum frame (not a 'rest' frame, waves are never at rest). The above is of course in contradistinction to Einstein's light quantum, for which the momentum \mathbf{P} is purely in one direction, and $cP = U$. The implication seems to be that we cannot form a model of the photon by any pulse wave-function satisfying Maxwell's equations. If the momentum \mathbf{P} and energy U formed a four-vector $(c\mathbf{P}, U)$, $U^2 - c^2P^2$ would be a Lorentz invariant. This holds for point particles, but not universally for wavepackets. We show however that $u^2 - c^2p^2$ is a Lorentz invariant, non-negative at all space-time points (u and \mathbf{p} are the energy and momentum densities).

We also discuss the helicity of electromagnetic pulses, and the counter-intuitive relation between the helicity and angular momentum of certain exactly calculable examples.

1. INTRODUCTION

Maxwell's equations, with the electric and magnetic fields expressed in terms of the vector potential $\mathbf{A}(\mathbf{r}, t)$ and scalar potential $\Phi(\mathbf{r}, t)$ via

$$\mathbf{E} = -\nabla\Phi - \partial_{ct}\mathbf{A}, \quad \mathbf{B} = \nabla \times \mathbf{A} \quad (1)$$

and with \mathbf{A} and Φ satisfying the Lorenz condition $\nabla \cdot \mathbf{A} + \partial_{ct}\Phi = 0$, lead (in free space) to Φ and all components of \mathbf{A} satisfying the wave equation

$$\nabla^2\psi - \partial_{ct}^2\psi = 0 \quad (2)$$

Electromagnetic pulses can then be constructed from solutions of (2). For example, the choice $\Phi = 0$, $\mathbf{A} = \nabla \times (0, 0, \psi) = (\partial_y, -\partial_x, 0)\psi$ gives us the transverse electric (TE) pulse with

$$\mathbf{E} = -\partial_{ct}\mathbf{A} = (-\partial_y\partial_{ct}, \partial_x\partial_{ct}, 0)\psi, \quad \mathbf{B} = \nabla \times \mathbf{A} = (\partial_x\partial_z, \partial_y\partial_z, -\partial_x^2 - \partial_y^2)\psi \quad (3)$$

The wave Equation (2) has an infinity of solutions, for example $\psi = f(z-ct)$, with f an arbitrary twice differentiable function. These solutions, and the textbook plane wave $\exp i(\mathbf{K} \cdot \mathbf{r} - \omega t)$ and spherical waves $r^{-1} \exp [\pm iK(r \pm ct)]$ (both with $\omega = cK$) are not localized in space-time. The spherical wave solutions generalize to $r^{-1}f(r \pm ct)$, with f again any twice-differentiable function. These solutions are singular at the origin.

Bateman [1] obtained a general solution of the wave equation in integral form. For solutions with axial symmetry (independent of the azimuthal angle ϕ) the Bateman solution is, with $\rho = [x^2 + y^2]^{\frac{1}{2}}$ being the distance from the z -axis,

$$\psi(\rho, z, t) = \frac{1}{2\pi} \int_0^{2\pi} d\theta f(z + i\rho \cos \theta, ct + \rho \sin \theta) \quad (4)$$

We outline a proof (different from Bateman's): the wave equation in cylindrical polars, with no azimuthal dependence, reads

$$\left(\partial_\rho^2 + \frac{1}{\rho}\partial_\rho + \partial_z^2 - \partial_{ct}^2 \right) \psi = 0 \quad (5)$$

Carrying out the partial differentiations in $(\nabla^2 - \partial_{ct}^2)f$, and comparing with $\partial_\theta^2 f$ gives us

$$\left(\partial_\rho^2 + \frac{1}{\rho}\partial_\rho + \partial_z^2 - \partial_{ct}^2 \right) f = -\rho^{-2}\partial_\theta^2 f \quad (6)$$

Operating on (4) with $\nabla^2 - \partial_{ct}^2$ therefore gives

$$-2\pi\rho^2 (\nabla^2 - \partial_{ct}^2) \psi = \int_0^{2\pi} d\theta \partial_\theta^2 f = \partial_\theta f \Big|_0^{2\pi} = 0 \quad (7)$$

On the propagation axis ($\rho = 0$) the beam wavefunction becomes

$$\psi(0, z, t) = f(z, ct) \quad (8)$$

For example, if the on-axis wavefunction takes the form

$$f(z, t) = \frac{ab}{[a - i(z + ct)][b + i(z - ct)]} \psi_0 \quad (9)$$

the corresponding full wavefunction obtained by integrating (4) is

$$\psi(\rho, z, t) = \frac{ab}{\rho^2 + [a - i(z + ct)][b + i(z - ct)]} \psi_0 \quad (10)$$

This wavefunction has been obtained by other means (see references in [3–6]).

2. CONSERVATION LAWS, ENERGY-MOMENTUM INEQUALITIES

The energy, momentum and angular momentum densities of an electromagnetic field, in free space and in Gaussian units, are [2]

$$u(\mathbf{r}, t) = \frac{1}{8\pi} (E^2 + B^2), \quad \mathbf{p}(\mathbf{r}, t) = \frac{1}{4\pi c} \mathbf{E} \times \mathbf{B}, \quad \mathbf{j}(\mathbf{r}, t) = \mathbf{r} \times \mathbf{p}(\mathbf{r}, t) \quad (11)$$

$\mathbf{E}(\mathbf{r}, t)$ and $\mathbf{B}(\mathbf{r}, t)$ are the real electric and magnetic fields at position \mathbf{r} and time t . The total energy, momentum and angular momentum at time t of an electromagnetic pulse are

$$U = \int d^3r u(\mathbf{r}, t), \quad \mathbf{P} = \int d^3r \mathbf{p}(\mathbf{r}, t), \quad \mathbf{J} = \int d^3r \mathbf{j}(\mathbf{r}, t) \quad (12)$$

It will come as no surprise that these are all conserved quantities: the integrals in (12) are all independent of time.

The energy and momenta of electromagnetic pulses based on the solution (10) of the wave equation were evaluated in [3]. Proofs of the constancy of U and of \mathbf{P} were sketched in [4]. The conservation of angular momentum was proved in [5]. In all cases, the proofs follow from taking the time derivatives of the quantities U , \mathbf{P} and \mathbf{J} defined in (12), applying Maxwell's free-space equations

$$\begin{aligned} \nabla \cdot \mathbf{B} &= 0 & \nabla \cdot \mathbf{E} &= 0 \\ \nabla \times \mathbf{E} + \partial_{ct} \mathbf{B} &= 0 & \nabla \times \mathbf{B} - \partial_{ct} \mathbf{E} &= 0 \end{aligned} \quad (13)$$

and using elementary analytical techniques.

In order for the quantities U , \mathbf{P} and \mathbf{J} to *exist* (let alone be conserved), the corresponding electromagnetic pulse has to be localized. The first evaluation of U for any localized pulse was in [6]; later evaluation of energy, momentum and angular momentum for various electromagnetic pulses found [3] that all had $U > cP_z$, with the transverse momenta P_x and P_y zero. Thus these pulses could be Lorentz-transformed into their zero momentum frames, in which the pulse converges onto its focal region and then diverges from it, maintaining zero net momentum at all times. The proof that $U > cP_z$ for all localized electromagnetic pulses is elementary [4]: let the total momentum vector \mathbf{P} point along the z direction, and consider the energy and momentum densities $u(\mathbf{r}, t)$ and $p_z(\mathbf{r}, t)$. From (11), we have

$$\begin{aligned} 8\pi(u - cp_z) &= \mathbf{E}^2 + \mathbf{B}^2 - 2(\mathbf{E} \times \mathbf{B})_z \\ &= E_x^2 + E_y^2 + E_z^2 + B_x^2 + B_y^2 + B_z^2 - 2(E_x B_y - E_y B_x) \\ &= (E_x - B_y)^2 + (E_y + B_x)^2 + E_z^2 + B_z^2 \geq 0 \end{aligned} \quad (14)$$

Equality of U and cP_z would require $u - cp_z$ to be zero everywhere and at all times, which from (14) requires $E_z = 0 = B_z$ (purely transverse fields) and also $E_x = B_y$ and $E_y = -B_x$. The divergence equations in (13) then give

$$-\partial_x E_y + \partial_y E_x = 0 \quad \text{and} \quad \partial_x E_x + \partial_y E_y = 0 \quad (15)$$

Thus E_x and $-E_y$ would be a Cauchy-Riemann pair in the variables x and y , and satisfy

$$(\partial_x^2 + \partial_y^2) E_x = 0, \quad (\partial_x^2 + \partial_y^2) E_y = 0 \quad (16)$$

Such harmonic functions cannot have a maximum except at the boundary of their domain, and thus cannot be localized in x and y (for any z and t). For localized electromagnetic pulses we therefore always have the total energy greater than c times the net total momentum

$$U > cP_z \quad (17)$$

U and \mathbf{P} are defined by (12) as spatial integrals, independent of time in any given inertial frame. If together they formed the four-vector $(c\mathbf{P}, U)$, $U^2 - c^2 P^2$ would be a Lorentz invariant, the same in all inertial frames.

Such four-vectors exist for point particles, but cannot be associated (in general) with extended wavepackets. Consider however the squares of the volume densities, $u^2(\mathbf{r}, t)$ and $\mathbf{p}^2(\mathbf{r}, t)$. From (11), we have

$$\begin{aligned} (8\pi)^2(u^2 - c^2 \mathbf{p}^2) &= (E^2 + B^2)^2 - 4(\mathbf{E} \times \mathbf{B})^2 \\ &= (E^2 + B^2)^2 - 4E^2 B^2 + 4(\mathbf{E} \cdot \mathbf{B})^2 \\ &= (E^2 - B^2)^2 + 4(\mathbf{E} \cdot \mathbf{B})^2 \end{aligned} \quad (18)$$

Hence $u^2 - c^2 \mathbf{p}^2$ is everywhere non-negative, and further it is a Lorentz invariant, since $E^2 - B^2$ and $\mathbf{E} \cdot \mathbf{B}$ are Lorentz invariants. The Appendix has further discussion of the Lorentz transformation of wavepackets.

3. ANGULAR MOMENTUM, HELICITY

We have seen that the energy U , momentum \mathbf{P} and angular momentum \mathbf{J} are all conserved (do not change with time) for any electromagnetic pulse. The energy and momentum are also independent of the choice of origin of the spatial coordinates (which are integrated over, see (12)). However, the angular momentum does depend on the choice of origin: in the translation $\mathbf{r} \rightarrow \mathbf{r} - \mathbf{a}$, $\mathbf{J} \rightarrow \mathbf{J} - \mathbf{a} \times \mathbf{P}$. Textbooks make statements such as ([7], p569) ‘the photon has vanishing mass and cannot be brought to rest in any Lorentz frame of reference’. As we have seen, any localized electromagnetic pulse satisfying Maxwell’s equations does have a zero momentum frame (not a ‘rest’ frame). In the frame where \mathbf{P} is zero the angular momentum is independent of the choice of origin, and thus we can associate an *intrinsic angular momentum* with a localized electromagnetic pulse.

Suppose (as we have in this paper) that the net momentum of a pulse is along the z -direction, $\mathbf{P} = (0, 0, P_z)$. A Lorentz boost at speed $c^2 P_z / U$, along the z -axis, will bring the pulse to its zero momentum frame. The component J_z of the angular momentum is unchanged in this Lorentz transformation. This is because the four-tensor of angular momentum $J_{ij} = X_i P_j - X_j P_i$ (X_i and P_i represent components of the space-time and momentum-energy four-vectors) has the same structure as the electromagnetic field four-tensor composed of \mathbf{E} and \mathbf{B} ([8], Section 2–6)

$$[J_{ij}] = \begin{pmatrix} 0 & J_z & -J_y & J_{14} \\ -J_z & 0 & J_x & J_{24} \\ J_y & -J_x & 0 & J_{34} \\ J_{41} & J_{42} & J_{43} & 0 \end{pmatrix} \quad (19)$$

where

$$\begin{aligned} J_{41} &= -J_{14} = i(ctP_x - xU/c) \\ J_{42} &= -J_{24} = i(ctP_y - yU/c) \\ J_{43} &= -J_{34} = i(ctP_z - zU/c) \end{aligned} \quad (20)$$

For comparison, the field four-tensor, also in the Minkowski notation, is

$$[F_{ij}] = \begin{pmatrix} 0 & B_z & -B_y & -iE_x \\ -B_z & 0 & B_x & -iE_y \\ B_y & -B_x & 0 & -iE_z \\ iE_x & iE_y & iE_z & 0 \end{pmatrix} \quad (21)$$

Since B_z is unchanged by a Lorentz boost along the z -axis, J_z will also be unchanged by such a transformation. Thus we can regard the component of the angular momentum along the momentum (J_z , in this paper) as the intrinsic angular momentum of the pulse.

The helicity of the pulse is $+1$ if the sign of J_z is the same as that of P_z (in a frame with $P_z \neq 0$), -1 if the signs are opposite. There is no helicity (or the helicity is zero) if J_z is zero.

We shall give some examples of results for electromagnetic pulses based on the wavefunction (10). The first is for the TE+iTM pulse for which

$$\mathbf{A} = \nabla \times (0, 0, \psi) = (\partial_y, -\partial_x, 0)\psi \quad (22)$$

$$\mathbf{B} = \nabla \times \mathbf{A} + i\partial_{ct}\mathbf{A}, \quad \mathbf{E} = i\mathbf{B} \quad (23)$$

(Here $\mathbf{B}(\mathbf{r}, t)$ and $\mathbf{E}(\mathbf{r}, t)$ are complex; their real and imaginary parts are separately solutions of Maxwell's equations.) The energy, momentum and angular momentum found in [3] are

$$U = \frac{\pi}{8} \frac{a+b}{ab} \psi_0^2, \quad cP_z = \frac{\pi}{8} \frac{a-b}{ab} \psi_0^2, \quad J_z = 0 \quad (24)$$

For this pulse, a Lorentz boost at speed βc , $\beta = cP_z/U = (a-b)/(a+b)$, will bring the pulse to its zero-momentum frame [3].

If instead we take the vector potential to be

$$\mathbf{A} = \nabla \times [i\psi, \psi, 0] \quad (25)$$

with \mathbf{B} and \mathbf{E} defined by (23) as before, we obtain [3]

$$U = \frac{\pi}{8} \frac{a+3b}{a^2} \psi_0^2, \quad cP_z = \frac{\pi}{8} \frac{a-3b}{a^2} \psi_0^2, \quad cJ_z = \frac{\pi}{4} \frac{b}{a} \psi_0^2 \quad (26)$$

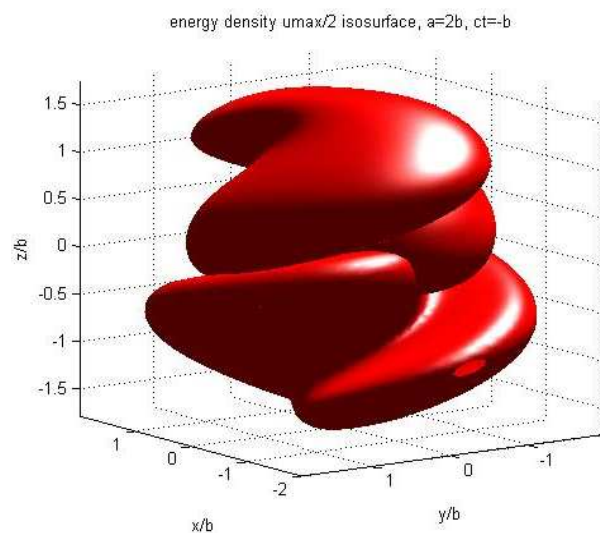


Figure 1: The energy density isosurface at $u = \frac{1}{2}u_{\max}$, $ct = -b$ for the wavefunction given in the text. The pulse is travelling upward, and has negative angular momentum about the propagation direction. In contrast, the energy isosurface consists of two short right-handed screw threads.

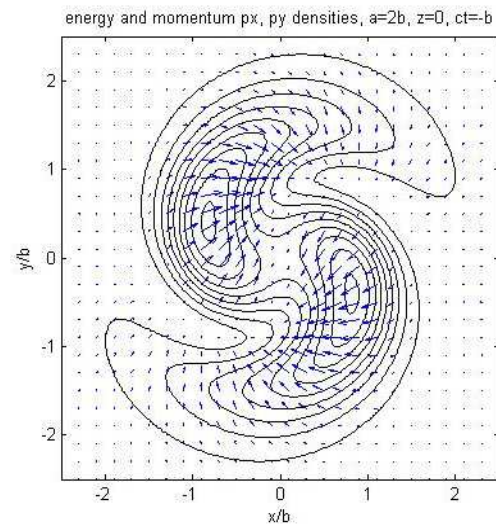


Figure 2: The energy density (contours) and the transverse momentum densities p_x , p_y (arrows) in the $z = 0$ plane, for the same pulse and at the same time as in Figure 1. The pulse is travelling up out of the page.

This example shows that non-zero angular momentum can result from a wavefunction without azimuthal dependence: the curl operator supplies the twist.

More complex exact solutions of the wave equation have been tried, and the energy, momentum and angular momentum evaluated [9, 10]. There we find the surprising result that when the wavefunction ψ has an $e^{im\phi}$ azimuthal dependence, the helicity is opposite to the sign of m . Since J_z is represented by the operator $-i\hbar\partial_\phi$ in quantum mechanics, $J_z e^{im\phi} = \hbar m e^{im\phi}$, so there the $e^{im\phi}$ dependence produces $J_z = \hbar m$, the same sign as m . It is not understood physically why electromagnetic pulses do the opposite.

Figure 1 illustrates a pulse based on ψ equal to $\rho e^{i\phi}/[b + i(z - ct)]$ times the wavefunction in (10), with \mathbf{A} given by (22) and \mathbf{E} and \mathbf{B} by (1) (with Φ zero). The resulting energy, momentum and angular momentum are [10]

$$U = \frac{\pi}{16} \frac{3a + b}{b^2} \psi_0^2, \quad cP_z = \frac{\pi}{16} \frac{3a - b}{b^2} \psi_0^2, \quad cJ_z = -\frac{\pi}{8} \frac{a}{b} \psi_0^2 \quad (27)$$

Note that energy isosurface has positive helicity (right-handed), opposite to that of the angular momentum.

4. DISCUSSION

The established universal properties of localized electromagnetic pulses are the constancy of their energy, momentum and angular momentum in time, and the fact that their energy is always greater than c times their momentum. As a consequence, localized electromagnetic pulses have a zero-momentum frame. A further consequence is that we can define an intrinsic angular momentum for such pulses.

Localized solutions of the classical Maxwell equations thus stand in contradistinction to Einstein's light quantum [11], for which $U = cP$, and which cannot be transformed to a zero momentum frame.

APPENDIX: LORENTZ TRANSFORMATION OF WAVEPACKETS

For point particles of mass M , the energy and momentum are related by $U^2 = M^2 c^4 + P^2 c^2$, and the combination $(c\mathbf{P}, U)$ is a four-vector, meaning that it transforms in the same way as (\mathbf{r}, ct) . It follows that $U^2 - c^2 P^2$ is a Lorentz invariant, in this case $M^2 c^4$.

Electromagnetic wavepackets are extended objects, evolving in space-time, and the transformation between inertial frames is more complicated. However, as we have seen in Equation (18), $u^2 - c^2 p^2$ is a non-negative Lorentz invariant, for any electromagnetic pulse.

Consider the transformation of a scalar wavefunction such as (10). A Lorentz boost along the direction of motion (i.e. along the z -axis) at speed βc leaves the transverse coordinate ρ unchanged, and changes z and t to z' and t' :

$$z = \gamma (z' + \beta ct'), \quad ct = \gamma (ct' + \beta z'), \quad \gamma = (1 - \beta^2)^{-\frac{1}{2}} \quad (A1)$$

The effect is to change the weight of the $z \pm ct$ components of ψ :

$$z + ct = \sqrt{\frac{1 + \beta}{1 - \beta}} (z' + ct'), \quad z - ct = \sqrt{\frac{1 - \beta}{1 + \beta}} (z' - ct') \quad (A2)$$

For the wavefunction in (10), a Lorentz boost with $\beta = (a - b)/(a + b)$ or $(1 + \beta)/(1 - \beta) = a/b$ transforms ψ to [3]

$$\psi(\mathbf{r}', t') = \frac{ab\psi_0}{\rho^2 + \left[\sqrt{ab} - i(z' + ct') \right] \left[\sqrt{ab} + i(z' - ct') \right]} \quad (A3)$$

in which the forward and backward propagations are balanced. Such a choice of β brings the TE + iTM pulse to its zero momentum frame, as we have seen in Equations (22) to (24). Moreover, the energy in the zero momentum frame, $U_0 = \frac{\pi}{4} \psi_0^2 / \sqrt{ab}$, is equal to the square root of $U^2 - c^2 P_z^2$, so in this respect the pulse momentum and energy behave as four-vector components.

However, other pulses constructed from the same wavefunction require a different β to bring them to their zero momentum frame, as in the example specified by (25) and (26) for which $\beta = (a - 3b)/(a + 3b)$. For this β the wavefunction (10) is transformed to

$$\psi(\mathbf{r}', t') = \frac{ab\psi_0}{\rho^2 + \left[\sqrt{ab} - i/\sqrt{3}(z' + ct') \right] \left[\sqrt{ab} + i\sqrt{3}(z' - ct') \right]} \quad (\text{A4})$$

The transformed momentum is zero, and the transformed energy is

$$U_0 = \frac{\pi}{4}\psi_0^2/\sqrt{3ab} \quad (\text{A5})$$

This is not (unless $a = 3b$) equal to the square root of $U^2 - c^2P_z^2$, for which the values in (26) give

$$\sqrt{U^2 - c^2P_z^2} = \frac{\pi}{4}\psi_0^2\sqrt{\frac{3b}{a^3}} \quad (\text{A6})$$

Thus the same solution of the wave equation can lead to pulses for which the energy and momenta may or may not behave like four-vectors. In general, the Lorentz transformation of electromagnetic wavepackets is more complicated than that of point particles, as may be expected.

REFERENCES

1. Bateman, H., "The solution of partial differential equations by means of definite integrals," *Proc. Lond. Math. Soc.*, Vol. 1, 451–458, 1904.
2. Jackson, J. D., *Classical Electrodynamics*, 2nd Edition, Wiley, New York, 1975.
3. Lekner, J., "Electromagnetic pulses which have a zero momentum frame," *J. Opt. A: Pure Appl. Opt.*, Vol. 5, L15–L18, 2003.
4. Lekner, J., "Angular momentum of electromagnetic pulses," *J. Opt. A: Pure Appl. Opt.*, Vol. 6, S128–S133, 2004.
5. Lekner, J., "Energy and momentum of electromagnetic pulses," *J. Opt. A: Pure Appl. Opt.*, Vol. 6, 146–147, 2004.
6. Feng, S., H. G. Winful, and R. W. Hellwarth, "Spatiotemporal evolution of focused single-cycle electromagnetic pulses," *Phys. Rev. E*, Vol. 59, 4630–4649, 1999.
7. Merzbacher, E., *Quantum Mechanics*, 3rd Edition, Wiley, New York, 1998.
8. Landau, L. and E. Lifshitz, *The Classical Theory of Fields*, Addison-Wesley, Reading, 1951.
9. Lekner, J., "Localized electromagnetic pulses with azimuthal dependence," *J. Opt. A: Pure Appl. Opt.*, Vol. 6, 711–716, 2004.
10. Lekner, J., "Helical light pulses," *J. Opt. A: Pure Appl. Opt.*, Vol. 6, L29–L32, 2004.
11. Einstein, A., "On the quantum theory of radiation," *Physik. Zeits.*, Vol. 18, 121–128, 1917; English Translation in *Laser Theory*, Barnes, F. S. Ed., New York, IEEE, 1972.

Universal Properties of Electromagnetic Beams

John Lekner

MacDiarmid Institute and School of Chemistry and Physics
Victoria University, Wellington, New Zealand

Abstract— We survey the existing known universal properties of electromagnetic beams, and discuss the possibility of a new one. The established universal properties are the existence of beam invariants, which follow from conservation laws, and various non-existence theorems arising out of beam localization transversely to the direction of propagation. In both cases the theorems follow directly from Maxwell’s equations. The conservation of energy, momentum and angular momentum lead to seven beam invariants, the simplest of which is the integral across a transverse section of an electromagnetic beam of the time-averaged longitudinal component of the momentum density. This integral is the same for any transverse section: it is an *invariant*. This particular invariant comes from the conservation of energy; the conservation of momentum leads to three invariant integrals over components of the electromagnetic stress tensor, and likewise three more invariants come from the conservation of angular momentum. The non-existence theorems show that the properties of the textbook electromagnetic plane wave cannot be realized for real (transversely finite) beams. They assert the non-existence of: (i) Pure TEM beam modes, (ii) Beams of fixed linear polarization, (iii) Beams which are everywhere circularly polarized in a fixed plane, and (iv) Beams within which the energy velocity is everywhere in the same direction and magnitude c . In addition to these established facts, we give an elementary topological argument for the universality of rings of zeros of the beam wave function in the focal plane, leading to wave vortices.

1. INTRODUCTION

This paper is concerned with *universal* properties of electromagnetic beams, by which we mean properties that all physical beams must have (or cannot have). It is useful however to have a summary of the existing exact solutions of Maxwell’s equations representing electromagnetic beams, which we give in this introduction.

For monochromatic beams, in which the time dependence of the complex fields is contained in the factor $e^{-i\omega t}$, all the components of \mathbf{E} and \mathbf{B} satisfy the Helmholtz equation,

$$(\nabla^2 + K^2)\psi = 0, \quad K = \omega/c \quad (1)$$

This follows from Maxwell’s equations by expressing the magnetic and electric fields in terms of the vector and scalar potentials \mathbf{A} and Φ ,

$$\mathbf{B} = \nabla \times \mathbf{A}, \quad \mathbf{E} = -\nabla\Phi - \partial_{ct}\mathbf{A} \quad (2)$$

and choosing the Lorenz gauge

$$\nabla \cdot \mathbf{A} + \partial_{ct}\Phi = 0 \quad (3)$$

In free space, Φ and all components of \mathbf{A} satisfy (1) (see for example [1, pp.218ff]), and so do their derivatives such as \mathbf{E} and \mathbf{B} .

The textbook solutions of (1) are the plane wave $\exp(i\mathbf{K}\cdot\mathbf{r})$ and the spherical waves $\exp(\pm iKr)/r$. Physical beams are localized transversely to the direction of propagation, in contradistinction to the textbook solutions. Deschamps [2] noted that a complex shift along the propagating direction (the z -axis, in this paper) gives an exact solution of (1) localized transversely:

$$\psi = \frac{e^{ikR}}{R}, \quad R^2 = x^2 + y^2 + (z - ib)^2 = \rho^2 + (z - ib)^2 \quad (4)$$

This solution is singular on the circle $\{\rho = b, z = 0\}$, and so cannot represent a physical beam. One can regularize by subtracting the complex-shifted spherically converging wave $\exp(-iKR)/R$ [3]

$$\psi = \frac{\sin KR}{KR} = j_0(KR) \quad (5)$$

and generalize to [4]

$$\psi_{\ell m} = j_{\ell}(KR) P_{\ell}^m \left(\frac{z - ib}{R} \right) e^{im\phi} \quad (6)$$

but problems remain in the divergence of some invariants (see [5] and Section 3 below), and in the backward-propagating components associated with the terms proportional to $\exp(-iKR)/R$.

The Helmholtz Equation (1) is separable in cylindrical coordinates (ρ, ϕ, z) : it reads

$$\left[\partial_{\rho}^2 + \frac{1}{\rho} \partial_{\rho} + \frac{1}{\rho^2} \partial_{\phi}^2 + \partial_z^2 + K^2 \right] \psi = 0 \quad (7)$$

This is solved by $J_m(k\rho)e^{im\phi}e^{iqz}$ provided $k^2 + q^2 = K^2$, and thus also by the *generalized Bessel beams* [6]

$$\psi_m(\mathbf{r}) = e^{im\phi} \int_0^K dk f(k) J_m(k\rho) e^{iqz}, \quad k^2 + q^2 = K^2 \quad (8)$$

Note that k is restricted to the interval $[0, K]$, so $q = \sqrt{K^2 - k^2}$ is a real mapping onto $[0, K]$. These beams are purely forward propagating, by construction. The weight function $f(k)$ can be complex; it is constrained by the necessary finiteness of integral invariants (Section 3). In the next section we shall see how $f(k)$ is related to Bateman's weight function.

2. BATEMAN INTEGRAL SOLUTION OF THE WAVE EQUATION

Bateman [7] considered integral representations of solutions to the wave equation $(\nabla^2 - \partial_{ct}^2)\psi = 0$. The simplest case is that where the solution is independent of the azimuthal angle ϕ , in which case it takes the form

$$\Psi(\rho, z, t) = \frac{1}{2\pi} \int_0^{2\pi} d\theta F(z + i\rho \cos \theta, ct + \rho \sin \theta) \quad (9)$$

We can adapt this to find the general solution of the Helmholtz Equation (1) which is independent of the azimuthal angle. For time-dependence $e^{-i\omega t} = e^{-iKct}$, the function F must take the form

$$F(z + i\rho \cos \theta, ct + \rho \sin \theta) = g(z + i\rho \cos \theta) e^{-iK(ct + \rho \sin \theta)} \quad (10)$$

and then the spatial part of Ψ in (9) becomes

$$\psi(\rho, z) = \frac{1}{2\pi} \int_0^{2\pi} d\theta g(z + i\rho \cos \theta) e^{-iK\rho \sin \theta} \quad (11)$$

We can verify that this is a solution of the Helmholtz equation as follows. Let $G(\rho, z, \theta) = g(z + i\rho \cos \theta) e^{-iK\rho \sin \theta}$. A short calculation shows that $(\nabla^2 + K^2)G = -\rho^{-2} \partial_{\theta}^2 G$ and so $2\pi(\nabla^2 + K^2)\psi = -\rho^{-2} \partial_{\theta} G|_0^{2\pi} = 0$. Thus the $\psi(\rho, z)$ of (11) is the most general form of the scalar wavefunction corresponding to axially symmetric monochromatic beams.

Note that on the beam axis ($\rho = 0$) we get

$$\psi(0, z) = g(z) \quad (12)$$

Thus the amplitude function g in (11) given by the axial value of the beam wavefunction.

There is a one-to-one correspondence between (11) and the $m = 0$ generalized Bessel beam solution (8). Since $k^2 + q^2 = K^2$ we can write $\psi_0(\mathbf{r})$ as an integral over q instead of over k :

$$\psi_0(\mathbf{r}) = \int_0^K dq h(q) J_0 \left(\rho \sqrt{K^2 - q^2} \right) e^{iqz} \quad h(q) = \frac{q}{\sqrt{K^2 - q^2}} f \left(\sqrt{K^2 - q^2} \right) \quad (13)$$

The zero-order Bessel function containing the square root can be rewritten by using Bessel's integral ([8, Section 2.21]), which transforms (13) into

$$\psi_0(\rho, z) = \frac{1}{2\pi} \int_0^{2\pi} d\theta e^{-iK\rho \sin \theta} \int_0^K dq h(q) e^{iq(z + i\rho \cos \theta)} \quad (14)$$

Comparison of (11) and (14) shows that, for the $m = 0$ generalized Bessel beams, the amplitude function g is given by

$$g(z + i\rho \cos \theta) = \int_0^K dq h(q) e^{iq(z + i\rho \cos \theta)} \quad (15)$$

The axial form of ψ is thus equal to the finite Fourier transform of $h(q)$:

$$\psi(0, z) = g(z) = \int_0^K dq h(q) e^{iqz} \quad (16)$$

3. CONSERVATION LAWS AND BEAM INVARIANTS

The energy, momentum and angular momentum densities of an electromagnetic field in free space are, in Gaussian units, given by [1]

$$u(\mathbf{r}, t) = \frac{1}{8\pi} (E^2 + B^2), \quad \mathbf{p}(\mathbf{r}, t) = \frac{1}{4\pi c} \mathbf{E} \times \mathbf{B}, \quad \mathbf{j}(\mathbf{r}, t) = \mathbf{r} \times \mathbf{p}(\mathbf{r}, t) \quad (17)$$

Here $\mathbf{E}(\mathbf{r}, t)$ and $\mathbf{B}(\mathbf{r}, t)$ are the real fields. For monochromatic fields it is convenient to work in terms of complex fields $\mathbf{E}(\mathbf{r})$ and $\mathbf{B}(\mathbf{r})$ with the real electric field being given by

$$\mathbf{E}(\mathbf{r}, t) = \text{Re}\{\mathbf{E}(\mathbf{r})e^{-i\omega t}\} = \text{Re}\{[\mathbf{E}_r(\mathbf{r}) + i\mathbf{E}_i(\mathbf{r})][\cos \omega t - i \sin \omega t]\} = \mathbf{E}_r(\mathbf{r}) \cos \omega t + \mathbf{E}_i(\mathbf{r}) \sin \omega t \quad (18)$$

The average of $u(\mathbf{r}, t)$ over one period $2\pi/\omega$ is

$$\bar{u}(\mathbf{r}) = \frac{1}{8\pi} \{\mathbf{E}(\mathbf{r}) \cdot \mathbf{E}^*(\mathbf{r}) + \mathbf{B}(\mathbf{r}) \cdot \mathbf{B}^*(\mathbf{r})\} \quad (19)$$

Likewise the cycle-averaged momentum density is

$$\bar{\mathbf{p}}(\mathbf{r}) = \frac{1}{16\pi c} [\mathbf{E}(\mathbf{r}) \times \mathbf{B}^*(\mathbf{r}) + \mathbf{E}^*(\mathbf{r}) \times \mathbf{B}(\mathbf{r})] \quad (20)$$

The conservation of energy equation, $\nabla \cdot \mathbf{S} + \partial_t u = 0$, where $\mathbf{S} = c^2 \mathbf{p}$ is the energy flux density, has the cycle-average

$$\nabla \cdot \bar{\mathbf{p}} = \partial_x \bar{p}_x + \partial_y \bar{p}_y + \partial_z \bar{p}_z = 0 \quad (21)$$

Applying $\int d^2r = \int_{-\infty}^{\infty} dx \int_{-\infty}^{\infty} dy = \int_0^{\infty} d\rho \rho \int_0^{2\pi} d\phi$ to (21) gives, for transversely finite beams propagating in the z direction [9]

$$\partial_z \int d^2r \bar{p}_z = 0, \quad \text{or} \quad P'_z = \int d^2r \bar{p}_z = \text{constant} \quad (22)$$

We use the notation P'_z , since $dP'_z = P'_z dz$ is total z -component momentum contained in a transverse slice of the beam, of thickness dz . Equation (22) states that the momentum content per unit length, along the direction of net propagation of the beam, is an *invariant*. Note that the invariance of the *momentum* content per unit length is derived from the conservation of *energy*.

The conservation of momentum equation is expressed in terms of the stress (or momentum flux density) tensor

$$\partial_t p_i + \sum_j \partial_j \tau_{ij} = 0, \quad \tau_{ij} = \frac{1}{4\pi} \left[\frac{1}{2} (E^2 + B^2) \delta_{ij} - E_i E_j - B_i B_j \right] \quad (23)$$

Taking the cycle average gives $\sum_j \partial_j \bar{\tau}_{ij} = 0$, and operating with $\int d^2r$ gives $\partial_z \int d^2r \bar{\tau}_{iz} = 0$ ($i = x, y, z$). Thus momentum conservation leads to three invariants [9]

$$\begin{aligned} T'_{xz} &= \int d^2r \bar{\tau}_{xz} = -\frac{1}{4\pi} \int d^2r [\overline{E_x E_z} + \overline{B_x B_z}] \\ T'_{yz} &= \int d^2r \bar{\tau}_{yz} = -\frac{1}{4\pi} \int d^2r [\overline{E_y E_z} + \overline{B_y B_z}] \\ T'_{zz} &= \int d^2r \bar{\tau}_{zz} = \frac{1}{8\pi} \int d^2r [\overline{E_x^2 + E_y^2 - E_z^2} + \overline{B_x^2 + B_y^2 - B_z^2}] \end{aligned} \quad (24)$$

Three more invariants follow from the conservation of angular momentum, $\partial_t j_i + \sum_{\ell} \partial_{\ell} \mu_{\ell i} = 0$, where the angular momentum flux density tensor $\mu_{\ell i} = \sum_j \sum_k \varepsilon_{ijk} x_j \tau_{k\ell}$ is defined in terms of the momentum flux density tensor τ_{ij} [10]. These invariants are [9]

$$\begin{aligned} M'_{zx} &= \int d^2r \bar{\mu}_{zx} = \int d^2r [y\bar{\tau}_{zz} - z\bar{\tau}_{yz}] \\ M'_{zy} &= \int d^2r \bar{\mu}_{zy} = \int d^2r [z\bar{\tau}_{xz} - x\bar{\tau}_{zz}] \\ M'_{zz} &= \int d^2r \bar{\mu}_{zz} = \int d^2r [x\bar{\tau}_{yz} - y\bar{\tau}_{xz}] \end{aligned} \quad (25)$$

Thus there are seven universal invariants of electromagnetic beams, arising from the conservation of energy, momentum and angular momentum. Perhaps surprisingly, the energy per unit length of the beam, $U' = \int d^2r \bar{u}$, is not always an invariant, although it is constant for the types of generalized Bessel beams discussed in [6], as is $J'_z = \int d^2r \bar{j}_z$.

4. NON-EXISTENCE THEOREMS

In textbooks a light beam is usually represented by a plane wave, with \mathbf{E} , \mathbf{B} and the propagation vector \mathbf{k} everywhere mutually perpendicular. This ‘beam’ can be everywhere linearly polarized in the same direction, or everywhere circularly polarized in the same plane, and its energy is everywhere transported in a fixed direction at the speed of light. It has been shown in [11] that *none* of these properties can hold for a transversely finite beam. We shall just state the theorems, except for the one relating to linear polarization, for which the proof in [11] is incomplete.

- (i) Pure TEM beams do not exist.
- (ii) Beams of fixed linear polarization do not exist.
- (iii) Beams which are everywhere circularly polarized in the same direction do not exist.
- (iv) Beams or pulses within which the energy velocity [12] is everywhere in the same direction and of magnitude c do not exist.

Proof of (ii): Suppose $\mathbf{E} = (F(x, y, z), 0, 0)$, so the beam is linearly polarized along $\hat{\mathbf{x}}$, everywhere. Then from the Maxwell curl equations, with e^{-iKct} time dependence, we have $iK\mathbf{B} = \nabla \times \mathbf{E} = (0, \partial_z, -\partial_y)F$, and $iK\nabla \times \mathbf{B} = (-[\partial_y^2 + \partial_z^2], \partial_x \partial_y, \partial_x \partial_z)F = K^2\mathbf{E}$. Hence $(\partial_y^2 + \partial_z^2 + K^2)F = 0$ and $\partial_x \partial_y F = 0 = \partial_x \partial_z F$. The last two equations imply $F(x, y, z) = f(x) + g(z) + h(y, z)$, which cannot represent a beam localized transversely in the x direction.

5. FOCAL PLANE ZEROS, AND DISCUSSION

We have seen that electromagnetic beams can be constructed from solutions of the scalar Helmholtz Equation (1). In particular the TM, TE, ‘LP’ and ‘CP’ beams have their vector potentials proportional (respectively) to

$$(0, 0, \psi), \quad (\partial_y \psi, -\partial_x \psi, 0), \quad (\psi, 0, 0) \quad \text{and} \quad (-i\psi, \psi, 0) \quad (26)$$

(The quotation marks indicate that the ‘LP’ and ‘CP’ beams are fully linearly and circularly polarized only in the plane wave limit: compare theorems (ii) and (iii) of the previous section.)

What are the universal properties of physically acceptable solutions ψ ? We have already seen that seven beam invariants must exist. We also saw that certain textbook properties of electromagnetic beams cannot hold for laterally finite beams. Here we argue that an infinity of zeros of ψ must occur in the focal plane.

The solutions $\psi(\mathbf{r})$ of the Helmholtz equation are, in general, complex functions of position, $\psi = \psi_r + i\psi_i$. The real and imaginary parts ψ_r and ψ_i are (in free space) smooth functions of position. These functions are zero on surfaces S_r and S_i , and where these surfaces meet (on curves C in space) both ψ_r and ψ_i are zero. If we write

$$\psi(\mathbf{r}) = M(\mathbf{r})e^{iP(\mathbf{r})} = [\psi_r^2 + \psi_i^2]^{\frac{1}{2}} \exp\left(i \arctan \frac{\psi_i}{\psi_r}\right) \quad (27)$$

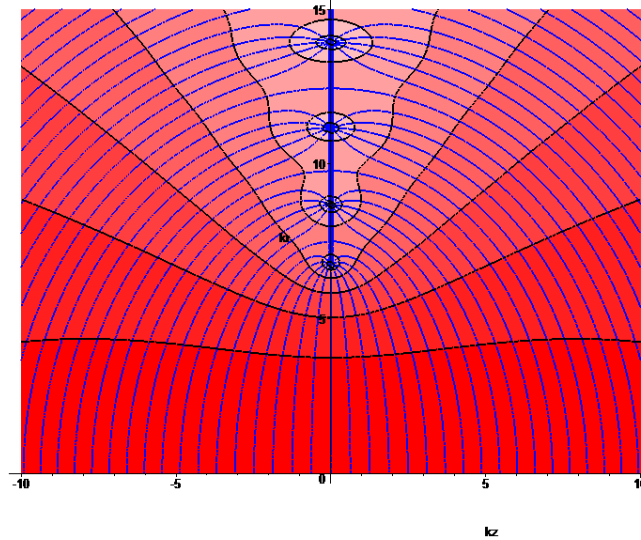


Figure 1: Isophase surfaces (blue) of the $j_0(KR)$ beam, Equation (5), plotted for $Kb = 6$, at intervals of $\pi/6$. (The three-dimensional picture is obtained by rotating about the z -axis.) The surfaces with phase equal to an integer multiple of π converge onto the circles $\rho = [(X/K)^2 + b^2]^{\frac{1}{2}}$, where $\tan X = X$. The other isophase surfaces converge onto the zeros of $j_0(KR)$ in the $z = 0$ plane, namely on the circles $\rho_n = [(n\pi/K)^2 + b^2]^{\frac{1}{2}}$. Surfaces of constant modulus are shown in black.

we see that, on any such curve C , the modulus $M(x)$ is zero, and the phase $P(\mathbf{r})$ is indeterminate. Nye and Berry [13] called these curves wave dislocations; Chapter 5 of Nye's book [14] gives illustrations of such phase singularities.

We give a topological argument for the existence of zeros of ψ in the focal plane, on the assumption that the isophase surfaces intersect the focal plane. At the zeros of ψ the phase can be any real number, but we exclude integer multiples of π , as explained below.

The focal plane is a plane of symmetry for an ideal beam; we can take it to be the $z = 0$ plane, and can also take the phase of ψ to be zero at the origin. Then the isophase surfaces correspond to negative $P(\mathbf{r})$ for $z < 0$ and positive $P(\mathbf{r})$ for $z > 0$. The surfaces $P = -n\pi$ and $P = n\pi$ can meet where ψ is not zero, since the phase difference is an integer (n) multiple of 2π . These isophase surfaces are concave toward the origin, since a physical beam is converging toward the focal region for $z < 0$ and diverging from it for $z > 0$. The other isophase surfaces can only meet on the focal plane if on it there exist curves where ψ is zero. On such curves (circles, in the simplest case) the phase surfaces $P = -\pi/2$ and $P = +\pi/2$ can meet, for example. The surfaces with $0 < |P| < \pi$ meet on the first zero curve, $\pi < |P| < 2\pi$ meet on the next, and so on. Figure 1 illustrates phenomenon, which I conjecture to be universal at the focal plane. Because of the topological nature of the above argument, we expect the zeros to persist even when the beam is perturbed (for example, focused by an imperfect lens or mirror). The focal plane would then be distorted to a nearly-planar surface, and the circles of zeros to approximately circular closed curves, where the perturbed phase surfaces $\pm P$ meet.

One counter-example to the above conjecture (of the universality of rings of zeros in the focal plane) appears to be separable spheroidal beams, for which $\psi(\xi, \eta, \phi) = R(\xi)S(\eta)e^{im\phi}$, with $\rho = b[(\xi^2 + 1)(1 - \eta^2)]^{\frac{1}{2}}$, $z = b\xi\eta$. The focal plane $z = 0$ corresponds to $\xi = 0$ for $\rho \leq b$ and $\eta = 0$ for $\rho \geq b$. Thus if $S(\eta)$ is zero for $\eta = 0$, $\psi = 0$ for $\rho \geq b$ in the focal plane, and the $-P$ and $+P$ isophase surfaces can meet anywhere on the focal plane outside of the central disk $\rho \leq b$. However, such spheroidal wavefunctions have been shown to be non-physical [15].

REFERENCES

1. Jackson, J. D., *Classical Electrodynamics*, 2nd Edition, Wiley, New York, 1975.
2. Deschamps, G. A., "Gaussian beam as a bundle of complex rays," *Electron. Lett.*, Vol. 7, 684–685, 1971.
3. Sheppard, C. J. R. and S. Saghafi, "Beam modes beyond the paraxial approximation: A scalar treatment," *Phys. Rev. A*, Vol. 57, 2971–2979, 1998.

4. Ulanowski, Z. and I. K. Ludlow, “Scalar field of nonparaxial Gaussian beams,” *Opt. Lett.*, Vol. 25, 1792–1794, 2000.
5. Lekner, J., “TM, TE and ‘TEM’ beam modes: Exact solutions and their problems,” *J. Opt. A: Pure Appl. Opt.*, Vol. 3, 407–412, 2001.
6. Lekner, J., “Invariants of three types of generalized Bessel beams,” *J. Opt. A: Pure Appl. Opt.*, Vol. 6, 837–843, 2004.
7. Bateman, H., “The solution of partial differential equations by means of definite integrals,” *Proc. Lond. Math. Soc.*, Vol. 1, 451–458, 1904.
8. Watson, G. N., *A Treatise on the Theory of Bessel Functions*, 2nd Edition, Cambridge University Press, 1966.
9. Lekner, J., “Invariants of electromagnetic beams,” *J. Opt. A: Pure Appl. Opt.*, Vol. 6, 204–209, 2004.
10. Barnett, S. M., “Optical angular momentum flux,” *J. Opt. B: Quantum Semiclass.*, Vol. 4, S7–S16, 2002.
11. Lekner, J., “Polarization of tightly focused laser beams,” *J. Opt. A: Pure Appl. Opt.*, Vol. 5, 6–14, 2003.
12. Lekner, J., “Phase and transport velocities in particle and electromagnetic beams,” *J. Opt. A: Pure Appl. Opt.*, Vol. 4, 491–499, 2002.
13. Nye, J. F. and M. V. Berry, “Dislocations in wave trains,” *Proc. Roy. Soc. Lond. A*, Vol. 336, 165–190, 1974.
14. Nye, J. F., *Natural Focusing and Fine Structure of Light*, Inst. Phys. Publishing, Bristol, 1999.
15. Boyack, R. and J. Lekner, “Non-existence of separable spheroidal beams,” *J. Opt.*, Vol. 13, 085701(3), 2011.

Wide Band Open Ended Air Gap RLSA Antenna at 26 GHz Frequency Band

I. M. Ibrahim¹, T. A. Rahman², M. I. Sabran², U. Kesavan², and T. Purnamirza²

¹Faculty of Electronics and Computer Engineering, Universiti Teknikal Malaysia Melaka, Malaysia

²Wireless Communication Centre, Universiti Teknologi Malaysia, Malaysia

Abstract— RLSA antenna is a popular candidate for many applications such as Direct Broadcast Satellite Reception, Point to Point Microwave Link, RFID and Wimax Application. This is due to its capability of carrying high speed signal with high directivity characteristic and capability of beam steering and beam shaping. This paper will introduce the RLSA antenna designed at the frequency of 26 GHz for wireless backbone application. The antenna design was utilize open ended air gap as a separator between radiation surface and ground plane. The open air gap cavity structure normally implemented in broadband planar antennas. This structure normally provide a wide bandwidth and good return loss on the desired frequency. Therefore, an investigation of this technique and hybrid with FR4 board as a cavity material will be very interesting due to condition of easy to manufacture, lighter the antenna weight and durable. The model of RLSA antenna at 26 GHz has been simulated. The results obtained a -25 dB of reflection coefficient, 23.68 dBi of directivity gain with wide antenna bandwidth capability. This research found an opportunity of utilizing RLSA antenna concept for extreme high frequency band application.

1. INTRODUCTION

RLSA antenna was developed for Direct Broadcast Satellite application, point to point microwave link application, RFID application and Wimax application [1–3]. Many design method and technique was introduced to increase the efficiency of the antenna. For point to point application, the RLSA has been designed and developed at the frequency range of 5725–5875 MHz by few researchers [2, 3]. The polypropylene has been used as a slow wave element in the RLSA structure. This material normally give 2.3 dielectric value [2, 3]. The other potential application for this antenna is point to point microwave link at 26 GHz frequency. Normally, parabolic antenna was used at this frequency due to minimum loss and pencil beam characteristic. The 26-GHz frequency band is allocated to broadband wireless access (BWA) in many parts of the world. The 26-GHz band offers advantages such as relatively high bandwidth resulting in a much higher bit rates available to individual users when compared to frequency of around 10 GHz used typically in tropical regions [4]. It also allows the reuse of spectrum with a higher density of smaller cells resulting in a higher network capacity in urban and rural areas. These networks are particularly suited for network connection to small offices or suburban homes to high-capacity public switching and backbone networks for wireless multimedia services. Wireless information required by customers on the move includes internet, multimedia, and voice.

2. THE STRUCTURE DESIGN

The RLSA at 26 GHz antenna for Point to Point Application was designed based on Linear Polarised Beam Squint technique. The RLSA antenna structure normally consists of a dielectric material sandwiched by copper plate. The front plate bears the radiating element while rear plate acts as a ground plane with feed element at the centre. The dielectric constant $\epsilon_r > 1$ was chosen to suppress the grating lobes. The radiating elements are arrayed so that their radiation are added in phase along the beam direction [5, 6]. The structure of the investigated single-layer RLSA antenna is shown in Figure 1(a). The orientation of slots is in such a direction so as to transmit and receive waves of proper polarization, linear, and proper coupling inside the cavity.

In this research, the FR4 board with air gap distance to the ground plane has been introduced. The thickness of overall cavity is 3.6 mm where the thickness of open air gap is 2 mm. A $50\ \Omega$ single coaxial probe coated with Teflon is used to feed the signal into the cavity as shown in Figure 1(b). The aluminium plate is used as a platform to hold the antenna and also become a ground plane. The FR4 with 1.6 mm thickness with 5.4 permittivity value is used as a first layer substrate to the radiating surface.

The theoretical slot arrangement is similar to what was proposed in [2, 3]. Slot pattern has been arranged on the aperture to provide a linear polarization. A unit radiator is defined as an

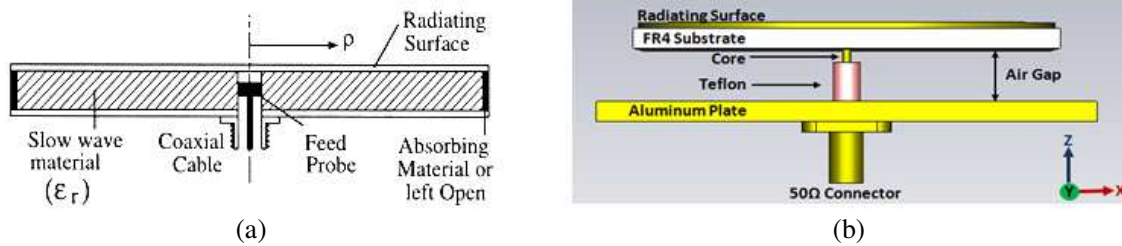


Figure 1: (a) Conventional structure within the cavity of RLSA antenna, (b) open ended air-gap structure of RLSA antenna.

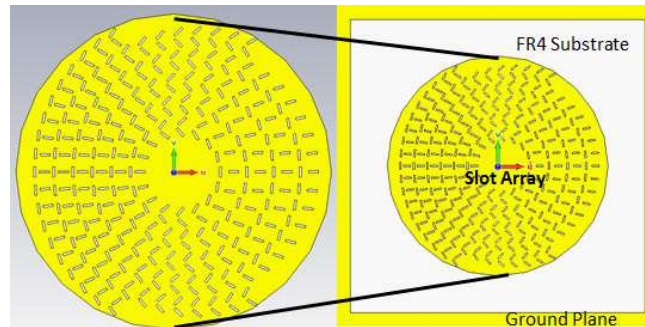


Figure 2: The slots arrangement on the surface of Air Gap RLSA.

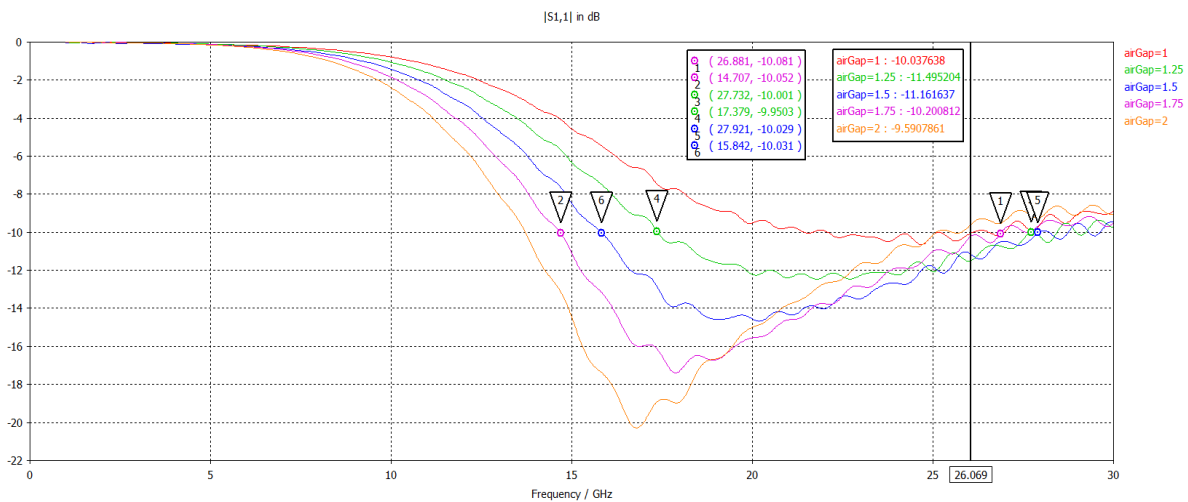


Figure 3: Simulated reflection coefficient of Air Gap RLSA.

adjacent slot pair #1, #2, lying along the constant direction (Φ). The 180 mm diameter of RLSA was chosen. The dielectric value has influenced the number of slots and the slots length on the surface of the antenna. The radial arrangement of slots pair has been constructed in the area of 180 mm diameter as shown in Figure 2.

3. SIMULATION RESULTS

The Air Gap RLSA was simulated using CST Studio software. Figure 3 shows the simulated reflection coefficient of the RLSA. The air gap has been optimized from 1 mm to 2 mm of thickness. An air gap function is tuning the resonant frequency at desired target frequency. From simulated result, the air gap of 1.25 mm response efficiently at 26 GHz. However, for practical reason and easy to fabricate the antenna, the air gap of 1.5 is also acceptable since the different is only 0.3 dB. The reflection coefficient started at 15.84 GHz to 27.92 GHz. When the air gap distances increase, the bandwidth will shift towards the lower frequency. From the simulation, the dominant resonant frequency is between 15–20 GHz. This is maybe because of the slot length is not purely resonate

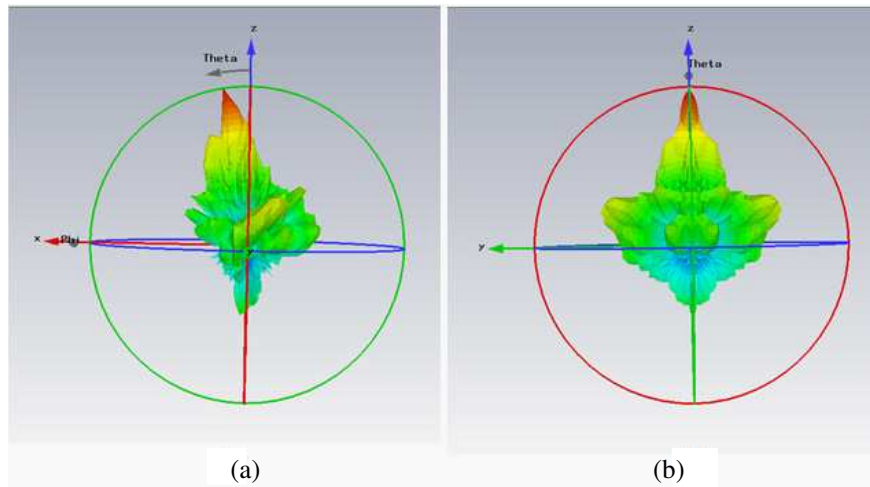


Figure 4: Simulated Radiation pattern for Air Gap RLSA, (a) E -plane, (b) H -plane.

at desired frequency. However, the result on 26 GHz is acceptable.

Figure 4 illustrates the radiated radiation pattern of the Air Gap RLSA at E -plane. The antenna directivity gain recorded at 23.68 dBi with -10.4 dB side lobe level at E -plane and -13.8 dB at H -plane. This antenna also provide 22 dB of front to the back lobe ratio at E -plane and 10 dB at H -plane. The main lobe squinted at 9 degree from 0 degree. The radiation pattern shows high directivity characteristic that suitable for the target application. Low side lobe and back lobe has increase the gain of the front side of the antenna. The beamwidth of the main lobe is 6.2 degree. From the 3D pattern, it is clearly show the concentration of the radiated energy is on the main beam. In overall, the radiation pattern shown directive characteristic and have a potential to be implement at point to point application.

4. CONCLUSIONS

A model of Air Gap RLSA has been simulated using hybrid air gap and FR4 dielectric material. The 50% wide bandwidth has been recorded through this approach. A 23.68 dBi directive gain also recorded from the simulation. The 6.2 degree beamwidth of the radiation pattern is sufficient for high directional application. Since the proposed application was for Point to Point Link, this study proposed the Air Gap RLSA can be a new candidate for this application.

ACKNOWLEDGMENT

The author would like to acknowledge and express sincere appreciation to Universiti Teknologi Malaysia and Ministry of Higher Education Malaysia (MOHE) for funding this project. Appreciation also goes to University Teknikal Malaysia Melaka and MOHE for funding the author's scholarship.

REFERENCES

1. Jamlos, M. F. B., T. A. Rahma, M. R. B. Kamarudin, P. Saad, O. Abdul Aziz, and M. A. Shamudin, "Adaptive beam steering of RLSA antenna with RFID technology," *Progress In Electromagnetics Research*, Vol. 108, 65–80, 2010.
2. Ibrahim, I. M., T. A. Rahman, P. S. Wei, and J. Ahmad, "A study on effectiveness of FR4 as a dielectric material for radial line slot array antenna for wireless backhaul application," *The 17th Asia-Pacific Conference on Communications (APCC 2011)*, Sutera Harbour Resort, Kota Kinabalu, Sabah, Malaysia, Oct. 2–5, 2011.
3. Ibrahim, I. M., A. Riduan, A. R. Tharek, and A. Hasnain, "Beam squinted radial line slot array antenna (RLSA) design for point-to-point WLAN application," *Asia Pacific Applied Electromagnetics Conference (APACE 2007)*, Melaka, Malaysia, Dec. 4–6, 2007.
4. Fong, B., A. C. M. Fong, G. Y. Hong, and H. Ryu, "Measurement of attenuation and phase on 26-GHz wide-band point-to-multipoint signals under the influence of rain," *Antennas and Wireless Propagation Letters*, Vol. 4, 20–21, 2005.

5. Ando, M., K. Sakurai, and N. Goto, “Characteristics of a radial line slot antenna for 12 GHz band satellite TV reception,” *IEEE Transactions on Antennas and Propagation*, Vol. 34, No. 10, 1269–1272, Oct. 1986.
6. Yamamoto, T., M. Takahashi, M. Ando, and N. Goto, “Measured performances of a wide band radial line slot antenna,” *Antennas and Propagation Society International Symposium, 1994, AP-S. Digest*, Vol. 3, 2204–2207, 1994.

Design of Wideband Monopole Antennas Using a Simple Tapered Feed Line and Slot

L. Liu, X. J. Yang, and S. W. Cheung

Department of Electrical and Electronic Engineering
The University of Hong Kong, Hong Kong, China

Abstract— This paper presents two simple techniques, a tapered feed line and small ground slot, to significantly increase the bandwidth of planar monopole antenna with microstrip-fed. An antenna having a half-elliptical-shaped radiator with a total size of $24 \times 30 \times 0.762 \text{ mm}^3$ is used for illustration of the two techniques. Results show that, with the use of the two techniques, an extremely wideband characteristic of 3.1–40 GHz can be achieved.

1. INTRODUCTION

Planar monopole antennas, due to low cost, low complexity and ease of fabrication, have been developed rapidly for uses in Ultra Wideband (UWB) wireless communications [1]. To achieve wideband operation and stable performance for planar UWB antennas, different methods have been proposed. These methods included using resonant structures [2], parasite elements [3], filters [4], slots [5], different shaped radiators [6], modifying the shape of the radiator [7], adding slots on the ground plane [8–11], and modifying the shapes of the ground planes [9, 10]. Some researchers also combined several methods together to optimize the designs [14–17].

In this study, we propose to use two very simple approaches, i.e., a tapered microstrip feed-line and a simple square ground slot underneath the feed line on the ground plane, to increase the bandwidth of a microstrip-feed antenna to 40 GHz. For illustration of the two approaches, we simply use a planar monopole antenna with a half-elliptical-shaped radiator. The effects of the tapered feed line and the ground slot on the bandwidth of the antenna are studied using computer simulation. Results show that, with a compact antenna size $24 \times 30 \times 0.762 \text{ mm}^3$, an extremely bandwidth of 3.1–40 GHz can be easily obtained by optimizing the dimensions of the tapered profile for the feed line and the slot.

2. ANTENNA DESIGN

The geometry of the proposed antenna is shown in Fig. 1. It consisted of a half-elliptical-shaped radiator fed by a microstrip line on one side of the substrate. The feed line had a tapering shape towards the radiator and acted as impedance transformer. The width and length of the microstrip feed line were set at $W_l = 1.7 \text{ mm}$ and $L_l = 5 \text{ mm}$, respectively, to achieve a $50\text{-}\Omega$ impedance for matching the feeding cable. For good matching, the tapered impedance transformer in the upper part of the feed line had an upper width of $W_t = 1.12 \text{ mm}$ and a length of $L_t = 3 \text{ mm}$. The ground plane on the other side of the substrate had a dimension of $W_s \times L_g$. A small square-shaped slot

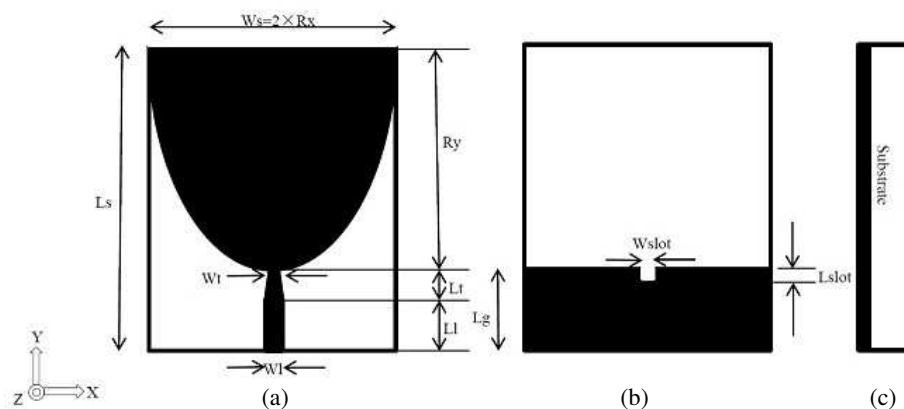


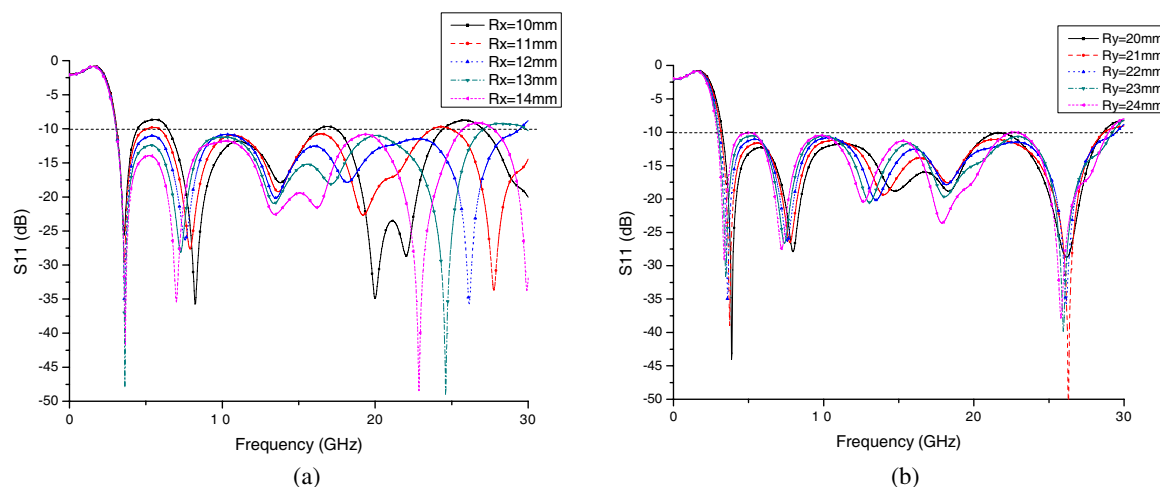
Figure 1: Geometry of proposed antenna: (a) front view, (b) bottom view, and (c) side view.

Table 1: Dimensions of antenna (mm).

W_s	L_s	R_x	R_y	W_1	L_1	W_t	L_t	L_g	W_{slot}	L_{slot}
24	30	12	22	1.7	5	1.12	3	8	1	1



Figure 2: Photograph of prototyped antenna.

Figure 3: Simulated S_{11} with different (a) R_x , and (b) R_y .

was cut at the upper edge of the ground plane right underneath the microstrip feed line to further improve matching at higher frequencies and hence to widen the operating bandwidth. The small ground slot had a size of $W_{\text{slot}} \times L_{\text{slot}}$. The half-elliptical shaped radiator had a minor axis of $2 \times R_x$ in the horizontal direction and a major axis of $2 \times R_y$ in the vertical direction. The width W_s of the substrate was same as the length of the minor axis. The antenna was designed on a Rogers substrate, RO4350B, having an area of $W_s \times L_s$, a thickness of 0.762 mm, a permittivity of 3.48 and a loss tangent of 0.004. The antenna was studied and optimized using computer simulation with the optimized dimensions listed in Table 1. The antenna was also fabricated as shown in Fig. 2 using the optimized dimensions.

3. BANDWIDTH IMPROVEMENT MECHANISM

3.1. Effects of Radiator Dimensions

The dimensions of the radiator are important factors for impedance matching the feed line. Figs. 3(a) and (b) show the simulated S_{11} with different R_x and R_y of the radiator. No ground slot was used to obtain these results. Fig. 3(a) shows that the minor axis R_x mainly affected the operating bandwidth ($S_{11} < -10$ dB) at high frequencies and had little effect at low frequencies. With $R_x = 12$ mm, the bandwidth seemed to be widest in our design. While Fig. 3(b) shows that the major axis R_y obviously affected the bandwidth at lower frequencies. The low-cutoff frequency was inversely proportional to R_y . It also had some effects at high frequencies.

3.2. Effects of Tapered Feed Line

The feed line had a tapering shape toward the radiator. The tapering shape could be considered as a trapezoid or also could be considered as a triangle, as shown in Fig. 4, with the upper part overlapping with the radiator. In such case, only the height d of the triangle needed to be studied as shown in Fig. 4. Fig. 5 shows the simulated S_{11} of the antenna with different d , and other parameters fixed at those shown in Table 1. In the study, no ground slot was used. It can be seen that d mainly affected the bandwidth at high frequencies. It had no effect on the low-cut-off frequency.

3.3. Effects of Ground Slot

Figure 6 shows the simulated S_{11} of the antenna with different values of W_{slot} and L_{slot} , and other parameters maintained as in Table 1. It can be seen in Fig. 6(a) that increasing W_{slot} from 1 mm seriously degraded impedance matching. Fig. 6(b) shows that increasing L_{slot} from 1 mm also made matching worse. Thus W_{slot} and L_{slot} were both set to 1 mm. Without the ground slot, Fig. 5 shows that the antenna had a bandwidth of 3.1–30 GHz. However, with using the small ground slot, the impedance bandwidth could be significantly increased to 3.1–40 GHz as shown in Fig. 6. Clearly, the ground slot could be used for improving impedance matching at high frequencies.

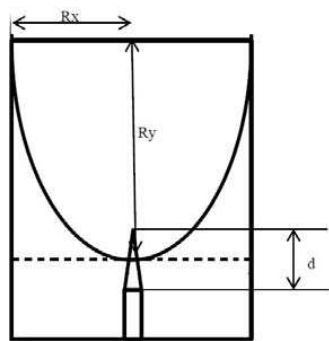


Figure 4: Front view of the antenna using half-elliptical radiator with tapered transformer.

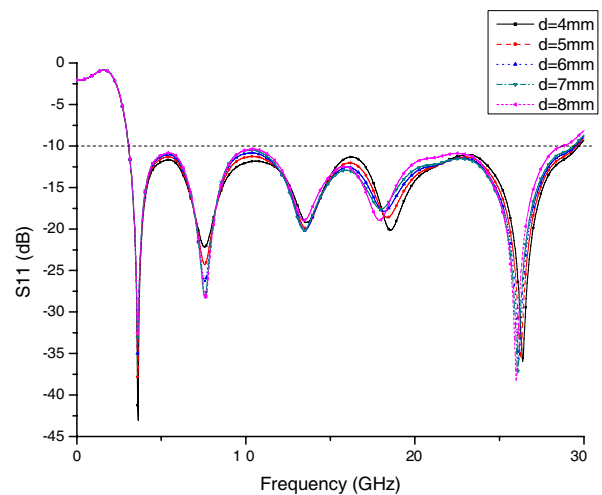


Figure 5: Simulated S_{11} with different d in antenna with tapered transformer.

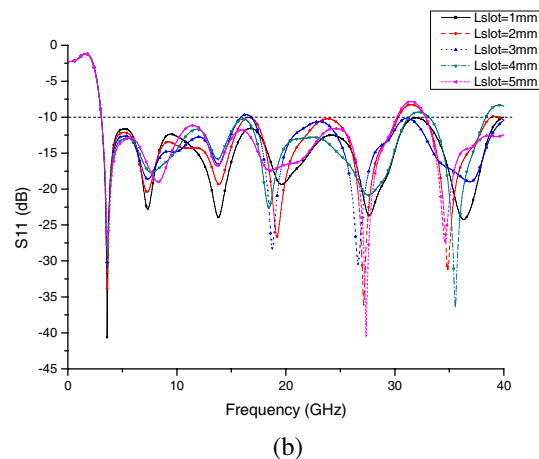
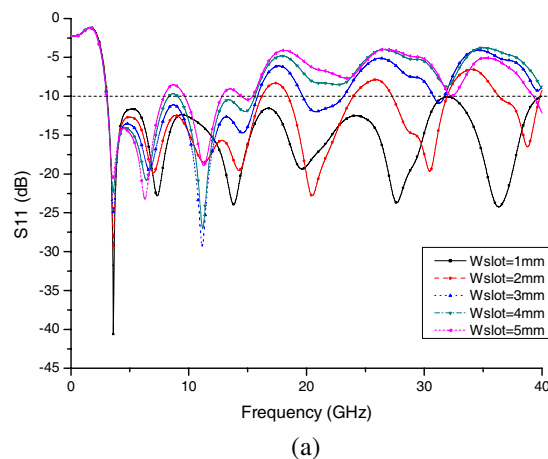


Figure 6: Simulated S_{11} of the antenna with tapered transformer and ground slot with (a) different W_{slot} , and (b) L_{slot} .

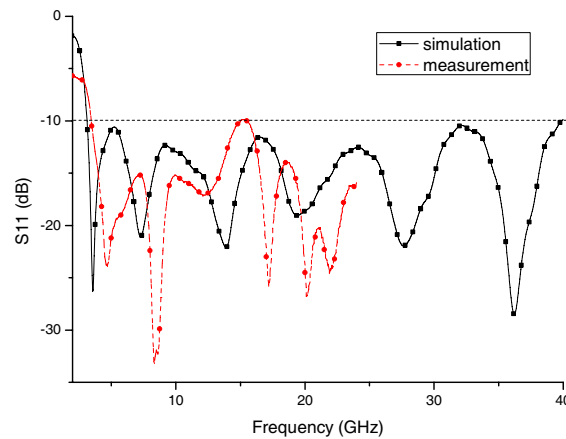


Figure 7: Simulated and measured S_{11} of proposed antenna.

4. RESULTS AND DISCUSSIONS

The S_{11} of the prototyped antenna was measured using the Vector Network Analyzer (VNA) Rohde & Schwarz ZVA 24. The simulated and measured S_{11} of the proposed antenna with tapered feed line and ground slot is shown in Fig. 7. The measured S_{11} is only shown up to 24 GHz due to the frequency range of the VNA. It can be seen that the antenna had an impedance bandwidth ($S_{11} < -10$ dB) of 3.1–40 GHz.

5. CONCLUSIONS

The design of a wideband planar monopole antenna using a simple tapered feed line and ground slot has been presented. A planar monopole antenna having a half-elliptical-shaped radiator with microstrip-fed has been used for illustration and studied using computer simulation. Results have shown that a feed line with a tapering shape can increase the high-cutoff frequency to 30 GHz and a ground slot can further increase it to 40 GHz.

REFERENCES

1. Chen, Z. N., M. J. Ammann, X. Qing, X. H. Wu, T. S. P. See, and A. Cai, "Planar antennas," *IEEE Microwave Magazine*, Vol. 7, 63–73, 2006.
2. Sadeghzadeh-Sheikhan, R. A., M. Naser-Moghadasi, E. Ebadifallah, H. Rousta, M. Katouli, and B. S. Virdee, "Planar monopole antenna employing back-plane ladder-shaped resonant structure for ultra-wideband performance," *IET Microwaves, Antennas & Propagation*, Vol. 4, No. 9, 1327–1335, September 2010.
3. Martins, T. C., R. M. S. de Oliveira, and C. L. S. Sobrinho, "Use of square parasite elements to increase the bandwidth of planar monopole antenna for UWB systems," *2007 SBMO/IEEE MTT-S International Microwave and Optoelectronics Conference*, 427–431, October–November 2007.
4. Barakat, A. and M. El-Khamy, "Bandwidth extension of UWB planar antenna with band-notched characteristics," *2010 IEEE Middle East Conference on Antennas and Propagation (MECAP)*, 1–5, October 2010.
5. Wang, H. and Y. Li, "Bandwidth enhancement of a wide slot UWB antenna with a notch band characteristic," *2011 IEEE 3rd International Conference on Communication Software and Networks (ICCSN)*, 365–368, May 2011.
6. Naktong, W. and A. Ruengwaree, "Increasing bandwidth of flambeau-shape monopole antenna for UWB application," *2011 8th International Conference on Electrical Engineering/Electronics, Computer, Telecommunications and Information Technology (ECTI-CON)*, 172–175, May 2011.
7. Zaker, R. and A. Abdipour, "A very compact ultrawideband printed omnidirectional monopole antenna," *IEEE Antennas and Wireless Propagation Letters*, Vol. 9, 471–473, 2010.
8. Sun, Y. Y., M. T. Islam, S. W. Cheung, T. I. Yuk, R. Azim, and N. Misran, "Offset-fed UWB antenna with multi-slotted ground plane," *2011 International Workshop on Antenna Technology (iWAT)*, 432–436, March 2011.

9. Liu, L., S. W. Cheung, and T. I. Yuk, "Bandwidth improvements using ground slots for compact UWB microstrip-fed antennas," *PIERS Proceedings*, 1420–1423, Suzhou, China, September 12–16, 2011.
10. Azim, R., M. T. Islam, N. Misran, S. W. Cheung, and Y. Yamada, "Planar UWB antenna with multi-slotted ground plane," *Microwave and Optical Technology Letters*, Vol. 53, No. 5, May 2011.
11. Liu, L., S. W. Cheung, R. Azim, and M. T. Islam, "A compact circular-ring antenna for ultra-wideband applications," *Microwave and Optical Technology Letters*, Vol. 53, 2283–2288, October 2011.
12. Chang, D., J. Liu, B. Zeng, and M. Liu, "Impedance bandwidth enhancement for UWB slot antenna," *2007 International Workshop on Antenna Technology: Small and Smart Antennas Metamaterials and Applications*, 184–187, March 2007.
13. Leib, M., M. Frei, and W. Menzel, "A microstrip-fed ultra-wideband slot antenna," *2009 IEEE Antennas and Propagation Society International Symposium*, 1–4, June 2009.
14. Nashaat, D., H. A. Elsadek, E. Abdallah, H. Ellhenawy, and M. F. Iskander, "Enhancement of ultra-wide bandwidth of microstrip monopole antenna by using metamaterial structures," *2009 IEEE Antennas and Propagation Society International Symposium*, 1–4, June 2009.
15. Wu, Q., R. Jin, J. Geng, and M. Ding, "Printed omni-directional UWB monopole antenna with very compact size," *IEEE Transactions on Antennas and Propagation*, Vol. 56, No. 3, 896–899, March 2008.
16. Koohestani, M., M. N. Moghadasi, and B. S. Virdee, "Miniature microstrip-fed ultra-wideband printed monopole antenna with a partial ground plane structure," *IET Microwaves, Antennas and Propagation*, Vol. 5, No. 14, 1683–1689, November 2011.
17. Zhang, J., X. L. Sun, S. W. Cheung, and T. I. Yuk, "CPW-coupled-fed elliptical monopole antenna for UWB applications," *IEEE Radio Wireless Week 2012 (RWW2012)*, Santa Clara, CA, USA, 2012.

A Grounded CPW Transparent UWB Antenna for UHF and Microwave Frequency Application

T. Peter¹, S. W. Cheung², S. K. A. Rahim³, and A. R. Tharek³

¹Department of Electronics and Computer Engineering
Brunel University, Uxbridge, Middlesex, UK

²Department of Electronics and Electrical Engineering
University of Hong Kong, Pokfulam Road, Hong Kong, China

³Wireless Communication Centre, Faculty of Electrical Engineering
University Technology Malaysia, Malaysia

Abstract— A grounded CPW transparent ultra-wideband (UWB) antenna for Ultra High Frequency (UHF) and microwave frequency application is proposed in this paper. The proposed antenna covers a bandwidth starting from as low as 500 MHz to the upper limit of the FCC UWB bandwidth of 10.6 GHz. This enables the antenna to be used for a very wide range of applications ranging from narrow band UHF devices to high data rate UWB transceivers. The antenna is fabricated using AgHT-8 for the CPW and radiator patch on a 1 mm thick glass substrate with an Indium Tin Oxide (ITO) ground. The AgHT-8 has a sheet resistance of $8 \Omega \cdot \text{m}$ while the ITO, a sheet resistance of $4 \Omega \cdot \text{m}$. The overall size of the antenna is $64 \times 67 \text{ mm}^2$. The antenna has a consistent flat 10 dB return loss across the entire bandwidth. The antenna is suitable for integrating onto window glass of homes and buildings as it does not affect the aesthetics of the building. The AgHT-8 layer of the antenna additionally provides sun-shielding from harmful sun-rays and keeps the building cool thus conserving energy required for air-conditioning in hot climates. As such the antenna provides an integrated wireless communication and energy conservation solution for modern day homes and buildings.

1. INTRODUCTION

Since the approval by the FCC in 2002, much research has been undertaken on UWB especially for wireless communications. Although the FCC regulated frequency range is from 3.1 GHz to 10.6 GHz, research into extreme wide bands to cover the lower frequencies in the Megahertz range to the microwave frequencies in the Gigahertz range was also continuously being carried out in the background [1]. An extreme wideband enables the size of the antenna to be kept small for the lower frequencies and big enough for the higher frequencies. However, the gain is compromised especially at the lower frequencies. Nevertheless, such antennas could be used for short and medium range communications. Designing such antennas with transparent materials enables them to be used on window glass of homes and buildings [2, 3]. In this regard, a transparent grounded CPW microstrip patch antenna is designed to cover from 500 MHz to 18 GHz. The antenna thus covers GSM's 900 MHz and 1800 MHz; UMTS' 1900 MHz and 2100 MHz; and the 2.4 GHz and 5 GHz WLAN frequency bands besides FCC's 3.1 GHz to 10.6 GHz regulated range. The antenna comprises of a microstrip patch and an extended CPW ground designed using AgHT-8 on a 1 mm glass substrate that is layered with an ITO ground on the other side of the glass.

2. ANTENNA DESIGN

The geometry of the proposed antenna along with its parameters is as shown in Figure 1(a) and Table 1. It is a grounded coplanar waveguide (CPW) fed microstrip patch antenna inscribed on a thin transparent conductive oxide (TCO) polymer film, AgHT-8. The overall size of the antenna is $64 \times 67 \text{ mm}^2$. The microstrip rectangular patch is designed as an inset in the enclosed and extended ground of the CPW. The rectangular patch of size, $27 \times 21 \text{ mm}^2$ is fed by a feed line of width 3.5 mm. The feed gap between the feed line and extended CPW ground is 0.25 mm. The prototype of the antenna is shown in Figure 1(b). The SMA connector is connected to the antenna using conductive epoxy. The DC resistance of the conductive portion of the AgHT-8 is around 25 Ohms and has a conductivity of 125,000 S/m. The surface resistivity of the AgHT-8 as noted from its trademark name is $8 \Omega \cdot \text{m}$. The AgHT film has a thickness of 0.175 mm making it suitable for use on glass of windows and buildings.

3. EXPERIMENTAL RESULTS

The measured return loss of the antenna prototype is as given in Figure 2. The measured -10 dB bandwidth ranged from 800 MHz to above 18 GHz. The measured gain is shown in Figure 3. The gain is noticed to increase gradually above 10 GHz which may provide potentials for its use in other higher frequency applications. The gain could be effectively improved if the antenna is designed using AgHT-4 which has a higher conductivity and lesser surface resistance of $4 \Omega \cdot m$.

The measured radiation patterns are given in Figure 4. The proposed transparent antenna has a quasi omni-directional radiation pattern at 1.8 GHz and above.

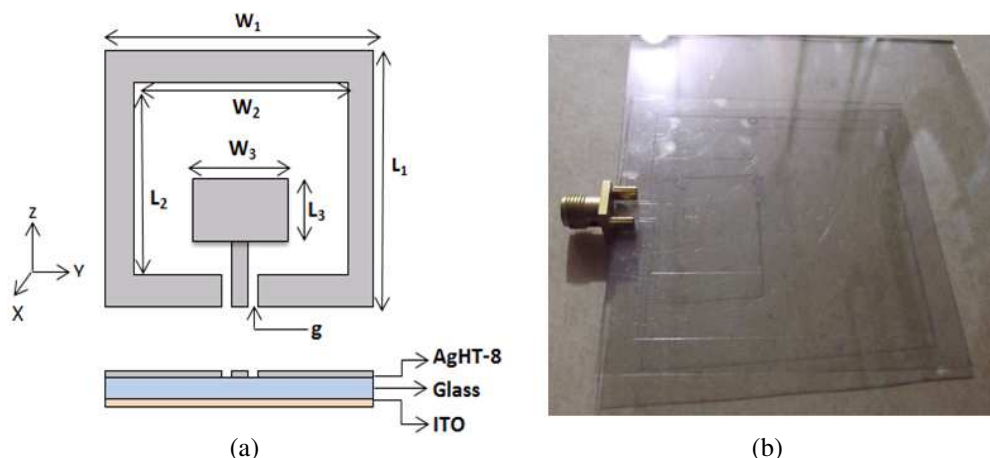


Figure 1: (a) Geometry of the proposed transparent UWB antenna. (b) Prototype of the proposed antenna.

Table 1: Dimensions of the antenna geometry in Figure 1.

Parameters	L_1	W_1	L_2	W_2	L_3	W_3	g
Size (mm)	67	64	54	52	21	27	0.25

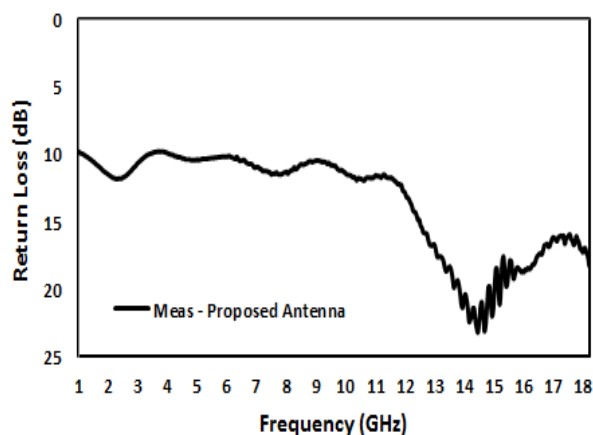


Figure 2: Return loss of the proposed.

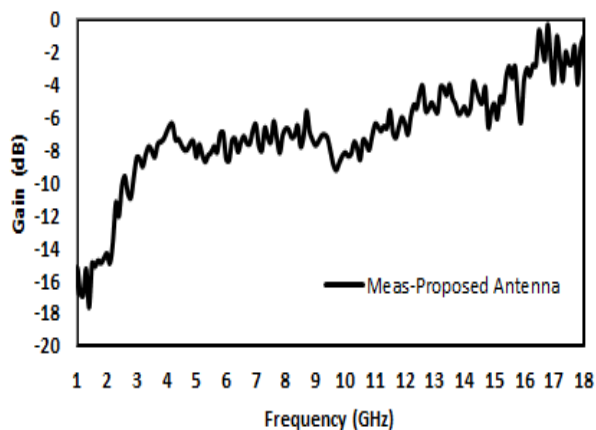
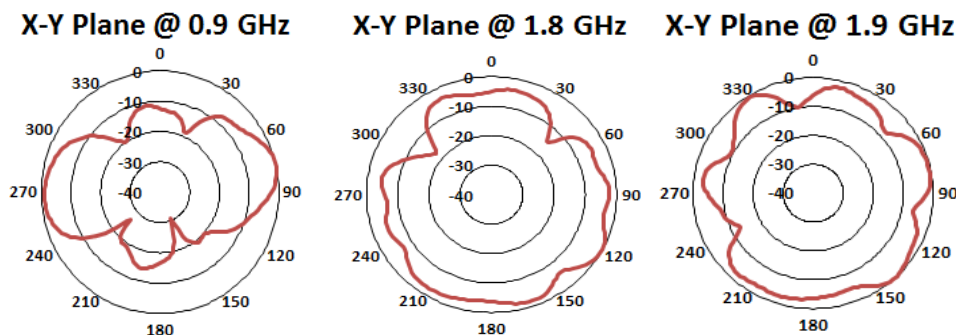


Figure 3: Gain of the proposed antenna.



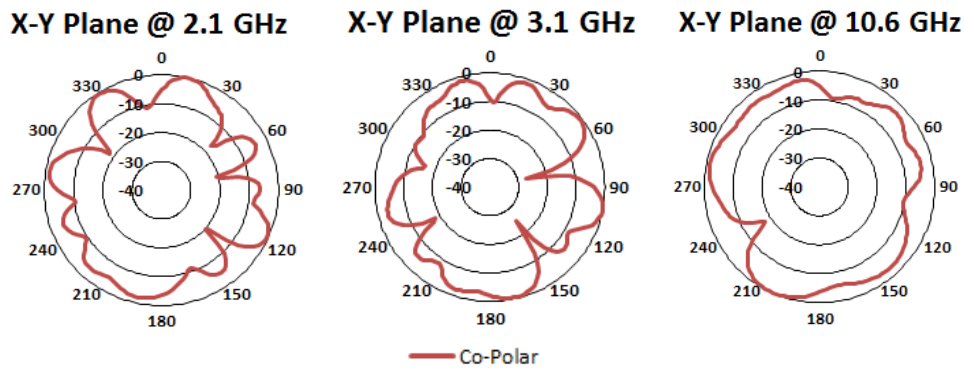


Figure 4: Measured radiation patterns of the antenna at 0.9 GHz, 1.8 GHz, 1.9 GHz, 2.1 GHz, 3.1 GHz and 10.6 GHz.

4. CONCLUSIONS

A small and transparent grounded CPW UWB antenna capable of receiving and transmitting signals at UHF and microwave frequency applications has been proposed and presented. The antenna can be incorporated onto window glass and glass panels of buildings to support GSM, UMTS, WLAN and UWB applications. Being transparent it maintains the aesthetics of the building while the AgHT-8 film material it is made from provides shielding from harmful sun-rays and keeps the building cool.

ACKNOWLEDGMENT

The authors wish to acknowledge CPFilms, UK for their support in providing the AgHT-8 film used in this research.

REFERENCES

1. Wang, N.-B., Y. Song, Y.-C. Jiao, L. Zhang, and F.-S. Zhang, "Extreme wideband tapered slot antenna with impedance bandwidth in excess of 21.6 : 1," *Journal of Electromagnetic Waves and Applications*, Vol. 23, Nos. 2–3, 231–238, 2009.
2. Peter, T., Y. Y. Sun, T. I. Yuk, H. F. AbuTarboush, R. Nilavalan, and S. W. Cheung, "Miniature transparent UWB antenna with tunable notch for green wireless applications," *2011 International Workshop on Antenna Technology (iWAT)*, 25962, March 7–9, 2011.
3. Peter, T., "Optically transparent UWB antenna for wireless application & energy harvesting," Ph.D. dissertation, Dept. Electronics and Computer Eng., Brunel Univ., Uxbridge, Middlesex, UK, 2012.

A Printed Dipole Antenna with U-line Matched for Dual-band WiFi Applications

Chung-Jou Tsai and Bo-Yuan Tsai

Graduate School of Computer and Communication, Kun Shan University, Tainan, Taiwan, R.O.C.

Abstract— A dual-band WiFi printed dipole antenna is presented in this paper, the PCB size is $7\text{ mm} \times 45.9\text{ mm} \times 1\text{ mm}$. This long and narrow PCB antenna will be applied to the wireless AP and has the omni-directional radiation pattern. This double-sided antenna uses parasitic capacitance and U-shaped microstrip line to match and control the bandwidth to reduce the sensitivity of gap size between the ground and radiator of a dipole antenna. This antenna only has the low frequency bandwidth $2.36 \sim 2.75\text{ GHz}$ (390 MHz, 15.5%) and the high frequency bandwidth $4.90 \sim 5.83\text{ GHz}$ (930 MHz, 17.0%), these bands meet the applications of WiFi communication. The simulation results of the return loss, pattern, pattern and current distribution will be presented in this paper by using the software of Ansoft HFSS.

1. INTRODUCTION

With the vigorous development of the wireless communications industry, the quality of wireless communications services needs to increase performance. Wireless communication systems keep increasing emphasis on performance, how to make the characteristics of the antenna can be more perfect, so that the overall performance can improve. Because the dipole antenna is simple, stable, easily-manufactured and omni-radiation, already widely used in the wireless communications industry, especially the printed PCB dipole antenna is commonly used in wireless communication systems. The WiFi AP commonly used the dipole antenna as the main antenna, the frequency band of 802.11b/g/n/a/p/h applications are $2.4 \sim 2.483\text{ GHz}$, $5.15 \sim 5.35\text{ GHz}$ and $5.725 \sim 5.875\text{ GHz}$, if only for the WiFi application, the other bands should not exist to reduce interference from other communication systems.

In [1] inserts the U-shaped slot in the symmetrical dipole arms to generate 2.4/5.2 GHz WLAN frequency bands, whose size is $5\text{ mm} \times 50\text{ mm} \times 0.4\text{ mm}$. The frequency bands of this antenna are 2290–2790 MHz (500 MHz) and 5140–5510 MHz (370 MHz). In [2] presents a dipole antenna through the symmetrical arm of different lengths to produce the WLAN frequency band, the resonant points are 2.45 GHz, 4.25 GHz and 5.5 GHz, the antenna size is $5.6\text{ mm} \times 53\text{ mm} \times 0.8\text{ mm}$. In [3] describes how to change the length and width of arms of dipole antenna to adjust the location and bandwidth of the frequency band. In [4] describes how to adjust the frequency band by changing the spacing of both ends of the dipole antenna pairs to generate 2.4 GHz and 5 GHz dual-band. The U-shaped slot can be used to do a better impedance matching to achieve the effective bandwidth by the fine-tuning function were discussed in [5, 6].

In this paper, we propose one type of the WiFi dipole antenna suitable for the AP, and the sensitivity of the pitch size of the dipole antenna to the frequency band can be reduced by the impedance matching of the U-shaped microstrip line and the parasitic capacitance. The oscillation point are only at 2.4/5.5 GHz, reducing the possible interference of other communications systems, but also the frequency band, radiation pattern and gain of antenna are more stable. The remainder of this paper will propose the simulation results of the relationship of antenna parameters to the bandwidth, and will show the simulation results of current distribution, radiation pattern and gain value to highlight the characteristics of this antenna.

2. ANTENNA STRUCTURE

This paper presents the antenna structure as shown in Figure 1. The feeding point of this double-sided dipole antenna is at the middle of the upper side. The ground arm $L1$ and the radiator arm $L2$ are the main body of the antenna placed on upper side of the substrate of thickness H . $G1$ represents the intermediate position and the gap between the $L1$ and $L2$. The metal parasitic capacitance $L3$ and the U-shaped microstrip line $L4$ on the back side are used to adjust the performance of the impedance matching to be easier to adjust the band characteristic of the antenna, thereby reducing the affect of the $G1$ size on the band. This antenna is printed on FR4 substrate with the relative dielectric constant 4.4 of thickness $H = 1\text{ mm}$, and the antenna area is $7\text{ mm} \times 45.9\text{ mm}$. This narrow type of antenna design is used to the WiFi AP application, the

frequency bands are 2.36 ~ 2.75 GHz (390 MHz, 15.5%) and 4.90 ~ 5.83 GHz (930 MHz, 17.0%), the gain value is maintained 1.55 ~ 1.95 dBi at the low frequency band, and is 3.05 ~ 3.41 dBi at the high frequency band. The radiation pattern is omni-directional. After the simulation of various parameters, the final size of parameters are $L1 = 31$ mm, $L2 = 13$ mm, $L3 = 19$ mm, $L4 = 9$ mm, $G1 = 1.9$ mm, $W1 = 6.5$ mm, $W2 = 7$ mm, $W3 = 1$ mm, $L = 45.9$ mm, $H = 1$ mm. The simulation results will be presented in the following to show the influence to the bandwidth, pattern and gain of the antenna of the various parameters, and to indicate that the antenna can indeed achieve dual band 2.4/5.4 GHz WiFi communication requirements.

3. PARAMETERS ANALYSIS AND SIMULATION RESULTS

In the architecture of Figure 1, the total parameters are $L1, L2, G1, L3, L4, G2, W2, W3$, etc.. In general, $G1$ is a parameter having the great influence of the band of antenna. The simulation of relationship of $G1$ and the impedance matching effect does firstly. The curves of the return loss of $G1 = 1.5$ mm, 1.7 mm, 1.9 mm, 2.1 mm, 2.3 mm are shown in Figure 3. The change of $G1$ does not affect the bandwidth of the low frequency band which maintained at 370 MHz (15.1%), and has a larger effect to the high frequency band. When the length of $G1$ become larger, the corresponding high frequency band increases from 820 MHz to 950 MHz. For achieving the requirements of the WiFi bandwidth to select $G1 = 1.9$ mm, the low frequency band of 2.36 ~ 2.75 GHz and a bandwidth of 390 MHz (15.5%), the high-frequency band of 4.90 ~ 5.83 GHz and a bandwidth of 930 MHz (17.0%). From this result, the influence of $G1$ of the band in this architecture is smaller than it of the single-sided dipole antenna. The curves of the return loss of $L1 = 25$ mm, 27 mm, 29 mm, 31 mm, 33 mm are shown in Figure 4. The change of $L1$ affects the bandwidth of the low and high frequency bands simultaneously. When the length of $L1$ become smaller from 33 mm to 25 mm, the corresponding low frequency band increases from 350 MHz to 500 MHz, the corresponding high frequency band increases from 860 MHz to 1140 MHz. For achieving the requirements of the WiFi bandwidth to select $L1 = 31$ mm, the low frequency band of 2.36 ~ 2.75 GHz and a bandwidth of 390 MHz (15.5%), the high-frequency band of 4.90 ~ 5.83 GHz and a bandwidth of 930 MHz (17.0%).

The curves of the return loss of $L2 = 15$ mm, 14 mm, 13 mm, 12 mm, 11 mm are shown in Figure 5. When the length of $L2$ become smaller from 15 mm to 11 mm, the corresponding low

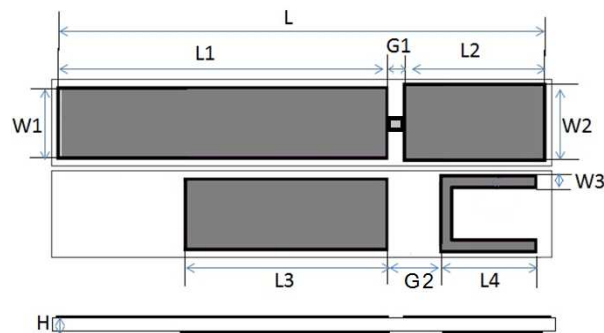


Figure 1: Architecture of the proposed antenna.

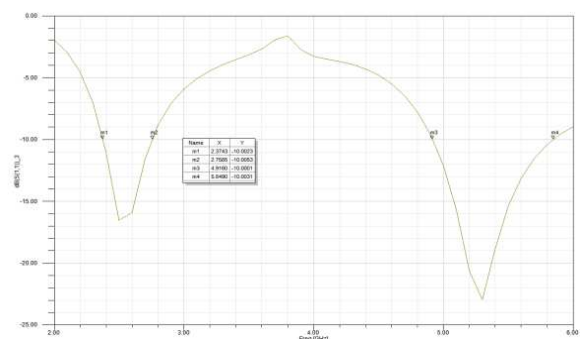


Figure 2: Return loss characteristics of the proposed antenna.

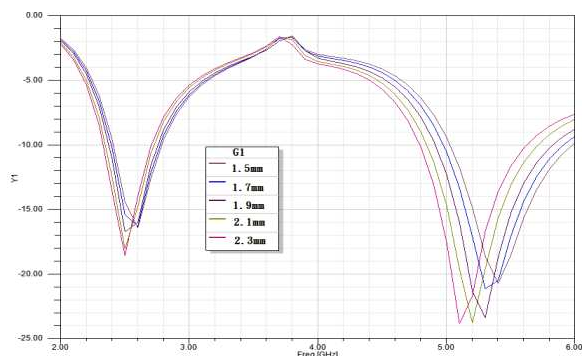


Figure 3: Return losses vs. different values of $G1$.

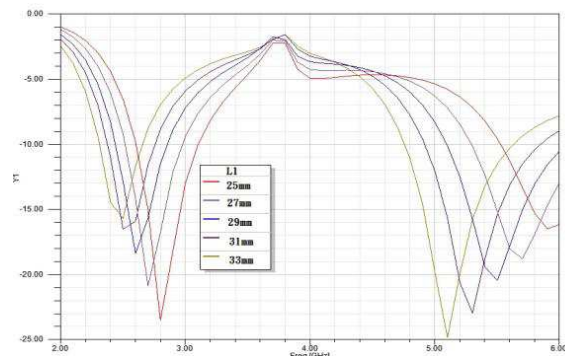
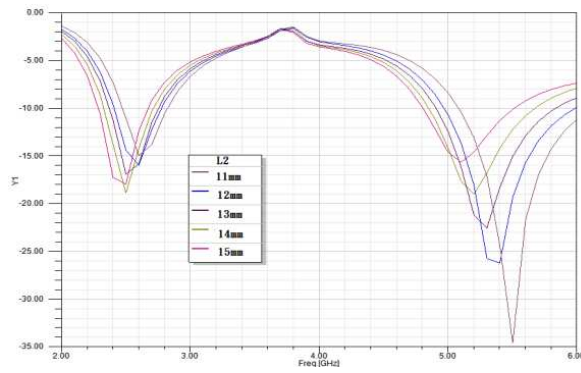
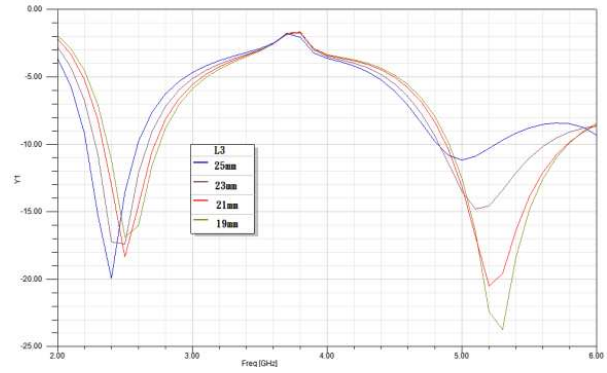
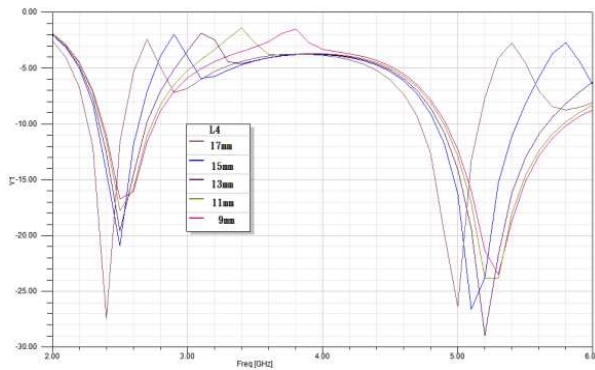
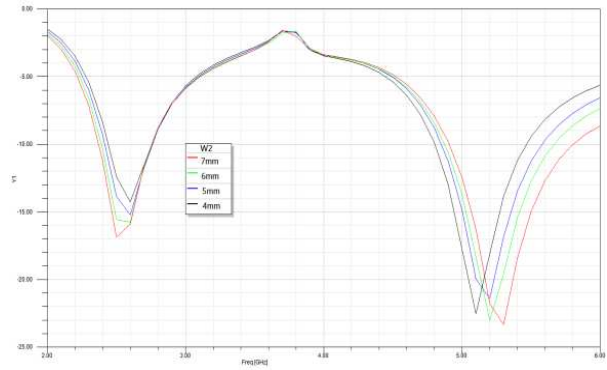


Figure 4: Return losses vs. different values of $L1$.

Figure 5: Return losses vs. different values of $L2$.Figure 6: Return losses vs. different values of $L3$.Figure 7: Return losses vs. different values of $L4$.Figure 8: Return losses vs. different values of $W2$.

frequency band becomes larger and then smaller, the bandwidth increase from 339 MHz (13.8%) to 390 MHz (15.9%) and back to 350 MHz (14.2%), the corresponding high frequency band increases from 700 MHz (12.9%) to 1060 MHz (19.6%). For achieving the requirements of WiFi bandwidth select $L2 = 13$ mm, the low frequency band of 2.36 ~ 2.75 GHz and a bandwidth of 390 MHz (15.5%), the high-frequency band of 4.90 ~ 5.83 GHz and a bandwidth of 930 MHz (17.0%). The curves of the return loss of $L3 = 25$ mm, 23 mm, 21 mm, 19 mm are shown in Figure 6. The change of $L3$ does not affect the bandwidth of the low frequency band which maintained at 370 MHz (15.1%), and has a larger effect to the high frequency band. When the length of $L3$ become shorter from 25 mm to 19 mm, the corresponding high frequency band increases from 400 MHz (7.4%) to 930 MHz (17.0%). For achieving the requirements of the WiFi bandwidth to select $L3 = 19$ mm, the low frequency band of 2.36 ~ 2.75 GHz and a bandwidth of 390 MHz (15.5%), the high-frequency band of 4.90 ~ 5.83 GHz and a bandwidth of 930 MHz (17.0%).

The curves of the return loss of $L4 = 17$ mm, 15 mm, 13 mm, 11 mm, 9 mm are shown in Figure 7. When the length of $L4$ become shorter, the corresponding low frequency band increases from 250 MHz (10.2%) to 370 MHz (15.1%), and the corresponding high-frequency bandwidth increase from 430 MHz (7.9%) to 930 MHz (17.0%). For achieving the requirement of the WiFi bandwidth to select $L4 = 9$ mm, the low frequency band of 2.36 ~ 2.75 GHz and a bandwidth of 390 MHz (15.5%), the high-frequency band of 4.90 ~ 5.83 GHz and a bandwidth of 930 MHz (17.0%). The curves of the return loss of $W2 = 7$ mm, 6 mm, 5 mm, 4 mm are shown in Figure 8. When the length of $W2$ becomes shorter, the corresponding bandwidths of the low frequency band and the high frequency band decrease. The corresponding low frequency band decreases from 380 MHz (15.5%) to 302 MHz (12.3%), and the corresponding high-frequency bandwidth decreases from 930 MHz (17.0%) to 650 MHz (12.0%). For achieving the requirement of the WiFi bandwidth to select $W2 = 7$ mm, the low frequency band of 2.36 ~ 2.75 GHz and a bandwidth of 390 MHz (15.5%), the high-frequency band of 4.90 ~ 5.83 GHz and a bandwidth of 930 MHz (17.0%).

Following the simulation results of the above parameters, the final size of parameter are $L1 = 31$ mm, $L2 = 13$ mm, $L3 = 19$ mm, $L4 = 9$ mm, $G1 = 1.9$ mm, $G2 = 4$ mm, $W1 = 6.5$ mm, $W2 = 7$ mm, $W3 = 1$ mm and $L = 45.9$ mm, $H = 1$ mm. The changing of the size $G2$ and $W3$ only

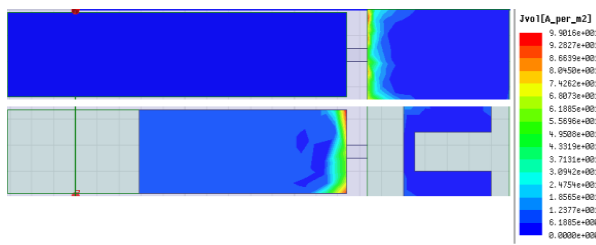


Figure 9: Current distribution of 2.45 GHz.

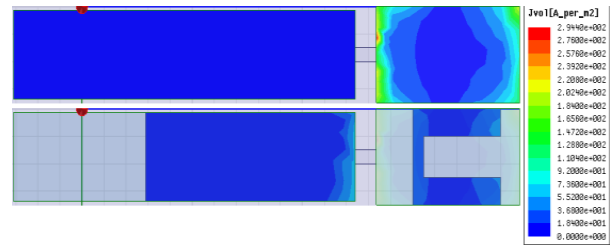


Figure 10: Current distribution of 5.4 GHz.

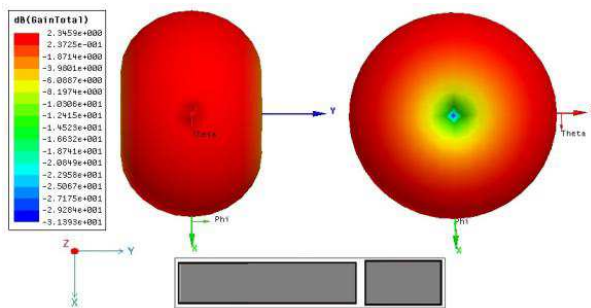


Figure 11: 3D radiation patterns of 2.45 GHz.

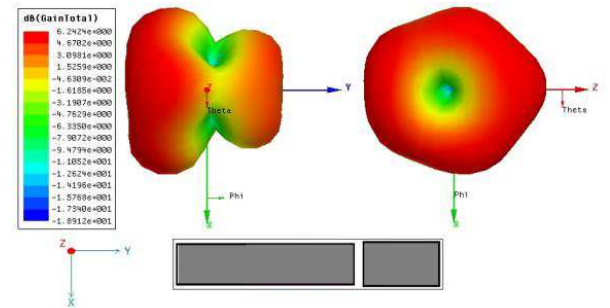


Figure 12: 3D radiation patterns of 5.4 GHz.

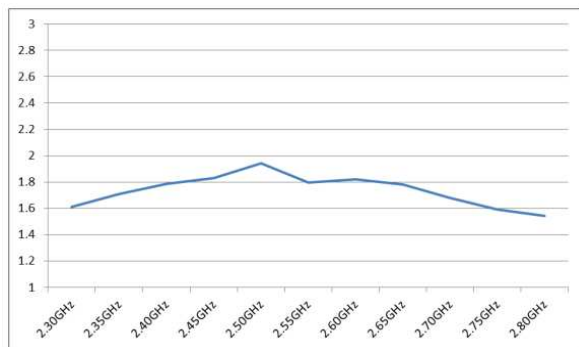


Figure 13: Gain values of 2.3 ~ 2.8 GHz.

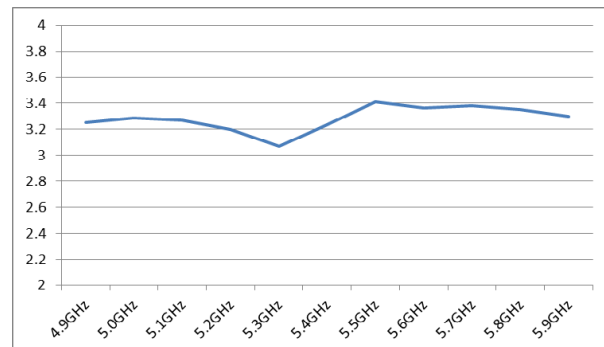


Figure 14: Gain values of 4.9 ~ 5.9 GHz.

has a small impact on the band, so there is no discussion about them. The return loss of the antenna meets WiFi requirement shown in Figure 2. The whole frequency band for the low frequency band is 2.36 ~ 2.75 GHz, a bandwidth of 390 MHz (15.5%), the high-frequency band of 4.90 ~ 5.83 GHz, a bandwidth of 930 MHz (17.0%). Figure 11 presents 2.45 GHz 3D patterns. Figure 12 presents 5.4 GHz 3D pattern. These patterns show that the antenna has a good omnidirectional and has a good corresponding relationship to the current distributions of Figure 9 and Figure 10. The current in the middle position of Figure 9 is a maximum, the wavelength of 2.45 GHz can generate a good oscillation condition, so there is good omni-directional and stable gain, the current of Figure 10 is gathered in the above, the wavelength of 5.4 GHz can generate a good oscillation condition, so there will be a good field and stable gain. The gain value of low-frequency is also stable at the 1.55 ~ 1.95 dBi, and the gain value of high-frequency stabilized at 3.05 ~ 3.41 dBi, and the gain value having a stable characteristic.

4. CONCLUSION

In this paper, an antenna structure is presented to meets the requirements of WiFi dual-band communications. This antenna has the omni-directional radiation pattern, and has a stable gain value changing within 0.4 dBi. Owing to the design of the parasitic capacitance and the U-shaped microstrip line, the sensitivity of the size changing of $G1$, $G2$ to the frequency band is reduced. This effect reducing the frequency shift due to poor welding result makes the mass production having better reliability, which is the characteristic of this antenna architecture.

REFERENCES

- 1 Su, C.-M., H.-T. Chen, and K. L. Wong, “Printed dual-band dipole antenna with U-slotted arms for 2.4/5.2 GHz WLAN operation,” *Electronics Letters*, Vol. 38, No. 22, Oct. 24, 2002.
- 2 Chen, T.-L., “Multi-band printed sleeve dipole antenna,” *Electronics Letters*, Vol. 39, No. 1, Jan. 9, 2003.
- 3 Zhang, Z., M. F. Iskander, J.-C. Langer, and J. Mathews, “Dual-band WLAN dipole antenna using an internal matching circuit,” *IEEE Transactions on Antenna and Prop.*, Vol. 53, No. 5, May 2005.
- 4 Webster, J., ed., *Wiley Encyclopedia of Electrical and Electronics Engineering*, John Wiley & Sons, Inc, 1999.
- 5 Singh, V. K. and Z. Ali, “Dual band U-shaped microstrip antenna for wireless communication,” *International Journal of Engineering Science and Technology*, Vol. 2, No. 6, 1623–1628, 2010.
- 6 Chu, C. Y., “Printed dipole antenna design for wireless communications,” Department of Electrical & Computer Engineering, McGill University, Montreal, Canada, Jul. 2005.

Compact Dual-band Monopole Antenna for 2.4/3.5 GHz WiMAX Applications

X. L. Sun, S. W. Cheung, and T. I. Yuk
 Department of Electrical and Electronic Engineering
 The University of Hong Kong, Hong Kong, China

Abstract— The paper presents the design of a dual-band monopole antenna with microstrip-fed for use in wireless devices in the worldwide interoperability for microwave access (WiMAX) system. The antenna radiator, with a compact size of only $14.5 \times 8.7 \text{ mm}^2$, consists of a short stem and two branches resonating at around 2.4 GHz and 3.5 GHz for the WiMAX bands. The antenna performance in terms of reflection coefficient, radiation pattern, peak gain and efficiency is studied using computer simulation through the EM simulator CST.

1. INTRODUCTION

The rapid development in wireless technology has increased the demand for compact-size antennas to be able to operate in dual-band or multi-band, e.g., for the different frequency bands in the WiMAX system, 3G system, GSM systems, etc.. As users tend to like using thinner wireless devices more, planar monopole antenna, due to its low profile and easy fabrication, is becoming more popular. Many techniques using planar technology have been proposed in literature for the designs of dual-band or multi-band antennas [1–9]. In [1–5], dual-band or multi-band monopole antennas were designed using multi-branches. In [6], the dual-band monopole antenna was achieved by modifying the radiator to create multiple current paths. In [7, 8], parasitic elements were used in the monopole antennas to generate multiple resonances.

In this paper, a dual-band monopole antenna is proposed for wireless applications in the WiMAX system. The radiator of the antenna consists of a short stem with two branches acting as monopoles to generate two frequency bands at around 2.4 and 3.5 GHz. One branch of the radiator is folded and the other one is meandered to achieve a compact size of only $14.5 \times 8.7 \text{ mm}^2$. Computer simulation using CST is used to study the performance of the antenna.

2. ANTENNA DESIGN

The geometry of the proposed dual-band monopole antenna with microstrip-fed is shown in Fig. 1. The antenna is designed on a Rogers substrate, RO4350, with a size of $W \times L \times h = 40 \times 35 \times 0.8 \text{ mm}^3$, a relative permittivity of $\epsilon_r = 3.5$ and a loss tangent of $\tan \delta = 0.004$. The microstrip feed-line has a width of $W_f = 1.8 \text{ mm}$ to achieve a $50\text{-}\Omega$ characteristic impedance. The radiator has a short stem and two branches, branches 1 and 2, acting as two monopoles. Branch 1 is folded and designed to resonate at 2.4 GHz, while branch 2 is meandered and designed to resonate at around 3.5 GHz. With such designs, the radiator achieves a compact size of only $(L_1 + L_5 - W_5) \times L_6 = 14.5 \times 8.7 \text{ mm}^2$. The antenna is studied, designed and optimized using the EM simulation tool CST. The optimized dimensions are listed in Table 1.

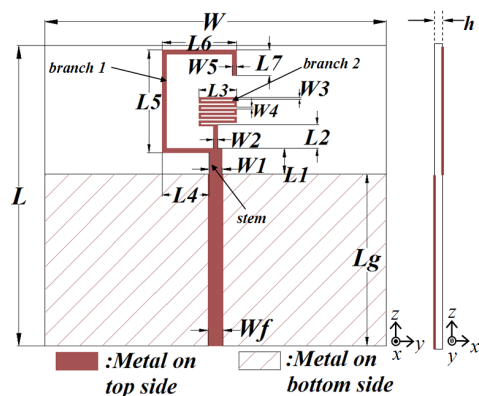


Figure 1: Geometry of proposed dual-band antenna for WiMAX.

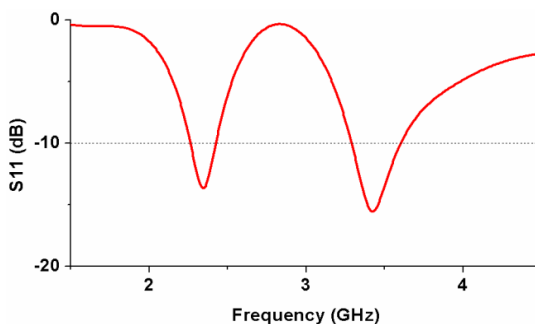


Figure 2: Simulated S_{11} .

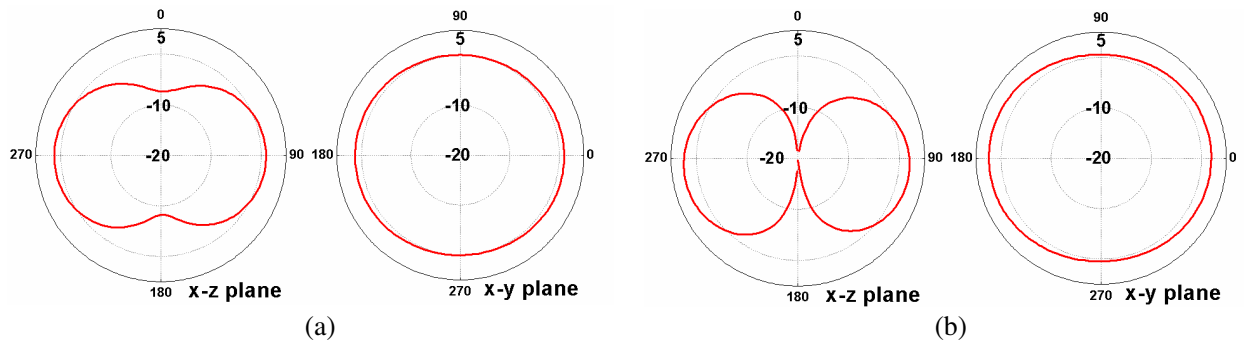


Figure 3: Simulated radiation patterns at (a) 2.4 and (b) 3.5 GHz.

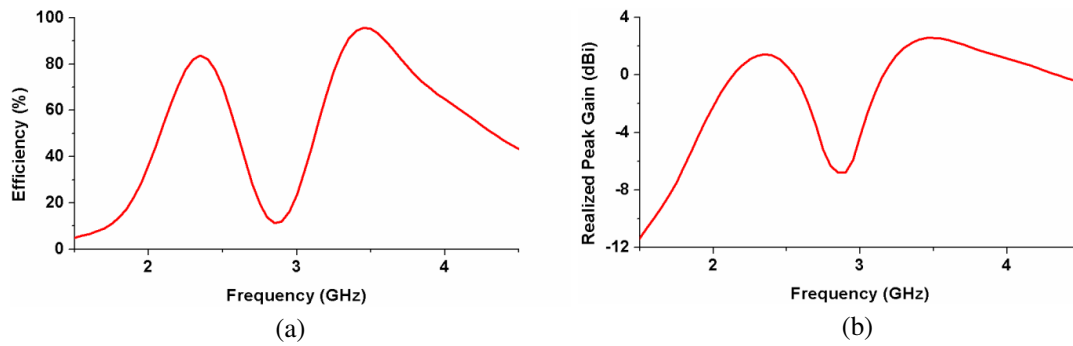


Figure 4: Simulated (a) efficiencies and (b) realized peak gains of proposed antenna.

Table 1: Optimized dimensions of antenna (mm).

W	40	L_1	3	L_5	12	W_1	1.5
L	35	L_2	2.8	L_6	8.7	W_2	0.5
h	0.8	L_3	4.4	L_7	3	W_3	0.2
L_g	20	L_4	5.5	W_f	1.8	W_4	0.25

3. SIMULATION AND MEASUREMENT RESULTS

With the use of the dimensions listed in Table 1, the S_{11} and radiation patterns are studied using computer simulation. The simulated S_{11} is shown in Fig. 3 which indicates that the antenna has bandwidths ($S_{11} < -10$ dB) of 2.26–2.42 GHz and 3.29–3.6 GHz for the lower and higher bands, respectively. The simulated result shows that the antenna can cover the 2.3–2.4 GHz and 3.4–3.6 GHz bands for the WiMAX system.

The simulated radiation patterns at 2.4 and 3.5 GHz in the x - z and x - y planes are shown in Figs. 3(a) and (b), respectively. It can be seen that the antenna behaves like a monopole antenna both at 2.4 and 3.5 GHz.

The simulated efficiencies and realized peak gains of the antenna are shown in Fig. 4. It can be seen that, at the frequencies of 2.4 and 3.5 GHz, the simulated efficiencies are quite high at 83% and 95%, respectively, with the corresponding gains of 1.35 and 2.5 dBi. However, these values have to be confirmed using measurement.

4. CONCLUSIONS

A compact dual-band monopole antenna has been studied for WiMAX application using computer simulation. The antenna radiator consists of a short stem and two branches having resonance at about 2.4 and 3.5 GHz. The simulated results on S_{11} , radiation pattern, gain and efficiency have been presented. It has been shown that the antenna can cover the frequency bands for the WiMAX system. The radiator of the antenna has a compact size of only 14.5×8.7 mm² and so is suitable for wireless devices.

REFERENCES

1. Sun, X. L., S. W. Cheung, and T. I. Yuk, “Frequency-tunable antenna for dual-band WLAN applications,” *PIERS Proceedings*, 819–822, Kuala Lumpur, Malaysia, Mar. 27–30, 2012.
2. Chu, Q. X. and L. H. Ye, “Design of compact dual-wideband antenna with assembled monopoles,” *IEEE Trans. Antennas Propag.*, Vol. 58, No. 12, 4063–4066, 2010.
3. Lu, J. H. and W. C. Chou, “Novel design of planar multi-band U-shape monopole antenna with compact operation for WiMAX application,” *2010 Asia-Pacific Microwave Conference Proceedings*, 2212–2215, 2010.
4. Sun, X. L., J. Zhang, S. W. Cheung, and T. I. Yuk, “A triple-band monopole antenna for WLAN and WiMAX applications,” *IEEE AP-S/USNC-URSI*, Chicago, USA, 2012.
5. Thomas, K. G. and M. Sreenivasan, “Compact triple band antenna for WLAN/WiMAX applications,” *Electronic Letters*, Vol. 45, 811–813, 2009.
6. Sun, X. L., S. W. Cheung, and T. I. Yuk, “Coplanar waveguide-fed dual-band antenna for wireless local area network applications,” *Microwave and Optical Technology Letters*, Vol. 54, No. 6, 1391–1396, 2012.
7. Lu, J. H. and Y. S. Cai, “Planar compact multi-band monopole antenna for WiMAX system,” *2012 IEEE Antenna and Propagation Society International Symposium*, 1–2, 2012.
8. Lin, K. C., C. H. Lin, and Y. C. Lin, “A planar multiband antenna with parasitic-element design for multistandard mobile terminals,” *IEEE Antennas and Propagation Society International Symposium*, 1–4, 2009.

Dual-band Transparent Antenna for ISM Band Applications

M. S. A. Rani¹, S. K. A. Rahim¹, A. R. Tharek¹, T. Peter², and S. W. Cheung³

¹Wireless Communication Centre, Faculty of Electrical Engineering

University Technology Malaysia, Malaysia

²Department of Electronics and Computer Engineering

Brunel University, Uxbridge, Middlesex, UK

³Department of Electronics and Electrical Engineering

University of Hong Kong, Pokfulam Road, Hong Kong, China

Abstract— A compact dual-band transparent antenna with co-planar waveguide (CPW)-fed for wireless applications in the unlicensed industrial, scientific and medical (ISM) band is proposed in this paper. The proposed antenna generates two bands at 2.4 and 5.8 GHz for Wireless Local Area Network (WLAN) access points and point-to-point applications, respectively. The CPW technique is used to feed the circular radiating element. Two slots line are introduced in the antenna to obtain the desired resonating frequencies. Results and analysis from introduction of the slot lines are highlighted in this paper. The antenna utilizes a conductive silver coated film (AgHT) as the core material as the substrate, making the antenna almost 82% transparent. The proposed antenna is very small, having an overall size of $60 \times 60 \times 0.175 \text{ mm}^3$, when compared to other conventional non-transparent antenna operating at the same frequencies of 2.45 and 5.8 GHz. The combination of transparency and small size enables the antenna to be integrated into any flat surface with low chances of being noticed. The antenna can be integrated into the window glass of a building and performs as an access point to provide wireless signal around it. In addition, the antenna can also serve as a tinted film to provide an extra layer of protection from the sun radiation when integrated into the buildings' windows. The integration of the antenna into building windows will reduce the space consumption and remove the space limitation problems faced when using the conventional non-transparent antenna. The proposed prototype antenna has acceptable performances in terms of return loss, gain, efficiency and omni-directional radiation pattern. Simulated and experimental results are discussed.

1. INTRODUCTION

Wireless Local Area Network (WLAN) is one of the best network used in the communication system. According to the Federal Communications Commission (FCC), WLAN frequency is allocated under unlicensed spectrum category, where it falls under the ISM band (802.11a,b,g) covering 2.400–2.484 GHz and 5.150–5.350/5.725–5.825 GHz [1]. Since WLAN frequency is under unlicensed spectrum category, its frequency has been used in many applications and devices, such as Bluetooth, microwave oven, and cordless phone. This networks usually uses 2.4–2.5 GHz frequency for the Access Points and 5.8 GHz for the point-to-point application.

Currently, thin film is one of the emerging technologies in the recent antenna technology and it has been rapidly adapted into the wireless communication system over these few years. It has attracted major attention to antenna designers due to its major advantage; very low thickness. Thin film technology has been implemented widely in product areas, such as in x-ray detectors, thin film photovoltaic and as well as smaller but possibly growing areas of OLED displays or e-book readers [2]. One of the popular thin film materials is the transparent silver conductive material (AgHT-4), which is almost transparent to the human eye with 90% transparency percentage.

Many researches have been done that combine both WLAN dual-band and CPW-fed antenna. A simple slotted-dipole antenna fed using CPW has produced a dual-band antenna at 2.45 GHz and 5.8 GHz [3]. A novel rhombus slot antenna that consists of CPW feeding and rhombic ring can also produce dual-band characteristic [4]. Then, CPW-fed monopole antennas in [5] and [6] will produce dual-band characteristic if proper slots and rings are added to the antenna design. Most of the previous antenna works are using non-transparent material and the thickness of the antenna is quite significant.

In this paper, a transparent dual-band antenna fed with CPW feeding is proposed. The proposed antenna will utilize a new thin film material, conductive silver coated thin film (AgHT-4) that is 90% transparent as the main material. The transparent antenna will cover the dual-band frequencies of 2.45 GHz and 5.8 GHz; WLAN band. The proposed antenna is very compact and easy to manufacture. The proposed transparent antenna is integrated to existing commercial window glass and the performances were measured.

2. ANTENNA DESIGN

The design of the dual-band transparent antenna consists of a circular radiating element fed with a $50\text{-}\Omega$ CPW feeding. This proposed antenna utilizes a new transparent thin film material, conductive silver coated thin film (AgHT-4) as its main substrate. Most of the conventional antenna uses non-transparent material such as FR-4, Rogers, Duroid and Taconic for the substrate. The proposed antenna is based on a conventional CPW-fed circular patch antenna as in Figure 1(a). Then, a U-slot is added to the design to enhance the reflection coefficient of the proposed antenna at the first resonant frequency, 2.45 GHz, as in Figure 1(b). Another slot is then added in the proposed design, as in Figure 1(c) to introduce a second resonant frequency at 5.8 GHz. The combination of these two slots and the circular patch antenna will provide a dual-band antenna. The proposed antenna is integrated to a 1.9 mm thick glass. The geometries of the proposed design are shown in Figure 2. This design is simulated using Computer Simulation Technology software. Overall size of the antenna is only $60 \times 60 \times 2.075 \text{ mm}^3$.

3. RESULTS AND DISCUSSIONS

Figure 3(a) and Figure 3(b) show the current distribution at 2.45 GHz and 5.8 GHz respectively. As shown in the figure, at 2.45 GHz, most of the current are distributed at the edge of the U-slot. Thus, the reflection coefficient of the proposed antenna at 2.45 GHz is enhanced by adding the U-slot. Meanwhile, most of the current distributed at the line slot at 5.8 GHz. It shows that the introduction of the line slot had produced the second resonant frequency.

Figure 4 shows the reflection coefficient of the proposed antenna with and without slot. The proposed antenna doesn't resonate at lower frequency band when there are no slots introduced. This may happen due to the small size of the circular patch that resonating at higher frequency band. The proposed antenna shows a resonating frequency at 2.45 GHz when the U-slot is introduced. This has proven that the U-slot has produced the 2.45 GHz. Then, another resonating frequency at 5.8 GHz is produced after the introduction of the line slot. The reflection coefficient for the proposed antenna at 2.45 GHz and 5.8 GHz are -14.2 dB and -14.4 dB respectively. These coefficient is acceptable because it is below the standard -10 dB set by the FCC. The bandwidth at 2.45 GHz is 50 MHz, which is very narrow and it is very good to reduce interference with other frequency band. However, the bandwidth at 5.8 GHz is slightly broad compared to the bandwidth

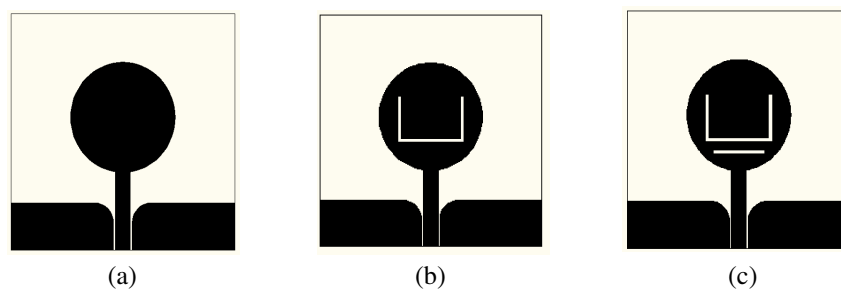


Figure 1: Proposed antenna design with (a) no slot, (b) U-slot, (c) U-slot and line slot.

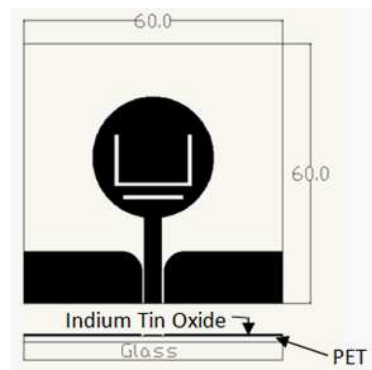


Figure 2: Geometries of proposed antenna design.

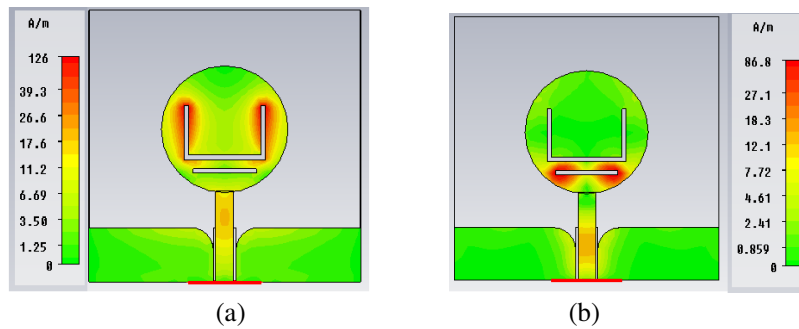


Figure 3: Surface current distribution at (a) 2.45 GHz, (b) 5.8 GHz.

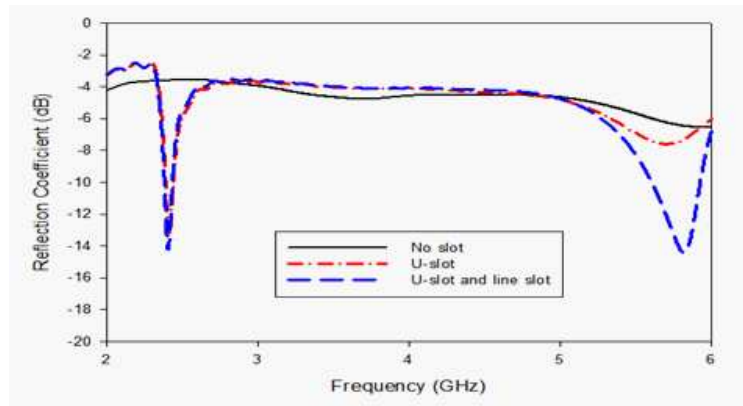


Figure 4: Simulated reflection coefficient of the proposed slotted antenna.

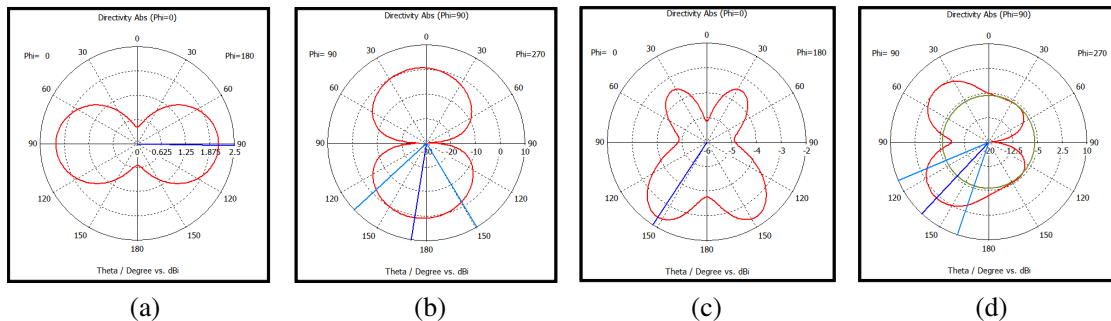


Figure 5: Simulated radiation pattern at (a) 2.45 GHz H -plane, (b) 2.45 GHz E -plane, (c) 5.8 GHz H -plane, (d) 5.8 GHz E -plane.

at 2.45 GHz, with 350 MHz.

Figure 5 shows the simulated radiation pattern at 2.45 GHz and 5.8 GHz for both E -plane and H -plane. The proposed antenna has a bi-directional radiation pattern at the first resonating frequency, with maximum directivity gain of 2.2 dBi. This gain is comparable to other conventional antenna in [5] and [6] that are using FR-4 substrate. Then, the radiation pattern of this antenna become more directional and shifted in its radiating direction at the second resonant frequency, 5.8 GHz. However, the maximum directivity gain at 5.8 GHz is very high, with 6.38 dBi.

4. CONCLUSION

A CPW-fed transparent dual band antenna operating at 2.45 GHz and 5.8 GHz has been presented. The main advantage of this proposed antenna is its transparency and its compact size. The antenna is very thin, that it can be integrated to glass with ease. The antenna also has a good reflection coefficient at both resonating frequencies. Then, the gain of this proposed transparent antenna is comparable to the existing non-transparent antenna with a maximum of 2.2 dBi and 6.38 dBi at 2.45 GHz and 5.8 GHz respectively. This proposed antenna can be used in WLAN applications, where the integration with the existing system can be done easily due to its transparency and

compact size.

ACKNOWLEDGMENT

The authors would like to acknowledge their gratitude and sincerest appreciation to Ministry of Higher Education and Research Management Centre of Universiti Teknologi Malaysia for financing this project (Q.J13000.2423.00G35). Also, special thanks go to all the members of Wireless Communication Centre, Faculty of Electrical Engineering, Universiti Teknologi Malaysia, for their kind assistance.

REFERENCES

1. Zhao, G., F.-S. Zhang, Y. Song, Z.-B. Weng, and Y.-C. Jiao, "Compact ring monopole antenna with double meander lines for 2.4/5 GHz dual-band operation," *Progress In Electromagnetics Research*, Vol. 72, 187–194, 2007.
2. Jackson, T., "Advances and challenges in active thin film electronics," *International Semiconductor Device Research Symposium, 2009, ISDRS '09*, 1, December 9–11, 2009.
3. Tsai, C.-J., C.-H. Lin, W.-C. Chen, C.-L. Lu, and J.-K. Guo, "A CPW-feed printed antenna for dual-band WLAN operations," *2011 International Conference on Consumer Electronics, Communications and Networks (CECNet)*, 4638–4641, April 16–18, 2011.
4. Lin, C.-C., E.-Z. Yu, and C.-Y. Huang, "Dual-band rhombus slot antenna fed by CPW for WLAN applications," *IEEE Antennas and Wireless Propagation Letters*, Vol. 11, 362–364, 2012.
5. Kim, T. H. and D. C. Park, "CPW-fed compact monopole antenna for dual-band WLAN applications," *Electronics Letters*, Vol. 41, No. 6, 291–293, March 17, 2005.
6. Wu, C.-M., "Dual-band CPW-fed cross-slot monopole antenna for WLAN operation," *Microwaves, Antennas & Propagation, IET*, Vol. 1, No. 2, 542–546, April 2007.

Developing Alternatives of Small Monopole Antenna Design for Achieving 4G-LTE Requirements in a Limited Antenna Size

N. I. Mohamed, T. A. Rahman, and A. Y. Abdulrahman

Wireless Communication Center (WCC), Faculty of Electrical Engineering
Universiti Teknologi Malaysia (UTM), Malaysia

Abstract— Achieving Long Term Evolution (LTE) frequency bands (the second generation (2G), third generation (3G), and the proposed fourth generation (4G) frequency bands) using a small-size antenna in a compact device remains a major technical challenge. This paper surveys the recent literature on two types of Universal Serial Bus (USB) LTE antennas, the Meander Line Antenna (MLA) which is one of the alternatives of the small monopole antenna and the Slot Patch multiband antenna (SPA), which is vital for multiband through slotting patch radiators. Consequently a new geometrical design of multiband antenna is proposed in this paper. The proposed antenna design operates at four separate bands: 1.5, 1.8, 1.9, and 2.6 GHz for supporting LTE wireless device of USB dongle.

1. INTRODUCTION

In designing an antenna for any application, a number of parameters must be considered. For instance, the antenna casing determines the antenna size, while the antenna operating environment determines the antenna type; and the antenna applications (or, frequency bands), determine the antenna performance. Such parameters as the impedance bandwidth, antenna gain, efficiency, and radiation pattern are used for gauging the antenna performance. Therefore the design of LTE-USB device antenna has two main challenges; the first one is attaining the required efficiency on a small size antenna, and the second challenge is achieving the highest number of LTE application bands in a separate multiband pattern. Accordingly, a considerable amount of research works have attempted to increase the efficiency of small antennas and to optimize the characteristics of LTE antennas. This article surveys the recent literature on two types of USB LTE antennas, the MLA which is one of the alternatives of the small monopole antenna and the SPA, which is vital for multiband through slotting patch radiators. The main focus is on the key features that are required in designing LTE antennas. These are multiband features which can be achieved by making slots over patch antennas and the wider band width; and shrink size features which can be achieved by meandering the monopole antenna as a MLA [2].

2. MEANDERED LINE ANTENNA (MLA)

All LTE application frequency bands are in the frequency range of 700 MHz \sim 3.8 GHz, whereas $\lambda/4$ monopole is too long to be integrated in a USB device [1]. Decreasing the height (while maintaining fixed frequency) creates short and straight-wire monopole antenna that has a high capacity and low radiation resistance which causes increase in voltage standing wave ratio (VSWR), loss, and consequently a drop in radiation efficiency [1]. Creation of monopole resonant frequency and matching it to the desired characteristic impedance can be achieved by bending the short monopole in inverted-L shape. Meandered antenna is a developed configuration or modification of the inverted L-antenna. Tuning monopole antenna capacitive reactance (or the total feeding point reactance is equal to zero) can be achieved by meandering the horizontal part of the inverted L-wire antenna in any geometric configuration [1]. The technique of meandered wire antenna was initiated as a new design to reduce the size of the existing wire antennas such as log-periodic dipole arrays antennas and Yagi-Uda [2]. The meander wire antenna proposed in [2] was tested by changing the main design variables, such as the number of sections per wavelength (N) and antenna reduction ratio β (where $\beta = l/L$, l is the reduced length after meandering and L is overall length of the wire). It was found that the lower the value of N , the better the antenna performance. However, the resonant resistance and bandwidth decrease as β decreases. Therefore in most of the recently published research works, two sections per wavelength ($N = 2$) were proposed for print planar meander line antennas designs [3, 4]. Table 1 shows various compact meander antenna designs and their corresponding frequencies, bandwidths, and antenna size, as reported in the literature. LTE requires bandwidth of 100 MHz or at least 40 MHz to cover the downlink and uplink channels. The previously proposed LTE antenna models of meandered line designs were able

Table 1: Various compact meander antenna designs and their corresponding parameters.

Reference	Frequency	Bandwidth	Antenna size
[6]	710 MHz	70 MHz	$50 \times 110/2 \text{ mm}^2$
[3]	897 MHz	185 MHz	$23.5 \times 43 \text{ mm}^2$
[4]	2600 MHz	200 MHz	$10 \times 20 \text{ mm}^2$
[7]	619 MHz	182 MHz	$12 \times 50 \text{ mm}^2$
[8]	2.4 GHz	100 MHz	$12 \times 20 \text{ mm}^2$

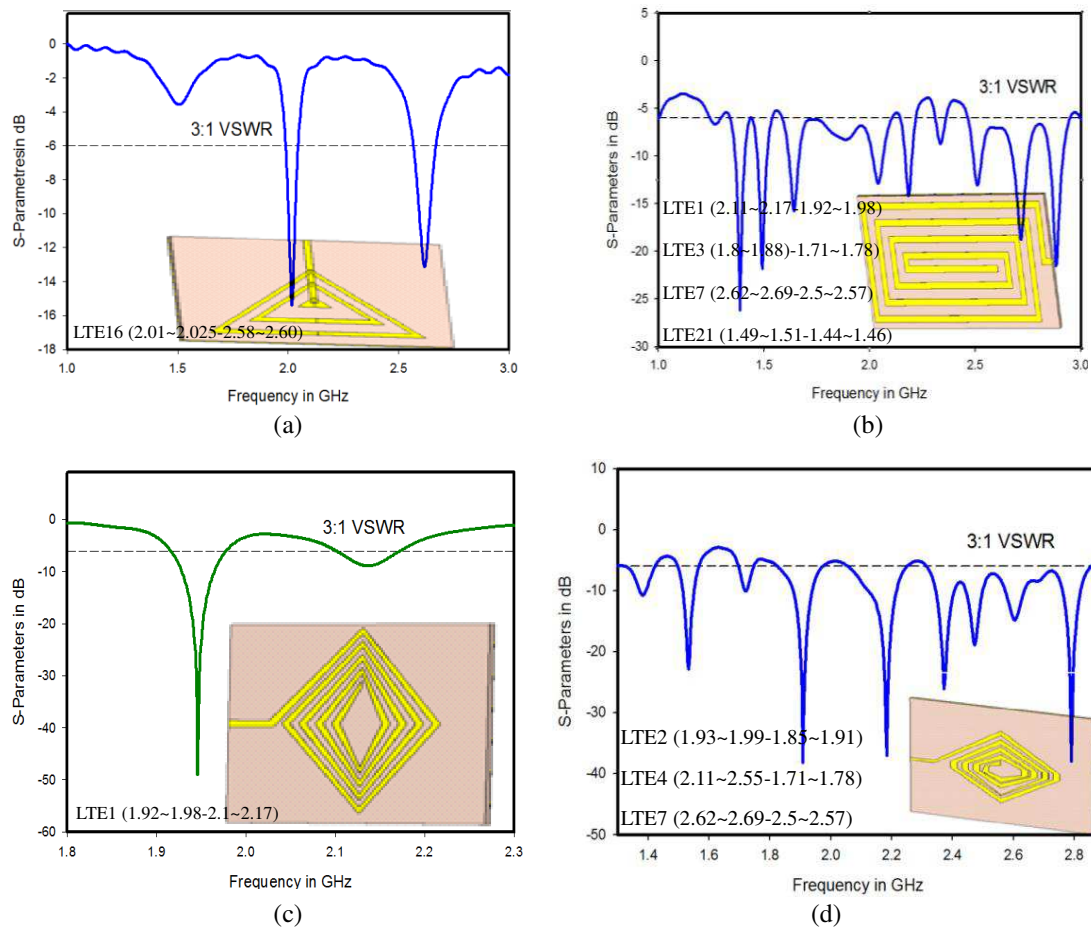


Figure 1: Simulated multiband slot patch antennas optimized for wider impedance bandwidth through geometrical designs of: (a) triangle, (b) squire, (c) trapezoid, and (d) hexagonal patch antennas.

to attain enough bandwidth for the required application band. As reported in [5], for instance, a bandwidth of 200 MHz was achieved at a frequency of 2.6 GHz through a compact size meander antenna of dimensions $10 \text{ mm} \times 20 \text{ mm}$. These are 6 and 12 times lower in dimensions, compared to the operating wavelength.

3. SLOT PATCH ANTENNA

A multiband antenna may be designed by simply making slots over patch antenna. However, patch antennas suffer from the narrow band width [1]. The band width is usually less than the required uplink or downlink of one of LTE-FDD application band. Therefore slot patch multiband antennas operate at few of LTE application frequency bands [9, 10] compared to the LTE wide band antennas reported in [11, 13]. Figures 1(a)–(d) show the various models (slot triangle, squire, diamond, trapezoid, hexagonal) of patch antennas have been optimized for increasing the impedance bandwidth. These types of antennas are able to operate at a few numbers of LTE application frequency bands. Moreover they can only work as transmitter antennas for the possibility of

inserting Antenna Tuning Unit (ATU) which can improve the narrow band efficiency [14]. Generally small multiband antennas efficiency can be improved by using the matching networks. These networks are usually located between the transmitter and the antenna input. More so, it has been found that by placing the matching network components on the antenna structure at any specific points, the best radiation efficiency can be achieved. But, such matching networks must be tuned for each transmitting frequency band, where it cannot be tuned while the matching network is mounted on the antenna [14]. Consequently those types of antennas are valid only for transmitter antenna applications.

4. PROPOSED DESIGN

The proposed antenna is achieved by combining the two characteristics of the separate bands (which can be achieved by making slots over patch antennas) and the wider band width (which is achieved by meandering line antennas). The design has both electrical and mechanical features which allow convenient placement of tuning elements when configured as an electrically small transmitting antenna. The design is printed on one surface of an FR-4 substrate (relative permittivity $\epsilon_r = 4.7$, loss tangent $\delta = 0.02$, thickness $T = 1.6$ mm), which is mounted above a copper USB size ground plane. The proposed multiband antenna has been simulated using the CST microwave studio software. A network analyser was used for measuring the antenna matched frequencies bands, a good agreement was attained between the simulation and measurement results. The proposed antenna design matches four distinct bands (1450 ~ 1510 MHz, 1.701 ~ 1.824 MHz, 1.83 ~ 2.202 MHz and 2.49 ~ 2.775 MHz). Furthermore the new antenna design has good radiation power pattern characteristics.

5. CONCLUSIONS

The most recently published works on the LTE MLA and SPA have been surveyed. All of the surveyed antenna designs were analysed in order to investigate the geometrical concepts for achieving multiband and, therefore improving the impedance bandwidth. A new electrically small antenna (ESA) design, based on the geometrical shapes of MLA and SPA, was presented. The proposed antenna design can successfully function as a multiband antenna and can operate at four separate frequency bands. The antenna has been simulated by using the CST microwave studio software, and fabricated. There is good agreement between the simulated and measured results. The antenna is intended for use in the LTE frequency bands of 1.5, 1.8, 1.9, and 2.6 GHz for USB-Dongle wireless devices.

ACKNOWLEDGMENT

The authors would like to acknowledge and express sincere appreciation to Malaysian Communications and Multimedia Commission (MCMC) for financing the research project under the Contract Research, conducted by Universiti Teknologi Malaysia (UTM). Title: The Long Term Evolution (LTE) Laboratory Establishment, vote No. R.J130000.7323.4B050.

REFERENCES

1. Sanchez-Hernandez, D. A., *Multiband Integrated Antennas for 4G Terminals, Antenna and Propagation*, Artech House, London, 2008.
2. Rashed, J. and C. T. Tai, "A new class of resonant antennas," *IEEE Transactions on Antennas and Propagation*, Vol. 39, 1428–1430, 1991.
3. Sharawi, M. S., Y. S. Faouri, and S. S. Iqbal, "Design and fabrication of a dual electrically small MIMO antenna system for 4G terminals," *2011 German Microwave Conference (GeMIC)*, 1–4, 2011.
4. Ssorin, V., A. Artemenko, A. Sevastyanov, and R. Maslennikov, "Compact bandwidth-optimized two element MIMO antenna system for 2.5–2.7 GHz band," *Proceedings of the 5th European Conference on Antennas and Propagation (EUCAP)*, 319–323, 2011.
5. Ssorin, V., A. Artemenko, A. Sevastyanov, and R. Maslennikov, "Compact bandwidth-optimized two element MIMO antenna system for 2.5–2.7 GHz band," *Proceedings of the 5th European Conference on Antennas and Propagation (EUCAP)*, 319–323, 2011.
6. Bhatti, R. A., S. Yi, and S. O. Park, "Compact antenna array with port decoupling for LTE-standardized mobile phones," *IEEE Antennas and Wireless Propagation Letters*, Vol. 8, 1430–1433, 2009.

7. Bae, S. and Y. Mano, "A small meander VHF & UHF antenna by magneto-dielectric materials," *Asia-Pacific Conference Proceedings Microwave Conference Proceedings, APMC 2005*, 3, 2005.
8. Lin, C. C., S. W. Kuo, and H. R. Chuang, "A 2.4-GHz printed meander-line antenna for USB WLAN with notebook-PC housing," *IEEE Microwave and Wireless Components Letters*, Vol. 15, 546–548, 2005.
9. Lizzi, L. and A. Massa, "Dual-band printed fractal monopole antenna for LTE applications," *IEEE Antennas and Wireless Propagation Letters*, Vol. 10, 760–763, 2011.
10. Abutarboush, H. F., R. Nilavalan, S. W. Cheung, K. M. Nasr, T. Peter, D. Budimir, and H. Al-Raweshidy, "A reconfigurable wideband and multiband antenna using dual-patch elements for compact wireless devices," *IEEE Transactions on Antennas and Propagation*, Vol. 60, 36–43, 2012.
11. Chen, S. C. and K. L. Wong, "Wideband monopole antenna coupled with a chip-inductor-loaded shorted strip for LTE/WWAN mobile handset," *Microwave and Optical Technology Letters*, Vol. 53, 1293–1298, 2011.
12. Kang, T. W. and K. L. Wong, "Simple two-strip monopole with a parasitic shorted strip for internal eight-band LTE/WWAN laptop computer antenna," *Microwave and Optical Technology Letters*, Vol. 53, 706–712, 2011.
13. Yang, C. W., Y. B. Jung, and C. W. Jung, "Octaband internal antenna for 4G mobile handset," *IEEE Antennas and Wireless Propagation Letters*, Vol. 10, 817–819, 2011.
14. Warnagiris, T. J. and T. J. Minardo, "Performance of a meandered line as an electrically small transmitting antenna," *IEEE Transactions on Antennas and Propagation*, Vol. 46, 1797–1801, 1998.

Investigation on CPW Koch Antenna Durability for Microwave Imaging

R. Yahya^{1,2}, M. R. Kamarudin², N. Seman², M. I. Sabran², and M. F. Jamlos³

¹Department of Communication Engineering, Faculty of Electrical and Electronic Engineering
Universiti Tun Hussein Onn Malaysia (UTHM), Parit Raja, Batu Pahat, Johor 86400, Malaysia

²Wireless Communication Center (WCC)

Universiti Teknologi Malaysia (UTM), Skudai, Johor Bahru, Johor 81310, Malaysia

³Advanced Communication Engineering Center (ACE)

School of Computer and Communication Engineering

Universiti Malaysia Perlis (UniMAP), Kampus Pauh Putra

Arau, Perlis 02600, Malaysia

Abstract— In this paper, the investigation on the durability of Coplanar Waveguide (CPW) Koch antenna is presented. Increasing demands in the use of flexible antenna makes the fabric material being concerned. This antenna is made of fully fabric material. The radiating element is made of pure copper fabric and patched onto a denim jean substrate with relative permittivity, $\epsilon_r \approx 2.3$. The antenna is measured on the conditions of crumpled, ironed, wetted, washed, and dried for durability investigation. It produces very well performance results for all conditions except after it is washed. In washed condition, the return loss value decreases to -7.83 dB. It is due to the high water content in the substrate which is influencing the originality of the substrate's permittivity value. Thus, it leads to the decreases of antenna's performance. However, the return loss value is still accepted for the fabric based antenna in wideband applications. Therefore, the durability of the antenna to maintain its wideband frequency characteristic in various conditions makes it has high potential to be implemented into microwave imaging application.

1. INTRODUCTION

Antenna is the main part in microwave imaging system. Recent studies are trying to apply an antenna for microwave imaging due to the cost of using well known devices such as Computed Tomography (CT) and Magnetic Resonance Imaging (MRI) are very expensive. Therefore, it will limit the devices to be used frequently which cause delay in diagnose purpose [1].

Several numbers of antennas have been proposed for microwave imaging purpose [2–6]. Vivaldi [2] and triangular shape [3] antenna are proposed for brain cancer detection while 'Dark Eyes' [4], compact ultra wideband [5] and rectangular ring microstrip antenna [6] are proposed for breast tumor detection. However, all those proposed antennas are based on either microstrip or metal materials which cannot be flexed or bent towards the human body shape. Therefore, a fabric material is seen to be the best substrate for flexibility and bending requirement. In addition, it is easy to integrate with clothes, lightweight, and compact which increases demand on its usage.

An important antenna characteristic for microwave imaging application is the wideband frequency. Therefore, pulse excitation can be generated and higher resolution will be produced. A simple wideband antenna in [7] posses 3400 MHz bandwidth (1270–4670 MHz). The antenna is developed on FR-4 microstrip substrate which is not flexible and cannot be bent. Therefore, a fabric based antenna is inspired.

In the other hand, fabric antenna should be robust and durable to promise it can be used frequently and long lasting for years. Therefore, an antenna using robust and durable fabric is considered in this research. Nevertheless, the condition of antenna during crumpled, ironed, wetted, washed, and dried is investigated. The experimental results are then discussed in the following part.

2. THE GEOMETRY OF THE ANTENNA

The geometry of the CPW Koch antenna is given in Figure 1. This fully fabric antenna is fabricated on a robust denim jean substrate with relative permittivity, $\epsilon_r \approx 2.3$ and thickness, $h = 0.7$ mm while its radiating element is made of pure copper polyester taffeta fabric. The fabrication process is using simple cutting and sewing by hand technique. The prototype of the fabricated fabric Koch antenna is shown in Figure 2. The antenna is fed using microstrip line with feeder gap, $g = 0.5$ mm.

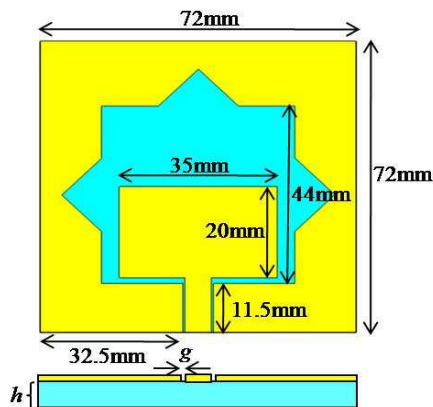


Figure 1: Geometry of fabric Koch antenna.

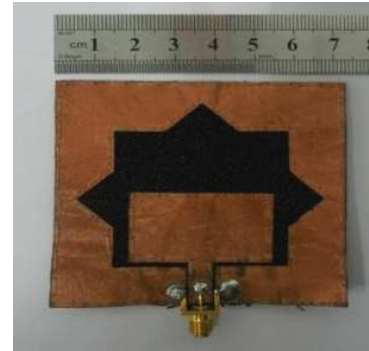


Figure 2: Prototype of fabric Koch antenna.

The durability of the antenna is first examined on crumpled condition. The antenna is crumpled and folded for resulting crinkly lines on the radiating element. The crumpled antenna is then ironed to make it evenly similar to the original. For the wet condition, the antenna is wiped using wet tissues for several times. Different to wash condition, the antenna is washed and rinsed under running tap water. Lastly, the antenna is dried under the sun to dry.

3. RESULTS AND DISCUSSIONS

The antenna is observed on its upper and lower frequencies for bandwidth determination. Figure 3 shows the simulation and measurement result of S_{11} . Based on the figure, measured fabric antenna has wider operating frequency from 1.2–8.2 GHz which consumes 6 GHz or 149% impedance bandwidth. This width of 6 GHz is 2.6 GHz bandwidth greater than antenna in [7].

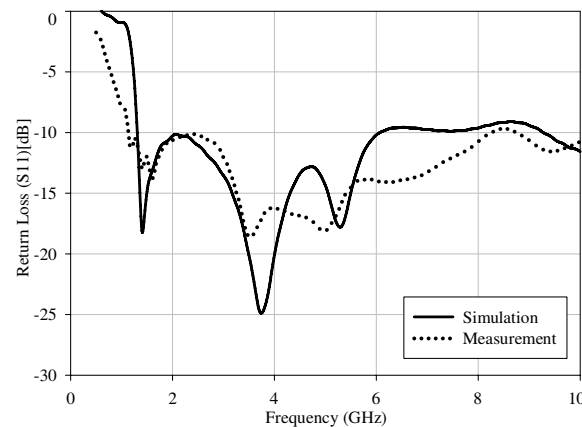


Figure 3: Return loss of the fabric Koch antenna.

The measured result of crumpled and ironed effect is presented in Figure 4. Although the antenna circumstance has changed, it still gives good results, even better than the original condition. During crumpled, it covers 1.16–8.29 GHz while after ironed, it covers 1.02–7.91 GHz. The bandwidths are improved for 151% and 154% respectively. These promises the antenna can be used even in crumpled condition. However, the performance becomes better while the antenna is ironed.

Other condition is during the antenna is wetted using wet tissues. Referring to Figure 5, wetted antenna covers wider frequency range from 1.17–9.91 GHz except 1.83–1.93 GHz and 2.07–2.12 GHz. It shows that the antenna still performs well even though in the wet condition. After it is washed, the performance is still good. It can operate from 1.12 GHz to more than 10 GHz. However, at the middle frequency range, the reflection coefficient decreases to -7.83 dB. Even if the reflection coefficient is decreases at the mid frequency, the return loss value of fabric antenna is still acceptable for most cases [8]. The return loss decrement is due to the high water content in the antenna substrate. It will change the original permittivity of the substrate and consequently decreasing the performance of the antenna.

The final process is to dry the antenna under the sun. Once again the antenna shows a good performance from 1.17 GHz to more than 10 GHz as shown in Figure 5. There are certain values between 1.45–2.12 GHz that the return loss changes and decreases to -9.34 dB. However, it still accepted for fabric antenna operations.

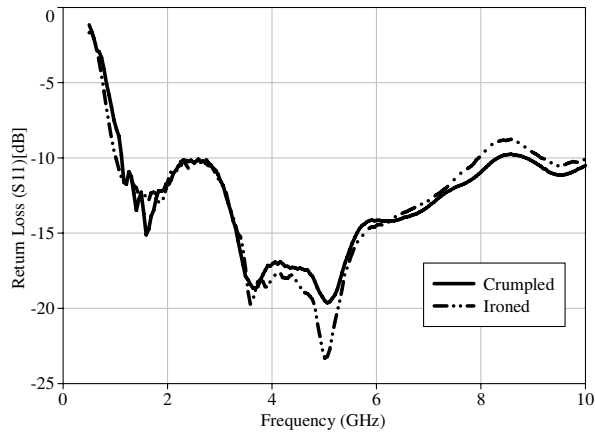


Figure 4: Measured return loss of crumpled and ironed antenna.

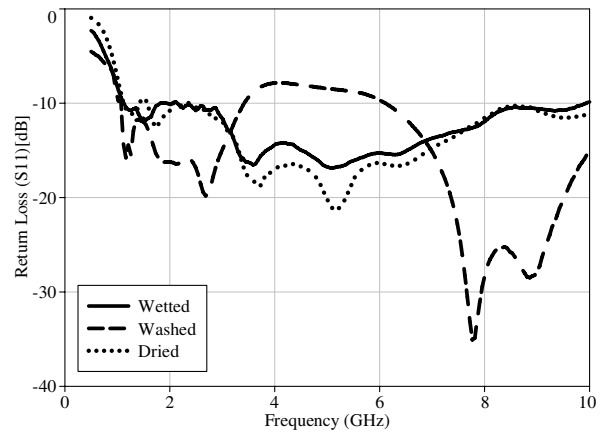


Figure 5: Measured return loss of wetted, washed, and dried antenna.

Table 1: Radiation pattern of the fabric Koch antenna.

Frequency (GHz)	3D	E-plane ($\phi=0$)	H-Plane ($\theta=0$)
2			
4			
6			

According to measurement results of the fabric CPW Koch antenna, it shows a good agreement between simulation and measurement result is obtained. Nevertheless, measurement result is better than the simulation. This happened due to imperfection in fabrication process which is done using hand-sewn instead of sewing machine. Therefore, there is an air trapped between substrate and the radiating elements (patch and ground) which lead to widen the bandwidth [9]. As a result, the proposed antenna provides a wider bandwidth in measurement compared to simulation.

The E -plane and H -plane radiation of the fabric Koch antenna is provided in Table 1. It produces bidirectional radiation pattern with multiple changes at different frequencies. The antenna's gain is also changes in range 3.69 dB to 5.893 dB from frequency 2 GHz to 6 GHz respectively. Nonetheless, the antenna also provides 59% to 91.2% efficiency within the operating bandwidth which can be used in many applications especially for microwave imaging.

4. CONCLUSION

There are several numbers of antennas proposed for microwave imaging. However, the flexibility and bending factor limits the implementation of microstrip antenna towards the multiple shape and size of human body. Therefore, the fabric based antenna is seen as the most suitable substrate for the flexible and bending purpose for microwave imaging. The antenna is investigated on its durability for long lasting usage. The condition of crumpled, ironed, wetted, and dried shows a good measurement results are obtained.

ACKNOWLEDGMENT

The authors would like to thank the Ministry of Science, Technology An Innovation (MOSTI) under Science Fund (Vote 4S056: Development of Head Monitoring System Using Array Transceiver for Microwave Imaging Application), Minister of Higher Education (MOHE) and Universiti Teknologi Malaysia for funding this project under GUP Grant (Vote 01H00, Vote 00G36, and Vote 04H36). Besides, thanks to the members of Wireless Communication Center (WCC), UTM for helping and providing resources to enable this work to be completed. Authors also would like to thanks to Universiti Tun Hussein Onn Malaysia for the sponsor.

REFERENCES

- Guardiola, M., L. Jofre, and J. Romeu, "3D UWB tomography for medical imaging applications," *IEEE Antennas and Propagation Society International Symposium (APSURSI)*, Vol. 1, No. 1, 3–6, 2010.
- Zhang, H. and A. El-Rayis, "A smart antenna array for brain cancer detection," *IEEE Antennas and Propagation Conference (LAPC)*, Vol. 2, 14–17, Loughborough, November 2011.
- Trefna, H. and M. Persson, "Antenna array design for brain monitoring," *IEEE Antennas and Propagation Society International Symposium, AP-S 2008*, 1–4, 2008.
- Kanj, H. and M. Popovic, "A novel ultra-compact broadband antenna for microwave breast tumor detection," *Progress In Electromagnetics Research*, Vol. 86, 169–198, 2008.
- Adnan, S., R. A. Abd-Alhameed, C. H. See, H. I. Hraga, I. T. E. Elfergani, and D. Zhou, "A compact UWB antenna design for breast cancer detection," *PIERS Online*, Vol. 6, No. 2, 129–132, 2010.
- Singh, S. and A. Singh, "UWB rectangular ring microstrip antenna with simple capacitive feed for breast cancer detection," *PIERS Proceedings*, 1639–1642, Beijing, China, March 23–27, 2009.
- Zhang, H., H.-Y. Xu, B. Tian, and X.-F. Zeng, "CPW-fed fractal slot antenna for UWB application," *International Journal of Antennas and Propagation*, Vol. 2012, 1–4, 2012.
- Bai, Q. and R. Langley, "Crumpled textile antennas," *Electronics Letters*, Vol. 45, No. 9, 436, 2009.
- Islam, M. T., M. N. Shakib, and N. Misran, "Broadband E-H shaped microstrip patch antenna for wireless systems," *Progress In Electromagnetics Research*, Vol. 98, 163–173, 2009.

P-shape Monopole Antenna Design for WBAN Application

Ebrahim Sailan Aabidi, M. R. Kamarudin, T. A. Rahman, and Hashimu Uledi Iddi

Wireless Communication Centre (WCC)

Universiti Teknologi Malaysia, UTM Skudai, Johor 81310, Malaysia

Abstract— This paper presents P-shaped monopole antenna for WBAN application for 3.1 to 5.1 GHz frequency band. The design and simulation of proposed antenna for WBAN applications in the free space and close proximity of body surface has been done using CST Microwave Studio. The proposed antenna was designed on the FR4 substrate with dielectric constant, ϵ_r of 4.4 and thickness of 1.6 mm. The final optimized design is $32 \times 28 \text{ mm}^2$. The antenna is suitable to be deployed for WBAN application.

1. INTRODUCTION

We are driven by communication systems in the future through the concept of being connected anywhere at any time. An essential part of this concept is an approach that focuses on the user in the services that are available continuously and provide systems re-configurable, modesty and the correct guidance of the human mind. A wireless body area network that focuses on networks consisting of the number of nodes, and units put on the human body or in the vicinity such as everyday clothing [1].

UWB technology full bandwidth covers from 3.1 to 10.6 GHz for UWB communication applications by the Federal Communication Commission (FCC) in 2002 [2], but the full bandwidth is inefficient system, so UWB system divided to the lower band at (3.1–5.1 GHz) and higher band at 6–10.6 GHz for more efficient system [3].

The antenna is an essential element of WBAN applications for off-body, in-body and on-body communication system [4]. The antenna designed must be considered a small size for human body application. In addition, The antenna designed must be a consideration three layers of body tissues (skin, fat and muscle) with relative permittivity and different thickness [5].

This paper presents a P-shaped monopole antenna for WBAN application for the lower frequency band from 3.1 to 5.1 GHz of the UWB band. The simulation results of the P-shaped monopole antenna in free space and close proximity to body tissues has been presented taken into consideration of different dimensions of the antenna and the human body tissues.

2. ANTENNA DESIGN

The P-shape monopole antenna is designed to be operated from 3.1 GHz to 5.1 GHz frequency band. The antenna is printed on the FR4 substrate with dielectric constant of 4.4, loss tangent of 0.02 a thickness of 1.6 mm. The optimized dimension of the propose antenna is $32 \times 28 \times 1.6 \text{ mm}^3$. The geometry and dimension of proposed P-shaped monopole antenna is shown in Figure 1.

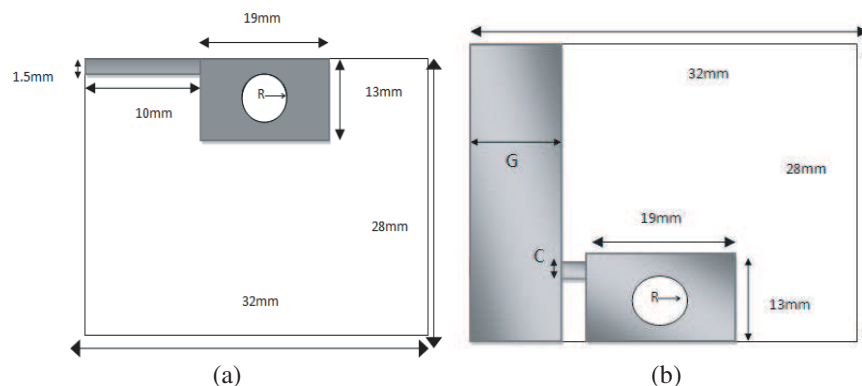


Figure 1: Geometry of the proposed P-shaped monopole antenna. (a) Front view. (b) Back view.

3. RESULTS AND DISCUSSION

The P-shaped monopole antenna is simulated in the free space and with the presence of numerical human body phantom. Figure 2 shows a comparison of VSWR of the proposed antenna in free space and close to the human body. It can be seen that, the P-shaped monopole antenna has achieved $VSWR < 2$ in the frequency range of 3.0 to 5.6 GHz in the free space and close to human body tissues. The distance between antenna and body surface is represented by d . In this analysis, the P-shaped antenna is placed very close to the body ($d = 2$ mm). The VSWR shown in Figure 2 is for d is about 2 mm. It can be concluded that the antenna VSWR or return loss is more stable although the distance is very much closer as long as the antenna is not directly touched with the human body.

In this work, three layers of human body tissues are consist of muscle, fat and skin. The human body dimensions are about $100 \times 100 \times 36$ mm³, in which the thickness of skin is 1 mm, fat is 5 mm and muscle is 30 mm.

This human body effect on the performances of P-shape monopole antenna in term of gain and SAR are tabulated in Table 1. It can be seen that the gain of the antenna when it is proximity to the body is degraded as expected when compared with the gain in free space. In addition, the

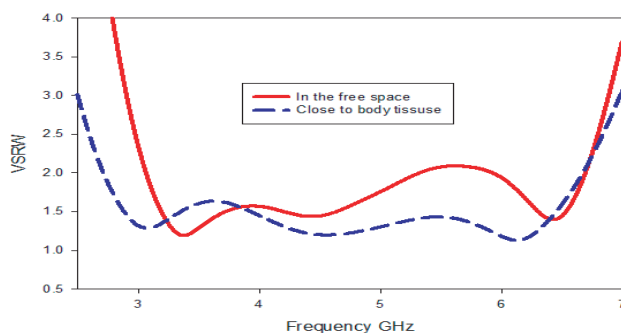
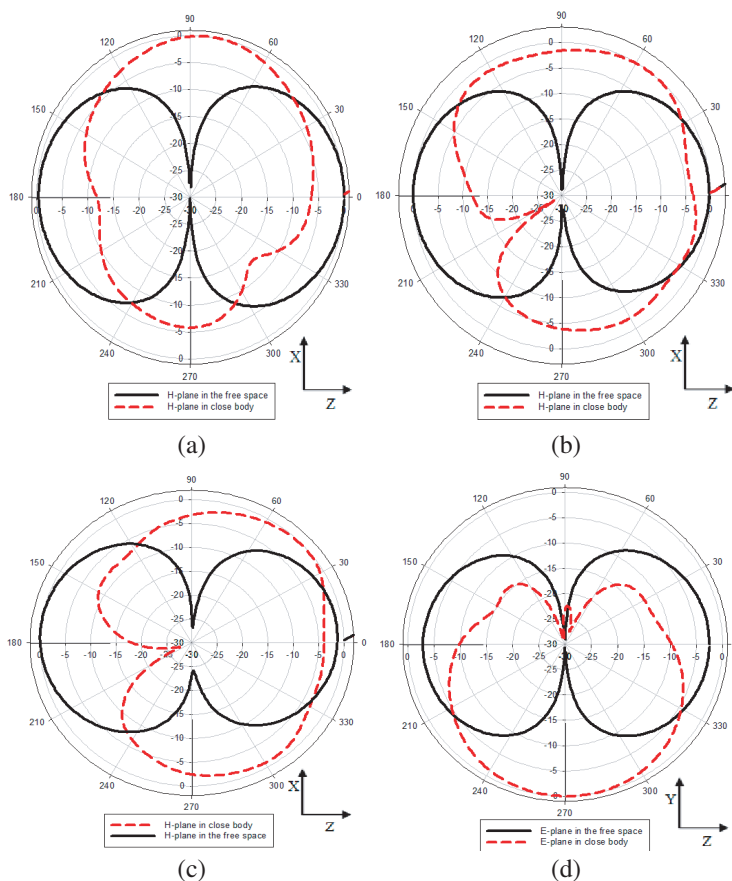


Figure 2: Comparison of VSWR of the antenna in the free space and close to human body.



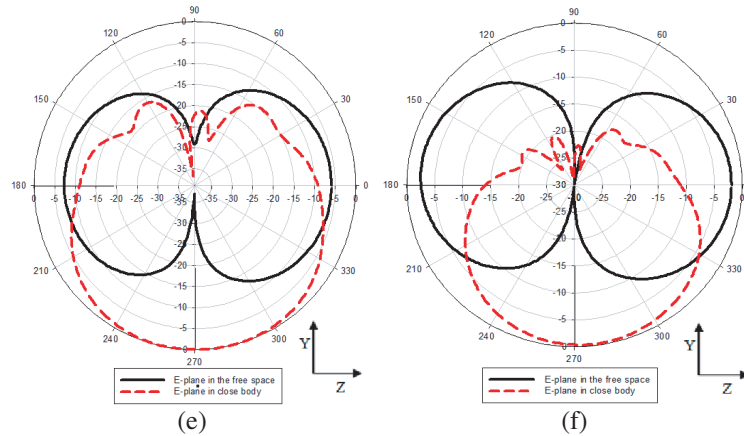


Figure 3: The radiation pattern of the P-shape antenna. (a) H -plane pattern at 3.1 GHz. (b) H -plane pattern at 4.1 GHz. (c) H -plane pattern at 5.1 GHz. (d) E -plane pattern at 3.1 GHz. (e) E -plane pattern at 4.1 GHz. (f) E -plane pattern at 5.1 GHz.

Table 1: Comparison of gain and SAR of the antenna in the free space and close to human body.

	Frequency	3.1 GHz	4.1 GHz	5.1 GHz
In the free space	Gain	2.4	3	2.4
	SAR (10 g)	17.3 W/kg	18 W/kg	19.92 W/kg
In close body tissue	Gain	0.7	0.9	1.1
	SAR (10 g)	17.3 W/kg	18 W/kg	19.92 W/kg

numerical SAR value (reference is 1 W) can be seen increased from lower frequency (3.1 GHz) to higher frequency (5.1 GHz). If the reference power of 1 mW is used, the SAR values will be in the limit of allowable SAR.

Figure 3 shows that the E - and H -plane patterns in 3.1, 4.1 and 5.1 GHz of the proposed antenna in the free space and close to human body tissues at $d = 2$ mm. It can be seen that the E -plane and H -plane radiation pattern is affected when the antenna placed close to the body.

4. CONCLUSIONS

In this paper P-shaped monopole antenna has been presented investigating the VSWR, gain, radiation patterns and SAR in the free space and close proximity to the human body. The proposed antenna provided an impedance bandwidth VSWR < 2 from 3.1 to 5.1 GHz. The VSWR was not affected by the proposed antenna in free space and when placed near the body at different distances from the body surface. In addition, SAR effect is increased when the antenna placed near the body surface and with increasing frequency. The SAR of the proposed antenna are 17.3, 18 and 19.92 W/kg at 3.1, 4.1 and 5.1 GHz respectively. The simulated gain obtained were 0.7, 0.9 and 1.1 to 3.1 GHz, 4.1 GHz and 5.1 GHz respectively. The value of gain was reduced when the proposed antenna is placed close to the body.

ACKNOWLEDGMENT

The authors would like to thank to Ministry of Higher Education (MOHE) and UTM GUP (vote 01H00 and vote 00G36) for sponsoring this work. Besides, thanks to the members of Wireless Communication Center (WCC), UTM for helping and providing resources to enable this work to be completed.

REFERENCES

1. Alomainy, A., A. Sani, A. Rahman, J. G. Santas, and H. Yang, "Transient characteristics of wearable antennas and radio propagation channels for ultrawideband body-centric wireless communications," *IEEE Transactions on Antennas and Propagation*, Vol. 57, No. 4, 875–884. 2009.
2. Hongsan, S., P. Orlik, A. M. Haimovich, L. J. Cimini, Jr., and Z. Jinyun, "On the spectral

- and power requirements for ultra-wideband transmission,” *IEEE International Conference on Communications*, 2003.
3. Tuovinen, T., K. Y. Yazdandoost, and J. Iinatti, “Ultra wideband loop antenna for on-body communication in Wireless Body Area Network,” *2012 6th European Conference on Antennas and Propagation (EUCAP)*, 2012.
 4. Hall, P. S., Y. Hao, and S. L. Cotton, “Advances in antennas and propagation for body centric wireless communications,” *2010 Proceedings of the Fourth European Conference on Antennas and Propagation (EuCAP)*, 2010.
 5. Yazdanboost, K. Y. and R. Kohno, “Ultra wideband L-loop antenna,” *2005 IEEE International Conference on Ultra-wideband*, 2005.

Can There Be WDM Solitons in Fibers?

Cavour Yeh and F. I. Shimabukuro

California Advanced Studies, 2432 Nalin Dr., Los Angeles, CA 90077, USA

Abstract— The existence of solitons on single wavelength beam in fiber is a marvel of nature. For a pulse propagating on a single wavelength beam in a fiber, it is amazing that the linear dispersive effect of pulse broadening can be cancelled exactly by the non-linear self-phase modulating effect of pulse compression such that the pulse will not degrade as it propagates along the fiber. This pulse is called a soliton. This delicately balanced condition can easily be perturbed or destroyed, when there are co-propagating pulses on different wavelength beams, called wavelength division multiplexed (WDM) beams, in this fiber. This degradation is due to the presence of the non-linear cross-phase modulation effect which can act on co-propagating pulses on WDM beams. Can nature provide another condition under which pulses on WDM beams can be formed into WDM solitons? This paper will address this problem.

1. INTRODUCTION

The discovery in 1973 that an optical soliton [1, 2] on a single wavelength beam can exist in a fiber is one of the most significant events since the introduction of low-loss optical fiber communication. This means that, in principle, data pulses may be transmitted in a fiber without degradation for long distances. This soliton discovery sets the ultimate goal in information carrying capacity for optical fiber communication on a single wavelength beam. The existence of solitons is made possible by adjusting the delicate balance between the dispersion effect and the non-linear effect such that a specially shaped optical pulse can propagate in the fiber without degradation. Further increase in information carrying capacity can be achieved if solitons on wavelength division multiplexed (WDM) beams in a single mode fiber can be formed. However, due to the presence of complex non-linear cross-phase modulation interaction (CPM or XPM or Kerr effect) between co-propagating pulses on different wavelength beams, the delicate balance achieved for single wavelength solitons can be perturbed, and it is not certain that WDM solitons can exist. This paper will examine the possibility of forming WDM solitons, which was proposed earlier [3, 4]. Added here are examples of how WDM solitons may be used to transmit information.

2. BIT PARALLEL WDM SOLITONS

In a wavelength division multiplexed (WDM) system, the cross-phase modulation (CPM or XPM) effects caused by the nonlinearity of the optical fiber are unavoidable [5]. These CPM effects occur when two or more optical beams co-propagate simultaneously and affect each other through the intensity dependence of the refractive index. This CPM phenomenon can be used to produce an interesting pulse shepherding effect [6]. It may be utilized to align the arrival time of pulses that are otherwise misaligned, to produce a highly compressed pulse on a different wavelength beam [7], or to generate time-aligned pulses in the picoseconds range of WDM beams [8].

The traditional way of transmitting solitons on WDM beams in a single-mode fiber is to make sure that soliton pulses on each WDM beam do not overlap with those on the other WDM beams. If overlapping occurs, rapid walk-off is designed in the system so that the overlapping time is kept at a minimum. So, basically this type of soliton propagation on WDM beams is not much different from the soliton propagation on a single beam case except new deleterious effects to destroy the integrity of a soliton are added due to the overlapping and walk-off interaction problem. Therefore the CPM effect due to the presence of neighboring WDM beams is considered to be undesirable.

On the contrary, investigations presented in References [5–7] show that the CPM effect may be used to gain constructive new approaches to solve problems of importance. The case-in-point is the discovery of bit parallel WDM solitons. Inspection of previous work on CPM effect [6–8] shows that it tends to provide certain adhesion among co-propagating overlapping pulses even in the presence of walk-off. This stabilizing effect increases the tendency for co-propagating overlapping pulses to stay together. It was under this influence that the bit-parallel WDM solitons were found.

Let us start with an idealized fiber which is lossless (i.e., $\alpha_i = 0$ for all beams) and which possesses uniform group-velocity dispersion (GVD), i.e., $v_{gi} = v_g$ for all beams, within the wavelength range

under investigation. The equations governing the propagation characteristics of signal pulses are

$$-j \frac{\partial u_i}{\partial \xi} = -\frac{1}{2} \frac{\partial^2 u_i}{\partial \tau^2} - \frac{L_D}{L_{NL}} \left(|u_i|^2 + 2 \sum_{m \neq i}^I |u_m|^2 \right) u_i \quad (i=1, 2, 3, \dots, I), \quad I = \text{number of WDM beams.} \quad (1)$$

In Eq. (1), $\tau = (t - z/v_g)/T_0$, $\xi = z/L_D$, $L_D = T_0^2/|\beta_2|$, $L_{NL} = 1/(\gamma P_0)$, β_2 is the dispersion coefficient $= dv_g^{-1}/d\omega$, v_g is the group velocity, and γ is the non-linear index coefficient. T_0 and P_0 are, respectively, the initial pulse width and the peak power of the initial pulse, u_i is the field envelope of the propagating pulse on the i th beam.

The anomalous GVD case in which $\text{sgn}(\beta_{2i}) = -1$ is considered [3, 4]. It is seen from the above equation that the summation term representing the cross phase modulation effect is twice as effective as the self-phase modulation (SPM) effect for the same intensity. This observation also provides the idea that cross phase modulation may be used in conjunction with self-phase modulation on the WDM pulses to counteract the GVD effect, thus producing WDM solitons. Comparing the non-linear term for a single beam with that for the co-propagating multiple WDM beams in Eq. (1) shows that if we choose the correct amplitudes for the initial pulses on WDM beams and retain the hyperbolic secant pulse form, it may be possible to construct a set of initial pulses which will propagate in the same manner as the single soliton pulse case, i.e., undistorted and without change in shape for arbitrarily long distances. Let us choose the initial pulses as follows [3, 4],

$$u_i(0, \tau) = [1 + 2(I - 1)]^{-1/2} \text{sech}(\tau) \quad (i = 1, 2, 3, \dots, I) \quad (2)$$

where I is the number of WDM beams.

Using these initial pulse forms numerical simulation was carried out to solve Eq. (1). The split-step Fourier method was used [9–12]. The fiber parameters used for the simulation are L , length of fiber equal to 1000 km; β_2 , dispersion coefficient, equal to $-2 \text{ ps}^2/\text{km}$; nonlinear index coefficient, γ , equal to $20 \text{ W}^{-1}\text{km}^{-1}$; T_0 , pulse width, equal to 10 ps; $L_D = 50 \text{ km}$; and $L_{NL} = 50 \text{ km}$. Four cases with $I = 1, 2, 3, 4$ were treated. The $I = 1$ case corresponds to the well-known single soliton case; here, the amplitude for the fundamental soliton is 1. For the two-beam case, the amplitude is $3^{-1/2} = 0.57735$. For the three-beam case it is $5^{-1/2} = 0.4472136$. For the four-beam case, it is $7^{-1/2} = 0.37796447$. It is noted that the amplitude of the fundamental solitons on WDM multibeams becomes successively smaller as the number of beams is increased. This is because the non-linear effect becomes more pronounced when more beams are present. Numerical simulation shows that after propagating 1000 km through this fiber the original pulse shape for all these WDM pulses remains unchanged. It thus appears that the initial forms chosen for the pulses on WDM beams are the correct soliton forms for WDM beams.

An example on how bit-parallel WDM (BP-WDM) solitons may carry digital data streams on 4 WDM beams is demonstrated in Fig. 1. It shows how a bit-parallel word may be transmitted by this scheme. The key to form BP-WDM solitons is to set the magnitude of each bit to a predetermined value for a bit parallel word based on the number of bits used to represent this word. Another example on the comparison between single-wavelength soliton with solitons on BP-WDM beams on a single mode fiber is shown in Fig. 2.

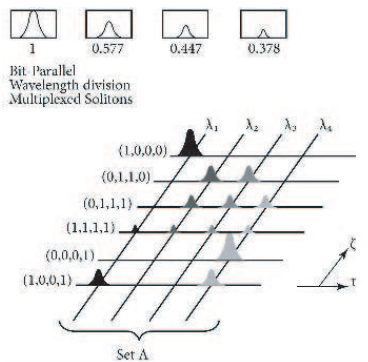


Figure 1: An example of Bit-parallel WDM solitons in their information transmission.

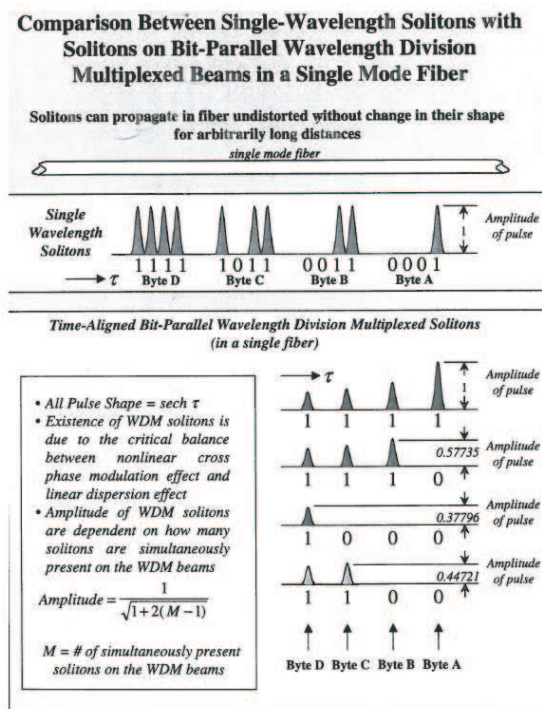


Figure 2: Comparison between single-wavelength solitons with solitons on bit-parallel wavelength division multiplexed beams on a single mode fiber.

Preliminary results have shown that if the relative walk-off is kept below a certain value, all co-propagating pulses tend to stay together and co-propagate at an average group velocity. The shapes of these pulses may also be altered somewhat, but the information carrying ability is maintained. This means the BP-WDM solitons are quite robust [13]. Furthermore, because of the cohesive effects, due to CPM and pulse shepherding, some of the deleterious effects (such as Raman effect, the third order dispersion effect, and self-steepening effect) that may be present for the case of soliton propagation on a single beam may be diminished.

The existence of optical solitons on wavelength division multiplexed beams in a fiber is not only of fundamental interest but also has enormous implications in the field of optical fiber communications. It is conceivable that multiple terabits of information can be sent through a single fiber in the bit-parallel wavelength division multiplexed format without degradation.

REFERENCES

1. Hasegawa, A. and T. Tappert, "Transmission of stationary nonlinear optical pulses in dispersive dielectric fibers. I. Anomalous dispersion," *Appl. Phys. Lett.*, Vol. 23, 142–144, 1973.
2. Mollenauer, L. F., R. H. Stolen, and L. P. Gordon, "Experimental observation of picosecond pulse narrowing and solitons in optical fibers," *Phys. Rev. Lett.*, Vol. 45, 1095, 1980.
3. Yeh, C. and L. A. Bergman, "Existence of optical solitons on wavelength division multiplexed beams," *Phys. Rev. E*, Vol. 60, 2306–2308, 1999.
4. Yeh, C. and L. A. Bergman, "Wavelength division multiplexed optical solitons," US Patent 6612, 743B1, Sep. 2, 2003.
5. Agrawal, G. P., *Nonlinear Fiber Optics*, 3rd Edition, Elsevier, Singapore, 2001.
6. Yeh, C. and L. A. Bergman, "Pulse shepherding in nonlinear fiber optics," *J. Appl. Phys.*, Vol. 80, 3174–3178, 1996.
7. Yeh, C. and L. A. Bergman, "Enhanced pulse compression in a nonlinear fiber by a wavelength division multiplexed optical pulse," *Phys. Rev. E*, Vol. 57, 2398–2404, 1998.
8. Yeh, C., L. A. Bergman, J. Moroodian, and S. Monaco, "Generation of time-aligned picosecond pulses on WDM beams in a nonlinear fiber," *Phys. Rev. E*, Vol. 57, 6135–6139, 1998.
9. Yeh, C., J. E. Pearson, and W. P. Brown, "Enhanced focal-plane irradiance in the presence of thermal blooming," *Appl. Opt.*, Vol. 15, 2913–2916, 1976.

10. Pearson, J. E., C. Yeh, and W. P. Brown, "Propagation of laser beams having an on-axis null in the presence of thermal blooming," *J. Opt. Soc. Am.*, Vol. 66, 1384–1388, 1976.
11. Yeh, C., L. Casperson, and B. Szejn, "Propagation of truncated gaussian beams in multimode fiber guides," *J. Opt. Soc. Am.*, Vol. 68, 989–993, 1978.
12. Yeh, C., W. P. Brown, and B. Szejn, "Multimode inhomogeneous fiber couplers," *Appl. Opt.*, Vol. 18, 489–495, 1979.
13. Ostrovskaya, E. A., Y. S. Kivshar, D. Mihalache, and J. C. Crasovan, "Multichannel soliton transmission and pulse shepherding in bit-parallel wavelength optical fiber links," *IEEE Journ. Selected Topics in Quantum Electronics*, Vol. 8, 591–596, 2002.

Investigation of Two Bidirectional C + L Band Fiber Amplifiers with Pumping Sharing and Wavelength Reused Mechanisms

S. K. Liaw¹, Y. L. Yu¹, Y. C. Wang¹, W. F. Wu², and R. Y. Liu³

¹Department of Electronic Engineering

National Taiwan University of Science and Technology, Taipei 106, Taiwan

²Department of Mechanical Engineering, National Taiwan University, Taipei 106, Taiwan

³National Space Organization, Hsin Chu 300, Taiwan

Abstract— Two types of bidirectional fiber amplifier are proposed and experimentally demonstrated, including EDFA and hybrid fiber amplifier in C + L band. A single-wavelength pump source is used to pump both the C band and L band fiber amplifiers. Using different pumping power and wavelength the average gains are about 10.72 dB for the hybrid fiber amplifiers and 15.4 dB for the EDFA, respectively, with a launched wavelength tunable signal power of -10 dBm. The average noise figures are about 5.17 dB and 5.1 dB for the C band and L band EDFA, respectively.

1. INTRODUCTION

The rapid growth of data traffic in optical communications and optical networks demands extensive research into wideband optical amplifiers as the roles they play have become increasingly important. Both L and Erbium-doped fiber amplifier (EDFA) and Raman fiber amplifier operating in C + L band wavelength-division-multiplexing (WDM) systems are now a mature technology. So far, there are many methods to amplify the C + L band signals such as EDFA, Raman fiber amplifier (RFA) and semiconductor optical amplifier (SOA). For the C band, EDFA is a mature and widely used technology, owing to its higher gain and lower noise figure (NF) than other methods. RFA is a convenient method to amplify various wavebands, and it has even lower NF than that of EDFA [1]. We have studied theoretically both serial-type scheme and parallel-type hybrid amplifier scheme [2, 3]. Both dispersion compensation and power equalization are realized by adjusting the fiber Bragg grating (FBG) reflectivity and the pumping ratio. In addition, compared to the unidirectional EDFA, bidirectional EDFAs can not only reduce the complexity of the optical system, but also reduce the cost of transmission optical fiber. In this paper, we proposed and experimentally demonstrated two kinds of bidirectional fiber amplifiers. The amplification range covers both the C band and L band signals. We use a single wavelength pump laser diode for both the C band and L band. Moreover, we employ concept of residual pumping power reuse to optimize both the gain efficiency of C + L band signals.

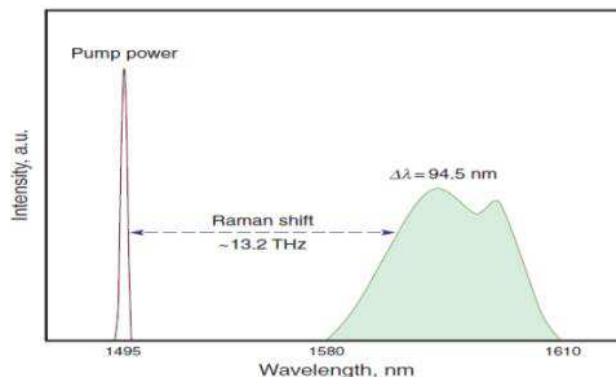


Figure 1: Pump-sharing to C-band EDFA and L-band RFA concept.

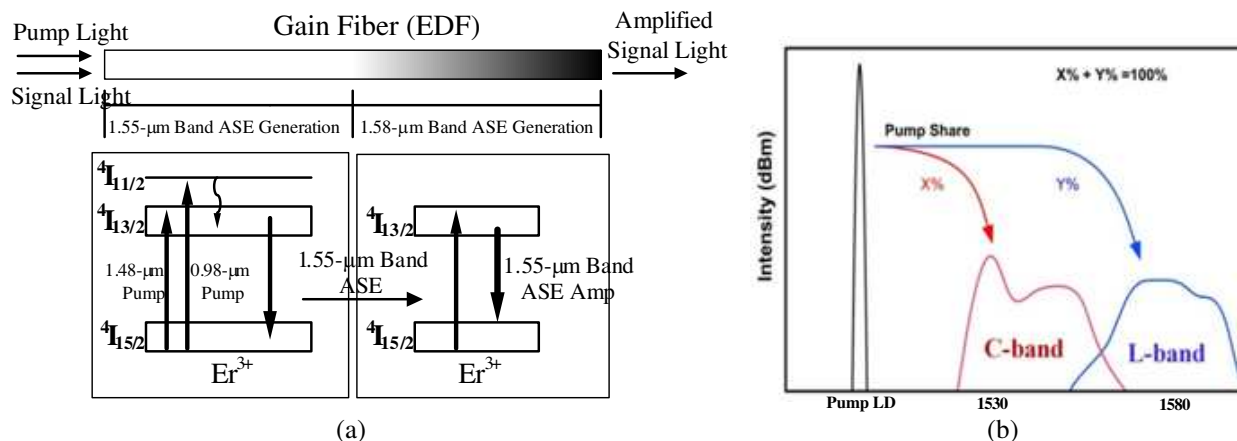


Figure 2: (a) Amplification mechanism of EDF [4], (b) distribution of pump power.

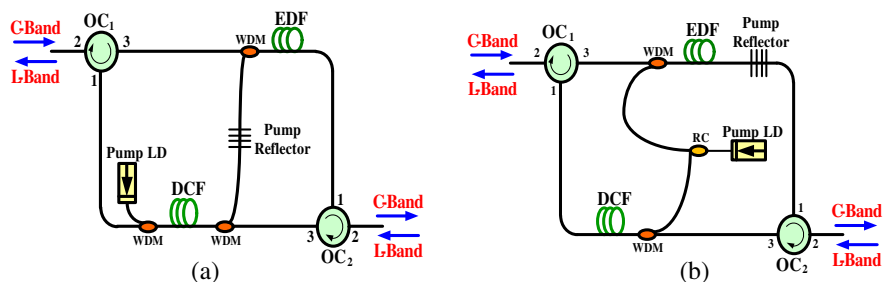


Figure 3: (a) The proposed C + L band hybrid amplifiers using a single-wavelength pump laser source, and (b) the proposed C + L band Erbium doped fiber amplifiers using a single-wavelength pump laser source.

2. THEORY

2.1. Raman

The Raman shift concept is illustrated in Fig. 1. For a pump source at 1495 nm for example, the corresponding gain peak can be described using the following equation [5]:

$$\Delta\lambda = -\lambda \frac{\Delta f}{f} = -\lambda^2 \frac{\Delta f}{c} = 94.9 \text{ nm} \quad (1)$$

where $\Delta f = -13 \text{ THz}$ and $\Delta\lambda = 94.9 \text{ nm}$ are the total amount of detuning with respect to the pump frequency and wavelength, respectively. The maximum gain occurs at 1589.5 nm in the L-band region. The C-band EDFA can also use the same 1495 nm pump laser diode (LD). The gain is only a little smaller than that using 1480 nm.

2.2. EDFA

The amplified concept of EDFA using single wavelength pump LD in C + L band is illustrated in Fig. 2(a). First, the pump LD injected into the front-ends of EDF, the population inversion enables the EDF to absorb pump light and generate C band amplified spontaneous emission (ASE). After the pump light running out, C-band amplified spontaneous emission is absorbed by the rear end EDF again and generates L band ASE. Therefore, the length of EDF is key factor on generating L band ASE.

2.3. Pump Sharing

We use concept of pump sharing for gain equalization and saving cost. Fig. 2(b) depicts the pump sharing concept. We provide the $X\%$ and $Y\%$ of pump power for the C band and L band fiber amplifier, respectively. ($X + Y = 100\%$). We divide pump power by an optical ratio coupler (RC) and a pump reflector, respectively.

3. EXPERIMENTAL SETUP

3.1. Hybrid Fiber Amplifiers

Figure 3(a) shows the proposed bidirectional hybrid, C + L-band EDFA/RFA for WDM applications. The C-band EDFA is for the downstream signal amplification. In this case, the length and absorption coefficient of EDF are 3 m, 12.4 dB/m@979 nm and 18.79 dB/m@1531 nm, respectively. The L-band RFA for the upstream signal amplification consists of a dispersion compensating fiber (DCF). Here, the fiber loss, dispersion and dispersion slope for the DCF are 0.4 dB/km, -95 ps/nm/km and -0.62 ps/nm²/km, respectively. The residual pump power was then routed to the C-band erbium-doped fiber (EDF) via a pair of WDM couplers. Since the residual pump power may still be too much for the EDFA, a ratio pump reflector was placed between the WDM pair to reflect part of the residual pump back to the L-band RFA for further pumping. The left hand side optical circulator (OC) is used to add the C-band signals to the EDFA as well as receive the L-band signals from the RFA. The right hand side OC is used to add the L-band signals to the RFA as well as receive the C-band signals from the EDFA. The signals for both bands have unidirectional paths thank to the inter-port isolation of the OCs. Note that the DCF plays a dual role as both the gain medium and dispersion compensator for the RFA.

3.2. EDFA

Figure 3(b) depicts the proposed bidirectional C + L band EDFAs for WDM application. The C band EDFA is for the downstream signal amplification at the upper path, and the L band EDFA is for the upstream signal amplified at the lower path. The C-band EDFA consists of a wavelength division multiplexer (WDM), EDF parameters are identical to the case in Fig. 3(a). The residual pumping power can be re-absorbed and reused by the EDF₁ after it loops back to the EDF₁ by the FBG-based pump reflector. The L-band EDFA is constructed by a WDM and 10 m-long EDF. The absorption coefficient of EDF₂ (RightWaveTM EDF LRL Reduced Length) is 10 dB/m@1480 nm and 33.5 dB/m@1530 nm. The pump power of 200 mW was used only one pump LD. We assign 60 mW of pumping power to C-band EDFA. The residual pumping power can be reabsorbed by C-band EDFA again.

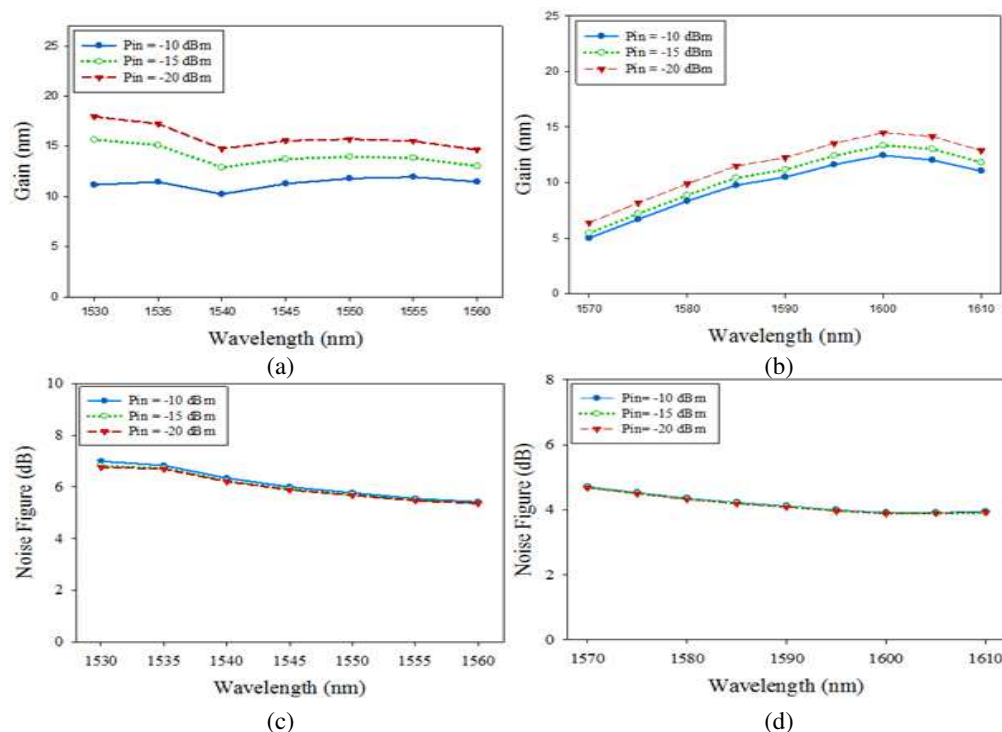


Figure 4: Measured gain and NF profiles using a tunable laser source, respectively, for (a) C-band EDFA gain, (b) L-band RFA gain, (c) C-band EDFA NF, (d) L-band RFA NF.

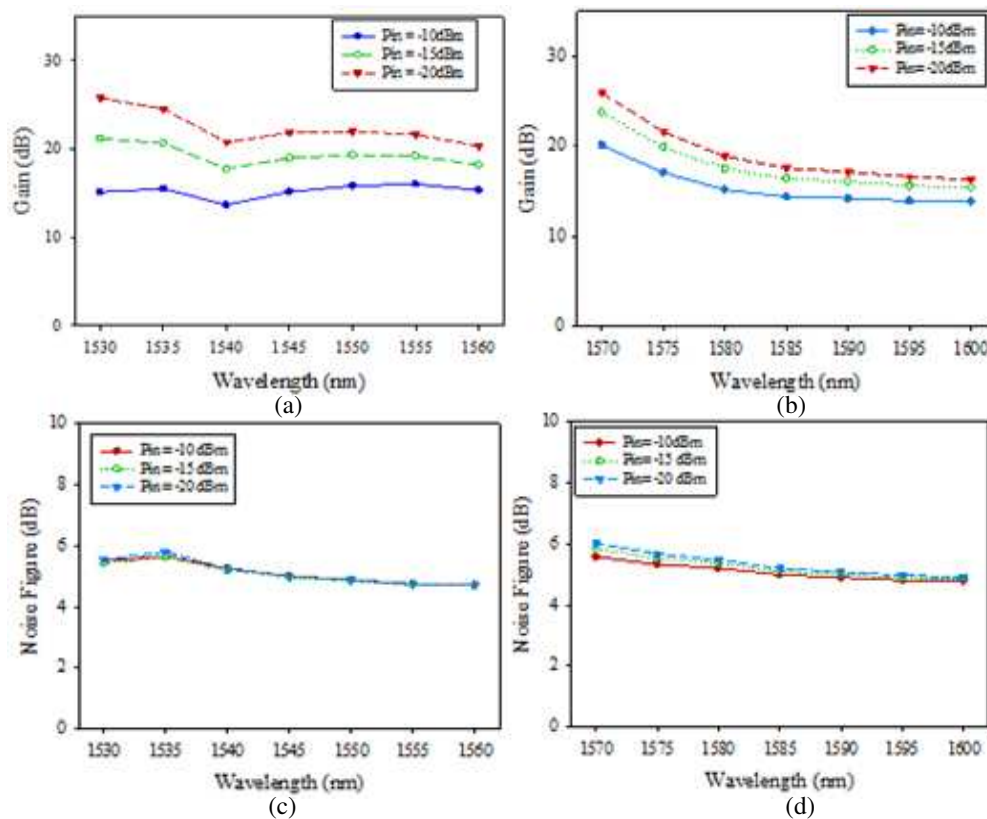


Figure 5: Measured gain and NF profiles using a tunable laser source, respectively, for (a) C-band EDFA gain, (b) L-band EDFA gain, (c) C-band EDFA NF, (d) L-band EDFA NF.

4. RESULTS AND DISCUSSION

Three input power conditions of $-20/-15/-10$ dBm were set for each channel into the C + L band fiber amplifier. Seven WDM channels were measured step by step, in 5 nm spacing, from 1530–1560 nm for the C-band signals. Similarly, seven WDM channels were measured step by step, in 5 nm spacing from 1570–1610 nm for the L-band signals.

4.1. Hybrid Fiber Amplifier

Figures 4(a) and 4(b) show the gain profiles of the EDFA and RFA, respectively, for different launched power (P_{in}) levels. The average gains are 11.35 dB for the C-band EDFA and 10.08 dB for the longer band of L-band RFA, respectively, for -10 dBm launched power for each channel. The power variation between C- and L-bands could be further smaller if the pump reflector have precisely controlled at 43% in reflectance. Figs. 4(c) and Fig. 4(d) show the NF characteristics of the EDFA and RFA, respectively, for different launched power levels (P_{in}). The average NF is 6.13 dB for the C-band EDFA and 4.20 dB for the L-band RFA, respectively.

4.2. EDFA

Figures 5(a) and (b) show the gain profiles of the C-band and L band EDFAs, respectively, for different launched powers (P_{in}). For -10 dBm launched power, the average gains are 15.25 dB for the C band EDFA and 15.54 dB for the L band EDFA, respectively. Figs. 5(c) and (d) show the noise figure (NF) characteristics of the C band and L band EDFAs, respectively, for different launched power levels (P_{in}). The average NFs are 5.11 dB for the C band EDFA and 5.08 dB for the L band EDFA, respectively.

5. CONCLUSION

Two C + L band amplifiers, either hybrid EDFA/RFA or EDFA were experimentally investigated and demonstrated. A single-wavelength pump source was shared between the C-band and L-band fiber amplifier. Gain equalization between these two bands can be further improved by adjusting the pump reflector reflectivity. In hybrid EDFA/RFA. Using 550 mW pump power at 1495 nm and a launched signal power of -10 dBm, the average gains were 11.35 dB for the EDFA and 10.08 dB

for the RFA, respectively. The average NFs were 6.13 dB for the EDFA and 4.20 dB for the RFA, respectively. In C + L band EDFA, with -10 dBm signal power, the average gains were 15.25 dB for the C-band EDFA and 15.54 dB for the L-band EDFA. The average NFs were 5.11 dB for the C-band EDFA and 5.08 dB for the L-band EDFA, respectively.

ACKNOWLEDGMENT

The work was partially support by NSC 100-2622-E-011-014-CC2, NSC 101-2811-E-011-008-MY2, and NSPO-S-100178.

REFERENCES

1. Zhou, X., C. Lu, P. Shum, and T. H. Cheng, "A simplified model and optimal design of a multiwavelength backward-pumped fiber raman amplifier," *IEEE Photon. Technol. Lett.*, Vol. 13, No. 9, 945–947, 2001.
2. Liaw, S.-K. and Y.-S. Huang, "C + L-band hybrid amplifier using FBGs for dispersion compensation and power equalisation," *Electron. Lett.*, Vol. 44, No. 14, 844–845, 2008.
3. Liaw, S.-K., L. Dou, A. Xu, and Y.-S. Huang, "Optimally gain-flattened and dispersion-managed C + L-band hybrid amplifier using a single-wavelength pump laser," *Opt. Commun.*, Vol. 282, No. 20, 4087–4090, 2009.
4. Ono, H. and M. Yamada, "1.58- μ m band gain-flattened Erbium-Doped fiber amplifiers for WDM transmission systems," *Journal of Light. Tech.*, Vol. 17, No. 3, 490–496, 1999.
5. Hecht, J., *Understanding Fiber Optics*, Upper Saddle River, Pearson Prentice Hall, New Jersey, 2006.

Optical-circulator-based Single-frequency Fiber Laser Using Absorber and Subring Cavity in the Linear Cavity

S. K. Liaw¹, H. Wang¹, H. I. Hsu¹, C. S. Shin², and R. Y. Liu³

¹Department of Electronic Engineering

National Taiwan University of Science and Technology, Taipei 106, Taiwan

²Department of Mechanical Engineering, National Taiwan University, Taipei 106, Taiwan

³National Space Organization, Hsin Chu 300, Taiwan

Abstract— We report a single-frequency fiber laser using a saturable absorber Incorporated subring cavity as mode filters. The linear-cavity based fiber laser is constructed using an optical circulator and a partial reflectance fiber Bragg grating as the cavity ends. At 1550.82 nm, the laser output is 6.25 dBm and the signal-to-noise-ratio is 53.2 dB and with linewidth less than 1 MHz in stable operation. The pumping efficiency is 10% improved by recycling the residual pump power to gain medium.

1. INTRODUCTION

Single frequency lasers have attracted much research interest because of their potential applications in long-haul and/or high-speed optical communications [1, 2]. Up to now, various techniques have been investigate to obtain a stable single frequency operation, such as using fiber Bragg gratings (FBGs), the Fabry-Pérot etalon, saturable-absorber filter inside the cavity, passive multiple-ring cavities, integrating two cascaded FFP filters, using an un-pumped erbium doped fiber (EDF) as a narrow bandwidth auto tracking filter for fiber ring lasers and so on [3–5]. Some high output power fiber lasers have also been demonstrated [6, 7]. For short length fiber lasers, low-pump absorption typically limits the output power for single-frequency EDF lasers. Linear cavity fiber laser requires fewer intracavity components and connecting fiber than that of a unidirectional ring-cavity fiber laser. This makes it more attractive. However, the requirement for several to ten meters of cavity length is still unavoidable. Several linear-cavity fiber laser issues were studied such as mode-locked laser or multiple wavelength laser [8, 9]. However, single frequency operation in a linear-cavity fiber laser is seldom addressed when compares to ring-cavity fiber lasers. In this paper, we experimentally demonstrate, for the first time to our knowledge, the linear cavity fiber laser by incorporating a piece of un-pumped EDF as the saturable absorber and a subring cavity as mode filter. Experimental results are given for fiber laser characteristics and wavelength stability.

2. LINEAR-CAVITY FIBER LASER SCHEME

The original diagram of fiber laser cavity shown in Fig. 1(a) consists of an OC, a FBG, a segment of erbium doped fiber (EDF) as the gain medium. The gain medium EDF is 3 m in length which has absorption of 18.79 dB/m at 1531 nm. The Er^{3+} ion density, fiber diameter, numerical aperture and meta-stable lifetime are 5.0×10^{24} ($1/\text{m}^3$), 125 μm , 0.22 and 10 ms respectively. A 1480/1550 nm wavelength division multiplexing (WDM) coupler and a 1480 nm pumping source in backward pumping scheme is used to recycling the residaul pumping power. At the cavity end, the OC has low inter-port insertion of 0.5 dB for the lasing signal and 80% reflectance for the pumping source. Fig. 1(b) shows the proposed single frequency operation by adding one subring cavity and a piece of un-pumped EDF as saturable absorber. The Er^{3+} ion density, fiber diameter, numerical aperture and meta-stable lifetime are 5.0×10^{24} ($1/\text{m}^{3+}$), 125 μm , 0.22 and 10 ms, respectively. And the fiber loss is 6.24 dB/m at 1530 nm.

In experiment, the residual pumping power can travel back to the gain medium to increase the pumping efficiency up to 10%. A C-band FBG has 3 dB bandwidth of 0.2 nm (25 GHz) and 40% transmission for lasing serves as a mode-restricting element to restrict the possible noise. The narrow band FBG thus provide enough discrimination to prevent one polarization state from lasing and keep the laser output at a linearly polarized state. However, the fiber laser can be tuned over the gain bandwidth of the EDF, from 1530 to 1565 nm, using a tunable FBG as either mechanism in our research described previously [10, 11]. To analyze the laser characteristics, Fig. 2(a) shows lasing power stability of < 0.09 dB and wavelength variation of < 0.03 nm are observed in 30 minutes interval. Fig. 2(b) shows laser power and optical signal-to-noise ratio (SNR) versus various lengths

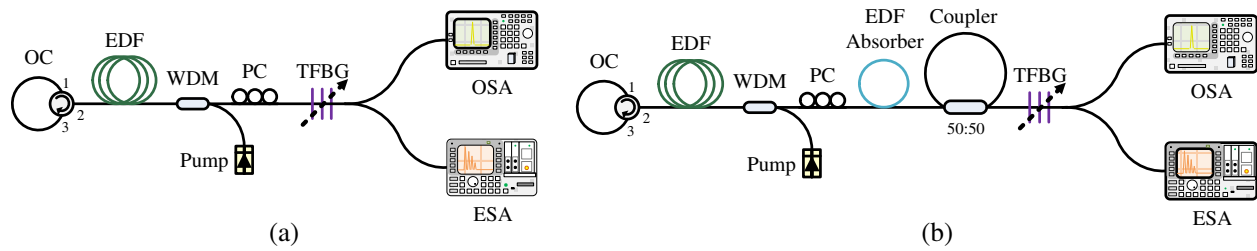


Figure 1: (a) The OC-based linear-cavity fiber laser and (b) the proposed linear-cavity fiber laser including a subring cavity incorporated a piece of absorber.

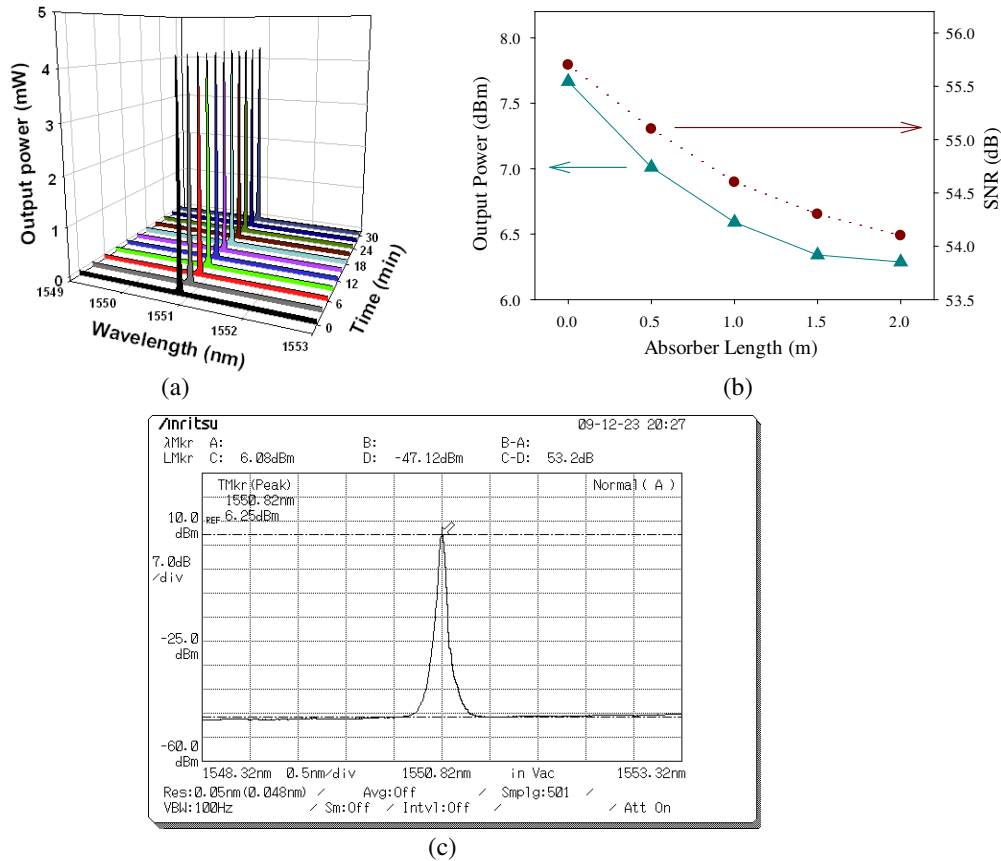


Figure 2: (a) Lasing power stability and wavelength variation in 30 minutes observation, (b) lasing power and optical signal-to-noise ratio (SNR) against various lengths of saturable absorber, and 2(c) lasing wavelength at 1550.82 nm using 2 m saturable absorber.

(namely, 0.0, 0.5, 1.0, 1.5 and 2.0 m) of unpumped saturable absorber. Both of them are decreased in dB but values are still in acceptable range even the saturable absorber length is increased up to 2 m. Fig. 2(c) shows the emission spectrum of the fiber laser at 1550.82 nm using 2 m saturable absorber. The SNR is determined by the amplified spontaneous emission (ASE) and is larger than 53.2 dB and its output power is 6.25 dBm.

3. SINGLE-FREQUENCY OPERATION

The single frequency operation is verified using a subring cavity integrated saturable pump absorber. Consider the effect of subring cavity, the round-trip cavity length of the main cavity and subring cavity are 36 m and 2 m, corresponding to 5.5 MHz and 102.1 MHz of free spectra range (FSR), respectively. The laser mode oscillates only at a frequency that satisfies the resonant conditions of all cavities [2]. One polarization controller (PC) inside the linear cavity is used to align the polarization state of lasing signal for optimization. According to the Vernier effect for mode suppression, the effective FSR becomes the least common multiple number of all FSR's. Considering the effect of saturable absorber, spatial-hole burning effect is generated which leads to slight refractive index

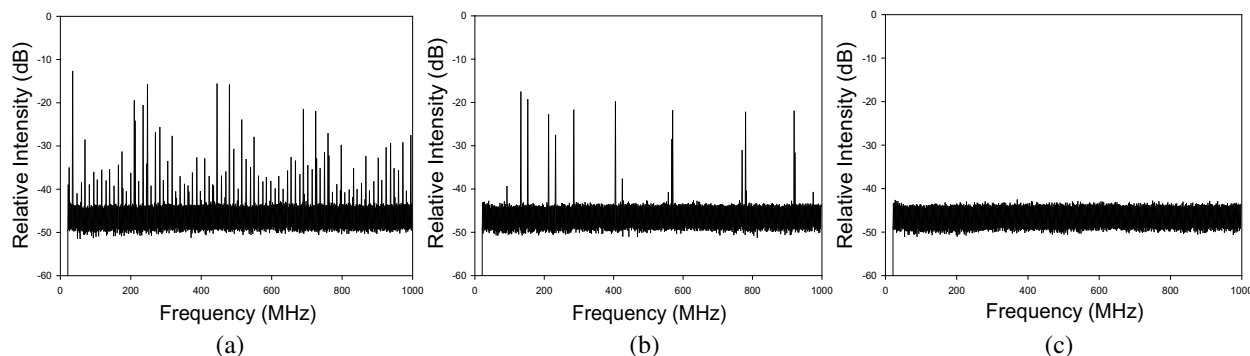


Figure 3: Measured frequency spectra for the proposed fiber laser, (a) without subring cavity or absorber, (b) with subring cavity only, and (c) with both subring cavity and absorber, respectively.

change in the absorber, and a weak Bragg grating with very narrow reflection bandwidth is thus generated. Tests were first carried out for Fig. 3(a) without an un-pumped EDF as the saturable absorber nor subring cavity, (b) with subring cavity only to reduce most of the modes numbers and (c) with both subring cavity and 2m saturable absorber, respectively. The laser can successfully suppress multimode operation and obtain a narrow line width of 967 kHz. The single-frequency operation is realized using this EDF saturable absorber. Compares the optical SNR of Figs. 3(a) and (c), its value is reduced from 57.6 dB to 53.2 dB and the signal power is 3.59 dB decreased after using subring cavity integrated saturable absorber. These experimental results reveal another interesting feature that as the threshold values increase with length of the saturable absorber but the slope efficiency remains constant around 10%. The slope efficiency may further improved if the mode-mismatch between fibers and fusion splice losses are reduced.

4. CONCLUSION

A single frequency linear-cavity OC-based fiber laser has been demonstrated using a subring cavity integrated a saturable absorber. The pumping efficiency is improved up to 10% by recycling the residual pump power to the gain medium using the OC. Experimental results show this fiber laser has high optical SNR of 53.2 dB and narrow line width of less than 1 MHz. Beside the power and wavelength are stable, the fiber laser is compact, easily to construct and cost-effective. With these merits as mentioned above, the proposed linear cavity fiber laser has a number of potential applications in long-haul and high-speed optical communications.

ACKNOWLEDGMENT

The work was partially support by NSC 100-2622-E-011-014-CC2 and NSC 101-2811-E-011-008-MY2. And also NSPO-P-101228.

REFERENCES

1. Wang, F., E. M. Xu, J. J. Dong, and X. L. Zhang, "A tunable and switchable single-longitudinal-mode dual-wavelength fiber laser incorporating a reconfigurable dual-pass Mach-Zehnder interferometer and its application in microwave generation," *Optics Communications*, Vol. 284, No. 9, 2337–2340, 2011.
2. Yeh, C. H., C. W. Chow, Y. F. Wu, Y. H. Lin, B. C. Cheng, and J. H. Chen, "Using optimal cavity loss and saturable-absorber passive filter for stable and tunable dual-wavelength erbium fiber laser in single-longitudinal-mode operation," *Laser Phys. Lett.*, Vol. 8, No. 9, 672–677, 2011.
3. Chen, D., H. Fu, and W. Liu, "Single-longitudinal-mode erbium-doped fiber laser based on a fiber Bragg grating Fabry-Perot filter," *Laser Physics*, Vol. 17, No. 10, 1246–1248, 2007.
4. Lee, C. C., Y. K. Chan, and S. K. Liaw, "Single-longitudinal-mode fiber laser with a passive multiple-ring cavity and its application for video transmission," *Opt. Lett.*, Vol. 23, No. 5, 358–360, 1998.
5. Wei, Y. and B. Sun, "Wavelength spacing tunable dual-wavelength single-longitudinal-mode fiber ring laser based on fiber Bragg gratings," *Laser Physics*, Vol. 19, No. 6, 1252–1256, 2009.

6. Pan, S., X. Zhao, and C. Lou, “Switchable single-longitudinal-mode dual-wavelength erbium-doped fiber ring laser incorporating a semiconductor optical amplifier” *Opt. Lett.*, Vol. 33, No. 8, 764–766, 2008.
7. Polynkin, P., A. Polynkin, M. Mansuripur, J. Moloney, and N. Peyghambarian, “Single-frequency laser oscillator with watts-level output power at 1.5 μm by use of a twisted-mode technique,” *Opt. Lett.*, Vol. 30, No. 20, 2745–2747, 2005.
8. Zhang, M., L. L. Chen, C. Zhou, Y. Cai, L. Ren, and Z. G. Zhang, “Mode-locked ytterbium-doped linear-cavity fiber laser operated at low repetition rate,” *Laser Phys. Lett.*, Vol. 6, No. 9, 657–660, 2009.
9. Fu, Z. H., Y. X. Wang, D. Z. Yang, and Y. H. Shen, “Single-frequency linear cavity erbium-doped fiber laser for fiber-optic sensing applications,” *Laser Phys. Lett.*, Vol. 6, No. 8, 594–597, 2009.
10. Liaw, S. K. and G. S. Jhong, “Tunable fiber laser using a broadband fiber mirror and a tunable FBG as laser-cavity ends,” *IEEE J. Quantum Electronics*, Vol. 44, No. 6, 520–527, 2008.
11. Liaw, S. K., W. Y. Jang, C. J. Wang, and K. L. Hung, “Pump efficiency improvement of a C-band tunable fiber laser using optical circulator and tunable fiber gratings,” *Appl. Opt.*, Vol. 46, No. 12, 2280–2285, 2007.

Generation of Terahertz, Microwave, Radio Waves from a Laser-excited Wire Antenna

Kuan-Yan Huang, Chia-Hsiang Chen, Ming-Hsiung Wu, and Yen-Chieh Huang

HOPE Laboratory, Institute of Photonics Technologies
National Tsinghua University, Hsinchu 30013, Taiwan

Abstract— We report a laser-excited wire antenna (LEWA) generating radiation covering a spectrum from radio to THz frequencies. When the wire was irradiated by a mode-locked Ti:sapphire laser with a 160-fs pulse width, focused to 280 GW/cm^2 intensity on the wire, we detected the THz radiation with a 3-THz bandwidth, reaching the detection limit of our electro-optic sampling system. The amplitude of the detected THz signal was comparable to that generated from a ZnTe emitter under the same experimental condition. The microwave LEWA was driven by a Nd:YAG laser amplifier producing 40-mJ pulse energy in a 460-ps pulse width. We installed the LEWA in front of an S-band metal waveguide, which functions as a spectral filter to pass and reject the radiation above and below the cutoff frequency of 2.08 GHz for the dominant TE_{10} waveguide mode. By using a ring antenna, we measured 1.7 and 2.6 GHz microwave signal before and after the waveguide, respectively. In a separate experiment, the radio wave was further produced from a LEWA with its laser-excited tip biased at an anode voltage +500 V. When irradiated by a laser pulse with 42 mJ energy in a 7 ns pulse width, the LEWA generated radiation power 3–4 orders of magnitude higher than that from a direct laser-excited antenna without the biased voltage. The radiation power scales with the square of the laser induced photocurrent between the antenna tip and the anode (800 A in our case). With a higher biased anode field and shorter-wavelength excitation laser, this antenna has a potential to reach MW-GW radiation power in the microwave or even in the millimeter-wave spectrum.

1. INTRODUCTION

There are many methods to generate a THz radiation pulse. One of the methods is to irradiate a voltage-biased photoconductive switch with an ultrafast laser pulse to create a transient radiation current [1]. In this scheme, the carrier recombination time of the photoconductive material limits the radiation bandwidth. Optical rectification (OR) which is induced by the incidence of ultra-fast laser pulse in a nonlinear optical material can be used to generate THz radiation pulses. The THz radiation generated by this method often suffers from dispersion and absorption of the material. A metal-rod antenna with a driven electronic circuit is often used in transmitting and receiving the radio-wave and microwave signals. Since the relaxation time in a metal is extremely short (on the order of 10–19 s) [2], it has a great potential to generate ultra-broadband radiation from a fast transient current in a metal. According to some earlier experimental data [3, 4], the near-zone radiation signal was measured from an ns-laser excited metal rod with a 4-GW/cm^2 laser intensity on the rod tip. However, the far-zone radiation signal was too small to be measured with the same experimental conditions. The transient current is the source of the radiation, and it is induced by thermionic emission of electrons at the laser irradiating area. Recently, a group in at Rice University reported that a thin metal wire with a cross-section area comparable to the THz wavelengths can function as a low-loss THz waveguide [5], although, to our knowledge, such a thin wire has never been used as an active element to generate THz radiation. Theoretically, it is possible to use a high-power fs laser to kick out electrons from the tip of a short metal wire to emit THz radiation [6]. It was also theoretically proposed that the ponderomotive force of a short pulse laser incident on dense hot plasma could induce low-frequency radiation [7]. In the following, we first report an experimental demonstration of THz-wave radiation from a direct laser-excited wire antenna (LEWA) in comparison with that from a ZnTe OR emitter under the same laser focusing condition. We further present microwave and radio-wave radiation from a sub-ns laser excited thin wire as a supporting evidence to the measured THz radiation.

2. LASER EXCITED THz-WAVE ANTENNA

Figure 1 illustrates the device of the LEWA. The electric-discharge-machining (EDM) brass wire with a 250- μm diameter is LEWA radiation component. An EDM brass wire with a diameter of 0.25 mm is sandwiched between two 2.1-mm thick grounded copper frames each having a 1-mm diameter aperture at the center. One surface of the input frame was ruled with a groove to hold

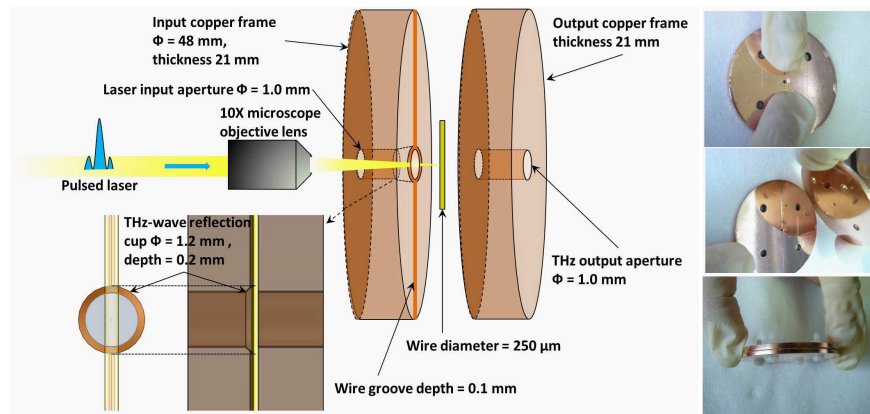


Figure 1: The LEWA device for generating THz radiation. A thin wire with a diameter of 0.25 mm is sandwiched between two circular copper frames each having a 1-mm diameter aperture at the center. One surface of the input frame was ruled with a groove to hold the wire across the aperture. A 10× microscope objective lens focuses the laser pulse on the wire. Photographs below show (left to right) inserting the wire into the groove, covering the input frame with the output one, and bolting together the two frames.

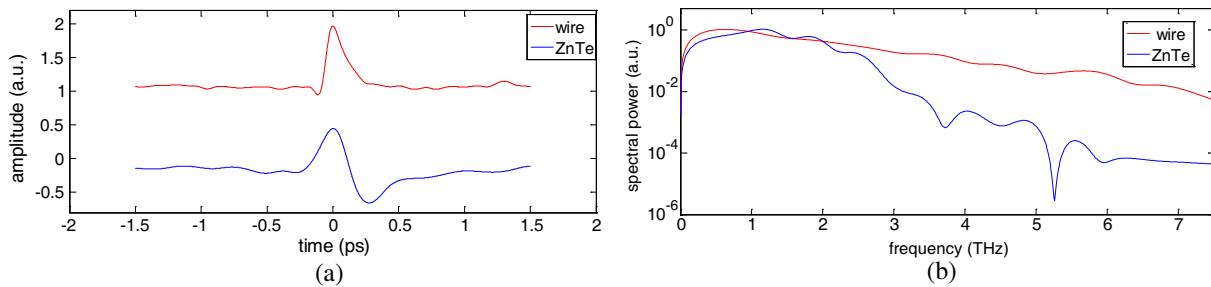


Figure 2: (a) Detected time-domain THz signal from the LEWA and the ZnTe emitter. The two signals are comparable in amplitude. (b) The power spectrum of the LEWA is clearly broader than that of the ZnTe emitter.

the wire across the aperture. The laser aperture on the ruled surface was further machined into a cone shape to collect the THz radiation in the forward direction. The experiments pump laser using a mode-locked Ti:sapphire laser (Mai Tai HP) with pulse width of 160 fs (inferred from a 230-fs autocorrelation width with an assumed Gaussian pulse shape) and a 80-MHz repetition rate, producing a maximum average power of 2.2 W at 800 nm. The laser pulse was first split 250-mW power for the probe beam of the EO sampling system and sent the remaining laser power to the pump beam of the THz emitter. The laser pulse was focused at normal incidence on the wire target with a 5- μm radius by a 10× microscope objective lens. The peak laser intensity on the LEWA wire was about 280 GW/cm². Since a plane polarized light is more absorptive to copper [8], the laser polarization was aligned perpendicular to the axial direction of the wire. At normal incidence, the incident laser is plane polarized to the curved surface of the wire.

Our THz pulse was detected by the standard electro-optic (EO) sampling technique [9, 10] with a 1-mm thick $\langle 110 \rangle$ ZnTe crystal (~ 3 THz detection bandwidth [11]). The THz pulse was collected and focused to the ZnTe crystal at normal incidence by using a pair of off-axis parabolic mirrors with the F number = 1.5. We installed a black polyethylene filter between the two mirrors to block the scattered pump laser. The probe beam passed below the 2nd off-axis mirror to reach the ZnTe crystal with a 10-deg. incidence angle. The experiment was carried out in a clean-room environment with humidity maintained between 40 and 45%.

Figure 2(a) shows the measured THz pulse from the LEWA (red curve) with its full amplitude normalized to one, indicating a temporal width of about 160 fs (FWHM). For comparison, the plot also shows the detected THz signal from a 1-mm thick $\langle 110 \rangle$ ZnTe emitter (blue curve) installed at the same location of the LEWA. Under the same experimental condition, the field amplitude of the THz signal measured from the ZnTe emitter is comparable to that measured from the LEWA. The temporal width of the THz radiation from the LEWA is smaller than that of the ZnTe emitter,

implying a broader radiation bandwidth for the LEWA. Figure 2(b) shows the power spectra of the THz signals generated from the LEWA (red curve) and the ZnTe crystal (blue curve). The 7.5 THz plot range is set by the 40- μm step size of our scanner in the EO sampling system. Indeed, the spectral bandwidth of the LEWA is evidently broader than that of the ZnTe emitter.

The measured 160-fs THz pulse width has reached the detection limit of the 1-mm thick ZnTe crystal ($0.44/3\text{ THz} \sim 150\text{ fs}$ for a Gaussian pulse). We should point out that each spectral curve in Figure 2(b) is a multiplication of the radiation spectrum and the transfer function of the measurement system [11]. Although the plot range has exceeded the detector bandwidth, the ratio of the two curves, which is independent of the measurement system's transfer function, can still be informative for bandwidth comparison.

In the EO sampling measurement, we use an optical chopper to modulate the pump laser beam at 10 Hz with a modulation duty cycle of 50%. The 250- μm diameter EDM wire showed no degradation in radiation performance after tens of hours of laser irradiation. However, a thinner EDM wire with a 100- μm diameter was melt in a few minutes under the same incident laser power.

3. LASER EXCITED MICROWAVE ANTENNA

We attached the same EDM wire with a 250- μm diameter to the metal frame of an S-band copper waveguide, as illustrated in Figure 3. The waveguide's three dimension width (along x), height (along y), and length (along z) are 7.2, 3.4, 30.0 cm, respectively. Both ends of the wire were grounded to the waveguide edges. The waveguide having a cutoff frequency of 2.08 GHz and dominant mode is TE_{10} . The next higher-order mode is TE_{20} , having a cutoff frequency of 4.16 GHz. The axial direction of the LEWA is aligned along y and centered to the waveguide, so that TE modes are the preferred modes of excitation in the waveguide. To efficiently excite the S-band radiation with a short and strong enough laser pulse, we employed a flash-lamp pumped Nd:YAG laser amplifier to increase the pulse energy of a passively Q-switched Nd:YAG laser from 70 μJ to about 40 mJ in a 460-ps laser pulse width. The laser was focused to the wire with an intensity of 30 TW/cm^2 for an estimated laser radius of 14 μm .

Figures 4(a) and (b) show the temporal radiation signals detected by a receiver antenna installed before and after the waveguide, respectively. Figures 4(c), (d) are the corresponding power spectra of (a), (b). It is seen from Figure 4(c) that the reflected radiation is peaked at 1.7 GHz, having a high frequency cutoff at about 2 GHz. In Figure 4(d), the transmitted radiation is peaked at 2.6 GHz, having a low frequency cutoff slightly above 2 GHz. The copper waveguide simply functions as a radiation filter, passing and rejecting radiations with frequencies above and below the frequency cutoff of the TE_{10} mode at 2.08 GHz.

4. LASER EXCITED VOLTAGE-BIASED RADIO WAVE ANTENNA

Figure 5 shows our experimental setup of the proposed voltage-biased antenna. The transmitting antenna is a 20-cm long copper wire with a 2-mm diameter. One end of the antenna is grounded through a 0.05-resistor and the other end is mounted on an insulator frame as a photocathode. A laser pulse is incident on the photocathode to induce electron emission in air. The photoemission from the photocathode generates a pulsed return current in the antenna rod entering the ground.

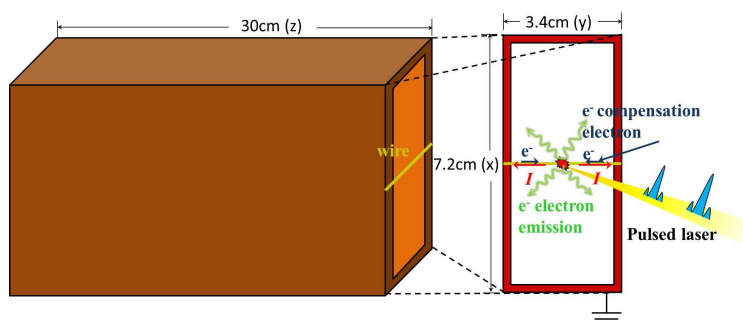


Figure 3: The experimental setup to further verify radiation from a direct laser excited thin wire. A sub-n laser pulse is incident on a thin wire with its both ends grounded to a copper waveguide. The copper waveguide functions as a spectral filter to pass and reject the radiation above and below the cutoff frequency of the dominant TE_{10} mode.

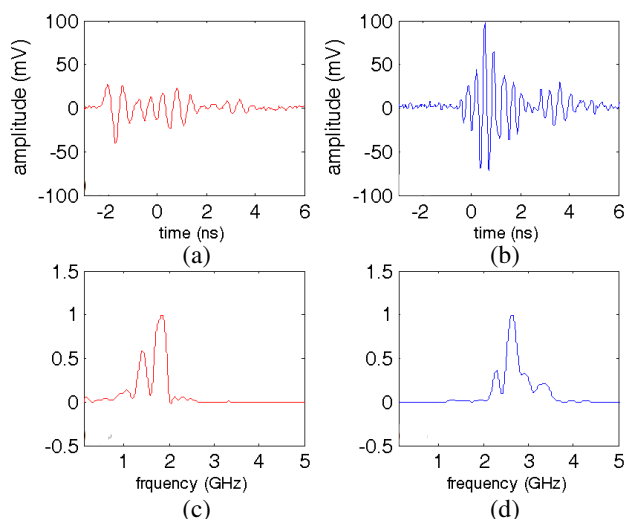


Figure 4: (a), (b) The temporal radiation signals measured by a receiver antenna before and after the waveguide, respectively. (c) The power spectrum of (a), showing reflected radiation with spectral components below the TE_{10} cutoff frequency. (d) The power spectrum of (b), showing transmitted spectral components above the TE_{10} cutoff frequency.

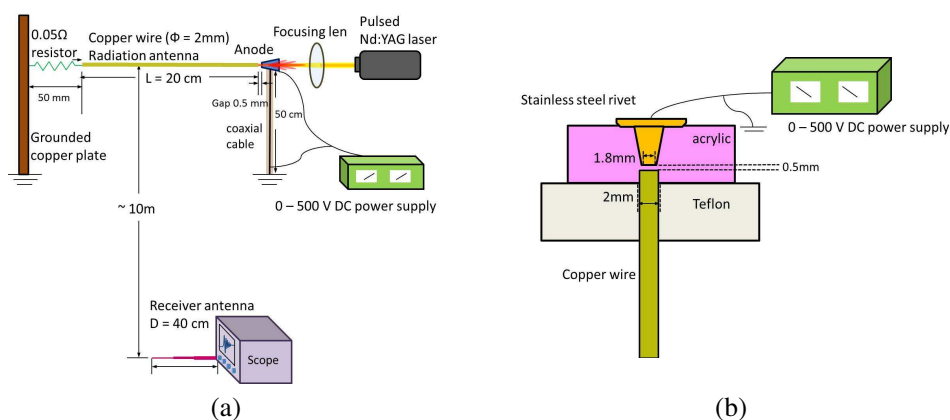


Figure 5: (a) Experimental setup of the photo-plasma switched radiation antenna. (b) The detail equipment of voltage-biased anode, the anode consists of a hollow rivet with a 1.8 mm diameter holding on a thin acrylic plate. The Teflon disc locks with the acrylic plate mounting on an optical transition stage.

The antenna current can be deduced from a measured voltage across the 0.05-resistor. In front of the photocathode we installed a tube anode with an inner diameter of 1.8 mm and a length of 3 mm. The gap between the tube anode and photocathode is 0.5 mm. The tube anode is biased with a voltage between 0 and 500 V during our experiment. At 500 V, the peak electric field on the cathode surface is about 1 kV/mm, which is approximately one third of the air-breakdown field. A Nd:YAG Q-switched laser, producing a maximum energy of 42 mJ at 1064 nm over a 7 ns pulse width, is incident on the antenna tip with an intensity of 10.2 TW/cm^2 . We detect the electromagnetic radiation by using a 40-cm monopole antenna situated at a location 10 m away from the transmitting antenna. The receiving antenna is directly connected to the coaxial input port of an oscilloscope with 50-termination. Both the longitudinal axes of the transmitting and receiving antennas were aligned along the primary polarization direction of the radiation field.

Figure 6 shows (a) the temporal and (b) the spectral signals of the far-field radiation measured at 10 m away from the photo-plasma switched antenna for several anode voltages. It is seen from the plots that, without the anode voltage, the signal is undetectable and buried under noise. This could be the reason that no far-field radiation data were presented in previous publications [4, 5]. On the other hand, with the anode voltage $> 100 \text{ V}$, clear radiation signals were recorded in the far zone by our 40-cm monopole receiver antenna. The spectrum of the measured far-zone signal is

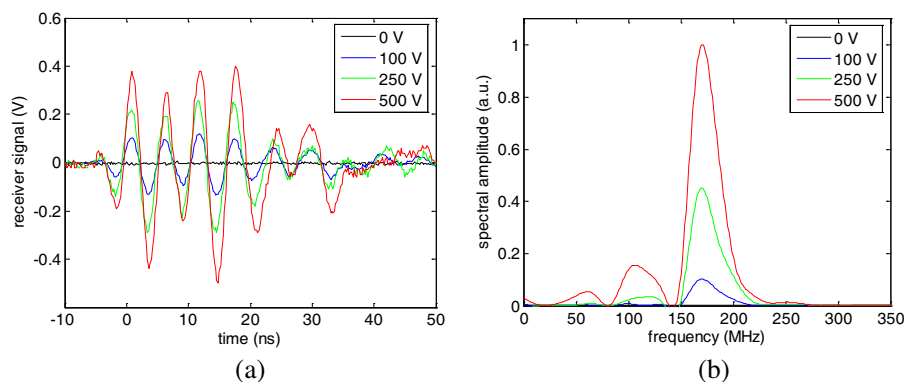


Figure 6: (a) The temporal and (b) the spectral signals of far-field radiation measured at 10 m away from the photo-plasma switched antenna for several anode voltages. Without the anode voltage, the radiation signal is undetectable by our receiver antenna. The radiation spectrum is peaked at ~ 170 MHz, which is slightly larger than the inverse of the laser-pulse duration.

peaked at about 170 MHz, which is slightly larger than the inverse of the 7-ns laser pulse width due to the multi-photon emission process at the photocathode. The low frequency spectral components are attributable to oscillations in some circuit elements.

5. CONCLUSION

In this paper, we report the THz-wave radiation, microwave radiation and radio waves from a thin copper wire directly be illuminated by a 160 fs laser a sub-ns laser and ns laser, respectively. A thin metal wire helps to confine a highly directional current for radiation generation. The relaxation time order of metal is 10^{-19} s, insinuate the possibility of generating ultra-broadband radiation from a fleet transient state current and a dominant mechanism is photoemission in an LEWA [3, 12]. In our experiment, the work function of the copper wire is 4.7 eV [13], which is about three times of the incident photon energy. The pulse width of generated THz radiation pulse is shorter than the original incident laser pulse because of the multi-photon emission process, giving rise to a radiation bandwidth wider than the incident laser bandwidth. For the THz LEWA experiment, we could not study the pulse-shortening effect in details due to the bandwidth limit of our ZnTe detector. Actually, we did not calibrate our EO sampling detector to determine the absolute power radiated but the measured radiation amplitude was comparable to that generated from a ZnTe THz emitter under the same laser system. To compare the THz LEWA and THz air-plasma technique [14], the first one just need a moderate laser power from a Ti:sapphire laser oscillator but the other one necessitate a high-power laser amplifier. In our design, the THz LEWA emitter is simply a short EDM wire, whose cost is cheap, compared with that of a THz photoconductive antenna or an OR crystals. The LEWA radiation technique presented in this paper is remarkably simple, economic, and broadband.

ACKNOWLEDGMENT

This work is supported in part by National Science Council under Contract NSC 99-2112-M-007-013-MY3 and by the Top-Center Program of NTHU under Project Code 100N7015E1.

REFERENCES

1. Auston, D. H., K. P. Cheung, and P. R. Smith, "Picosecond photoconducting Hertzian dipoles," *Appl. Phys. Lett.*, Vol. 45, 284–286, 1984.
2. Cheng, D. K., *Field and Wave Electromagnetics*, Addison-Wesley, Massachusetts, 1989.
3. Meadors, J. G. and M. A. Poirier, "Laser induced transient excitation of conducting targets by thermionic emission," *J. Appl. Phys.*, Vol. 52, 449–454, 1981.
4. Peake, W. H., J. G. Meadors, and M. A. Poirier, "Laser-induced transient excitation of conducting targets," *Appl. Phys. Lett.*, Vol. 37, 844–845, 1980.
5. Wang, K. and D. M. Mittleman, "Metal wires for terahertz wave guiding," *Nature*, Vol. 432, 376, 2004.
6. Li, Z.-C. and J. Zheng, "Terahertz radiation from a wire target irradiated by an ultra-intense laser pulse," *Physics of Plasma*, Vol. 14, 054505, 2007.

7. Uryupin, S. A. and A. A. Frolov, “Generation of low-frequency radiation by dense hot plasma under pondermotive action of a short laser pulse,” *Journal of Experimental and Theoretical Physics*, Vol. 114, 878, 2012.
8. Srinivasan-Rao, T., J. Fischer, and T. Tsang, “Optical field enhanced multiphoton photoemission in copper mirrors,” *Appl. Phys. Lett.*, Vol. 63, 1595, 1993.
9. Wu, Q. and X.-C. Zhang, “Ultrafast electrooptic field sensors,” *Appl. Phys. Lett.*, Vol. 68, 1604, 1996.
10. Nahata, A., A. S. Weling, and T. F. Heinz, “A wideband coherent terahertz spectroscopy system using optical rectification and electrooptic sampling,” *Appl. Phys. Lett.*, Vol. 69, 2321, 1996.
11. Gallot, G., J. Zhang, R. W. McGowan, T. I. Jeon, and D. Grischowski, “Measurements of the THz absorption and dispersion of ZnTe and their relevance to the electro-optic detection of THz radiation,” *App. Phys. Lett.*, Vol. 74, 3450, 1999.
12. Chen, C.-H., K.-Y. Huang, M.-H. Wu, and Y.-C. Huang, “Photo-plasma-switched radiation antenna,” *Journal of Electromagnetic Waves and Applications*, Vol. 26, Nos. 17–18, 2452–2458, 2012.
13. Lide, D. R., *CRC Handbook of Chemistry and Physics*, CRC, New York, 1997.
14. Dai, J., X. Xie, and X. C. Zhang, “Detection of broadband terahertz waves with a laser-induced plasma in gases,” *Phys. Rev. Lett.*, Vol. 97, 103903, 2006.

Arc-induced Long Period Fiber Gratings Based on Flat-clad Fibers

Zhi-Zong Zheng, Chai-Ming Li, Cheng-Ling Lee, and Jing-Shyang Horng

Department of Electro-Optical Engineering, National United University, Miaoli 360, Taiwan, R.O.C.

Abstract— This work demonstrates a successful fabrication of an arc-induced long period fiber grating (AI-LPFG) based on a flat-clad fiber (FCF) with arbitrary grating periods. The FCF with asymmetric structure would make the characteristics of the FCF-AI-LPFG anisotropic. The spectral transmissions and sensing capabilities of the proposed FCF-AI-LPFGs have been experimentally investigated. The measurement results show that the optical and sensing properties of the FCF-AI-LPFGs are very similar to those of the general LPFGs based on the single-mode fiber (SMF).

1. INTRODUCTION

Arc-induced long-period fiber gratings (AI-LPFGs) written by electric-arc discharge techniques [1] are so popular because they do not need to be hydrogen loaded or highly germanium-doped for the expensive UV-laser exposure fabrication [2] or custom grooved [3]. Many kinds of AI-LPFGs, based on single mode fibers (SMF) [4], dual concentric core fibers, special-doped (nonstandard) fibers, hollow core fibers [5], pure-silica-core fibers [6] photonic crystal fibers [7], and photonic band gap hollow fibers have been presented. By use of the heating and thermal effect, a flexible and low-cost arc-induced technique which can fabricate a periodical LPFG structure in any kinds of material and structure waveguides will become possible and easier.

In this study, we experimentally demonstrated a new AI-LPFG by using another type of fiber that called flat-clad fiber (FCF). The used FCF is only a traditional single-mode fiber but with a flat-cladding. This FCF with asymmetric structure of cladding diameters respectively of about $120\ \mu\text{m}$ and $80\ \mu\text{m}$ causes the sensing characteristics of the AI-LPFG to be anisotropic. Experimental results show that the optical and sensing properties of the FCF-AI-LPFGs are very similar to those of the general LPFGs based on the single-mode fiber (SMF). However, fabricating method of arc-induced LPFG by point to point writing would be much easier, more flexible, and moreover the expensive UV-writing laser is not required. We believe such a simple and inexpensive FCF-AI-LPFG may be very useful in many applications, especially in directional bending measurement.

2. EXPERIMENTS AND RESULTS

The experimental set up for fabricating the proposed FCF-AI-LPFG is shown in Fig. 1. The original FCF is only a traditional single-mode fiber with flat-cladding as shown in the inset (a) of Fig. 1. The FCF-AI-LPFG was fabricated simply by using an Ericsson FSU-975 commercial fusion splicer, and as it does not rely on any particular tapering station or precise optical stages. The bare FCF without its protective coating was placed between the electrodes of a fusion splicer, while its electrode-arc direction was fixed along the short axis of cladding of the FCF. Given an

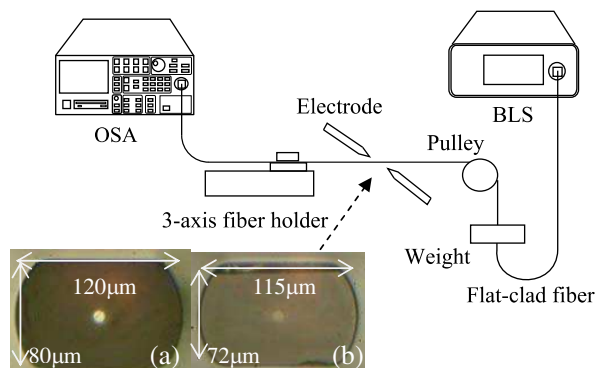


Figure 1: Schematic diagram of the experimental setup and cross-sectional views of the FCF with (a) before and (b) after arc-discharged.

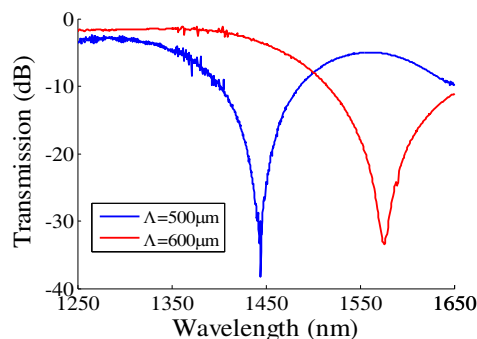


Figure 2: The transmission spectra of the fabricated FCF-AI-LPFGs with $\Lambda = 500$ and $600\ \mu\text{m}$, respectively.

appropriate arc power, arc duration, and stretching distance, the arc processes can be successively fabricated to form the proposed FCF-AI-LPFGs. The cross-sectional views of the flat-clad fiber before and after arc-discharging are also displayed in the inset (a) and (b) of the Fig. 1 respectively. One can see the photography; there is a slightly different size of the AI-FCF to the original FCF. The diameter of the cladding was reduced to a cladding diameter of about $115\ \mu\text{m}$ (long axis: d_L) and $72\ \mu\text{m}$ (short axis: d_S) from original diameters of $120\ \mu\text{m}$ (long axis) and $80\ \mu\text{m}$ (short axis) respectively. In the measurement, a broadband light source (BLS) is launched into the fiber device and the transmission spectra are readily measured by using an optical spectrum analyzer (OSA).

The transmission spectra of the fabricated FCF-AI-LPFGs with grating period of $\Lambda = 500$ and $600\ \mu\text{m}$ are respectively shown in Fig. 2. We can fabricate the FCF-AI-LPFGs has only one resonant wavelength dip within the whole measurement range of $1250\sim 1650\ \text{nm}$. The resonant wavelength dip at $1444\ \text{nm}$ even over $35\ \text{dB}$ is achieved by the method in the case of $\Lambda = 500\ \mu\text{m}$ FCF-AI-LPFG with only six periods.

To further investigate the sensing capability of the FCF-AI-LPFGs, the devices are tested under strain, bending and refractive index sensing. Spectral responses of the $\Lambda=600\ \mu\text{m}$ FCF-AI-LPFG with different strains are displayed in Fig. 3. The wavelength dip is shifted toward the shorter wavelength side as the strain is increased. The strain was applied by moving the fiber holder on the optical translation stage. The strain is expressed by the parameter ε , $\varepsilon = \Delta L/L_0$, where the L_0 is original length, and ΔL denotes stretched length. The sensitivity of the strain responses of the proposed FCF-AI-LPFG are shown in Fig. 4. The strain sensitivity of the wavelength shift has a linear relationship with $-2.8\ \text{pm}/\mu\varepsilon$ in the case. Furthermore, wavelength shifts of the dip of the same device with different bending curvature are also plotted in Fig. 5. Bending sensitivity presents a quadratical relation to the bending curvature (m^{-1}), as shown in Fig. 6.

Figure 7 shows the experimental spectra of the proposed FCF-AI-LPFG at different surrounding. The wavelength dip is shifted toward the shorter wavelength side as the refractive index increased and further demonstrated similar results to those of the general UV-writing LPFG.

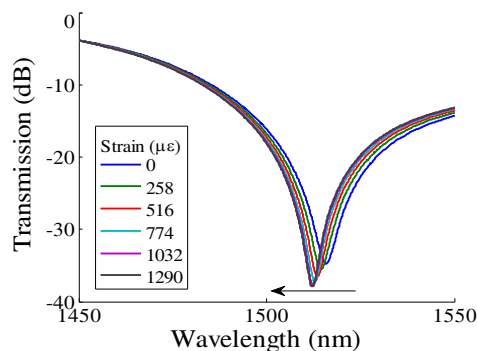


Figure 3: Transmission spectra of the $\Lambda = 600\ \mu\text{m}$ FCF-AI-LPFG with different strains.

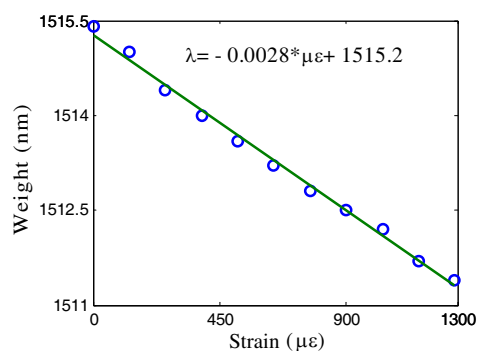


Figure 4: Wavelength shifts of the dips of the FCF-AI-LPFG with different strains based on the results of Fig. 3.

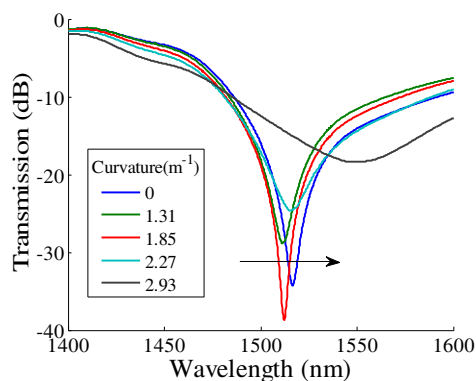


Figure 5: Transmission spectra of the $\Lambda = 600\ \mu\text{m}$ FCF-AI-LPFG with different bending curvature.

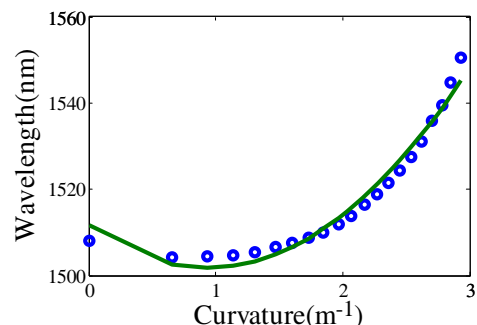


Figure 6: Dip wavelength shifts of the FCF-AI-LPFG with different bending curvature based on the results of Fig. 5.

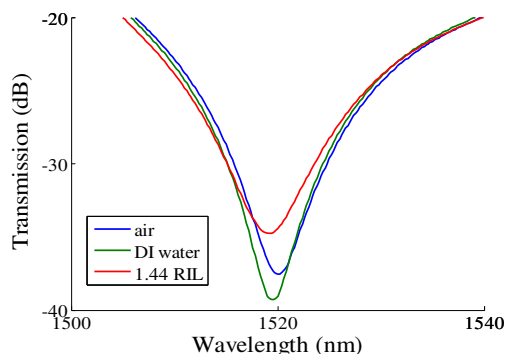


Figure 7: Transmission spectra of the $\Lambda=600\ \mu\text{m}$ FCF-AI-LPFG with different external refractive index surrounding.

3. CONCLUSIONS

Arc-induced long-period fiber gratings based on the flat-clad fiber have been fabricated and demonstrated in the study for the first time. The successfully fabricated FCF-AI-LPFGs with different grating period have been obtained and measured under sensing parameters of strain, bending and external refractive index. The properties of the proposed devices with simple, flexible fabrication, large extinction ratio (35 dB) and narrow bandwidth even with anisotropic properties which are very practical in many fields of applications, especially in directional bending measurement. The related results will be discussed in the forthcoming paper.

REFERENCES

1. Hwang, I. K., S. H. Yun, and B. Y. Kim, "Long-period fiber gratings based on periodic microbends," *Optics Letters*, Vol. 24, No. 18, 1263–1265, 1999.
2. Dianov, E. M., D. S. Stardubov, S. A. Vasiliev, A. A. Frolov, and O. I. Medvedkov, "Refractive-index gratings written by near-ultraviolet radiation," *Optics Letters*, Vol. 24, No. 4, 221–223, 1997.
3. Cardenas-Sevilla, G. A., D. Monzon-Hernandez, I. Torres-Gomez, and A. Martinez-Rios, "Mechanically induced long-period fiber gratings on tapered fibers," *Optics Communications*, Vol. 282, No. 14, 2823–2826, 2009.
4. Monzón-Hernández, D., I. Torres-Gómez, A. Martínez-Ríos, and K. Salas-Alcántara, "Fine-tuning of the transmission characteristics of an arc-induced longperiod fiber grating by local heating," *Proc. of SPIE*, Vol. 7503, 75033Q-1, 2009.
5. Iadicicco, A., S. Campopiano, and A. Cusano, "Long-period gratings in hollow core fibers by pressure-assisted arc discharge technique" *IEEE Photonics Technology Letters*, Vol. 23, No. 21, 1567–1569, 2011.
6. Rego, G. and O. Ivanov, "Investigation of the mechanisms of formation of long-period gratings arc-induced in pure-silica-core fibres" *Optics Communications*, Vol. 284, No. 8, 2137–2140, 2011.
7. Dobb, H., K. Kalli, and D. J. Webb, "Measured sensitivity of arc-induced long-period grating sensors in photonic crystal fibre" *Optics Communications*, Vol. 260, No. 1, 184–191, 2006.

Transmitted Characterization of 625 Mbps/15 GHz ROF Signal Using a Direct Modulated Baseband Signal and Twice Optical Carrier Suppression Modulation

Yu-Peng Chang¹, Wen-Jeng Ho¹, Jhe-Min Lin¹, Peng-Chun Peng¹, and Hai-Han Lu^{1,2}

¹Institute of Electro-Optical Engineering, National Taipei University of Technology, Taipei 106, Taiwan

²Department of Information Technology and Communication, Tunghnan University
New Taipei City, 222, Taiwan

Abstract— In this paper, we experimentally demonstrated the optical frequency quadrupling generation and characterized a directly modulated 625 Mbps baseband data carried up on a 15 GHz radio over fiber (ROF) signal by using twice optical carrier suppression (OCS) modulation. The measured results show that the 625 Mbps/15 GHz signal was successfully transmitted and the low power penalty of only 0.5 dB was obtained. The effectiveness of the proposed technique was feasible without high frequency mixer and narrow band optical notch filter to generate 15 GHz frequency quadrupling ROF signal.

1. INTRODUCTION

The distribution of radio frequency (RF) signals over optical fiber link has advantages of low attenuation, high capacity, broadband bandwidth, and low cost. Under these advantages, radio over fiber (ROF) system is interested for the applications such as mobile communications, wireless large area networks, and fixed wireless access services [1]. The optical millimeter-wave (mm-wave) used in ROF is a promising frequency resource for optical-wireless access networks. But the optical mm-wave is difficult to generate in electrical domain which it must be spend more costs to purchase electrical configure devices to achieve. Hence, it is a attracting way that mm-waves/microwave is generated and processed in optical domain. The most common way to generate an mm-wave signal was to use the optical heterodyne technique. The important issue associated with this technique was that the two wavelengths applied to a photo-detector (PD) for heterodyne must be phase-correlated. Recently, a few schemes for realizing this technique have been reported, such as using single-sideband modulation (SSB) with low-frequency local oscillator (LO) signals [2], using an optical phase-locked loop (OPLL) as two pumps to generate the four-wave mixing (FWM) process in the semiconductor optical amplifier (SOA) [3], and SSB modulation based on an injection-locked distributed-feedback laser diodes (DFB-LDs) laser [4]. The first method must be based on a stable notch filter for wavelength collimation, and it was not easy to achieve because of the sensitivity of environmental factors. The second method, to achieve effective OPLL, the two lasers should be selected to have narrow line-widths, and have a positive impact on the signal quality of the microwave/mm-wave. The last method using external-injection technology has a difficult problem in wavelength collimation.

In this work, we proposed the generation of optical microwave using two cascaded low-speed optical intensity modulators (IMs) and a tunable electrical phase shifter without any optical filter. A directly modulated baseband signal can be casually up-conversion on the microwave frequency at minimum transmission point of the modulator. Finally, we analyzed the transmitted characterization of 625 Mbps/15 GHz ROF signal.

2. EXPERIMENT SETUP

A direct modulated optical carrier based on cascade carrier suppression modulation quadruple frequency technique for micrometer-wave ROF signals over PON was proposed as shown in Fig. 1. A distributed-feedback laser diodes (DFB-LDs), operated at central wavelength of 1550 nm and directly modulated with a 625 Mbps baseband signal, was used as an optical carrier. Instead of using external modulation with a high frequency electrical mixer, the proposed direct modulation in this work is a low cost approach. The 1550 nm modulated optical carrier is then coupled into the first optical modulator (IM1) via a polarization controller (PC). A 3.75 GHz RF driving signal was split two branches, one branch directly applied to IM1. Another branch of RF signal was first coupled to a tunable electrical phase shifter, which can adjust the phase of RF signal, then applied to the second modulator (IM2). The DC bias voltage applying on two modulators was adjusted to

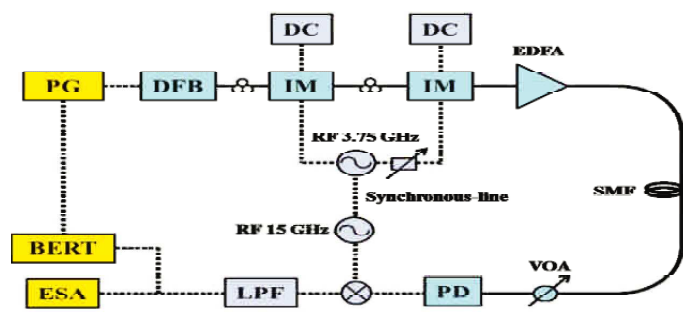


Figure 1: Experiment setup (PG: pattern generator; VOA: variable optical attenuator; LPF: low pass filter).

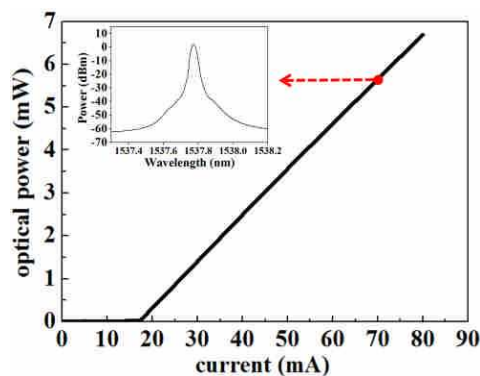


Figure 2: L-I curve of the used DFB-LD at 25°C and the inset is optical spectrum of DFB-LD with directly modulating 625 Mbps baseband signal.

a value of the minimum transmission point of optical modulator to obtain two second-order optical sideband with optical carrier suppression. Two polarization controllers are used to adjust the polarization states of the light-waves entering the MZMs to minimize the polarization-dependence loss. The technique of quadruple frequency will be discussed in the following [5].

The output of continue light wave from a DFB-LD can be expressed as

$$E_o(t) = E_o \cos(\omega_o t)$$

where E_o is optical field amplitude, and ω_o is the frequency of laser source. The voltage of a RF driving signal for the first modulator can be expressed as

$$V_1(t) = V_{e1} \cos(\omega_e t + \varphi_1)$$

where V_{e1} is amplitude of the electric signal, and ω_e and φ_1 are frequency and phase of electric signal, respectively. If the DC voltage of the modulator is tuned to suppress all even-order optical sideband, the optical field at the output of the first modulator can be approximately expressed as

$$E_{out1}(t) = J_1(\beta_1) E_o \{ \cos[(\omega_o - \omega_e)t - \varphi_1] + \cos[(\omega_o + \omega_e)t + \varphi_1] \}$$

where β_1 is the phase modulation index of the first modulator. The voltage of RF driving signal for the second modulator can be expressed as

$$V_2(t) = V_{e2} \cos(\omega_e t + \varphi_2)$$

where V_{e2} is amplitude of the electric signal, and φ_2 is phase of electric signal. The DC bias voltage of the second modulator was also operation in the case to suppressing all even-order optical sidebands. Similarly, the optical field at the output of this modulator can be appropriately expressed as

$$\begin{aligned} E_{out2}(t) = & J_1(\beta_1) J_1(\beta_2) E_o \{ \cos[(\omega_o - 2\omega_e)t - \varphi_1 - \varphi_2] \\ & + J_1(\beta_1) J_1(\beta_2) E_o \{ \cos[(\omega_o + 2\omega_e)t + \varphi_1 + \varphi_2] + J_1(\beta_1) J_1(\beta_2) E_o \cos(\omega_o t - \varphi_1 + \varphi_2) \\ & + J_1(\beta_1) J_1(\beta_2) E_o \cos(\omega_o t + \varphi_1 - \varphi_2) \} \end{aligned}$$

where β_2 is the phase modulation index of the second modulator. The phase deviation, $\varphi_1 - \varphi_2$, can be adjusted by the tunable electrical phase shifter. The overlap of two sidebands on the ω_o will be interfered and contracted when the phase deviation is $\pi/2$. Therefore, the two optical sidebands separated by four times the RF driving frequency of 15 GHz are obtained.

The obtained 625 Mbps/15 GHz signal was then amplified by an Erbium doped fiber amplifier (EDFA) for optical loss compensation before transmitted through a 10 km single mode fiber (SMF). After transmission, the optical carrier coupled into an optical attenuator in keeping with the sensitivity of photo-detector (PD). Then, the ROF signal was detected by a PD with 3-dB bandwidth of 20 GHz and down-converted by an electrical mixer with a 15 GHz RF signal. The optical spectrum and the electric spectrum were characterized by optical spectrum analyzer (OSA,

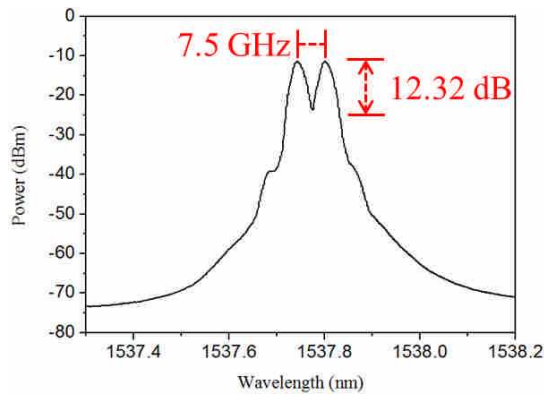


Figure 3: Optical spectrum of the output of the first the intensity modulator.

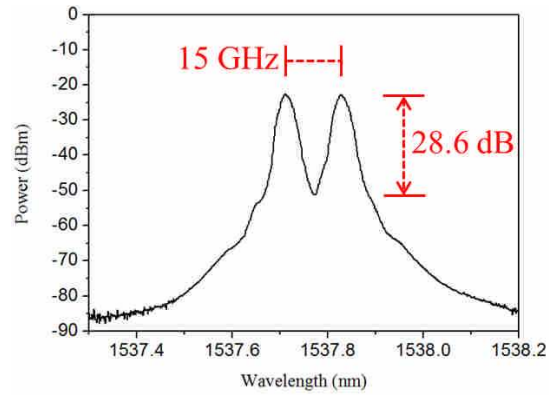


Figure 4: Optical spectrum of the output of second intensity modulator.

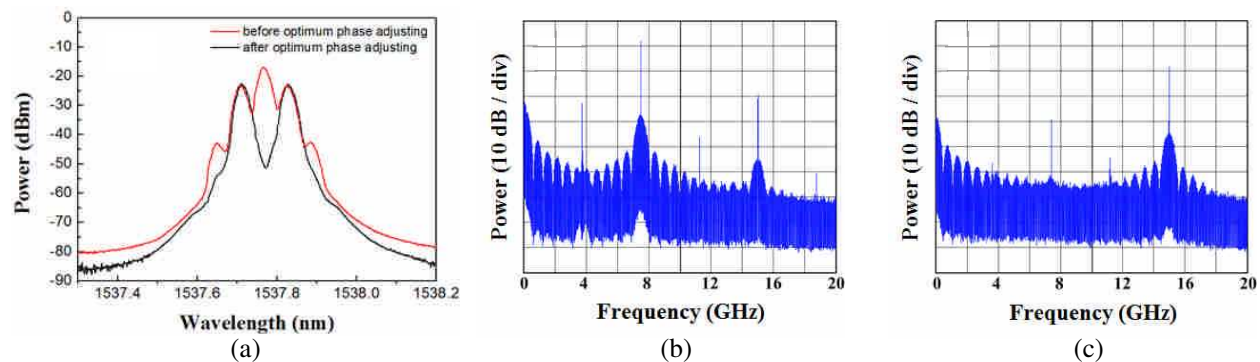


Figure 5: Optical and electrical spectrum measured at the output of the second modulator. (a) Optical spectrum before optimum phase adjusting or after optimum phase adjusting. (b) Electrical spectrum without optical overlap sideband suppression. (c) Electrical spectrum with optical overlap sideband suppression.

Advantest Q8384) and electrical spectrum analyzer (ESA, Rohde & Schwarz FSEK30), respectively. In addition, the recovered 625 Mbps baseband signal was examined in electrical eye diagram and bit-error-rate (BER) by a 20 GHz digital communication analyzer (DCA) and a signal quality analyzer (SQA).

3. RESULTS AND DISCUSSION

Figure 2 shows the light-current (L-I) characteristics of the used distributed feedback laser diode at temperature of 25°C the inset is the spectrum of DFB laser diode biasing at DC 70 mA and modulating with 625 Mbps baseband signal. The total power of DFB laser diode is 6.53 dBm and the central wavelength is 1537.8 nm.

Figure 3 is the output spectrum of the first intensity modulator. Optical carrier suppression and two sidebands are observed when the 3.75 GHz RF driving signal was applied on this modulator. The spacing of two sidebands is 7.5 GHz and the carrier suppression ratio is 12.32 dB. Fig. 4 shows the output spectrum of the second intensity modulator with carrier suppression after an optimum phase adjusting of RF signal. Here, we can see that the spacing of two sidebands is up-conversion to 15 GHz and the carrier suppression ratio is increasing to 28.6 dB.

Figure 5(a) shows the optical spectrum at the output of the second modulator before and after adjusting the phase of RF signal between two modulators to an optimum value by a tunable electrical phase shifter. Fig. 5(b) shows the electric spectrum at the output of the second modulator before phase adjusting to optimum value. Here, the highest intensity of this electric spectrum is at the 7.5 GHz due to the constructive interference of the overlap sideband. Fig. 5(c) shows the electric spectrum with the highest intensity of 15 GHz after the phase adjusting to an optimum value which because the overlap sideband are destructive interference.

The 625 Mbps/15 GHz ROF signal was down-converting by an electrical mixer with a 15 GHz RF signal. The eye diagrams of the 625 Mbps signals measured at back-to-back (B2B) and 10 km

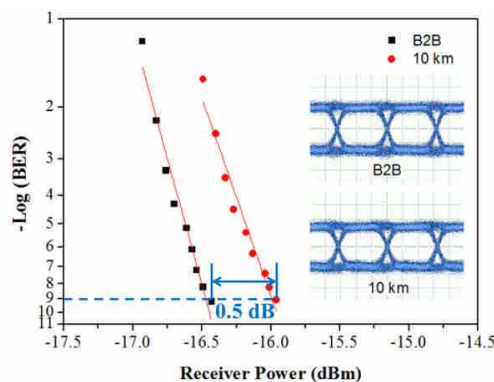


Figure 6: Bit-Error-Rate measurement curves and eye diagrams of 625 Mbps/15 GHz signals of BTB and with 10 km transmission.

fiber link are shown in the inset of Fig. 6. The qualities of the obtained eye diagrams are very clear at B2B and after transmitting 10 km SMF. The Bit-Error-Rate (BER) as a function of the receiver power at B2B and transmitting 10 km SMF is shown in Fig. 6. The receiver powers at B2B and 10 km are -16.43 dBm and -15.96 dBm, respectively. The power penalties which are about 0.5 dB after 10 km transmission are presented in our system.

4. CONCLUSIONS

The proposed a direct modulated optical carrier based on cascade carrier suppression modulation quadruple frequency technique for microwave ROF signals over PON was successfully demonstrated in this paper. The DC bias voltage applied on two modulators is adjusted to a value of the minimum transmission point of optical modulator to obtain two second-order optical sideband with optical carrier suppression. The central carrier will be eliminated without using an optical filter and can be appropriately adjusted by an electrical phase shifter. The receiver power of -15.96 dBm was obtained, and the power penalty of about 0.5 dB after 10 km transmission is presented in our system. The proposed technique has a great potential for application in wireless access networks operating at mm-wave band.

ACKNOWLEDGMENT

The authors would like to thank the National Science Council of the Republic of China for financial support under grants NSC-100-2622-E-027-029-CC3.

REFERENCES

1. Wake, D., M. Webster, G. Wimpenny, K. Beacham, and L. Crawford, "Radio over fiber for mobile communications," *Proc. Int. Top. Meeting Microw. Photon*, 157–160, Oct. 4–6, 2004.
2. Wang, Q., H. Rideout, F. Zeng, and J. Yao, "Millimeter-wave frequency tripling based on four-wave mixing in a semiconductor optical amplifier," *IEEE Photon. Technol. Lett.*, Vol. 18, No. 23, 2460–2462, Dec. 1, 2006.
3. Yu, J., M.-F. Huang, Z. Jia, T. Wang, and G.-K. Chang, "A novel scheme to generate single-sideband millimeter-wave signals by using low-frequency local oscillator signal," *IEEE Photon. Technol. Lett.*, Vol. 20, No. 7, 478–480, Apr. 1, 2008.
4. Hong, C., C. Zhang, M. Li, L. Zhu, L. Li, W. Hu, A. Xu, and Z. Chen, "Single-sideband modulation based on an injection-locked DFB laser in radio-over-fiber systems," *IEEE Photon. Technol. Lett.*, Vol. 22, No. 7, 462–464, Apr. 1, 2010.
5. Zhang, J., H. Chen, M. Chen, T. Wang, and S. Xie, "A photonic microwave frequency quadrupler using two cascaded intensity modulators with repetitious optical carrier suppression," *IEEE Photon. Technol. Lett.*, Vol. 19, No. 14, 1057–1059, Jul. 15, 2007.

A Fault-tolerant Mechanism on Star-ring Based Ethernet Passive Optical Networks

Z. D. Shyu¹, I. S. Hwang², and I. C. Lin³

¹Department of General Education, Army Academy, Taoyuan City, Taiwan

²Department of Information Communication, Yuan-Ze University, Taoyuan City, Taiwan

³Department of Computer Science and Engineering, Yuan-Ze University, Taoyuan City, Taiwan

Abstract— Ethernet Passive Optical Networks (EPONs) are proposed to overcome the bandwidth bottleneck at access networks due to its simplicity, cost effectiveness and wide spread deployment. The traditional PON architecture is bounded by the nature of tree topology, where data must be transmitted from node to central node before it could be redirected to another node which causes performance waste. To resolve this issue, a Sub-OLT component is assigned on the proposed star-ring based EPON architecture to control the partial traffic in the ring. All ONU's AF and BE traffics will be sent to Sub-OLT then transport to the OLT. On the other hand, all ONU's EF traffic (including Sub-OLT traffic) is transmitted directly at the assigned DBA time. In addition, to achieve high reliability and low-cost for deployment, a significant fault-tolerant mechanism on star-ring based EPON architecture is proposed in this article to provide protection against link fiber failure and ring fiber failure. This paper also proposes a Star-Ring Dynamic Bandwidth Allocation (SR-DBA) scheme on star-ring based EPON to handle dynamic bandwidth allocation process by OLT and Sub-OLT respectively. The simulation results show that the fault-tolerant SR-DBA can provide high system performance for different failure situations in terms of packet delay and expedited forwarding (EF) jitter, especially in high traffic loads.

1. INTRODUCTION

The Passive Optical Network (PON) technology, which features data deployment through passive components, has gained the most attention in the industry. It deploys a single optical fiber through a passive star coupler to transmit signal to multiple premises. There are no active components found in PON architecture between the optical line terminal (OLT) that resides in a Central Office (CO) and multiple optical network units (ONUs), therefore, it is considered a great deployment advantage. EPON offers low transmission waste, low deployment cost, and high-speed broadband, thus making it a leading direction for broadband communication research. EPON can support downstream broadcast; data is broadcast downstream from the OLT to multiple ONUs. Packets are transmitted from OLT go through a splitter before reaching multiple ONUs. When the data reaches the ONU, it accepts or discards the packets according to the logical link ID (LLID) which is uniquely addressed for each ONU. To avoid packets collisions, the upstream traffic of EPON utilizes Time-division Multiplexing (TDM), in which an ONU can only transmit packets in a dedicated time-slot. Since EPON lacks packet segmentation and reassembly mechanism, whenever the dedicated time-slot is insufficient for transmitting a packet, the packet must be resend in the next dedicated time-slot hence reducing efficiency. In addition, a considerable amount of bandwidth is wasted when time slots are not being allocated to full capacity.

Due to the fundamental limitation of EPON, numerous dynamic bandwidth allocation (DBA) techniques [1, 6, 7] were innovated to enhance the efficiency of upstream traffic. The Interleaved Polling with Adaptive Cycle Time (IPACT) [1] mainly uses a polling scheme to deliver packets to a central OLT and then controls the allocation of bandwidth to ONUs based on the *Grant* and *Report* messages provided by the Multi-Point Control Protocol (MPCP) mechanism in EPON. Bandwidth is allocated to each ONU according to the capacity indicated on the Service Level Agreement (SLA). In addition, based on the upstream mechanism of EPON, the OLT computes the bandwidth needed by each ONU upon receiving report message from each ONU. This polling mechanism, however, produces an idle period during each computation. Prediction-based bandwidth allocation may improve both fairness issues and idle period issues. On the other hand, under non-uniform or burst of traffic, efficiency could be compromised because inaccurate predictions.

The ITU-T Recommendation G.983.1 [5] describes four types of protection network. The first type of protection network is the link protection between OLT and splitter connection. Any error occurs in the OLT or splitter note may cause failure. Second type of protection network is to add a backup OLT module to eliminate the shortcoming of the first type of protection. The third

protection network is to add a feeder fiber between all links and nodes. Data will be sent to both working link and backup link simultaneously to form a full protection when a fault occurs. However, this type of protection network not only increases deployment cost, it also wastes resource because the ineffectiveness of loading share between protection link and backup link. The fourth type of protection network can offset the drawback of the third type of protection by adding more splitters and feeder fiber even though the cost of deployment is the highest.

In [2], the authors proposed a star-ring based architecture in PON to protect the network when challenged with failure through operations of different components with an emphasis on hardware enhancement. The operation principle behind the network protection is using two backup feeder fibers to connect OLT and Remote Nodes (RN). A $2 \times N$ Array Waveguide Grating (AWG) is used in RN to connect to ONUs through tree-based network. The ring-based part is formed by connecting all ONUs with one optical fiber. When link failure occurs between RN and ONU, the effected ONU will be connected to neighboring ONU through ring and still be able to receive data. However, this architecture cannot provide protection between RN and ONU. In this paper, we propose a bandwidth allocation algorithm for OLT and Sub-OLT in a star-ring architecture and the corresponding protection mechanisms that enable the star-ring architecture to categorize traffic into different classes (such as EF, AF and BE) and solve the issues of low outbound and inbound (within ONUs) transmission efficiency with a traditional point-to-multipoint tree-based structure combined with a high transmission efficiency of the ring architecture. Moreover, through these two different networks, an uplink redundant solution is provided. This architecture possesses two independent DBA scheme for OLT and Sub-OLT respectively to support efficient bandwidth allocation under error or normal condition.

2. PROPOSED METHOD

We propose the bandwidth allocation algorithms for OLT and Sub-OLT in star-ring architecture and designs both ONU and Sub-OLT components of ring network in reference to [4] to ensure that data can be transmitted in speed of light in a ring network. This architecture utilizes the traditional tree-based structure within its network to transmit delay sensitive traffic with narrow-band nature (like the EF Traffic). In addition, it utilizes ring architecture to transmit inbound (within ONUs) EF traffic and all AF and BE traffics to OLT. The QoS-based DBA scheduling mechanism for star-ring architecture [3] was our previously research result, however, the DBA of Sub-OLT was not studied in this thesis. In ring architecture, data transfer between ONUs accounts for a significant proportion of the traffic. Without an appropriate Sub-OLT DBA that provides higher transmission efficiency, both inefficiency and waste of bandwidth may become issues. The Sub-OLT DBA that we propose will allow ONUs on the ring to transmit data on each uplink time slot. To avoid data collision, AF and BE traffic will be uniformly uploaded by Sub-OLT, thus resolving the issue of without appropriate Sub-OLT DBA. In terms of fault-tolerance, this paper proposes the protection mechanism featured by the star-ring architecture. There are dual optical fibers in this architecture that can support backup for one another. When an error occurs in tree-based structure or in the ring architecture, it can quickly be detected and recovered.

The DBA within [4] operates in a ring topology, where OLT controls and dedicates time slot according to the grand/report message provided by MPCP for EPON. Report message and data transmitted by ONU are transferred or exchanged from one ONU to the next in a ring, hence, every ONU receives report message and data frame of other ONUs. The action of data transfer by any ONU will prompt a DBA algorithm to secure the time slot for next cycle in order to avoid data collision. In other words, the next uplink bandwidth is predicted based on the current needs in the ring and the need of that ONU. A report message will always be placed before the data transmission when any ONU uploads data for transmission to eliminate idle period. This architecture is extremely suitable for local traffic. However, it is inefficient for situations where large volume of outbound data transmission is required.

The method we propose can improve the issues generated in [2, 4] by categorizing different classes of traffics. The EF traffic of each ONU is sent by tree structure, and AF and BE traffic of each ONU is transmitted by ring architecture. This architecture can enhance the efficiency of transmission between ONUs and distinguish inbound and outbound traffic as well as use feeder fiber to achieve protection function. It is able to improve the utilization efficiency of all classes of traffic in the entire ring. Figure 1 shows the star-ring architecture. As the figure indicates, EF traffic is transmitted by traditional tree structure. OLT broadcasts the downstream traffic to each ONU through PSC. For upstream traffic, OLT designates the uplink time slot to each ONU then respectively uploads

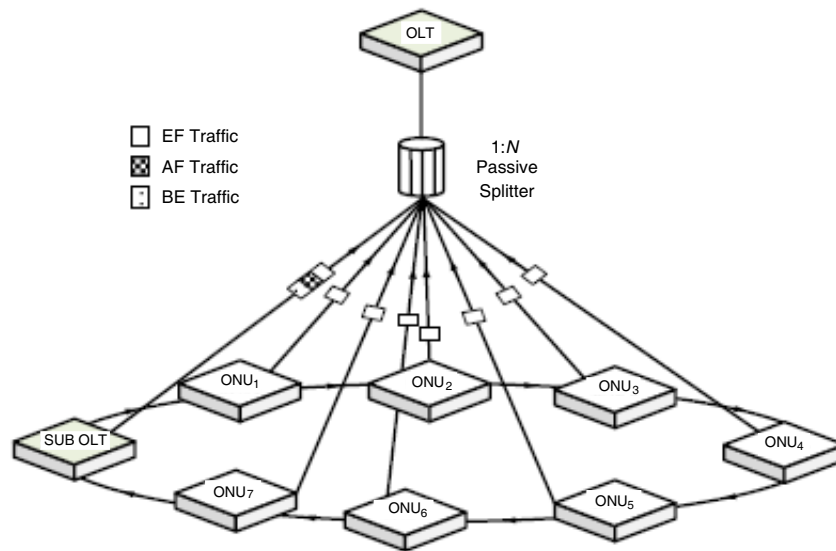


Figure 1: Proposed star-ring architecture.

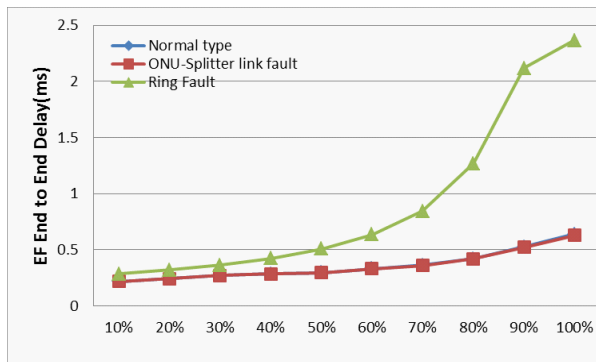


Figure 2: EF end-to-end delay.

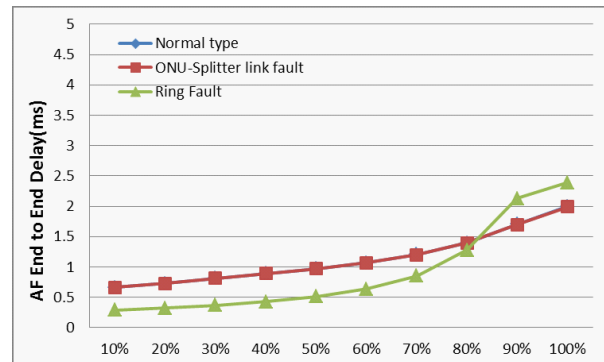


Figure 3: AF end-to-end delay.

ONU EF traffic through the upstream process. AF and BE traffic are uploaded through Sub-OLT in a single-direction ring, which connects ONUs in a ring topology. Upon receiving outbound AF and BE traffic from ONU and/or EF traffic in the ring, Sub-OLT uploads the traffic to OLT. For inbound traffic, the Sub-OLT takes the processed traffic and downstream it to star-ring for transmission.

3. PERFORMANCE ANALYZE

The results show the performance in one normal situation and two kinds of fault situation: ONU-Splitter link fault and ring fault. ONU-Splitter link fault means the fault on the link between ONU and splitter, and ring fault means the fault on the link of the ring. When ONU-Splitter link fault occurred, EF traffic on the fault ONU are transmitted to its neighbor ONU and the neighbor ONU will relay it to OLT. In addition, AF and BE traffic on the fault ONU are still transmitting to Sub-OLT. In the ring fault situation, the proposed mechanism renews the original star-ring structure to traditional tree structure. The DBA scheme is changed from our previous SRDBA [8] to IPACT DBA.

In Figure 2, ONU-Splitter link fault situation is almost the same with the normal type. The reason is that only one ONU's EF traffic are effected because of fiber fault between ONU and splitter, the influence is not worth mentioning. In the ring fault situation, the DBA algorithm is changed to IPACT DBA That's why the EF traffic delay is worse than the other two situations In Figure 3, the AF traffic has to be transmitted to sub-OLT before it is transmitted to OLT in the star-ring structure Therefore, the AF delay is higher than ring fault situation which renews the original star-ring structure to traditional tree structure and the DBA scheme is changed from SRDBA to IPACT DBA. However, the AF delay in ring fault situation is well at loading is higher

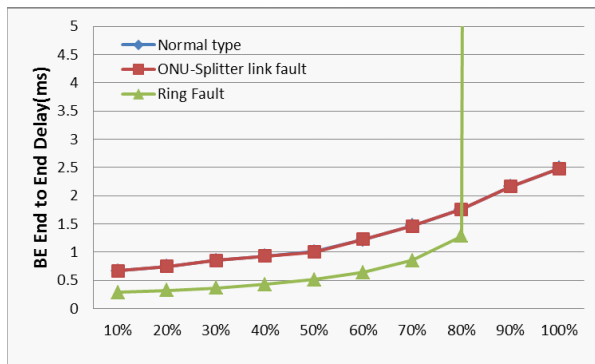


Figure 4: BE end-to-end delay.

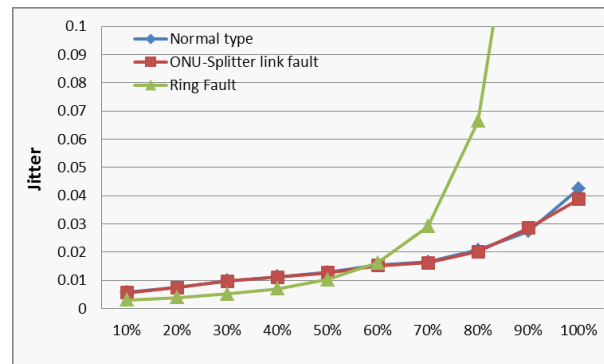


Figure 5: Jitter.

than 80%. In Figure 4, the result of BE delay is similar to AF traffic. The star-ring structure has a good performance before 80%. However, the BE traffic delay is raised tremendously when loading is over 80%. The reason is that BE traffic is starvation in IPACT DBA scheme when loading is over 80%. SRDBA keeps performance well then BE End-to-End delay is stable and acceptable.

In Figure 5, SRDBA has a great result in jitter. Because the EF traffic is transmitted to OLT directly by tree structure without any competition with AF and BE traffic. We can see that the result is similar when loading is small, but it has a tremendous difference in hard loading. The jitter performance is raised tremendously when loading is over 70% in IPACT DBA scheme.

4. CONCLUSIONS

In this paper, a meaningful star-ring based EPON architecture is proposed to reduce the local traffic transmitted to OLT and enhance bandwidth efficiency. This research also proposed using a Sub-OLT component to control the partial traffic in the ring. In addition, we modify the ONU structure in all optical to reduce the optical-electrical conversion delay. The highest priority traffic (EF) of each ONU is sent to OLT by tree structure; meanwhile, the minor priority traffic (AF and BE) of each ONU are transmitted to Sub-OLT by ring architecture to ensure Quality of Service (QoS). In this paper, we proposed a Sub-OLT DBA in star-ring architecture. By improving the components of ONU, the SR-DBA work successfully. The aims of this paper are improving EF end to end delay, jitter, and system performance between ONUs. Not only that we have proved our aims, we have also proven that the hierarchical DBA can improve the system throughput. Because the local ring bandwidth still has redundant bandwidth, it seems that we can increase the local traffic by letting each ONU get more bandwidth. In the future, we will discuss the DBA mechanism and prediction scheme in the proposed architecture.

ACKNOWLEDGMENT

This work was supported by the National Science Council of Taiwan (NSC 100-2218-E-539-002-MY2 and NSC 101-2221-E-155-051).

REFERENCES

1. Kramer, G., B. Mukherjee, and G. Pesavento, "Interleaved polling with adaptive cycle time (IPACT): A dynamic bandwidth distribution scheme in an optical access network," *Photonic Network Communications*, Vol. 4, No. 1, 89–107, 2002.
2. Sun, X. F., Z. X. Wang, C. K. Chan, and L. K. Chen, "A novel star-ring protection architecture scheme for WDM passive optical access networks," *Conference on Optical Fiber Communication, Technical Digest Series*, Vol. 3, 563–565, Anaheim, California, Mar. 2005.
3. Hwang, I. S., Z. D. Shyu, J. Y. Lee, and C. H. Lee, "A novel distributed QOS-based DBA scheduling mechanism for star-ring architecture on ethernet passive optical networks," *International Conference on Network-Based Information System*, 238–243, Japan, Sep. 14–16, 2010.
4. Hossain, A. S. M. D., R. Dorsinville, M. Ali, A. Shami, and C. Assi, "Supporting private networking capability in EPON," *Proc. of IEEE ICC*, Vol. 6, 2655–2660, Jun. 2006.
5. ITU-T, Study Group 15, "G.983: High speed optical access systems based on passive optical network (PON) techniques," 2001.

6. Chen, B., J. Chen, and S. He, “Efficient and fine scheduling algorithm for bandwidth allocation in ethernet passive optical networks,” *IEEE Journal of Selected Topics in Quantum Electronics*, Vol. 12, No. 4, 653–660, Jul.–Aug. 2006.
7. Assi, C., Y. Ye, S. Dixit, and M. A. Ali, “Dynamic bandwidth allocation for quality-of-service over ethernet PONs,” *IEEE Journal on Selected Areas in Communications*, Vol. 21, No. 9, 1467–1477, Nov. 2003.
8. Shyu, Z. D., I. S. Hwang, and C. W. Huang, “A comprehensive dynamic bandwidth allocation on star-ring based EPON,” *International Conference on Optics & Photonics Taiwan (OPTIC)*, 133, National Taiwan University, Taiwan, Dec. 6–8, 2012.

A New Mechanism to Improve Bandwidth Utilization and QoS of IPTV in Ethernet Passive Optical Network

I-Shyan Hwang^{1,2}, Andrew Tanny Liem², Ali Akbar Nikoukar², and Ku Chieh Chen²

¹Department of Information Communication, Yuan-Ze University, Chung-Li 32003, Taiwan

²Department of Computer Science and Engineering, Yuan-Ze University, Chung-Li 32003, Taiwan

Abstract— IPTV is one of the killer multimedia applications for the next-generation network, yet provides exciting new revenue and opportunities for service providers. Despite all the attractive IPTV services, it also requires high-speed access networks with the functions of multicasting and Quality-of-Services (QoS) guarantee. In the access networks, Ethernet Passive Optical Network (EPON) is regarded as one of the best solutions to meet the higher bandwidth demands. In this paper, we propose a broadcasting mechanism for IPTV in EPON by using the Single Copy Broadcast (SCB). In our mechanism, a table is constructed in the Reconciliation Sublayer (RS) of ONUs and OLT to handle the IPTV requests. Simulation results have shown that our proposed mechanism can improve the QoS metrics in terms of bandwidth consumption, packet loss, and queue length.

1. INTRODUCTION

Newly evolving multimedia applications such as high-definition television (HDTV), Internet Protocol Television (IPTV), and Video-on-Demand (VoD) in recent times become one of the most key services for network operators. It is predicted that 1.2 million minutes of video content will cross the network every second in 2016 and the sum of all forms of video traffics (TV, VoD, Internet, and P2P) will be approximately 86 percent of global consumer traffic by 2016 [1]. These applications have brought the network operators to offer higher bandwidth to their residential and business subscribers. Among these applications, IPTV is one of the killer multimedia applications for the next-generation network, yet provides exciting new revenue and opportunities for service providers. IPTV offers digital television services over Internet Protocol (IP) for the subscribers at a lower cost. These IPTV services include the live television, time-shifted television, and video on demand (VoD) [2]. Despite all the attractive IPTV services, it also requires high-speed access networks with functions of multicasting, Quality-of-Services (QoS) guarantee and so on. In the access networks, Ethernet Passive Optical Network (EPON) is considered as one of the best solutions due to its simplicity, low-cost and high data rate. The EPON architecture consists of a centralized optical line terminal (OLT) and number of splitters. The OLT is connected to multiples associated optical network units (ONUs) over point-to-multipoint topologies to deliver the packets and reduce the costs relative to the maintenance power. Because EPON is a broadcasting by nature in the downstream direction, therefore the OLT will broadcast the control messages and data packets and is selectively extracted by their destination ONU. In addition, the SCB is introduced so that the OLT can forward the broadcast packets to multiple recipients without multiple duplications for each ONU [3].

To carry the IPTV traffic in the EPON several multicasting algorithms based on Mac Address, LLID, and IGMP snooping are proposed [4–6]. Most of the previous works used the IGMP to deliver the multicasting for IPTV service. The IGMP is a protocol to maintain the multicast membership between the routers in order to support multicast communication. To implement IGMP multicasting, the ONU needs a processor to perform IGMP snooping and the 802.1D entity should be added in ONU. The OLT should broadcast multicast traffic to run IGMP snooping; and also needs software to snoops IGMP and configures 802.1D entity in ONU through OAMPDUs. Moreover, the use of multicast LLID is not scalable since the limitation of Logical Group ID, which essentially for ONUs to identify the number of multicast group address. Finally, the previous studies also have not mentioned of how to distinguish the IPTV traffic from the other traffics in real PON-based networks. Consequently, to tackle the aforementioned problems and challenges, in this paper, we propose a new mechanism, which emulates the multicasting mechanism by using the SCB and a table that manages the IPTV requests. Simulation results have shown that our proposed mechanism can improve the QoS metrics in terms of bandwidth consumption, packet loss, and queue length.

2. PROPOSED ARCHITECTURE

In our proposed mechanism we construct a table at the ONU and a table at the OLT in RS to manage the IPTV requests. The ONU table contains channel name, user MAC address, and user IP address fields, whereas the OLT table consists of channel name and the ONU LLID. In the downstream direction, the OLT sets the broadcast LLID to the IPTV packets and sends it via SCB port thus all ONUs will accept these packets. The tables are used to manage the requests and broadcast the streams to ONUs. This table also helps the OLT to decide whether to start/stop the broadcasting channel. We use a ONU to support routing function in layer three. We add a record to the routing table to distinguish the IPTV request sent by the user. When the request comes from the user the ONU table checks to find any previous request from the user. If the user has a record (value) in the table first the current value should be deleted from the table and new value adds to the table. Deleting the value from the table means to leave the channel and adding a new value means to join a channel in the proposed mechanism. In the other words each user can have a record in the ONU table. The join algorithms is shown in Fig. 1(a). If the requested channel is already broadcasted by the OLT and the name of the broadcast channel exists in the ONU table, the ONU will start to broadcast the requested channel to the user and add the user MAC and the requested channel in the table by *Add_ONU* (*user_MAC*, *ch_name*) function. If the request is not in the ONU table that means it is not broadcasted from the OLT. The request should be sent to the OLT. Consequently the OLT passes it to the IPTV server. When the data starts to send from the IPTV, the OLT receives these packets and by examining the source address of the packets are sent via SCB port. When the OLT starts to broadcast the channel the function *Add_OLT*() is executed to add the channel name to the OLT table. The operation in OLT is shown in Fig. 1(b). After any change to the OLT table it is necessary that OLT informs the ONUs to know about current broadcasted channel. The OLT should decide to continue or stop the channel broadcasting. Fig. 1(c) shows the algorithms for the continue/stop broadcasting. When a user leaves the channel, the corresponding ONU removes the user's MAC address from the ONU's table with the *Remove_ONU* (*User_MAC*, *Ch_name*) function. The function *Filter_ONU_Table* (*Ch_name*) is designed to filter the ONU's table. This function return removes LLID request to the OLT if no longer user watching the channel after the OLT uses *Remove_OLT* (*ONU_LLID*, *Ch_name*) to remove ONU's LLID from the OLT's table. At the same time, OLT uses *Filter_OLT.Table* (*Ch_name*) to filter the OLT's table if the OLT finds no ONU for the channel in the table, it will stop broadcasting the channel.

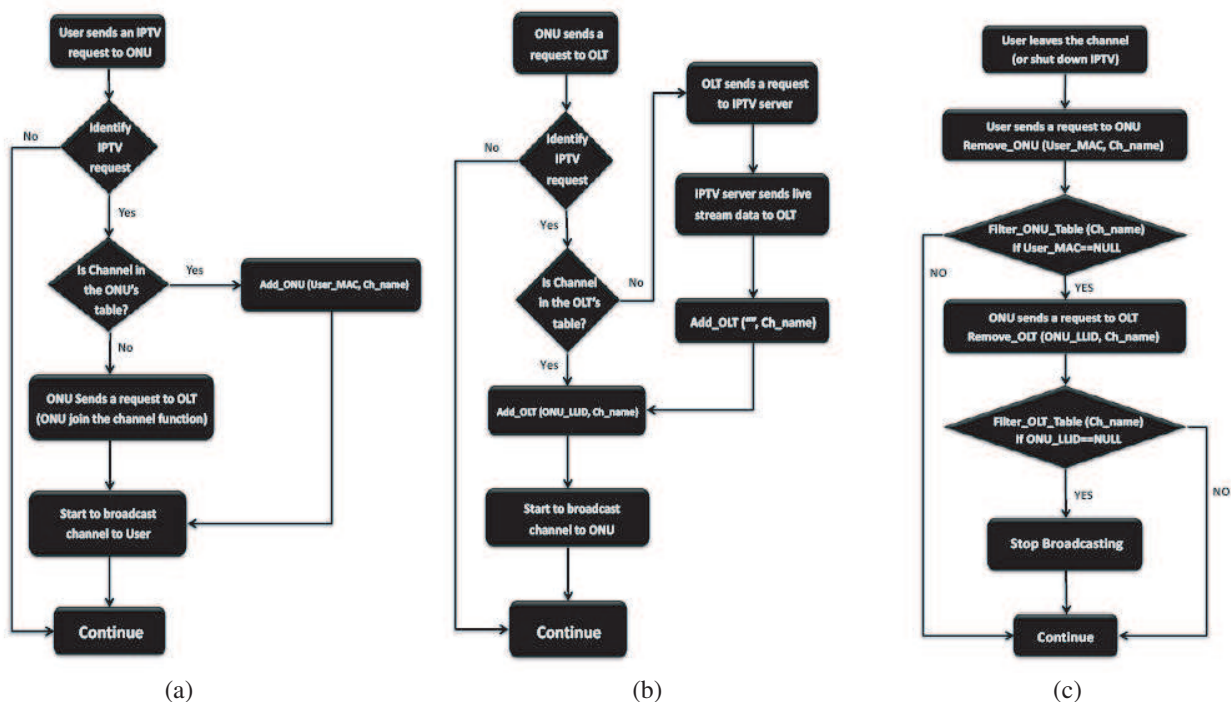


Figure 1: (a) ONU operation; (b) OLT operation; (c) algorithm to stop the broadcasting.

3. SYSTEM PERFORMANCE

In this section, we present the results from our simulation experiments conducted to evaluate the bandwidth consumption, packet loss, and packet delay in the downstream direction. The OLT uses the First-In-First-Out (FIFO) for the packet queuing with finite buffer space. The system model is set up with 5 to 40 HD channels with 10 Mbps bit rate per channel. We assume that up to 20% of the total traffic is used for IPTV traffic. The distance from ONUs to OLT is assumed to range between 10 to 20 km. Moreover, for the traffic model considered here, the packet generation followed the self-similarity and Long Range Dependence (LRD) [8], and the packet size is followed the trimodal [9]. The access number of the user for each channel is followed the same as in [10] and compared our proposed mechanism (i.e., “SCB”) with unicast and multicast mechanisms. The simulation parameters are summarized in Table 1.

3.1. Bandwidth Consumption

Figure 2 shows the bandwidth usage of unicast, multicast and the proposed mechanism (i.e., SCB) versus the number of channels. It can be observed the unicast mechanism has the highest bandwidth usage because it is required to send the dedicate data to the users. The bandwidth usage is rapidly increased, and it occupied the available bandwidth with just around 40 channels. The multicast

Table 1: Simulation Parameters.

Parameters	Value
Number of HD channels in the system	5, 10, 20, 25, 30, 35, 40
Downstream link capacity	1 Gbps (200 Mbps for IPTV traffic) [1]
OLT-ONU distance (uniform)	10–20 km
OLT processing time	5 μ s
HD channel Bit rate	10 Mbps

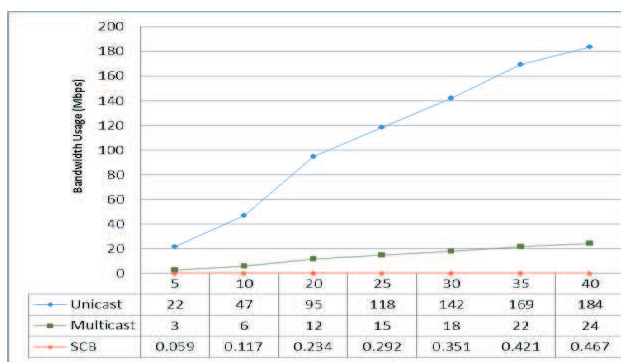


Figure 2: Bandwidth usage.

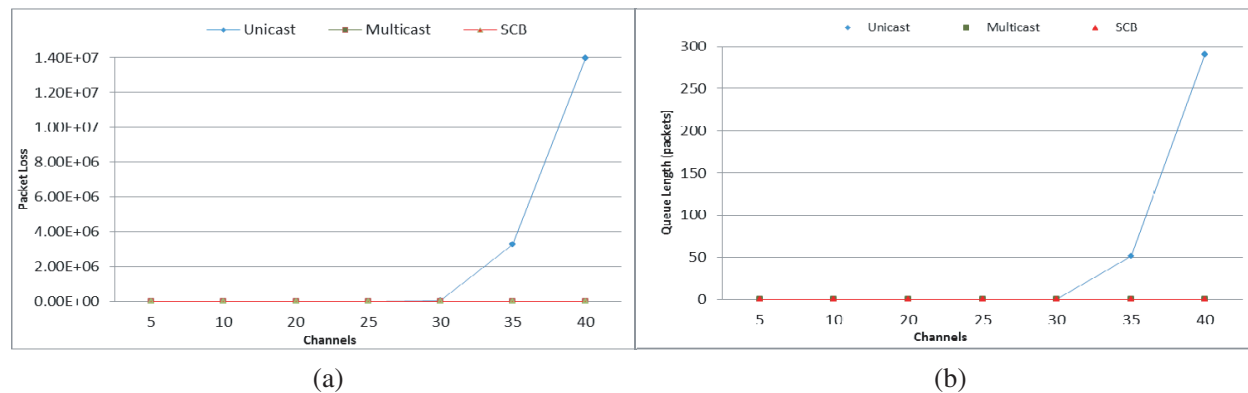


Figure 3: (a) Packet loss; (b) queue length.

mechanism can reduce the bandwidth usage around 10% of the available bandwidth. On the other hand, our proposed mechanism has the lowest bandwidth consumption because the OLT will send the packet by using SCB, thus each packet needs broadcast once. Our proposed mechanism can improve the bandwidth utilization to over 90% compared with the unicast mechanism and improve 9% compared to the multicast mechanism.

3.2. Packet Loss and Queue Length

Figure 3(a) shows the packet loss of the unicast, multicast and SCB mechanisms, respectively. We define the packet loss is where there is no bandwidth available and no buffer space to provision the IPTV traffic. It is shown that the unicast mechanism begins to drop the packet when the number of channel exceeds 25. Because there is no longer available bandwidth to satisfy the IPTV traffic in the downstream direction. The packet loss for both multicast and SCB mechanisms are zero because the bandwidth can satisfy the IPTV traffic sent by the IPTV server. Fig. 3(b) compares the queue length of unicast, multicast and SCB mechanisms versus the number of channels, respectively. It is shown that the unicast mechanism needs bigger buffer space to accommodate the packets in the OLT buffer space. However, for the multicast and SCB, the number of packet in the queue is always zero, because the bandwidth is available and there is no need to buffer the packets in the OLT buffer space.

4. CONCLUSIONS

In this paper, we proposed a mechanism to manage the IPTV request by constructing the tables in the ONUs and OLT R Sublayer (RS). We developed three algorithms to maintain the tables in ONUs and OLT. In the ONU, if there is a record for the requested channel, the broadcasted packet is sent to the user without going to the OLT and IPTV server; otherwise, the request will send to the ONU queue. Furthermore, if there is a change in the ONU table or when the new channel starts to broadcast, the OLT table will be updated. Finally, an algorithm is proposed to aware the OLT to stop broadcasting the channel. Simulation results have shown that our proposed mechanism outperforms the bandwidth usage up to 90% compared to the unicast and 9% compared to the multicast mechanism.

REFERENCES

1. Cisco, "Cisco visual networking index: Forecast and methodology," 2011–2016, 2012.
2. Xiao, Y., X. Du, J. Zhang, F. Hu, and S. Guizani, "Internet protocol television (IPTV): The killer application for the next-generation internet," *IEEE Communications Magazine*, Vol. 45, No. 11, 126–134, Nov. 2007.
3. <http://standards.ieee.org/getieee802/download/802.3av-2009.pdf>.
4. Sue, C. C., C. Y. Hsu, Y. S. Su, and Y. Y. Shieh, "A new IPTV channel zapping scheme for EPON," *First International Conference on Ubiquitous and Future Networks*, 131–136, Jun. 2009.
5. Cheng, C. and L. Wang, "Research on a method to carrying IPTV in EPON," *4th International Conference on Wireless Communications, Networking and Mobile Computing*, 1–4, Oct. 2008.
6. Ikeda, H., J. Sugawa, Y. Ashi, and K. Sakamoto, "High-definition IPTV broadcasting architecture over gigabit-capable passive optical network," *Global Telecommunications Conference*, 2242–2246, Nov. 2007.
7. Wu, J., Y. Nie, H. Yoshiuchi, and H. Ikeda, "Building multicast controller for carrier-grade IPTV service over ethernet passive optical network," *Second International Conference on Systems and Networks Communications*, 47, Aug. 2007.
8. Erramilli, A., P. Pruthi, and W. Willinger, "Fast and physically-based generation of self-similar network traffic with applications to ATM performance evaluation," *29th Conference on Winter Simulation*, 997–1004, Dec. 1997.
9. http://www.ieee802.org/3/efm/public/jul01/presentations/sala_1_0701.pdf.
10. Choi, J., A. S. Reaz, and B. Mukherjee, "A survey of user behavior in VoD service and bandwidth-saving multicast streaming schemes," *IEEE Communications Surveys and Tutorials*, Vol. 14, No. 1, 156–169, 2012.

The Influence of the Electromagnetic Wave on the Nonlinear Quantum Acoustoelectric Current in a Quantum Well

N. V. Hieu^{1,2}, N. Q. Bau¹, and N. V. Nghia¹

¹Faculty of Physics, Hanoi University of Science, Vietnam National University, Hanoi, Vietnam

²Faculty of Physics, Danang University of Education, Danang, Vietnam

Abstract— The influence of the electromagnetic wave on the nonlinear quantum acoustoelectric (QAE) current in a quantum well (QW) is investigated for an acoustic wave whose wavelength $\lambda = 2\pi/q$ is smaller than the mean free path l of the electrons and in the region $ql \gg 1$ (where q is the acoustic wave number). The dependence of the QAE current j^{QAE} on the frequency of external acoustic wave ω_q , the temperature T , the amplitude E_0 and frequency Ω of the electromagnetic wave are obtained by using the quantum kinetic equation in the case of relaxation time of momentum τ constant approximation. Numerical calculation is done, and the result is discussed for a typical AlGaAs/GaAs/AlGaAs QW. The computational results show that the dependence of the QAE current j^{QAE} on the external acoustic wave frequency ω_q , the frequency of electromagnetic wave Ω and the QW's width L is non-monotonic, the cause of appearance peaks attributes the transition between mini-bands $n \rightarrow n'$. The quantum theory of the QAE current in a QW is newly developed.

1. INTRODUCTION

When an acoustic wave is absorbed by a conductor, the transfer of the momentum from the acoustic wave to the conduction electron may give rise to a current usually called the acoustoelectric (AE) current, j^{AE} , in the case of an open circuit, a constant electric field, E^{AE} . The study of this effect is crucial, because of the complementary role it may play in the understanding of the properties of the low-dimensional systems (superlattices, QW, quantum wire . . .) which, we believe, should find an important place in the acoustoelectronic devices. The study of the AE effect in bulk materials have received a lot of attention [1–5].

It is well known that in low-dimensional systems, the energy levels of electrons become discrete and are different from other dimensionalities [1]. In certain conditions, the decrease in dimensionality of the system for semiconductors can lead to dramatically enhanced nonlinearities [2]. So the nonlinear properties, especially electrical and optical properties of semiconductor quantum wells, superlattices (SL), quantum wires, and quantum dots have attracted much attention in the past few years, for example, the linear absorption of a weak electromagnetic wave caused by confined electrons in low-dimensional systems has been investigated [3–5]. Calculations of the nonlinear absorption coefficients of an intense electromagnetic wave by using the quantum kinetic equation for electrons in bulk semiconductors [6], in quantum well [7] and in quantum wire [8] have also been reported. Also, the AE effect have been studied in detail in bulk semiconductors by using both the Boltzmann classical kinetic equation and quantum method [9–15].

In recent years, the acoustoelectric effect in low-dimensional structures have been extensively studied experimentally and theoretically. So far, however, almost all those works [16–24] have been studied theoretically by using the Boltzmann classical kinetic equation method, and are, thus, limited to the case of the electron-external acoustic wave interaction. The acoustoelectric effect in superlattices [16–18], the acoustoelectric current in one-dimensional channel [19], acoustoelectric effect in a finite-length ballistic quantum channel [20], AC in a ballistic quantum point contact [21], AC through a quantum wire containing a point impurity and AC in submicron-separated in a quantum wire [22, 23], and acoustoelectric effect in a carbon nanotube [24] have also been studied. In addition, the influence of the electromagnetic wave on the acoustoelectric effect has been studied theoretically in a SL by using the Boltzmann classical kinetic equation [25]. However, the calculation of the QAE current j^{QAE} and influence of the electromagnetic wave on QAE current in QW by using the quantum kinetic equation method is still open for study. In the present work, we use the quantum kinetic equation method to study the influence of the electromagnetic wave on the acoustoelectric current j^{QAE} induced by the electron-external acoustic wave interactions and the electron-internal acoustic wave (internal phonons) scattering in a QW and the present work is different from previous works [16–24] because 1) the QAE current is not only a result of the electron-external acoustic wave interaction, but also due to the electron-internal phonons scattering in the

sample, 2) we use the quantum kinetic equation method, 3) we calculated the influence of a strong electromagnetic wave on j^{QAE} .

This paper is organized as follows. In Section 2, we outline a quantum kinetic equation for electrons confined in a QW. The analytical expression for QAE current in the case of the electron-external acoustic wave and electron-internal phonons scattering is obtained in Section 3. The numerical results and brief discussions are presented for a specific QW AlGaAs/GaAs/AlGaAs are in Section 4. Finally, we come to a conclusion in Section 5.

2. QUANTUM KINETIC EQUATION FOR ELECTRONS IN A QUANTUM WELL IN THE PRESENCE OF AN ELECTROMAGNETIC WAVE

We use a simple model for a QW, in which an electron gas is confined by the infinite potential along the Oz direction (along the Oz direction, the energy spectrum of electron is quantized or the motive direction of electron is limited) and electrons are free on the $(x-y)$ plane. It is well known that the motion of an electron is confined QW and that its energy spectrum is quantized into discrete levels in the Oz direction. Let us suppose that the external acoustic wave of frequency ω_q is propagating along the quantum well axis (Oz). When

$$\omega_q/\eta = c_s q/\eta \ll 1; \quad ql \gg 1, \quad (1)$$

where η is the frequency of the electron collisions, q is the modulus of the external acoustic wave-vector and l is the electron mean free path. The acoustic wave is considered in the region $ql \gg 1$. Under such circumstances, the external acoustic wave can be interpreted as monochromatic phonons having the 3D phonon distribution function $N(\vec{k})$, and can be presented the acoustic flux by a δ -function distribution in \vec{k} -space $N(\vec{k}) = \frac{(2\pi)^3}{\omega_{\vec{q}}c_s} \Phi \delta(\vec{k} - \vec{q})$, where Φ is the flux density of external acoustic wave (external phonon) with frequency $\omega_{\vec{q}}$. In the presence of an external acoustic wave with frequency $\omega_{\vec{q}}$, the Hamiltonian of the electron-external phonon and electron-internal phonon system in a QW in second quantization representation can be written as (we select $\hbar = 1$):

$$H = H_0 + H_{e-ph}; \quad H_0 = \sum_{n, \vec{p}_\perp} \varepsilon_n \left(\vec{p}_\perp - \frac{e}{c} \vec{A}(t) \right) a_{n, \vec{p}_\perp}^+ a_{n, \vec{p}_\perp} + \sum_{\vec{k}} \omega_{\vec{k}} b_{\vec{k}}^+ b_{\vec{k}}, \quad (2)$$

$$H_{e-ph} = \sum_{n, \vec{p}_\perp, n', \vec{q}} C_{\vec{q}} U_{n, n'}(\vec{q}) a_{n, \vec{p}_\perp + \vec{q}_\perp}^+ a_{n', \vec{p}_\perp} c_{\vec{q}} \exp(-i\omega_{\vec{q}}t) + \sum_{n, \vec{p}_\perp, n', \vec{k}} D_{\vec{k}} I_{n, n'}(\vec{k}_z) a_{n, \vec{p}_\perp + \vec{k}_\perp}^+ a_{n', \vec{p}_\perp} (b_{\vec{k}} + b_{-\vec{k}}^+), \quad (3)$$

where n denotes the quantization of the energy spectrum in the Oz direction, $n = 1, 2, \dots$; a_{n, \vec{p}_\perp}^+ and a_{n, \vec{p}_\perp} ($b_{\vec{k}}^+$ and $b_{\vec{k}}$) are the creation and the annihilation operators of the electron (internal phonon), respectively, $c_{\vec{q}}$ is the annihilation operators of the external phonon. $|n, \vec{p}_\perp\rangle$ and $|n', \vec{p}_\perp + \vec{k}_\perp\rangle$ are electron states before and after scattering, $\vec{A}(t)$ is the vector potential of an external electromagnetic wave $\vec{A}(t) = \frac{e}{\Omega} \vec{E}_0 \sin(\Omega t)$, Ω is the frequency of electromagnetic wave. The electron energy takes the simple form

$$\epsilon_{n, \vec{p}_\perp} = \frac{\vec{p}_\perp^2}{2m} + \frac{n^2 \pi^2}{2mL^2} \quad (4)$$

Here, m is the effective mass of electron, L is the width of the QW, and \vec{p}_\perp is the transverse component of the quasi-momentum in the $(x-y)$ plane. $U_{n, n'}(\vec{q})$ is the matrix element of the operator $U = \exp(iqy - \lambda_l z)$:

$$U_{n, n'}(\vec{q}) = \frac{(-1)^{n+n'} \exp(-\lambda_l L) - 1}{\lambda_l L + \frac{(n+n')^2 \pi^2}{\lambda_l L}} - \frac{(-1)^{n-n'} \exp(-\lambda_l L) - 1}{\lambda_l L + \frac{(n-n')^2 \pi^2}{\lambda_l L}}, \quad (5)$$

where $\lambda_l = (q^2 - \omega_q^2/c_s^2)^{1/2}$ is the spatial attenuation factor of the potential part the displacement field, $C_{\vec{q}}$ and $D_{\vec{k}}$ are the electron-external and electron-internal phonon interaction factor, respectively and takes the form:

$$C_{\vec{q}} = i\Lambda c_l^2 (\omega_{\vec{q}}^3 / 2\rho_0 \Xi S)^{1/2}, \quad \Xi = q \left[\frac{1 + \sigma_l^2}{2\sigma_l} + \left(\frac{\sigma_l}{\sigma_t} - 2 \right) \frac{1 + \sigma_t^2}{2\sigma_t} \right], \quad (6)$$

$$\sigma_l = (1 - c_s^2/c_l^2)^{1/2}, \quad \sigma_t = (1 - c_s^2/c_t^2)^{1/2}, \quad |D_{\vec{k}}|^2 = \frac{\Lambda^2 \vec{k}}{2\rho_0 c_s},$$

here Λ is the deformation potential constant, c_l and c_t are the velocities of the longitudinal and the transverse bulk acoustic wave, c_s is the velocity of the acoustic wave, ρ_0 is the mass density of the medium, $S = L_x L_y$ is the surface area and

$$I_{n',n}(k_z) = \frac{2}{L} \int_0^L dz \sin\left(\frac{n'\pi}{L}z\right) \sin\left(\frac{n\pi}{L}z\right) \exp(ik_z z). \quad (7)$$

In order to establish the quantum kinetic equations for electrons in QW, we use the electron distribution function $f_{n,\vec{p}_\perp} = \langle a_{n,\vec{p}_\perp}^+ a_{n,\vec{p}_\perp} \rangle_t$:

$$i \left(\frac{\partial f_{n,\vec{p}_\perp}}{\partial t} \right)_{ac} = \langle [a_{n,\vec{p}_\perp}^+ a_{n,\vec{p}_\perp}, H] \rangle_t, \quad (8)$$

where $\langle \Psi \rangle_t$ denotes a statistical average value at the moment t ; $\langle \Psi \rangle_t = Tr(\widehat{W}\Psi)$ (\widehat{W} is the density matrix operator). Starting from the Hamiltonian Eqs. (2) and (3), Eq. (8) and realizing operator algebraic calculations, we obtained the quantum kinetic equation for electrons in QW:

$$\begin{aligned} \left(\frac{\partial f_{n,\vec{p}_\perp}}{\partial t} \right)_{ac} &= - \sum_{n',\vec{q}} |C_{\vec{q}}|^2 |U_{n,n'}(\vec{q})|^2 N(\vec{q}) \sum_{l,s} J_l \left(\frac{e\vec{E}_0 \vec{q}_\perp}{m\Omega^2} \right) J_{l+s} \left(\frac{e\vec{E}_0 \vec{q}_\perp}{m\Omega^2} \right) \exp(-is\Omega t) \\ &\times \left\{ - \frac{f_{n,\vec{p}_\perp} - f_{n',\vec{p}_\perp + \vec{q}_\perp}}{i(\epsilon_{n',\vec{p}_\perp + \vec{q}_\perp} - \epsilon_{n,\vec{p}_\perp} - \omega_{\vec{q}} - l\Omega + i\delta)} - \frac{f_{n,\vec{p}_\perp} - f_{n',\vec{p}_\perp - \vec{q}_\perp}}{i(\epsilon_{n',\vec{p}_\perp - \vec{q}_\perp} - \epsilon_{n,\vec{p}_\perp} + \omega_{\vec{q}} - l\Omega + i\delta)} \right. \\ &+ \left. \frac{f_{n',\vec{p}_\perp - \vec{q}_\perp} - f_{n,\vec{p}_\perp}}{i(\epsilon_{n,\vec{p}_\perp} - \epsilon_{n',\vec{p}_\perp - \vec{q}_\perp} - \omega_{\vec{q}} - l\Omega + i\delta)} + \frac{f_{n',\vec{p}_\perp - \vec{q}_\perp} - f_{n,\vec{p}_\perp}}{i(\epsilon_{n,\vec{p}_\perp} - \epsilon_{n',\vec{p}_\perp - \vec{q}_\perp} + \omega_{\vec{q}} - l\Omega + i\delta)} \right\} \\ &- \sum_{n',\vec{k}} |D_{\vec{k}}|^2 |U_{n,n'}(\vec{q})|^2 N(\vec{q}) \sum_{l,s} J_l \left(\frac{e\vec{E}_0 \vec{q}_\perp}{m\Omega^2} \right) J_{l+s} \left(\frac{e\vec{E}_0 \vec{q}_\perp}{m\Omega^2} \right) \exp(-is\Omega t) \\ &\times \left\{ - \frac{f_{n,\vec{p}_\perp} - f_{n',\vec{p}_\perp + \vec{q}_\perp}}{i(\epsilon_{n',\vec{p}_\perp + \vec{q}_\perp} - \epsilon_{n,\vec{p}_\perp} - \omega_{\vec{q}} - l\Omega + i\delta)} - \frac{f_{n,\vec{p}_\perp} - f_{n',\vec{p}_\perp - \vec{q}_\perp}}{i(\epsilon_{n',\vec{p}_\perp - \vec{q}_\perp} - \epsilon_{n,\vec{p}_\perp} + \omega_{\vec{q}} - l\Omega + i\delta)} \right. \\ &+ \left. \frac{f_{n',\vec{p}_\perp - \vec{q}_\perp} - f_{n,\vec{p}_\perp}}{i(\epsilon_{n,\vec{p}_\perp} - \epsilon_{n',\vec{p}_\perp - \vec{q}_\perp} - \omega_{\vec{q}} - l\Omega + i\delta)} + \frac{f_{n',\vec{p}_\perp - \vec{q}_\perp} - f_{n,\vec{p}_\perp}}{i(\epsilon_{n,\vec{p}_\perp} - \epsilon_{n',\vec{p}_\perp - \vec{q}_\perp} + \omega_{\vec{q}} - l\Omega + i\delta)} \right\} \quad (9) \end{aligned}$$

Eq. (9) is fairly general can be applied for any mechanism of interaction. In the case of vanishing electron-internal phonon interaction, it give the same results as these obtained in [16–18].

3. ACOUSTOELECTRIC CURRENT

It is assumed that the external acoustic wave propagates perpendicularly the Oz axis of the QW. After a new equilibrium has been established, the distribution function f of the electrons will obey the condition

$$\partial f_{n,\vec{p}_\perp} / \partial t = (\partial f_{n,\vec{p}_\perp} / \partial t)_{ac} + (\partial f_{n,\vec{p}_\perp} / \partial t)_{th} = 0, \quad (10)$$

$(\partial f_{n,\vec{p}_\perp} / \partial t)_{ac}$, the rate of change caused by the electron-external acoustic wave and inertial phonons interaction; $(\partial f_{n,\vec{p}_\perp} / \partial t)_{th}$, the rate of change due to the interaction of the electron with thermal phonons, with the impurities, and with one another. Substituting Eq. (9) into Eq. (10) we obtained

the basic equation of the problem:

$$\begin{aligned}
(\partial f_{n,\vec{p}_\perp}/\partial t)_{th} = & \pi \sum_{n',\vec{q}} |C_{\vec{q}}|^2 |U_{n,n'}(\vec{q})|^2 N(\vec{q}) \sum_{l,s} J_l \left(\frac{e\vec{E}_0\vec{q}_\perp}{m\Omega^2} \right) J_{l+s} \left(\frac{e\vec{E}_0\vec{q}_\perp}{m\Omega^2} \right) \\
& \times \left\{ [f(\epsilon_{n,\vec{p}_\perp}) - f(\epsilon_{n',\vec{p}_\perp+\vec{q}_\perp})] \delta(\epsilon_{n',\vec{p}_\perp+\vec{q}_\perp} - \epsilon_{n,\vec{p}_\perp} - \omega_{\vec{q}} - l\Omega) \right. \\
& + [f(\epsilon_{n,\vec{p}_\perp}) - f(\epsilon_{n',\vec{p}_\perp+\vec{q}_\perp})] \delta(\epsilon_{n',\vec{p}_\perp+\vec{q}_\perp} - \epsilon_{n,\vec{p}_\perp} + \omega_{\vec{q}} - l\Omega) + [f(\epsilon_{n,\vec{p}_\perp}) - f(\epsilon_{n',\vec{p}_\perp-\vec{q}_\perp})] \\
& \times \delta(\epsilon_{n',\vec{p}_\perp-\vec{q}_\perp} - \epsilon_{n,\vec{p}_\perp} + \omega_{\vec{q}} - l\Omega) + [f(\epsilon_{n,\vec{p}_\perp}) - f(\epsilon_{n',\vec{p}_\perp-\vec{q}_\perp})] \delta(\epsilon_{n',\vec{p}_\perp-\vec{q}_\perp} - \epsilon_{n,\vec{p}_\perp} - \omega_{\vec{q}} - l\Omega) \left. \right\} \\
& + \pi \sum_{n',\vec{k}} |D_{\vec{k}}|^2 |I_{n,n'}(k_z)|^2 N(\vec{k}) \sum_{l,s} J_l \left(\frac{e\vec{E}_0\vec{q}_\perp}{m\Omega^2} \right) J_{l+s} \left(\frac{e\vec{E}_0\vec{q}_\perp}{m\Omega^2} \right) \\
& \times \left\{ [f(\epsilon_{n,\vec{p}_\perp}) - f(\epsilon_{n',\vec{p}_\perp+\vec{k}_\perp})] \delta(\epsilon_{n',\vec{p}_\perp+\vec{k}_\perp} - \epsilon_{n,\vec{p}_\perp} + \omega_{\vec{q}} - \omega_{\vec{k}} - l\Omega) \right. \\
& \left. + [f(\epsilon_{n,\vec{p}_\perp}) - f(\epsilon_{n',\vec{p}_\perp-\vec{k}_\perp})] \delta(\epsilon_{n',\vec{p}_\perp-\vec{k}_\perp} - \epsilon_{n,\vec{p}_\perp} - \omega_{\vec{q}} + \omega_{\vec{k}} - l\Omega) \right\}. \tag{11}
\end{aligned}$$

We linearize Eq. (11) by replacing $f(\epsilon_{n,\vec{p}_\perp})$ with $f_F(\epsilon_{n,\vec{p}_\perp}) + f_1$, where $f_F(\epsilon_{n,\vec{p}_\perp})$ is the equilibrium Fermi contribution function. As indicated in [26] $(\partial f_{n,\vec{p}_\perp}/\partial t)_{th} = -f_1/\tau_{\vec{p}}$; $\tau_{\vec{p}}$ is the momentum relaxation time. Thus,

$$\begin{aligned}
f_1 = & \tau_{\vec{p}} \pi \sum_{n',\vec{q}} |C_{\vec{q}}|^2 |U_{n,n'}(\vec{q})|^2 N(\vec{q}) \sum_{l,s} J_l \left(\frac{e\vec{E}_0\vec{q}_\perp}{m\Omega^2} \right) J_{l+s} \left(\frac{e\vec{E}_0\vec{q}_\perp}{m\Omega^2} \right) \\
& \times \left\{ [f(\epsilon_{n,\vec{p}_\perp}) - f(\epsilon_{n',\vec{p}_\perp+\vec{q}_\perp})] \delta(\epsilon_{n',\vec{p}_\perp+\vec{q}_\perp} - \epsilon_{n,\vec{p}_\perp} - \omega_{\vec{q}} - l\Omega) \right. \\
& + [f(\epsilon_{n,\vec{p}_\perp}) - f(\epsilon_{n',\vec{p}_\perp+\vec{q}_\perp})] \delta(\epsilon_{n',\vec{p}_\perp+\vec{q}_\perp} - \epsilon_{n,\vec{p}_\perp} + \omega_{\vec{q}} - l\Omega) + [f(\epsilon_{n,\vec{p}_\perp}) - f(\epsilon_{n',\vec{p}_\perp-\vec{q}_\perp})] \\
& \times \delta(\epsilon_{n',\vec{p}_\perp-\vec{q}_\perp} - \epsilon_{n,\vec{p}_\perp} + \omega_{\vec{q}} - l\Omega) + [f(\epsilon_{n,\vec{p}_\perp}) - f(\epsilon_{n',\vec{p}_\perp-\vec{q}_\perp})] \delta(\epsilon_{n',\vec{p}_\perp-\vec{q}_\perp} - \epsilon_{n,\vec{p}_\perp} - \omega_{\vec{q}} - l\Omega) \left. \right\} \\
& + \pi \sum_{n',\vec{k}} |D_{\vec{k}}|^2 |I_{n,n'}(k_z)|^2 N(\vec{k}) \sum_{l,s} J_l \left(\frac{e\vec{E}_0\vec{q}_\perp}{m\Omega^2} \right) J_{l+s} \left(\frac{e\vec{E}_0\vec{q}_\perp}{m\Omega^2} \right) \\
& \times \left\{ [f(\epsilon_{n,\vec{p}_\perp}) - f(\epsilon_{n',\vec{p}_\perp+\vec{k}_\perp})] \delta(\epsilon_{n',\vec{p}_\perp+\vec{k}_\perp} - \epsilon_{n,\vec{p}_\perp} + \omega_{\vec{q}} - \omega_{\vec{k}} - l\Omega) \right. \\
& \left. + [f(\epsilon_{n,\vec{p}_\perp}) - f(\epsilon_{n',\vec{p}_\perp-\vec{k}_\perp})] \delta(\epsilon_{n',\vec{p}_\perp-\vec{k}_\perp} - \epsilon_{n,\vec{p}_\perp} - \omega_{\vec{q}} + \omega_{\vec{k}} - l\Omega) \right\}. \tag{12}
\end{aligned}$$

The quantum acoustoelectric current j^{QAE} in the direction of external acoustic wave vector \vec{q} is expressed:

$$j^{QAE} = \sum_n \frac{2e}{(2\pi)^2} \int v_{\vec{p}} f_1 d\vec{p}_\perp, \tag{13}$$

$v_{\vec{p}}$ is the electron velocity is given by $v_{\vec{p}} = \partial \epsilon_{n,\vec{p}} / \partial \vec{p}$.

Substituting Eq. (12) into Eq. (13) and solving for a non-degenerate electron gas, $\tau_{\vec{p}}$ is taken to be constant, we obtain for the acoustoelectric current:

$$\begin{aligned}
j^{QAE} = & A_1 \sum_l \frac{1}{l[(l\Omega\tau)^2 + 1]} \sum_{n,n'} |U_{n,n'}|^2 \exp\left(-\frac{\pi^2 n^2}{2mL^2 k_B T}\right) (B_+ - B_-) \\
& + A_2 \sum_l \frac{1}{l[(l\Omega\tau)^2 + 1]} \sum_{n,n'} \frac{\pi}{L} (2 + \delta_{n,n'}) \exp\left(-\frac{\pi^2 n^2}{2mL^2 k_B T}\right) (C_+ - C_-), \tag{14}
\end{aligned}$$

where

$$A_1 = \frac{(2\pi \cdot e)^2 \Phi \wedge^2 \tau c_l^4 \omega_{\vec{q}}^3 E_0}{4\rho_0 c_s^2 m \Omega^3} \exp\left(\frac{\epsilon_F}{k_B T}\right), \quad A_2 = \frac{2e^2 \wedge^2 \tau (2mk_B T \pi)^{1/2} E_0}{8m^2 (2\pi)^3 \rho_0 c_s \omega_{\vec{q}} \Omega^3} \exp\left(\frac{\epsilon_F}{k_B T}\right),$$

$$\begin{aligned}
B_{\pm} &= \left(1 + \frac{D_{\pm}^2}{mk_B T}\right) \exp\left(-\frac{D_{\pm}^2}{2mk_B T}\right), \quad D_{\pm} = \frac{q}{2} + \frac{m\Delta_{n,n'}}{q} \pm \frac{m(\omega_{\bar{q}} - \omega_{\bar{k}} - \Omega)}{q}, \\
C_{\pm} &= \exp(-F_{\pm}) \left[\frac{1}{2} \left(\frac{d_{\pm}}{c}\right)^{3/2} K_3[2(d_{\pm}c)^{1/2}] + 2a_{\pm} \frac{d_{\pm}}{c} K_2[2(d_{\pm}c)^{1/2}] + 2b_{\pm} \left(\frac{d_{\pm}}{c}\right)^{1/2} K_1[2(d_{\pm}c)^{1/2}] \right], \\
F_{\pm} &= -\frac{\Delta_{n,n'} - \Omega \pm \omega_{\bar{k}}}{2k_B T}, \quad a_{\pm} = mk_B T + m\Delta_{n,n'} - m\Omega \pm m\omega_{\bar{k}}, \quad b_{\pm} = (m\Delta_{n,n'} - m\Omega \pm m\omega_{\bar{k}}), \\
d_{\pm} &= \frac{(m\Delta_{n,n'} - m\Omega \pm m\omega_{\bar{k}})^2}{2mK_B T}, \quad c = \frac{1}{8mk_B T}, \quad \Delta_{n,n'} = \frac{\pi^2}{2mL^2}(n^2 - n'^2),
\end{aligned}$$

here, ϵ_F is the Fermi energy, k_B is the Boltzmann constant, $K_n(x)$ is the Bessel function of 2nd order.

The Eq. (14) is the analytical expression of QAE current in QW in the case momentum relaxation time is a constant. In the case of the vanishing electron-internal phonon interaction. This result give the same result obtained by using Boltzmann kinetic equation in a quantum well.

4. NUMERICAL RESULTS AND DISCUSSIONS

To clarify the results that have been obtained, in this section, we consider the AE current. This quantity is considered as a function of the temperature T , the acoustic wave number q , the acoustic intensity Φ , and the parameters of the AlGaAs/GaAs/AlGaAs QW. The parameters used in the calculations are: $\sigma = 5300 \text{ kgm}^{-3}$, $\tau = 10^{-12} \text{ s}$, $m = 0.067m_0$, m_0 being the mass of free electron, $\Phi = 10^4 \text{ W m}^{-2}$, $c_l = 2.10^3 \text{ m s}^{-1}$, $c_t = 18.10^2 \text{ m s}^{-1}$, $c_s = 8.10^2 \text{ m s}^{-1}$.

Figure 1 present the dependence of the QAE current density on the frequency ω_q of the external acoustic wave at different values for the frequency of electromagnetic wave. Fig. 1 shown some maxima when the condition $\omega_{\bar{q}} = \omega_{\bar{k}} \pm \Delta_{n,n'} + l\Omega$ ($n \neq n'$) is satisfied. This result is different from the acoustoelectric current in a bulk semiconductor [9–15], because in a bulk semiconductor, when the $\omega_{\bar{q}}$ increase, the acoustoelectric current increases linearly. The cause of the difference between the bulk semiconductor and the QW is characteristics of a low-dimensional system, in low-dimensional systems, the energy spectrum of electron is quantized and exists even if the relaxation time τ of the carrier does not depend on the carrier energy. In Fig. 1, there are two peaks. This is attributed to the transitions between mini-bands ($n \rightarrow n'$), and the two peaks correspond to ($n = 1 \rightarrow n' = 2$) and ($n = 2 \rightarrow n' = 3$) transitions or intersubband transitions as the main contribution to j^{QAE} . When we consider the case $n = n'$. Physically, we merely consider transitions within sub-bands (intrasubband transitions), and from the numerical calculations we obtain $j^{QAE} = 0$, where mean that only the intersubband transition ($n \neq n'$) contribute to the j^{QAE} . In superlattices [16–18], the acoustoelectric current density appears even if the intrasubband transitions. This can be explained by assuming that only electrons whose momenta comply with the condition $\omega_{\bar{q}} = \omega_{\bar{k}} \pm \Delta_{n,n'} + l\Omega$

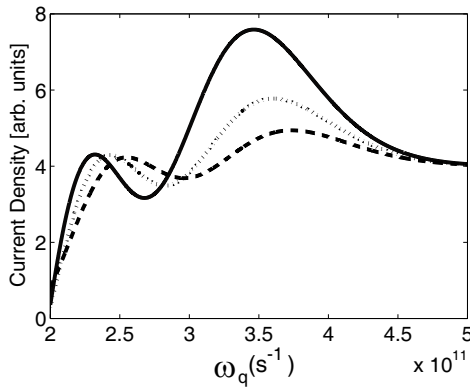


Figure 1: Dependence of the j^{QAE} current density on the frequency ω_q of the external acoustic wave at different values of the frequency of electromagnetic wave $\Omega = 8 \times 10^{13} \text{ s}^{-1}$ (solid line), $\Omega = 9 \times 10^{13} \text{ s}^{-1}$ (dot line), $\Omega = 10 \times 10^{13} \text{ s}^{-1}$ (dashed line). Here $T = 50 \text{ K}$, $\epsilon_F = 0.038 \text{ eV}$, $n = 1 \rightarrow 3$, $n' = 1 \rightarrow 3$.

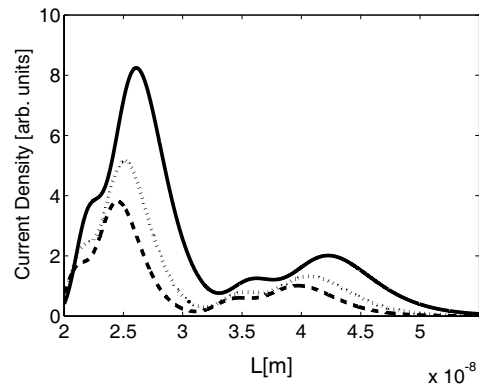


Figure 2: Dependence of the j^{QAE} current density on the width of the quantum well at different values of the frequency of electromagnetic wave $\Omega = 7 \times 10^{13} \text{ s}^{-1}$ (solid line), $\Omega = 7.5 \times 10^{13} \text{ s}^{-1}$ (dot line), $\Omega = 8 \times 10^{13} \text{ s}^{-1}$ (dashed line). Here $T = 50 \text{ K}$, $\epsilon_F = 0.038 \text{ eV}$, $n = 1 \rightarrow 3$, $n' = 1 \rightarrow 3$.

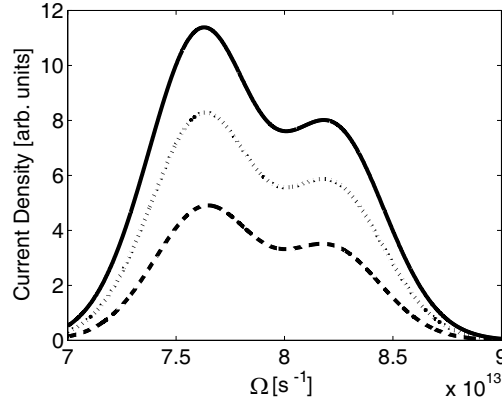


Figure 3: Dependence of the j^{QAE} current density on the frequency of electromagnetic wave at different values of temperature $T = 50$ K (solid line), $T = 53$ K (dot line), $T = 55$ K (dashed line), $\epsilon_F = 0.038$ eV, $n = 1 \rightarrow 3$, $n' = 1 \rightarrow 3$.

($n \neq n'$) contribute considerably to the effect.

Figure 2 shows the dependence of the j^{QAE} on the width of the QW for different values of the electromagnetic wave frequency Ω . Fig. 2 shows that influence of electromagnetic wave on the j^{QAE} is strong, when the frequency of electromagnetic wave increase the position of the peaks change and the peaks move to the smaller QW width when the frequency of the electromagnetic wave increases. Fig. 3 shows the dependence of the j^{QAE} on the electromagnetic wave frequency. The figures show that the dependence of j^{QAE} on the electromagnetic wave frequency is strong and nonlinear. The figures also show that when we consider different transitions, we obtain peaks at different values of L when the condition $\omega_{\vec{q}} = \omega_{\vec{k}} \pm \Delta_{n,n'} + l\Omega$ ($n \neq n'$) is satisfied. Moreover, Fig. 2 shows that the peaks move to the smaller width when the frequency of electromagnetic wave increases. In contrast, Fig. 3 shows that the position of the maxima nearly are not move as the temperature is varied, because the condition $\omega_{\vec{q}} = \omega_{\vec{k}} \pm \Delta_{n,n'} + l\Omega$ ($n \neq n'$) does not depend on the temperature.

5. CONCLUSION

In this paper, we have obtained analytical expressions for the j^{QAE} in presence of the external electromagnetic wave in a QW by using the quantum kinetic equation for the distribution function of electrons interacting with an external acoustic wave and internal phonons. We have shown the strong nonlinear dependence of j^{QAE} on the frequency ω_q of the external acoustic wave, the width L of the QW and the frequency of electromagnetic wave. The importance of the present work is the appearance of peaks when the condition $\omega_{\vec{q}} = \omega_{\vec{k}} \pm \Delta_{n,n'} + l\Omega$ ($n \neq n'$) is satisfied, the results are complex and different from those obtained in bulk semiconductors [9–15] and the superlattices [16–18]. Our result indicates that the dominant mechanism for such a behavior is electron confinement in the QW and transitions between mini-bands $n \rightarrow n'$. The j^{QAE} exists even if the relaxation time τ of the carrier does not depend on the carrier energy, and the results are similar to those for superlattices [16, 18]. This differs from bulk semiconductors, because in bulk semiconductors [9–15], the acoustoelectric current vanishes for a constant relaxation time.

The numerical results obtained for the AlGaAs/GaAs/AlGaAs QW show that influence of the electromagnetic wave on the j^{QAE} is strong.

ACKNOWLEDGMENT

This work was completed with financial support from the Vietnam National University, Ha Noi (No. QGTD.12.01) and Vietnam NAFOSTED (No. 103.01-2011.18).

REFERENCES

1. Zhang, Y., K. Suenaga, C. Colliex, and S. Iijima, *Science*, Vol. 281, 973, 1998.
2. Schmitt-Rink, S., D. S. Chemla, and D. A. B. Miller, *Adv. Phys.*, Vol. 38, 89, 1989.
3. Phong, T. C. and N. Q. Bau, *J. Korean Phys. Soc.*, Vol. 42, 647, 2003.
4. Shmelev, G. M., L. A. Chaikovskii, and N. Q. Bau, *Sov. Phys. Semicond.*, Vol. 12, 1932, 1978.

5. Bau, N. Q. and T. C. Phong, *J. Phys. Soc. Japan.*, Vol. 67, 3875, 1998.
6. Pavlovich, V. V. and E. M. Epshtein, *Sov. Phys. Semicond.*, Vol. 11, 809, 1977.
7. Bau, N. Q., D. M. Hung, and N. B. Ngoc, *J. Korean Phys. Soc.*, Vol. 54, 765, 2009.
8. Bau, N. Q. and H. D. Trien, *J. Korean Phys. Soc.*, Vol. 56, 120, 2010.
9. Parmenter, R. H., *Phys. Rev. B*, Vol. 89, 990, 1953.
10. Johri, G. and H. N. Spector, *Phys. Rev. B*, Vol. 15, 4955, 1959.
11. Kogami, M. and S. Tanaka, *J. Phys. Soc. Japan*, Vol. 30, 775, 1970.
12. Eckstein, S. G., *J. Appl. Phys.*, Vol. 35, 2702, 1964.
13. Epshtein, E. M. and V. G. Yu, *Sov. Phys. Solid State.*, Vol. 9, 288, 1967.
14. Weinreich, G., T. M. Sanders, and H. G. White, *Phys. Rev. B*, Vol. 1, 114, 1959.
15. Johri, G. and H. N. Spector, *Phys. Rev. B*, Vol. 15, 4955, 1977.
16. Mensah, S. Y. and F. K. A. Allotey, *J. Phys Condens. Matter.*, Vol. 12, 5225, 2000.
17. Mensah, S. Y. and N. G. Mensah, *J. Phys Superlatt. Micros.*, Vol. 37, 87, 2005.
18. Bau, N. Q., N. V. Hieu, N. T. Thuy, and T. C. Phong, *Coms. Phys. Vn.*, Vol. 3, 249, 2010.
19. Shilton, J. M., D. R. Mace, and V. I. Talyanskii, *J. Phys Condens.*, Vol. 8, 337, 1996.
20. Wohlman, O. E., Y. Levinson, and Y. M. Galperin, *Phys. Rev. B*, Vol. 62, 7283, 2000.
21. Levinson, Y., O. Entin-Wohlman, and P. Wolfle, *J. Appl. Phys. Lett.*, Vol. 85, 635, 2000.
22. Kokurin, I. A. and V. A. Margulis, *J. Exper and Theor Phys.*, Vol. 1, 206, 2007.
23. Cunningham, J., M. Pepper, and V. I. Talyanskii, *J. Appl. Phys. Lett.*, Vol. 86, 152105, 2005.
24. Astley, M. R., M. Kataoka, and C. J. B. Ford, *J. Appl. Phys.*, Vol. 103, 096102, 2008.
25. Bau, N. Q., N. V. Hieu, and N. V. Nhan, “The influence of the electromagnetic wave on the nonlinear acoustoelectric effect in a superlattice,” *PIERS Proceeding*, 1048–1053, Kuala Lumpur, Malaysia, March 27–30, 2012.
26. Zavaritskii, N. V., M. I. Kaganov, and S. T. Mevlyut, *JETP Lett.*, Vol. 28, 205, 1978.

Dyson Equations for Dense Random Media Composed of Dielectric or Metallic Nanoscale Scatterers

Gerard Berginc
Thales, France

Abstract— We develop a general formalism based upon Green functions to calculate the electromagnetic field scattered by a random medium with rough boundaries. We give an expression of the effective permittivity, which is extended to random media with different types of particles bounded with randomly rough interfaces.

1. INTRODUCTION

In this paper, we consider the coherent component of the electromagnetic wave field inside random media bounded with randomly rough surfaces. The subject of our interest concerns a random medium consisting of statistical ensembles of different scattering species and artificial material structures developed on base of dielectric or metallic resonant particles. The intent of this paper is to establish new formulas for the effective dielectric constant which characterizes the coherent part of an electromagnetic wave propagating inside a random medium with randomly rough interfaces. The starting point of our theory is the multiple scattering theory. Quantum multiple scattering theory has been transposed in this electromagnetic case. We give a formal solution for the scattering operator by introducing the T-operator formalism. We show that the T-operator satisfies a Lippman-Schwinger equation. Then we introduce the Quasi-Crystalline Coherent Potential Approximation (QC-CPA), which takes into account the correlation between the particles with a pair-distribution function. This function describes the correlation between two distinct particles.

2. DYSON EQUATION AND EFFECTIVE PERMITTIVITY

In the following we consider harmonic waves with $\exp(-i\omega t)$ pulsation. The structure, we consider in this paper is defined by a first semi-infinite medium (medium 0) with a permittivity ϵ_0 , a random layer (medium 1) with a permittivity $\epsilon_1(\omega)$ bounded by rough interfaces and another semi-infinite medium (medium 3) with a permittivity $\epsilon_2(\omega)$. The layer contains discrete scatterers randomly distributed. To calculate the scattered field we introduce the Green functions associated with the different media. With the source inside the medium 1 the Green functions satisfy the following propagation equations:

$$\nabla \times \nabla \times \bar{\mathbf{G}}_{SV}^{01}(\mathbf{r}, \mathbf{r}_0) - \epsilon_0(\omega) K_{vac}^2 \bar{\mathbf{G}}_{SV}^{01}(\mathbf{r}, \mathbf{r}_0) = 0, \quad (1)$$

$$\nabla \times \nabla \times \bar{\mathbf{G}}_{SV}^{11}(\mathbf{r}, \mathbf{r}_0) - \epsilon_V(\mathbf{r}, \omega) K_{vac}^2 \bar{\mathbf{G}}_{SV}^{11}(\mathbf{r}, \mathbf{r}_0) = \delta(\mathbf{r} - \mathbf{r}_0) \bar{\mathbf{I}}, \quad (2)$$

$$\nabla \times \nabla \times \bar{\mathbf{G}}_{SV}^{21}(\mathbf{r}, \mathbf{r}_0) - \epsilon_2(\omega) K_{vac}^2 \bar{\mathbf{G}}_{SV}^{21}(\mathbf{r}, \mathbf{r}_0) = 0, \quad (3)$$

The superscripts indicate respectively, the receiver location and the source location in the media 0, 1 and 2 and the subscript SV shows the interactions between the random volume and the rough interfaces are taken into account in the Green function, $K_{vac} \equiv \omega/c$. Inside the medium with the permittivity $\epsilon_1(\omega)$, we consider a set of N scatterers which we take spherical with a radius r_s and a permittivity $\epsilon_s(\omega)$. In the following we consider two types of scatterers with different radii and permittivities, they are noted a and b . The formulas can be generalized to N types of particles. The permittivity ϵ_V for the layer is given by:

$$\epsilon_V(\mathbf{r}, \omega) = \epsilon_1(\omega) + \sum_{a=1}^{N_a} (\epsilon_a(\omega) - \epsilon_1(\omega)) \Theta_a(\mathbf{r} - \mathbf{r}_a) + \sum_{b=1}^{N_b} (\epsilon_b(\omega) - \epsilon_1(\omega)) \Theta_b(\mathbf{r} - \mathbf{r}_b), \quad (4)$$

where $\mathbf{r}_1, \dots, \mathbf{r}_N$ are the positions of the centers of the particles, $N_a + N_b = N$ is the total number of particles and $\Theta_{a,b}$ describes the shape of the particles. We can notice that the results can be generalized to non-spherical particles:

$$\Theta_{a,b}(\mathbf{r}) = \begin{cases} 1 & \text{if } \|\mathbf{r}\| < r_{a,b} \\ 0 & \text{if } \|\mathbf{r}\| > r_{a,b} \end{cases}, \quad (5)$$

with $r_{a,b}$ the radii of the particles. We impose boundary conditions on the two rough surfaces. The solutions of the propagation equations are unique if we impose the radiation condition at infinity. We now define the potential function, which describes the interaction between the wave and the particles and then we give the expression of the Green function. The previous system of differential equations with boundary conditions can be transformed into integral equations. With the source in the medium 1 we have the following system of integral equations related to the potential function:

$$\bar{\mathbf{G}}_{SV}^{01} = \bar{\mathbf{G}}_S^{01} + \bar{\mathbf{G}}_S^{01} \cdot \bar{\mathbf{V}}^{11} \cdot \bar{\mathbf{G}}_{SV}^{11}, \quad (6)$$

$$\bar{\mathbf{G}}_{SV}^{11} = \bar{\mathbf{G}}_S^{11} + \bar{\mathbf{G}}_S^{11} \cdot \bar{\mathbf{V}}^{11} \cdot \bar{\mathbf{G}}_{SV}^{11}, \quad (7)$$

$$\bar{\mathbf{G}}_{SV}^{21} = \bar{\mathbf{G}}_S^{21} + \bar{\mathbf{G}}_S^{21} \cdot \bar{\mathbf{V}}^{11} \cdot \bar{\mathbf{G}}_{SV}^{11}, \quad (8)$$

where the Green functions $\bar{\mathbf{G}}_S^{ij}$ are given in [1]. They describes the field scattered by a slab with rough boundaries where the scatterers have been replaced by an homogeneous medium characterized by an effective permittivity $\epsilon_e(\omega)$. The following operator notation is used:

$$[\bar{\mathbf{A}} \cdot \bar{\mathbf{B}}](\mathbf{r}, \mathbf{r}_0) = \int_{V_1} d^3 \mathbf{r}_1 \bar{\mathbf{A}}(\mathbf{r}, \mathbf{r}_1) \cdot \bar{\mathbf{B}}(\mathbf{r}_1, \mathbf{r}_0). \quad (9)$$

And the potential function can be written as:

$$\bar{\mathbf{V}}^{11}(\mathbf{r}, \mathbf{r}_0, \omega) = \delta(\mathbf{r} - \mathbf{r}_0) \bar{\mathbf{V}}^1(\mathbf{r}), \quad (10)$$

$$\bar{\mathbf{V}}^1(\mathbf{r}, \omega) \equiv K_{vac}^2(\epsilon_V(\mathbf{r}, \omega) - \epsilon_e(\omega)) \bar{\mathbf{I}}, \quad (11)$$

The effective permittivity will be determined using the Coherent-Potential Approximation (CPA) and the Quasi-Crystalline Approximation (QCA). Our aim in this paper is to find a system of equations, with which we can calculate the effective permittivity. The Equation (7) is solved by iteration and we have the development:

$$\bar{\mathbf{G}}_{SV}^{11} = \bar{\mathbf{G}}_S^{11} + \bar{\mathbf{G}}_S^{11} \cdot \bar{\mathbf{V}}^{11} \cdot \bar{\mathbf{G}}_S^{11} + \bar{\mathbf{G}}_S^{11} \cdot \bar{\mathbf{V}}^{11} \cdot \bar{\mathbf{G}}_S^{11} \cdot \bar{\mathbf{V}}^{11} \cdot \bar{\mathbf{G}}_S^{11} + \dots \quad (12)$$

We can rewrite the Lipmann-Schwinger Equation (7) in introducing the transition operator $\bar{\mathbf{T}}_{SV}^{11}$, which is defined by:

$$\bar{\mathbf{G}}_{SV}^{11} = \bar{\mathbf{G}}_S^{11} + \bar{\mathbf{G}}_S^{11} \cdot \bar{\mathbf{T}}_{SV}^{11} \cdot \bar{\mathbf{G}}_S^{11}. \quad (13)$$

With the definition of (13) and the Equation (7) we can deduce the expression of the operator $\bar{\mathbf{T}}_{SV}^{11}$ in function of $\bar{\mathbf{V}}^{11}$:

$$\bar{\mathbf{T}}_{SV}^{11} = \bar{\mathbf{V}}^{11} + \bar{\mathbf{T}}_{SV}^{11} \cdot \bar{\mathbf{G}}_S^{11} \cdot \bar{\mathbf{V}}^{11}. \quad (14)$$

The transition operator $\bar{\mathbf{T}}_{SV}^{11}$ contains all the scattering processes involved in the random medium. This T -operator is useful to calculate the average field over the volume disorder $\langle \bar{\mathbf{G}}_{SV}^{11} \rangle_V$. We obtain the Dyson equation in which the potential operator is replaced by the mass operator, which contains all irreducible diagrams in the Feynman representation. The mass operator can be expressed with $\langle \bar{\mathbf{T}}_{SV}^{11} \rangle_V$. The averaged electric field satisfies a Dyson equation with a mass operator related to the effective dielectric permittivity of the homogenized structure. To determine $\epsilon_e(\omega)$ we use the coherent potential approximation (CPA), which is defined by:

$$\langle \bar{\mathbf{G}}_{SV}^{11} \rangle_V = \bar{\mathbf{G}}_S^{11}. \quad (15)$$

Using (13), we can demonstrate that (15) is equivalent to:

$$\langle \bar{\mathbf{T}}_{SV}^{11} \rangle_V = \bar{\mathbf{0}}. \quad (16)$$

3. EXPRESSION OF THE DIFFERENT SCATTERING OPERATORS

The scattering operator $\bar{\mathbf{t}}_{\mathbf{r}_i}^{11}$ for a particle with a permittivity ϵ_{si} located at the point \mathbf{r}_i inside an infinite homogeneous medium is given by the following equations with the scattering potential $\bar{\mathbf{v}}_{\mathbf{r}_i}^{11}$:

$$\bar{\mathbf{t}}_{\mathbf{r}_i}^{11} = \bar{\mathbf{v}}_{\mathbf{r}_i}^{11} + \bar{\mathbf{v}}_{\mathbf{r}_i}^{11} \cdot \bar{\mathbf{G}}_1^\infty \cdot \bar{\mathbf{t}}_{\mathbf{r}_i}^{11}, \quad (17)$$

$$\bar{\mathbf{v}}_{\mathbf{r}_i}^{11}(\mathbf{r}, \mathbf{r}_0) = (2\pi)^2 \delta(\mathbf{r} - \mathbf{r}_0) \bar{\mathbf{v}}_{\mathbf{r}_i}^1(\mathbf{r}), \quad \bar{\mathbf{v}}_{\mathbf{r}_i}^1(\mathbf{r}) = K_{vac}^2(\epsilon_{si} - \epsilon_1) \Theta_s(\mathbf{r} - \mathbf{r}_i) \bar{\mathbf{I}}. \quad (18)$$

$\bar{\mathbf{G}}_1^\infty$ is the Green function in an unbounded homogeneous medium with the effective permittivity ϵ_e . And the operator $\bar{\mathbf{T}}_{SV}^{11}$ can be written as:

$$\bar{\mathbf{T}}_{SV}^{11} = \sum_{j=1}^N \bar{\mathbf{t}}_j^{11} + \sum_{\substack{i,j=1 \\ i \neq j}}^N \bar{\mathbf{t}}_j^{11} \cdot \bar{\mathbf{G}}_S^{11} \cdot \bar{\mathbf{t}}_i^{11} + \sum_{\substack{i,j,m=1 \\ i \neq j, i \neq m}}^N \bar{\mathbf{t}}_j^{11} \cdot \bar{\mathbf{G}}_S^{11} \cdot \bar{\mathbf{t}}_i^{11} \cdot \bar{\mathbf{G}}_S^{11} \cdot \bar{\mathbf{t}}_m^{11} + \dots \quad (19)$$

$\bar{\mathbf{t}}_{S,\mathbf{r}_a}^{11}$ is the scattering operator for a particle located at \mathbf{r}_a inside the layer, this operator takes into account the interactions of the field with the rough surfaces.

$$\bar{\mathbf{t}}_{S,\mathbf{r}_a}^{11} = [\bar{\mathbf{I}} - \bar{\mathbf{v}}_{\mathbf{r}_a}^{11} \cdot \bar{\mathbf{G}}_S^{11}]^{-1} \cdot \bar{\mathbf{v}}_{\mathbf{r}_a}^{11}, \quad (20)$$

We write $\bar{\mathbf{G}}_S^{11} = \bar{\mathbf{G}}_1^\infty + \delta\bar{\mathbf{G}}_S^{11}$, $\delta\bar{\mathbf{G}}_S^{11}$ is the Green function describing the wave interactions with the boundaries of the effective medium. We can show that:

$$\bar{\mathbf{t}}_{S,\mathbf{r}_i}^{11} = \bar{\mathbf{t}}_{\mathbf{r}_i}^{11} + \bar{\mathbf{t}}_{\mathbf{r}_i}^{11} \cdot \delta\bar{\mathbf{G}}_S^{11} \cdot \bar{\mathbf{t}}_{S,\mathbf{r}_i}^{11}, \quad (21)$$

If we renormalize the permittivity of the particle by $\bar{\epsilon}_s = \epsilon_{si} - (\epsilon_1 - \epsilon_e)$, we have the relations:

$$\bar{\mathbf{V}}_{\mathbf{r}_i}^1(\mathbf{r}) = K_{vac}^2(\epsilon_{si} - \epsilon_1)\Theta_s(\mathbf{r} - \mathbf{r}_i)\bar{\mathbf{I}}, \quad (22)$$

$$= K_{vac}^2(\bar{\epsilon}_s - \epsilon_e)\Theta_s(\mathbf{r} - \mathbf{r}_i)\bar{\mathbf{I}}. \quad (23)$$

Hence the operator $\bar{\mathbf{t}}_{\mathbf{r}_i}^{11}$ is the scattering operator for a particle with a permittivity $\bar{\epsilon}_s$ surrounded by a medium of permittivity ϵ_e (see Fig. 1). The operator $\bar{\mathbf{t}}_{S,\mathbf{r}_i}^{11}$ describes the scattering from a particle located at the point \mathbf{r}_i inside the volume V_1 bounded by the rough interfaces. If we iterate the Equation (21), we obtain:

$$\bar{\mathbf{t}}_{S,\mathbf{r}_i}^{11} = \bar{\mathbf{t}}_{\mathbf{r}_i}^{11} + \bar{\mathbf{t}}_{\mathbf{r}_i}^{11} \cdot \delta\bar{\mathbf{G}}_S^{11} \cdot \bar{\mathbf{t}}_{\mathbf{r}_i}^{11} + \bar{\mathbf{t}}_{\mathbf{r}_i}^{11} \cdot \delta\bar{\mathbf{G}}_S^{11} \cdot \bar{\mathbf{t}}_{\mathbf{r}_i}^{11} \cdot \delta\bar{\mathbf{G}}_S^{11} \cdot \bar{\mathbf{t}}_{\mathbf{r}_i}^{11} + \dots, \quad (24)$$

The first term of the Equation (24) describes the scattering from the particle and the following terms represent the interaction between the particle and the rough surfaces, which is given by $\delta\bar{\mathbf{G}}_S^{11}$ (see Fig. 1). We now introduce the scattering operator $\bar{\mathbf{C}}_{SV,\mathbf{r}_i}^{11}$, which represents the field scattered by a particle located at \mathbf{r}_i taking into account the interactions between the other particles and the rough surfaces (see Fig. 1). We can show that this operator is given by:

$$\bar{\mathbf{C}}_{SV,\mathbf{r}_i}^{11} = \bar{\mathbf{t}}_{S,\mathbf{r}_i}^{11} + \sum_{j=1, j \neq i}^N \bar{\mathbf{t}}_{S,\mathbf{r}_i}^{11} \cdot \bar{\mathbf{G}}_S^{11} \cdot \bar{\mathbf{t}}_{S,\mathbf{r}_j}^{11} + \sum_{j=1, j \neq i}^N \sum_{k=1, k \neq j}^N \bar{\mathbf{t}}_{S,\mathbf{r}_i}^{11} \cdot \bar{\mathbf{G}}_S^{11} \cdot \bar{\mathbf{t}}_{S,\mathbf{r}_j}^{11} \cdot \bar{\mathbf{G}}_S^{11} \cdot \bar{\mathbf{t}}_{S,\mathbf{r}_k}^{11} + \dots \quad (25)$$

4. AVERAGING OPERATORS

We now average $\bar{\mathbf{C}}_{SV,\mathbf{r}_i}^{11}$ with the conditional average $\langle \dots \rangle_{V;\mathbf{r}_i}$ using the conditional probability of finding a particle at \mathbf{r}_i given a particle at \mathbf{r}_j and the CPA hypothesis ($i = a$ or b). We obtain the expression:

$$\langle \bar{\mathbf{C}}_{SV,\mathbf{r}_i}^{11} \rangle_{V;\mathbf{r}_i} = \bar{\mathbf{t}}_{S,\mathbf{r}_i}^{11} + n_i \bar{\mathbf{t}}_{S,\mathbf{r}_i}^{11} \cdot \bar{\mathbf{G}}_S^{11} \cdot \int_{V_1} d^3\mathbf{r}_j \left[g(\|\mathbf{r}_j - \mathbf{r}_i\|) \langle \bar{\mathbf{C}}_{SV,\mathbf{r}_j}^{11} \rangle_{V;\mathbf{r}_i,\mathbf{r}_j} - \langle \bar{\mathbf{C}}_{SV,\mathbf{r}_j}^{11} \rangle_{V;\mathbf{r}_j} \right], \quad (26)$$

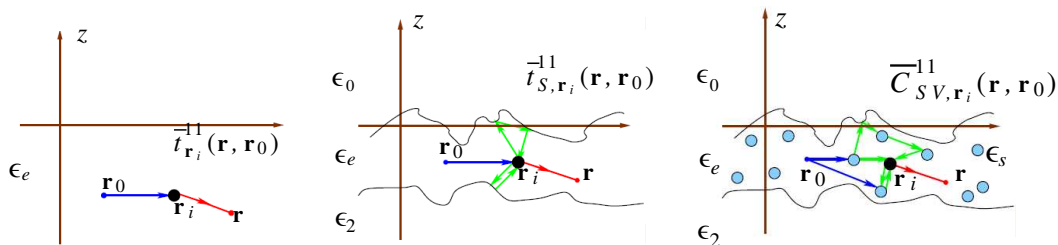


Figure 1: Representation of the operators $\bar{\mathbf{t}}_{\mathbf{r}_i}^{11}$, $\bar{\mathbf{t}}_{S,\mathbf{r}_i}^{11}$, $\bar{\mathbf{C}}_{SV,\mathbf{r}_i}^{11}$.

where we used the approximation $n_i \simeq (N_i - 1)/\mathcal{V}_1$ which is valid for a large number of particle ($N \gg 1$). We also defined a pair-distribution function $g(\|\mathbf{r}_j - \mathbf{r}_i\|) = p(\mathbf{r}_j|\mathbf{r}_i)/p(\mathbf{r}_j)$. It only depends on the distance between the two particles if we suppose that the distributions of the particles are statistically homogeneous and isotropic. $p(\mathbf{r}_j)$ defines the density probability to find a particle at the point \mathbf{r}_j . $p(\mathbf{r}_j|\mathbf{r}_i)$ is the conditional probability to find a particle at \mathbf{r}_j given a particle at \mathbf{r}_i . The Quasi-Crystalline Approximation (QCA) states that $\langle \bar{\mathbf{C}}_{SV,\mathbf{r}_j}^{11} \rangle_{V;\mathbf{r}_i,\mathbf{r}_j} = \langle \bar{\mathbf{C}}_{SV,\mathbf{r}_j}^{11} \rangle_{V;\mathbf{r}_j}$. This approximation is strictly valid when the particles have a fixed position, as in a crystal. The Quasi-Crystalline Approximation consists in omitting the fluctuation of the electromagnetic field, interacting with a particle located at \mathbf{r}_j , due to a deviation of a particle located at \mathbf{r}_i from its average position. Under the QC Approximation the effective permittivity $\epsilon_e(\omega)$ satisfies the following system of equations:

$$(2\pi)^2 \delta(\mathbf{r} - \mathbf{r}_0) \epsilon_e K_{vac}^2 \bar{\mathbf{I}} = (2\pi)^2 \delta(\mathbf{r} - \mathbf{r}_0) \epsilon_1 K_{vac}^2 \bar{\mathbf{I}} + n_a \int_{V_1} d^3 \mathbf{r}_a, \langle \bar{\mathbf{C}}_{SV,\mathbf{r}_a}^{11}(\mathbf{r}, \mathbf{r}_0) \rangle_{V;\mathbf{r}_a} \\ + n_b \int_{V_1} d^3 \mathbf{r}_b, \langle \bar{\mathbf{C}}_{SV,\mathbf{r}_b}^{11}(\mathbf{r}, \mathbf{r}_0) \rangle_{V;\mathbf{r}_b}, \quad (27)$$

$$\langle \bar{\mathbf{C}}_{SV,\mathbf{r}_i}^{11} \rangle_{V;\mathbf{r}_i} = \bar{\mathbf{t}}_{S,\mathbf{r}_i}^{11} + n_i \bar{\mathbf{t}}_{S,\mathbf{r}_i}^{11} \cdot \bar{\mathbf{G}}_S^{11} \cdot \int_{V_1} d^3 \mathbf{r}_j [g(\|\mathbf{r}_j - \mathbf{r}_i\|) - 1] \langle \bar{\mathbf{C}}_{SV,\mathbf{r}_j}^{11} \rangle_{V;\mathbf{r}_j}. \quad (28)$$

The Equation (28) can be simplified by omitting the contribution $\delta \bar{\mathbf{G}}_S^{11}$ due to the rough boundaries in $\bar{\mathbf{G}}_S^{11} = \bar{\mathbf{G}}_1^\infty + \delta \bar{\mathbf{G}}_S^{11}$ if the following condition is satisfied: $K_e'' H \gg 1$ with $K_e'' = \text{Im} K_e$. We define the extinction length as $l_e = 1/2K_e''$. The previous condition means that the slab thickness must be greater than the extinction length. With this condition we replace in (28) the Green function $\bar{\mathbf{G}}_S^{11}$ by $\bar{\mathbf{G}}_1^\infty$ and the operator $\bar{\mathbf{t}}_{S,\mathbf{r}_i}^{11}$ by $\bar{\mathbf{t}}_{\mathbf{r}_i}^{11}$.

5. CONCLUSION

The expression of the permittivity developed in this paper has been extended to random media with different types of particles and bounded by rough surfaces. This extended formulation of the effective permittivity is then used to calculate the coherent fields and incoherent intensities scattered from a three-dimensional disordered medium with discrete scatterers and randomly rough interfaces.

REFERENCES

1. Soubret, A. and G. Berginc, "Electromagnetic Wave Scattering from a random layer with rough interfaces I: Coherent field," arXiv:physics/0312133, 2003.
2. Soubret, A. and G. Berginc, "Effective dielectric constant for random medium," arXiv:physics/0312117, 2003.
3. Berginc, G. and C. Bourrelly, "Light scattering from 3-D nanoscale disordered media," *PIERS Online*, Vol. 6, No. 8, 730–734, 2010.
4. Barabanenkov, Y. N., M. Y. Barabanenkov, and S. A. Nikitov, "Artificial magnetism in theory of wave multiple scattering by random discrete non-magnetic conducting media," arXiv:1009.4770v1, 2010.
5. Berginc, G., "Light scattering from nanostructured media," *PIERS Proceedings*, 273–276, Moscow, Russia, August 19–23, 2012.

Analysis of Parameter Sensitivity of Electromagnetic Railgun System

Na Pan¹, Zejun Shen², Peng Zuo², and Jiansheng Yuan²

¹Department of Electrical Engineering, Northeast Dianli University, Jilin 132012, China

²Department of Electrical Engineering, Tsinghua University, Beijing 100084, China

Abstract— By using the simulation of the electromagnetic railgun system, the influence effect of several parameters to the performance of the system characteristics is analyzed, including the number of capacitance groups in the pulse power source, the value of capacitances and their sequence trigger time, the value of adjustable wave inductance and resistance, current-carrying diode resistance and thyristor resistance, rail resistance gradient and inductance gradient parameters. The acceleration time and the exit velocity of armature are taken as the system performance. On the basis of parameter sensitivity analysis, more reasonable values of the parameters can be determined and designed, which can help the design of electromagnetic rail gun systems.

1. INTRODUCTION

The operation process of electromagnetic railgun system is involved with the mutual coupling of mechanical, electromagnetic, thermal, and other physical processes [1]. The design of the system may concern with the principle of electromagnetic emission, the technique of pulsed power sequence control, the numerical simulation or modeling, the dynamic load characteristics, the material property of armature and rails, and so on [2–13]. The numerical simulation or modeling of the system is of significance for the design. From the circuit point view, Software Simulink is widely used for the simulation [5–10]. While the electromagnetic field distribution in the railguns are usually analyzed the finite element method software, such as ANSYS software [11].

By the simulation, the parameter sensitivity of the system can be obtained, which can help the design. The influence effect of the parameters to the performance of the system characteristics can be analyzed in details by the numerical simulation, which is the main advantage of the simulation relative to the physical experiment. The parameters of the electromagnetic railgun system may include the value of capacitances, the value of adjustable wave inductance and resistance, current-carrying diode resistance and thyristor resistance, rail resistance and inductance gradient parameters. The acceleration time and the exit velocity of armature are taken as the system performance. Those parameters are analyzed in this paper.

2. ELECTROMAGNETIC RAILGUN CIRCUIT MODEL

The basic structure of electromagnetic railgun is composed of high pulsed power supply, two root conductor rails, and an armature sandwiched between the rails. The armature can slide forward. The working principle of the system is that: a huge value of current produced by the high pulse power source flows through the rails and the armature, the current produces a big magnetic field interacted with the current inside the armature, and the electromagnetic force is formed which speeds the armature forward.

The electromagnetic railgun lumped parameter model of the equivalent circuit diagram is shown as Fig. 1, in which C_i is the energy storage capacitance, D_j is the thyristor that controls C_i discharge sequence. R_{ci} is the equivalent current-carrying diode resistance of capacitance branch. D_k is the current-carrying diode that is for inductance discharge provide current-carrying diode loop after capacitance putting out, R_{xi} is the current-carrying diode equivalent resistance, L_{si} is the adjustable wave inductance, R_{si} is the adjustable wave resistance, R_{bi} is the cable equivalent resistance of the capacitance connected to the orbit, L_{bi} is the cable equivalent inductance, R_x and L_x are the armature movement equivalent resistance and the inductance respectively. R_a is the armature resistance, $R_x = R_{x0} + R'x$, $L_x = L_{x0} + L'x$, R_{x0} and L_{x0} are the orbit equivalent resistance and the armature inductance in the initial position respectively, R and L' are the rail resistance and the rail inductance gradient respectively. The variable footnote is $i = 1, 2, \dots, n$, $j = 1, 3, 5, \dots, n$, $k = 2, 4, 6, \dots, n$ to indicate different groups of the pulse power modules.

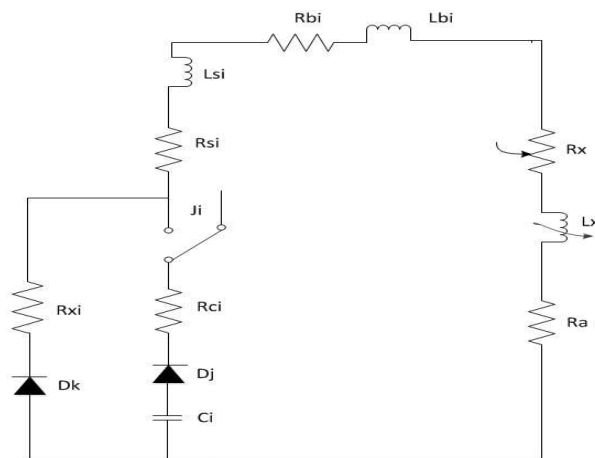


Figure 1: Electromagnetic railgun lumped circuit model.

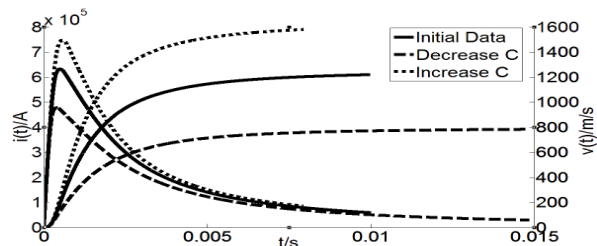


Figure 2: Influence to the current and the velocity by the value of capacitance.

3. ANALYSIS OF SYSTEM PARAMETER SENSITIVITY

A simulation model and the parameters come from the model in [13]. The simulation in [13] was conducted with PSPICE. The results were verified by the test data provided by Miguel Del Güercio in U.S. Army Research Laboratory [7]. A set of railgun experimental apparatus were given in [7], which gave the value of the capacitor, inductor, cable parameters and the power module. Totally eighteen power modules were used and operated at the same time or discharge as trigger time sequence. Based on this model, we have analyzed the parameter sensitivity.

3.1. System Parameter Setting

The total energy of test capacity storage is 4.5 MJ. The pulsed power source consists of 18 groups of modules, which can be operated at the same time and by sequential discharge. The value of capacitance is 4.2422 mF. The charged voltage on the capacitance is 5 kV and 6.5 kV respectively for two different experiments. The thyristor resistance R_c is 3.65 m Ω . The current-carrying diode resistance R_x is 6.65 m Ω . R' is 0 $\mu\Omega$ /m and L' is 0.46 μ H/m. The armature quality is 0.23 kg. The initial position x_0 is 0 m. The rail length l is 3 m. The cable resistance R_b is 9.18 m Ω . The cable inductance L_b is 3.22 μ H. Adjustable wave inductance L_s of the former 9 modules is 60 μ H at the same time trigger. The adjustable wave resistance R_s is 2 m Ω . L_s and R_s of other 9 modules are 24 μ H and 1 m Ω . The former 9 modules adopted time sequence trigger, other 9 modules are according to the delay in 0.3 ms time sequence trigger.

3.2. Influence by the Capacitance Parameter

The charging capacitance C determines the energy storage, which provides necessary energy to the system operation. The value of capacitance is set to three different situations, but the voltage on the capacitance keeps the same, by which the influence of its characteristic parameters to the system output is observed, i.e., the velocity of the armature. In Fig. 2, the current $i(t)$ and the armature velocity $v(t)$ are given for three value of capacitance. It comes to the conclusion that the value of capacitance influences the pulse current peak and the armature outlet velocity.

3.3. Influence by the Adjustable Wave Inductance L_s

In order to see the influence of the adjustable wave inductance with the current waveform and the armature velocity, three values of the inductance is chosen. Fig. 3 gives the results. By observing the current waveform regulation characteristics, it comes to the conclusion that functions of the adjustable wave inductance are almost the same as the capacitance. The value of adjustable wave inductance mainly influences the pulse current peak and the arriving time, as well as the armature acceleration time. Ultimately, it affects the armature outlet velocity. When the adjustable wave inductance is down to smaller, the pulse current peak is higher, the descent is faster and the armature acceleration time is shorter. Therefore L_s has some effect on the armature final exit velocity.

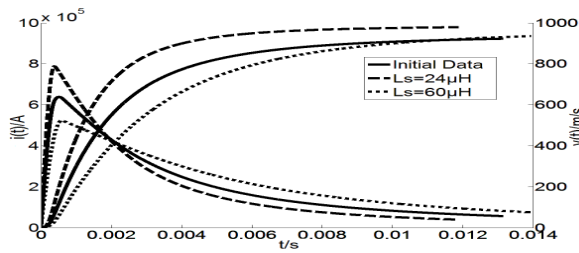


Figure 3: Influence to the current and the velocity by the adjustable inductance.

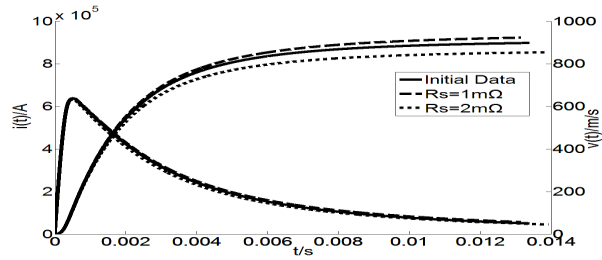


Figure 4: Influence to the current and the velocity by the adjustable resistance.

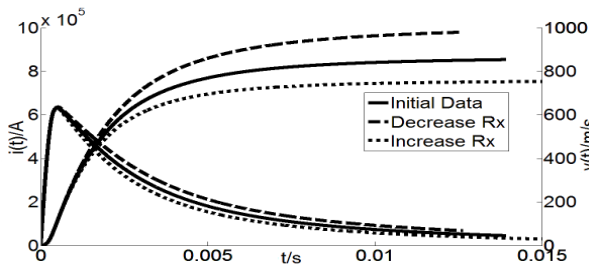


Figure 5: Influence to the current and the velocity by the current-carrying diode resistance.

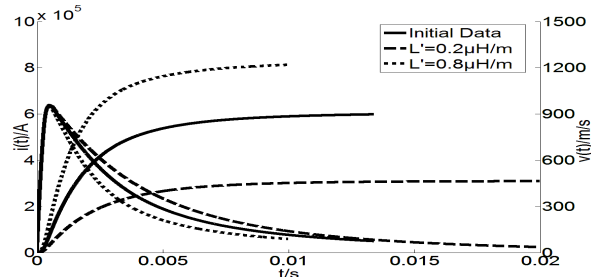


Figure 6: Influence to the current and the velocity by the rail inductance gradient.

3.4. Influence by the Adjustable Wave Resistance R_s

The adjustable wave resistance only produces negative effects to the system. By analyzing the influence of R_s can get the maximum resistance which is allowed in the system. Fig. 4 gives the results of current and velocity with three values of the resistance. By observing the resistance parameters characteristic curve, we can see that R_s does not have apparent effect on the pulse current peak and the peak time. In a similar way, R_s has no obvious effect on the armature acceleration time. Ultimately R_s is not of obvious influence for the armature outlet velocity.

3.5. Influence by the Current-carrying Diode Resistance R_x

The analysis of current-carrying diode resistance R_x is similar with the adjustable wave resistance Fig. 5 shows the influence to the current and the velocity. From the results with three different value of R_x and the influence of other resistances, we can see that R_x has a significant impact on the pulse current peak and the peak time. R_x mainly plays a role in the pulse current decline, and reduces the acceleration time of the armature. Consequently, it leads to the decrease of armature outlet velocity.

3.6. Influence by the Thyristor Resistance R_c and the Rail Resistance R

The analysis of thyristor resistance R_c and the rail resistance R is similar to the analysis of other resistances. The simulation results indicate that R_c has no obvious influence on the pulse current peak and the peak time as well as armature acceleration time and the armature outlet velocity. Resistance R mainly effects the pulse current decline stage. The value of the resistance is smaller, the current decline is slower, and the armature acceleration time is longer. Consequently, the armature velocity is greater.

3.7. Influence by the Rail Inductance Gradient L'

The rail inductance gradient L' , i.e., the changing ratio of the inductance against the length of the rails, is proportional to the electromagnetic force on the armature. In principle, the bigger is the inductance gradient, the better to the system. The simulation results as shown in Fig. 6 indicate that the relationship between the armature acceleration and the inductance gradient. By the results we can see that the rail inductance gradient mainly influences the pulse current decline stage. The value of rail inductance gradient is larger, the pulse current descent speed is faster, and the armature acceleration time is shorter. The rail inductance gradient effects the armature acceleration greatly.

4. CONCLUSION

The charging capacitance C determines the energy storage. Therefore, the value of capacitance influences the pulse current peak and the armature outlet velocity greatly. The rail inductance gradient is proportional to the electromagnetic force on the armature. Therefore, the value of rail inductance gradient determines the armature acceleration.

The resistance in the system only produces negative effects to the system, which decreases the efficiency of the system. The current-carrying diode resistance R_x has a significant impact on the pulse current peak and the peak time. The rail resistance R effects the pulse current decline stage. The adjustable wave resistance R_s and the thyristor resistance R_c have slight effect on the armature acceleration.

REFERENCES

1. Wang, Y. and F. Xiao, *Electric Gun Principle*, National Defence Industry Press, Beijing, Mar. 1995.
2. Wang, Y., S. Cheng, and P. Zheng, "Widely developing electric launch technology in China," *IEEE Transactions on Magn.*, Vol. 39, No. 1, 39–41, 2003.
3. Marshall, R. A. and Y. Wang, *Rail Guns: Their Science and Technology*, China Machine Press, Beijing, 2004.
4. Gully, J. H., "Power supply technology for electric guns," *IEEE Transactions on Magn.*, Vol. 27, No. 1, 329–334, 1991.
5. Fair, H. D., "Electromagnetic launch science and technology in the United States enters a new era," *IEEE Transactions on Magn.*, Vol. 41, No. 1, 158–164, Jan. 2005.
6. Chen, Q. and Y. Wang, "Computer simulation of electromagnetic process in the capacitor driven rail gun," *Transactions of China Electrotechnical Society*, Vol. 4, No. 4, 69, 2006.
7. Yang, Y. and J. Wang, "Design and simulation of power source for capacitive EM gun," *High Voltage Apparatus*, Vol. 44, No. 5, 435–437, 2008.
8. Yang, Y. and J. Wang, "Influence of pulse forming network on rail gun launching efficiency," *Journal of Gun Launch & Control*, No. 4, 41–45, 2011.
9. Tan, S. and J. Lu, "The electric parameters characteristics and optimum design of electromagnetic railgun," *Marine Electric Technology*, Vol. 32, No. 2, 2012.
10. Zhou, Y., P. Yan, W. Yuan, and L. Sun, "Effect of rail geometrical parameters on inductance gradient of EML," *Advanced Technology of Electrical Engineering and Energy*, Vol. 28, No. 3, 23–27, 2009.
11. Ju, L. and B. Zhang, "Barrel structural design and research on electromagnetic railgun," *Ship Science and Technology*, Vol. 33, No. 7, 94–98, 2011.
12. Tao, M., "Electromagnetic railgun solid armature characteristic research," Chinese Academy Sciences Institute, 1998.
13. Miguei, D. G., "A 4.5-MJ pulsed power supply for railgun experiments," *IEEE Trans. on Magn.*, Vol. 39, No. 1, 934–938, 2003.

Analysis of Approaches for Modeling the Contact Resistance on Conductor Interface by the Finite Element Method

Zejun Shen, Li Hao, Peng Zuo, and Jiansheng Yuan

Department of Electrical Engineering, Tsinghua University, Beijing 100084, China

Abstract— There may be an additional contact resistance on the interface of conductor regions caused by the change of material property, i.e., the resistivity. The simulation of the contact resistance is very important to get the Joule-heat losses of the conductors. However, it is difficult or impossible to model and calculate the contact resistance by using the traditional finite element method (FEM). A new method to model the contact resistance has been proposed in this article, with the help of the contact element in FEM software ANSYS. The contact element meshes the interface between conductors directly. With the parameter of “surface conductivity”, equations can be set up to couple the value elements of the conductors. We have implemented the simulation of contact resistance on the interface of different shape regions. Some examples of contact resistance calculation under different contact conditions are given and compared to those given by other methods. It is shown that using the contact element of ANSYS can model the contact resistance more easily and accurately, with a great advantage over other methods.

1. INTRODUCTION

There is an additional contact resistance on the interface when two conductors meet together, caused by the change of material property. Contact resistance is made up of two parts, according to traditional electrical contact theory. One part is called shrinking resistance caused by current shrinking at contact spots, the area of which occupies only a small proportion of the whole interface. The other part is called membrane resistance caused by membrane attached to the interface [1].

The contact resistance is normally much greater than the resistance of the conductors, and so with the Joule heat losses. Therefore, it is very important to calculate the contact resistance to get the Joule heat losses. There are some problems to calculate the contact resistance by using the traditional finite element method. First, the contact domain is much smaller than the domains of conductors, which makes the size of elements used very small and the numbers huge. The other problem is that it is difficult to model the complex contact conditions on the interface with the finite element method.

A “thin-layer” model has been proposed by some articles, which use a thin layer with a different resistivity from the conductors to model the contact resistance [2–4]. However, the domain of the thin layer is still very small compared to the domains of the conductors, so elements with small size are still needed and the number of the elements is also huge. The other problem with the “thin-layer” model is that the accuracy of the calculated contact resistance has a great dependence on the choice of the length and the resistivity of the layer. The relationships between the contact resistance and the two factors have also been studied in these articles.

Other articles focus on modeling the shape of the interface to solve the current distribution under different contact conditions [5]. However, the shape of the interface can be very complex to model accurately.

2. APPROACH FOR MODELING THE CONTACT RESISTANCE BASED ON ANSYS

It is very convenient and efficient to use the contact element provided by the software ANSYS to solve contact problems. The contact element in ANSYS is a special surface element to identify and mesh the interface. The contact element has many real constants to reflect contact conditions. Surface conductivity is one of the real constants to reflect the conductive performance of the interface between conductors. Its definition is given as follows:

$$J = ECC \times (V_1 - V_2) \quad (1)$$

where J is the current density in a contact element on the interface, ECC is the surface conductivity of the contact element, V_1 and V_2 are the voltage of the two sets of conductors' nodes on the interface respectively.

The traditional concept of conductivity is based on volume. Suppose a block of conductor is inserted with current I , and the voltage of the two faces where the current goes into and out are

V_1 and V_2 respectively. The conductor is so thin that the section which is perpendicular to the current is of the same size all along the current, and the area of the section is S . The length of the conductor is l and the conductance of the conductor is G . The definition of the traditional conductivity γ is given as follows:

$$I = G \times (V_1 - V_2) = \gamma S/l \times (V_1 - V_2) \quad (2)$$

The current density in the conductor is J , so that $I = JS$. With this, (2) can be changed to:

$$J = \gamma/l \times (V_1 - V_2) \quad (3)$$

The relationship between the traditional conductivity and the surface conductivity can be obtained by comparing (3) with (1). Then we can get:

$$ECC = \gamma/l \quad (4)$$

It is shown that the surface conductivity is traditional conductivity divided by the length of the conductor with the unit of S/m^2 . As to the contact problems, conductivity γ can be seen as an equivalent conductivity of the contact domain, and the length l is the length of the contact domain. According to (4), a smaller value of ECC means a smaller value of the conductivity of the contact domain γ or a greater value of the length of the contact domain l , which means that the conductive performance of the interface is worse. While a greater value of ECC means a better conductive performance of the interface.

3. IMPLEMENTATION OF CONTACT RESISTANCE SIMULATION

Figure 1 gives a model where there are two blocks of conductors with the same size and material. The length, width and the height of the conductors are all 20 mm, and the material is copper with a resistivity of $1.72 \times 10^{-8} \Omega \cdot m$. The two conductors contact through a whole surface. The mesh is also shown in Fig. 1.

The procedure of implementing the contact resistance simulation by ANSYS is: (1) open the Contact Wizard to create contact elements, (2) choose the two surfaces of the conductors comprising the interface and define them as contact surface and target surface respectively, (3) set the surface conductivity to $1 \times 10^8 S/m^2$, (4) mesh the interface by the contact elements as shown in Fig. 2, (5) apply a current of 1 A on the surface at the end of a conductor (against the interface), (6) couple the electric potential of the nodes on the surface to make the surface equipotential, (7) set the electric potential of the surface at the end of the other conductor to zero, (8) choose static solving type to solve the problem.

The resistance for the whole system is $R = (U_1 - U_2)/I$, where U_1 and U_2 are the electric potential on the surfaces at the end of the two conductors respectively, and I is the current in the conductors with the value of 1 A. U_2 has been set to zero and U_1 can be got in post process, with a value of $2.672 \times 10^{-5} V$. Therefore, it can be calculated as $R = 2.672 \times 10^{-5} \Omega$. The resistance for the two conductors with a perfect contact is $R_0 = \rho l/S$, where ρ is the resistivity of the conductors equaling to $1.72 \times 10^{-8} \Omega \cdot m$, l is the length of the two conductors with a value of $2 \times 20 \text{ mm} = 40 \text{ mm}$, and S is the area of the section of the conductors equaling to $20 \text{ mm} \times 20 \text{ mm} = 400 \text{ mm}^2$. Consequently, it can be calculated that $R_0 = 1.72 \times 10^{-6} \Omega$. It can be seen that the value of R is greater

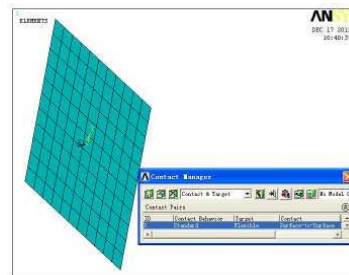
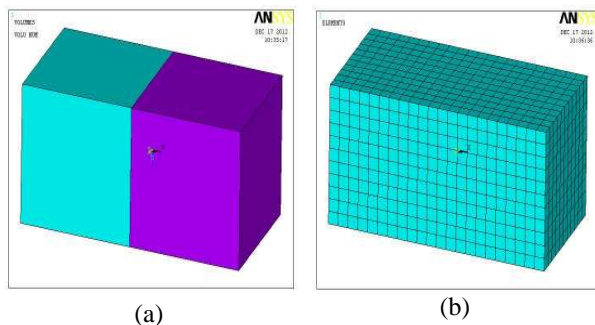


Figure 1: (a) The geometry model of the two conductors and (b) the elements of the meshed conductors.

Figure 2: Contact elements.

than the value of R_0 , with an additional contact resistance R_c . Therefore, the contact resistance $R_c = R - R_0 = 2.5 \times 10^{-5} \Omega$.

Different contact resistances under different contact conditions can be got by altering the value of surface conductivity with other options as the same approach described above. The results are listed in Table 1. It is shown in Table 1 that the contact resistance declines linearly as the value of surface conductivity increases. When the surface conductivity is greater, the contact resistance gets closer to zero. On the other hand, if the surface conductivity is smaller, the contact resistance is of a greater value.

In addition to modeling two conductors contacting through surface, using the contact element in ANSYS can also model conductors contacting through several spots, which is more similar to the real contact conditions. This can be realized by setting different values of surface conductivity to contact elements at different positions on the interface. Different contact shapes on the interface can be modeled and more accurate contact resistances can be got with this function.

Take the two blocks of conductors shown above for example. Suppose that two conductors contact through one spot in the centre of the interface. First, create the geometry models of the conductors in ANSYS and mesh them with element type SOLID69. Then, use the Contact Wizard to define contact surface and target surface respectively, with the value of ECC set to 0.1. This means the whole interface has a poor conductive performance. After that, create a new real constant set (menu in ANSYS: Preprocessor — Real Constants — Add) with the value of ECC set to 1×10^{12} . Then come the key option: choose the contact element in the centre of the interface and modify the real constant set of the element to the new one just created, using the function of modifying elements in ANSYS (menu in ANSYS: Preprocessor — Modeling — Move/Modify — Elements — Modify Attributes). By this option, only the centre of the interface has a good conductive performance and the model of two conductors contacting through one spot in the centre is created, as shown in Fig. 3. Apply the same excitations and boundary conditions as the example above and solve the model. The distributions of current density in the conductors and on a section perpendicular to the current are shown in Fig. 4 and Fig. 5 respectively. It can be seen that the current density in the centre of the interface is much higher than at other positions. Contact resistance of this model can be calculated with a value of $5.148 \times 10^{-6} \Omega$. Nakamura gave a formula for the contact resistance at a square conductive spot [6], as shown in (5):

$$R_c = \rho/2L \quad (5)$$

where ρ is the resistivity of the conductors and L is the length of the square spot on one side, which is the length of the elements on one side here. Using (5), contact resistance of this example can be calculated with a result of $4.73 \times 10^{-6} \Omega$. The value calculated using contact element in ANSYS is close to this value and the accuracy of the contact element method is testified.

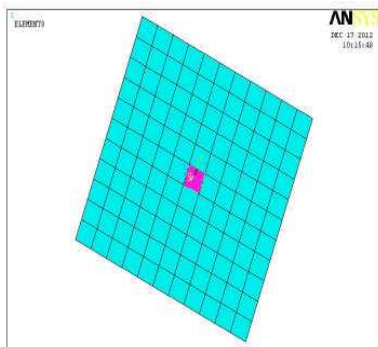


Figure 3: The model of single spot.

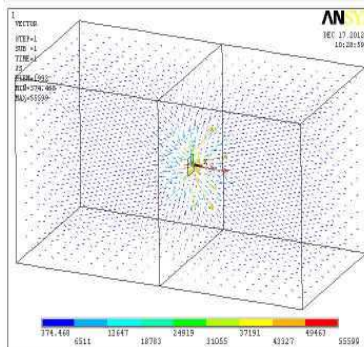


Figure 4: Current density in conductors under single-spot contact.

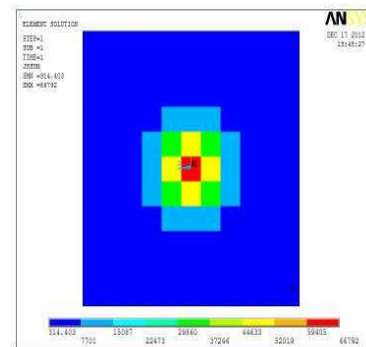


Figure 5: Current density on a section of conductors under single-spot contact.

Table 1: Different contact resistances with different values of surface conductivity.

Surface Conductivity (S/m ²)	10 ⁴	10 ⁶	10 ⁸	10 ¹⁰	10 ¹²
Contact Resistance (Ω)	0.25	2.5 × 10 ⁻³	2.5 × 10 ⁻⁵	2.5 × 10 ⁻⁷	2.5 × 10 ⁻⁹

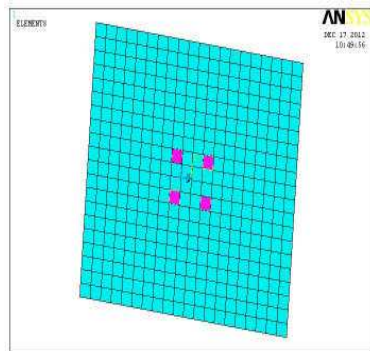


Figure 6: The model of several spots.

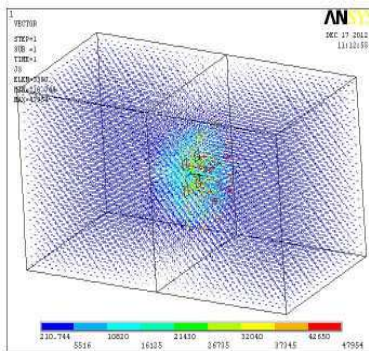


Figure 7: Current density in conductors under several-spots contact.

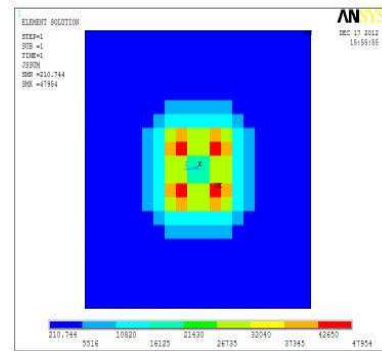


Figure 8: Current density on a section of conductors under several-spots contact.

Similar to the example in part B, modeling of conductors contacting through several spots can also be done using the function of modifying elements in ANSYS. After creating the geometry model of the two conductors and meshing them, choose the contact element at four positions in the centre of the interface as contacting spots, as shown in Fig. 6. Using the options introduced in part B to set the surface conductivity of the contact elements at the four spots to 1×10^{12} , while others set to 0.1. After solving the model, the distributions of current density in the conductors and on a section perpendicular to the current are shown in Fig. 7 and Fig. 8 respectively. It can be seen that the current density at the four spots on the interface are much higher than at other positions. Contact resistance of this model can be calculated, with a result of $3.236 \times 10^{-6} \Omega$. Greenwood proposed a formula to calculate the contact resistance at several round conductive spots [7], as shown in (6):

$$R_c = \frac{\rho}{2 \sum a_i} + \frac{\rho}{\pi n^2} \sum_{i \neq j} \sum \frac{1}{d_{ij}} \quad (6)$$

where ρ is the resistivity of the conductors, n is the number of round spots, a_i is the radius of the i th spot ($1 \leq i \leq n$), d_{ij} is the distance between the centre of the i th spot and the j th spot.

Square spots are modeled in this example instead of round ones, so the former part of (6) should be modified to (5), the formula to calculate contact resistance at a square spot. So we get a new formula to calculate contact resistance at several square conductive spots, as shown in (7):

$$R_c = \frac{\rho}{2nL} + \frac{\rho}{\pi n^2} \sum_{i \neq j} \sum \frac{1}{d_{ij}} \quad (7)$$

where L is the length of the square spot on one side. Other parameters have the same definitions as in (6). Using (7), contact resistance of this example can be calculated with a result of $3.385 \times 10^{-6} \Omega$. The result using contact element in ANSYS is close to this value and the accuracy of the contact element method is testified.

4. CONCLUSION

Calculating the contact resistance by using the contact element in ANSYS has a great advantage over the traditional finite element method. The interface between conductors is meshed by the contact elements in ANSYS, which makes it not necessary to employ volume elements with small size and a great number of elements. The different contact resistance under different contact conditions can be modeled easily by modifying the surface conductivity of contact element. Besides, by setting different values of surface conductivity to contact elements at different positions on the interface, the different contact shapes can be modeled and more accurate contact resistance and the Joule-heat loss can be obtained.

ACKNOWLEDGMENT

Project 51177075 supported by National Natural Science Foundation of China.

REFERENCES

1. Braunovic, M., V. V. Konchitsand, and N. K. Myshki, *Electrical Contacts Fundamentals, Applications and Technology*, 148–150, Translated by Liangjun Xu, China Machine Press, Beijing, Oct. 2010.
2. Coffo, M. I. R. and J. Gallant, “Modeling of the contact resistance and the heating of the contact of a multiple brush projectile for railguns with the final element code ANSYS,” *Proceedings of 2009 IEEE Pulsed Power Conference (PPC)*, 753–756, Washington, DC, USA, Jul. 2009.
3. Kim, B.-K., K.-T. Hsieh, and F. X. Bostick, “A three-dimensional finite element model for thermal effect of imperfect electric contacts,” *IEEE Transactions on Magn.*, Vol. 35, No. 1, 170–174, Jan. 1999.
4. Ho, S. L., Y. Li, X. Lin, H. C. Wong, and K. W. E. Cheng, “A 3-D study of eddy current field and temperature rises in a compact bus duct system,” *IEEE Transactions on Magn.*, Vol. 42, No. 4, 987–990, 2006.
5. Pennec, F., D. Peyrou, D. Leray, P. Pons, R. Plana, and F. Courtade, “Impact of the surface roughness description on the electrical contact resistance of ohmic switches under low actuation forces,” *IEEE Transactions on Components, Packaging and Manufacturing Technology*, Vol. 2, No. 1, 85–94, Jan. 2012.
6. Nakamura, M. and I. Minowa, “Computer simulation for the conductance of a contact interface,” *IEEE Transactions on Components, Hybrids, and Manufacturing Technology*, Vol. 9, No. 2, 150–155, Jun. 1986.
7. Greenwood, J. A., “Constriction resistance and the real area of contact,” *Brit. J. Appl. Phys.*, Vol. 17, 1621–1632, 1966.

Analysis of the Electric Field Environment around Railway Platform

Yuyi Lin, Li Hao, Zejun Shen, Jun Zou, and Jiansheng Yuan

Department of Electrical Engineering, Tsinghua University, Beijing 100084, China

Abstract— The calculation of the power frequency electric and magnetic fields around the high-speed railway is of importance to evaluate the living environment situation of residents along railway. In this paper, the electric field is calculated by the finite element method (FEM). In the calculation, the mesh generation with the freedom coupling method on interfaces is adopted to model the thin transmission lines and the large surrounding air region. This method is able to reduce the demand of element number and increase the calculation accuracy greatly. By the calculation results, a conclusion is made that the electric field intensity on the platform of the ordinary railway structure is less than the environment standard limit.

1. INTRODUCTION

With the rapid development of high-speed railway, the power frequency electric and magnetic fields around high-speed railway have been more and more concerned. The calculation of the power frequency electric and magnetic fields is of importance to evaluate the living environment situation of residents along railway.

Presently, the railway power supply in China mainly contains direct supply, booster transformer (BT) supply and auto transformer (AT) supply. The AT power supply is the main style in the development of the high-speed railway. Therefore, the research of the electric and magnetic fields by AT power supply is an important issue in the construction of railways. In the past, the research of the similar issue was made by simplified model, which only considered a piece of contact line and track. Thus, the calculation results couldn't satisfy the practical engineering requirements. Besides, the power frequency electric and magnetic fields emitted by three kinds of power supply modes can be calculated by the image method, which provides important reference [1].

However, considering the influence of the boundary such as the roof of the platform shell and the train carriage, the power frequency electric field can't be calculated by the image method. The FEM has advantages in calculation of the irregular electric field region in comparison with the image method [2]. Whereas in this issue, the size of the transmission lines (in mm) are much shorter than the computation region (in m). Obviously, it is a thin transmission lines and large surrounding air region issue. The mesh generation plays an important role in increasing the calculation accuracy and efficiency.

2. VALIDATION OF THE CALCULATE BY THE FEM

2.1. Freedom Coupling Method

The traditional FEM requires the continuity of the mesh on the interface of domains, i.e., all the nodes on the interface must be used by the neighborhood domain (Fig. 1(a)). The characteristic of the simulation is that the size of transmission lines is very small, but the air region from the line to the ground is very large relatively. Therefore, if the transmission lines with small region are generated small size of elements, the size of elements in the air and near the transmission lines must be also small, which will generate huge number of elements in the air with large region. Consequently, large computer resource is needed for the simulation by the traditional FEM.

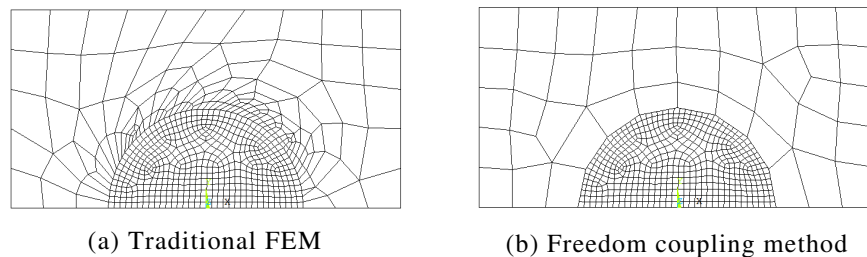


Figure 1: Comparison of the mesh generation by the traditional FEM or the freedom coupling method.

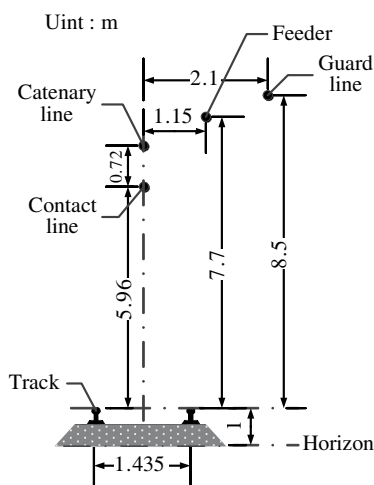


Figure 2: Geometry of the transmission lines by AT power supply mode.

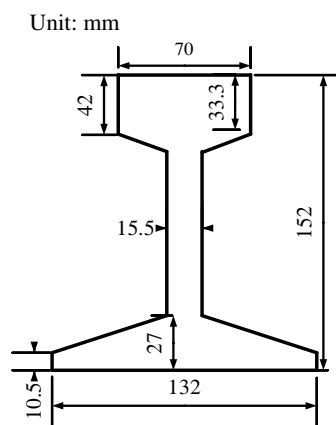


Figure 3: Geometry of the track.

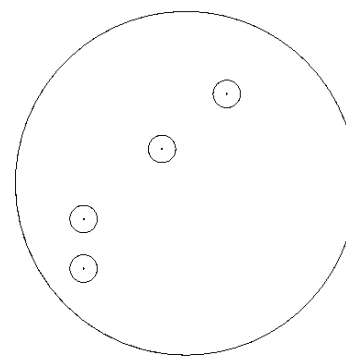


Figure 4: Sketch of the transmission lines.

Table 1: Selection of the parameters in model.

	Contact line	Catenary line	Feeder	Guard line	Track
Radius (mm)	6.6	5.9	7.7	4.7	
Voltage (V)	27.5 k	27.5 k	-27 k	250	250

An efficient method is adopted for the simulation, which is the freedom coupling method. By this method, the continuity of mesh is not required, and the mesh can be generated as shown in Fig. 1(b), in which the circle can be the transmission line. It is clear that the number of mesh in the air can be made much less than the traditional FEM. The freedom coupling method is included in software ANSYS. By the freedom coupling method, we calculate the electric field on the ground, and acceptable results have been obtained.

The following is its basic process: First, when establishing geometric model, the two computation regions shouldn't do the Boolean operation to make sure the interface of domains is independent. Second, mesh is generated without regard of the continuity of mesh on the interface. Then, select all the nodes on the interface belonged to the region, which is generated small size of elements, and define the nodes as node component. Similarly, define the elements as element component, which belong to the other region. Finally, the node component and the element component should be coupled by the freedom coupling method.

2.2. Validation of the Freedom Coupling Method

The geometry of the transmission lines is showed in Fig. 2. The geometry of the polyline track is showed in Fig. 3. And the selection of parameters is show in Table 1.

As the transmission lines are very small, each line is enclosed by a circle as showed in Fig. 4. In the other hand, the transmission lines are very close. Therefore, a region can be created to enclose all the lines, in which small size elements are generated in circles. And the interface between the big circle and the small one is coupled by the freedom coupling method. The sketch of the mesh generation in the local region is showed in Fig. 5.

The calculation points out that with the same level of mesh generation accuracy, the total number of elements is 9,217 by the freedom coupling method, and the one is 23,043 when calculated by the traditional FEM. So the number of elements is reduced heavily and the calculation efficiency is increased greatly. In the other hand, the results indicate the maximum relative error of voltage between the two methods is lower than 1.5%. In summary, the freedom coupling method has a great advantage in calculation efficiency.

In addition, the distribution of equipotential lines is given in Fig. 6, which is calculated in the regular electric field region. Considering the image method is available in this situation, the electric field is calculated by the image method as well. The maximum relative errors of voltage between the two methods are showed in Table 2, where the horizontal distance from the origin to 50 m in different vertical height. As is showed in Table 2, the maximum relative errors are lower than

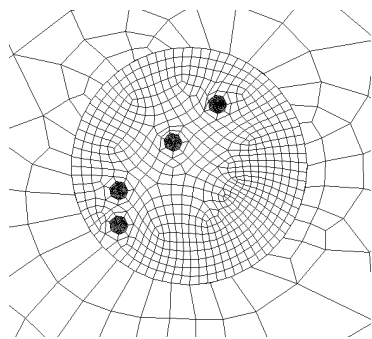


Figure 5: Sketch of the mesh generation.

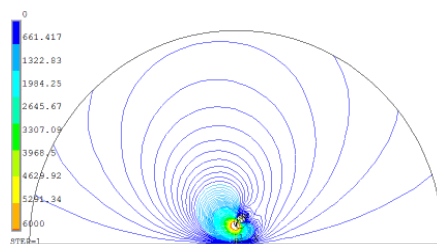


Figure 6: Distribution of space equipotential lines.

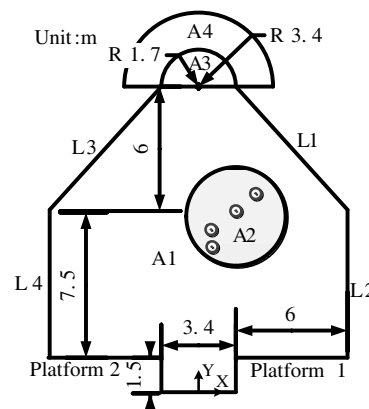


Figure 7: Geometry of railway platform.

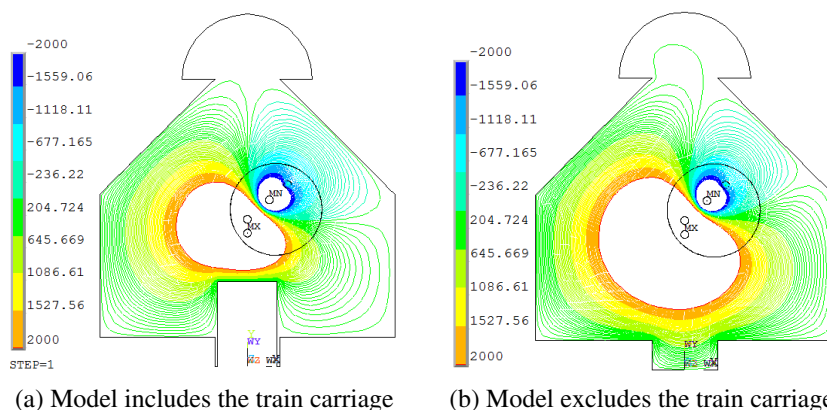


Figure 8: Distribution of equipotential lines on the platform.

Table 2: Maximum relative error compared with the results by image method in different height.

Vertical height (m)	Maximum relative error
2	1.72%
3	0.71%
4	0.69%
5	0.70%

2.0%. So the results can satisfy the practical engineering requirements. In conclusion, the freedom coupling method has high calculation accuracy, and can be applied to practical engineering issue.

3. ANALYSIS OF THE ELECTRIC FIELD AROUND RAILWAY PLATFORM

The geometry of the railway platform is showed in Fig. 7, in which the selection of the parameters is showed as well. The region A2 is the transmission line region and the parameters is described above. The region A4 uses the infinite boundary elements to simulate the infinite boundary, to indicate that the filed spreads to the infinite space. The region A1 (or A3) is the air region. The boundary L2 (or L4) simulates the platform wall and L1 (or L3) simulates the roof of the platform shell.

The distribution of equipotential lines on the platform is showed in Fig. 8, where the part (a) is the situation that includes the train carriage, and part (b) is the other one. As can be seen from Fig. 8, due to the influence of the train carriage, the voltages decrease greatly adjacent to the ground. What is more, Fig. 9 shows the comparison of electric intensity in different vertical height in the platform. We can draw a conclusion that the maximum of the electric field intensities is less than 1,200 V/m.

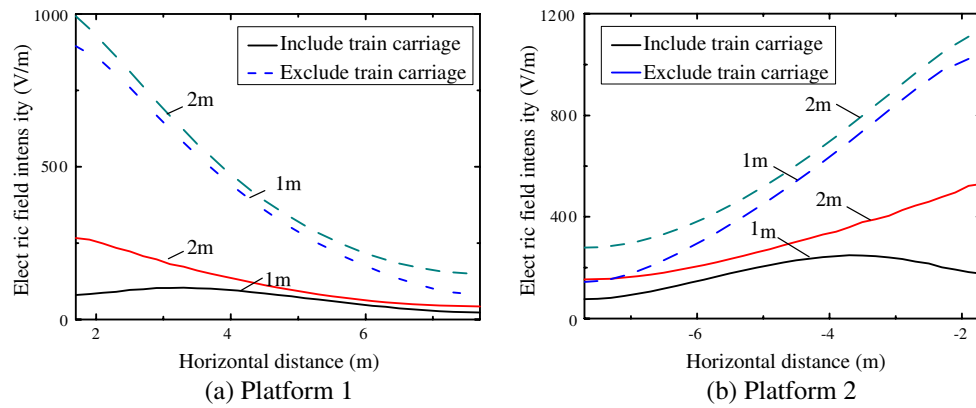


Figure 9: Comparison of electric field intensity in different height.

According to the recommended standard of the China state environmental protection administration, the limited value of the power frequency electric field intensity is 4 kV/m in the residential area [3]. In addition, the literature [4] indicates that it is safe to the health of residents if the power frequency electric field intensity is less than 5 kV/m. Obviously, the electric field intensity of the railway is less than the standard limit within 2 m of the platform ground.

4. CONCLUSIONS

In the simulation by the FEM, the mesh generation with the freedom coupling method on interfaces is an efficient and powerful approach to model the thin transmission lines and the large surrounding air region, as well as the problems composed by relatively small and huge regions. Software ANSYS has the coupling method. This method is able to increase the calculation accuracy and efficiency greatly. Besides, by the calculation results, the electric field intensity of the ordinary structure railway is less than the national environment standard limit within 2 m of the platform ground.

ACKNOWLEDGMENT

Project Supported by the China Ministry of Railways Research Funds of Science and Technology.

REFERENCES

1. Zhao, Z., "Calculation and analysis of the 50 Hz electromagnetic field emitted by different kinds of electric traction system of railways," China Academy of Railway Science, Beijing, 2001.
2. Jin, J., *Electromagnetic FEM*, Xidian University Press, Xian, 1998.
3. The State Environmental Protection Administration, "500 kV EHV conversion engineering electromagnetic radiation environmental impact assessment technical specifications," China Environmental Science Press, Nov. 1998.
4. Pan, L., Z. Yu, et al. "Electric traction power frequency high electromagnetic field effects on human health," *Chinese Journal of Industrial Hygiene and Occupational Diseases*, Vol. 11, No. 6, 359–361, 1993.

The Multi-component Signal Model and Learning Algorithm of Blind Source Separation

T.-J. Zeng¹, Q.-Y. Feng¹, X.-H. Yuan¹, and H.-B. Ma²

¹School of Information Science and Technology, Southwest Jiaotong University, Sichuan 610031, China

²School of Electric Engineering, Southwest Jiaotong University, Sichuan 610031, China

Abstract— The current study proposes a polynomial mixture model that has better precision than general models for describing real situations. Signal separation can be achieved using an information maximization criterion that does not require the probability density function of observed signals. Numerical simulation was performed in the current study to illustrate the efficiency of the proposed method.

1. INTRODUCTION

The separation of instantaneous linear mixtures has been extensively studied in the past. However, a nonlinear mixture model is generally more realistic and accurate than a linear model in many practical applications. The current study aims to investigate and develop efficient solutions for BSS. The proposed model is different from general models [1, 2], and it is simpler than the PNL mixture. The elements of mixing and separating matrix are polynomial expression no long real numbers like in [1, 2], it is clear that the real number is an especial case of polynomial expression, nonlinear polynomial model is more realistic and accurate.

The rest of the current paper is organized as follows. Section 2 presents the polynomial model. Section 3 discusses the information maximization criterion. Finally, experimental results and related discussions are given in Section 4.

2. MULTI-COMPONENT SIGNAL MODEL

Equations, figures, tables and references should follow a sequential numerical scheme in order to ensure a logical development of subject matter.

For **equations**, Assuming that the number of sensors and sources are M and N , respectively, then BSS algorithms can be separated into the following three categories: under-determined ($M < N$), determined ($M = N$), and over-determined ($M > N$). In the current study, the under-determined algorithms were not considered, and the over-determined BSS problem can be described using the following noise-free linear model:

$$X(t) = A \cdot S(t), \quad A = (A_{ij})_{M \times N}, \quad A_{ij} \in R \quad (1)$$

where $X(t) = \{x_i(t), i = 1, 2, \dots, M\}^T$ are sensor signals, $S(t) = \{s_i(t), i = 1, 2, \dots, N\}^T$ are source signals, and A is the mixing matrix. Based on some assumptions were made to solve the problem [3], any N independent signals of M sensor signals exist. Without loss of generality, let $x_1(t), x_2(t), \dots, x_N(t)$ be independent of one another. Therefore,

$$x_i(t) = \sum_{j=1}^N b_{ij} x_j(t), \quad \exists b_{ij} \neq 0, \quad i = N+1, N+2, \dots, M$$

$$\begin{pmatrix} x_{N+1}(t) \\ x_{N+2}(t) \\ \vdots \\ x_M(t) \end{pmatrix} = \begin{pmatrix} b_{N+1,1} & b_{N+1,2} & \dots & b_{N+1,N} \\ b_{N+2,1} & b_{N+2,2} & \dots & b_{N+2,N} \\ \vdots & \vdots & \dots & \vdots \\ b_{M1} & b_{M2} & \dots & b_{MN} \end{pmatrix} \begin{pmatrix} x_1(t) \\ x_2(t) \\ \vdots \\ x_N(t) \end{pmatrix} = \tilde{B}_{(M-N) \times N} \begin{pmatrix} x_1(t) \\ x_2(t) \\ \vdots \\ x_N(t) \end{pmatrix} \quad (2)$$

Let

$$B = \begin{pmatrix} I_{N \times N} & 0_{N \times (M-N)} \\ -\tilde{B}_{(M-N) \times N} & I_{(M-N) \times (M-N)} \end{pmatrix}_{M \times M} \quad (3)$$

where I is the unitary matrix. Multiplying the two sides of Equation (1) by B yields

$$\begin{pmatrix} I_{N \times N} & 0_{N \times (M-N)} \\ -\tilde{B}_{(M-N) \times N} & I_{(M-N) \times (M-N)} \end{pmatrix} \begin{pmatrix} x_1(t) \\ x_2(t) \\ \vdots \\ x_M(t) \end{pmatrix} = \begin{pmatrix} I_{N \times N} & 0_{N \times (M-N)} \\ -\tilde{B}_{(M-N) \times N} & I_{(M-N) \times (M-N)} \end{pmatrix} A \begin{pmatrix} s_1(t) \\ s_2(t) \\ \vdots \\ s_N(t) \end{pmatrix} \quad (4)$$

Based on Equations (2) and (3)

$$\begin{pmatrix} I_{N \times N} & 0_{N \times (M-N)} \\ -\tilde{B}_{(M-N) \times N} & I_{(M-N) \times (M-N)} \end{pmatrix} \begin{pmatrix} x_1(t) \\ x_2(t) \\ \vdots \\ x_M(t) \end{pmatrix} = \begin{pmatrix} x_1(t) \\ \vdots \\ x_N(t) \\ \dots \\ 0_{(M-N) \times 1} \end{pmatrix} \quad (5)$$

Let $A = \begin{pmatrix} A_1 \\ \dots \\ A_2 \end{pmatrix}$, where A_1 is the $N \times N$ sub-matrix of A , and A_2 is the $(M-N) \times N$ sub-matrix of A .

$$\begin{pmatrix} I_{N \times N} & 0_{N \times (M-N)} \\ -\tilde{B}_{(M-N) \times N} & I_{(M-N) \times (M-N)} \end{pmatrix} A = \begin{pmatrix} I_{N \times N} & 0_{N \times (M-N)} \\ -\tilde{B}_{(M-N) \times N} & I_{(M-N) \times (M-N)} \end{pmatrix} \begin{pmatrix} A_1 \\ \dots \\ A_2 \end{pmatrix} = \begin{pmatrix} A_1 \\ \dots \\ -\tilde{B}A_1 + A_2 \end{pmatrix}. \quad (6)$$

Based on Equations (4)–(6), the following equation can be obtained:

$$\begin{pmatrix} x_1(t) \\ \vdots \\ x_N(t) \\ \dots \\ 0_{(M-N) \times 1} \end{pmatrix} = \begin{pmatrix} A_1 \\ \dots \\ -\tilde{B}A_1 + A_2 \end{pmatrix} \begin{pmatrix} s_1(t) \\ s_2(t) \\ \vdots \\ s_N(t) \end{pmatrix}. \quad (7)$$

If $-\tilde{B}A_1 + A_2 \neq 0$, then at least one non-zero element, b_1, b_2, \dots, b_k ($1 \leq k \leq N$), exists. Based on Equation (7), the equation can be obtained: $\sum_k b_k s_k(t) = 0$. $s_k(t)$ are independent of one another;

therefore, $\forall b_k = 0$. This assumption conflicts with the former assumption; thus, $-\tilde{B}A_1 + A_2 = 0$. Equation (7) is then transformed into the following equation:

$$\begin{pmatrix} x_1(t) \\ x_2(t) \\ \vdots \\ x_N(t) \end{pmatrix} = A_1 \begin{pmatrix} s_1(t) \\ s_2(t) \\ \vdots \\ s_N(t) \end{pmatrix}, \quad A_1 = (a_{ij})_{N \times N} \quad (8)$$

Based on the derivation above, we can conclude that (1) \Rightarrow (8). That is, the obtained simplifying over-determined model can be turned into the determined case ($M = N$). Without loss of generality, let $M = N$. Thus, A is a non-singular $N \times N$ mixing matrix. Based on Equation (1), the following equation can be obtained:

$$x_i = \sum_k a_{ik} s_k \quad (9)$$

In Equation (9), the mixing signal x_i consists of linear source signals s_k ($k = 1, 2, \dots, N$). The model is simple and easy to understand, but it is too deliberately restricted in the real world. Thus, a more general model was considered as follows: $x_i = \sum_k f_k(s_k)$, where the function f_k is

continuous in $(-\infty, +\infty)$. Based on Weierstrass function approximation theory, $f_k(s_k) \approx \sum_{j=0}^n a_j s_k^j$.

The current study presents the polynomial mixing model in Figure 1(a), where the elements of A are polynomials rather than real numbers as in usual models [1, 2]. In the proposed model,

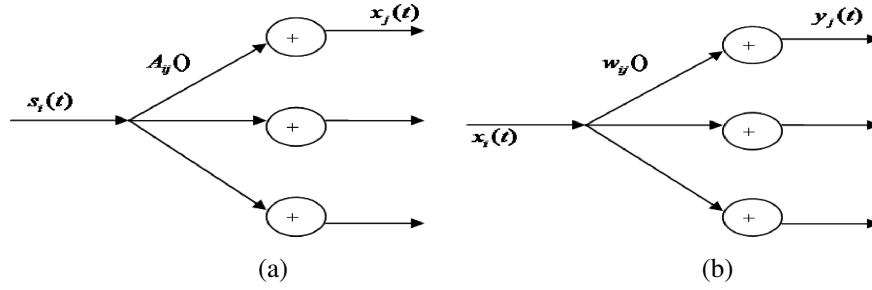


Figure 1: Block diagram of the proposed polynomial, (a) mixing structure and (b) separating structure.

$A_{ij}() = a_{ij_0} + a_{ij_1}() + a_{ij_2}()^2 + \dots + a_{ij_n}()^n$. Moreover, the polynomial mixing model turns into the usual mixing model when $a_{ij_0} = a_{ij_2} = \dots = a_{ij_n} = 0$. Thus, the polynomial mixing model is considered more general than the usual mixing model, which is a particular case of the polynomial mixing model. Symmetrically, the corresponding separation structure is shown in Figure 1(b). Similarly, $W_{ij}() = w_{ij_0} + w_{ij_1}() + w_{ij_2}()^2 + \dots + w_{ij_n}()^n$. Definition

$$\begin{aligned} A_{ij}() * s_k &= a_{ij_0} + a_{ij_1} s_k + a_{ij_2} s_k^2 + \dots + a_{ij_n} s_k^n \\ W_{ij}() * x_k &= w_{ij_0} + w_{ij_1} x_k + w_{ij_2} x_k^2 + \dots + w_{ij_n} x_k^n \quad (i, j, k = 1, 2, \dots, N) \end{aligned} \quad (10)$$

Thus, the mixing data mode can be expressed in matrix form as follows:

$$X(t) = \begin{bmatrix} A_{11}() & A_{12}() & \dots & A_{1N}() \\ A_{21}() & A_{22}() & \dots & A_{2N}() \\ \dots & \dots & \dots & \dots \\ A_{N1}() & A_{N2}() & \dots & A_{NN}() \end{bmatrix} * \begin{bmatrix} s_1(t) \\ s_2(t) \\ \dots \\ s_N(t) \end{bmatrix} = A * S, \text{ and the separating mode is given}$$

by

$$Y(t) = \begin{bmatrix} W_{11}() & W_{12}() & \dots & W_{1N}() \\ W_{21}() & W_{22}() & \dots & W_{2N}() \\ \dots & \dots & \dots & \dots \\ W_{N1}() & W_{N2}() & \dots & W_{NN}() \end{bmatrix} * \begin{bmatrix} x_1(t) \\ x_2(t) \\ \dots \\ x_N(t) \end{bmatrix} = W * X.$$

3. INFORMATION-MAXIMIZATION FOR BLIND SEPARATION

A set of signals is independent if its joint PDF $p(s_1, s_2, \dots, s_N)$ can be decomposed as: $p(s_1, s_2, \dots, s_N) = \prod_{i=1}^N p_i(s_i)$, where $p_i(s_i)$ is the PDF of source signal $s_i(t)$. The statistical independence of the sources is the main assumption. Let $Y = (y_1, y_2, \dots, y_N)$ be the estimated source signal vector and p_Y its PDF. As proposed by author [4], the statistical independence of the output signal can be measured using the Kullback-Liebler (KL) divergence between p_Y and $\prod_{i=1}^N p(y_i)$: $\text{KL}(p_Y, \prod_{i=1}^N p(y_i)) = \int p_Y \log \frac{p_Y}{\prod_{i=1}^N p(y_i)} dY$, which is equal to Shnnon's mutual information $I(Y)$ between the components of

output vector Y . $I(Y)$ can be rewritten as: $I(Y) = \sum_{i=1}^N H(y_i) - H(Y)$. $H(y) = - \int p(y) \log p(y) dy$ denotes the entropy of y . $I(Y)$ is nonnegative and reaches its minimum value or vanishes if and only if $p_Y = \prod_{i=1}^N p(y_i)$. In other words, minimizing the KL divergence can make the estimated source signals independent [1]. Considering the separation structure in Figure 2, the joint probability density function of output Y can be expressed as follows:

$$\begin{aligned} p_Y(y) &= \frac{p_X(x)}{|\det J|}, \\ J &= \frac{\partial Y}{\partial X} = \frac{\partial(y_1, y_2, \dots, y_N)}{\partial(x_1, x_2, \dots, x_N)} = \begin{bmatrix} \frac{\partial y_1}{\partial x_1} & \dots & \frac{\partial y_1}{\partial x_N} \\ \dots & \dots & \dots \\ \frac{\partial y_N}{\partial x_1} & \dots & \frac{\partial y_N}{\partial x_N} \end{bmatrix} = \begin{bmatrix} \frac{\partial W_{11} * x_1}{\partial x_1} & \dots & \frac{\partial W_{1N} * x_N}{\partial x_N} \\ \dots & \dots & \dots \\ \frac{\partial W_{N1} * x_1}{\partial x_1} & \dots & \frac{\partial W_{NN} * x_N}{\partial x_N} \end{bmatrix} \quad (11) \end{aligned}$$

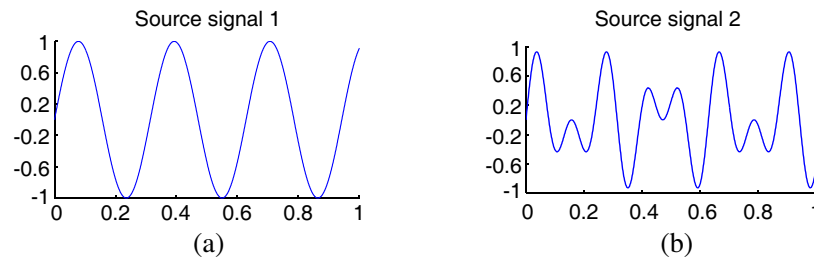


Figure 2: The source signals.

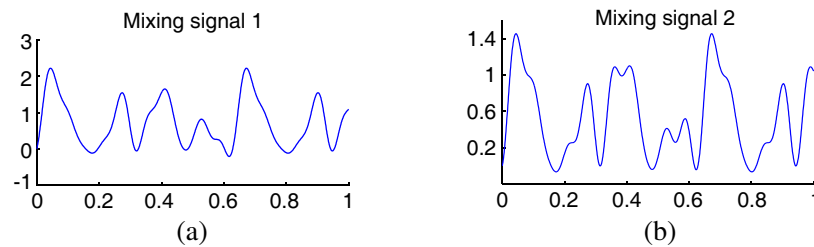


Figure 3: The polynomial mixing signals.

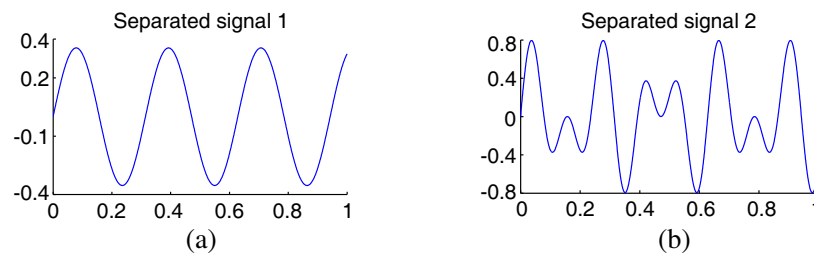


Figure 4: The separated signals.

where $\det(\cdot)$ denotes the operation for computing the determinant. Therefore, the joint entropy of Y is given by $H(Y) = H(X) + \log |\det J|$ (12). The optimal solution for the information-theoretic criterion can be obtained when the maximum entropy of Y is reached. $H(x)$ does not contain any parameters of the separation system; therefore, it will become zero when its gradient is considered with respect to the parameters. Using the gradient ascent learning algorithm to maximize the second term, the derivative of the entropy function $H(Y)$ should be considered with respect to the parameter Ω . Based on Equations (10)–(12), the following can be obtained: $J = (J_{ij})_{N \times N}$, $J_{ij} = \sum_{k=1}^n k w_{ij_k} x_j^{k-1}$. Let $\Omega = \{\Omega_{ij}, 1 \leq i, j \leq N\}$, $\Omega_{ij} = (w_{ij_1}, w_{ij_2}, \dots, w_{ij_N})$. $\frac{\partial \log |\det J|}{\partial \Omega} = \frac{\partial \log |\det J|}{\partial J} \cdot \frac{\partial J}{\partial \Omega}$,

$$\frac{\partial \log |\det J|}{\partial J} = (J^{-1}(\Omega, X)), \frac{\partial J}{\partial \Omega} = \sum_{i,j=1}^N \frac{\partial J}{\partial \Omega_{ij}}, \frac{\partial J}{\partial \Omega_{ij}} = \begin{bmatrix} 0 & 0 & 0 \\ 0 & J_{ij} & 0 \\ 0 & 0 & 0 \end{bmatrix}, J_{ij} = \sum_{n=1}^k n x_j^{n-1}.$$

4. SIMULATION RESULTS

This section presents the two experiments conducted to test the efficiency and performance of the proposed algorithm. The following sub-Gaussian signals are used as source signals: $s_1(t) = \sin(20t)$ and $s_2(t) = \sin(40t) \cos(10t)$. These signals are mixed using the following matrix:

$$M = \begin{pmatrix} 0.45(\cdot) + 0.96(\cdot)^2 & 0.72(\cdot) + 0.84(\cdot)^2 \\ 0.37(\cdot) + 0.65(\cdot)^2 & 0.21(\cdot) + 0.76(\cdot)^2 \end{pmatrix}$$

Figures 2–4 show the source signals, the polynomial mixtures $X(t)$, and the separated signals, respectively. As shown in Figure 4, the proposed algorithm provides a clear separation of the original source signals without any knowledge.

ACKNOWLEDGMENT

This work was supported by the National Natural Science Foundation of China (NNSF) under Grants 60990320, 60990323 and 61271090, the National 863 Project of China under Grant 2012AA012305, Sichuan Provincial Science and technology support Project under Grant 2012GZ0101, and Chengdu Science and technology support Project under Grant 12DXYB347JH-002.

REFERENCES

1. Solazzi, M. and A. Uncini, “Spline neural networks for blind separation of post-nonlinear-linear mixtures,” *IEEE Trans. Circuits and Systems I*, Vol. 51, No. 4, 817–829, Apr. 2004.
2. Barros, A. K., J. C. Principe, and D. Erdogmus, “Independent component analysis and blind source separation,” *Signal Processing*, Vol. 87, Sp. Iss. SI, 1817–1818, Elsevier, Aug. 2007.
3. Amari, S. and A. Cichocki, “Adaptive blind signal processing — Neural network approaches,” *Proceedings of the IEEE*, Vol. 86, No. 10, 2026–2048, Oct. 1998.
4. Deville, Y., S. Hosseini, and A. Deville, “Effect of indirect dependencies on maximum likelihood and information theoretic blind source separation for nonlinear mixtures,” *Signal Processing*, Vol. 91, 793–800, Elsevier, Apr. 2011.

Near-weightlessness Movements in Electromagnetic Fields

Zi-Hua Weng

School of Physics and Mechanical & Electrical Engineering, Xiamen University
Xiamen 361005, China

Abstract— The ‘near-weightlessness’ movement in electromagnetic fields can be described with the octonion. The octonion is separated into two parts, the quaternion and S -quaternion. The quaternion is propitious to depict the feature of gravitational fields, while the S -quaternion is suitable to describe the property of electromagnetic fields. The comparability of the quaternion and S -quaternion enable the concept of weightlessness and near-weightlessness in the gravitational field to extend into the electromagnetic field. From the condition of similar ‘near-weightlessness’ in the electromagnetic field, it reveals that the electromagnetic potential will impact the ‘orbital’ movement of the trial charge in the S -quaternion space, and then to interfere the measurement precision. The deduction coincides with the Aharonov-Bohm experimental result as well as the uncertainty principle in the quantum mechanics. This means that adopting the existing electric measuring method is unable to avoid the electromagnetic potential to interfere the ‘orbital’ movement of trial charges and other physical quantities in the S -quaternion space.

1. INTRODUCTION

J. C. Maxwell was the first to describe simultaneously the feature of electromagnetic field with two methods, the quaternion and the vector terminology. However the existing study reveals that it is not successful to adopt directly the quaternion to depict the electromagnetic field. The octonion can be separated into two components, the quaternion and the S -quaternion. The S -quaternion is similar to the imaginary number of the complex number. The quaternion is propitious to depict the feature of gravitational fields, while the S -quaternion is suitable to describe the property of electromagnetic fields [1].

In the quaternion space for gravitational fields, the radius vector and the integral of gravitational potential can be combined together to become the compounding radius vector, and the related function space is called the quaternion compounding space. The latter is suitable to describe the movement feature of particle, which is in weightlessness and near-weightlessness in the gravitational field. The inference can explain the overspeed phenomenon of stars on the fringe of galaxy [2]. The concept of weightlessness and near-weightlessness in the gravitational field can be extended into the electromagnetic field, to depict the movement feature of trial charge.

In the S -quaternion space for the electromagnetic field, the radius vector and the integral of electromagnetic potential can be combined together to become the compounding radius vector, and the related function space is called the S -quaternion compounding space. The latter is suitable to depict the movement feature of charged particle, which is in similar ‘weightlessness’ and ‘near-weightlessness’, in the electromagnetic field. The deduction is consistent with the Aharonov-Bohm test result [3] and the uncertainty principle in the quantum mechanics to a certain extent.

2. QUATERNION COMPOUNDING SPACE

In the quaternion space, the basis vector is $\{\mathbf{i}_i\}$. The quaternion radius vector is $\mathbb{R}_g(r_i) = \mathbf{i}_i r_i$, the quaternion velocity is $\mathbb{V}_g(v_i) = c\mathbb{D} \circ \mathbb{R}_g$, the quaternion angular velocity is $\mathbb{Y}_g(y_i) = \mathbb{D} \circ \mathbb{V}_g$, and the quaternion angular acceleration is $\mathbb{Z}_g(z_i) = -\mathbb{D}^* \circ \mathbb{Y}_g$. Herein \circ denotes the quaternion multiplication. $\mathbb{D} = \mathbf{i}_i \partial_i$, with $\partial_i = \partial/\partial r_i$. $\nabla = \mathbf{i}_i \partial_i$. $\mathbf{i}_0 = 1$. $i = 0, 1, 2, 3$. $j = 1, 2, 3$.

In the quaternion space for the gravitational field, the quaternion physical quantity is $\mathbb{X}_g(x_i)$, which is the integral of quaternion field potential $\mathbb{A}_g(a_i)$, that is, $\mathbb{A}_g(a_i) = \mathbb{D} \circ \mathbb{X}_g$. The quaternion field strength is $\mathbb{B}_g(h_i) = \mathbb{D} \circ \mathbb{A}_g$, the quaternion field source is $\mathbb{S}_g(s_i) = -\mathbb{D}^* \circ \mathbb{B}_g/\mu_g$. Herein the gravitational constant is $\mu_g < 0$. By comparison with the classical gravitational theory, there is, $\mathbb{S}_g = m\mathbb{V}_g$. m is the mass density. $r_0 = v_0 t$. v_0 is the speed of light, and t is the time.

According to the definition of quaternion physical quantity and the feature of quaternion operator \mathbb{D} , the definition of gravitational field source deduces the gravitational field equations in the quaternion space, including the law of gravitation.

$$\nabla \cdot \mathbf{b} = 0, \quad \nabla^* \times \mathbf{g}/v_0 + \partial_0 \mathbf{b} = 0, \quad (1)$$

$$-\mu_g s_0 = \nabla^* \cdot \mathbf{g}/v_0, \quad -\mu_g \mathbf{s} = \nabla^* \times \mathbf{b} + \partial_0 \mathbf{g}/v_0, \quad (2)$$

where $\mathbb{S}_g = s_0 + \mathbf{s}$, $\mathbb{B}_g = h_0 + \mathbf{h}$, $\mathbf{h} = \mathbf{b} + \mathbf{g}/v_0$. The gauge equation is chosen as $h_0 = 0$.

In the gravitational theory, the planet revolving around the sun M can be considered as one particle. The above equations are able to describe the planetary orbital movement, when the planet movement is in weightlessness.

In the quaternion space for the gravitational field, the quaternion radius vector \mathbb{R}_g and the quaternion physical quantity \mathbb{X}_g can be combined together to become the quaternion compounding radius vector $\bar{\mathbb{R}}_g = \mathbb{R}_g + k_{rx}\mathbb{X}_g$, or the quaternion compounding physical quantity $\bar{\mathbb{X}}_g = \mathbb{X}_g + K_{rx}\mathbb{R}_g$, with $K_{rx} = 1/k_{rx}$. The quaternion compounding radius vector $\bar{\mathbb{R}}_g$ can be considered as the radius vector in the quaternion compounding space (function space). In the quaternion compounding space, the compounding velocity is $\bar{\mathbb{V}}_g = v_0\bar{\diamond} \circ \bar{\mathbb{R}}_g = \mathbb{V}_g + v_0k_{rx}\mathbb{A}_g$, the compounding angular velocity is $\bar{\mathbb{Y}}_g = \bar{\diamond} \circ \bar{\mathbb{V}}_g$, and the compounding angular acceleration is $\bar{\mathbb{Z}}_g = -\bar{\diamond}^* \circ \bar{\mathbb{Y}}_g$. Similarly in the gravitational field, the compounding field potential is $\bar{\mathbb{A}}_g = \bar{\diamond} \circ \bar{\mathbb{X}}_g = \mathbb{A}_g + (K_{rx}/v_0)\mathbb{V}_g$, the compounding field strength is $\bar{\mathbb{B}}_g = \bar{\diamond} \circ \bar{\mathbb{A}}_g = \mathbb{B}_g + (K_{rx}/v_0)\mathbb{Y}_g$, and the compounding field source is $\bar{\mathbb{S}}_g = -\bar{\diamond}^* \circ \bar{\mathbb{B}}_g/\mu_g$. Herein $\bar{\mathbb{S}}_g = m\bar{\mathbb{V}}_g$, $\bar{\mathbb{S}}_g = \mathbb{S}_g + \mathbb{Z}_g/(\mu_g k_{rx})$, $\mathbb{Z}_g = (\mu_g k_{rx}^2 m v_0)\mathbb{A}_g$.

According to the definition of quaternion compounding physical quantity and the feature of quaternion operator $\bar{\diamond}$, the definition of compounding field source deduces the gravitational field equations in the quaternion compounding space, including the field equation similar to the law of gravitation. In the gravitational theory, the planet revolving around the sun M is considered as one particle still. The above equations are able to describe the deviation amplitude of the planetary orbital movement relative to the weightlessness movement.

3. GRAVITATIONAL NEAR-WEIGHTLESSNESS

In the quaternion compounding space, expanding the definition of compounding field source, $\bar{\mathbb{S}}_g = -\bar{\diamond}^* \circ \bar{\mathbb{B}}_g/\mu_g$, yields the gravitational field equations as follows,

$$\nabla \cdot \bar{\mathbf{b}} = 0, \quad \nabla^* \times \bar{\mathbf{g}}/v_0 + \partial_0 \bar{\mathbf{b}} = 0, \quad (3)$$

$$-\mu_g \bar{s}_0 = \nabla^* \cdot \bar{\mathbf{g}}/v_0, \quad -\mu_g \bar{\mathbf{s}} = \nabla^* \times \bar{\mathbf{b}} + \partial_0 \bar{\mathbf{g}}/v_0, \quad (4)$$

where $\bar{\mathbb{S}}_g = \bar{s}_0 + \bar{\mathbf{s}}$, $\bar{\mathbb{B}}_g = \bar{h}_0 + \bar{\mathbf{h}}$, $\bar{\mathbf{h}} = \bar{\mathbf{b}} + \bar{\mathbf{g}}/v_0$. The gauge equation is chosen as $\bar{h}_0 = 0$.

In case $\bar{\mathbb{S}}_g = 0$, one solution of the above is $\bar{\mathbb{B}}_g = 0$. When $\bar{\mathbf{h}} = 0$, the planet movement is in weightlessness in the gravitational field of the sun M . That is, $\bar{\mathbf{g}} = \mathbf{g} + \mathbf{a} = 0$ and $\bar{\mathbf{b}} = \mathbf{b} + \mathbf{y} = 0$. Herein the linear acceleration is, $\mathbf{a} \approx d\mathbf{v}/dt$, in the quaternion space. $\mathbb{R}_g = r_0 + \mathbf{r}$, $\mathbf{r} = \mathbf{i}_j r_j$. The angular velocity is $\mathbf{y} \approx \nabla \times \mathbf{v}$, $\mathbb{V}_g = v_0 + \mathbf{v}$, $\mathbf{v} = \mathbf{i}_j v_j$.

In the movement model for the revolution and rotation of the planet orbiting around the sun M , the equation $\bar{\mathbf{g}} = 0$ determines the ellipse trajectory for the revolution, while $\bar{\mathbf{b}} = 0$ ascertains the angular speed for the rotation. In the static gravitational field, there are, $\bar{\mathbf{s}} = 0$ and $\bar{\mathbf{b}} = 0$. When $\bar{s}_0 \neq 0$, Eq. (4) reveals that the field strength is, $\bar{\mathbf{g}} = \mathbf{g} + \mathbf{a} \neq 0$. When the planet orbiting around the sun M is considered as one particle, the above is applied to describe the radii variation of trajectory for the planet in near-weightlessness. The above deduces three kinds of cases,

(1) $\bar{\mathbf{g}} = 0$. It means that $\mathbf{g} + \mathbf{a} = 0$, and the planetary orbital movement is in weightlessness. According to classical gravitational theory, the calculation yields the planetary radii r and the area speed C . In the polar coordinate system (r, φ) , the sun M is on the point of origin, the planetary orbital radii is $r = p/\{1 + e \cos(\varphi - \delta)\}$. Herein $p = C^2/(f_1 M)$, the gravitational constant is $f_1 > 0$, and the solar mass is M . e and δ are the coefficients.

(2) $|\mathbf{g}'| < |\mathbf{g}|$, with $\mathbf{g}' = \mathbf{g} - \bar{\mathbf{g}}$. It means that $\mathbf{g}' + \mathbf{a} = 0$, and the gravitational strength becomes weakened, the planetary orbital movement deviates from the weightlessness, and the planetary orbital radii increases. In the polar coordinate system (r, φ) , the sun M is on the point of origin, in case $\bar{\mathbf{g}}$ is proportional to (f/r^2) , the planetary orbital radii is $r = p/\{1 + e \cos(\varphi - \delta)\}$. Herein $p = C^2/(f_2 M)$, f_2 is the equivalent gravitational constant, $0 < f_2 < f_1$, and f is the coefficient. According to the conservation of angular momentum and the invariance of area speed, the planetary orbital radii increases, while the planetary orbital speed decreases.

(3) $|\mathbf{g}'| > |\mathbf{g}|$, with $\mathbf{g}' = \mathbf{g} - \bar{\mathbf{g}}$. It means that $\mathbf{g}' + \mathbf{a} = 0$, and the gravitational strength becomes strong, the planetary orbital movement deviates from the weightlessness, and the planetary orbital radii decreases. In the polar coordinate system (r, φ) , the sun M is on the point of origin, in case $\bar{\mathbf{g}}$ is proportional to (f/r^2) , the planetary orbital radii is $r = p/\{1 + e \cos(\varphi - \delta)\}$. Herein $p = C^2/(f_3 M)$, f_3 is the equivalent gravitational constant, $f_3 > f_1$, and f is the coefficient. According to the conservation of angular momentum and the invariance of area speed, the planetary orbital radii

decreases, while the planetary orbital speed increases. Similarly in the movement model for the star orbiting around the galaxy center M' , the stars on the fringe of the galaxy can be considered as one particle, the orbital speed of stars could be different to the theoretical value of classical gravitational theory. The prediction coincides with the experimental measuring results.

The above states that the mass density m , velocity \mathbb{V}_g , and field potential \mathbb{A}_g of the quaternion compounding field source $\bar{\mathbb{S}}_g$ will impact the planetary orbital radii and speed. In the case of $\bar{\mathbf{g}} \neq 0$, the planetary orbit is still ellipsoidal and stable in the static gravitational field. Similarly in the quasi-static gravitational field, in case the quaternion compounding field source $\bar{\mathbb{S}}_g$ alters endlessly, it will cause the field strength $\bar{\mathbf{g}}$ and the planetary orbital radii r to change continuously and accordingly. This will impact the planetary orbital radii of the solar system during it is in the growth phase, stable phase, and decline phase.

4. S-QUATERNION COMPOUNDING SPACE

The octonion can be separated into two components, the quaternion and S -quaternion. Similarly the complex number is able to be decomposed into two parts, the real number and the imaginary number. The contrast reveals that the S -quaternion is similar to the imaginary number of complex number. The quaternion is propitious to depict the feature of gravitational fields, while the S -quaternion is suitable to describe the property of electromagnetic fields. The method adopting the quaternion to study the feature of gravitational field can be extended to introduce the S -quaternion to explore the property of electromagnetic field.

In the S -quaternion space for the electromagnetic field, the basis vector is $\{\mathbf{I}_i\}$. The S -quaternion radius vector is $\mathbb{R}_e(R_i) = \mathbf{I}_i R_i$, the S -quaternion velocity is $\mathbb{V}_e(V_i) = v_0 \diamond \circ \mathbb{R}_e$, the S -quaternion angular velocity is $\mathbb{Y}_e(Y_i) = \diamond \circ \mathbb{V}_e$, and the S -quaternion angular acceleration is $\mathbb{Z}_e(Z_i) = -\diamond^* \circ \mathbb{Y}_e$.

In the electromagnetic field, the S -quaternion physical quantity is $\mathbb{X}_e(X_i)$, which is the integral of field potential $\mathbb{A}_e(A_i)$, that is, $\mathbb{A}_e(A_i) = \diamond \circ \mathbb{X}_e$. The physical quantity $\mathbb{X}_e(X_i)$ can be considered as the generalizing of the magnetic flux and Hertz vector. The S -quaternion field strength is $\mathbb{B}_e(H_i) = \diamond \circ \mathbb{A}_e$, and the S -quaternion field source is $\mathbb{S}_e(S_i) = -\diamond^* \circ \mathbb{B}_e/\mu_e$. By comparison with the classical theory, there are, $\mathbb{V}_e = \mathbb{V}_g \circ \mathbf{I}_0$, and $\mathbb{S}_e = q\mathbb{V}_e$. Herein q is the density of electric charge, and the electromagnetic constant is $\mu_e > 0$.

According to the definition of S -quaternion physical quantity and the feature of quaternion operator \diamond , the definition of electromagnetic field source deduces the electromagnetic field equations in the S -quaternion space, including the Maxwell's equations.

$$\nabla \cdot \mathbf{B} = 0, \quad \nabla^* \times \mathbf{E}/v_0 + \partial_0 \mathbf{B} = 0, \quad (5)$$

$$-\mu_e \mathbf{S}_0 = \nabla^* \cdot \mathbf{E}/v_0, \quad -\mu_e \mathbf{S} = \nabla^* \times \mathbf{B} + \partial_0 \mathbf{E}/v_0, \quad (6)$$

where $\mathbb{S}_e = \mathbf{S}_0 + \mathbf{S}$. $\mathbb{B}_e = \mathbf{H}_0 + \mathbf{H}$. $\mathbf{H} = \mathbf{B} + \mathbf{E}/v_0$. $\mathbf{S}_0 = S_0 \mathbf{I}_0$. $\mathbf{H}_0 = H_0 \mathbf{I}_0$, with $H_0 = 0$.

After transferring the above equations into that in the quaternion space, it is found that the above is identical with Maxwell's equations in the classical electromagnetic theory, except for the opposite plus-minus sign of term $\partial_0 \mathbf{E}$. Moreover expanding the above into the scalar equation will yield the same conclusion.

In the S -quaternion space for the electromagnetic field, the trial charge revolving around the electric charge can be considered as one particle. The above equations are able to describe the 'orbital' movement and 'radii' of the trial charge, when the movement of trial charge is in similar 'weightlessness'. In the octonion space, the octonion radius vector is, $\mathbb{R} = \mathbb{R}_g + k_{eg} \mathbb{R}_e$, with k_{eg} being the coefficient. For the trial charge, the quaternion radius vector \mathbb{R}_g is independent to the S -quaternion radius vector \mathbb{R}_e . In some simple cases, the radius vector \mathbb{R}_g is able to be solved from the weightlessness condition, while the radius vector \mathbb{R}_e from the similar 'weightlessness'.

In the S -quaternion space for the electromagnetic field, the S -quaternion radius vector \mathbb{R}_e and the S -quaternion physical quantity \mathbb{X}_e can be combined together to become the S -quaternion compounding radius vector $\bar{\mathbb{R}}_e = \mathbb{R}_e + k_{rx} \mathbb{X}_e$, or the S -quaternion compounding physical quantity $\bar{\mathbb{X}}_e = \mathbb{X}_e + K_{rx} \mathbb{R}_e$. The S -quaternion compounding radius vector $\bar{\mathbb{R}}_e$ can be considered as the radius vector in the S -quaternion compounding space (function space). In the S -quaternion compounding space, the compounding velocity is $\bar{\mathbb{V}}_e = v_0 \diamond \circ \bar{\mathbb{R}}_e = \mathbb{V}_e + v_0 k_{rx} \mathbb{A}_e$, the compounding angular velocity is $\bar{\mathbb{Y}}_e = \diamond \circ \bar{\mathbb{V}}_e$, and the compounding angular acceleration is $\bar{\mathbb{Z}}_e = -\diamond^* \circ \bar{\mathbb{Y}}_e$. Similarly in the electromagnetic field, the compounding field potential is $\bar{\mathbb{A}}_e = \diamond \circ \bar{\mathbb{X}}_e = \mathbb{A}_e + (K_{rx}/v_0) \mathbb{V}_e$, the compounding field strength is $\bar{\mathbb{B}}_e = \diamond \circ \bar{\mathbb{A}}_e = \mathbb{B}_e + (K_{rx}/v_0) \mathbb{Y}_e$, and the compounding field source is $\bar{\mathbb{S}}_e = -\diamond^* \circ \bar{\mathbb{B}}_e/\mu_e$. Herein $\bar{\mathbb{S}}_e = q\bar{\mathbb{V}}_e$. $\bar{\mathbb{S}}_e = \mathbf{S}_e + \mathbb{Z}_e/(\mu_e k_{rx})$. $\mathbb{Z}_e = (\mu_e k_{rx}^2 q v_0) \mathbb{A}_e$.

According to the definition of S -quaternion compounding physical quantity and the feature of quaternion operator \diamond , the definition of compounding field source deduces the electromagnetic field equations in the S -quaternion compounding space, including the Maxwell's equations. In the electromagnetic theory, the trial charge revolving around the electric charge can be considered as one particle still. The above equations are able to describe the deviation amplitude of the 'orbital' movement of the trial charge relative to the 'weightlessness' status.

5. ELECTROMAGNETIC NEAR-WEIGHTLESSNESS

In the S -quaternion compounding space, expanding the definition of compounding field source, $\bar{\mathbb{S}}_e = -\diamond^* \circ \bar{\mathbb{B}}_e/\mu_e$, yields the electromagnetic field equations as follows,

$$\nabla \cdot \bar{\mathbf{B}} = 0, \quad \nabla^* \times \bar{\mathbf{E}}/v_0 + \partial_0 \bar{\mathbf{B}} = 0, \quad (7)$$

$$-\mu_e \bar{\mathbf{S}}_0 = \nabla^* \cdot \bar{\mathbf{E}}/v_0, \quad -\mu_e \bar{\mathbf{S}} = \nabla^* \times \bar{\mathbf{B}} + \partial_0 \bar{\mathbf{E}}/v_0, \quad (8)$$

where $\bar{\mathbb{S}}_e = \bar{\mathbf{S}}_0 + \bar{\mathbf{S}}$. $\bar{\mathbb{B}}_e = \bar{\mathbf{H}}_0 + \bar{\mathbf{H}}$. $\bar{\mathbf{H}} = \bar{\mathbf{B}} + \bar{\mathbf{E}}/v_0$. $\bar{\mathbf{S}}_0 = \bar{S}_0 \mathbf{I}_0$. $\bar{\mathbf{H}}_0 = \bar{H}_0 \mathbf{I}_0$, with $\bar{H}_0 = 0$.

In case $\bar{\mathbb{S}}_e = 0$, one solution of the above is $\bar{\mathbb{B}}_e = 0$. When $\bar{\mathbf{H}} = 0$, the movement of the trial charge is in similar 'weightlessness' in the electromagnetic field of the positive charge Q . That is, $\bar{\mathbf{E}} = \mathbf{E} + \mathbf{a}_e = 0$, and $\bar{\mathbf{B}} = \mathbf{B} + \mathbf{Y} = 0$. Herein the linear acceleration is, $\mathbf{a}_e \approx d\mathbf{V}/dt$, in the S -quaternion space. $\mathbb{R}_e = \mathbf{R}_0 + \mathbf{R}$. $\mathbf{R} = \mathbf{I}_j R_j$. $\mathbf{R}_0 = R_0 \mathbf{I}_0$. The angular velocity is $\mathbf{Y} \approx \nabla \times \mathbf{V}$. $\mathbb{V}_e = \mathbf{V}_0 + \mathbf{V}$. $\mathbf{V} = \mathbf{I}_j V_j$. $\mathbf{V}_0 = V_0 \mathbf{I}_0$.

In the movement model for the 'revolution' and 'rotation' of the trial charge 'orbiting' around the positive charge Q , the equation $\bar{\mathbf{E}} = 0$ determines the radii of ellipse 'trajectory' for the trial charge 'revolution', while $\bar{\mathbf{B}} = 0$ ascertains the angular speed for the trial charge 'rotation'.

It should be noted that the equations $\bar{\mathbf{E}} = 0$ and $\bar{\mathbf{B}} = 0$ belong to the S -quaternion space, and cannot be measured directly in the quaternion space. That is because that the measurement method of the physical quantity in the S -quaternion space is different to that in the quaternion space. For instance, the electromagnetic strength \mathbf{E} and the electromagnetic source \mathbf{S}_0 belong to the S -quaternion space, and are only measured indirectly until to now. As the octonion product of \mathbf{E} and \mathbf{S}_0 , the Coulomb force, $\mathbf{F} = \mathbf{E} \cdot \mathbf{S}_0 = \mathbf{i}_j F_j$, belongs to the quaternion space, and is able to be measured directly in the quaternion space.

In the static electric field, there are, $\mathbf{S} = 0$ and $\bar{\mathbf{B}} = 0$. When $\bar{\mathbf{S}}_0 \neq 0$, Eq. (8) reveals that the field strength is, $\bar{\mathbf{E}} = \mathbf{E} + \mathbf{a}_e \neq 0$. When the trial charge orbiting around the positive charge Q is considered as one particle, the above is applied to describe the trajectory variation of the trial charge, which is in similar 'near-weightlessness'. The above deduces three kinds of cases,

(1) $\bar{\mathbf{E}} = 0$. It means that $\mathbf{E} + \mathbf{a}_e = 0$, and the 'orbital' movement of the trial charge is in similar 'weightlessness'. The calculation yields the radii R and the area speed C of the trial charge. In the polar coordinate system (R, ϕ) , for the S -quaternion space and (r, φ) for the quaternion space, the positive charge Q is on the point of origin, the 'orbital' radii of trial charge are $r = (k_1 Q/f)^{1/2}$ and $R = p/\{1 + e \cos(\phi - \theta)\}$, when f is one constant. Herein $p = (-C^2/f)^{1/3}$, the electromagnetic constant is $k_1 > 0$. e and θ are the coefficients.

(2) $|\mathbf{E}'| < |\mathbf{E}|$, with $\mathbf{E}' = \mathbf{E} - \bar{\mathbf{E}}$. It means that $\mathbf{E}' + \mathbf{a}_e = 0$, and the electric strength will become weakened, the 'orbital' movement of the trial charge deviates from the 'weightlessness', and the orbital radii of the trial charge increases. In the polar coordinate system (R, ϕ) , for the S -quaternion space and (r, φ) for the quaternion space, the positive charge Q is on the point of origin, the 'orbital' radii of trial charge are $R = p/\{1 + e \cos(\phi - \theta)\}$ and $r = (k_2 Q/f)^{1/2}$, in case $\bar{\mathbf{E}}$ is proportional to (k/R^2) and f is one constant. It means that the 'orbital' radii R of the trial charge keeps unchanged, while r decreases. Herein $p = (-C^2/f)^{1/3}$, k_2 is the equivalent electromagnetic constant, $0 < k_2 < k_1$, and k is the coefficient.

(3) $|\mathbf{E}'| > |\mathbf{E}|$, with $\mathbf{E}' = \mathbf{E} - \bar{\mathbf{E}}$. It means that $\mathbf{E}' + \mathbf{a}_e = 0$, and the electric strength will become strong, the 'orbital' movement of the trial charge deviates from the similar 'weightlessness', and the 'orbital' radii of the trial charge decreases. In the polar coordinate system (R, ϕ) , for the S -quaternion space and (r, φ) for the quaternion space, the positive charge Q is on the point of origin, the 'orbital' radii of trial charge are $r = (k_3 Q/f)^{1/2}$ and $R = p/\{1 + e \cos(\phi - \theta)\}$, in case $\bar{\mathbf{E}}$ is proportional to (k/R^2) and f is one constant. It means that the 'orbital' radii R of the trial charge keeps unchanged, while r increases. Herein $p = (-C^2/f)^{1/3}$, k_3 is the equivalent electromagnetic constant, $k_3 > k_1$, and k is the coefficient.

The above states that the charge density q , velocity \mathbb{V}_e , and field potential \mathbb{A}_e of the S -quaternion compounding field source $\bar{\mathbb{S}}_e$ will impact the 'orbital' radii and speed of the trial charge. In the

case of $\bar{\mathbf{E}} \neq 0$, the ‘orbit’ of the trial charge is still ellipsoidal and stable in the static electric field. Similarly in the quasi-static electric field, in case the S -quaternion compounding field source $\bar{\mathbb{S}}_e$ alters endlessly, it will cause the field strength $\bar{\mathbf{E}}$ and the orbital radii R of the trial charge to change continuously and accordingly. This will impact the ‘orbital’ radii of the trial charge, during it is in the growth phase, stable phase, and decline phase.

At the present time, the physical quantity being able to measure directly belongs to the quaternion space. And the physical quantity in the S -quaternion space is only measured indirectly, including the electromagnetic potential, the ‘orbital’ radii of trial charge, and the velocity of charged particle etc.. The above analysis reveals that the electromagnetic potential has an influence on the ‘orbital’ radii and velocity of charged particle. This prediction coincides with the Aharonov-Bohm test in the quantum mechanics, in which the magnetic flux impacts the electron movement.

Moreover adopting existing electric measurement method cannot obviate the electromagnetic potential to interfere the electron movement to a certain extent. It means that the electric measurement system will disturb the ‘orbital’ movement of trial charge during the measuring period, and then to interfere the measurement precision further. This conclusion is consistent with the uncertainty principle in the quantum mechanics.

6. CONCLUSIONS

The octonion compounding space can be separated into the quaternion compounding space and the S -quaternion compounding space. The quaternion compounding space can be used to describe the particle movements in weightlessness and near-weightlessness in the gravitational field, while the S -quaternion compounding space can be applied to depict that in the electromagnetic field.

In the quaternion compounding space for gravitational fields, the condition that the quaternion compounding field strength is equal to zero can be used to describe the movement trajectory of particles in weightlessness. The condition that the quaternion compounding field strength is not equal to zero can be used to depict the trajectory of particles in near-weightlessness. The conception of weightlessness and near-weightlessness can be extended to the electromagnetic field.

In the S -quaternion compounding space for electromagnetic fields, the condition that the S -quaternion compounding field strength is equal to zero can be used to describe the movement ‘trajectory’ of trial charges in similar ‘weightlessness’. The condition that the S -quaternion compounding field strength is not equal to zero can be used to depict the movement ‘trajectory’ of trial charges in similar ‘near-weightlessness’.

It should be noted that the research for the movement ‘trajectory’ of trial charges in similar ‘weightlessness’ and ‘near-weightlessness’ has examined only one simple case, which the compounding field strength of the static electric field is direct proportional to (k/R^2) . Despite its preliminary characteristics, this study can clear indicate that the field potential of the static electric field has an influence on the movement ‘trajectory’ of trial charges in similar ‘near-weightlessness’. The static electric field potential of measuring instruments is able to force the movement ‘trajectory’ of trial charge deviate from that in similar ‘weightlessness’. The inference agrees with the Aharonov-Bohm test and the uncertainty principle in the quantum mechanics to a certain extent.

ACKNOWLEDGMENT

This project was supported partially by the National Natural Science Foundation of China under grant number 60677039.

REFERENCES

1. Weng, Z.-H., “Velocity curl and spin in electromagnetic fields,” *PIERS Proceedings*, 352–356, Marrakesh, Morocco, Mar. 20–23, 2011.
2. Zwicky, F., “On the masses of nebulae and of clusters of nebulae,” *Astrophysical Journal*, Vol. 86, No. 3, 217–246, 1937.
3. Aharonov, Y. and D. Bohm, “Significance of electromagnetic potentials in quantum theory,” *Physical Review*, Vol. 115, No. 3, 485–491, 1959.

Focusing on the Moiré Effect

S. L. Vesely¹ and A. A. Vesely²

¹I.T.B. — C.N.R., Italy

²Via L. Anelli 13, Milano, Italy

Abstract— The moiré effect usually is not considered a fundamental topic of theories of radiation, even though it is quite commonly observed. It concurs to the characterization of images obtained by catadioptric systems, but escapes geometrical optics constructions. For the purpose of imaging in other frequency ranges, it could be worth to recognize it.

1. INTRODUCTION

This paper proposes some considerations on the moiré effect, a rather common effect that owes its name to the visual appearance of some silk fabric. It is often identified with a wavy pattern, and explained as beat between two periodical structures differing from each other in orientation or period dephasing only. It is deployed in various ways in the analysis of mechanical structures, but it may cause some inconveniences during image sampling.

As an optical effect, it is held subject of explanations within the framework of radiation theories. In addition, for any linear theory such explanations are expected to extend smoothly over all frequency ranges where the theory holds. The *small signals* detected in electromedical applications, or surveying, for example, behave linearly, therefore the moiré effect is expected to occur in those frequency ranges too. However, scattering targets do not behave linearly, let alone their emissions. If the electrical constitutive parameters of bodies behaved linearly, by now the underlying codes would have been cracked. Instead, in order to interpret the received signal, one has to laboriously recognize the effects brought about by the illumination supplied. As regards pictures, data acquired from a given subject in a different frequency band may not match the corresponding photography, and such recognition can be more difficult in non-optical ranges. Thus, even when handling imaging issues, information and telecommunications theories tend to lean on the modern theoretical approaches to fundamental physics, and concentrate on statistical models of matter and radiation. On the other hand, telecommunications breakthroughs could ease alternative approaches, such as the analysis of SAR data transposed into the optical band, pioneered in the 60s by Leith and Upatnieks. In that case, electromagnetism could be made to develop its own distinctive approach to the interpretation of received signals.

As the moiré is a wavy effect *belonging* to stigmatic images, in the following we summarize how analytical mechanics associates systems of points to their normal vibration modes, the energetic interpretation of such modes, and their dualism interpretation in relation to Fourier optics, as the wave part of quantum mechanics. Indeed, the moiré shows up mostly in diffractive optics applications.

2. POINTS AND WAVES IN ANALYTICAL MECHANICS

The efficiency of the conversion of mechanical vibrations to electrical emissions depends on many experimental parameters, even though the conversion itself is reversible. Moreover, the electrical signals can be made much cleaner than the mechanical vibrations that they originate from, or can be generated with no mechanical counterpart. In the golden era of mechanical reductionism, however, those kinds of vibrations were assimilated, since electromagnetic oscillations were attributed to aether.

The general problem of determining the motion of a linear mechanical system was tackled by Lagrange. He hypothesizes that the reversible motion of a system of N material points of mass m_j ($j = 1, \dots, N$) can be brought back to statics by balancing small independent displacements of the active forces against the inertial ones, for each tiny time interval¹ δt . Let's write active forces as $P_s \delta p_s$ ($s = 1, \dots, r$), where p_s is the line of action of P_s , while the x component of the inertial displacement of the j -th mass is $m_j \ddot{x}_j \delta x_j$. If system constraints are holonomic² and time-independent, then the inertia too varies along constant directions $p_s \forall \delta t$. Constraint equations let

¹Spatial and temporal variables are not symmetric.

²An holonomic constraint is a finite expression that can be used to reduce the *degrees of freedom* of the system and express free coordinates q_n as a function of Cartesian ones (x_j, y_j, z_j) .

us introduce free coordinates q_n ($n \equiv s = 1, \dots, r \leq 3N$), and write the difference between the work done by inertial forces and the active ones along those lines of action as:

$\delta L(q, dq) = \sum_{n=1}^r (\frac{d\delta T}{\delta dq_n} - \frac{\delta T}{\delta q_n} + \frac{\delta V}{\delta q_n}) \delta q_n = 0$, where the δq_n quantities can be varied independently from one another³. T is a quadratic expression of the dq_n , while V corresponds to the potential energy only if the forces P_n are conservative. In the latter case T is not only quadratic but also homogeneous in the dq_n , and the Lagrangian $L = T(dq_n) + V(q_n)$ represents total energy.

For small oscillations, the elastic restoring force on each mass m_j vanishes at equilibrium. Now, for each m_j , the displacement from its equilibrium position $(\bar{x}_j, \bar{y}_j, \bar{z}_j)$ can be referred as three free coordinates q_n , yielding a total of $r = 3N$ in this case. The values of q_n are very small, and vanish at equilibrium. Furthermore, as $\delta V / \delta q_n |_{(\bar{x}_j, \bar{y}_j, \bar{z}_j)} = 0$, the first significant term in the expansion of V is the quadratic one. Discarding higher order terms, the Euler-Lagrange equations become: $d(\frac{\delta L}{\delta dq_n}) - \frac{\delta L}{\delta q_n} = 0$ ($n = 1, \dots, r$). If the motion of each m_j is actually cyclic⁴, then one obtains homogeneous wave equations $\ddot{q}_n + Kq_n = 0$. However, $q_n = A_n \sin(t\sqrt{K} + \theta_n)$ is not the n -th general solution: This motion depends indeed on the initial conditions $(q_n|_{t=t_0}, \dot{q}_n|_{t=t_0})$, which determine A_n and θ_n , but the K depends on the coupling between the other masses. If all of the N masses are identical and equidistant to one another, and each mass has but a single free coordinate, then the n -th general solution $q_n = \sum_{j=1}^N A_j \sin(t\sqrt{K_{nj}} + \theta_j)$ is the sum of N harmonic functions. Since the motion of each mass is given by q_n , knowledge of the normal modes — to wit, the spectrum — is not sufficient to determine the motion of the system. In order to compute the latter, it is necessary to invert the matrix of the normal modes $A_n \sin(t\sqrt{K_{jn}} + \theta_n)$. Analytical mechanics provides for no dualism: The partial solution consisting of the determination of the normal modes is not equivalent to the determination of the motion.

For the conceptual developments of statistical mechanics, and for the representations of quantum mechanics dualism, descriptions based on the phase space became increasingly popular. They stem from the Hamiltonian function $H = \sum_{n=1}^r (\frac{\delta L}{\delta dq_n}) dq_n - L$, which differs from the Lagrangian by a Legendre transformation with respect to the δq_n . The Hamiltonian introduces kinetic momenta $p_n = \delta L / \delta dq_n = \sum_{m=1}^r a_{mn} dq_m + a_n$ as conjugate variables of the q_n , which vary independently of them. The variation $\delta H = \sum_{n=1}^r (\frac{\partial H}{\partial p_n} \delta p_n + \frac{\partial H}{\partial q_n} \delta q_n)$ gives the canonical equations⁵ $dq_n = \partial H / \partial p_n$ and $dp_n = -\partial H / \partial q_n$, which, given $2r$ initial conditions, describe in the phase space the motion of the point that represents the system. Probabilistic interpretations, $r \rightarrow \infty$, attribute a spectrum with countably infinitely many frequencies to the resonator.

3. SPECTRAL ISSUES

For an alternative to the elastic theory of aether, electromagnetic energy has been assimilated to *heat radiation*. To deal with heat conduction, Fourier introduced serial expansions based on trigonometric functions, that allow successive approximations more easily than those based on polynomials. He determined analytical expressions of the temperature $T(q_n)$ as functions of the positions q_n along homogeneous rods⁶. He found out that the law of heat flow variation per unitary cross-section, $\delta Q / \delta t = -k \Delta T / \Delta q$ ($\Delta q = q_n - q_{n-1}$ for a sample subdivided into segments of the same length), also holds when the temperature of one end of the rod is driven according to a given periodical rule. Fourier didn't bother considering thermodynamical equilibrium. According to him, variations of temperature are independent causes, and sum up at each point q_n . His conclusion is that each term of the expansion represents a real oscillation of the flow, which cannot be seen because of the damping effect of the medium. Boltzmann described the oscillating heat flow by assigning cyclic coordinates $\langle q_n \rangle$ in each point⁷, and represented thermodynamical quantities by potentials. Statistical mechanical reduction of thermodynamics brings to the Hamiltonian formulation.

Fourier believed that his method to do oscillating conduction flow could be extended to the

³By δ and d , we denote the two kinds of variations, independent of one another. The former variations are compatible with the constraints. The latter ones are determined so as to counter the active forces, thus their directions are near the corresponding kinematic velocities.

⁴Since the spring constant is a tensor, its components along the three coordinate directions have to be in a simple ratio among themselves, possibly equal to one another.

⁵The first, for example, is obtained reversing the kinetic motion matrix $\sum_{m=1}^r a_{mn} (p_m - a_m)$.

⁶The experiments were carried out using rods of various sections and lengths, whose ends were in thermal contact with heat reservoirs of different temperatures.

⁷Cyclic coordinates were introduced by Helmholtz to treat steady flows in thermodynamic cycles. They are called *cyclic* because, in the Lagrangian, their kinetic energy $T = T(dq_n)$ does not depend on the free coordinates.

oscillations of radiant heat. Instead, it took quantum theory to assign normal modes to radiant heat⁸. Classical statistics derives the vibration modes of a radiation inside a cavity as a function of temperature in two ways. The first one, from a statistic thermodynamics point of view, considers a gas of N independent molecules with mean energy $\bar{\epsilon}$, and associates an energy distribution $\langle E \rangle \propto \exp(-\bar{\epsilon}/k_B T)$ to its temperature T . It is valid at high frequencies only. The second one, of analytical mechanics derivation, counts the amount of steady synchronous oscillation frequencies of aether comprised in the interval $[\nu, \nu + d\nu]$ in a unitary volume, and comes to the asymptotic value $N(\nu) = 8\pi\nu^2/c^3$. Turning to the energy density, one gets $u(\nu, T) = N(\nu)k_B T$ by the equipartition theorem. That formula holds also replacing aether with N oscillator molecules at thermal equilibrium that absorb and emit heat radiation. In either case, the formula approximates the black body radiation at low frequencies only. However, by *quantizing energy*, one gets an interpolation that approximates the curves obtained by Rubens and Kurlbaum at any frequency, the Planck's curve: $u(\nu, T) = \frac{8\pi\nu^2}{c^3} \frac{\bar{\epsilon}}{e^{\frac{\bar{\epsilon}}{k_B T}} - 1} = \frac{8\pi h\nu^3}{c^3} \frac{1}{e^{\frac{h\nu}{k_B T}} - 1}$. Planck's constant, $h = \iint dp_n dq_n = \oint p_n(q_n) dq_n$, $n = 1, \dots, r$, dimensioned as energy times time, implies that the system phase space is subdivided into cells of volume Ω . N linear oscillators in a volume Ω_N yield energy $E = Nh\nu = \Omega_N \nu$ and entropy $S = k_B N \ln(\Omega/\Omega_N)$. In general, those N linear oscillators are spread among M energy level cells, which is what differentiates Planck's statistics from the equipartition of energy. Thus, normal modes are not attributed to the molecules, but to the cells. Atomic spectra don't display those energies, but behave according to Ritz's combination principle. The correspondence principle — the beginning of quantum interpretation — considers $\lim_{N \rightarrow \infty} dE/dN = h\nu$ rather than E .

4. DUALIST APPROACHES

After it was clarified that perturbation theory is not about deformation of electrons' orbits, but about transitions between different orbits, electromagnetic waves were included back into quantum theory as entities complementary to matter. The purpose of that early dualism — wave as radiation vs. particle as matter — was a microscopic description of electrodynamics, analogous to the statistical mechanics description of thermodynamics. Bohr regarded radiation's absorption as related to refraction, in the same way as diffraction was related to Bragg reflection. But Einstein showed that the absorption and emission processes correspond to energetic jumps, and require that the exchanged energy be located in the photon. Before recognizing the necessity of field quantization, dualism was considered an ability to describe atomic systems according to either Schrödinger's wave theory or Heisenberg's particle theory. In both cases, the uncertainty principle⁹ requires the operators corresponding to conjugates dynamical variables q_n and p_n to assume values in mutually reciprocal spaces. Therefore, the phase space was split into a configuration space and an impulse space. But the photoelectric process of detection requires the field to be quantized. That so-called second quantization derailed the concept of wave-photon dualism. Indeed, the eigensolutions of the wave equation — quantized according to Dirac — are constructed by creating and annihilating photons, basing on eigenstates of the particle number operator, known as Fock states. Incoherent solutions are interpreted as fluctuations of the number of photons. Coherent solutions correspond to the probability of having N photons in a coherent state. Coherent states, which are linear combinations of Fock states, were introduced by Glauber in order to describe laser radiation, thereby founding quantum optics. Rather than being the quantity mapped out by an interference pattern, the phase is the expected value of the phase part of the annihilation operator. Finally, quantum electrodynamics (QED) requires the uncertainty principle to be extended to the time-energy pair of conjugate variables. Such extension conflicts with Lagrange's conception of time as a parameter rather than a dynamical variable. In 1931, Landau and Peierls discussed with Bohr the conceptual difficulties raised in quantum theories about the ability to make predictable measurements of

⁸Boltzmann derives the relationship $u \propto T^4$ (Stefan-Boltzmann law) of the radiant energy density u from absolute temperature T after thermodynamics. From $Q = TS = E + pV = uV + pV$ differentiating with respect to V and then positing $V = 1$ and taking into account $(\partial S/\partial V)_T = (\partial p/\partial T)_V$, one has $T(\partial p/\partial T)_V = p + u$. Substituting $p = 1/3u$, which is the radiation pressure, one has $T(\partial u/\partial T)_V = 4u$.

⁹The uncertainty principle dates 1927. It precludes the possibility to measure a coordinate and its conjugate momentum in a precise manner at the same time. In Heisenberg's picture, it originates from Schwarz inequality $(1/2\hbar|\dot{X}|)^2 = |\langle XH - HX \rangle|^2 \leq \Delta X^2 \Delta H^2$ when c -numbers are replaced by q -numbers. In Schrödinger's picture, the same uncertainty principle is expressed by Fourier transform. Originally, Schrödinger formulated his wave equation by analogy with the Hamiltonian optics of rays and wave fronts. He interpreted eigenstates of the wave function of atoms in the *momentum space* as steady oscillations having $p = \hbar k$, transitions between eigenstates (as per Ritz's combination principle) as spatial beats, and associated a wave packet to any free particle. If, in the corresponding *position space*, that wave function represents a density, then, by the analysis of the Lagrangian given in Section 2 for a finite number of points, such density must be interpreted probabilistically.

the physical quantities that they deal with. Notwithstanding Bohr's and Rosenfeld's exhaustive reply, and the discovery of the Lamb shift, and many others quantum effects of radiation, including squeezed states, that argument clarified the importance of new points of view on this subject.

5. DIFFRACTION PATTERNS IN THE STIGMATIC IMAGES

Fourier optics derived from physical optics, spurred on by telecommunication theory. While it shares with physical optics the representations of photon trajectories and wave fronts, duality obtains an independent meaning. *Telecommunications* don't relate signals and spectra: They deal with the transmission of whatever encoded information, irrespective of its meaning, and are just concerned with defining the frequency band to transmit signals, as determined by Shannon's findings. However, *analog optical information processing* relates diffraction with the images. It regards holograms as a means to capture the optical field, and deals with them as if they were frequency filters, in the sense that a zone-plate can replace a lens¹⁰. Therefore, in Fourier optics the wave pattern ceases to act as an approximation of order higher than that of the light ray, and becomes the dual counterpart of the image point in the same approximation, i.e., that of linear response. In the following, we'll investigate the moiré. It lends itself to illustrate a duality suitable for imaging purposes, inasmuch as it is often related to an interference pattern *observed on the image plane*. To say that a moiré is a spatial beat among gratings of similar periods means that it is a composition of either the gratings' pitches and hence the beat is an image — or that the moiré is an interference and hence the gratings are diffraction patterns, too. While a dual transformation between a (flat) image and its diffraction pattern can be performed by means of a lens, setting up reciprocal spaces to represent image points and spatial frequency points is futile unless radiation is encoded. Let's examine some specific cases as examples. Hutley et al. [1] used the moiré to magnify the average graphical element of a motif. In their experiments, the fringes are caused by the beat of an array of lenticular lenses with the underlying graphics, and are observed onto the support frame. Each fringe appears as a possibly magnified image of the repeated graphical element. However, since the graphics is in the lenses' focal plane, the images should not appear sharp to an eye looking at the frame. Nevertheless, they do, because the light sources that illuminate gratings appear on focus together with their diffraction patterns [2]. In Ramachandran's paper, the images of the source appear in the scattering pattern of lycopodium powder¹¹. In practice, interferential effects confer a distinctive aspect to the image, and disallow its point-by-point construction. That argument is also relevant for the general understanding of diffraction. For another example, consider the irregular grating formed by foliage protruding above a track on a sunny day: When watched against the light, that is interpreted as *light diffraction*, while, looking downward, it is interpreted as shadows cast against the ground. Instead, the above discussion implies that the shadow is the diffraction pattern of the branches and the light spots belong to the moiré. In fact, in case of partial solar eclipse those spots are crescent-shaped. Thus, if diffraction is considered an attribute of the received signal, rather than a feature of light, then it is natural to recognize that object images are not, in general, either stigmatic or wavy.

In telecommunications, it is customary to encode images to be transmitted, and decode them with a prior established error bounds. Therefore, especially in surveying, it may make sense to ask whether illuminating a scene with some encoded radiation might make the image processing similar to that adopted for encoded signals. To acquire the pictures, a grating with two independent pitches is conceptually superimposed to the signal¹². Subsequently, the encoded part of the echoes gets decoded, but, differently from telecommunications, that part is not the one that contains

¹⁰Crystallography originates from physical optics and involves dualism too. However, its crystal lattice models are abstracted from diffractograms considered in the reciprocal space, for example according to Ewald. Instead, holograms, as well as diffraction patterns of diffractive optics, have a visible relationship with stigmatic images. Moreover, X rays can only be collimated whereas both diffraction pattern and images are obtained by focusing. That kind of visible dualism — of a space onto itself — can be made explicit by establishing a specific geometrical model.

¹¹Ramachandran demonstrates that bright spots in the diffraction patterns obtained with lycopodium powder are copies of the light source, and that such behavior is typical of diffraction patterns obtained from non-point sources. The single components of the motif, those ones magnified by moiré effect in Hutley et al., are situated at the focal plane of the lenses, and therefore their images are projected at infinity. In diffractive-optical terms a diffraction pattern is observed together with the image when the corresponding planes coalesce. In such conditions, it is hard to tell whether the beat is an interference between the gratings rather than their diffraction patterns.

¹²Roughly, in airborne radar systems microwave impulses are encoded in part directly by the emitting device and in part due to the aircraft motion relative to the target. Magnetic resonance imaging is based on a similar encoding: The frequency response of the hydrogen resonating peak of water depends on the magnetic field, which is varied according to two independent linear functions. In principle, the value of the frequency allows to locate the region that originated the response. In both cases, the aliasing due to the encoding is known and gets filtered off.

the information sought. The returned echoes contain also the information-carrying part, to which physical theories assign characteristic properties. That part has neither photon nor wave properties, as far as interpreting the images goes: It only becomes a kind of signal when received. In fact, the conversion step for the scattered radiations is performed differently by different receivers¹³: Typically, unencoded parts that a human eye would recognize as moiré, if any, are not necessarily decoded as such if they are reconstructed point by point.

6. CONCLUSIONS

Image analysis is usually based on statistical models of both the radiation and active or passive radiators. The wave-particle dualism, to which wave theories relate the Fourier transform, is among the most influential concepts in telecommunications. We examined the moiré effect in order to bring out a distinction between the radiation, as usually considered, and signals. At least in its original acceptation, the moiré is a non-local effect of the weft, observable together with the fabric. We interpreted it as an interferential effect seen with the image. Accordingly, the moiré would fit in the framework of a geometric model that goes beyond geometrical optics, by providing alternatives to one-to-one relationships between object points and image points. In the optical range, the moiré is focused and recognized as such. However, it might contribute to signals — or noise — during image acquisition in any frequency range.

REFERENCES

1. Hutley, M. C., R. Hunt, R. F. Stevens, and P. Savander, “The moiré magnifier,” *Pure Appl. Opt.*, Vol. 3, 133–142, 1994.
2. Ramachandran, G. N., “Fluctuations of light intensity of coronæ formed by diffraction,” *J. Astrophys. Astr.*, Vol. 15, 357–371, 1994; Origin in *Proc. Indian Acad. Sci.*, 1943.

¹³Signal reception can be emulated by algorithmic methods for the whole linear part; that is, up to the receiver’s transduction.

Response of Multilayer Materials to Electromagnetic Waves

R. Kadlec, P. Marcoň, E. Kroutilová, and P. Fiala

Department of Theoretical and Experimental Electrical Engineering
Brno University of Technology, Kolejní 2906/4, Brno 612 00, Czech Republic

Abstract— The authors report on an analytical solution of the propagation, reflection and refraction of broadband electromagnetic signals within multilayer optical materials. The presented solution is processed in the Matlab program, which is suitable for a specifically oriented detailed analysis of a general problem.

The paper includes a theoretical analysis and references to the generated algorithms. Comparison of the parameter changes is supported by graphical outputs of the algorithms. Algorithms created in the Matlab environment are verified by means of programs based on the finite element method, namely the ANSYS program.

Inhomogeneities and regions with different parameters generally appear even in the cleanest materials. During the electromagnetic wave passage through a material there occurs an amplitude decrease and a wave phase shift; these phenomena are due to the material characteristics such as conductivity, permittivity, or permeability. Any incidence of a wave on an inhomogeneity results in a change in its propagation. The change manifests itself in two forms, namely in the reflection and refraction. In addition to this process, polarization and interference may appear in these waves.

The methods described in this paper are well-suited for the analysis of beam refraction to the other side from the perpendicular line during the passage through the boundary. This phenomenon occurs in metamaterials.

1. INTRODUCTION

Inhomogeneities and regions with different parameters generally appear even in the cleanest materials. During the electromagnetic wave passage through a material there occur an amplitude decrease and a wave phase shift; these phenomena are due to the material characteristics such as conductivity, permittivity, or permeability. If a wave impinges on an inhomogeneity, there occurs a change in its propagation. The change manifests itself in two forms, namely in reflection and refraction. In addition to this process, polarization and interference may appear in these waves.

It should be notify that in terms of the general theory is the frequency interval from 0 to 100 GHz (the area that deals with electricity and magnetism) and the interval 0.1 to 10 THz PHZ (studied in optics) no principled difference. The idea of a solid as the atomic structure of the opposite assumption connection environment, it is necessary to understand the material properties that describe the response of the environment, such as mean values of a sufficient number of atoms.

In the Matlab program, algorithms were created that simulate reflection and refraction in a lossy environment on the boundary between two dielectrics. The reflection and refraction are in accordance with Snell's law for electromagnetic waves as shown in Fig. 1(a). The form of Snell's law is as follows [1]:

$$\frac{\sin \theta_0}{\sin \theta_2} = \frac{\mathbf{k}_2}{\mathbf{k}_1} = \frac{\sqrt{j\omega\mu_2 \cdot (\gamma_2 + j\omega\varepsilon_2)}}{\sqrt{j\omega\mu_1 \cdot (\gamma_1 + j\omega\varepsilon_1)}}, \quad (1)$$

where \mathbf{k} is the wave number, γ is the conductivity, ε the permittivity, μ the permeability, θ_0 angle of incidence and θ_2 angle of refraction. Relation (1) is defining for the boundary line between the dielectrics medium. Interpretation of the Fresnel equations and Snell's laws is simple in the case of the refraction on boundary line between the dielectrics medium. In case of refraction in a lossy medium, according to relation (1), angle θ_2 depends on wave numbers \mathbf{k}_1 and \mathbf{k}_2 , which are generally complex; then, in medium 2 an inhomogeneous wave is propagated.

This complicates the physical nature of the phenomena and brings qualitatively new phenomena. Areas of constant phase generally do not merge with areas of constant amplitude, then wave is not completely transverse. Areas of constant amplitude are parallel to the interface, but the same areas of phases are generally oblique to it. The resulting EMG waves are propagated in the coordinate system in the direction \mathbf{u}_{n2} . An electromagnetic wave is understood as the electric field strength and the magnetic field strength.

For simplicity, we will analyse separately the \mathbf{E} vector parallel to the boundary (also known as TE wave) as indicated in Fig. 1(a) and the \mathbf{H} vector parallel to the boundary (also known as TM wave). For the TE wave, electric field strength of the reflection and transmission beams is expressed according to the equation

$$\mathbf{E}_r = \mathbf{E}_1 e^{-jk_1 \mathbf{u}_{n1} \times \mathbf{r}}, \quad \mathbf{E}_t = \mathbf{E}_2 e^{-jk_2 \mathbf{u}_{n2} \times \mathbf{r}}, \quad (2)$$

where \mathbf{E}_1 is calculated from the intensity on boundary line \mathbf{E}_0 and reflection coefficient ρ_E , and \mathbf{E}_2 is calculated from the intensity on boundary line \mathbf{E}_0 and transmission factor τ_E . For numerical modelling, there is a suitable relation in the form:

$$\begin{aligned} \mathbf{E}_r &= \frac{\mu_2 k_1 \cos \theta_0 - \mu_1 \sqrt{k_2^2 - k_1^2 \sin^2 \theta_0}}{\mu_2 k_1 \cos \theta_0 + \mu_1 \sqrt{k_2^2 - k_1^2 \sin^2 \theta_0}} \mathbf{E}_0 \cdot e^{-jk_1 \mathbf{u}_{n1} \times \mathbf{r}}, \\ \mathbf{E}_t &= \frac{2\mu_2 k_1 \cos \theta_0}{\mu_2 k_1 \cos \theta_0 + \mu_1 \sqrt{k_2^2 - k_1^2 \sin^2 \theta_0}} \mathbf{E}_0 \cdot e^{-jk_2 \mathbf{u}_{n2} \times \mathbf{r}}. \end{aligned} \quad (3)$$

These relations are calculated from the basic variable and they facilitate an acceleration of the calculation process. We use atypical formulas for calculating the magnetic components:

$$\begin{aligned} \mathbf{H}_r &= -\frac{\frac{\mu_2}{\mu_1} \mathbf{k}_1 \cos \theta_0 - \sqrt{\mathbf{k}_2^2 - \mathbf{k}_1^2 \sin^2 \theta_0}}{\mu_2 \cos \theta_0 + \frac{\mu_1}{\mathbf{k}_1} \sqrt{\mathbf{k}_2^2 - \mathbf{k}_1^2 \sin^2 \theta_0}} \frac{\mathbf{E}_0}{\omega} \cdot e^{-jk_1 \mathbf{u}_{n1} \times \mathbf{r}} \\ \mathbf{H}_t &= -\frac{2\mathbf{k}_2 \cos \theta_0}{\mu_2 \cos \theta_0 + \frac{\mu_1}{\mathbf{k}_1} \sqrt{\mathbf{k}_2^2 - \mathbf{k}_1^2 \sin^2 \theta_0}} \frac{\mathbf{E}_0}{\omega} \cdot e^{-jk_2 \mathbf{u}_{n2} \times \mathbf{r}} \end{aligned} \quad (4)$$

2. OBLIQUE INCIDENT WAVE ON A LAYERED MEDIUM

For a layered heterogeneous medium, an algorithm is derived for the reflection of the electric component on several layers, Fig. 1(a). Interpretation of the propagation of electromagnetic waves on a layered heterogeneous medium is expressed by the relation

$$\mathbf{E}_{rl} = \mathbf{E}_{il} \rho_{El} \cdot e^{-j\mathbf{k}_l \mathbf{u}_{nr} \times \mathbf{r}_l}, \quad \mathbf{E}_{tl} = \mathbf{E}_{il} \tau_{El} \cdot e^{-j\mathbf{k}_l \mathbf{u}_{nt} \times \mathbf{r}_l}, \quad (5)$$

where \mathbf{E}_{rl} and \mathbf{E}_{tl} are the reflection and refraction electromagnetic waves on the boundary line ($l = 1, \dots, \max$) according to Fig. 1(a), \mathbf{E}_{il} is the amplitude electric field strength on boundary line l , ρ_{El} and τ_{El} are the reflection coefficient and transmission factor on boundary line l , \mathbf{k}_l is the wave number of the layer, \mathbf{r}_l is the electromagnetic wave positional vector on boundary line l , \mathbf{u}_{nt} and \mathbf{u}_{nr} are the unit vectors of propagation direction.

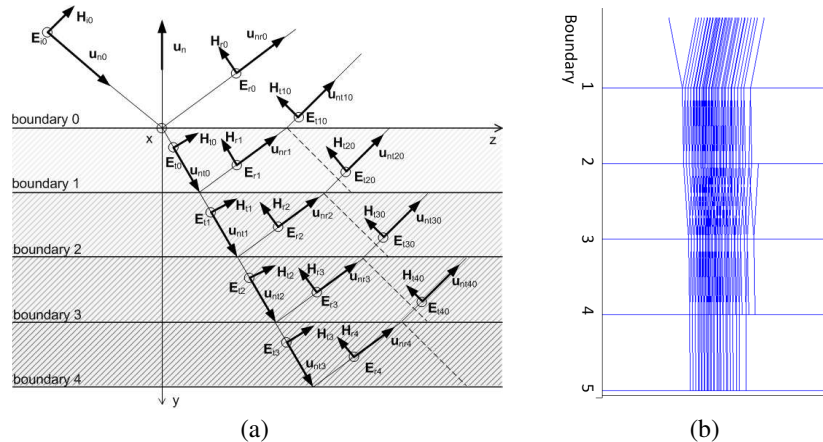


Figure 1: Reflection and refraction of the electromagnetic waves on a layered medium for the TE wave: (a) layout, (b) in Matlab for 5000 cycles.

3. OBLIQUE INCIDENT WAVE IN MATLAB PROGRAM

Response is dependent on the thickness d of each layer. Figs. 2 and 3 show the response of the environment 5 layers of the same thickness. Wave at a frequency of 700 THz during the transmission from a material with parameters $\varepsilon_r = 1$, $\mu_r = 1$ and $\gamma = 0 \text{ S/m}$ at the incidence of the wave on the boundary 1 at the angle of 30° (according to Fig. 1(b)), into a material 1 with parameters $\varepsilon_r = 2.5$, $\mu_r = 1$ and $\gamma = 870 \text{ S/m}$, where the wave is reflected and refracted. Furthermore, the wave propagates through material 2 with parameters $\varepsilon_r = 81.6$, $\mu_r = 1$ and $\gamma = 4.4 \cdot 10^{-6} \text{ S/m}$, material 3 with parameters $\varepsilon_r = 2.5$, $\mu_r = 1$ and $\gamma = 1200 \text{ S/m}$, 4 with material parameters $\varepsilon_r = 8.5$, $\mu_r = 1$ and $\gamma = 150 \text{ S/m}$. In the material 5 with parameters ($\varepsilon_r = 81.6$, $\mu_r = 1$ and $\gamma = 4.4 \cdot 10^{-6} \text{ S/m}$), the wave reflects only, because we assume no backward waves in the most bottom medium. Selection of material parameters is only a test, thus has not special meaning.

Figure 2 shows the response of layers of thickness $d = 10 \cdot \lambda$, where λ is the wavelength of

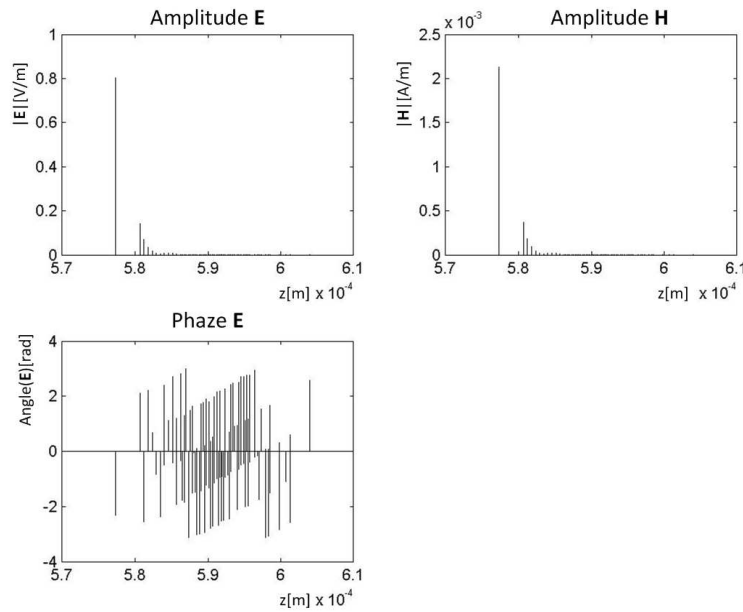


Figure 2: The intensity of electric and magnetic component of TE wave outside layered medium for $d = 10 \cdot \lambda$.

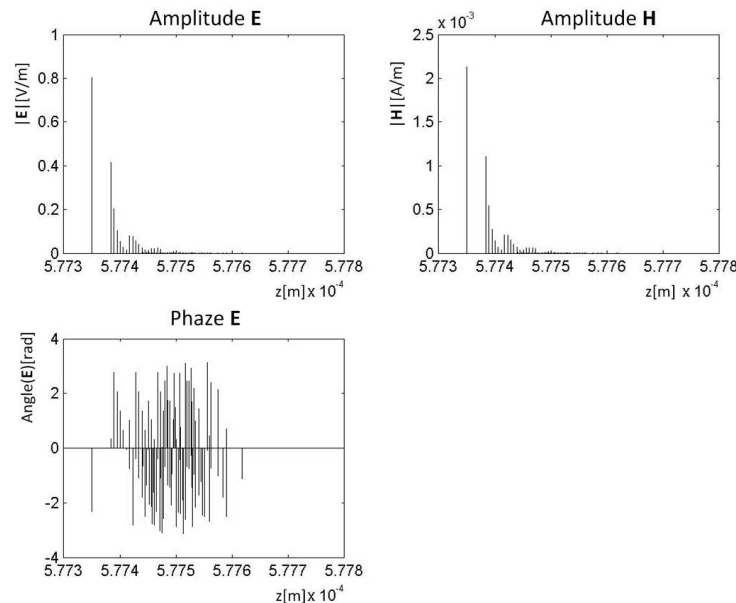


Figure 3: The intensity of electric and magnetic component of TE wave outside layered medium for $d = \lambda/10$.

the wave, which is sent from a source in the form of a single pulse. All five layers have the same thickness. The response is shown for the electric field strength \mathbf{E} and magnetic field strength \mathbf{H} for TE wave, i.e., the amplitude and the phase. Fig. 3 shows the same response, but for the layer thickness $d = \lambda/10$. From Figs. 2 and 3, it is obvious different shape. For thicknesses $d > \lambda$ waveforms have the same character as in Fig. 2 and for thicknesses $d < \lambda$ waveforms have the same character as in Fig. 3.

4. CONCLUSIONS

The paper includes a theoretical analysis of and various references to the generated algorithms, which are verified using numerical models. Analytical solution of the propagation, reflection, and refraction of wideband electromagnetic signals within multilayer optical materials is very time-intensive if realized in the Matlab program; this fact is further illustrated in Fig. 1(a), which shows both components of the electromagnetic waves.

This method is nevertheless suitable for a specifically oriented detailed analysis of a general problem. Algorithms created in the Matlab environment are verified by means of programs based on the finite element method, namely such programs as Comsol and ANSYS.

Methods described in this article are well-suited for the analysis of beam refraction to the other side from the perpendicular line during the transmission through the interface. This phenomenon occurs in metamaterials.

ACKNOWLEDGMENT

The research described in the paper was financially supported by the research program of Ministry of Industry and Trade of the CR (Diagnostics of Superfast Objects for Safety Testing, FR-TI1/368), Czech Science Foundation (102/09/0314), project of the BUT Grant Agency FEKT-S-11-5/1012 and project from Education for Competitiveness Operative Programme CZ.1.07.2.3.00.20.0175, (Electro-researcher).

REFERENCES

1. Dedek, L. and J. Dedková, *Elektromagnetismus 2*, 232, Vitium, Brno, 2000, ISBN 80-214-1548-7.
2. Nešpor, D., “Electromagnetic wave propagation study in heterogeneous structures,” 20 s, Supervisor, Doc. Ing. Pavel Fiala, Ph.D., 2009.
3. Steinbauer, M. and K. Bartušek, “Numerical method of simulation of material influences in MR tomography,” *PIERS Proceedings*, 1077–1080, Hangzhou, China, Mar. 24–28, 2008.
4. Fiala, P., E. Kroutilová, M. Steinbauer, P. Dohnal, M. Hadinec, and K. Bartušek, “Experiments with the effect of non-homogenous parts in materials,” *PIERS Proceedings*, 1081–1084, Hangzhou, China, Mar. 24–28, 2008.
5. Hadinec, M., P. Fiala, E. Kroutilová, M. Steinbauer, and K. Bartušek, “Method for magnetic field approximation in MR tomography,” *PIERS Proceedings*, 1179–1183, Hangzhou, China, Mar. 24–28, 2008.

Analysis of Distortion Factor of Three Phase Linear Synchronous Motor

Koichi Nakaiwa¹ and Hiroyuki Wakiwaka²

¹Tamagawa Seiki Corporation, Japan

²Shinshu University, Japan

Abstract— The relationship between the E.M.F and the distortion factor in a magnet arrangement was compared and verified. The use of a linear motor suitable for each magnet arrangement was determined from the perspective of magnetic energy efficiency. (e.g., generator use, industrial use, high speed drive use, etc.).

1. INTRODUCTION

It is important to take into account the influence of the distortion factor in the design of a linear motor. A distortion factor expresses the grade of distortion of a wave, and it is a ratio of the effective value of the overall higher harmonic wave contained in the distorted wave to the effective value of the fundamental wave. Since an effective current value will also increase if the distortion factor becomes high, electric power increases at I^2R , and it becomes important to know whether high thrust can lower the distorted rate of the E.M.F wave pattern from vibration and overheating [1]. Past research has been published about the Distortion Factor. The types of motor techniques of this research are also varied [2–5]. This report describes the E.M.F and the distortion factor.

2. STRUCTURE AND PRINCIPLE OF LINEAR SYNCHRONOUS MOTOR

A schematic structure of the Linear Synchronous Motor (abbreviated as LSM) is shown in Fig. 1. The length units used are mm. The mover is composed of permanent magnets and shaft. The shaft has $\phi 5$ in the outer diameter. A rare earth Ne-Fe-B ($B_r = 1.29$ T) type permanent magnet is used for the magnets. The Radial array has a magnetic material shaft, and the Halbach array and Interior array have a shaft made of a non-magnetic material. The core of the stator is made of a silicon steel (35H300). The excitation coil has a three-phased structure. The number of windings in one slot is 37 turns. Detailed specifications are shown in Table 1 [6–11].

3. FINITE ELEMENT ANALYSIS OF LSM

3.1. Calculation of Interlinkage Flux

First, Interlinkage flux was calculated. The software used in this analysis was developed by our group [12]. A finite element model and the calculated results are shown below. The number of elements is 74000. The calculated value of the Interlinkage flux is shown in Fig. 2.

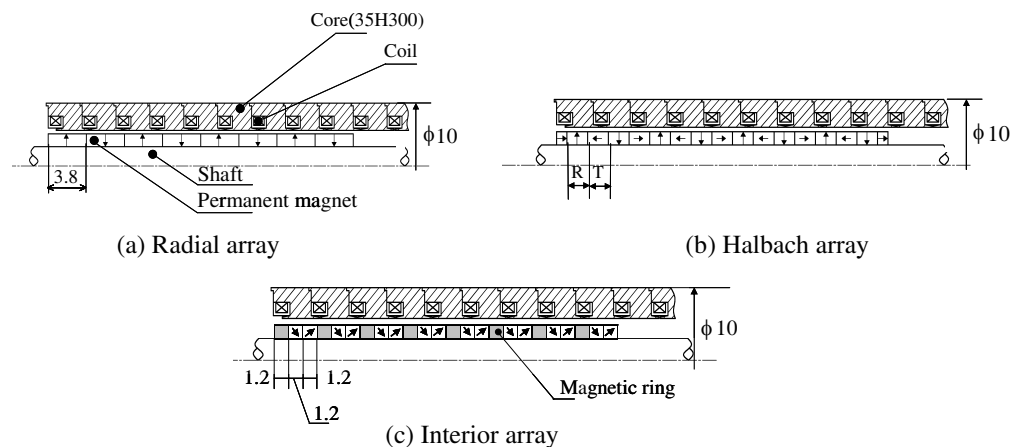


Figure 1: A schematic structure of LSM.

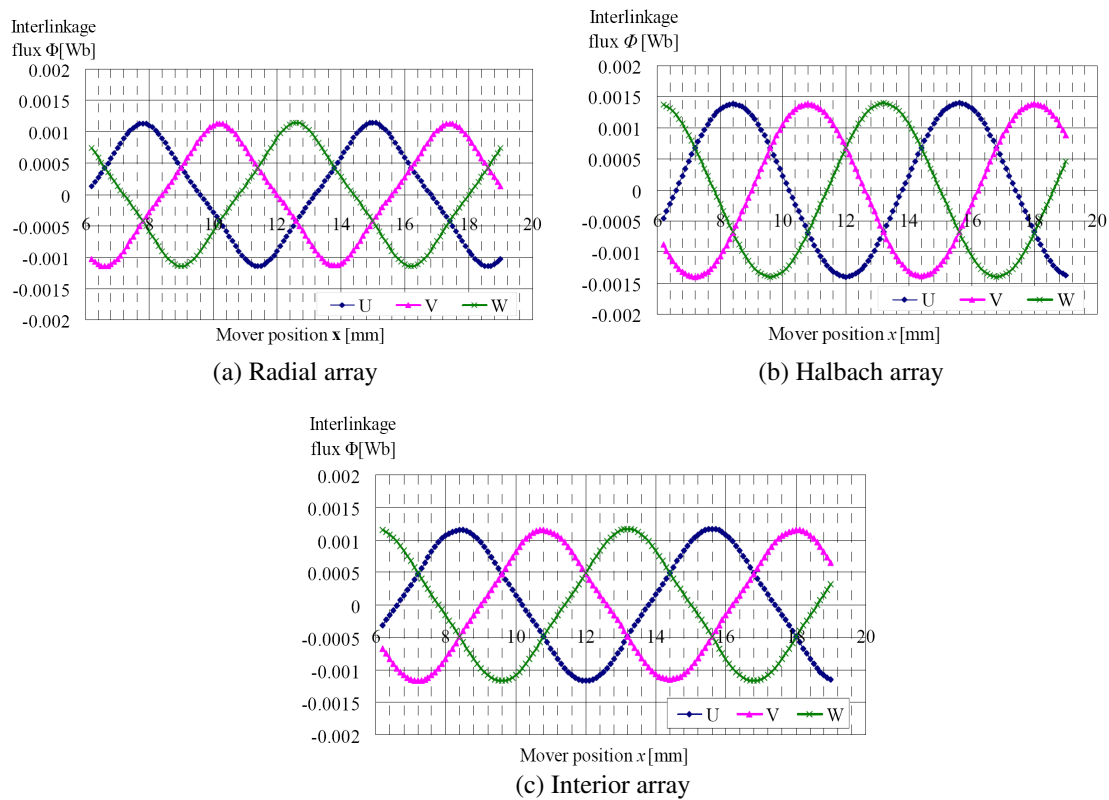


Figure 2: Calculated value of Interlinkage flux.

Table 1: Summary specification.

Item \ Type	Radial array	Halbach array	Interior array
External dimensions	12 mm		
stroke	30 mm		
Number of magnet	8	24	16
Number of pole & slot	8p-18s		
Number of phase	3		
Structure of magnet	Radial magnet	Radial & Thrust magnet	Radial & Thrust magnet +
shaht material	magneric	non-magnetic	

3.2. Calculation of the E.M.F and the Distortion Wave

The Distortion wave is considered as a superposition of sine wave, and if $y(t)$ is defined as the time function of distortion wave with cycle T ,

$$\begin{aligned}
 y(t) &= y(t + T) = b_0 + b_1 \cos(\omega t) + b_2 \cos(2\omega t) \\
 &\quad + b_3 \cos(3\omega t) + \dots a_1 \sin(\omega t) + a_2 \sin(2\omega t) + a_3 \sin(3\omega t) + \dots \\
 &= b_0 + \sum_n^{\infty} [a_n \sin(n\omega t) + b_n \cos(n\omega t)] = b_0 + \sum_n^{\infty} A_n \sin(n\omega t + \theta_n)
 \end{aligned} \tag{1}$$

where, A_1 is the amplitude of the basic wave, A_n is the n harmonic, b_0 is the average value of the Distortion wave. The purpose of a Distortion factor is to express the grade of distortion of a waveform. Generally it is defined as a ratio of the total of the effective value of an overall height harmonic ingredient ($V_2 \sim V_n$) and the effective value of a fundamental wave (V_1) which is included

in the waveform. Generally it is expressed with the following.

$$v(t) = V_0 + \sum_n V_n \sin(n\omega t - \theta_n) \quad (2)$$

An effective value is expressed below,

$$|V| = \sqrt{\frac{1}{T} \int_0^T v^2(t) dt} \quad (3)$$

$$|V| = \sqrt{V_0^2 + |V_1|^2 + |V_2|^2 + |V_3|^2 + \dots} \quad (4)$$

It becomes a sin wave of the sum of the square of the effective value of each higher harmonics wave. Also, the definition of the rate of harmonic distortion,

$$D = \frac{\sqrt{|V_2|^2 + |V_3|^2 + \dots}}{\sqrt{|V_1|^2}} \quad (5)$$

where, V_1 is the Basic wave, V_2 is the second higher harmonics wave, V_3 is the third higher harmonics wave.

The calculated value of the E.M.F and the Distortion factor is shown in Fig. 3.

Next, I calculated the thrust due to current. Fig. 4 shows the Magnetic flux density of the Halbach array. The result series is shown in Table 2.

In all the arrangement, Distortion factor was about 10%. There is no big problem at the object for dynamos, or slow running, but during high speed driving, there is a concern that heat generation becomes high.

Next, In order to lower the Distortion factor, the magnetic aspect ratio was fluctuated. (refer Fig. 5).

The analysis results are shown in Table 3 and Fig. 6.

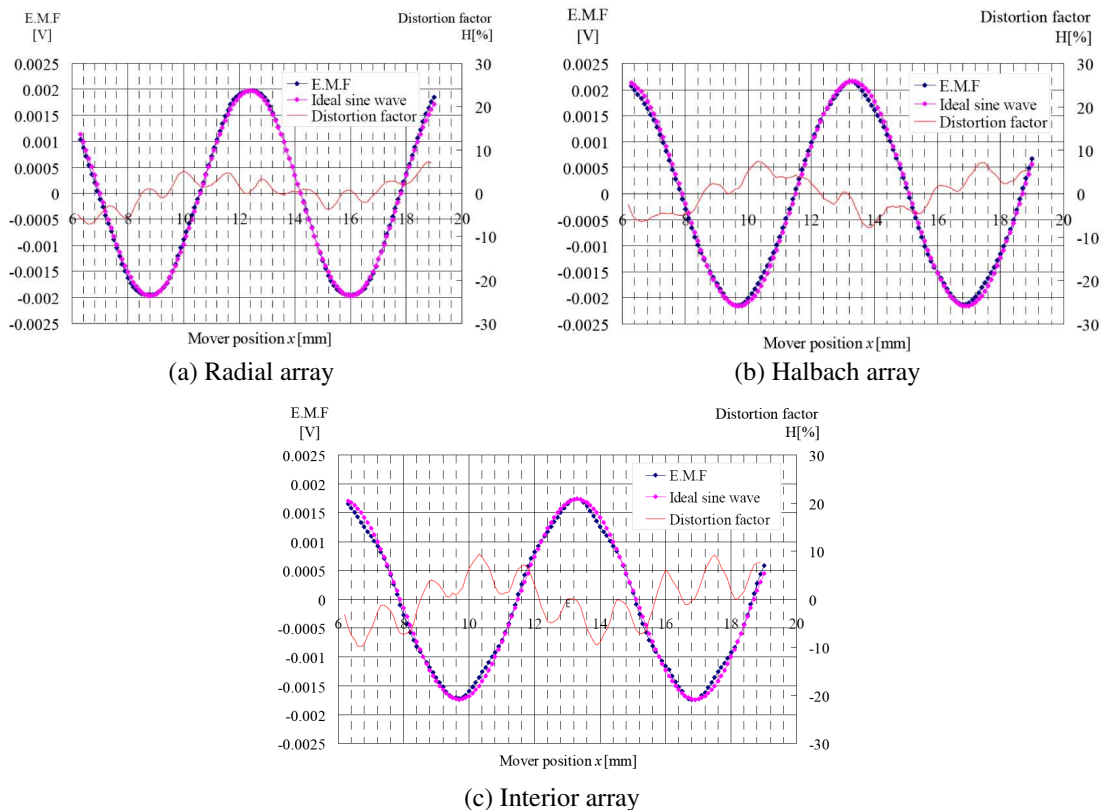


Figure 3: Calculated value of the E.M.F wave and the Distortion factor.

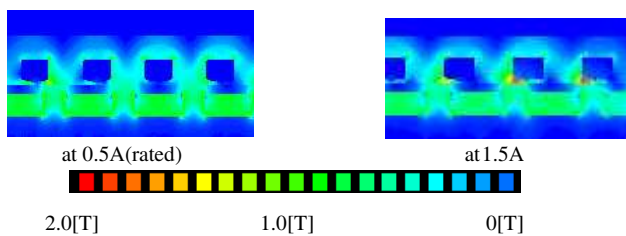


Figure 4: Magnetic flux density.

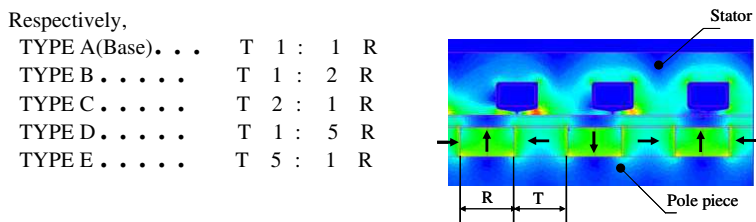


Figure 5: Aspect ratio.

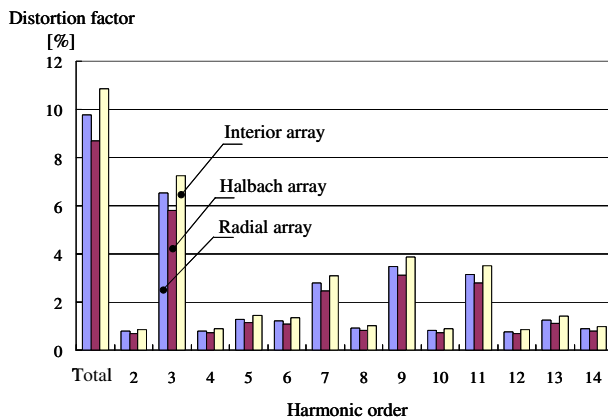


Figure 6: Higher harmonic wave.

Table 2: Series of result.

Type \ Item [Unit]	Radial array	Halbach array	Interior array
Interlinkage flux [wb]	0.00126	0.00140	0.00116
E.M.F [V]	0.00197	0.00216	0.00173
Distortion facto [%]	9.76	8.68	10.85
Thrust [N]	at 0.5 A	1.09	1.28
	at 1.5 A	3.24	3.78

Table 3: Calculated results of aspect change.

Type \ Item [Unit]	Type A	Type B	Type C	Type D	Type E
Interlinkage flux [wb]	0.00140	0.00136	0.00137	0.00113	0.00128
E.M.F [Wb/s]	0.00216	0.00214	0.00222	0.00152	0.00208
Distortion factor [%]	8.68	6.38	9.11	9.91	9.05

4. CONCLUSION

The E.M.F of three distinct models and the relation of their Distortion factors were checked, and the fundamental cause and effect relationship between the Distortion factor from fluctuating a Halbach type aspect ratio and the induction voltage was checked. E.M.F has a downward tendency when the rate of an aspect ratio is large. In the future, I would like to pursue tests which lower the Distortion factor.

REFERENCES

1. Tsai, N.-C. and C.-W. Chiang, "Design and analysis of magnetically drive actuator applied for linear compressor," *Mechatronics*, Vol. 20, The Science of Intelligent Machines, 596–603, 2010.
2. Hajime, H., T. Yoshio, U. Kenji, I. Yukinori, and M. Shigeo, "New torque estimation method considering spatial harmonics and torque ripple reduction in permanent magnet synchronous motors," *The Transactions of the Institute of Electrical Engineers of Japan, D*, Vol. 130, No. 9, 1051–1058, A Publication of Industry Applications Society, 2010.
3. Nonaka, S. and K. Ogawa, "Slot harmonics and end effect of high-speed linear induction motor," *T. IEE Japan*, Vol. 108-D, No. 6, 598–602, 1988.
4. Kusumalatha, Y., C. Saibabu, and Y. P. Obulesu, "Minimization of harmonic distortion of industrial motor drives with active power filter in paper mill-a case study," *Proceeding of the International Multi Conference of Engineers and Computer Scientists*, Vol. 2, 2012.
5. Ishibashi, F., R. Takemasa, M. Matsushita, T. Nishizawa, and S. Noda, "Harmonic fluxes and electromagnetic forces of concentric winding brushless permanent magnet motor," *The Transactions of the Institute of Electrical Engineers of Japan, D*, Vol. 127, No. 12, 1231–1237, A Publication of Industry Applications Society, 2007.
6. Nakaiwa, K., A. Yamada, K. Tashiro, and H. Wakiwaka, "Comparison of thrust characteristics of pencil size cylinder type linear motor with different magnet array," *Journal of the Japan Society of Applied Electro Magnetism and Mechanics*, 481–484, 2009.
7. Nakaiwa, K., H. Wakiwaka, and K. Tashiro, "Thrust characteristic comparison of interior magnet type pencil size cylinder linear motor," *Journal of the Japan Society of Applied Electro Magnetism and Mechanics*, 509–512, 2011.
8. Mishima, M., K. Hirata, and H. Ishiguro, "Study halbach array of linear actuator for android," LD07-15, 73–76, 2007.
9. Mison, N., H. Wakiwaka, A. Kamiya, H. Yajima, N. Fujiwara, M. Hosono, and S. Takeda, "Design of a high thrust interior permanent magnet linear synchronous motor and its characteristics," *Proceeding of LDIA2001*, 248–251, 2001.
10. Lee, S.-Q., K.-H. Park, M.-C. Paek, and K.-Y. Kang, "Halbach magnet array based focusing actuator for small-form-factor optical storage device," *Jpn. J. Appl. Phys.*, Vol. 45, No. 2B, 1131–1136, Japan Society of Applied Physics through the Institute of Pure and Applied Physics, 2006.
11. Kakihara, M., T. Hoshi, T. Shikayama, and M. Ohto, "Development of high force density iron core linear synchronous motor," *The Transactions of the Institute of Electrical Engineers of Japan, D*, Vol. 132, No. 4, 480–486, A Publication of Industry Applications Society, 2012.
12. Kokue, K., M. Nirei, and K. Shiroshita, "Development of a tool that executes finite element analysis automatically," *Proceedings of MAGDA Conference in Sapporo Conference on Electro-magnetic Phenomena and Dynamics*, 629–632, 2010.

Simulation of 3-D SAR Imaging Based Outdoor RCS Measurement Technique

Kefei Liao¹, Sanyuan Xu², Xiaoling Zhang¹, and Jun Shi¹

¹Lab. B504, School of Electronic Engineering
University of Electronic Science and Technology of China, Chengdu, China

²Unit 95784 of PLA, China

Abstract— To avoid the limitation of being used in the anechoic chamber, a new 3-D SAR imaging based RCS Measurement technique is developed, which can be used outdoor. The basic idea of the RCS Measurement technique is come from 3-D SAR imaging technique, which can reconstruct the target's 3-D distribution of scattering characteristics. Owing to its advantages of 3-D resolving power, it can spatially distinguish the targets' RCS from environment. The scattering explanation and the RCS prediction principle of the technique are introduced. As validation, the measurement simulations of RCS for 3-D complex-shaped perfect electric conductor electric-large targets, such as a car-like object, are presented.

1. INTRODUCTION

Most traditional RCS Measurement systems need to be placed in an anechoic chamber to reduce the environment noise, but the sizes of targets are limited by the anechoic chamber [1, 2]. To overcome this defect, the RCS Measurement technique based on 3-D SAR imaging is developed, which can be used outdoor and measure large targets, such as flights and tanks.

The basic idea of the RCS Measurement technique is come from 3-D SAR imaging technique, which acquire the scattering electric field in a large 2-D/3-D spatial scale, and reconstruct the target's shape and scattering characteristics by signal processing techniques [3, 4]. The mechanism of RCS Measurement via 3-D SAR imaging can accurately be explained using the Stratton-Chu equation. For perfect conductor, the 3-D image is related to the electric current density [5], and the received Electric-field is related to the electric current density, as a result, the RCS can be calculated as the ratio of the received Electric-field to the transmit Electric-field.

Owing to its advantages such as high resolution and 3-D imaging, 3-D SAR imaging technique can spatially distinguish the scattering characteristic of the different parts of complex objects, or distinguish the targets' RCS from environment. By selecting the region of interested (ROI) manually (pick out the electric/magnetic currents in the ROI using the prior information on the target's shape), we can obtain the scattering characteristic in the ROI, and calculate its RCS easily.

As validation, the scattering fields are computed using widely accepted software FEKO based on physical optics. The IFFT algorithm is adopted for step-frequency data to form a high-resolution range image, and the 3-D BP algorithm is adopted to form a focused 3-D image. The technique of imaging and the measurement of RCS for a 3-D complex-shaped perfect electric conductor electric-large target, such as a car-like object, are presented.

2. PRINCIPLE

In this section, the scattering explanation of 3-D SAR image will be introduced. Then, by using 3-D SAR image, the RCS prediction technique is presented.

2.1. Scattering Explanation of 3-D SAR Image

3-D SAR imaging technique acquire the scattering electric field in a large 2-D/3-D spatial scale, and reconstruct the target's shape and scattering characteristics by signal processing techniques. When the transmitter is fixed, since the transmitted signal and the geometry of the transmitter and targets remain unchanged during the observation session, the coherence of scattering electric field is well preserved, which is crucial for SAR system. Under this consideration, the mechanism of 3-D SAR imaging can be explained using the scattering theory, which separates the scattering phenomenon into three stages:

Firstly, the incident electromagnetic wave inspires the induced electric/magnetic currents on the targets;

Secondly, the induced electric/magnetic currents produce the receiver array propagating in free space;

Thirdly, the 3-D imaging method is employed to obtain 3-D image.

This procedure is accurately described by the Stratton-Chu equation [6, 7], or electric (magnetic) field integral equation (EFIE/MFIE) for perfect conductor. Due to limitation of length, this paper will only discuss the perfect conductor situation.

The aim of 3-D SAR imaging is to reconstruct the targets' scattering characteristics from the acquired data. For perfect conductor, the magnetic current density $\vec{\mathbf{M}}$ can be ignored, and the imaging results of 3-D SAR with fixed transmitter are the estimations of the electric current density $\vec{\mathbf{J}}$ for perfect conductor [5].

2.2. RCS Prediction Using 3-D SAR Image

In this section, we will discuss the RCS prediction using 3-D SAR image with fixed transmitter.

Since 3-D image can completely separate the electric/magnetic current of target and ambient interference (such as ground, wall and turntable, etc.) spatially, RCS prediction using 3-D SAR image can relax the requirement to the measurement environment, which is available for outdoor measurement.

As we stated in last subsection, for perfect conductor, 3-D SAR image reflects the accurate electric current density. By selecting the electric current density of object, we can reconstruct the scattering field (received and reconstructed voltage exactly) as:

$$v_{\text{ROI}} = \int_{\text{ROI}} j\omega \vec{\mathbf{J}} \psi d\mathbf{p}' \quad (1)$$

where, ROI means region of interested, i.e., the region that includes the target and excludes the environmental disturbance. $\vec{\mathbf{J}}$ denotes the volume electric current density, ψ denotes the green function ω enotes the temporal frequency, \mathbf{p}' denotes the coordinates of target.

By set a reference point, we can easily calculate the RCS of ROI:

$$\sigma_{\text{ROI}} = \left(\frac{v_{\text{ROI}}}{v_r} \right)^2 \left(\frac{R_{\text{ROI}}}{R_r} \right)^2 \sigma_r \quad (2)$$

where, R_{ROI} means the range from the target to the center of the virtual receiving array, v_r means the received and reconstructed voltage of reference point, R_r means the range from the reference point to the center of the virtual receiving array, σ_r means the RCS of reference point.

Equation (2) indicates that using 3-D SAR image, we can predict the backscattering RCS of the target in the ROI. Owing to using of a reference point to be the RCS criterion, we can avoid many system errors (such as the interchannel phase incoherence and amplitude of variation).

3. SIMULATION EXPERIMENT

In this section, to study the EM characteristic of complex-targets, the well-known electromagnetic calculation software which named FEKO is used to calculate the scattered fields and RCS of targets. The IFFT algorithm is adopted for step-frequency data to form a high-resolution range image, and

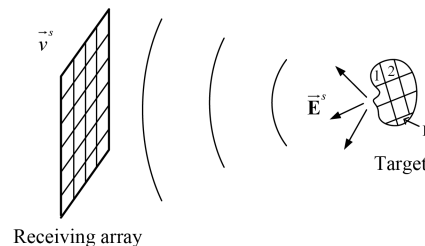
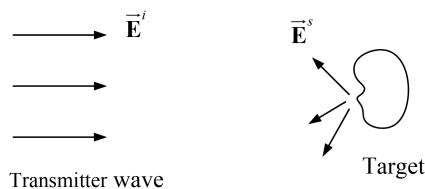


Figure 1: Geometry of transmitter and target, since the geometry remains unchanged during the observation session, the electric/magnetic current is always same.

Figure 2: Geometry of receiver array and scattering field, the receiver acquires the scattering electric field over a large spatial scale, then 3-D image can be obtained by using 3-D imaging method.

Table 1: The system parameters.

carrier frequency	2 GHz
Bandwidth	1 GHz
Size of receive array	2 m × 2 m
system resolution	0.15 m × 0.15 m × 0.15 m

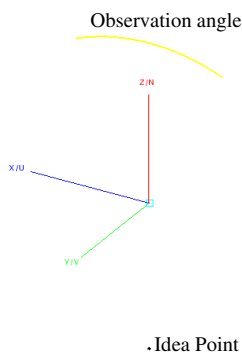


Figure 3: Geometry of the ideal point model.

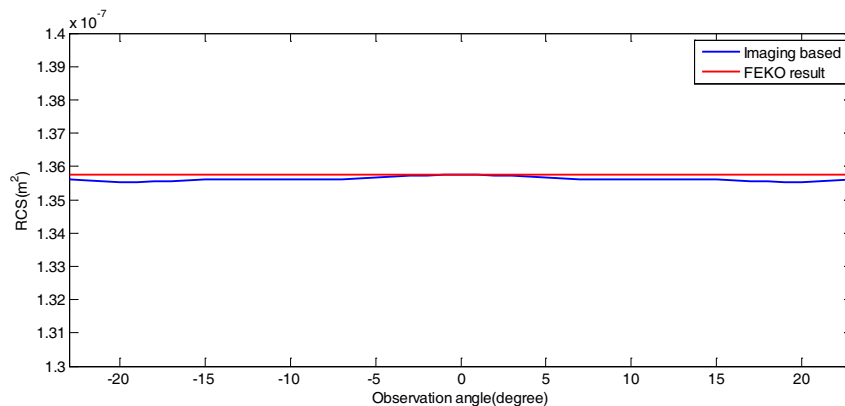


Figure 4: Comparison of imaging based result and FEKO result for RCS of the ideal point.

the 3-D BP algorithm is adopted to form a focused 3-D image. Three examples are presented to verify the precision of 3-D SAR imaging based RCS prediction by compared with FEKO results.

The system parameters are listed in Table 1.

3.1. Ideal Point Model

The EM characteristic of ideal point accords with the traditional scattering centers model, which has no spatial variation of scattering characteristic from different observation angle. Fig. 4 shows the comparison of imaging based result and FEKO result for RCS of the ideal point.

From it, we can find that, the imaging based result is mainly consistent with FEKO result, which indicates that the 3-D SAR imaging based RCS measurement is capable of measuring the RCS of the ideal point.

3.2. Flare Model

The EM characteristic of flare does not accord with the traditional scattering centers model, and the spatial variation of scattering characteristic from different observation angle is significant, which will cause slight system derivation of RCS. Fig. 6 shows the comparison of imaging based results and FEKO results for RCS of an flare.

From it, we can find that, the variation trend of imaging based result is approximately consistent with FEKO result, but there is a difference between the values of two RCS results. The difference is caused by two reasons:

The discrete 3-D resolution will cause some loss of small scattering characteristic during the changing of observation angle;

The receive array acquire the scattering electric field in a large 2-D/3-D spatial scale which has the spatial variation of scattering characteristic, as a result, the RCS result of imaging based method can be considered as the sum of RCSes in the range of a large observation angle, but not the exactly the RCS of a single observation angle.

According to above two reasons, the correction and optimization of this method will be studied in the future to predict the exactly RCS.

3.3. Car-like Model

Figure 8 shows the comparison of imaging based results and FEKO results for RCS of a car-like model with size of 1 m by 1 m, which does not accord with the traditional scattering centers model.

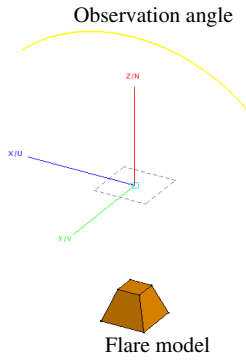


Figure 5: Geometry of the flare model.

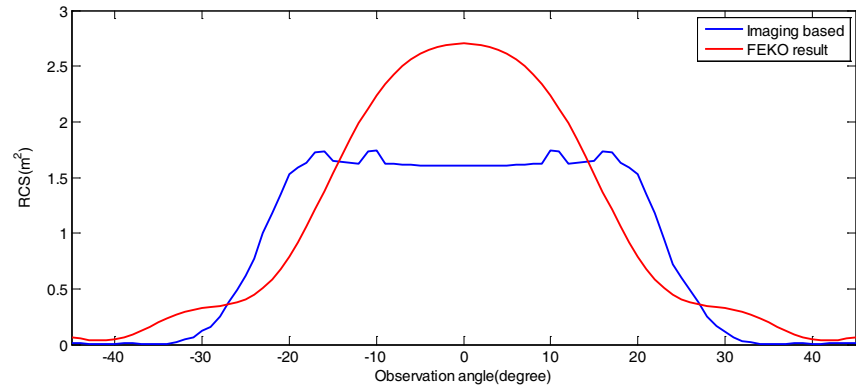


Figure 6: Comparison of imaging based result and FEKO result for RCS of a flare model.

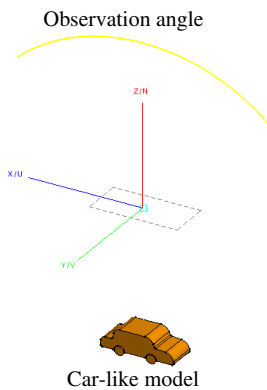


Figure 7: Geometry of the car-like model.

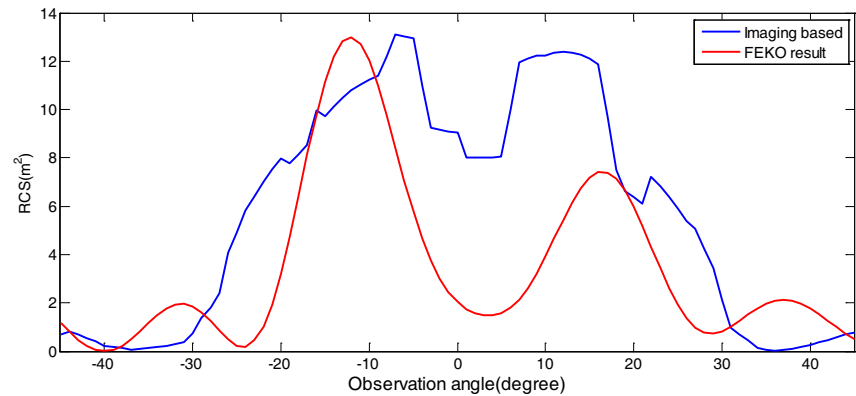


Figure 8: Comparison of imaging based result and FEKO result for RCS of a car-like model.

From it, we can find that, the variation trend of imaging based result is approximately consistent with FEKO result, but there is a difference between the values of two RCS results, which are consistent with the conclusions and reasons in last subsection.

4. CONCLUSIONS

Since the 3-D image can separate the electric/magnetic current of target and ambient interference, the 3-D SAR imaging based RCS Measurement technique is available for outdoor measurement. From simulations, this technique is capable of measuring the RCS of ideal point which accords with the traditional scattering centers model. Due to the discrete 3-D resolution and using large array to receive data, the measuring of RCS of actual target is roughly accurate and has some errors, which will be studied in the future.

ACKNOWLEDGMENT

This work was supported by National Natural Science Foundation of China under Grant (No. 61101170) and Ph.D. Programs Foundation of Ministry of Education of China (No. 2011018511001).

REFERENCES

1. Cown, B. J. and C. E. Ryan, Jr., "Near-field scattering measurements for determining complex target RCS," *IEEE Transactions on Antennas and Propagation*, Vol. 31, No. 5, 1989.
2. Hu, C.-F., J.-D. Xu, N. J. Li, and L.-X. Zhang, "Indoor accurate RCS measurement technique on UHF band," *Progress In Electromagnetics Research*, Vol. 81, 279–289, 2008.
3. Chan, T.-K., Y. Kuga, and A. Ishimaru, "Experimental studies on circular SAR imaging in clutter using angular correlation function technique," *IEEE Transactions on Geoscience and Remote Sensing*, Vol. 37, No. 5, Part 1, 2192–2197, 1999.

4. Bryant, M. L., L. L. Gostin, and M. Soumekh, “3-D E-CSAR imaging of a T-72 tank and synthesis of its SAR reconstructions,” *IEEE Trans. on Aerospace and Electronic Systems*, Vol. 39, No. 1, 211–227, 2003.
5. Shi, J., K. Liao, and X. Zhang, “Three-dimensional SAR with fixed transmitter and its scattering explanation,” *Progress In Electromagnetics Research*, Vol. 133, 285–307, 2013.
6. Knott, E. F., J. F. Shaeffer, and M. T. Tuley, *Radar Cross Section, Its Prediction, Measurement and Reduction*, 47–187, Artech House Inc., Dedham, MA, 1985.
7. Sheppard, C. J. R., A. Choudhury, and J. Gannaway, “Electromagnetic field near the focus of wide-angular lens and mirror systems,” *Microwaves, Optics and Acoustics*, Vol. 1, No. 4, 129–132, 1977.

GRECO Based Spotlight SAR Imaging Simulation Method

Min Su, Jia Liu, Ning Fang, and Baofa Wang

School of Electronic Information Engineering, Beihang University, Beijing, China

Abstract— SAR (Synthetic Aperture Radar) simulation plays a significant role in radar target recognition for its convenience in data supporting. Radar signal and EM scattering characteristic are usually two independent sources of SAR simulation, which are based on different method. The former is currently the main contribution to SAR research. Since GRECO (Graphical Electromagnetic computing) could compute the EM scattering characteristic of complex electrically large target with fast speed and acceptable error, generating SAR image based on it has great practical values. This paper introduces a GRECO based spotlight SAR imaging simulation method, which simulates and calculates the target scattered field and generates the SAR data, and then further processes the SAR image. The result of the real complex target proves the method's effectiveness.

1. INTRODUCTION

SAR has wide attention in the world for its characteristic of all day long, all-weather and high resolution etc.. The SAR echo and image simulation technology of complex target, is not only the foundation to realize the model based automatic target recognition system, but also provides a large amount of data supporting for recognition algorithm research. Be different from simulation aim at SAR system, complex target simulation needs not only simulation of echo and imaging, more need to simulate various mechanisms of electromagnetic scattering waves, such as edge diffraction, multiple scattering, coating materials, etc.. Its formation echo should include information such as target scattering electromagnetic wave amplitude, phase, polarization, in-band response and response in aperture.

According to the difference of selected electromagnetic calculation method and SAR simulation model, domestic and overseas scholars have proposed many methods: Spanish scholars [1] using graphical electromagnetic computing method for SAR simulation, its advantage is electromagnetic calculation can be speed up by used graphics card, and calculating in real-time, it is mainly suitable for the high frequency calculation. Scattering calculation in literature [2] although has a comprehensive consideration, but its echo simulation model is simple, and does not apply to wide bandwidth, large aperture work mode. Literature [3] gives a kind of ISAR simulation method, but the plane wave incidence hypothesis may not apply to the near field imaging system.

In view of the above present research situation, this paper proposes a method of complex target SAR echo and image simulation based on target scattering characteristics. The method based on graphical electromagnetic computing, visual simulate target complex scattering field in different location and frequency to build echo, so as to avoid the stable scattering center hypothesis. The simulation echo contains the target response on changing frequency and angle of view, it is more suitable for the large angle and wide bandwidth work mode. Changing the traditional plane wave incident to spherical wave, can make accurate simulation of near or far field mode. In addition, the method can simulate the single and multiple scatter of target and the variable polarization effect, has the ability of the whole polarization simulation.

2. SYNTHETIC APERTURE RADAR IMAGING PRINCIPLE

Synthetic aperture radar's main working modes have Spotlight SAR, Stripmap SAR and ScanSAR, etc., this paper mainly aims at Spotlight SAR imaging simulation method.

Spotlight SAR imaging geometrical relationship as shown in Figure 1, set R_0 as the minimum slope distance of radar platform, V_p as the platform speed, ψ as angle of depression, φ as azimuthal central angle, and T as the flight time. SAR system launches a linear frequency modulation signal, pulse transmitting frequency is f_p and carrier frequency is f_0 , antenna's actual length is L_a , transmitted pulse bandwidth is B_0 , pulse width T_p , and LFM ratio is $|K_r| = B_0/T_p$, the transmit signal can be expressed as [4]:

$$s(\tau, \eta) = A_0 \omega_r(\tau) \omega_a(\eta - \eta_c) \cos(2\pi f_0 \tau + \pi K_r \tau^2) \quad (1)$$

In Equation (1), A_0 is transmitted pulse amplitude, for constant; τ is the range time; η is azimuth time; η_c is the deviating time of beam center. In the simulation, in order to simplify, assume SAR

for side looking, it has $\eta_c = 0$; $\omega_r(\tau) = \text{rect}(\tau/T_p)$ is the range envelope; $\omega_a(\eta) = [\text{sinc}(\alpha L_a/\lambda)]^2$ is azimuth envelope; λ is carrier wave length; α is angle of slant distance and the most short distance in oblique plane, as shown in Figure 1.

Target complex backscattering field is $\sigma(\tau, \eta, \theta)$, the echo signal is convolution of target complex backscattering field and radar signal, the SAR receives the echo signal can be expressed as

$$s'_r(\tau, \eta) = \sigma(\tau, \eta, \theta) \otimes \left\{ A_0 \omega_r(\tau - 2R(\eta)/c) \cdot \omega_a(\eta - \eta_c) \cdot \cos \left[2\pi f_0 (\tau - 2R(\eta)/c) + \pi K_r (\tau - 2R(\eta)/c)^2 \right] \right\} \quad (2)$$

SAR antenna receive signal like Equation (2), and the signal after quadrature demodulation is expressed as

$$s_r(\tau, \eta) = \sigma(\tau, \eta, \theta) \otimes \left\{ A_0 \omega_r(\tau - 2R(\eta)/c) \cdot \omega_a(\eta) \cdot \exp\{-4j\pi f_0 R(\eta)/c\} \cdot \exp\{j\pi K_r (\tau - 2R(\eta)/c)^2\} \right\} \quad (3)$$

Equation (3) is the expression of time domain SAR echo signal. In theory, directly based on Equation (3), through the time SAR echo signal calculation, it can be realized SAR image simulation by the imaging algorithm processing, but it has a huge computation and very low efficiency. This paper realize the SAR image simulation through calculating the frequency domain echo signal, and compared to the time domain method, the method can effectively improve the SAR image simulation efficiency. For quick calculation of echo signal, make Equation (3) to Fourier transform in range based on principle of stationary phase (POSP), it is

$$S_r(f_\tau, \eta) = \sigma'(f_\tau, \eta, \theta) \otimes \left\{ A_0 \omega_r(f_\tau) \cdot \omega_a(\eta) \cdot \exp\{-4j\pi f_0 R(\eta)/c\} \cdot \exp\{-4j\pi f_\tau R(\eta)/c\} \cdot \exp\{-j\pi f_\tau^2 / K_r\} \right\} \quad (4)$$

In the low angle, instantaneous slant distance between radar and target can approximate for parabolic:

$$R(\eta) = \sqrt{R_0^2 + V_p^2 \eta^2} \approx R_0 + V_p^2 \eta^2 / 2R_0 \quad (5)$$

While put Equation (5) into Equation (4)'s index items, and set $K_a = 2V_p^2/\lambda R_0 = 2V_p^2 f_0/c R_0$, it is

$$S_r(f_\tau, \eta) = \sigma'(f_\tau, \eta, \theta) \otimes \left\{ A_0 \omega_r(f_\tau) \cdot \omega_a(\eta) \cdot \exp\left\{-4j\pi (f_0 - f_\tau) \frac{R_0}{c}\right\} \cdot \exp\{-j\pi K_a \eta^2\} \cdot \exp\left\{-4j\pi f_\tau \frac{V_p^2 \eta^2}{2R_0 c}\right\} \cdot \exp\left\{-j\pi \frac{f_\tau^2}{K_r}\right\} \right\} \quad (6)$$

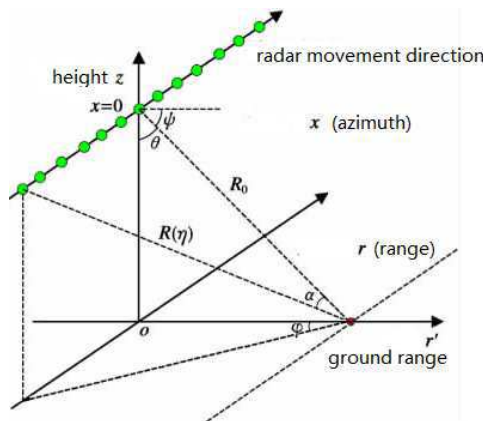


Figure 1: Spotlight SAR imaging geometrical relationship.

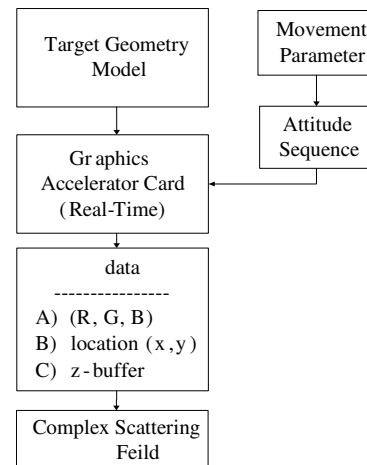


Figure 2: Process of scattering field calculation based on GRECO.

Further, according to the azimuth time-frequency relationship, $f_\eta = -K_a\eta$, substituting in Equation (6), the azimuth Fourier transform of signal is

$$S_r(f_\tau, f_\eta) = A_0\sigma'(f_\tau, f_\eta, \theta) \cdot \omega_r(f_\tau) \cdot \omega_a(f_\eta) \cdot \exp\left\{-4j\pi(f_0 - f_\tau)\frac{R_0}{c}\right\} \cdot \exp\left\{-j\pi\frac{f_\eta^2}{K_a}\right\} \cdot \exp\left\{-j\pi f_\tau\frac{f_\eta^2 R_0\lambda^2}{2V_p^2 c}\right\} \cdot \exp\left\{-j\pi\frac{f_r^2}{K_r}\right\} \quad (7)$$

And by $f_\eta = 2V_p \sin(\varphi)/\lambda$, it is

$$S_r(f_\tau, f_\eta) = A_0\sigma'(f_\tau, \varphi, \theta) \cdot \omega_r(f_\tau) \cdot \omega_a(f_\eta) \cdot \exp\left\{-4j\pi(f_0 - f_\tau)\frac{R_0}{c}\right\} \cdot \exp\left\{-j\pi\frac{f_\eta^2}{K_a}\right\} \cdot \exp\left\{-j\pi f_\tau\frac{f_\eta^2 R_0\lambda^2}{2V_p^2 c}\right\} \cdot \exp\left\{-j\pi\frac{f_r^2}{K_r}\right\} \quad (8)$$

Equation (8) is the two dimensional frequency domain SAR echo signal model. The key of frequency domain SAR echo signal simulation is to calculating target's complex scattering field, $\sigma'(f_\tau, \varphi, \theta)$.

3. GRAPHICAL ELECTROMAGNETIC COMPUTING

The calculation of target's RCS can use graphical electromagnetic computing method. Graphical Electromagnetic Computing is J. M. Rius's suggestion, to overcome shortcomings of traditional high frequency calculation method in the calculation of the memory space, calculation accuracy and calculation speed [5].

This is a kind of fast high-frequency RCS prediction method, using the OpenGL displayed target on a computer screen in real-time, the target view point set in monostatic radar position, is the part show on screen is the part of target where radar wave can exposure to, computer hardware automatic will blank off the invisible parts. Through the set of specific illumination model, light source characteristics and materials, from screen pixel point of red, green, blue three color component (R, G, B), it can be computed the pixel's normal vector (n_x, n_y, n_z) on the surface of the corresponding target. Z value can read from the depth buffer (z -buffer), target location coordinates x, y value is obtained from the relative position of the screen coordinate system. After acquired x, y, z, n_x, n_y, n_z by graphics accelerator card, we can calculate electromagnetic scattering characteristics of target by use high frequency numerical method, general process is shown in Figure 2.

Based on GRECO, using high frequency approximation method such as physical optics and physical diffraction, and subsequently obtain the scattering field:

$$\begin{bmatrix} E_h^s \\ E_v^s \end{bmatrix} = -\frac{jk \exp(-jkr)}{2\pi r (1 - n^2)} \cdot \int_{F_p} \begin{bmatrix} R_h n_x^2 - R_v n_y^2 & (R_h + R_v) n_x n_y \\ (R_h + R_v) n_x n_y & R_h n_y^2 - R_v n_x^2 \end{bmatrix} \begin{bmatrix} E_h^i \\ E_v^i \end{bmatrix} (\hat{z} \cdot \hat{n}) \exp(2jkz) ds \quad (9)$$

In which, F_p is the surface integral interval, E^i is the incident field, E^s is the scattering field, h and v respectively stands for horizontal and vertical polarization. $\hat{n}(n_x, n_y, n_z)$ is the normal vector of medium surface element. Put Equation (9) in the RCS definition equation, $\sigma = \lim_{R \rightarrow \infty} 4\pi R^2 |\vec{E}^s / \vec{E}^i|^2$, find out the target's complex scattering field under different polarization, $\sigma'(f_\tau, \varphi, \theta)$.

4. SAR IMAGING SIMULATION BASED ON GRECO

Figure 3 shows SAR simulation system solutions given in this paper. The system can calculate the target scattering field through the simulation, further process generating SAR image. The system mainly consists of three parts: the graphical electromagnetic computing module, GRECO post-processing module and SAR imaging processing module.

Graphical electromagnetic computing module, using graphical electromagnetic computing (GRECO) method which had been described above, according to the input of the target model, target motion parameters, and radar parameters, simulate the radar data acquisition process, and calculate relative posture sequence between the target and the radar. It calculates the target every gesture of complex scattering field $\sigma'(f_\tau, \varphi, \theta)$ visually in real-time.

GRECO post-processing module, this module will substitute the complex scattering field data $\sigma'(f_\tau, \varphi, \theta)$ in Equation (8), according to the input of the radar parameters, restore it to two

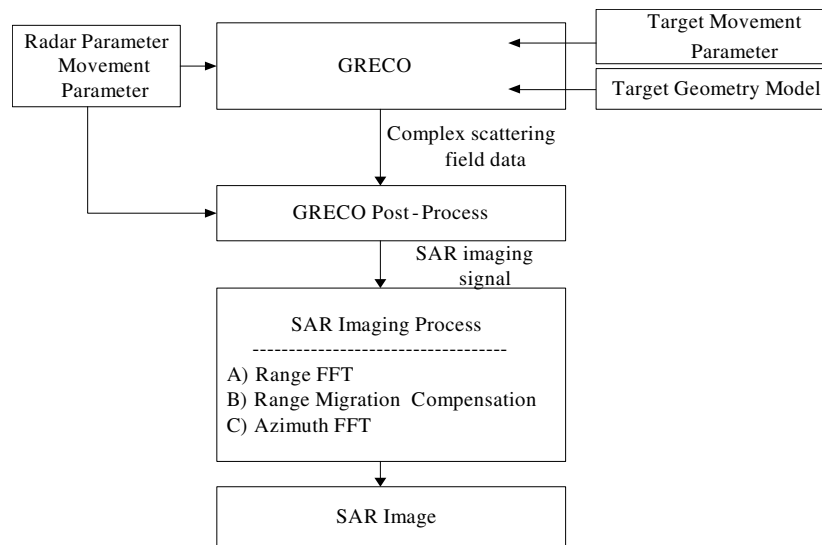


Figure 3: SAR simulate system scheme based on GRECO.

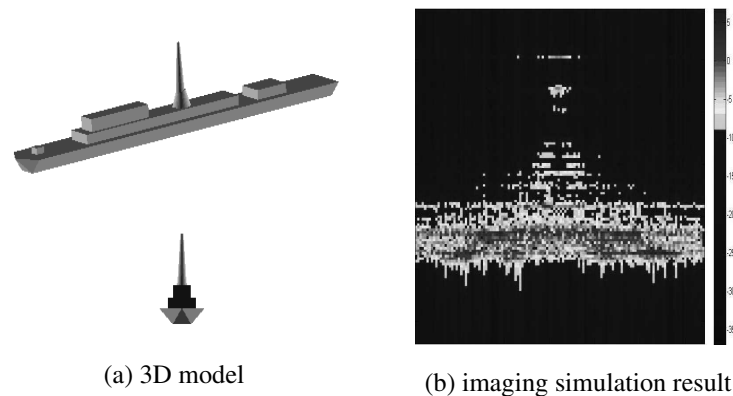


Figure 4: A ship's 3D module and simulate result.

dimensional frequency domain SAR echo signal model $S_r(f_\tau, f_\eta)$, provides a data basis for SAR image processing.

SAR image processing module, to verify the validity of the simulation system, this paper only simply using Range-Doppler imaging algorithm, namely to SAR echo signal range Fourier transform, range migration compensation, finally do azimuth Fourier transform and then can get target SAR image.

Using the above process, simulate a ship for SAR image, set radar's movement in 10000 meters high above target, radar move 500 meters, data sampling points is 128, radar wave center frequency is 10 GHz, bandwidth is 500 MHz, VV polarization, we can get a imaging results as shown in Figure 4(b).

We can see the target outline from the image, can see clearly that the distribution of strong scattering source, such as scattering points at the top of the image corresponding the small platform on ship top, deck and cabin top is flat structure, and radar observation direction is located in the radial direction of reflection, so most of the strong scattering point focus on deck and the cabin top surface. For simply, this paper adopts simple imaging algorithm, imaging results verify the validity of this method. This method can take further optimize measures to get a more clear image.

5. CONCLUSIONS

In this paper, aim at SAR imaging problems of complex target, research SAR image simulation method based on the GRECO high frequency electromagnetic scattering characteristics calculation. This method firstly according to SAR platform parameter and SAR imaging geometry, calculate target's electromagnetic scattering characteristics, based on this, it further according to SAR system

parameters, generate SAR raw echo data, and finally use the Range-Doppler imaging algorithm processing, get target's SAR image. This paper verifies the validity of this method, through the SAR image simulation results of actual target. As a SAR image simulation method study, in the present simulation, in order to simplify, this paper only consider a simple Range-Doppler imaging algorithm, the subsequent will further research and optimize the SAR imaging processing.

ACKNOWLEDGMENT

This paper is supported by the National Science Fund for Distinguished Young Scholars of NFSC. No. 61001003.

REFERENCES

1. Margarit, G., J. J. Mallorqui, J. M. Rius, and J. Sanz-Marcos, "On the usage of GRECOSAR, an orbital polarimetric SAR simulator of complex targets, to vessel classification studies," *IEEE Trans. on GRS*, Vol. 44, No. 12, 3517–3526, 2006.
2. Sun, J. and S. Hong, "Simulation of synthetic aperture radar image in natural scene," *Radar Science and Technology*, Vol. 1, No. 4, 210–214, 2003.
3. Franceschetti, G., M. Migliaccio, D. Riccio, et al., "SARAS: A synthetic aperture radar (SAR) raw signal simulator," *IEEE Trans. on GRS*, Vol. 30, No. 1, 110–123, 1992.
4. Li, R., K. Ji, et al., "Simulation of SAR imagery of target based on electromagnetic scattering characteristic computation," *Radar Science and Technology*, Vol. 8, No. 5, 395–400, 2010.
5. Rius, J. M., M. Ferrando, and L. Jofre, "High-frequency RCS of complex radar targets in real-time," *IEEE Transactions on Antennas and Propagation*, Vol. 41, No. 9, 1308–1319, 1993.

Bridgeless SEPIC-derived LED Driver without Electrolytic Capacitor for Multistring Application

H.-B. Ma¹, Q.-Y. Feng², T.-J. Zeng², and X.-H. Yuan²

¹School of Electrical Engineering, Southwest Jiaotong University, Chengdu, Sichuan 610031, China

²Institute of Microelectronics Technology, Southwest Jiaotong University, Chengdu, Sichuan 610031, China

Abstract— The widely used multi-stage cascade structure and the employed low-frequency diode rectified bridge in the front-end PFC rectifier, result in the low efficiency of LED drivers. Meanwhile, the electrolytic capacitor with large capacitance is used as decoupling capacitors is also an obstacle to the overall long-term reliability of the LED lighting product. To overcome these limitations, a bridgeless SEPIC-derived AC/DC converter without electrolytic capacitors is proposed in this paper. Furthermore its isolation type is easy to couple with our studied twin-bus configuration for increasing the overall efficiency of LED drivers. A 50-W hardware prototype has been designed, fabricated and tested in the laboratory to verify the converter validity under universal input voltage condition.

1. INTRODUCTION

Due to the rapid progress of in the semiconductor manufacture and package technology, LEDs have been considered for the general-purpose lighting [1]. Compared with conventional artificial light- sources, high power LEDs have numerous advantage, such as higher efficacy, a maximum of 100,000 h of lifetime, and so on [2]. Currently, to obtain sufficient luminance, many LEDs have to be connected and arranged in parallel LED strings. Driving multiple LED stings in parallel from an offline power source poses challenges in many aspects of power supply design. First of all, high power factor, and low-input-current harmonics are becoming the mandatory design criteria for LED drivers. In general lighting application, ballasts with input power exceeding 25-W are required to comply with stricter requirements as stated in IEC 61000-3-2-Class C [3] and Energy Star [4]. State-of-the-art LED driver shows that long lifetime and high efficiency are also the main design consideration of LED power supply for matching LED virtues. Additionally, the PWM dimming is also desired to further power saving.

A lot of work has been directed toward power factor correction (PFC) topologies and control schemes in LED application over the past decades [5–7]. These topologies are suitable for different power levels and customer requirements. However, these topologies have several common drawbacks. First of all, electrolytic capacitors with large capacitance are usually used as the storage capacitor in the previously mentioned LED lighting drivers. However, the lifetime of electrolytic capacitors is much shorter than the potential lifetime of LEDs. Hereafter, a low frequency diode rectified bridge is inserted between the EMI filter and the PFC stage, which degrade the overall system efficiency. Furthermore, the typical solution for LED drivers is employing the multi-stages cascade structure. Such a cascade configuration can help LEDs achieving good operating performance. However too many power handle stages results in the lower efficiency and relatively high cost.

This paper proposed a novel bridgeless SEPIC-derived AC/DC converter for LED lighting application. Though this topology appears similar to the presented bridgeless SEPIC circuit in [8], the operational characteristics are quite different. In the proposed circuit, the special DCM is employed to make the bus capacitor decouple the pulsating input power and constant output power. By allowing a relatively voltage ripple, the proposed AC/DC converter is able to eliminate electrolytic capacitors while maintaining desired the performances such as high power factor, low output ripple et al.. Additionally, this proposed circuit is not difficult to match our presented Twin-Bus configuration in [9]. The detailed operating principle and design consideration are described in the following sections. A laboratory prototype with 50-W power level has been built and tested to verify the presented topology.

2. PROPOSED BRIDGELESS AC/DC CONVERTER

Figure 1(a) shows the proposed bridgeless SEPIC-derived AC/DC converter. Though this topology appears similar to the presented bridgeless SEPIC circuit in [20], the operational characteristics

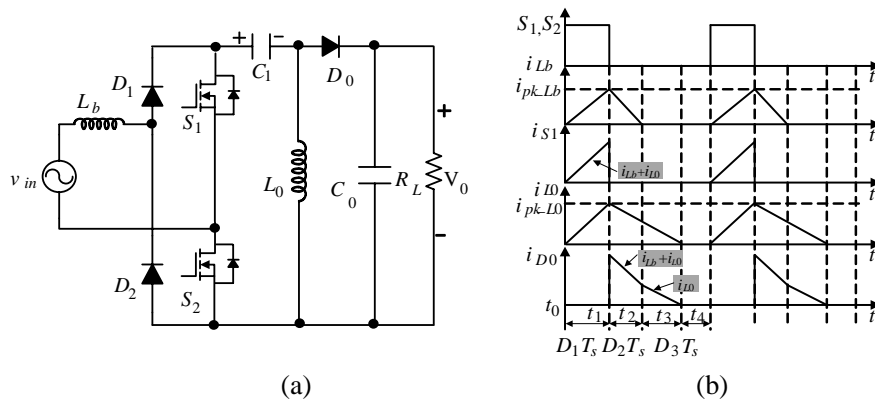


Figure 1: Proposed circuit and its main current waveforms in a switch cycle for positive half-line cycle. (a) Proposed bridgeless AC/DC Converter. (b) Theoretical waveforms in a switch cycle.

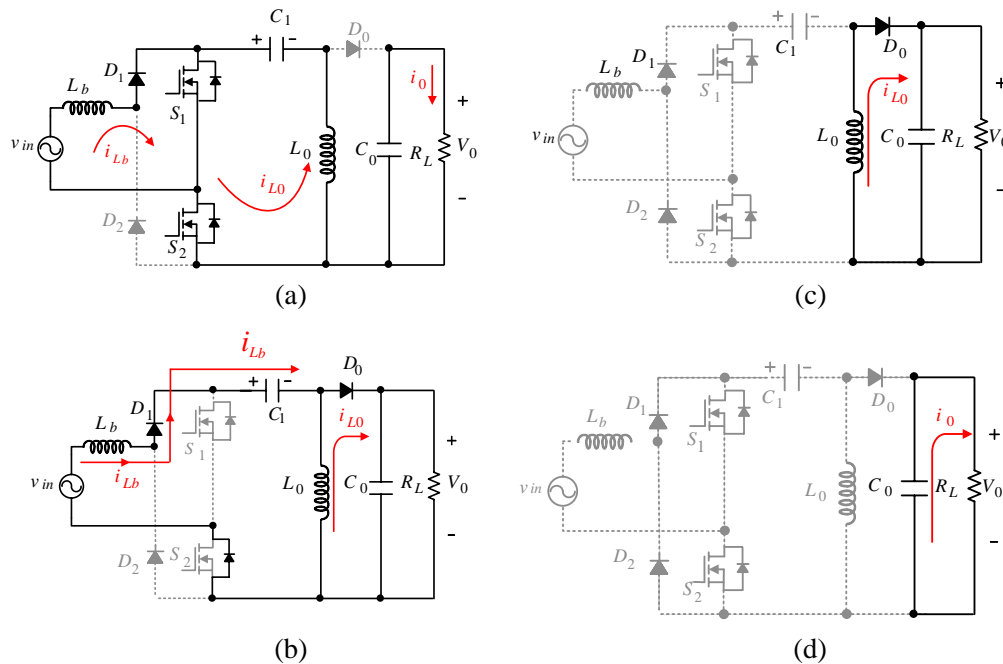


Figure 2: Equivalent circuit during the different interval. (a) Interval $[t_0, t_1]$. (b) Interval $[t_1, t_2]$. (c) Interval $[t_2, t_3]$. (d) Interval $[t_3, t_4]$.

are quite different. Before describing the operation principle, the following assumptions are made: (1) The input voltage v_{in} is ideal sinusoidal. (2) The switching frequency (f_s) is much higher than the ac line frequency (f_l). (3) The voltages V_{C1} , and V_0 can be considered constant during switching period T_s .

The operation of this converter is symmetrical in two half line cycles of input voltage. Therefore the converter operation is explained during one switching period in the positive half line cycle of the input voltage. The schematics operations during one switching cycle can be divided into four distinct intervals as shown by the equivalent circuits in Figure 2. The theoretical waveforms during a switching period are plotted in Figure 1(b). The converter analysis starts at the instant t_0 .

Interval 1: $[t_0, t_1]$: Prior to this interval, the currents through L_b and L_0 are at zero level. This mode starts by turning S_1 and S_2 on. When the switch S_1 and S_2 is turned on at t_0 simultaneously, the diodes D_0 is reverse biased. Therefore, capacitor C_1 is as the charging power supply of inductance L_0 . The corresponding equivalent circuit is shown in Figure 2(a). Hence, the currents i_{Lb} and i_{L0} begin to increase linearly by slope of v_{in}/L_b and V_{C1}/L_0 as shown as Figure 1(b), respectively. This interval ends by turning off the switch S_1 and S_2 . Based on the aforementioned operation,

the following equations can be derived:

$$i_{L_b}(t) = \frac{v_{in}}{L_b} t \quad (1)$$

$$i_{L_0}(t) = \frac{V_{C_1}}{L_0} t \quad (2)$$

$$i_{S_1} = i_{L_b}(t) + i_{L_0}(t) = \left(\frac{v_{in}}{L_b} + \frac{V_{C_1}}{L_0} \right) t \quad (3)$$

Interval 2: $[t_1, t_2]$: When the switch S_1 and S_2 are turned off, capacitor C_1 is as the discharging power supply of inductance L_b . Meanwhile the output diode D_0 begins to conduct carrying the sum of i_{L_b} and i_{L_0} . Thus, currents i_{L_b} and i_{L_0} decrease linearly at rates proportional to $(V_{C_1} + V_0 - v_{in})$ and V_0 , respectively. The corresponding current waveforms are shown in D_2T_s of Figure 1(b). Figure 2(b) shows the equivalent circuit at this interval. This interval is not ends until the current i_{L_b} reaches zero level. Similarly, the current of inductor L_b and L_0 (i_{L_b} and i_{L_0}) and diode current i_{D_0} can be described approximately as:

$$i_{L_b}(t) = \frac{v_{in}}{L_b} D_1 T_s + \frac{V_{in} - V_{C_1} - V_0}{L_b} t \quad (4)$$

$$i_{L_0}(t) = \frac{V_{C_1}}{L_0} D_1 T_s - \frac{V_0}{L_0} t \quad (5)$$

$$i_{D_0}(t) = \left(\frac{v_{in}}{L_b} + \frac{V_{C_1}}{L_0} \right) D_1 T_s + \frac{v_{in} - V_{C_1}}{L_b} t - \left(\frac{V_0}{L_0} + \frac{V_0}{L_b} \right) t \quad (6)$$

Interval 3: $[t_2, t_3]$: In this interval, the current i_{L_0} continues to decrease through the output diode D_0 . This interval ends when the current of D_0 reaches zero. The corresponding equivalent circuit is plotted in Figure 2(c).

Interval 4: $[t_3, t_4]$: This interval is a freewheeling stage where all semi-conductors are off and all branch currents are zero. The converter stays in this state until the switch S_1 and S_2 are turned on again.

3. CONTROL STRATEGY

It needs to note that the switches S_1 and S_2 can be driven in the following two ways: (1) as shown in Figure 3(b), the switch S_1 and S_2 are driven by the same signal with switching frequency f_s ; (2) the switch S_2 keep turning on at the positive half line cycle, the switch S_1 is turned on and off with switching frequency f_s . Accordingly, the switch S_1 keeps turning on at the negative half line cycle. In this paper, to make the control circuit be simply, the driven way (1) is employed.

From the operation principle described in Section 2, the voltage control mode only is good enough to adjust constant output voltage. Figure 3 shows the detailed implemented circuit of the aforementioned control strategy. Driver IC IR2110s is used to drive switch S_1 and S_2 with same control signal. Although control IC UCC38C44 is designed based on peak current mode, it is not difficult to modify as voltage control mode by adding resistor R_{S_1} , R_{S_2} and bipolar transistor Q_1 . In addition, FOD2742 is 8-PIN SOIC error amplifier optocoupler consisting of the popular KA431 precision programmable shunt reference and an optocoupler, which is employed to implement isolation and output feedback regulation.

4. EXPERIMENTAL VERIFICATION

To verify the presented bridgeless SEPIC-derived AC/DC converter, a laboratory prototype with the following specifications was designed and tested. The prototype is arranged with Twin-Bus output stage to comply with the Twin-Bus configuration. Universal input voltage: $v_{in} = 90v_{ac}$, 60 Hz. Twin-bus output voltage: $V_{01} = 50V_{dc}$, $V_{02} = 45V_{dc}$. Rated output power: $P_0 = 50 W$. Switching frequency: $f_s = 53 \text{ kHz}$.

The schematic diagram of the laboratory prototype is shown in Figure 4, which was used to convert the universal ac line voltage into the twin-bus voltage V_{01} and V_{02} , and provides a high power factor and low harmonics to meet the standard such as IEC 61000-3-2 Class C. The PFC inductor L_b is split into two smaller ones (L_{b1} and L_{b2}) integrated in same core to reduce the common-mode EMI.

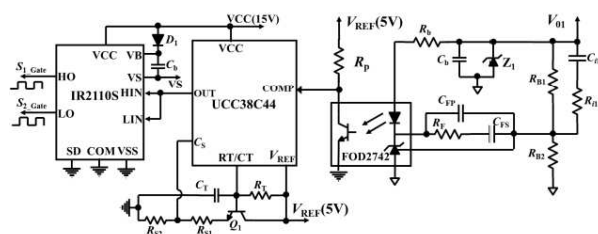


Figure 3: Control strategy and implemented circuit.

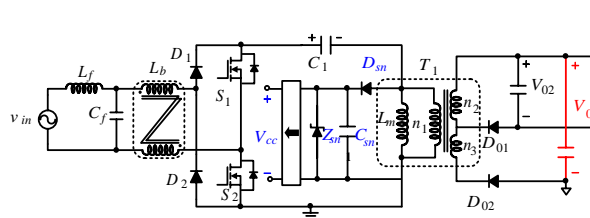


Figure 4: Bridgeless SEPIC-derived AC/DC converter with twin-bus output.

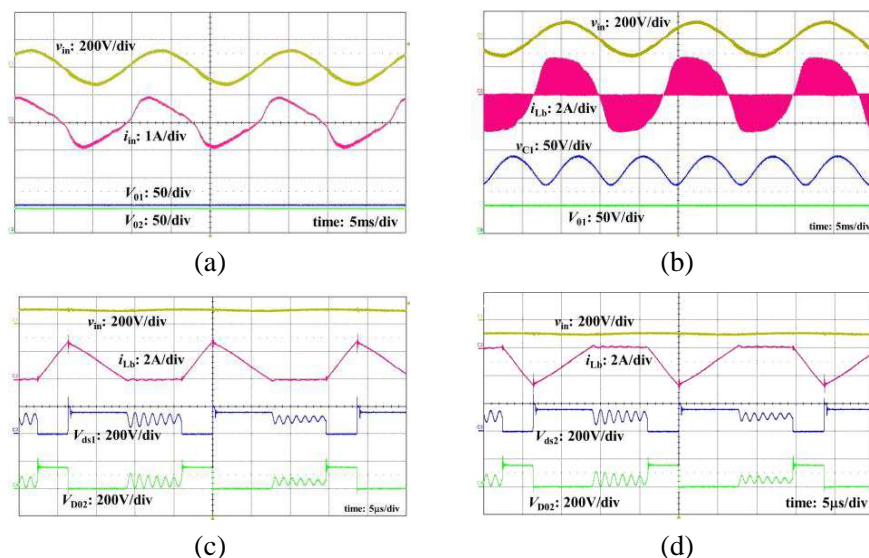


Figure 5: Experimental results under 90 V input voltage condition. (a) Measured v_{in} , i_{in} , V_{01} and V_{02} . (b) Measured v_{in} , i_{Lb} , v_{C1} and V_{01} . (c) Experimental waveform at peak value of the positive half cycle. (d) Experimental waveform at peak value of the negative half cycle.

Figure 5 shows the experimental waveform at 90 V input voltage and full load. In Figure 5(a), the input current i_{in} have a near-sinusoidal waveform and is in phase with the input voltage v_{in} . Thus the high PF with 0.96 can be achieved. The third and fourth channel in Figure 5(a) shows the measured waveform of output voltage V_{01} and V_{02} . As can be seen, the output voltage is regulated well with small voltage ripple. Figure 5(b) is the experimental waveforms of inductor current i_{Lb} and bus voltage v_{C1} . It can be observed that the capacitor voltage v_{C1} has the relatively large double line-frequency (120 Hz) ripple Δv_{C1} . Meanwhile, the waveforms of V_{ds1} , V_{ds2} , V_{D02} during the switching period T_s are provided for the positive and negative half line cycle of the input voltage v_{in} , respectively.

5. CONCLUSION

A bridgeless SEPIC-derived AC/DC topology without electrolytic capacitors is studied in this paper. The basic circuit operating principle and design consideration are described in detail to achieve the desired performance. Its isolation type is easy to couple with our proposed twin-bus configuration for increasing the total efficiency of LED drivers.

Additionally, it is noteworthy that the way (2) can be employed to further improve the efficiency. Future work is to improve the efficiency by this operation mode.

ACKNOWLEDGMENT

This work is supported by the National Natural Science Foundation of China (NNSF) under Grant 60990320, 60990323; 61271090, and the National 863 Project of China under Grant 2012AA012305, and Sichuan Provincial Science and technology support Project under Grant 2012GZ0101, and Chengdu Science and technology support Project under Grant 12DXYB347JH-002.

REFERENCES

1. Tsao, J. Y., “Solid-state lighting: Lamps, chips and materials for tomorrow,” *IEEE Circuits Devices Mag.*, Vol. 20, No. 3, 28–37, 2004.
2. Chiu, H.-J., H.-M. Huang, H.-T. Yang, and S.-J. Cheng, “An improved single-stage flyback PFC converter for high-luminance lighting LED lamps,” *International Journal of Circuit Theory and Applications*, Vol. 36, No. 2, 205–210, 2008.
3. “Electromagnetic compatibility (EMC) — Part 3–2: Limits for harmonic current emissions (equipment input current ≤ 16 A per phase),” Edition 2.1, IEC Standard 61000-3-2, Oct. 2001.
4. “ENERGY STAR program requirements for solid state lighting luminaires,” Online: http://www.energystar.gov/ia/partners/product_specs/program_reqs/SSL_prog_req_V1.1.pdf.
5. Ma, H., J.-S. Lai, Q. Feng, W. Yu, and C. Zheng, “A universal-input high-power-factor power supply without electrolytic capacitor for multiple lighting LED lamps,” *International Journal of Circuit Theory and Applications*, 2011, DOI: 10.1002/cta.816.
6. Ye, Z., F. Greenfeld, and Z. Liang, “Single-stage offline SEPIC converter with power factor correction to drive high brightness LEDs,” *Proceeding of IEEE APEC*, 546–553, 2009.
7. Gacio, D., J. M. Alonso, A. J. Calleja, and J. García, “A universal-input single-stage high-power-factor power supply for HB-LEDs based on integrated buck-flyback converter,” *Proceeding of IEEE APEC*, 15–19, 2009.
8. Mahdavi, M. and H. Farzanehfard, “Bridgeless SEPIC PFC rectifier with reduced components and conduction losses,” *IEEE Trans. Ind. Electron.*, Vol. 58, No. 9, 4153–4160, 2011.
9. Yu, W., J.-S. Lai, H. Ma, and C. Zheng, “High-efficiency DC-DC converter with Twin-Bus for dimmable LED lighting,” *IEEE Trans. Power Electron.*, Vol. 26, No. 8, 2095–2100, 2011.

Investigation of Irregularities Induced from Medium-scale Traveling Ionospheric Disturbances Using Global Positioning System and Digisonde

Wei-Sheng Chen¹, Chien-Chih Lee¹, and Fang-Dar Chu²

¹General Education Center, Chien Hsin University of Science and Technology, Taiwan

²National Standard Time and Frequency Lab, Chunghwa Telecom Co. Ltd., Taiwan

Abstract— This study is intended to investigate the irregularities induced from medium-scale traveling ionospheric disturbances (MSTIDs) over Wuhan (30.51°N, 114.41°E) in China. We employed the data came from the GPS receiver and the digisonde at Wuhan. The data were limited in 2000 when sun was in high solar activity period. The events of MSTIDs were derived from the perturbations of total electron content (TEC) of GPS data. The GPS phase fluctuation index and the spread F occurrences were calculated and examined from the GPS and digisonde observations, respectively. We explored the seasonal and nighttime occurrence rates as well as the one-to-one correspondences for these phenomena. We discovered that, for the seasonal variations, three phenomena all are highly active in summer, which confirms that irregularities over Wuhan mainly relate to MSTIDs. Moreover, all spread F types have a minor occurrence peak in winter but none for the MSTIDs and the GPS phase fluctuations. Besides, none of large GPS phase fluctuations event had occurred during observation periods, which indicates that the strength of irregularities related to MSTIDs are weaker than that of equatorial plasma bubbles. For the nighttime variations, the frequency spread F occurs earlier than other spread F types which implies that disturbances start at the altitude near the F -region peak. For the one-to-one correspondences, the occurrence rates of each spread F type and GPS phase fluctuations are low during MSTIDs occurred. This implies that smaller scale irregularities which are observed as spread F or GPS phase fluctuations may only appear in some phase of MSTIDs.

1. INTRODUCTION

In the mid-latitudes ionosphere, the most conspicuous irregularity phenomenon is Medium-Scale Traveling Ionospheric Disturbances (MSTIDs). The MSTIDs is a kind of wave-like perturbations which modulates ionospheric electron density and height. Its horizontal wavelength is about several

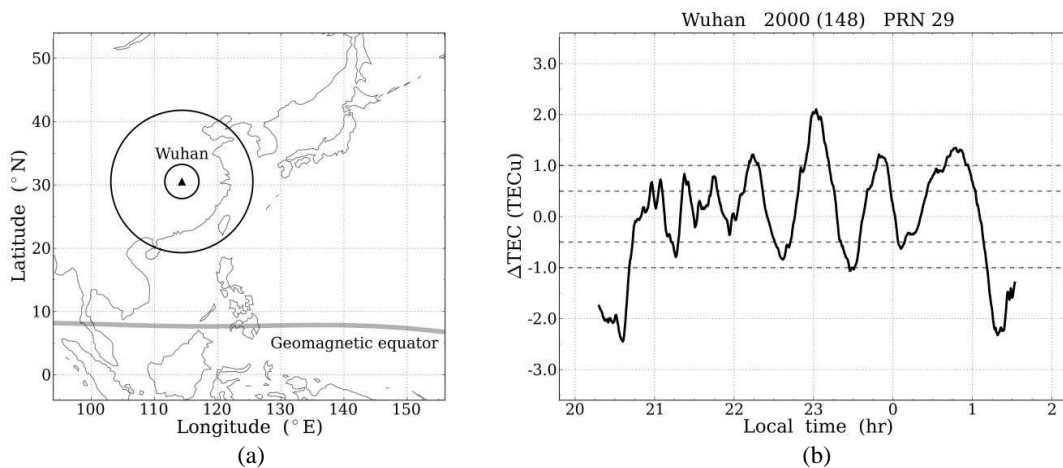


Figure 1: (a) The location of instruments and their field-of-view. The triangle represents the location of the GPS receiver and the digisonde. The larger and smaller circles represent the field-of-view of the GPS receiver and the digisonde, respectively. (b) An example of TEC temporal perturbations with MSTIDs signatures. The TEC perturbations is the TEC temporal variation subtracted its one hour running mean. The TEC temporal variation is derived from the pair of the Wuhan GPS receiver and the GPS satellite PRN 29 on the day 148 in 2000.

hundred kilometers and the period is 15–60 minutes. The wave front of most nighttime MSTIDs aligns from northwest to southeast, and which travels in the southwest direction with horizontal velocity 15–250 m/s [1]. It has been found that smaller scale irregularities can be generated and embed in MSTIDs structures [2]. Moreover, many statistical studies show that MSTIDs are common in two solstice seasons, especially in summer [3–6]. In this study, we choose the city Wuhan as our experiment location. We collect the GPS and the digisonde data, and explore nighttime occurrence rates of spread F , GPS phase fluctuations, and MSTIDs in 2000.

2. DATABASED

The data used in this study come from the GPS receiver and the digisonde which setup at Wuhan (30.5°N, 114.4°E, 20°N MLAT) in China (see Figure 1(a) for instrument locations and field-of-view). In this study, we focus on the nighttime date (18-06 local time) in 2000 when sun was in

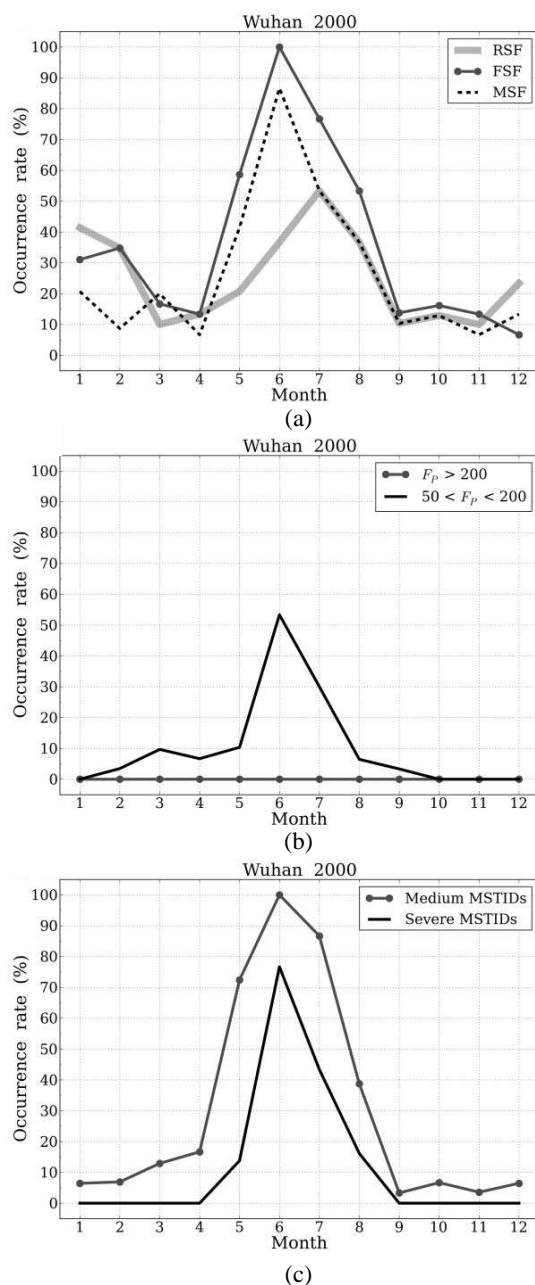


Figure 2: The monthly occurrence rates of spread F and F_p as well as MSTIDs. The occurrence rate in the figure is the percentage of days on which at least one event occurred in a day in a month.

the high solar activity phase. For the digisonde, we inspect each ionogram and categorize those into No Spread F (NSF), Frequency Spread F (FSF), Range Spread F (RSF), and Mixed Spread F (MSF) four types. Regarding the GPS, we derive the GPS phase fluctuation index (Fp) which represents the strength of irregularities [7]. The index has two criteria $Fp > 200$ and $50 < Fp < 200$ which represent the strong and medium irregularities, respectively. If $Fp < 50$, it will treat as the background noise. To retrieve the signature of MSTIDs, we adopt the method proposed by Kotake et al. (2006) [8]. We first select the Total Electron Content (TEC) temporal data with the length longer than two hours, and then subtract its one hour running mean to get the TEC perturbations (see Figure 1(b) for example). We manually inspect these perturbations and pick up whose period and amplitude corresponding to MSTIDs characteristics. Furthermore, we also categorize these MSTIDs events into severe and medium two levels in which the severe level indicates the TEC perturbation larger than one TECu ($1 \text{ TECu} = 10^{16} \text{ electrons/m}^2$) and the medium level is 0.5 TECu.

3. RESULTS

Figure 2 shows monthly occurrence rates of spread F and Fp as well as MSTIDs. The occurrence rate in the figure is the percentage of days on which at least one event occurred in a day in a month. The results of the figure can be summarized as follow: (1) Three spread F types, $50 < Fp < 200$, and two MSTIDs levels all are highly active in summer (May, June, July and August). (2) No $Fp > 200$ event occurs during whole observation periods. (3) All three spread F types have a minor occurrence peak in winter (January, February, November, and December). (4) The ionosphere seems very stable during equinoxes (March, April, September, and October) because all phenomena have very low occurrence rates.

Figure 3 displays the hourly occurrence rates of spread F and Fp in equinoxes, summer, and winter. The occurrence rate is the number of event divided the total number of data in an hour in the season. In the figure, the equinoxes and winter parts can be ignored because the occurrence rates are too low. For the summer part, two important results are (1) high spread F occurrence rates can last for a long time but Fp only occur around midnight, and (2) FSF occurs earlier than other spread F types.

In this study, the method we used to detect MSTIDs is inappropriate to examine the nighttime

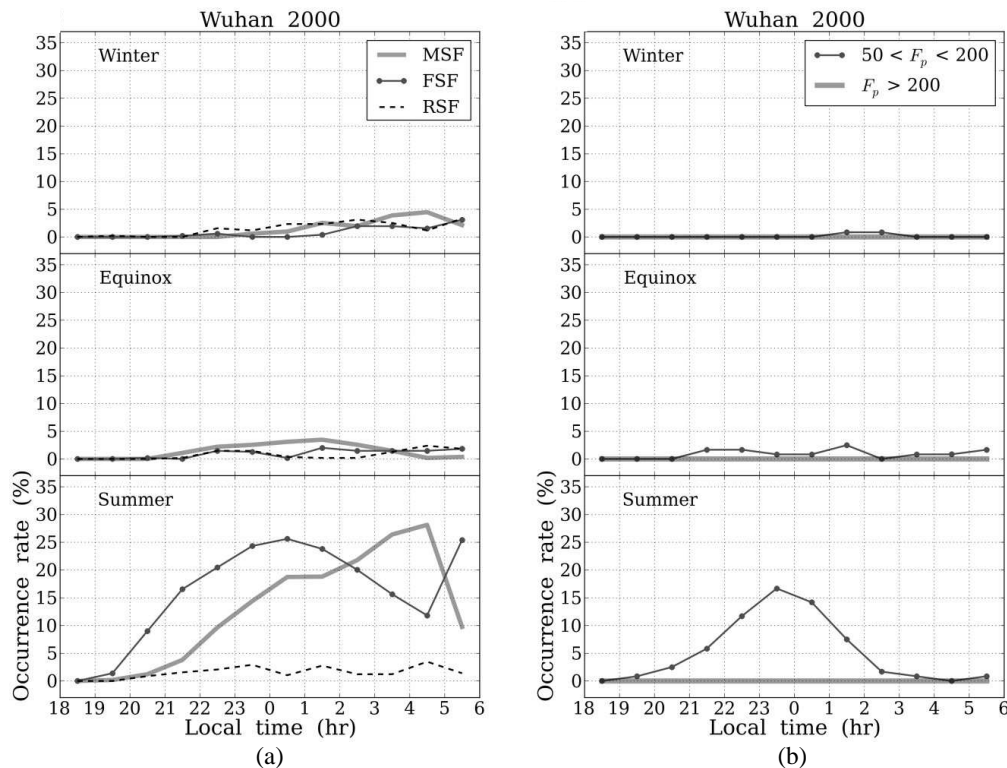


Figure 3: The hourly occurrence rates of spread F and Fp in summer, winter, and equinoxes three seasons. The occurrence rate is the number of event divided the total number of data in an hour in the season.

variations of MSTIDs occurrences because the distributions of data points changes from day to day. However, we have examined the one-to-one correspondences between MSTIDs and spread F or F_p . The results show that the occurrence rates of FSF, RSF, and MSF during severe MSTIDs are 39%, 1%, and 31%, respectively. In the same time, $50 < F_p < 200$ has 20% occurrence rates.

4. CONCLUSIONS

We spotlight five important points to draw our conclusions.

- (1) The high occurrence rates of three spread F types, $50 < F_p < 200$, and two MSTIDs levels in summer confirms that irregularities over Wuhan mainly relate to MSTIDs.
- (2) All spread F types have a minor occurrence peak in winter but none for MSTIDs and GPS phase fluctuations.
- (3) None of $F_p > 200$ event occurs during observations which indicates that the strength of irregularities related to MSTIDs is weaker than that of equatorial plasma bubbles in the low-latitudes ionosphere
- (4) The earliest occurrence of FSF implies that disturbances related to MSTIDs start at the altitude near the F -region peak.
- (5) The results of one-to-one correspondences implies that smaller scale irregularities which are observed as spread F or GPS phase fluctuations may only appear in some phase of MSTIDs.

ACKNOWLEDGMENT

The authors thank the International GNSS Service (IGS) for GPS data, and the Beijing National Observatory of Space Environment, Institute of Geology and Geophysics, Chinese Academy of Sciences for digisonde data.

REFERENCES

1. Hunsucker, R. D., "Atmospheric gravity waves generated in the high-latitude ionosphere: A review," *Rev. Geophys.*, Vol. 20, No. 2, 293–315, 1982.
2. Saito, A., N. Nishimura, M. Yamamoto, S. Fukao, T. Tsugawa, Y. Otsuka, S. Miyazaki, and M.C. Kelley, "Observations of traveling ionospheric disturbances and 3-m scale irregularities in the nighttime F region ionosphere with the MU radar and a GPS network," *Earth Planets Space*, Vol. 54, 31–44, 2002.
3. Evans, J., J. Holt, and R. Wand, "A differential-doppler study of traveling ionospheric disturbances from Millstone Hill," *Radio Sci.*, Vol. 18, No. 3, 435–451, 1983.
4. Jacobson, A., R. Carlos, R. Massey, and G. Wu, "Observations of traveling ionospheric disturbances with a satellite Beacon radio interferometer: Seasonal and local time behavior," *J. Geophys. Res.*, Vol. 100, No. A2, 1653–1665, 1995.
5. Kotake, N., Y. Otsuka, T. Ogawa, T. Tsugawa, and A. Saito, "Statistical study of medium-scale traveling ionospheric disturbances observed with the GPS networks in southern California," *Earth Planets Space*, Vol. 59, 95–102, 2007.
6. Shiokawa, K., C. Ihara, Y. Otsuka, and T. Ogawa, "Statistical study of nighttime medium-scale traveling ionospheric disturbances using midlatitude airglow images," *J. Geophys. Res.*, Vol. 108, No. A1, 1052, 2003.
7. Mendillo, M., B. Lin, and J. Aarons, "The application of GPS observations to equatorial aeronomy," *Radio Sci.*, Vol. 35, 885–904, 2000.
8. Kotake, N., Y. Otsuka, T. Tsugawa, T. Ogawa, and A. Saito, "Climatological study of GPS total electron content variations caused by medium-scale traveling ionospheric disturbances," *J. Geophys. Res.*, Vol. 111, A04306, 2006.

A Study of Equatorial Ionospheric Irregularities over the Indian-Ocean Sector during Solar Maximum by Using the Global Positioning System

F. D. Chu¹, W. S. Chen², C. C. Lee², W. H. Tseng¹, H. T. Lin¹ and C. S. Liao¹

¹National Time and Frequency Standard Lab, Chunghwa Telecom Co., Ltd., Taiwan

²General Education Center, Chien Hsin University of Science and Technology, Taiwan

Abstract— Ionospheric irregularities will exert scintillations on electromagnetic waves if the waves pass through them. So they are interesting for ionospheric propagation at the magnetic equator and low latitudes. The irregularities during solar maximum period were examined by tracking stations of the global position system, which were located in the India-Ocean sector in both southern and northern hemispheres. The results show that the significant nocturnal ionospheric irregularities appear equinoctial dominance at low latitudes. Besides, there is an equinoctial asymmetry of occurrence rate of irregularities, i.e., the rate seems larger during spring (March–April) than autumn (September–October) over the eastern sector, while appears larger during autumn than spring over the western sector. Moreover, the equinoctial asymmetry can reverse over the eastern sector when solar activity is going to reach maximum during the rising phase of a solar cycle.

1. INTRODUCTION

Ionospheric irregularities can exert amplitude and phase scintillations on electromagnetic waves if the waves traverse them [1]. This effect may cause severe signal fading and loss of lock at a receiver. Therefore, ionospheric irregularities are interesting for electromagnetic wave propagation.

Ionospheric irregularities usually occur in the F region of the ionosphere, and can be observed by high frequency (HF) radio sounding as spread F, which is a spread of HF echo trace on the ionogram [2]. In addition, the irregularities can also be observed by global navigation satellite system (GNSS), such as the global positioning system (GPS), and the observation result is consistent with that of spread-F echoes [3]. Furthermore, some strong irregularities can reach the top of the ionosphere and can be observed by satellite [4].

Although there have been a few studies of nocturnal ionospheric irregularities with HF sounding in a local geographical region [5] and with satellites at the top of the ionosphere [4] during high solar activity period, there may be some characteristics of irregularities which would not yet be revealed very well over the Indian-Ocean Sector. The objective of this study was to investigate the occurrence of nocturnal ionospheric irregularities over the Indian Ocean during solar maximum period by GPS signals observed from the ground. The noticeable results were equinoctial asymmetry of occurrence rate of irregularities and this asymmetry might be reverse during the transition from middle to high solar activity in the rapidly rising phase of a solar cycle.

2. DATABASE AND METHOD

Six GPS tracking stations of the International GNSS Service (IGS, <http://www.igs.org>; [6]) were found in the India-Ocean sector. Their marker names were BAHN, SEY1, IISC, MALD, LCKI, and DGAR. For the sake of readability, these stations are represented by Bahrain, Seychelles, Bangalore, Maldives, Lucknow, and Diego Garcia, respectively. The locations of the stations and the fields of view at the height of 400 km with 15° elevation angle over the stations are shown in Figure 1 as triangle marks and dash circles, respectively. Bangalore and Maldives are near and on the opposite sides of the magnetic equator (the 0° Nm magnetic latitude as shown in Figure 1); Seychelles and Diego Garcia are near the southern equatorial anomaly (about -15° Nm magnetic latitude) formed by the equatorial plasma fountain [7]; and finally, Bahrain and Lucknow are at the crest of the northern equatorial anomaly and close to middle latitudes.

Equatorial ionospheric irregularities are mainly plasma bubbles, which often occur in the F layer of the ionosphere after sunset over the geomagnetic equator. The irregularities are originally formed in the bottom-side region of the F layer and then rise and may up to the top of the ionosphere by nonlinear Rayleigh-Taylor instability [7]. They also elongate along geomagnetic fields off the equator to low latitudes. GPS phase fluctuations, which were practically the time variation of

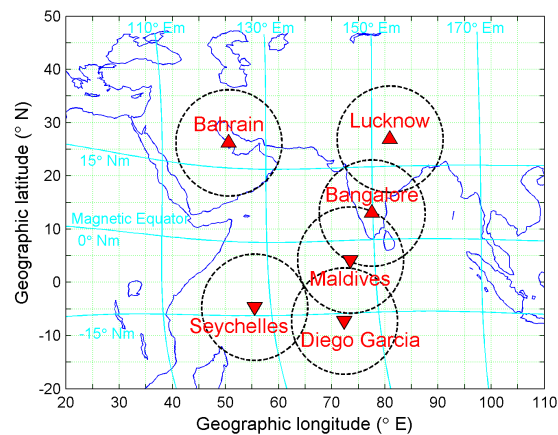


Figure 1: Locations of the GPS tracking stations in Indian-Ocean sector.

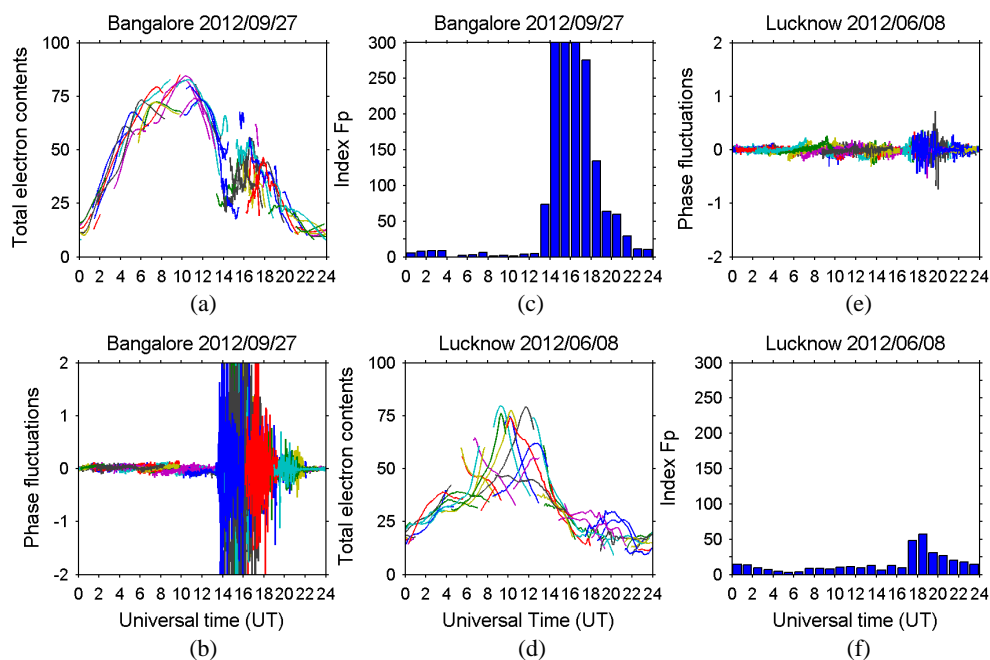


Figure 2: Examples of GPS phase fluctuations.

high-pass-filtered total electron contents (TEC), were used as an indicator to detect equatorial ionospheric irregularities [8]. For quantitatively characterizing GPS phase fluctuations, the hourly index Fp was defined for all satellites available to a station [9]. The index Fp is the average of all the quarterly index fp of available satellites in an hour multiplied by 1000. The index fp is the median value of absolute phase fluctuations of a satellite in a 15-minute interval. The magnitude of Fp indicates the strength of existing irregularities: $Fp \leq 50$ represents the GPS phase fluctuations come from background noise of irregularities; $Fp > 200$ means the GPS signal is severe influenced by strong irregularities; $50 \leq Fp < 200$ stands for the existence of moderate irregularities. An example of strong irregularities on September 27, 2012 at Bangalore is shown in Figures 2(a)–2(c), demonstrating TEC, phase fluctuations, and the index Fp , respectively. During 14–17 UT (19–22 LT), the TECs obtained by available satellites were not only deeply depleted but also severe fluctuated, and the index Fp was high, as shown in Figures 2(a) and 2(c).

Other kind of irregularities at low latitudes may come from middle latitudes, such as traveling ionospheric disturbances (TID) [10, 11]. They often cause GPS phase fluctuations at an Fp value of around 50, and fluctuate two or more TEC curves. An example on June 8, 2012 at Lucknow is shown in Figures 2(d)–2(f) demonstrating moderate irregularities during 17–18 UT (22–23 LT).

The significant high solar-activity years of the nearest past were 2000–2002, and their yearly sunspot numbers were 120, 111, and 104, respectively. The present year, 2012, was in the rising phase of the 24th solar cycle with sunspot numbers of about 65. It is middle and going to reach

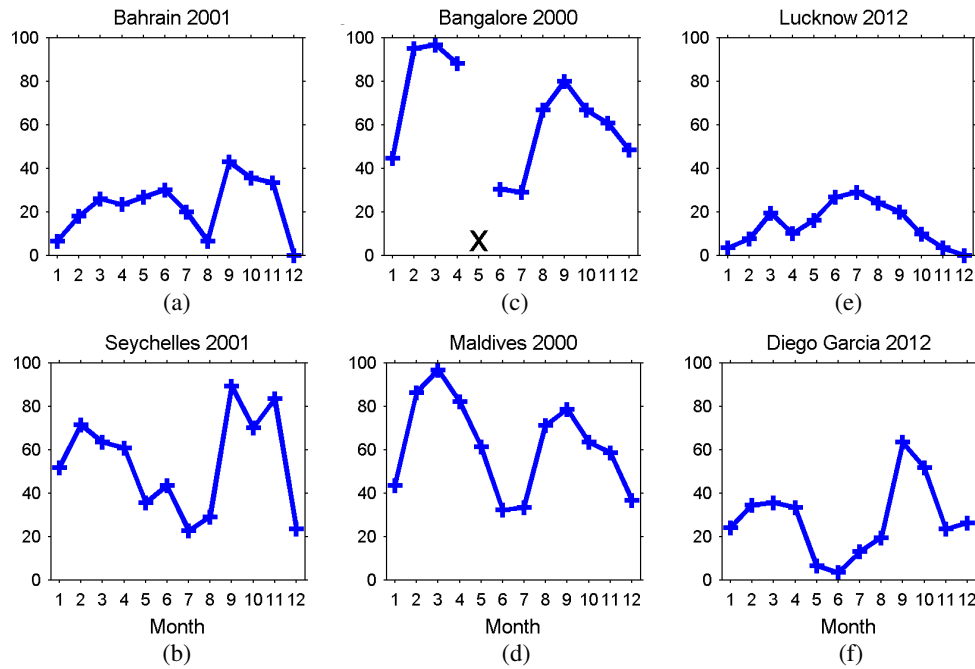


Figure 3: Monthly occurrence rates of nocturnal ionospheric irregularities.

high solar activity. Considering whether sufficient amount of data collected at these stations and for result comparisons between these stations, the data adopted in this study were those recorded at Bahrain and Seychelles during 2001, at Bangalore and Maldives during 2000, and at Lucknow and Diego Garcia during 2012. Thus, the nocturnal ionospheric irregularities occurred in the time interval of 1800–0600 LT were detected by examining the GPS phase fluctuations in Fp index derived from the aforementioned database, with the elevation angles of GPS satellites greater than 15° . Besides, both the bobble irregularities with $Fp > 50$ and the TID-like irregularities were processed in this study to describe the morphology of ionospheric irregularities at the equator and low latitudes.

3. RESULTS AND DISCUSSION

Figure 3 shows the monthly occurrence rates of nocturnal ionospheric irregularities over Bahrain, Seychelles, Bangalore, Maldives, Lucknow, and Diego Garcia. The number of observation days was at least 20 for each month. The cross symbol denotes not available or lack of data. The monthly occurrence rate of irregularities is the percentage of days on which at least one significant Fp occurred in a day in a month. First, over both Bangalore and Maldives near the magnetic equator, Figures 3(c)–3(d) show that the occurrence rates in general were dominant in equinoctial months (March–April and September–October). In addition, the occurrence rates in December-solstice months (D months: November–February) in general surpassed those in June-solstice months (J months: May–August). Moreover, the distributions of occurrence rate on the opposite sides of the magnetic equator (Bangalore and Maldives) accord with each other. Second, near the equatorial anomaly, over both Seychelles and Diego Garcia, the occurrence rates in general were also equinoctial dominant and minimum in J months as shown in Figures 3(b) and 3(f), similar to those over Bangalore and Maldives. Finally, over both Bahrain and Lucknow, the equinoctial dominance is not clear, and the occurrence rates in D months did not obviously surpass those in J months yet, as shown in Figures 3(a) and 3(e).

The results observed by GPS phase fluctuations over Bangalore are consistent with those of previous studies observed by spread-F echoes over the Indian region [5], indicating that the GPS can also be a useful tool to investigate the ionosphere. In addition, the results obtained by ground-based GPS stations are also similar to those obtained by satellites at the top of the ionosphere (top-side irregularities) [4], indicating that the low latitude irregularities mainly come from the magnetic equator (bobble irregularities generated by nonlinear Rayleigh-Taylor instability). Besides, comparing to in situ satellite observations [4], the occurrence rates of irregularities in this study are much higher, indicating that more irregularities are observed by the ground stations (i.e., bottom-side irregularities, developing under the top of the ionosphere). Finally, the irregularities

in J months at the crest of the northern equatorial anomaly seem not similar to the bobble irregularities at the equator, and probably come from middle latitudes; this is consistent with previous studies [4, 5, 10, 11].

There are two interesting findings in this study in the following. (1) The occurrence rates in equinoxes are asymmetry during solar maximum; the rate in spring (March–April) is slight higher than autumn (September–October) over the eastern Indian Ocean, while that is opposite over the western India Ocean. (2) The equinoctial asymmetry seems to have unusual solar-activity dependence in the eastern Indian Ocean; the rate in autumn is higher than spring when solar activity is going to reach maximum during the rapidly rising phase of a solar cycle. This can be seen at Diego Garcia during 2012 (Figure 3(f)), and also is consistent with that over Bangalore during 2012 although not shown here. Recently, a few studies have suggested that the transequatorial meridional neutral wind would play important roles in the Indian region, such as the probability for equatorial irregularities to occur in equinoxes [12]. Therefore, more data will be examined in the future to discover the mystery of ionospheric irregularities over the Indian-Ocean sector.

4. CONCLUSIONS

This work has investigated the equatorial ionospheric irregularities over the Indian-Ocean sector during solar maximum period by using the GPS. The aforementioned results and discussion can lead to the following conclusions. (1) The low latitude irregularities often develop in equinoctial and December-solstice months over the Indian-Ocean sector. (2) The low latitude irregularities mainly come from the magnetic equator. (3) At the crest of equatorial anomaly, the irregularities in June-solstice months should not be neglected and they probably come from middle latitudes. (4) The occurrence rates in equinoxes are asymmetric and maybe caused by the transequatorial meridional wind. (5) The equinoctial asymmetry of occurrence rates seems to have the opposite outcome during the transition from middle to high solar activity.

REFERENCES

1. Yeh, K. C. and C. H. Liu, "Radio wave scintillations in the ionosphere," *Proc. IEEE*, Vol. 70, No. 4, 324–360, 1982.
2. Davies, K., *Ionospheric Radio*, Peter Peregrinus Ltd., London, UK, 1990.
3. Chen, W. S., C. C. Lee, J. Y. Liu, F. D. Chu, and B. W. Reinisch, "Digisonde spread F and GPS phase fluctuations in the equatorial ionosphere during solar maximum," *J. Geophys. Res.*, Vol. 111, A12305, 2006.
4. Su, S.-Y., C. H. Liu, H. H. Ho, and C. K. Chao, "Distribution characteristics of topside ionospheric density irregularities: Equatorial versus midlatitude regions," *J. Geophys. Res.*, Vol. 111, A06305, 2006.
5. Dabas, R. S., R. M. Das, K. Sharma, S. C. Garg, C. V. Devasia, K. S. V. Subbarao, K. Niranjana, and P. V. S. R. Rao, "Equatorial and low latitude spread-F irregularity characteristics over the Indian region and their prediction possibilities," *J. Atmos. Solar Terr. Phys.*, Vol. 69, No. 6, 685–696, 2007.
6. Dow, J. M., R. E. Neilan, and C. Rizos, "The international GNSS service in a changing landscape of global navigation satellite systems," *J. Geod.*, Vol. 83, No. 3–4, 191–198, 2009.
7. Kelley, M. C., *The Earth's Ionosphere*, Elsevier, San Diego, California, USA, 2009.
8. Aarons, J., M. Mendillo, R. Yantosca, and E. Kudeki, "GPS phase fluctuations in the equatorial region during the MISETA 1994 campaign," *J. Geophys. Res.*, Vol. 101, 26851–26862, 1996.
9. Mendillo, M., B. Lin, and J. Aarons, "The application of GPS observations to equatorial aeronomy," *Radio Sci.*, Vol. 35, No. 3, 885–904, 2000.
10. Lee, C. C., Y. A. Liou, Y. Otsuk, F. D. Chu, T. K. Yeh, K. Hoshinoo, and K. Matunaga, "Night-time medium-scale traveling ionospheric disturbances detected by network GPS receivers in Taiwan," *J. Geophys. Res.*, Vol. 113, A12316, 2008.
11. Chen, W. S., C. C. Lee, F. D. Chu, and S.-Y. Su, "Spread F, GPS phase fluctuations, and medium-scale traveling ionospheric disturbances over Wuhan during solar maximum," *J. Atmos. Solar Terr. Phys.*, Vol. 73, No. 4, 528–533, 2011.
12. Maruyama, T., S. Saito, M. Kawamura, K. Nozaki, J. Krall, and J. D. Huba, "Equinoctial asymmetry of a low-latitude ionosphere-thermosphere system and equatorial irregularities: Evidence for meridional wind control," *Ann. Geophys.*, Vol. 27, 2027–2034, 2009.

Satellite Monitoring for Elasto-plastic Behavior of Plate around Epicenter in a Process Tsunami Earthquakes

Shigehisa Nakamura
Kyoto University, Japan

Abstract— This is a note to a basic understanding of an elasto-plastic behavior of plate around epicenter in a process of tsunami earthquake. In this work, the author introduces a concept of the dynamics for the problem noticed a case as is that in his manner in order to help for an evaluation of the interested process in nature. Formation of earth crust, linear process of crust, yielding and breaking process in nature are also introduced. Divergent and convergent zones are noted in relation to seismic and volcanic zone. Nonlinear process in energy release and energy transfer should be seen in a fault interface. A set of equivalent parameters should be introduced for updating the existing models. Some of applied magneto-hydrodynamics suggests to have an advanced research in order to construct an updated model for the purpose.

1. INTRODUCTION

This work is a note to a basic understanding of an elasto-plastic behavior of plate around epicenter in a process of tsunami earthquake. In this work, the author introduces a concept of the dynamics for the problem in a case as is seen in nature.

2. FORMATION OF EARTH CRUST

It has been well understood the earth is one of the planets in the solar system.

At the birth of the earth, some primitive particles consisted by an original elements found on the earth at present were in a stage of a nebular rotating around the sun. To the details about solar system of the related planets, it can be seen some illustrative publication introducing the planets in a scope of “Astronomy”.

The first phase of the earth is considered that was a spherical fire ball rotating on an orbit around the sun. The particles had gathered to the center to form the core of the earth. This process resulted to concentrate the particles energy when the heavy elements had been produced under a high temperature with a high pressure in the core.

The earth has been rotation itself during the rotating motion on the orbit and a thin sheath was formed to cover the core. The materials in the core had been electro-conductive property to produce the earth’s magnetic field.

Between the sheath as the earth surface layer and the earth’s core, a kind of the primitive magma had been existed to maintain the geomagnetic field.

A part of the energy inside the earth surface layer was radiated into the space to cooling down of the earth surface. This resulted to decrease the earth surface area, then, the magma and core had to be in a stage of higher temperature under a corresponding pressure in a balance of the forcing inside of the earth.

3. EARTH CRUST

Generally, it is understood that the properties of the elements existing on the earth surface in the field of physics and chemistry.

It can be taken that the earth crust is a spherical shell with an elastic property. A more exact note must be as that the crust could be understood to be formed by an equivalent material in order to introduce a concept of an equivalent elastic shell.

Assuming a slipper condition between the crust as the earth crust and the magma driven by the electromagnetic dynamo effect of the motions of the core consisting materials, then, the earth crust could be consisted by several plates to cover the earth surface. The magma acts to form a divergent belt zone of the crust, for example, as the mid-Atlantic ridge, and the convergent zone, as the grand trough of in the northeast Africa. There are various patterns can be seen as found in the map published for official use or citizen use in brief.

Now, assuming an equivalent elastic plate instead of the real earth crust, a formulation of stress-strain relation in a model crust which is isotropic and uniform.

Generally, this relation can be written as follows, that is, a displacement \mathbf{X} in relation to a external forcing \mathbf{F} in a Cartesian rectangular co-ordinate $Oxyz$,

$$\mathbf{X} = \mathbf{M} \times \mathbf{F}, \quad (1)$$

where, $\mathbf{X} = \mathbf{X}(x, y, z)$ for displacement vector, and, $\mathbf{F} = \mathbf{F}(x, y, z)$ for forcing vector, and, the notation \mathbf{M} is a tensor specifying the parameters of the elastic material which can be written as in following form, i.e.,

$$\mathbf{M} = |\mathbf{M}_{ijk}|, \left| \begin{array}{ccc} \mathbf{M}_{xx} & \mathbf{M}_{xy} & \mathbf{M}_{xz} \\ \mathbf{M}_{yx} & \mathbf{M}_{yy} & \mathbf{M}_{yz} \\ \mathbf{M}_{zx} & \mathbf{M}_{zy} & \mathbf{M}_{zz} \end{array} \right|, \quad \text{for (two of } x, y, \text{ and } z), \quad (2)$$

by using simple multiplier mark \mathbf{X} for convenience.

Assuming that density ρ and volume \mathbf{V} which are related to the interested forcing to the mass related to the displacement, it can be written as,

$$\mathbf{X} = \rho \mathbf{V}, \quad (3)$$

In case of the spherical co-ordinate $O(\mathbf{r}\theta\phi)$, the above tensor should be expressed after a proper mathematical transfer of the variables.

A simplest case must be the symmetric tensor, when the following conditions are satisfied, i.e., $\mathbf{M}_{xy} = \mathbf{M}_{yx} = O$, $\mathbf{M}_{xz} = \mathbf{M}_{zx} = O$, and, $\mathbf{M}_{yz} = \mathbf{M}_{zy} = O$, respectively. This case is one of the simplest examples so that the tensor can be degenerated as a case of equation for a vector field. In other word, the vector field of an elastic process in a solid material can be easily analyzed as a process of a linear process by using a linear differential equation.

This linear problem is understood as a case for Hook's law. In a case of the earth crust, it is essentially equivalent and same mathematical procedures can be applied. In the field of structural engineering, this linear problem had been developed so that an advanced work of an extended non-linear problem is their up-dated work.

The author is unfortunate that he could never have seen any step in some nonlinear seismic process in the field of seismology.

Then, the equation of motion for the interested elastic material in a solid phase can be written in a form of mathematical equation referring to the relation forcing and displacement as written in (1), i.e.,

$$d(\rho \mathbf{X})/dt = d(\mathbf{M} \times \mathbf{F})/dt. \quad (4)$$

where, $d()/dt = \partial()/\partial t + v \nabla()$ for the velocity vector the mass in motion.

4. YIELDING OF CRUST

As far as we concern that the elastic process in the range of the linear process, it is easy to solve if the considering elastic process in a solid material which is isotropic and uniform.

It is well understood that there is an yielding point where it is a critical stage for the solid material in the scope of elasticity.

In a case of a forcing action is beyond the critical condition, the interested solid material shift its motion of a linear process to another motion of nonlinear process under some condition to the next stage for breaking start as a nonlinear process. Then, the expression as seen in (4) cannot hold in the nonlinear process.

Apparent creeping must be a familiar process for us. Several materials familiar to us in the daily life or to structure engineers in the public productions at their research in advance, are the result of scientific applications of the creeping though any one of their processes never have been effectively formulated or applied for seismic event as earthquake.

In nature, the crust is in a stage of a complicated structure with some undulations after several processes of stratification were completed. So that it is necessary to introduce any one of the equivalent solid material model for the earth crust.

5. PLASTIC PROCESS

When it is a case of the minor yielding, the solid material can get some recovery of its elastic property. Degree of the recovery is depending on the effect of forcing and on the elasticity of the interested solid material.

In the phase of a yielding, any one of the elastic materials deformation starts to be fast even when any forcing or loading is faded out. In this phase, a creeping as a nonlinear process is significant up to get to the breaking phase.

This breaking phase can be seen even in the cases of some products produced with a consideration not to yield or not to break down.

6. BREAKING OF CRUST

The earth is radiating out its energy into the space, so that the earth surface is cooling down to make ease a growth in an apparent thickness of the crust.

Unfortunately, the amount of the energy loss at the earth surface radiation into the space is not evaluated yet in the author's concern. Nevertheless, this amount of the energy release should be effective to see the new crust formation time to time, for example, on the mid-Atlantic ridge where the magma is actively producing a new crust along the ridge from the Arctic Sea to the Antarctic zone in the Atlantic.

7. DIVERGENT OF EARTH CRUST

This belt covering the mid-Atlantic zone is one of the divergent zones of the earth plates. Nevertheless, there might be a little scientific work about the details of the degree of this crustal divergent in relation any energetics.

8. CONVERGENT OF EARTH CRUST

One of the convergent zones is just over-up location to the circum-Pacific seismic zone and the active volcanic zone.

The most significant convergent of the earth crusts must be in the northwestern Pacific. In this convergent zone, there might has been repeated several tsunami earthquake when the creeping and breaking of the related plates have been seen in order to maintain the earth's spherical shape which might be necessary to maintain the geomagnetic field generated by the conductive materials inside of the earth crust.

Then, the energetic magma actions must be closely related to the geomagnetism. This geomagnetic field is surely produced. after an inductive effect of the motions of conductive materials inside of the earth surface.

9. FAULT INTERFACE

As far a case of problems on a fault interface formed after an seismic event at and around an epicenter of an earthquake, the equation of motion noted above for an elastic body can be applied if rewriting the velocity vector c of the sound speed instead of $\mathbf{V} = (d\mathbf{X}/dt)$ in the Equation (4).

In this case, the elastic parameters defined at a static condition without any consideration of time. In some case, the time is introduced as a parametric factor though the author would not agree to use any factor defined for static conditions for any case of dynamic processes of the elastic material in a solid phase. Now, the author has to note that another parameters defined for dynamic conditions.

Nevertheless, it should be a careful application of the equation for any case after breaking in any elastic dynamics.

It should be some mechanisms of energy release and of energy transfer processes in the interested material of solid phase. Exactly speaking, a transitional zone around the fault interface should be realized in a solid mechanics of material.

Then, it can be found a way to introduce a set of equivalent parameters for the earth crust. With this, a proper model in an advanced scheme could be constructed.

10. MAGNETOHYDRODYNAMICS

In the historical age, geomagnetic field was understood as a simple dipole magnetic field.

In the last half of the 20 century, it was developed a model of magnetohydrodynamics (in brief, MHD) that the planets' magnetic fields could be formulated and understood.

In the early 21 century, this magnetohydrodynamics has been applied in order to realize the planets in the solar system after introducing the spacecraft monitoring of the magnetic fields of the planets though nobody knows what is appropriate for exactly realize the other planets even in an adjusted scaling for the earth.

It should be introduced an advanced research for finding new dynamical processes in a newly defined parameter.

11. CONCLUSIONS

Divergent and convergent zone of the earth surface are noted in relation to tsunami earthquakes observed on the earth crust. The motion of magma inside the earth crust is effective at considering the specific geophysical process found essentially at a nonlinear plastic process but a linear elastic process. Once a seismic fault is formed in the crust, an advanced understanding is required for realizing any dynamical processes on the fault interface. Problems on energy release and energy transfer are important even in a scope of plate mechanics.

As far as the author concerns, it can be noted that an application of magnetohydrodynamics is helpful for realizing geomagnetic field in a planet as well as for a global understanding of the earth crust process which might be closely related to significant seismic events on the earth.

As for the planets in the solar system, magnetohydrodynamics has been applied well for realizing the magnetic processes monitored by the spacecrafts.

A Geomagnetic Polar Drifting Path Evolution on the Geographic Earth Surface

Shigehisa Nakamura
Kyoto University, Japan

Abstract— This work concerns to a geomagnetic polar drifting path projected on the geographic earth surface. Under several assumptions, a specific sun spot positioning is considered for a convenient reference at modeling of the geomagnetic poloidal and toroidal modes is taken to be possible instead of the case of the solar spot model of eleven year cycle. This may lead to a consistent geomagnetic polar drifting path evolution on the geographic earth surface.

1. INTRODUCTION

This work concerns to a geomagnetic polar drifting projected on the geographic earth surface under several assumptions. A specific trend of the sun spot motion is considered a convenient reference at modeling of the geomagnetic poloidal and toroidal modes is taken to be possible to consider instead of the case of the solar spot model of eleven years cycle. This may lead to a consistent geomagnetic polar drifting path projected on the geographic earth surface.

2. REMANENT MAGNETISM

Nagata [1] had worked in the field of rock magnetism. He observed remanent magnetism of the rocks consisting the earth surface which could be taken when the solid rocks were formed after appeared on the surface of the spherical earth crust. His illustration for about 700 million years before present had been taken to show that the rock magnetism had been complicated processes on the earth surface. Then, Rikitake [2] simply introduced Nagata's illustration in brief in his text without any comment about a theoretical background though the fact has that the rock magnetism could give us the geomagnetism when the rock was to be solid as a memory of the solid rock was formed on the earth surface.

3. ASTRONOMICAL UNDERSTANDING

There have been an understanding of that the magma inside the spherical earth crust has a common reference of the pole positions as north pole Boreares and as south pole Austraius. The astronomers even at present say that the magma motion in the lower latitude is in a higher speed motion than that in the higher latitude. Now, the author tends to express it that is a certain constant angular velocity of the earth around the pole axis.

4. SIMILARITY OF MAGNETIC MODES

One of the theoretical solutions for the solar magnetic fields was obtained by Stix [3]. In his model, a solution was reduced on the basis of a magnetohydrodynamics for the spherical sun. The trend of the sun spot translation in a eleven year cycle was fit for his mathematical solution, His model did not to be considered a shell as a surface layer. Then, the author has get to consider an application of. Nevertheless, the author takes it not to be in geomagnetic polar wondering but to be in drifting.

5. MODELLING GEOMAGNETIC POLAR DRIFTING PATH

For the author's convenience, an application of Stix model is taken to introduce for constructing a model of the geomagnetic polar drifting path. In the past, it was taken to be a polar wondering. Then, taking as that problem is to find a geographical projection of the earth's magnetic polar drifting for the geological time scale of 700 million years under several bold assumptions. In this case, a spherical shell is considered not to affect to the geomagnetic field generated by a spherical material of high temperature and high pressure. Then, the solution can be reduced in a form quite similar to the case of Stix model for the poloidal mode and for the toroidal mode.

6. GEOGRAPHICAL EVOLUTION OF GEOMAGNETIC POLAR DRIFTING PATH

Now, A reference frame work is the geographical co-ordinating, that is, same to consider the earth's center as the origin for (r, ϕ, θ) , where, the notations r , ϕ , and θ denote radial distance from the origin to location on the earth surface, ϕ for latitude, and, θ for longitude, respectively.

Then, the geomagnetic pole with an inclination angle κ relative to the geographic frame can be written follows, i.e., the geomagnetic pole position projected on the geographic position on the earth surface can be written as that, (for convenience, when $\kappa = 0$),

$$r = R_0(\cos \theta), \quad \phi = r_0(\sin \theta), \quad \theta = (\omega t + \varepsilon) + \sum_{n=0}^N (2n\pi), \quad \text{for } n = 1, 2, 3, \dots, N (< 7 \times 10^8),$$

where, the notation of R_0 is the radius of the earth as an assumed sphere in rotating at an angular velocity ω (annual rotation rate is taken as 2π) at time t (unit is one year), and the notation ε is an arbitrary constant determined as the initial condition of the earth.

Assumptions are as that the initial and terminal geomagnetic positions are P_0 and P_t , respectively. This means that the position P_0 is at a location just neighbor the geographic equator in the northern hemisphere, and that the position P_t is at a location in the arctic zone of the geographic frame.

When time interval is taken as 700 million years, then, the expression of P_0 at $t = t_0$ is written as $P_0 = (r_0, \phi_0, \theta_0)$, for example, and, the expression of P_t at present is written as $(P_t = r_t, \phi_t, \theta_t)$.

Then, the spiral path is an expression of the geomagnetic drifting path.

This means that the magneto-hydrodynamic equation must be solved to fit for the above expression of the positioning for the geomagnetic drifting path.

Nevertheless, it should be considered that the above expression could be fit well to a model earth shaping an approximated spherical surface.

Adding to the above, the author has to note that this path tells only a consistency of the trend of the data for the rock magnetism, obtained, for example, by Nagata and the other scientists in the field of rock magnetism on the planet earth.

A more details should be discussed later for the exact shape of the earth or for the earth surface defined on the basis of the geoid as the reference of the most precise model of the earth. Then, satellite data for a geodetic process should be considered as much as for the other processes on the earth monitored by the satellites under the operation for the purpose of the earth surface observation.

7. ASSUMPTIONS AND CONDITIONS

Assume the earth's rotation is constant for the considering geological time period on the spherical earth which is formed as that a spherical thin shell corresponds to the earth surface crust, and that, the material inside the shell is acting to generate the geomagnetic field even it is under some conditions of a high temperature and a high pressure always steadily.

8. EXPECTED PATH

Consider that the north pole is in the tropical zone, first, just neighbor the equator in the northern hemisphere in the geographical frame work following the specific path for the sun spot starting the lower latitude neighbor the equator and moves on the north pole to the polar zone in a time of seven years on the surface of the planet sun. Similarly let us consider that the polar position of geomagnetic field moves from a certain position of lower latitude just neighbor the northern hemisphere to the magnetic north pole in the polar zone just neighbor the geographic north pole in a geological time of 700 million years. A schematic illustration could be shown for helping what path might be possible. In Figure 1, an expected geomagnetic polar drifting path. Tracking of this path, it could be seen when a specific zone was just neighbor the geomagnetic pole projected on the geographic frame work. Figure 2 might help what patter could be assumed for the purpose in this work. The author tends to consider the interested process as geomagnetic polar drift in a trend but polar wondering without at random. Nevertheless, the author would insist what should be right.

9. MERIDIONAL SPEED FROM TROPICAL ZONE TO ARCTIC ZONE

For a convenience, assuming the geomagnetic pole drifting path is starting at a point on a latitude of 20° north and terminate at a geomagnetic pole on a latitude of 70° north in the northern

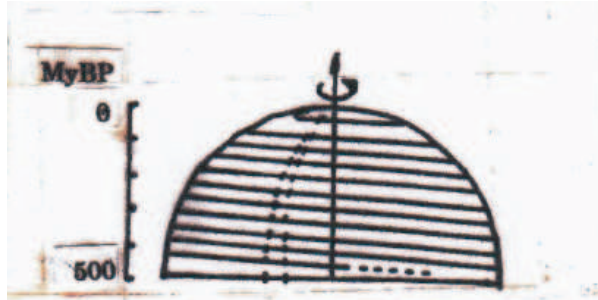


Figure 1: Geophysical polar drifting schematically illustrated for the geographic northern hemisphere during the time period for 500 million years before present (or 500 My BP).

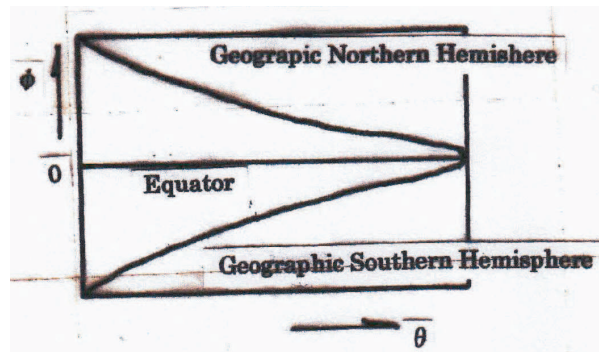


Figure 2: Geomagnetic polar drifting. Speed of the drifting on the path when the earth's rotation should be also taken to be account of consideration.

hemisphere, an approximate meridional speed to the north could be evaluated as 50 degree along a meridional line, for example, in 500 million years. That is, numeral a primitive evaluation gives that speed can be taken for 500 km (5×10^5 km) during 5×10^8 years, then, the interested speed is in an order of 10^{-3} meter per year (or an order of one mm per year). That is, the amount of the path shift is one cm per ten year on the earth surface. This amount of the path shift from south to north might be hard to distinguish out of the other displacements appeared after the other dynamical effects. This small numeral speed might had never considered in the ages of the geological dawn, then, the scientists in the fields of geology and the related scientific fields had taken it negligible for a long time.

10. CONCLUSIONS

The author introduced a possible dynamical process for the polar drifting path evolution under several assumptions. This looks as if it were so simple that no one of the scientists takes it to be important. In the age of rock magnetism about sixty or seventy year ago, the geomagnetic drifting was called as “geomagnetic polar wondering” which faintly suggesting it as that were irregular variations. Now, the author believes that it was not wondering with any effect out of the scientific factors and it should be much better to call as “geophysical drifting” on the bases of the scientific data, rather than “geophysical wondering” which suggests no scientific evaluation had been given.

REFERENCES

1. Nagata, T., *Rock Magnetism*, 350, Maruzen Publisher, Tokyo, 1961.
2. Rikitake, T., *Geo-Electromagnetism*, 354, Iwanami Publisher, Tokyo, 1972.
3. Stix, M., *The Sun*, 390, Springer-Verlag, Berlin, 1989.

Electromagnetic Process at a Crustal Fault Formation for Tsunami Earthquake on the Planet Earth

Shigehisa Nakamura
Kyoto University, Japan

Abstract— This work concerns to an electromagnetic process at a crustal fault as a seismic tsunami generation. Special references are the data of satellite monitoring, and of geophysical process at a specific tsunami earthquake. The data shows that the pattern of the earth surface displacement is quite similar to a water flow pattern out of a reservoir through a conduit in a hydraulic field. This fact tells us that the earth surface displacement pattern indicates the crust is in motion pointing to an epicenter of the earthquake for forcing the crust driven by the magma under the crust. This process might be consistent to induce an impulsive impact in the ionospheric layers just above the seismic epicenter.

1. INTRODUCTION

The author introduces his recent work which concerns to an electromagnetic process at a crustal fault as a seismic tsunami generation. Special references are the data of satellite monitoring, and of geophysical process at a specific tsunami earthquake. The data shows that the pattern of the earth surface displacement is quite similar to a water flow pattern out of a reservoir through a conduit or an orifice in a hydraulic field. This fact tells us that that the earth surface displacement pattern indicates the crust is in motion pointing to an epicenter of the earthquake for forcing the crust driven by the magma under the crust. This process might be consistent to induce an impulsive impact in the ionosphere just above the seismic epicenter. This could be named as an ionospheric tsunami earthquake.

2. DATA SOURCE

In this work, the author takes his reference out of the data obtained by the satellite monitoring, and of geophysical process at a specific tsunami earthquake.

Special reference is that obtained at the seismic event occurred on 11 March 2011. There are already many research works in a various form of publications. Though, the author would not introduce these publications in this work.

3. EARTH SURFACE DISPLACEMENT

The earth surface displacement pattern at the seismic event on 11 March 2011 was issued by the National Geographic Survey Institute after processing the satellite data. The reduced result shows that the pattern of the earth surface displacement is quite similar to the water outflow pattern around a conduit in the hydraulic field.

This must be a crustal motion under the earth surface driven by a certain active magma's global motion. Then, the crust motion should be forced to act as an elastic plate. When the forcing to the crust increases to get to the yield zone, it should be considered as a creeping process of an elasto-plastic material in a three-dimensional problem.

When the earth surface displacement gets to a point, the material of the crust should be in the phase of breaking. That is, the initial phase of the fault formation of the crust. Then, the seismic fault is started to grow.

Nevertheless, the seismologists have only a measure for specifying seismic event as earthquake on land by introducing a set of seismic parameters. Though these parameter are defined in a scope of phenomenological aspect so that any energetics could not be considered for the parameters.

Now, the author has to notice that the set of the seismic parameters for any one of the past tsunamis should not be applied as a set of the tsunami source without any consideration for energy transfer mechanism from the crust as the solid phase to the sea water layer as the liquid phase.

4. ELECTRIC POTENTIAL

Following to the above noted process of the earth surface displacement pointing the epicenter of the earthquake, the electric field pattern on the earth surface should be has never learned about such a process of any transitional electric field.

It must be possible to consider the maximum of the electric potential is just at the point of the epicenter of the interested earthquake if the pattern of the earth surface displacement corresponds to the pattern of the electric density variation.

Some piezoelectric effect must be also considered as one of the minor factors.

In the cases of our human daily life, the electric field of the earth surface is not considered important factor. Only the cases of thunder storm, it is necessary to escape from any destructive and harmful event at the electric discharge.

In this work, the author simply demonstrates that a maximum of the electronic potential is possible at the seismic epicenter.

5. ENERGY SOURCE

Now, let us consider about the energy source for the earth surface displacement and electric potential disturbance.

Generally, it has been to be rational to consider that the magma motion is effective to the present status of the crusts covering the planet earth.

As far as the author concern, the magnetic north pole (Mp) considered to be at the location at the north Siberia. An inclination of the magnetic north pole relative to the rotation axis of the planet earth must be taken into account of consideration.

On 14 April 2010, one of the subglacial volcanoes erupted in Iceland. This affected the human activities in the European area. The volcano is active yet but the magma at the volcano has been rocked so that never comes out to the ground surface. In 2011, several minor eruptions were seen at the other volcano in the Iceland.

6. PATH OF ENERGY TRANSFER

The author tend to easily consider that the magma at the volcanoes in Iceland released its enormous amount of energy by this time though the rest of its energy must be transferred on a path on the large circle to get to the east boundary of the Eurasian plate. Then, the magma transferred under the crust up to the Japan main land acted as a conduit just neighbor the east boundary of the Eurasian plate at the seismic event. That is, to say, the high energy of the magma at Iceland located on the Atlantic mid-ocean ridge must be possibly the energy source of the seismic event off the east coast of the Japan main island.

When the magma gets to a point area where is take as a target to concentrate to act a crust motion of elastic body, the force around the concentrating area the motion must be not to follow to Hook's law for a elastic property for the material of the crust, then, the interested elastic process shifts to a creeping process. As a final stage, it could be seen a start of breaking at the concentrating point area. This point area could be an epicenter of a seismic fault formation.

Then, it must be possibly seen boldly that the path of the magma motion along a latitudinal line and the referring earth magnetic meridian crosses rectangular in angle as an approximation.

Then, a motion of magma is effective to pull down in the point area of the crust, a fault is formed along a magnetic meridional line to pass the interested point area. In this case, a seismic fault as called "Normal Fault" must be the formed fault. The fault can be spread depending on the impulse-forcing effect at releasing to exhaust energy effective to the fault formation in the crust.

Motion of an impulsive magma push up in the point area of the crust, another fault formation process should be seen, i.e., a seismic fault as called "Reversal Fault".

It should be an advanced research on yielding and breaking process of elastic material as an equivalent material for realizing the earth surface displacement pattern just around the point area. This may be effective to have a more reasonable seismic model for a tsunami earthquake.

7. RESPONSE OF IONOSPHERE

As seen above, the electric field seems to reacted to form a pattern of convergent electric field in the author's assumption.

It must be fortunate that it was informed that a response of ionosphere to the seismic shock has been found. That is, a monitoring system of the Radio Communication Research Organization had cached some systematic disturbances at the time of the interested seismic event. It was reported that the observed disturbances in the ionosphere just above the were propagated radially to form a set of growing circles.

The increase of the maximum electric potential on the earth surface at the seismic event must be trigger of the disturbance in the ionosphere. The disturbance must surely be detected in the E layer and successively in the F_1 and F_2 layers.

When the peak of the electric potential is satisfies to discharge or release its energy, a lightning should be seen.

In our understanding of the lightning between the cloud (Cumulus) and the ground surface, a lightning originated at the bottom of the cloud to grow branching to get to the ground in an order of 10^{-3} sec as written by Schonland in the mid of the twentieth century. It is understood that the lightning is appears repeatedly so that our eye watch impression is a certain width of the lightning path though the path is not a straight line boldly.

8. IMPACT TO IONOSPHERE

The author noted above a response of ionosphere after an seismic fault formation with some consideration of the atmospheric layers covering the planet earth.

Assuming a process of a fault formation at a tsunami earthquake, the pattern of the earth surface displacement on land and undersea just around the interested epicenter, i.e., an empirical formula of a seismic disturbance R is described as follow,

$$R = \sum_{i=1}^N R_i(t) \exp[i(\mathbf{k}_i \mathbf{r}_i - f_i t)], \quad (1)$$

where, the notations of \mathbf{k}_i and \mathbf{f}_i are wave number and frequency in a space (\mathbf{r}, t) with the considering radial coordinate $\mathbf{r}(\mathbf{r}, \theta, \phi)$ in a time scale “ \mathbf{t} ”, for convenience. It should be strictly distinguished the suffix “ i ” from the mathematical term for the reaction of $i^2 = -1$.

The fault formation is a continuous process to form a discontinuous gap stretching from the epicenter to both sides for infinity on a fault line. This process is a release of an energy release on the earth crust out of the material in a solid state into the ocean water layer in a liquid phase and into the atmospheric layer in a phase of gas on the planet earth. The other expression of R described in (1) can be shown as follow, i.e.,

$$R = \int_0^t R_0(t) \exp[i(\mathbf{k}\mathbf{r} - ft)] d\mathbf{r} dt \quad (2)$$

Then, the released energy should be transferred in a mechanical energy for tsunamis and in an electromagnetic energy for induce disturbances in the ionospheres. Some ionization process of the gas molecules in the atmosphere must be found generally above the convection zone or at the altitude in the thermosphere or the much higher altitudes.

In the ionosphere just above the epicenter, the energy transferred from the earth surface gives an energetic impact to the ionosphere, for example, to the E layer.

In this work, the origin must be taken as a point for the convergence pattern of the earth surface displacement just around the epicenter. This suggests that a typical energy transfer from epicenter to the ionosphere must be seen along the vertical axis upward.

There must be induced a resonant response to the energetic impact. This response E can be described as shown below, i.e.,

$$E = \delta(k - k_0) \int_0^t E_0(t) \exp[i(\mathbf{k}\mathbf{r} - ft)] d\mathbf{r} dt. \quad (3)$$

The delta function in mathematics is introduced for a demonstration for a specific resonant mode induced in the interested ionosphere. That is,

$$\delta(x) = 1 \quad \text{for } x = 0, \quad \text{and,} \quad \delta(x) = 0 \quad \text{for } x \text{ as all of real numerals} \quad (4)$$

This expression of E in (3) must be well expected even when looking at the author’s experiment in relation to “Richtensbergsche Figuren” which is noted as in the next section, a phenomenological pattern is found to be similar to each other in a case of seismic fault formation in a process of energy transfer in a global scale and in a case of lightning at a high voltage as a high electric potential induced by an induction motor for an indoor experiment.

9. RICHTENBERGSCHE FIGUREN

What disturbance in the ionosphere monitored should be realized at present status of the knowledge in the fields of electromagnetics.

When the response of the ionosphere is an induction process of static electricity, the lightning could show a set of ring form disturbances in the layer.

Once, the author has had a chance to use an induction motor to produce several thousand volts or about a thousand volt for his purpose in order to see a specific pattern of electric discharge.

In 1957, Schonland had already published his photographic shots of the lightning patterns in every 4000 frame per a second in his text. In 1950s, Yuiti Tamura had had to promote an application of his model of lightning in Kyoto University.

An instrument was arranged to place a sheet of glass plate (ca20 cm square) 3 mm thick as an isolator between the pole tip (about 10 cm spacing). The glass surface was held to be horizontal. In the center part of the glass, a bit of mixed powders is set in a form of a small mound. Two kinds of the powders were used, i.e., the one is that of sulphur (S) and cinnabar (HgS) in this case. When the induced electric voltage is set to be 3000 volt between the two pole tips, lightning for releasing electric potential energy is performed.

A lightning for a short time less than 1 second is in a condition of voltage rate $3000/0.3$, i.e., 10^4 V/m. Then, the mixture of the two powders are separated, and each one of the powders showed different in their electric response to the lightning after a high voltage induced by the induction motor, i.e., a concentric reciprocally collared ring pattern by yellow and red powders around the pole tip position as the center point of the glass surface.

This ring pattern is obtained during the author's indoor experiment in 1952 to 1953 after introduction of "Richtenbergsche Figuren" by Dr. Takafusa Yoshida for about ten years since 1936. The author found the term of the "Richtenbergsche Figuren" in an Encyclopaedia in 1954 April though no details of any reference could not found even in the Electric Engineering School of Kyoto University.

10. SPLITE

It is informed that some of the astronauts reported about a lightning (called as "a splite") from the ground surface upward to the space. The splites has been observed at the eye-watch counting through the window of the space shuttle by the several astronauts.

Then, assuming the similar procedure for some conditions, it could be estimated well the splites must be appears when the electric potential difference between the ground surface and the E layer (altitude — 100 km) is, say, beyond 10^8 Volt under a bold assumption.

The scientists have had confirmed several splites which radiate a bright lightning shot at the ionization of the particles in a visible color band at altitude of 13 km. The brightness of the splites dissipates after the energy loss in the process of ionization.

It is sure that each of the splites must act a specific performance at the electric energy releases on the earth surface to the space even after aircraft monitoring of them through the ionospheric layers covering the atmospheric layers on the planet earth.

11. CONCLUSIONS

The author introduced his work concerning to electromagnetic process at a crustal fault as a seismic trigger of tsunami generation on the planet earth. Reference data were obtained by processing satellite monitoring signals. Pattern of the earth surface displacement for a specific case of the earthquake is noted in relation to seismic fault formation.

Electric potential disturbance is noted in relation to the monitored earth surface displacement at the seismic event. Energy source of the earthquake about the magnetic north pole of the planet earth is noted in relation to a volcanic activity on the Atlantic ocean-ridge. The energy transfer process is also noted in brief. Response of the ionosphere just above the seismic epicenter is noted with some consideration of electric energy release. A brief note is given about an indoor experiment of lightning as an electric discharge at a high electric voltage induced by an induction motor as a similar response can be seen though this fact was consistent to what noted before 1900 as "Richtenbergsche Figuren".

Scattering of Light from Rough Surfaces, the Limits of Validity of Geometric Optics Approximation Method

Imed Sassi and Mehdi Khemiri

Laboratory of Physico-chemical of Materials, Faculty of Science of Monastir
University of Monastir, Monastir, Tunisie

Abstract— The geometric optics approximation (GOA) for predicting wave scattering from rough surfaces is developed. The GOA consists of ray tracing the energy incident on a rough surface until it leaves the surface after having incurred multiple rebounds. The effects of the direction of incident light and optical properties of rough surfaces on the scattering and the backscattering of light are presented. For one-dimensional rough surfaces, the GOA is quantified by comparisons with the exact electromagnetic theory calculations. Shadowing affects and the multiple scattering are studied for Gaussian random rough surfaces. The regions of validity of the approximation method for *TE* and *TM* polarization are quantified. For dielectric rough surfaces, the integral method (IM) is used to determine the domains of validity of the GOA. Using that method represents a significant reduction in computational time and memory.

1. INTRODUCTION

The analytical approaches have considered both rigorous electromagnetic theory method and approximate models. Rigorous electromagnetic theory methods provides exact solutions without any restriction. Scattering of light by randomly rough surfaces is a multiple scattering problem. The Kirchhoff approximation (KA) and the first order perturbation solution account only for simple scattering. Therefore their domain of validity is restricted to small slopes. The geometric optics approximation (GOA) solution account for multiple scattering, and used for any rough surfaces. In this approach the energy incident on a rough surface is traced through multiple interactions with the surface until it leaves the surface, and Fresnel reflection is applied to each local point of interaction. The integral method (IM) has the advantages that it puts no restrictions on the surface roughness, optical constants of surface materials, incident angles and incident wavelength and shadowing are takes into consideration.

In this work, the influences of incident angle, the optical properties and the nature of polarization to reflectivity of random rough dielectric surfaces are presented. Our goal is to determine the domains of validity of GOA method for reflection. Therefore comparisons between GOA and IM solutions are quantified. We consider a one-dimensional Gaussian random rough surface characterized by the Gaussian distribution of heights [1, 2]. The surface is characterized by the correlation length and the rms deviation. The directional reflectivity from a material surface is the radiation property of interest. The regions of validity of the approximate method for one-dimensional dielectric surfaces are quantified by comparison with the integral method.

2. SURFACE REFLECTION FROM THE INTEGRAL METHOD

The incident field is:

$$U^{(inc)}(x, z) = \exp(i(\alpha_0 x - \beta_0 z)), \quad (1)$$

where: $\alpha_0 = k_0 \sin \theta_0$, $\beta_0 = (k_0^2 - \alpha_0^2)^{1/2}$ and $k_0 = 2\pi/\lambda$.

The total field y component is a solution of Helmholtz wave equations:

- in air (or vacuum) zone,

$$\nabla^2 U^{(1)}(x, z) + k_0^2 U^{(1)}(x, z) = 0, \quad z > h(x), \quad (2a)$$

- in the metal zone,

$$\nabla^2 U^{(2)}(x, z) + k_0^2 \varepsilon(\omega) U^{(2)}(x, z) = 0, \quad z < h(x), \quad (2b)$$

By the use of Green's second theorem and boundary conditions we can derive the integral equations for the scattered electromagnetic field. This field is expressed in terms of the unknown field and its normal derivative (source functions).

From integral equations giving a field at any point $M(x, z)$, one can obtain a pair of coupled integral equations for the source functions $H(x)$ and $L(x)$ for TM polarization case and the source functions $E(x)$ and $F(x)$ for TE polarization:

A numerical method used to solve these equations, as described in references [3, 4], consists in converting the infinite systems of integral equations into two a finite systems of linear equations as follows [1, 2].

In this subsection we define the surface radiative properties in both cases TE and TM polarization. Using the Poynting theorem relation [3, 4], the bi-directional reflection function is expressed as:

$$\rho''_{\lambda}(\theta_0, \theta_r) = \frac{\pi}{\cos \theta_r} \frac{d\Phi_r}{d\Omega_r}, \quad (3)$$

where Φ and Ω are the radiant power flow and solid angle, and the subscripts 0 and r denote incident and reflected respectively.

The directional hemispherical reflectivity is obtained by integrating the bidirectional reflectivity:

$$\rho'^{\square}_{\lambda}(\theta_0) = \int_{-\pi/2}^{\pi/2} \rho''_{\lambda}(\theta_0, \theta_r) \cos \theta_r d\theta_r, \quad (4)$$

3. DESCRIPTION OF THE GEOMETRIC OPTICS APPROXIMATION

We describe in this section the steps used to calculate the reflectivity of the rough surfaces in the geometric optics approximation method. Surface groove is assumed to be locally plane and smooth. This approximation to the electromagnetic theory predictions of surface scattering, traces ray from incidence until it leaves the surface asperities. Elements of analytic geometry and reflection Snell's law are considered to determine the number of local points of impact inside grooves, associated to an incident ray.

An incident monochromatic pencil of parallel rays strikes the surface under the incidence angle θ_0 . We consider N equally spaced points situated on the straight line defined by: $z = h_{\max}(x)$, depending on the geometrical shapes and the roughness of surface. In the most case, the number is equal to 512 for random rough surfaces, increased to 1024 for very rough surfaces. An incident ray from a point of coordinate $x_j = \frac{(2j-N)}{2N} L_x$ includes N_j local reflection points inside relief surface, which L_x is the length of the sample and j is an integer varied from 0 to N (N is the number of the incident rays). The ratio $(1 - \rho'_{\lambda}(\xi_1) \times \rho'_{\lambda}(\xi_2) \times \dots \times \rho'_{\lambda}(\xi_{N_j}))$, represents the power absorbed by the surface, with ξ_i designates the absolute of the local reflection angle and $\rho'_{\lambda}(\xi_i)$ is the directional spectral reflectivity which is determined by using Fresnel formula [2].

The directional hemispherical reflectivity of the surface is expressed as:

$$\rho'^{\square}_{\lambda}(\theta_0) = \frac{1}{N} \sum_{j=1}^N \left(\prod_{i=1}^{i=N_j} \rho'_{\lambda}(\xi_i) \right) \quad (5)$$

4. RESULTS

The radiative property quantified is the directional hemispherical reflectivity. The results about the random rough surfaces are averaged over 200 rough surface profiles, for a dielectric material of refractive index: $n = 1.41$ and 1.43 . The surface profile function $h(x)$ characterized by the correlation length τ and the *rms* deviation σ . From the comparison between IM and GOA solutions, we are able to quantify the limit value of τ/λ that defines the validity of geometric optics approximation (GOA), for a fixed values of σ/λ and θ_{inc} . In order to determine the domains of validity of the GOA, we define the criterion, **Cr**, is the absolute value of the ratio of the difference in the reflectivity calculated by the approximate and by the exact solutions to the reflectivity calculated by the exact solution. If **Cr** is less than a limit criterion Cr_{lim} (equal to 7%) the geometric optics approximation is considered valid.

The GOA is considered valid if the ratio τ/λ is greater than τ_{lim}/λ . In order to investigate how the validity of the approximate method depends on multiple reflection, we introduce the mean square slope $\gamma_{lim} = \sqrt{2}\sigma/\tau_{lim}$ and angle $\beta_{lim} = \arctg(\gamma_{lim})$. Thus, for transverse magnetic polarization the GOA is valid when the mean square slopes of surfaces is less than γ_{lim} . In other

words, these regions of validity are defined by $\beta < \beta_{\text{lim}}$ for the three considered values of σ/λ . The table below resume the results for the two case of polarization:

- Effects of the roughness and the nature of polarization for for the same parameters: $\lambda = 0.6328 \mu\text{m}$, $\theta_{\text{inc}} = 1^\circ$, $n = 1.43$.

σ/λ	$\tau_{\text{lim}}/\lambda$	$\gamma_{\text{lim}}(\text{TM})$	$\beta_{\text{lim}}(\text{TM})$	$\tau_{\text{lim}}/\lambda$	$\gamma_{\text{lim}}(\text{TE})$	$\beta_{\text{lim}}(\text{TE})$
1	28	0.050	2.89	13	0.11	6.21
1.5	46	0.046	2.64	36	0.058	3.37

- Effects of the optical properties for the same parameters: $\lambda = 0.6328 \mu\text{m}$, $\theta_{\text{inc}} = 1^\circ$ and $\sigma/\lambda = 1$.

n	$\tau_{\text{lim}}(\text{TM})$	$\gamma_{\text{lim}}(\text{TM})$	$\beta_{\text{lim}}(\text{TM})$	$\tau_{\text{lim}}(\text{TE})$	$\gamma_{\text{lim}}(\text{TE})$	$\beta_{\text{lim}}(\text{TE})$
1.41	30	0.047	2.69	15	0.094	5.38
1.43	28	0.050	2.89	13	0.108	6.21

5. CONCLUSION

We investigate the influence of the incident angle, the roughness and the dielectric permittivity on the accuracy of the geometric optics approximation. The influence of the multiple scattering and the nature of polarization are studied, in several different situations. The regions of validity of the geometric optics approximation for random rough surfaces are quantified. From the results obtained in this paper, some important conclusions can be drawn concerning the domains of validity of the GOA for reflection:

- The GOA has the ability to predict both specula and diffuse reflection. Using this method causes significant reduction in computational time and memory.
- The domains of validity of the geometric optics approximation for reflection become more extended when the dielectric permittivity of random rough surfaces increases.
- The range of validity of the geometric optics approximation is broader for TE than for TM.
- Using the geometric optics approximation represents a significant reduction in computational time and memory.

REFERENCES

1. Sanchez-Gil, J. A. and M. Nieto-Vesperinas, "Light scattering from random rough dielectric surfaces," *J. Opt. Soc. Am. A*, Vol. 8, 1270–1286, 1991.
2. Sassi, I. and M. S. Sifaoui, "Comparison of geometric optics approximation and integral method for reflection and transmission from microgeometrical dielectric surfaces," *J. Opt. Soc. Am. A*, Vol. 24, 451–462, 2007.
3. Stratton, J. A., *Electromagnetic Theory*, 1st Edition, 23–131, McGraw Hill, New York, 1941.
4. Maradudin, A. A., T. Michel, A. R. McGurn, and E. R. Méndez, "Enhanced scattering of light from a random grating," *Ann. Phys. (NY)*, Vol. 203, 255–307, 1990.

Modulation in the Spectral Degrees of Polarization of Stochastic Electromagnetic Higher-order Bessel-Gauss Pulsed Beams

Weimin Peng, Haixia Wang, and Chaoliang Ding*

College of Physics and Electronic Information, Luoyang Normal University, Luoyang 471022, China

Abstract— Taking the stochastic electromagnetic higher-order Bessel-Gauss pulsed (HBGP) beams as a typical example of stochastic spatially and spectrally partially coherent electromagnetic pulsed beams, the analytical expression for the spectral degree of polarization of stochastic electromagnetic HBGP beams propagating in free space is derived. The modulation of beam order, radial spatial frequency, pulse duration and temporal coherence length on the spectral degree of polarization of electromagnetic HBGP beams is illustrated through numerical calculations.

1. INTRODUCTION

In 2003 Wolf proposed the unified theory of coherence and polarization of stochastic stationary electromagnetic beams [1–3]. Since then, lots of work has been made on the propagation of stochastic stationary electromagnetic beams [4–6]. Some theoretical predictions were confirmed experimentally [7]. On the other hand, statistical optical pulses represent a wide class of partially coherent fields that find numerous applications in areas as diverse as optical imaging and fiber optics [8]. Recently, a scalar model of partially coherent pulses was introduced by Pääkkönen et al. [9]. Lajunen et al. described the coherent-mode representation for partially coherent Gaussian Schell-model scalar pulses [10]. In this paper, we extend the investigation of partially coherent pulses to vector case, and study the changes in the spectral degree of polarization of stochastic electromagnetic HBGP beams propagating in free space.

2. THEORETICAL FORMULATION

In the space-time domain the electric mutual coherence matrix of a stochastic electromagnetic HBGP beams at the source plane $z = 0$ is given by

$$\overleftrightarrow{\Gamma}^0(\rho_1, \rho_2, t_1, t_2) = [\Gamma_{ij}^0(\rho_1, \rho_2, t_1, t_2)] = [\langle E_i^*(\rho_1, t_1) E_j(\rho_2, t_2) \rangle],$$

$$(i = x, y; j = x, y \text{ unless otherwise stated}), \quad (1)$$

where E_i and E_j are components of the electric field $E(\rho, t)$ at the plane $z = 0$, The asterisk denotes the complex conjugate and the angular brackets denote the ensemble average.

To simplify the analysis it is assumed that the electric vector components in the x and y directions are uncorrelated at the plane $z = 0$ [3, 11], i.e.,

$$\Gamma_{ii}^0(\rho_1, \rho_2, t_1, t_2) = A_i J_n(\alpha_i \rho_1) J_n(\alpha_i \rho_2) \exp\left[-\frac{\rho_1^2 + \rho_2^2}{4\sigma^2}\right] \exp[in(\varphi_1 - \varphi_2)]$$

$$\times \exp\left[-\frac{t_1^2 + t_2^2}{2T_0^2} - \frac{(t_1 - t_2)^2}{2T_{ci}^2} + i\omega_0(t_1 - t_2)\right] \quad (2a)$$

$$\Gamma_{xy}^0(\rho_1, \rho_2, t_1, t_2) = \Gamma_{yx}^0(\rho_1, \rho_2, t_1, t_2) = 0, \quad (2b)$$

where n denotes the order of the Bessel function $J_n(\cdot)$ of the first kind α_i is the radial spatial frequency of the i component of the electric vector [12]. ρ_i and φ_i denote radial and azimuthal coordinates of position vector $\rho_i(r_i, \varphi_i)$, respectively. T_0 is the pulse duration and T_{ci} describes the temporal coherence length of the i component of the electric vector. σ denotes the waist of Gaussian beam ω_0 is the carrier frequency.

By using the Fourier-transform

$$W_{ij}^0(\rho_1, \rho_2, \omega_1, \omega_2) = \frac{1}{(2\pi)^2} \int_{-\infty}^{+\infty} \int_{-\infty}^{+\infty} \Gamma_{ij}^0(\rho_1, \rho_2, t_1, t_2) \exp[-i(\omega_1 t_1 - \omega_2 t_2)] dt_1 dt_2, \quad (3)$$

*Corresponding author: Chaoliang Ding (dingchaoliang2006@126.com).

the cross-spectral density matrix at the plane $z = 0$ can be derived and given by

$$\overleftrightarrow{\mathbf{W}}^0(\rho_1, \rho_2, \omega_1, \omega_2) = [\langle W_{ij}^0(\rho_1, \rho_2, \omega_1, \omega_2) \rangle], \quad (4)$$

where

$$W_{ii}^0(\rho_1, \rho_2, \omega_1, \omega_2) = \frac{T_0 A_i}{2\pi \Omega_{0i}} J_n(\alpha_i \rho_1) J_n(\alpha_i \rho_2) \exp\left(-\frac{\rho_1^2 + \rho_2^2}{4\sigma^2}\right) \exp[in(\varphi_1 - \varphi_2)] \\ \times \exp\left[-\frac{(\omega_1 - \omega_0)^2 + (\omega_2 - \omega_0)^2}{2\Omega_{0i}^2}\right] \exp\left[-\frac{(\omega_1 - \omega_2)^2}{2\Omega_{ci}^2}\right], \quad (5a)$$

$$W_{xy}^0(\rho_1, \rho_2, \omega_1, \omega_2) = W_{yx}^0(\rho_1, \rho_2, \omega_1, \omega_2) = 0, \quad (5b)$$

$$\Omega_{0i} = \sqrt{\frac{1}{T_0^2} + \frac{2}{T_{ci}^2}}, \quad (\text{Spectral width of the } i \text{ component of the electric vector}) \quad (6)$$

$$\Omega_{ci} = \frac{T_{ci}}{T_0} \Omega_{0i}. \quad (\text{Spectral coherence width of the } i \text{ component of the electric vector}) \quad (7)$$

The cross-spectral density matrix of stochastic electromagnetic HBGP beams at the plane $z > 0$ in the free-space propagation is expressed as [13]

$$\overleftrightarrow{\mathbf{W}}(\mathbf{r}_1, \mathbf{r}_2, z, \omega_1, \omega_2) = \frac{\omega_1 \omega_2}{4\pi^2 c^2 z^2} \exp[i(\omega_2 - \omega_1)z/c] \iint \overleftrightarrow{\mathbf{W}}^0(\rho_1, \rho_2, \omega_1, \omega_2) \\ \times \exp\left\{\frac{i}{2cz} [\omega_2(\mathbf{r}_2 - \rho_2)^2 - \omega_1(\mathbf{r}_1 - \rho_1)^2]\right\} d^2 \rho_1 d^2 \rho_2, \quad (8)$$

On substituting from Equation (4) into Equation (8), the elements of the cross-spectral density matrix of stochastic electromagnetic HBGP beams at the plane $z > 0$ are given by

$$W_{ii}(\mathbf{r}_1, \mathbf{r}_2, z, \omega_1, \omega_2) = \frac{T_0 A_i \omega_1 \omega_2}{2\pi \Omega_{0i} c^2 z^2} \exp\left[\frac{i(\omega_2 - \omega_1)z}{c}\right] \exp\left[\frac{i}{2cz} (\omega_2 r_2^2 - \omega_1 r_1^2)\right] \exp[in(\theta_1 - \theta_2)] \\ \times \exp\left[-\frac{(\omega_1 - \omega_0)^2 + (\omega_2 - \omega_0)^2}{2\Omega_{0i}^2}\right] \exp\left[-\frac{(\omega_1 - \omega_2)^2}{2\Omega_{ci}^2}\right] \\ \times \frac{1}{\left(\frac{1}{2\sigma^2} + \frac{i\omega_1}{cz}\right)} \times \frac{1}{\left(\frac{1}{2\sigma^2} - \frac{i\omega_2}{cz}\right)} \times \exp\left[-\frac{\alpha_i^2 + \left(\frac{\omega_1 r_1}{cz}\right)^2}{2\left(\frac{1}{2\sigma^2} + \frac{i\omega_1}{cz}\right)}\right] \\ \exp\left[-\frac{\alpha_i^2 + \left(\frac{\omega_2 r_2}{cz}\right)^2}{2\left(\frac{1}{2\sigma^2} - \frac{i\omega_2}{cz}\right)}\right] I_n\left[\frac{\alpha_i \omega_1 r_1}{\frac{1}{2\sigma^2} + \frac{i\omega_1}{cz}}\right] I_n\left[\frac{\alpha_i \omega_2 r_2}{\frac{1}{2\sigma^2} - \frac{i\omega_2}{cz}}\right], \quad (9a)$$

$$W_{xy}(\mathbf{r}_1, \mathbf{r}_2, z, \omega_1, \omega_2) = W_{yx}(\mathbf{r}_1, \mathbf{r}_2, z, \omega_1, \omega_2) = 0, \quad (9b)$$

Thus, the spectral degree of polarization of stochastic electromagnetic HBGP beams at the plane $z > 0$ can be derived by [2]

$$P(\mathbf{r}, z, \omega) = \sqrt{1 - \frac{4\text{Det}[\overleftrightarrow{\mathbf{W}}(\mathbf{r}, \mathbf{r}, z, \omega, \omega)]}{\left\{\text{Tr}[\overleftrightarrow{\mathbf{W}}(\mathbf{r}, \mathbf{r}, z, \omega, \omega)]\right\}^2}} = \left| \frac{W_{xx}(\mathbf{r}, \mathbf{r}, z, \omega, \omega) - W_{yy}(\mathbf{r}, \mathbf{r}, z, \omega, \omega)}{W_{xx}(\mathbf{r}, \mathbf{r}, z, \omega, \omega) + W_{yy}(\mathbf{r}, \mathbf{r}, z, \omega, \omega)} \right|, \quad (10)$$

where

$$W_{ii}(\mathbf{r}, \mathbf{r}, z, \omega, \omega) = \frac{T_0 A_i}{2\pi \Omega_{0i}} \frac{4\sigma^4 \omega^2}{c^2 z^2 + 4\sigma^4 \omega^2} \exp\left[-\frac{(\omega - \omega_0)^2}{\Omega_{0i}^2}\right] \\ \times \exp\left[-\frac{\alpha_i^2 + \left(\frac{\omega r}{cz}\right)^2}{\frac{1}{2\sigma^2} + \frac{2\sigma^2 \omega^2}{c^2 z^2}}\right] I_n\left[\frac{\alpha_i \omega r}{\frac{1}{2\sigma^2} + \frac{i\omega}{cz}}\right] I_n\left[\frac{\alpha_i \omega r}{\frac{1}{2\sigma^2} - \frac{i\omega}{cz}}\right]. \quad (11)$$

Equation (10) is the main analytical results obtained in this paper, which with Equation (11) describe the changes in the spectral degree of polarization of stochastic electromagnetic HBGP beams from the $z = 0$ plane to the z plane in free space z .

3. ILLUSTRATIVE EXAMPLES

Numerical calculation results for stochastic electromagnetic HBGP beams propagating in free space are presented to illustrate the modulation of beam order, radial spatial frequency, pulse duration and temporal coherence length on the spectral degree of polarization of stochastic electromagnetic HBGP beam. The calculations parameters are $\alpha_x = 1 \text{ mm}^{-1}$, $\alpha_y = 2\alpha_x$; $w_0 = 1 \text{ mm}$, $A_y/A_x = 1/2$, $T_0 = 3 \text{ fs}$, $T_{cx} = 5 \text{ fs}$, $T_{cy} = T_{cx}$, $\omega_0 = 4.72 \text{ rad}\cdot\text{fs}^{-1}$, $\omega/\omega_0 = 1$, $r = 0.5 \text{ mm}$. From Figure 1 it can be seen that the minimum of $P(r, z, \omega)$ is zero and the position z of the spectral degree of polarization $P = 0$ increases with increasing beam order.

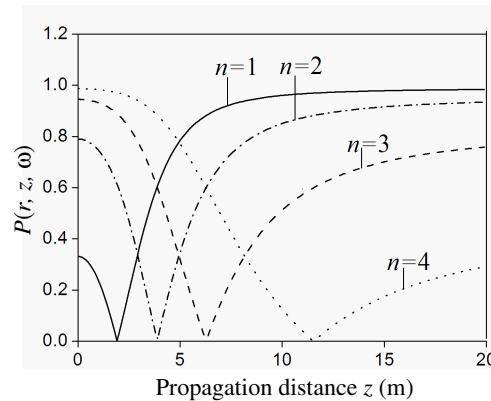


Figure 1: The spectral degree of polarization $P(r, z, \omega)$ versus the propagation distance z .

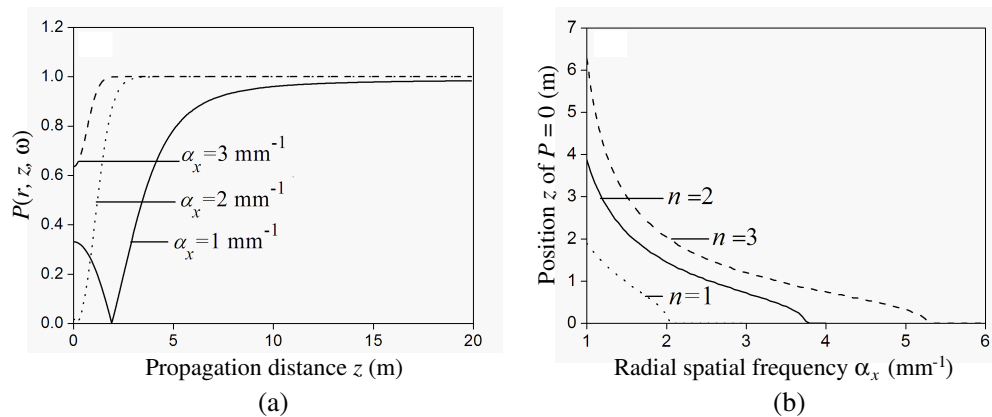


Figure 2: The spectral degree of polarization $P(r, z, \omega)$ versus (a) the propagation distance z , (b) the position z of $P = 0$ versus the radial spatial frequency α_x .

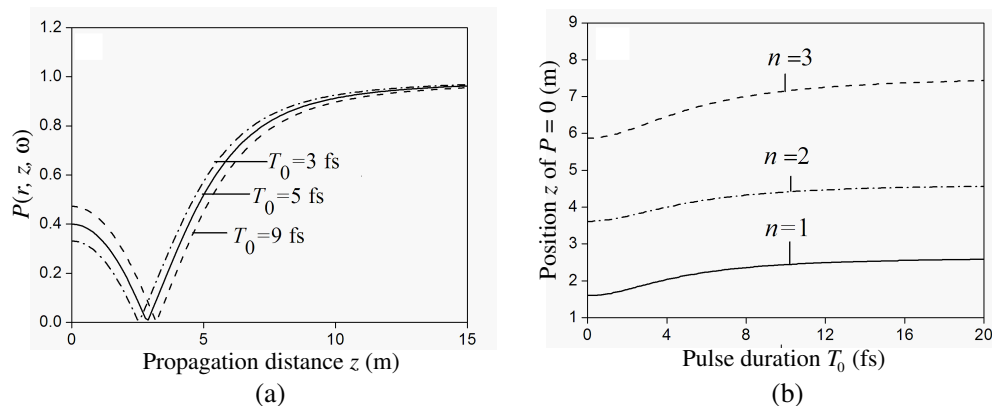


Figure 3: (a) The spectral degree of polarization $P(r, z, \omega)$ versus the propagation distance z , (b) the position z of $P = 0$ versus the pulse duration T_0 .

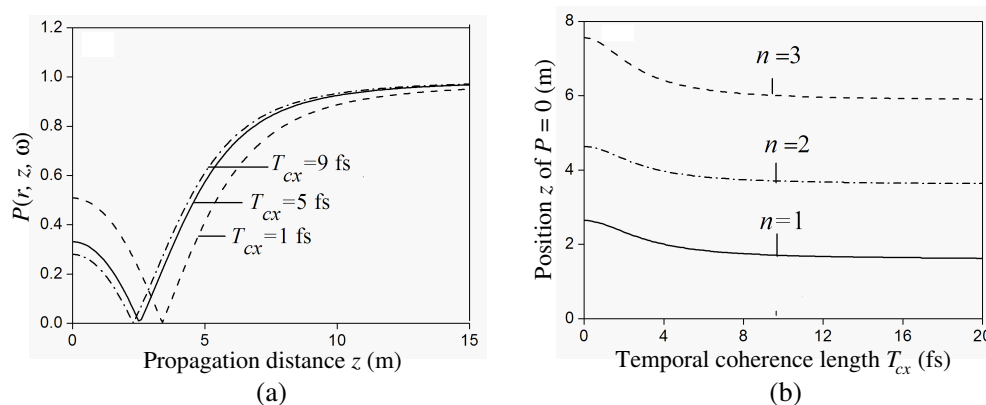


Figure 4: (a) The spectral degree of polarization $P(r, z, \omega)$ versus the propagation distance z , (b) the position z of $P = 0$ versus the temporal coherence length T_{cx} .

Figure 2 gives (a) the spectral degree of polarization $P(r, z, \omega)$ of stochastic electromagnetic HBGP pulsed beams versus the propagation distance z , (b) the position z of $P = 0$ versus the radial spatial frequency α_x . It is seen that the position z of $P = 0$ decrease with increasing radial spatial frequency, and when the radial spatial frequency is large enough, the position z of $P = 0$ disappears.

Figures 3 and 4 give the modulation of pulse duration T_0 and temporal coherence length T_{cx} on the spectral degree of polarization of stochastic electromagnetic HBGP pulsed beams. It can be seen that the position z of $P = 0$ increases with increasing pulse duration T_0 and decreases with increasing the temporal coherence length T_{cx} . Thus, we can modulate the spectral degree of polarization by T_0 and T_{cx} .

4. CONCLUSIONS

In this paper, we derive closed-form analytical expression of the spectral degree of polarization of stochastic electromagnetic HBGP pulsed beams propagating in free space. It has been shown that the position z of the spectral degree of polarization $P = 0$ increases with increasing beam order and pulse duration, whereas it decreases with increasing radial spatial frequency and temporal coherence length, respectively.

ACKNOWLEDGMENT

This work was supported by the National Natural Science Foundation of China under Grant Nos. 61275150, 61108090 and 61078077, and Natural Science Foundation of Henan Province under Grant Nos. 112300410062 and 13A140797.

REFERENCES

1. Wolf, E., "Unified theory of coherence and polarization of random electromagnetic beams," *Phys. Lett. A*, Vol. 312, No. 5–6, 263–267, 2003.
2. Wolf, E., "Correlation-induced changes in the degree of polarization, the degree of coherence, and the spectrum of random electromagnetic beams on propagation," *Opt. Lett.*, Vol. 28, No. 13, 1078–1080, 2003.
3. Wolf, E., *Introduction to the Theory of Coherence and Polarization of Light*, 1st Edition, Cambridge University, Cambridge, 2007.
4. Korotkova, O. and E. Wolf, "Changes in the state of polarization of a random electromagnetic beam on propagation," *Opt. Commun.*, Vol. 246, No. 1–3, 35–43, 2005.
5. Roychowdhury, H., S. A. Ponomarenko, and E. Wolf, "Change in the polarization of partially coherent electromagnetic beams propagating through the turbulent atmosphere," *J. Mod. Opt.*, Vol. 52, No. 11, 1611–1618, 2005.
6. Roychowdhury, H., G. P. Agrawal, and E. Wolf, "Changes in the spectrum, in the spectral degree of polarization, and in the spectral degree of coherence of a partially coherent beam propagating through a gradient-index fiber," *J. Opt. Soc. Am. A*, Vol. 23, No. 4, 940–948, 2006.

7. Roychowdhury, H. and E. Wolf, “Young’s interference experiment with light of any state of coherence and of polarization,” *Opt. Commun.*, Vol. 252, No. 4–6, 268–274, 2005.
8. Agrawal, G. P., *Application of Nonlinear Fiber Optics*, San Diego, Academic Press, 2007.
9. Pääkkönen, P., J. Turunen, P. Vahimaa, A. T. Friberg, and F. Wyrowski, “Partially coherent Gaussian pulses,” *Opt. Commun.*, Vol. 204, No. 1–6, 53–58, 2002.
10. Lajunen, H., P. Vahimaa, and J. Tervo, “Theory of spatially and spectrally partially coherent pulses,” *J. Opt. Soc. Am. A*, Vol. 22, No. 8, 1536–1545, 2005.
11. Korotkova, O., T. D. Visser, and E. Wolf, “Polarization properties of stochastic electromagnetic beams,” *Opt. Commun.*, Vol. 281, No. 4, 515–520, 2008.
12. Paterson, C. and R. Smith, “Higher-order Bessel waves produced by axicon-type computer-generated holograms,” *Opt. Commun.*, Vol. 124, No. 1–2, 121–130, 1996.
13. Mandel, L. and E. Wolf, *Optical Coherence and Quantum Optics*, Cambridge University, Cambridge, 1995.

Weighted Multi-frequency Imaging of Thin, Crack-like Electromagnetic Inhomogeneities

Y.-D. Joh, Y. M. Kwon, J. Y. Huh, and W.-K. Park

Department of Mathematics, Kookmin University, Seoul 136-702, Korea

Abstract— In recent works [4, 12, 14], a Multiple Signal Classification (MUSIC)-type algorithm has been designed and demonstrated to be a useful technique for imaging of thin, crack-like electromagnetic inhomogeneities. Unfortunately, this algorithm offers a result of poor resolution whenever one tried to obtain such inclusion both dielectric and magnetic contrasts with respect to the embedding homogeneous space, an improved multi-frequency based subspace migration has been considered [3, 10, 11, 13]. However, although this technique has been proven to be effective for imaging of such inhomogeneities, owing to its heuristic application, a mathematical study is still required in order to investigate its properties. In this paper, we discuss the structure and properties of existing subspace migration, introduce an improved weighted multi-frequency imaging algorithm, and explore some properties of the proposed algorithm. This is based on the fact that the measured scattered field can be written as an asymptotic expansion formula. Some numerical results are computed in order to demonstrate the feasibility of the proposed algorithm.

1. INTRODUCTION

An interesting topic in the inverse scattering problem is to identify the characteristics of unknown thin, curve-like electromagnetic inhomogeneities or perfectly conducting cracks from the measured scattered field or far-field patterns. Various algorithms for identifying the shape of unknown objects have been suggested in the literature, most of which are based on Newton-type iteration schemes. However, in order to obtain a good result, such a scheme must begin with a good initial guess that is close to the unknown object. To find a good initial guess, alternative non-iterative algorithms have been developed.

Among them, the multi-frequency based subspace migration algorithm has shown good imaging performance (see [7, 8, 10, 11]). However, a mathematical analysis of its structure needs to be performed for its heuristical applications. Motivated by this, the relationship between subspace migrations and Bessel functions of the first kind of the integer order were established in [9]. However, the indefinite integral of the square of the Bessel function of order one cannot be obtained explicitly in multi-frequency based subspace migration. Therefore, in this paper, we introduce a weighted multi-frequency based subspace migration imaging function and analyze its structure carefully.

This paper is organized as follows. In Section 2, we briefly discuss the two-dimensional direct scattering problem and multi-frequency imaging algorithm. In Section 3, we introduce a weighted multi-frequency imaging algorithm and analyze its structure. In Section 4, we present several numerical experiments. Finally, a brief conclusion is given in Section 5.

2. DIRECT SCATTERING PROBLEM AND MULTI-FREQUENCY IMAGING ALGORITHM

Let Γ be a two-dimensional homogeneous thin inclusion with a small thickness $2h$ with $h \ll \lambda$, where λ is a given wavelength:

$$\Gamma = \{\mathbf{x} + \eta \mathbf{n}(\mathbf{x}) : \mathbf{x} \in \sigma, \eta \in (-h, h)\},$$

where $\mathbf{n}(\mathbf{x})$ is the unit normal to σ at x , and σ denotes a simple, smooth curve in \mathbb{R}^2 , which describes the supporting curve of Γ . Throughout this paper, we assume that all materials are characterized by their dielectric permittivities and magnetic permeabilities. ε_0 and ε denote the dielectric permittivity of \mathbb{R}^2 and Γ , respectively, and μ_0 and μ are defined similarly. For the sake of simplicity, we define piecewise constant functions $\varepsilon(\mathbf{x})$ and $\mu(\mathbf{x})$ such that

$$\varepsilon(\mathbf{x}) = \begin{cases} \varepsilon & \text{for } \mathbf{x} \in \Gamma \\ \varepsilon_0 & \text{for } \mathbf{x} \in \mathbb{R}^2 \setminus \bar{\Gamma} \end{cases} \quad \text{and} \quad \mu(\mathbf{x}) = \begin{cases} \mu & \text{for } \mathbf{x} \in \Gamma \\ \mu_0 & \text{for } \mathbf{x} \in \mathbb{R}^2 \setminus \bar{\Gamma}. \end{cases}$$

At a given frequency ω , let $u_{\text{tot}}^{(l)}(\mathbf{x}; \omega)$ be the time-harmonic total field that satisfies the Helmholtz equation

$$\nabla \cdot \left(\frac{1}{\mu(\mathbf{x})} \nabla u_{\text{tot}}^{(l)}(\mathbf{x}; \omega) \right) + \omega^2 \varepsilon(\mathbf{x}) u_{\text{tot}}^{(l)}(\mathbf{x}; \omega) = 0 \quad \text{in } \mathbb{R}^2 \quad (1)$$

with transmission condition on the boundary of Γ . Let $u_{\text{in}}^{(l)}(\mathbf{x}; \omega)$ be the solution of (1) without Γ . Throughout this paper, we consider plane-wave illumination: for a vector $\boldsymbol{\theta}_l \in S^1$, $u_{\text{in}}^{(l)}(\mathbf{x}; \omega) = \exp(j\omega\boldsymbol{\theta}_l \cdot \mathbf{x})$. Here, S^1 denotes a two-dimensional unit circle.

Generally, the total field u_{tot} can be divided into the incident field u_{in} and the unknown scattered field u_{scat} , which satisfies the Sommerfeld radiation condition

$$\lim_{|\mathbf{x}| \rightarrow \infty} \sqrt{|\mathbf{x}|} \left(\frac{\partial u_{\text{scat}}(\mathbf{x}, \omega; l)}{\partial |\mathbf{x}|} - jk_0 u_{\text{scat}}^{(l)}(\mathbf{x}; \omega) \right) = 0, \quad k_0 = \omega\sqrt{\varepsilon_0\mu_0}$$

uniformly in all directions $\hat{\mathbf{x}} = \mathbf{x}/|\mathbf{x}|$.

The far-field pattern is defined as function $u_{\infty}(\hat{\mathbf{x}}, \boldsymbol{\theta}_l)$ that satisfies

$$u_{\text{scat}}(\mathbf{x}, \omega; l) = \frac{\exp(jk_0|\mathbf{x}|)}{\sqrt{|\mathbf{x}|}} u_{\infty}(\hat{\mathbf{x}}, \boldsymbol{\theta}_l) + o\left(\frac{1}{\sqrt{|\mathbf{x}|}}\right) \quad (2)$$

as $|\mathbf{x}| \rightarrow \infty$ uniformly on $\hat{\mathbf{x}}$. The asymptotic formula for the far-field pattern is represented as follows (see [5])

$$u_{\infty}(\hat{\mathbf{x}}, \boldsymbol{\theta}) = h \frac{k_0^2(1+i)}{4\sqrt{k_0\pi}} \int_{\sigma} \left(\frac{\varepsilon - \varepsilon_0}{\sqrt{\varepsilon_0\mu_0}} - \hat{\mathbf{x}} \cdot \mathbf{A}(\mathbf{y}) \cdot \boldsymbol{\theta} \right) e^{ik_0(\boldsymbol{\theta} - \hat{\mathbf{x}}) \cdot \mathbf{y}} d\sigma(\mathbf{y}) + o(h), \quad (3)$$

where $o(h)$ is uniform in $\mathbf{y} \in \sigma$ and $\hat{\mathbf{x}}, \boldsymbol{\theta} \in S^1$ and $\mathbf{A}(\mathbf{y})$ is a symmetric matrix (see [10]).

In [3, 7, 9–11, 13], multi-frequency based subspace migration was developed on the basis of the structure of singular vectors of Multi Static Response (MSR) matrix whose elements are far-fields. However, in the field of statistics, the efficiency of subspace migration is confirmed by on the statistical hypothesis testing, and therefore it cannot be explained on the basis of phenomena such as appearance of unexpected artifacts. Hence, the structure of subspace migration was investigated in [9], and the results are explained as follows. Assume that the thin inclusion is divided into M different segments of size of order half the wavelength $\lambda/2$. Having in mind the Rayleigh resolution limit, any detail less than one-half of the wavelength cannot be identified, and only one point, say \mathbf{y}_m for $m = 1, 2, \dots, M$, at each segment is expected to contribute at the image space of the response matrix $\mathbb{K}(\omega)$, refer to [4, 10–12, 14]. If the incident and observation directions are the same, i.e., $\hat{\mathbf{x}}_p = -\boldsymbol{\theta}_p$, for $p = 1, 2, \dots, R$, then the Singular Value Decomposition (SVD) of matrix $\mathbb{K}(\omega)$ can be represented as follows:

$$\mathbb{K}(\omega) = \left(u_{\infty}(\hat{\mathbf{x}}_p, \boldsymbol{\theta}_q) \right)_{p,q=1}^R = \mathbf{U}(\omega) \mathbf{S}(\omega) \bar{\mathbf{V}}^T(\omega) \approx \sum_{m=1}^M \mathbf{u}_m(\omega) s_m(\omega) \bar{\mathbf{v}}_m^T(\omega),$$

where $s_m(\omega)$ are the singular values, $\mathbf{u}_m(\omega)$ and $\mathbf{v}_m(\omega)$ are the left- and right-singular vectors of \mathbb{K} , respectively, for $m = 1, 2, \dots, M$. Based on the above SVD process, the imaging algorithm is developed as follows. For $c \in \mathbb{R}^3 \setminus \{0\}$, let us define a vector

$$\mathbf{d}(\mathbf{x}; \omega) = \left(c \cdot (1, \boldsymbol{\theta}_1) e^{ik_0\boldsymbol{\theta}_1 \cdot \mathbf{x}}, c \cdot (1, \boldsymbol{\theta}_2) e^{ik_0\boldsymbol{\theta}_2 \cdot \mathbf{x}}, \dots, c \cdot (1, \boldsymbol{\theta}_N) e^{ik_0\boldsymbol{\theta}_N \cdot \mathbf{x}} \right)^T \quad (4)$$

and a corresponding normalized unit vector $\hat{\mathbf{d}}(\mathbf{x}; \omega) = \mathbf{d}(\mathbf{x}; \omega)/|\mathbf{d}(\mathbf{x}; \omega)|$. Then, we can introduce subspace migration as follows (see [9]):

$$\mathbb{W}(\mathbf{x}; \omega) := \left| \sum_{m=1}^M \left(\hat{\mathbf{d}}(\mathbf{y}; \omega)^* \mathbf{u}_m(\omega) \right) \left(\hat{\mathbf{d}}(\mathbf{y}; \omega)^* \bar{\mathbf{v}}_m(\omega) \right) \right| \approx \sum_{m=1}^M J_0^2(\omega|\mathbf{y}_m - \mathbf{x}|). \quad (5)$$

Similarly, multi-frequency based subspace migration $\mathbb{W}(\mathbf{x}; \omega_N, \omega_1)$ is (see [9]) given as

$$\mathbb{W}(\mathbf{x}; \omega_N, \omega_1) \sim \frac{1}{N} \sum_{m=1}^M \left(\mathbf{\Pi}(\mathbf{x}; \omega_N) - \mathbf{\Pi}(\mathbf{x}; \omega_1) + \int_{\omega_1}^{\omega_N} J_1(\omega|\mathbf{y}_m - \mathbf{x}|) d\omega \right), \quad (6)$$

where

$$\mathbf{\Pi}(\mathbf{x}; \omega) = \frac{\omega}{\omega_N - \omega_1} \left(J_0^2(\omega|\mathbf{y}_m - \mathbf{x}|) + J_1^2(\omega|\mathbf{y}_m - \mathbf{x}|) \right).$$

Unfortunately, there is no finite representation of $\int J_1^2(x)dx$. Because of this term, the map of $\mathbb{W}(\mathbf{x}; \omega_N, \omega_1)$ should generate some afterimage. In order to overcome this problem by eliminating the last term of (6), we propose a weighted multi-frequency imaging algorithm in the next section.

3. WEIGHTED MULTI-FREQUENCY IMAGING ALGORITHM AND ITS STRUCTURE

To design a weighted multi-frequency imaging algorithm, we multiply (5) by each frequency ω_n . Then for a weighted multi-frequency case, the imaging function $\mathbb{W}_{\text{weight}}(\mathbf{x}; \omega_N, \omega_1)$ becomes

$$\begin{aligned} \mathbb{W}_{\text{weight}}(\mathbf{x}; \omega_N, \omega_1) &\approx \frac{1}{N} \left| \sum_{m=1}^M \omega_n \left(\hat{\mathbf{d}}(\mathbf{y}; \omega_n)^* \mathbf{u}_m(\omega) \right) \left(\hat{\mathbf{d}}(\mathbf{y}; \omega_n)^* \bar{\mathbf{v}}_m(\omega) \right) \right| \\ &\approx \frac{1}{\omega_N - \omega_1} \left| \sum_{m=1}^M \int_{\omega_1}^{\omega_N} \omega J_0^2(\omega|\mathbf{y}_m - \mathbf{x}|) d\omega \right|. \end{aligned}$$

Since the following indefinite integral holds (see [1])

$$\int \omega J_0^2(x) = \frac{\omega^2}{2} \left(J_0^2(x) + J_1^2(x) \right), \quad (7)$$

by switching to $\omega|\mathbf{y}_m - \mathbf{x}| = u$, we have

$$\begin{aligned} &\int_{\omega_1}^{\omega_N} \omega J_0^2(\omega|\mathbf{y}_m - \mathbf{x}|) d\omega = \frac{1}{|\mathbf{y}_m - \mathbf{x}|^2} \int_{\omega_1|\mathbf{y}_m - \mathbf{x}|}^{\omega_N|\mathbf{y}_m - \mathbf{x}|} u J_0^2(u) du \\ &= \frac{1}{2|\mathbf{y}_m - \mathbf{x}|^2} \left[\omega_N^2 |\mathbf{y}_m - \mathbf{x}|^2 \left(J_0^2(\omega_N|\mathbf{y}_m - \mathbf{x}|) + J_1^2(\omega_N|\mathbf{y}_m - \mathbf{x}|) \right) \right. \\ &\quad \left. - \omega_1^2 |\mathbf{y}_m - \mathbf{x}|^2 \left(J_0^2(\omega_1|\mathbf{y}_m - \mathbf{x}|) + J_1^2(\omega_1|\mathbf{y}_m - \mathbf{x}|) \right) \right] \\ &= \frac{1}{2} \left\{ \omega_N^2 \left(J_0^2(\omega_N|\mathbf{y}_m - \mathbf{x}|) + J_1^2(\omega_N|\mathbf{y}_m - \mathbf{x}|) \right) - \omega_1^2 \left(J_0^2(\omega_1|\mathbf{y}_m - \mathbf{x}|) + J_1^2(\omega_1|\mathbf{y}_m - \mathbf{x}|) \right) \right\}. \end{aligned}$$

Thus, in contrast to (6), the term $\int J_1^2(x)dx$ is eliminated and thus $\mathbb{W}_{\text{weight}}(\mathbf{x}; \omega_N, \omega_1)$ improves (6). Therefore, weighted subspace migration is of the form:

$$\mathbb{W}_{\text{weight}}(\mathbf{x}; \omega_N, \omega_1) = \sum_{m=1}^M \left(\mathbf{\Pi}(\mathbf{x}; \omega_N) - \mathbf{\Pi}(\mathbf{x}; \omega_1) \right) \quad (8)$$

where

$$\mathbf{\Pi}(\mathbf{x}; \omega) = \frac{\omega^2}{2(\omega_N - \omega_1)} \left(J_0^2(\omega|\mathbf{y}_m - \mathbf{x}|) + J_1^2(\omega|\mathbf{y}_m - \mathbf{x}|) \right).$$

4. NUMERICAL EXAMPLES

In this section, some numerical examples are shown in order to support our analysis in the previous section. For this purpose, two σ_i characteristics of thin inclusions Γ_i are chosen for illustration:

$$\begin{aligned} \sigma_1 &= \{ (z - 0.2, -0.5z^2 + 0.4) : z \in [-0.5, 0.5] \} \\ \sigma_2 &= \{ (z + 0.2, z^3 + z^2 - 0.5) : z \in [-0.5, 0.5] \}. \end{aligned}$$

Throughout this section, ε_i and μ_i denote the permittivities and permeabilities of Γ_i , respectively. The thickness h of Γ_i is set to 0.015, and parameters ε_0 and μ_0 are chosen as 1. The applied frequency is $\omega_n = \frac{2\pi}{\lambda_n}$; here λ_n , $n = 1, 2, \dots, 20$, is the given wavelength. In this paper, λ_n 's are

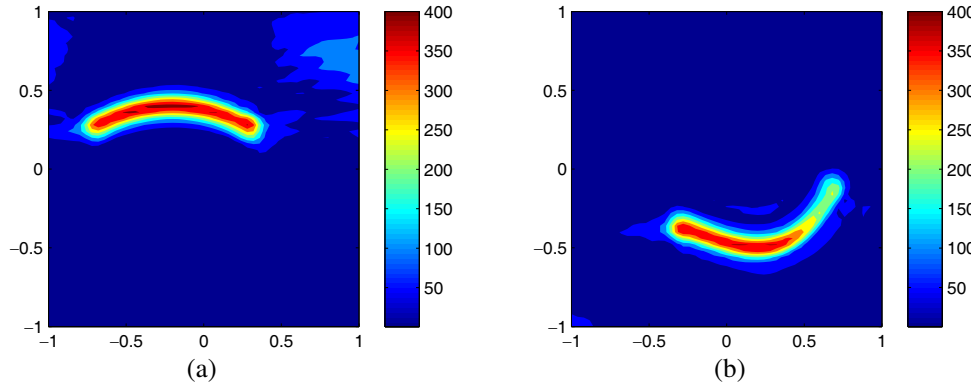


Figure 1: Imaging results via weighted subspace migration. (a) Shape of Γ_1 . (b) Shape of Γ_2 .

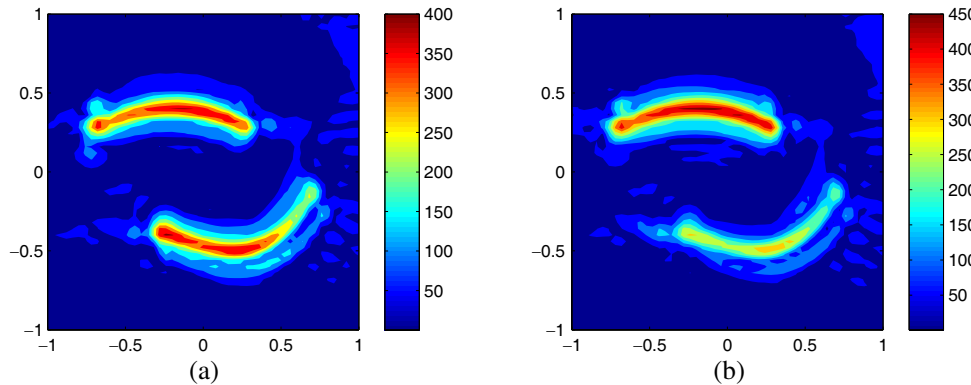


Figure 2: Imaging results via weighted subspace migration. Shapes of $\Gamma_1 \cup \Gamma_2$ (a) with the same material property and (b) with different material properties.

equi-distributed within the interval $[\lambda_{20}, \lambda_1] = [0.2, 0.5]$. Next, the illumination and observation directions $\boldsymbol{\theta}_l \in S^1$ they are selected as

$$\boldsymbol{\theta}_l = \left(\cos \frac{2\pi l}{L}, \sin \frac{2\pi l}{L} \right) \quad \text{for } l = 1, 2, \dots, L.$$

The data set of the MSR matrix \mathcal{K} is generated by the Finite Element Method (FEM) via a very fine meshes. Then, a white Gaussian random noise with 20 dB signal-to-noise ratio (SNR) is added to the unperturbed data in order to show the robustness.

Figure 1 shows the maps of $\mathbb{W}_{\text{weight}}(\mathbf{x}; \omega_N, \omega_1)$ for Γ_1 and Γ_2 . As expected in the previous section, the shape of the thin inclusions are clearly identified, and unexpected afterimages are successfully eliminated in comparison with the results in [10, 13]. Note that the proposed algorithm can be directly applied to the imaging of multiple inclusions. In Figure 2, maps of $\mathbb{W}_{\text{weight}}(\mathbf{x}; \omega_N, \omega_1)$ for $\Gamma_1 \cup \Gamma_2$ are illustrated. It is interesting to observe that although the shapes of Γ_1 and Γ_2 are identified, some afterimages are still observed. Moreover, when even the values of ε_i and μ_i are different to each other (in this section, we set $\varepsilon_1 = \mu_1 = 10$ and $\varepsilon_2 = \mu_2 = 5$), afterimages are not eliminated significantly.

5. CONCLUSION

In this contribution, we consider the multi-frequency based subspace migration by multiplying the applied frequency with the subspace migration. In order to identify the structure of the proposed imaging function, we investigated its relationship with the Bessel function of integer order of the first kind, and explained how the proposed imaging function eliminates unexpected artifacts. The presented results show that proposed algorithm works well for imaging of thin penetrable electromagnetic inclusions and successfully improves the traditional subspace migration. Note that the results obtained in this paper do not guarantee the true shape of thin inclusions. Fortunately, they can be a good initial guess of an iteration-based algorithm such as level-set evolution [2, 6, 15].

In this paper, we considered imaging in the presence of random noise. Analysis of the imaging function in the presence of random scatterers will be an interesting subject. Finally, it is expected that the present approach will be applicable to the case of supporting surfaces in the full three-dimensional framework of vector scattering, instead of the simple curves in this contribution and scalar scattering, which requires further numerical experimentation.

ACKNOWLEDGMENT

This work was supported by the Basic Science Research Program through the National Research Foundation of Korea (NRF) funded by the Ministry of Education, Science and Technology (No. 2012-0003207), and the research program of Kookmin University in Korea.

REFERENCES

1. Abramowitz, M. and I. A. Stegun, *Handbook of Mathematical Functions with Formulas, Graphs, and Mathematical Tables*, Dover, New York, 1996.
2. Álvarez, D., O. Dorn, N. Irishina, and M. Moscoso, “Crack reconstruction using a level-set strategy,” *J. Comput. Phys.*, Vol. 228, 5710–5721, 2009.
3. Ammari, H., J. Garnier, H. Kang, W.-K. Park, and K. Sølna, “Imaging schemes for perfectly conducting cracks,” *SIAM J. Appl. Math.*, Vol. 71, 68–91, 2011.
4. Ammari, H., H. Kang, H. Lee, and W.-K. Park, “Asymptotic imaging of perfectly conducting cracks,” *SIAM J. Sci. Comput.*, Vol. 32, 894–922, 2010.
5. Beretta, E. and E. Francini, “Asymptotic formulas for perturbations of the electromagnetic fields in the presence of thin imperfections,” *Contemp. Math.*, Vol. 333, 49–63, 2003.
6. Dorn, O. and D. Lesselier, “Level set methods for inverse scattering,” *Inverse Problems*, Vol. 22, R67–R131, 2006.
7. Griesmaier, R., “Multi-frequency orthogonality sampling for inverse obstacle scattering problems,” *Inverse Problems*, Vol. 27, 085005, 2011.
8. Huh, J. Y., Y. M. Kwon, Y.-D. Joh, and W.-K. Park, “Multi-frequency imaging of small electromagnetic inclusions via limited-view near-field data,” *Proceedings of the 5th International Congress on Image and Signal Processing*, 2465–2458, Chongqing, China, Oct. 2012.
9. Joh, Y.-D., Y. M. Kwon, J. Y. Huh, and W.-K. Park, “Structure analysis of single- and multifrequency subspace migrations in inverse scattering problems,” *Progress In Electromagnetics Research*, Vol. 136, 607–622, 2013.
10. Park, W.-K., “Non-iterative imaging of thin electromagnetic inclusions from multi-frequency response matrix,” *Progress In Electromagnetics Research*, Vol. 106, 225–241, 2010.
11. Park, W.-K., “On the imaging of thin dielectric inclusions via topological derivative concept,” *Progress In Electromagnetic Research*, Vol. 110, 237–252, 2010.
12. Park, W.-K. and D. Lesselier, “Electromagnetic MUSIC-type imaging of perfectly conducting, arc-like cracks at single frequency,” *J. Comput. Phys.*, Vol. 228, 8093–8111, 2009.
13. Park, W.-K. and D. Lesselier, “Fast electromagnetic imaging of thin inclusions in half-space affected by random scatterers,” *Random Complex Media.*, Vol. 22, 3–23, 2012.
14. Park, W.-K. and D. Lesselier, “MUSIC-type imaging of a thin penetrable inclusion from its far-field multi-static response matrix,” *Inverse Problems*, Vol. 25, 075002, 2009.
15. Park, W.-K. and D. Lesselier, “Reconstruction of thin electromagnetic inclusions by a level set method,” *Inverse Problems*, Vol. 25, 085010, 2009.